The influence of particle size distribution on measures of states for granular materials and implications for small strain stiffness

A thesis submitted in partial fulfilment of the requirements of the Doctor of Philosophy (PhD) degree and the Diploma of Imperial College (DIC)

By

Deyun LIU

Department of Civil and Environmental Engineering

Imperial College London

London SW7 2AZ

July 2022

Abstract

Gap-graded soils are poorly graded soils, which have a deficiency of certain particle sizes, one example is a mixture of coarse and finer sand grains with no intermediate-sized particles. While current knowledge of soil behaviour has been mainly established by considering the response of well-graded soils, natural soils encountered in geotechnical engineering practice can be gap-graded. In this research, both numerical and experimental approaches are applied to study the mechanical behaviour of gap-graded soils; materials with continuous particle size distributions are also investigated using the same analytical tools to provide a benchmark against which the gap-graded materials can be considered.

Using discrete element method (DEM) simulations, the stress transmission within granular materials with a broad range of particle size distributions was investigated. The first series of analyses took a rather simplistic binary approach and considered grains to be either active or inactive grains. These analyses showed that for both continuous and gap-graded soils, the proportion by volume of inactive grains can be sufficiently large to influence widely used measures of state such as void ratio and bulk density. The nature of the stress transmission was then analysed, which shows that for materials with a continuous, linear gradation, the proportion of stress carried by a particle aligns with its particle volume; this is not the case in gap-graded soils.

Using DEM, the small-strain stiffness of gap-graded soils was considered in detail. The results show that the particle-scale distribution of stress influences the stiffness of gap-graded soils. A new semi-empirical state variable, e_α, was proposed that weights the contribution of particles to the solids volume used in calculating e by the particle stress. The strong correlation of G_0 with e_α

shows how the heterogeneity of stress influences stiffness. The difference between the stiffness obtained from the quasi-static small strain probes and the stiffness obtained from the dynamic bender element tests can qualitatively capture the proportion of inactive particles. The potential to use this observation in physical laboratory experiments was explored.

Declaration

The work presented in this thesis was carried out in the Department of Civil and Environmental Engineering at Imperial College London. This thesis is the result of my own work and any quotation from, or description of the work of others is acknowledged herein by reference to the sources, whether published or unpublished. This thesis is not the same as any that I have submitted for any degree, diploma or other qualification at any other university. No part of this thesis has been or is being concurrently submitted for any such degree, diploma or other qualification. The copyright of this thesis rests with the author. Unless otherwise indicated, its contents are licensed under a Creative Commons Attribution-Non Commercial 4.0 International Licence (CC BY-NC). Under this licence, you may copy and redistribute the material in any medium or format. You may also create and distribute modified versions of the work. This is on the condition that: you credit the author and do not use it, or any derivative works, for a commercial purpose. When reusing or sharing this work, ensure you make the licence terms clear to others by naming the licence and linking to the licence text. Where a work has been adapted, you should indicate that the work has been changed and describe those changes. Please seek permission from the copyright holder for uses of this work that are not included in this licence or permitted under UK Copyright Law.

DEYUN LIU

London, July, 30

Acknowledgements

I wish to express my sincere gratitude to my academic supervisors Prof. Catherine O'Sullivan and Dr. J Antonio H Carraro their supervision, guidance, encouragement, and invaluable suggestions in the past three years.

I am grateful to the technical support from the technical team (Steve Ackerley, Prash (Prashant) Hirani, Stef Karapanagiotidis and Graham Keefe). I especially appreciate Mr. Steven Ackerley for his patience and passion to help develop the laboratory apparatus. My sincere thanks go to the examiners of this thesis Dr Béatrice Baudet and Dr. David M. G. Taborda.

I would like to express my gratitude to Ms. Camelia Dominguez for her helpful experiences and suggestions for the triaxial tests. I am also thankful for all my PhD colleagues and academic staff in the Geotechnics section, including Mrs. Tara Sassel, Mr. Tokio Morimoto, Mr. Peter Adesina, Mrs. Marina Schnaider Bortolotto, Mrs. Sara Bandera, Dr. Adnan Sufian, Mrs. Sihua Chen, Mr. Kai Wen, Mr. Zixiao Wang and Mr. Shuai Xue for their companionship and valuable suggestions.

This study was supported by China Scholarship Council (201908060057) and an Imperial College Dixon Scholarship. This research would not have been possible without their financial support.

Last but not least, I would like to thank my family for their support and help. I also would like to thank my wife, Mengting, for her unconditional support and my little boy, Zian. You make my life in London fruitful.

Table of Contents

Abstract....2
Declaration....4
Acknowledgements....5
List of figures....11
List of tables....36
List of notations....39
Chapter 1. Introduction....50
1.1. Background....50
1.2. Research questions....53
1.3. Scope of research....57
1.4. Outline of thesis....59
Chapter 2. Literature review....61
2.1. Introduction....61
2.2. Mechanical behaviour of soil mixtures: an experimental perspective 62
2.2.1. The effect of specimen reconstitution methods on shearing behaviour....62
2.2.2. The concept of a threshold finer fraction....64
2.2.3. State variables used for soil mixtures....68
2.2.4. Shearing behaviour....71
2.2.5. Small-strain stiffness....75
2.3. Mechanical behaviour of soil mixtures: DEM perspective....87
2.3.1. Isotropic compression behaviour of gap-graded soils....87
2.3.2. Shearing behaviour....90
2.3.3. Small-strain stiffness....96
2.4. Summary....103
Chapter 3. Methodology and research methods....105

3.1. Background to DEM 105
3.2. Introduction to DEM 109
3.3. Verification of the DEM code used 113
3.2.1. Plane strain loading condition 116
3.2.2. Triaxial loading condition 118
3.4. DEM setup 120
3.4.1. Numerical simulation approach (purely periodic boundaries) 121
3.4.2. Numerical simulation approach (mixed boundaries) 122
3.5. Summary 123
Chapter 4. Influence of inactive particles on quantifying the state of granular materials 124
4.1. Introduction 124
4.2. Overview of DEM simulations 127
4.3. $PSDs$ considered 128
4.3.1. Continuous particle size distribution 129
4.3.2. Gap-graded specimens 133
4.4. Results and discussion 141
4.4.1. Linear specimens 141
4.4.2. Fractal specimens 152
4.4.3. Bimodal specimens 158
4.4.4. Trimodal specimens 189
4.5. Summary 201
Chapter 5. The effect of particle size distribution on stress transmission 204
5.1. Introduction 204
5.2. Overview of DEM approach 206
5.3. $PSDs$ considered 206
5.3.1. Quantifying shape of the particle size distribution: the

introduction of the index of grading, I_G 207
5.4. Stress analysis approaches adopted 215
5.5. Analysis of stress distribution within the specimens 217
5.5.1. Specimens with continuous gradings 217
5.5.2. Specimens with bimodal gradings 225
5.5.3. Specimens with trimodal gradings 241
5.6. Summary 245
Chapter 6. Examining the small-strain stiffness of gap-graded soils 248
6.1. Introduction 248
6.2. Overview of DEM approach 252
6.2.1. Specimens with periodic boundaries only 253
6.2.2. Specimens with mixed rigid and periodic boundaries 254
6.3. $PSDs$ considered 255
6.3.1. Cubic specimen with periodic boundaries only 255
6.3.2. Cuboidal specimen with mixed boundaries 256
6.4. Analysis approaches adopted 258
6.4.1. Stress analysis approaches 258
6.4.2. Static method to determine shear stiffness 259
6.4.3. Dynamic method to determine shear stiffness 259
6.4.4. An example analysis of simulation data to obtain G_{sta} and G_{dyn} 261
6.4.5. Distribution of contact stiffnesses 262
6.4.6. Stiffness matrix method 263
6.5. Analysis of data for cubic specimens 267
6.5.1. Void ratio and coordination number 267
6.5.2. Analysis of results for linear specimens 270
6.5.3. Analysis of results for gap-graded specimens 273
6.5.4. Heterogeneity of contributions to stiffness 279

6.5.5. Heterogeneity of stress amongst particles 292
6.5.6. A new measure of state that accounts for stress heterogeneity 300
6.5.7. Perspective 306
6.6. Analysis of data for cuboidal specimens 307
6.6.1. Void ratio and coordination number 307
6.6.2. State-dependent soil behaviour 308
6.6.3. Comparison between G_{sta} and G_{dyn} and its implication ... 310
6.7. Summary 317
Chapter 7. Experimental investigation of the small-strain stiffness of uniform and gap-graded sands 320
7.1. Introduction 320
7.2. Experimental methods 321
7.2.1. Soils tested 321
7.2.2. Equipment 325
7.2.3. Specimen preparation 338
7.2.4. Analysis of specimen uniformity 340
7.2.5. Experimental methods used to quantify stiffness 350
7.3. Results and discussion 365
7.3.1. Void ratio data 365
7.3.2. Shear wave velocity data 367
7.3.3. Shear stiffness data 369
7.3.4. Data analysis of the experimental study 372
7.4. Summary 399
Chapter 8. Conclusions 401
8.1. Summary 401
8.2. Key observations 404
8.3. Recommendations for further research 406

8.3.1. The influence of particle shape effect on gap-graded soils. 406
8.3.2. The influence of the particle shear modulus of coarse and finer particles on gap-graded soils 407
8.3.3. The influence of soil fabric on the stiffness 407
8.3.4. The link between the soil liquefaction to the current study .. 407
8.3.5. The study of the large strain shearing behaviour 408
References 420

List of figures

Figure 1.1: Schematic drawings of gap-graded soil fabric (Modified from Shire et al., 2016) 50

Figure 1.2: A typical particle size distribution for a bi-modal gap-graded soils with $SR = 14.0,\ F_{finer} = 30\%$ 51

Figure 1.3: Evolution of fabric with two distinct SR values: (a) Small SR; (b) Large SR 54

Figure 1.4: SR values reported in several prior studies 55

Figure 1.5: Research methodology 57

Figure 2.1: Soil mixtures considered in prior studies: (a) Particle size distributions considered by Murthy et al. (2007); (b) Particle size distributions considered by Thevanayagam et al. (2002)..... 62

Figure 2.2: Variation in index properties, e_{min} and e_{max} with F_{finer}: (a) Modified from Lade et al., 1998; (b) Modified from Zuo & Baudet, 2015 66

Figure 2.3: Variation in intercepts (a) The normal compression line (Carrera et al., 2011); (b) The critical state line with fines content (Zuo & Baudet, 2015) 67

Figure 2.4: The effect of the addition of finer grains on the shearing behaviour of gap-graded soils (Modified from Yang & Wei, 2012): (a) Undrained stress-strain behaviour (q is the deviator stress, ε_a is the axial strain); (b) Critical state lines 71

Figure 2.5: The introduction of equivalent void ratio, e^*, to interpret the in shearing behaviour of soil mixtures; (a) CSL data presented in terms of the global void ratio, e; (b) CSL data presented in terms of the equivalent void ratio, e^*, calculated using equation 2.7 (Rahman et al., 2008) 72

Figure 2.6: Comparisons of shear stiffness measurements from bender

element tests and resonant column tests (Yang & Gu, 2013) 78
Figure 2.7: Schematic illustration of wave paths and force chains in bender element tests (Yang & Gu 2013) 79
Figure 2.8: Comparison of shear modulus measurements from the resonant column and bender element tests (Yang & Liu, 2016) 80
Figure 2.9: Variation of the small-strain shear modulus with soil state for sands with (a) 2% kaolin clay; (b) 5% kaolin clay; (c) 10% kaolin clay; and (d) 2% non-plastic silt (Carraro et al., 2009) 81
Figure 2.10: Particle size distribution of the soil mixtures considered by Wichtmann et al. (2015) 82
Figure 2.11: Shear stiffness of the soil mixtures considered by Wichtmann et al. (2015) 83
Figure 2.12: Comparison between global void ratio and the equivalent void ratio at effective confining stress of 200 kPa: (a) The effect of F_{finer} on the variation in G_0 with e; (b) The effect of F_{finer} on the variation in G_0 with $e*$ (Goudarzy et al., 2017) 84
Figure 2.13: Variation in shear modulus with state parameter at different confining stresses: (a) p' = 100 kPa; (b) p' = 200 kPa; (c) p' = 400 kPa; (d) p' = 500 kPa (Yang & Liu, 2016) 85
Figure 2.14: $PSDs$ of specimens analysed: (a) Wider gradations; (b) Narrower gradations (modified from Shire et al., 2014) 89
Figure 2.15: Variation of stress-reduction factor α with F_{finer} (Shire et al., 2014) 90
Figure 2.16: Stress reduction factor (α) and mechanical void ratio (e_m) (modified from Artigaut et al., 2019) 91
Figure 2.17: The granular void ratio calculated using different threshold mean stress values, p^* (Sufian et al., 2021) 93
Figure 2.18: Stress distribution for gap-graded soils during shearing from

the perspective of contacts. Note that only dense cases are considered in developing the contour. This contour represents approximate delineation (hence, the dashed lines) based on linear interpolation from the available data points shown by the markers (Sufian et al., 2021). 94

Figure 2.19: Proportion of the stress transferred by different groups of contacts during shearing: (a) Mean stress in coarse-coarse contacts versus axial strain; (b) Mean stress in coarse-fine contacts versus axial strain; (c) Mean stress in fine-fine contacts versus axial strain (modified from Sufian et al., 2021)..... 95

Figure 2.20: Relationship between the friction angle and F_{finer} (Zhu et al., 2020) 96

Figure 2.21: The G_0 of various specimens at a similar initial void ratio (e = 0.577) versus the confining pressure on a double log scale (Gong et al., 2019)..... 97

Figure 2.22: The effect of F_{finer} on G_0 for soils mixtures (Otsubo et al., 2019) 98

Figure 2.23: Relationship between f_{lp} and F_{finer}: (a) $p' = 100\ kPa$; (b) $p' = 50\ kPa$ 99

Figure 2.24: Relationship between f_{lp} and V_s for combined DEM and experimental data for GN samples at $p' = 50\ kPa$ 100

Figure 2.25: Relationship between V_s and packing properties observed in DEM simulations: (a) Mechanical void ratio; (b) The equivalent void ratio (modified from Otsubo et al., 2021 and Goudarzy et al., 2017) 101

Figure 3.1: Number of DEM-related papers per year (O'Sullivan, 2019; O'Sullivan et al., 2021)..... 105

Figure 3.2: Schematic of the spatial-partition parallel technique for a $2D$ problem: The simulation domain is divided into (a) Four subdomains; (b) 16 subdomains (C denotes core) (modified after Huang, 2014) 107

Figure 3.3: Scaling tests of the modified $LAMMPS$ code on the UK's national high-performance computing (HPC) facilities: (a) Triaxial compression simulation on a face-centred-cubic sample composed of 125,000 uniform spheres, run for 100,000 timesteps on HECToR Phase 3; (b) Constant volume simulation on a polydisperse sample comprising 351,248 spheres, run for 100,000-time steps on Hartree Blue Joule (O'Sullivan, 2014) 108

Figure 3.4: Scaling tests for a specimen with a linear grading considered in the current study (C_u of 4.5) 109

Figure 3.5: Transition calculation in each time step 110

Figure 3.6: FCC packing of uniform spheres: (a) Plan view; (b) View from the $x-$direction; (c) View from the $y-$direction; (d) Contact distribution for a single grain (modified from Huang, 2014) 114

Figure 3.7: Schematic drawing of a FCC packing of 7776 spherical grains: (a) Front view; (b) $3D$ view 116

Figure 3.8: FCC validation simulation for a plane strain loading condition (μ = 0.2): (a) Principal stresses; (b) Stress ratio; (c) Coordination number; (d) Contact force network before failure; (e) Contact force network after failure of another slice 118

Figure 3.9: FCC validation simulation for a triaxial loading condition (μ = 0.2): (a) Principal stresses; (b) Stress ratio; (c) Coordination number; (d) Contact force network before failure; (e) Contact force network after failure of another slice 119

Figure 3.10: Validation simulations of triaxial loading conditions with

various μ 119
Figure 3.11: Examples of specimens created under periodic boundaries and mixed boundaries: (a) Periodic boundary; (b) Mixed boundary (periodic boundaries in x and y directions); (c) Mixed boundary (rigid boundaries in the z direction) 123

Figure 4.1: Particle size distribution for specimens with continuous gradings: (a) Linear specimens; (b) Fractal specimens 129
Figure 4.2: Specimen size effect for linear specimens (i.e. C_u 2.4): (a) Cumulative distribution of connectivities by volume; (b) Percentage of inactive grains 131
Figure 4.3: Particle size distributions for gap-graded soils: (a) Bimodal specimens; (b) Trimodal specimens 134
Figure 4.4: Specimen size effect for bimodal specimens: (a) Cumulative distribution of connectivities by volume; (b) Percentage of inactive grains (d, m and l denote dense, medium and loose specimens, respectively). 136
Figure 4.5: Influence of specimen size on particle-scale data generated for a representative trimodal gradation, Tri 10_70: (a) Cumulative distribution of connectivities by volume; (b) Percentage of inactive grains. 139
Figure 4.6: Schematic drawing of connectivity value for the darker particle: (a) connectivity value of 1; (b) connectivity value of 2; (c) connectivity value of 3; (d) connectivity value of 4 142
Figure 4.7: Cumulative distribution of connectivities for linear specimens in the dense condition: (a) distribution by number; (b) distribution by volume 143
Figure 4.8: Percentage of inactive grains versus C_u for linear specimens:

(a) D_{50} of inactive, active and all particles for dense specimens; (b) D_{50} of inactive, active and all particles for loose specimens 144
Figure 4.9: Cumulative distribution of connectivities for linear specimens in the medium density: (a) distribution by number; (b) distribution by volume 145
Figure 4.10: Cumulative distribution of connectivities for linear specimens in the loose density: (a) distribution by number; (b) distribution by volume 146
Figure 4.11: Effect of density on cumulative distribution of connectivities for linear specimens when C_u = 1.5: (a) distribution by number; (b) distribution by volume 147
Figure 4.12: Effect of density on cumulative distribution of connectivities for linear specimens when C_u = 3.6: (a) distribution by number; (b) distribution by volume 148
Figure 4.13: Effect of density on cumulative distribution of connectivities for linear specimens when C_u = 6.0: (a) distribution by number; (b) distribution by volume 149
Figure 4.14: Percentage of inactive grains versus C_u for linear specimens: (a) percentage of inactive grains by number (b) percentage of inactive grains by volume 150
Figure 4.15: Comparison of measures of packing density for linear specimens, e versus e_m 151
Figure 4.16: Comparison of measures of packing density for linear specimens: (a) $(e\text{-}e_m)/e$ versus C_u; (b) $(\rho - \rho_m)/\rho$ versus C_u 152
Figure 4.17: Cumulative distribution of connectivities for dense fractal specimens: (a) distribution by number; (b) distribution by volume . 153
Figure 4.18: (a) D_{50} of inactive, active and all particles for dense specimens; (b) D_{50} of inactive, active and all particles for loose

specimens. 154
Figure 4.19: Effect of density on cumulative distribution of connectivities for a fractal specimen: (a) distribution by number for Fractal 0.1% L; (b) distribution by volume for Fractal 0.1% L 155
Figure 4.20: Variation in the percentage of inactive grains with C_u for linear specimens: (a) percentage of inactive grains by number (b) percentage of inactive grains by volume..... 156
Figure 4.21: Comparison of measures of packing density for fractal specimens, e versus e_m 157
Figure 4.22: Comparison of measures of packing density for fractal specimens: (a) (e -e_m)/ e versus C_u; (b) (ρ-ρ_m)/ ρ versus C_u 158
Figure 4.23: Influence of $Ffiner$ on global void ratio and mechanical void ratio when SR = 3.7: (a) e versus F_{finer}; e_m versus F_{finer} 159
Figure 4.24: Cumulative distribution of connectivities for bimodal specimens with F_{finer} = 10% (SR 3.7): (a) distribution by number; (b) distribution by volume (D, M and L denote dense, medium-dense and loose specimen respectively)..... 160
Figure 4.25: Cumulative distribution of connectivities for bimodal specimens with F_{finer} = 25% (SR 3.7): (a) distribution by number; (b) distribution by volume (D, M and L denote dense, medium-dense and loose specimen respectively)..... 161
Figure 4.26: Cumulative distribution of connectivities for bimodal specimens with F_{finer} = 50% (SR 3.7): (a) distribution by number; (b) distribution by volume (D, M and L denote dense, medium-dense and loose specimen respectively)..... 162
Figure 4.27: Percentage of inactive grains versus F_{finer} for bimodal specimens with SR = 3.7: (a) percentage of inactive grains by number (b) percentage of inactive grains by volume 163

Figure 4.28: Comparison between the F_{finer} of 15% and 20%: (a) by particle number; (b) by volume 164
Figure 4.29: Comparison between the F_{finer} of 15% and 20% in contact force network in the densest condition: (a) F_{finer} = 15%; (b) F_{finer} = 20% 164
Figure 4.30: Comparison of measures of packing density for bimodal specimens (SR = 3.7), e versus e_m (numbers in legend indicates the F_{finer} from 5% to 50%. D, M and L denote dense, medium-dense and loose specimen, respectively) 165
Figure 4.31: Comparison of measures of packing density for bimodal specimens (SR = 3.7): (a) (e - e_m)/ e versus F_{finer}; (b) (ρ - ρ_m)/ ρ versus F_{finer} 166
Figure 4.32: Different state variables for bimodal gap-graded soils (SR = 3.7): (a) Dense condition; (b) Medium condition; (c) Loose condition 168
Figure 4.33: Influence of F_{finer} on e and e_m ($SR = 8.4$): (a) e versus F_{finer}; e_m versus F_{finer} 169
Figure 4.34: Cumulative distribution of connectivities for bimodal specimens with F_{finer} = 10% (SR 8.4): (a) distribution by number; (b) distribution by volume (D, M and L denote dense, medium-dense and loose specimen, respectively) 170
Figure 4.35: Cumulative distribution of connectivities for bimodal specimens with F_{finer} = 25% (SR 8.4): (a) distribution by number; (b) distribution by volume (D, M and L denote dense, medium-dense and loose specimen respectively) 171
Figure 4.36: Cumulative distribution of connectivities for bimodal specimens with F_{finer} = 50% (SR 8.4): (a) distribution by number; (b) distribution by volume (D, M and L denote dense, medium-dense

and loose specimen respectively)..... 172
Figure 4.37: Percentage of inactive grains versus F_{finer} for bimodal specimens (SR = 8.4): (a) percentage of inactive grains by number (b) percentage of inactive grains by volume..... 173
Figure 4.38: Comparison between the dense and loose condition of F_{finer} of 25% in contact force network (SR = 8.4): (a) macro scale; (b) dense; (c) loose..... 174
Figure 4.39: Comparison of measures of packing density for bimodal specimens (SR = 8.4), e versus e_m (the numbers in the legend indicate the F_{finer}. D, M and L denote dense, medium-dense and loose specimen respectively)..... 175
Figure 4.40: Comparison of measures of packing density for bimodal specimens (SR = 8.4): (a) $(e - e_m)/e$ versus F_{finer}; (b) $(\rho - \rho_m)/\rho$ versus F_{finer}..... 176
Figure 4.41: Different state variables for bimodal gap-graded soils (SR = 8.4): (a) Dense condition; (b) Medium condition; (c) Loose condition 177
Figure 4.42: Influence of F_{finer} on global void ratio and mechanical void ratio (SR = 18.1): (a) e versus F_{finer}; (b) e_m versus F_{finer} 179
Figure 4.43: Cumulative distribution of connectivities for bimodal specimens with F_{finer} = 10% (SR 18.1): (a) distribution by number; (b) distribution by volume (D, M and L denote dense, medium-dense and loose specimen respectively)..... 180
Figure 4.44: Cumulative distribution of connectivities for bimodal specimens with F_{finer} = 25% (SR 18.1): (a) distribution by number; (b) distribution by volume (D, M and L denote dense, medium-dense and loose specimen respectively)..... 181
Figure 4.45: Cumulative distribution of connectivities for bimodal

specimens with F_{finer} = 50% (SR 18.1): (a) distribution by number; (b) distribution by volume (D, M and L denote dense, medium-dense and loose specimen respectively) 182
Figure 4.46: Percentage of inactive grains versus F_{finer} for bimodal specimens (SR = 18.1): (a) percentage of inactive grains by number (b) percentage of inactive grains by volume 183
Figure 4.47: Comparison of limiting measures of packing density for bimodal specimens (SR = 18.1), e versus e_m (numbers in legend indicates the F_{finer} from 5% to 50%. D, M and L denote dense, medium-dense and loose specimen respectively) 184
Figure 4.48: Comparison of limiting measures of packing density for bimodal specimens (SR = 18.1): (a) $(e - e_m)/e$ versus F_{finer}; (b) $(\rho - \rho_m)/\rho$ versus F_{finer} 185
Figure 4.49: Different state variables for bimodal gap-graded soils (SR = 18.1): (a) Dense condition; (b) Medium condition; (c) Loose condition 187
Figure 4.50: Cumulative distribution of connectivities for typical trimodal specimens (F_{finer} = 10%): (a) by particle number; (b) by particle volume (D, M and L denote dense, medium-dense and loose specimen respectively) 189
Figure 4.51: e versus e_m for trimodal specimens for F_{finer} of 10% (D, M and L denote dense, medium-dense and loose specimen respectively) 190
Figure 4.52: Percentage of inactive grains for trimodal specimens (F_{finer} = 10%): (a) by particle number; (b) by particle volume 191
Figure 4.53: Comparison of traditional measures for trimodal specimens (F_{finer} = 10%): (a) e and e_m; (b) ρ and ρ_m 192
Figure 4.54: Cumulative distribution of connectivities for typical trimodal

specimens (F_{finer} = 20%): (a) by particle number; (b) by particle volume (D, M and L denote dense, medium-dense and loose specimen respectively) 193
Figure 4.55: e versus e_m for trimodal specimens of a F_{finer} of 20% (D, M and L denote dense, medium-dense and loose specimen respectively) 194
Figure 4.56: Percentage of inactive grains for trimodal specimens (F_{finer} = 20%): (a) by particle number; (b) by particle volume 195
Figure 4.57: Comparison of traditional measures for trimodal specimens (F_{finer} = 20%): (a) e and e_m; (b) ρ and ρ_m 196
Figure 4.58: Cumulative distribution of connectivities for typical trimodal specimens (F_{finer} = 25%): (a) by particle number; (b) by particle volume (D, M and L denote dense, medium-dense and loose specimen respectively) 197
Figure 4.59: Cumulative distribution of connectivities for typical trimodal specimens (F_{finer} = 30%): (a) by particle number; (b) by particle volume (D, M and L denote dense, medium-dense and loose specimen respectively) 198
Figure 4.60: e versus e_m for trimodal specimens for a F_{finer} of 25% and 30% (D, M and L denote dense, medium-dense and loose specimen respectively) 199
Figure 4.61: Percentage of inactive grains for trimodal specimens (F_{finer}= 25%; 30%): (a) by particle number; (b) by particle volume 200
Figure 4.62: Comparison of traditional measures for trimodal specimens (F_{finer} = 25, 30%): (a) e and e_m; (b) ρ and ρ_m 201

Figure 5.1: Particle size distributions of bimodal gap-graded soils in Chapter 5 207

Figure 5.2: Variation in the I_G values for the linear specimens with C_u 209
Figure 5.3: Variation in the I_G values for the fractal specimens with C_u 210
Figure 5.4: Variation in the I_G values with increasing F_{finer} for the bimodal specimens with different size ratios (SR) 211
Figure 5.5: Variation in the I_G values for the trimodal specimens: (a) F_{finer} of 10%; (b) F_{finer} of 20%; (b) F_{finer} of 25% and 30% 214
Figure 5.6: Typical results for linear specimens in the densest condition: (a) PSD plots considering all particles; (b) PSD plots considering active particles; (c) PSD^{stress} plots; (d) CSD^{stress} plots, "D" denotes the densest case 219
Figure 5.7: Typical results for linear specimens in the medium-dense condition: (a) PSD plots considering all particles; (b) PSD plots considering active particles; (c) PSD^{stress} plots; (d) CSD^{stress} plots, "M" denotes the medium-dense case 220
Figure 5.8: Typical results for linear specimens in the loosest condition: (a) PSD plots considering all particles; (b) PSD plots considering active particles; (c) PSD^{stress} plots; (d) CSD^{stress} plots, "L" denotes the loosest case.....220
Figure 5.9: The effect of density on stress distribution for two linear gradations (i.e. C_u 1.5, 6.0): (a) PSD plots considering all particles; (b) PSD plots considering active particles; (c) PSD^{stress} plots; (d) CSD^{stress} plots, "D" denotes the densest case, "M" denotes the medium-dense case, "L" denotes the loosest case. 222
Figure 5.10: Comparison of I_G, I_G^{active} and I_G^{stress} data for linear gradations, "D" denotes the densest case, "L" denotes the loosest case 223

Figure 5.11: Typical results for fractal specimens: (a) PSD plots considering all particles; (b) PSD plots considering active particles; (c) PSD^{stress} plots; (d) CSD^{stress} plots , "D" denotes the densest case, "M" denotes the medium case, "L" denotes the loosest case. 224

Figure 5.12: Comparison of I_G, I_G^{active} and I_G^{stress} data for fractal gradations, "D" denotes the densest case, "L" denotes the loosest case 225

Figure 5.13: Representative results for the bimodal specimens with SR = 14.5 in the densest condition: (a) PSD plots considering all particles; (b) PSD plots considering active particles; (c) PSD^{stress} plots; (d) CSD^{stress} plots , "D" denotes the densest case 226

Figure 5.14: Representative results for the bimodal specimens, the effect of density: (a) PSD plots considering all particles; (b) PSD plots considering active particles; (c) PSD^{stress} plots; (d) CSD^{stress} plots , "D" denotes the densest case, "M" denotes the medium-dense case, "L" denotes the loosest case.....227

Figure 5.15: Representative results for the bimodal specimens in the densest condition, the effect of SR: (a) PSD plots, SR = 3.7; (b) PSD^{stress} plots, SR = 3.7; (c) PSD plots, SR = 8.4; (d) PSD^{stress} plots, SR = 8.4; (e) PSD plots, SR = 14.5; (f) PSD^{stress} plots, SR = 14.5 228

Figure 5.16: Stress contribution of finer and coarser particles, the effect of SR: (a) SR = 3.7; (b) SR = 8.4; (c) SR = 14.5; (d) SR = 18.1 229

Figure 5.17: Data for bimodal specimens with $SR = 14.5$ and F_{finer} = 10%: (a) CSD^{stress}; (b) Pie charts illustrating the numeric proportion of different contacts in the samples and the stress distribution amongst the different contacts 231

Figure 5.18: Data for bimodal specimens with $SR = 14.5$ and F_{finer} =

30%: (a) CSD^{stress}; (b) Pie charts illustrating the numeric proportion of different contacts in the samples and the stress distribution amongst the different contacts 232
Figure 5.19: Data for bimodal specimens with $SR = 14.5$ and F_{finer} = 50%: (a) CSD^{stress}; (b) Pie charts illustrating the numeric proportion of different contacts in the samples and the stress distribution amongst the different contacts 233
Figure 5.20: Variation in the proportion of stress transmitted by each of the three sets of contact with increasing F_{finer} when $SR = 3.7$: (a) Dense specimens; (b) Medium-dense specimens; (c) Loose specimens; (d) Example pie chart with equivalent data for F_{finer} of 30% 233
Figure 5.21: Variation in the proportion of stress transmitted by each of the three sets of contact with increasing F_{finer} when $SR = 8.4$: (a) Dense specimens; (b) Medium-dense specimens; (c) Loose specimens; (d) Example pie chart with equivalent data for F_{finer} of 30% 235
Figure 5.22: Variation in the proportion of stress transmitted by each of the three sets of contact with increasing F_{finer} when $SR = 14.5$: (a) Dense specimens; (b) Medium-dense specimens; (c) Loose specimens; (d) Example pie chart with equivalent data for F_{finer} of 30% 236
Figure 5.23: Variation in the proportion of stress transmitted by each of the three sets of contact with increasing F_{finer} in the dense condition with four distinct SRs: (a) SR = 3.7; (b) SR = 8.4; (c) SR = 14.5; (d) SR = 18.1 237
Figure 5.24: The averages values of these three normalized lengths for the three sets of contact in the densest condition: (a) SR = 3.7; (b) SR =

8.4; (c) SR = 14.5; (d) SR = 18.1 239

Figure 5.25: Comparison of IG, I_G^{active} and I_G^{stress} data for bimodal gradations: (a) SR = 3.7; (b) SR = 8.4; (c) SR = 14.5; (d) SR = 18.1, "D" denotes the densest case, "L" denotes the loosest case.....241

Figure 5.26: Representative results for trimodal specimens, the effect of density: (a) PSD plots considering all particles; (b) PSD plots considering active particles; (c) PSD^{stress} plots; (d) CSD^{stress} plots , "D" denotes the densest case, "L" denotes the loosest case. 242

Figure 5.27: Representative pie chart results for trimodal specimens, the effect of density: (a) PSD plots considering all particles; (b) PSD plots considering active particles; (c) PSD^{stress} plots; (d) CSD^{stress} plots , "d" denotes the densest case, "l" denotes the loosest case. 243

Figure 5.28: Comparison between the dense and loose conditions for Tri 25_45 in two-dimensional projections of contact force network: (a) Dense; (c) Loose 244

Figure 5.29: Comparison of I_G , I_G^{active} and I_G^{stress} data for trimodal specimens: (a) F_{finer} = 10%; (b) F_{finer} = 20%; (c) F_{finer} = 25%, 30%, "D" denotes the densest case, "L" denotes the loosest case. 245

Figure 6.1: Particle size distributions (periodic boundaries): (a) Linear specimens; (b) Bimodal gap-graded specimens; (c) Trimodal gap-graded specimens 256

Figure 6.2: Particle size distributions (mixed boundaries): (a) Linear specimens; (b) Bimodal gap-graded specimens.....257

Figure 6.3: The quantification of G_{sta} and G_{dyn} in DEM: (a) $q - \varepsilon_a$

relationship; (b) $G_{sta} - \varepsilon_q$ relationship; (c) V_s in time domain; (d) V_s in frequency domain 262
Figure 6.4: Variation of void ratio and coordination number for linear specimens: (a) e, e_m versus C_u; (b) Z, Z_m versus C_u 268
Figure 6.5: Variation in void ratio and coordination number with F_{finer} for bimodal specimens: (a) e and e_m data for SR = 3.7; (b) e and e_m data for SR = 8.4; (c) e and e_m data for SR = 18.1; (d) Z and Z_m data for SR = 3.7; (e) Z and Z_m data for SR = 8.4; (f) Z and Z_m data for SR = 18.1 270
Figure 6.6: Exploration of correlations between G_0 and various state variables for linear specimens (σ_3' = 500 kPa): (a) G_0 versus e; (b) G_0 versus e_m; (c) G_0 versus $Z/(1+e)$; (d) G_0 versus $Z_m/(1+e_m)$ 271
Figure 6.7: Performance of state variables for linear specimens in Hardin's equation: (a) The use of e; (b) The use of e_m; (c) The use of $Z_m/(1+e_m)$.....272
Figure 6.8: Variation in G_0 with e for bimodal specimens with various SR values (p' = 500 kPa): (a) G_0 versus e (SR = 3.7); (b) G_0 versus e (SR = 8.4); (c) G_0 versus e (SR = 14.5); (d) G_0 versus e (SR = 18.1) 274
Figure 6.9: Variation in G_0 with e for bimodal specimens with SR = 8.4 and various p' values: (a) G_0 versus e (p' = 100 kPa); (b) G_0 versus e (p' = 500 kPa); (c) G_0 versus e (p' = 1000 kPa).....275
Figure 6.10: Performance of state variables for bimodal specimens (SR = 8.4; p' = 500 kPa): (a) G_0 versus e; (b) G_0 versus em; (c) G_0 versus $Z/(1+e)$; (d) G_0 versus $Z_m/(1+e_m)$ 276
Figure 6.11: Performance of state variables for bimodal specimens in Hardin's equation (SR = 8.4): (a) The use of e; (b) The use of

$Z_m/(1+e_m)$ 277
Figure 6.12: Performance of state variables for trimodal specimens (p'= 500 kPa): (a) G_0 versus e; (b) G_0 versus $Z_m/(1+e_m)$ 278
Figure 6.13: Correlation between G_0 and state variables for linear, bimodal and trimodal specimens in Hardin's equation: (a) The use of e as the state variable; (b) The use of $Z_m/(1+e_m)$ as the state variable 279
Figure 6.14: Normal stiffness versus normal force for linear specimens in the dense condition 280
Figure 6.15: Normal stiffness characteristics for linear specimens: (a) Cumulative distribution of normal stiffness; (b) Cumulative distribution of normalised stiffness by average stiffness. "D" denotes the densest case, "L" denotes the loosest case 281
Figure 6.16: Normal stiffness versus normal force: (a) F_{finer} = 10%, SR = 3.7; (b) F_{finer} = 25%, SR = 3.7; (c) F_{finer} = 50%, SR = 3.7; (d) F_{finer} = 10%, SR = 8.4; (e) F_{finer} = 25%, SR = 8.4; (f) F_{finer} = 50%, SR = 8.4 282
Figure 6.17: Variation in normal contact stiffness values for bimodal specimens: (a) Cumulative distribution of normal stiffness values for specimens in the dense condition; (b) Cumulative distribution of normal stiffness values for specimens in the loose condition 284
Figure 6.18: Comparison of G_0 values obtained in small strain probes and using the stiffness matrix method for dense linear specimens (p' = 500 kPa): (a) G_0 values versus C_u; (b) $G_0/G_0^{C_u=1.2}$ values versus C_u; (c) $G_0^{500\,kPa}/G_0^{100\,kPa}$ values versus C_u 285
Figure 6.19: Comparison of G_0 values obtained in small strain probes and using the stiffness matrix method for medium linear specimens (p' = 500 kPa): (a) G_0 values versus C_u; (b) $G_0/G_0^{C_u=1.2}$ values versus C_u;

(c) $G_0^{500\,kPa}/G_0^{100\,kPa}$ values versus C_u 285

Figure 6.20: Comparison of G_0 values obtained in small strain probes and using the stiffness matrix method for loose linear specimens (p' = 500 kPa): (a) G_0 values versus C_u; (b) $G_0/G_0^{c_u=1.2}$ values versus C_u; (c) $G_0^{500\,kPa}/G_0^{100\,kPa}$ values versus C_u 286

Figure 6.21: Variation in G_0 values obtained using the probe and stiffness matrix methods with F_{finer} for bimodal specimens with p'= 500 kPa: (a) SR = 3.7; (b) SR = 8.4; (c) SR = 14.5 287

Figure 6.22: Comparison of G_0 values obtained using probes and using the stiffness matrix methods for bimodal gap-graded soils in the dense condition: (a) $G_0^{500\,kPa}/G_0^{100\,kPa}$ versus F_{finer}; (b) $G_0^{F_{finer}}/G_0^{F_{finer}=5\%}$ versus F_{finer} 288

Figure 6.23: Comparison of G_0 values obtained using probes and using the stiffness matrix methods for bimodal gap-graded soils in the medium condition: (a) $G_0^{500\,kPa}/G_0^{100\,kPa}$ versus F_{finer}; (b) $G_0^{F_{finer}}/G_0^{F_{finer}=5\%}$ versus F_{finer} 290

Figure 6.24: Comparison of G_0 values obtained using probes and using the stiffness matrix methods for bimodal gap-graded soils in the loose condition: (a) $G_0^{500\,kPa}/G_0^{100\,kPa}$ versus F_{finer}; (b) $G_0^{F_{finer}}/G_0^{F_{finer}=5\%}$ versus F_{finer} 291

Figure 6.25: Key cumulative distribution data for linear specimens in the densest condition: (a) PSD plots; (b) PSD^{stress} plots; (c) CSD^{stress} plots; (d) $CSD^{stiffness}$ plots 293

Figure 6.26: Key cumulative distribution data for linear specimens in the medium-dense condition: (a) PSD plots; (b) PSD^{stress} plots; (c) CSD^{stress} plots; (d) $CSD^{stiffness}$ plots 293

Figure 6.27: Key cumulative distribution data for linear specimens in the

loosest condition: (a) PSD plots; (b) PSD^{stress} plots; (c) CSD^{stress} plots; (d) $CSD^{stiffness}$ plots.....294
Figure 6.28: Typical results for bimodal specimens in the densest condition: (a) PSD plots considering all particles (SR = 3.7); (b) PSD^{stress} plots (SR = 3.7); (c) CSD^{stress} plots (SR = 3.7); (d) $CSD^{stiffness}$ plots (SR = 3.7); (e) PSD plots considering all particles (SR = 8.4);(f) PSD^{stress} plots (SR = 8.4);(g) CSD^{stress} plots (SR = 8.4); (h) $CSD^{stiffness}$ plots (SR = 8.4).....296
Figure 6.29: Variation in contribution of different contact types to overall stiffness for typical bimodal specimens when p' = 500 kPa: (a) SR = 3.7 in the dense condition; (b) SR = 3.7 in the loose condition; (c) SR = 8.4 in the dense condition; (d) SR = 8.4 in the loose condition..297
Figure 6.30: Typical results for bimodal specimens in the medium condition: (a) PSD plots considering all particles (SR = 3.7); (b) PSD^{stress} plots (SR = 3.7); (c) CSD^{stress} plots (SR = 3.7); (d) $CSD^{stiffness}$ plots (SR = 3.7); (e) PSD plots considering all particles (SR = 8.4);(f) PSD^{stress} plots (SR = 8.4);(g) CSD^{stress} plots (SR = 8.4); (h) $CSD^{stiffness}$ plots (SR = 8.4).....298
Figure 6.31: Typical results for bimodal specimens in the loosest condition: (a) PSD plots considering all particles (SR = 3.7); (b) PSD^{stress} plots (SR = 3.7); (c) CSD^{stress} plots (SR = 3.7); (d) $CSD^{stiffness}$ plots (SR = 3.7); (e) PSD plots considering all particles (SR = 8.4);(f) PSD^{stress} plots (SR = 8.4);(g) CSD^{stress} plots (SR = 8.4); (h) $CSD^{stiffness}$ plots (SR = 8.4).....299
Figure 6.32: Particle scale stress distribution: (a) Stress reduction factors with increasing F_{finer} (SR = 3.7); (b) Stress reduction factors with increasing F_{finer} (SR = 8.4).....302
Figure 6.33: Performance of e_α for bimodal specimens (SR = 8.4; p'= 500

kPa) 303
Figure 6.34: Optimal surface as described using Hardin's equation with e_α as the measure of state (SR = 8.4) 303
Figure 6.35: Performance of state variables as assessed by fitting the surface defined by Hardin's equation to all the bimodal specimen data: (a) Use of e as the measure of state; (b) Use of e_α as the measure of state. 304
Figure 6.36: Performance of e_α for all bimodal and trimodal specimens: (a) $Z_m/(1+e_m)$ versus e_α (b) The use of e_α 306
Figure 6.37: The variation of e (p' = 500 kPa): (a) e versus C_u; (b) e versus F_{finer} (SR = 8.0) 308
Figure 6.38: Assessment of the performance of various state variables (p' = 500 kPa): for linear specimens (a) G_{sta} versus e; (b) $G_{dyn}(e)$ versus e; (c) $G_{dyn}(e_m)$ versus e_m; for bimodal gap-graded specimens (SR = 8); (d) G_{sta} versus e; (e) $G_{dyn}(e)$ versus e; (f) $G_{dyn}(e_m)$ versus e_m 310
Figure 6.39: Comparison between G_{dyn} and G_{sta} values: for linear specimens (a) $G_{dyn}(e)$ versus G_{sta}; (b) $G_{dyn}(e_m)$ versus G_{sta}; for bimodal gap-graded specimens (SR = 8) (c) $G_{dyn}(e)$ versus G_{sta}; (d) $G_{dyn}(e_m)$ versus G_{sta} 311
Figure 6.40: The variation of $G_{sta}/G_{dyn}(e)$ (left vertical axis) and e/e_m & ρ_m/ρ (right vertical axis) with increasing C_u: (a) Dense condition; (b) Medium-dense condition 312
Figure 6.41: The relationship between $G_{sta}/G_{dyn}(e)$ and e/e_m & ρ_m/ρ for linear specimens: (a) $G_{sta}/G_{dyn}(e)$ versus e/e_m; (b) $G_{sta}/G_{dyn}(e)$ versus ρ_m/ρ 313
Figure 6.42: Variation in $G_{sta}/G_{dyn}(e)$ with F_{finer} ($SR = 8$; $500\ kPa$): (a) Dense samples, with right axes giving e/e_m and ρ_m/ρ; (b) Medium-

dense samples, with right axis giving e/e_m and ρ_m/ρ; (c) Dense samples, with right axes giving e/e_α and ρ_α/ρ; (d) Medium-dense samples, with right axis giving e/e_α and ρ_α/ρ 314

Figure 6.43: The trend of $G_{sta}/G_{dyn}(e)$ with increasing F_{finer} ($SR = 14$; dense): (a) p' of 500 kPa, with right axes giving e/e_m and ρ_m/ρ; (b) p' of 1000 kPa, with right axes giving e/e_m and ρ_m/ρ; (c) p' of 500 kPa, with right axes giving e/e_α and ρ_α/ρ; (d) p' of 1000 kPa, with right axes giving e/e_α and ρ_α/ρ 315

Figure 6.44: The relationship between $G_{sta}/G_{dyn}(e)$ and relative difference in state variables: (a) Ratio of e/e_m; (b) Ratio of ρ_m/ρ; (c) Ratio of e/e_α; (d) Ratio of ρ_α/ρ 316

Figure 7.1: Images of sands used in experiments: (a) Finer sand; (b) Coarse sand 322

Figure 7.2: Particle characterization for the experimental specimens: (a) Particle size distributions; (b) Particle shape parameters 323

Figure 7.3: Schematic illustration of particle characterisation technique: (a) Aspect ratio; (b) Convexity; (c) Sphericity (modified from Yang & Luo, 2015) 324

Figure 7.4: Triaxial apparatus indicating internal and external instrumentation 326

Figure 7.5: Schematic diagram of the bender element set-up (Alvarado & coop, 2012)..... 327

Figure 7.6: An example of a bender element test in this study 328

Figure 7.7: Budenberg dead weight calibrator (Images from Budenberg Gauge Co Ltd; www.budenberg.co.uk) 329

Figure 7.8: Best-fit calibration regression line for the cell pressure transducer..... 330

Figure 7.9: Best-fit calibration regression line for the load cell.....331
Figure 7.10: Best-fit calibration regression line for the vertical $LVDT$ 1 333
Figure 7.11: Error quantification for the vertical $LVDT$ 1.....334
Figure 7.12: Best-fit calibration regression line for the radial $LVDT$ 1...335
Figure 7.13: Best-fit calibration regression line for the volume gauge ..336
Figure 7.14: Simple sketch of specimen preparation for loose specimens 338
Figure 7.15: Specimen preparation of dense cases: (a) Side view; (b) Front view 339
Figure 7.16: Simple sketch of specimen preparation for the desired dense state: (a) First step; (b) Second step; (c) Third step; (d) Fourth step 340
Figure 7.17: Separate moulds used to check specimen uniformity for the loose state (Dominguez-Quintans et al., 2019).....342
Figure 7.18: The saw used to cut the solidified specimen.....342
Figure 7.19: An example of the solidified soil mixture layer ($F_{finer} = 50\%$) 343
Figure 7.20: The washing out of a solidified soil slice layer 344
Figure 7.21: Specimen uniformity quantification for the dense state: (a) Density gradient mould used to check specimen uniformity for the dense state; (b) Vibration machine used for densifying the specimen (Dominguez-Quintans et al., 2019).....344
Figure 7.22: Adding of de-aired water into the specimen: (a) The vacuum machine used to generate de-aired water; (b) The procedure of adding de-air water.....351
Figure 7.23: Quantifying the specimen dimensions: (a) Measurement of diameter at three locations; (b) The vernier calliper.....352
Figure 7.24: The relative error identified for a vertical transducer.....353

Figure 7.25: The instalment of transducers for a specimen 353
Figure 7.26: An example of an originally recorded dataset 354
Figure 7.27: The increase in both cell and back pressures before the consolidation stage 356
Figure 7.28: Key data recorded during the consolidation stage: (a) Change of back pressure; (b) Change of cell pressure; (c) Change of one of these vertical transducers; (d) Change of one of these radial transducers 358
Figure 7.29: An example of data analysis for the bender element test: (a) V_s in time domain; (b) V_s in frequency domain (F_{finer} 35%-1, relatively dense).....360
Figure 7.30: The quantification of stiffness values from the static method in experiments (relatively dense F_{finer} 35%-1): (a) $q - \varepsilon_a$ relationship; (b) $\varepsilon_a - time$ relationship 363
Figure 7.31: The relationship between ε_q and G_0 364
Figure 7.32: An example of divergent $LVDT$ responses that were sometimes observed (F_{finer} 50%-1, relatively dense).....365
Figure 7.33: Variation in post-consolidation e with F_{finer} : (a) post-consolidation e versus F_{finer} (p' = 100 kPa); (b) post-consolidation e versus F_{finer} (p' = 400 kPa) 367
Figure 7.34: Quantification of the shear wave velocities with increasing F_{finer}: (a) V_s versus F_{finer} (p' = 100 kPa); (b) V_s versus F_{finer} (p' = 400 kPa) 368
Figure 7.35: Relationship between V_s and e for four p' values: (a) $p' = 100\ kPa$; (b) $p' = 200\ kPa$; (c) $p' = 300\ kPa$; (d) $p' = 400\ kPa$....369
Figure 7.36: Relationship between G_{dyn} and e with four increasing p': (a) p' = 100 kPa; (b) p' = 200 kPa; (c) p' = 300 kPa; (d) p' = 400 kPa ; (e) The G_{dyn} versus e when p' = 200 kPa ; (f) Cyclic

resistance ratio $(CRR)_{7.5}$ versus e (modified from Carraro et al., 2003) 371
Figure 7.37: Relationship between G_{sta} and e with four increasing p': (a) p' = 100 kPa; (b) p' = 200 kPa; (c) p' = 300 kPa; (d) p' = 400 kPa 372
Figure 7.38: The relationship between stiffness values and e for specimens comprising only coarse particles: (a) G_{dyn} versus e; (b) G_{sta} versus e 375
Figure 7.39: The comparison between G_{dyn} and G_{sta} for the specimens comprising only coarse particles.....376
Figure 7.40: Best fit surface obtained by fitting Hardin's equation to the stiffness data for the specimens comprising only coarse particles and assuming c = 2.17 and n = 0.4: (a) G_{dyn} values; (b) G_{sta} values 377
Figure 7.41: The relationship between stiffness values and e for the specimens with F_{finer} = 10%: (a) G_{dyn} versus e; (b) G_{sta} versus e 379
Figure 7.42: The comparison between G_{dyn} and G_{sta} for the specimens with F_{finer} = 10%.....380
Figure 7.43: Best fit surface obtained by fitting Hardin's equation to the stiffness data for the specimens with F_{finer} = 10% and assuming c = 2.17 and n = 0.4: (a) G_{dyn} values; (b) G_{sta} values.....381
Figure 7.44: The relationship between stiffness values and e for the specimens with F_{finer} = 25%: (a) G_{dyn} versus e; (b) G_{sta} versus e 383
Figure 7.45: The comparison between G_{dyn} and G_{sta} for the specimens with F_{finer} = 25%.....384
Figure 7.46: Best fit surface obtained by fitting Hardin's equation to the

stiffness data for the specimens with F_{finer} = 25% and assuming c = 2.17 and n = 0.4: (a) G_{dyn} values; (b) G_{sta} values.....385
Figure 7.47: The relationship between stiffness values and e for the specimens with F_{finer} = 50%: (a) G_{dyn} versus e; (b) G_{sta} versus e 388
Figure 7.48: The comparison between G_{dyn} and G_{sta} for the specimens with F_{finer} = 50%.....388
Figure 7.49: Best fit surface obtained by fitting Hardin's equation to the stiffness data for the specimens with F_{finer} = 50% and assuming c = 2.17 and n = 0.4: (a) G_{dyn} values; (b) G_{sta} values.....389
Figure 7.50: The relationship between stiffness values and e for specimens comprising only finer particles: (a) G_{dyn} versus e; (b) G_{sta} versus e 391
Figure 7.51: The comparison between G_{dyn} and G_{sta} for the specimens comprising only finer particles 392
Figure 7.52: Best fit surface obtained by fitting Hardin's equation to the stiffness data for the specimens comprising only finer particles and assuming c = 2.17 and n = 0.4: (a) G_{dyn} values; (b) G_{sta} values 393
Figure 7.53: Variation in best-fit A value with F_{finer}: (a) $G_{dyn}(e)$ with increasing F_{finer} in DEM; (b) G_{sta} with increasing F_{finer} in DEM; (c) $G_{dyn}(e)$ with increasing F_{finer} in experiments; (d) G_{sta} with increasing F_{finer} in experiments.....396
Figure 7.54: The comparison between $G_{dyn}(e)$ and G_{sta} for experimental results.....397
Figure 7.55: The ratio of G_{sta}/G_{dyn} with increasing F_{finer}: (a) Relatively dense condition; (b) Relatively loose condition.....398

List of tables

Table 2.1: The summary of several prior experimental studies for shearing behaviour 73

Table 2.2: Summary of prior research that has considered the stiffness of gap-graded materials with a non-plastic finer fraction 86

Table 4.1: Key data for linear specimens 131

Table 4.2: Key data for fractal specimens 133

Table 4.3: Key data for bimodal gap-graded specimens with SR = 3.7 136

Table 4.4: Key data for bimodal gap-graded specimens with SR = 8.4 137

Table 4.5: Key data for bimodal gap-graded specimens with SR = 13.0 137

Table 4.6: Key data for bimodal gap-graded specimens with SR = 18.1 138

Table 4.7: Key data for bimodal gap-graded specimens with F_{finer} = 10% 140

Table 4.8: Key data for bimodal gap-graded specimens with F_{finer} = 20% 140

Table 4.9: Key data for bimodal gap-graded specimens with F_{finer} = 25%, 30% 141

Table 5.1: Measures of PSD shape for the linear specimens..... 209

Table 5.2: Measures of PSD shape for the fractal specimens..... 210

Table 5.3: Measures of PSD shape for the bimodal specimens with SR = 3.7 212

Table 5.4: Measures of PSD shape for the bimodal specimens with SR = 8.4 212

Table 5.5: Measures of PSD shape for the bimodal specimens with SR =

14.5 213
Table 5.6: Measures of PSD shape for the bimodal specimens with SR = 18.1 213
Table 5.7: Measures of PSD shape for the trimodal specimens ($F_{finer} = 10\%$) 214
Table 5.8: Measures of PSD shape for the trimodal specimens ($F_{finer} = 20\%$) 215
Table 5.9: Measures of PSD shape for the trimodal specimens ($F_{finer} = 25\%,\ 30\%$) 215

Table 6.1: The fitting results within the Hardin's equation 307

Table 7.1: Key size and shape measures for each sample presented as a function of F_{finer} 325
Table 7.2: Summary of calibration results used in triaxial tests 337
Table 7.3: Quantifying uniformity of dense specimen with F_{finer} = 10%. 346
Table 7.4: Quantifying uniformity of loose specimen with F_{finer} = 10%. 346
Table 7.5: Quantifying uniformity of dense specimen with F_{finer} = 25%. 347
Table 7.6: Quantifying uniformity of loose specimen with F_{finer} = 25%. 348
Table 7.7: Quantifying uniformity of dense specimen with F_{finer} = 50%. 348
Table 7.8: Uniformity quantification of 50% loose specimen 349
Table 7.9: B-values and initial e for the specimens 355
Table 7.10: Results for specimens comprising only coarse particles 374

Table 7.11: Results for specimens with $F_{finer}r$ = 10% 378
Table 7.12: Results for specimens with F_{finer} = 25% 382
Table 7.13: Results for specimens with F_{finer} = 50% 387
Table 7.14: Results for specimens comprising only finer particles, i.e. F_{finer} = 100% 390
Table 7.15: Results for specimens with F_{finer} = 30% 394
Table 7.16: Results for specimens with F_{finer} = 35% 395

List of notations

Symbol	Meaning
a_F	Ratio of the other two principal strain-increments in Thornton (1979) expressions
A	Fitting parameter for the Hardin's empirical equation
AP	Air pluviation method
A_c	Circular contact area
b	Variable that quantifies the relative contribution of the finer grains to the overall stress transmitted
b_F	Ratio of the other two principal strain-increments in Thornton (1979) expressions
c	Fitting parameter for the void ratio function
c_u	Uniformity coefficient
C_z	Coefficient of curvature
CSL	Critical state line
C	Coarse-dominated behaviour
C_{ij}	Elasticity tensor
C_{ij}^{all}	Overall stiffness for all contacts
C_{ij}^{CC}	Overall stiffness for coarse-coarse contacts
C_{ij}^{CF}	Overall stiffness for coarse-finer contacts
C_{ij}^{FF}	Overall stiffness for finer-finer contacts
COV	Coefficient of variation
CRR	Cyclic resistance ratio
CSD^{stress}	Cumulative distribution of the contribution of each contact to the overall stress

$CSD^{stiffness}$	Cumulative distribution of the contribution of each contact to the overall stiffness
d_{10}	10% of the finer particles are smaller than d_{10}
d_{50}	Median diameter of finer fraction
d_{60}	60% of the finer particles are smaller than d_{60}
d_i	Particle size of particle i
d_{min}^{p}	Minimum particle diameters
d_{int}^{p}	Intermediate grain diameter
d_{max}^{p}	Maximum particle diameters
d^{p}	Particle diameter
d_i^{p}	Specific measured diameter
D^*	Fractal dimension
D_{10}	10% of the coarser particles are smaller than D_{10}
D_{50}	Median diameter of the coarser particles
D_r	Relative density
DD	Dry deposition method
$D_{c,10}$	10% of the coarser fraction particles are smaller than D_{10}
$D_{c,50}$	median diameter of the coarse fraction
$d_{f,50}$	median diameter of the finer fraction
DEM	Discrete element method
D^{Fmin}	The minimum Feret diameter
D^{Fmax}	The maximum Feret diameter
e	Global void ratio
e^*	Equivalent void ratio
$e_{\max\,(coarser)}$	Maximum global void ratio of the coarser fraction
$e_{\max\,(finer)}$	Maximum global void ratio of the finer fraction
$e_{\min\,(\mathrm{coarser})}$	Minimum global void ratio of the coarser fraction

$e_{\min\,(\text{finer})}$	Minimum global void ratio of the finer fraction
$e_{\min}$	Minimum void ratio
$e_{\max}$	Maximum void ratio
e_{Low}	Lowest void ratios
e_{High}	Highest void ratios
e_G	Granular void ratio
e_f	Interfines void ratio
e_g	Intergranular void ratio
e_m	Mechanical void ratio
e_{sk}	Skeleton void ratio
e_α	Void ratio measure where particle contributions are weighted by particle stress
E_0	Small strain Young's modulus of the specimen
E_p^*	The relative Young's modulus
E_{p1}	Young's modulus values for contacting particle 1
E_{p2}	Young's modulus values for contacting particle 2
f_x^c	$x-$component of contact force for contact c
f_y^c	$y-$component of contact force for contact c
f_z^c	$z-$component of contact force for contact c
$\boldsymbol{f}_i^c$	Force vector for contact c
f_{lp}	The low-pass frequency
f	Frequency
FCC	Face-centred cubic
FC	Fines content
$F(e)$	Void ratio function in Hardin's equation
$F_{coarser}$	Percentage by mass of coarser grains in the specimen
F_{finer}	Percentage by mass of finer grains in the

	specimen
F_{int}	Percentage by mass of intermediate-sized grains in the specimen
F	Fines-dominated behaviour
F_p	Force applied on an individual grain
F_t	Tangential contact force
F_n	Normal force
F_{Pa}	Ratio used for calculating peak stress ratio proposed in Parkin (1965)
$\boldsymbol{F}_j^c$	Force (vector) applied at contact c
g	Gravitational acceleration
G_p	Shear modulus of a single grain
G_0	Small-strain stiffness
G_{max}	Maximum shear stiffness
G_{sta}	Stiffness determined from the static method
G_{dyn}	Stiffness determined from the dynamic method
$G_{dyn}(e)$	Stiffness determined from the dynamic method using e
$G_{dyn}(e_m)$	Stiffness determined from the dynamic method using e_m
$G_{dyn}(e_\alpha)$	Stiffness determined from the dynamic method using e_α
G_{zx}	Stiffness measured using a shear wave that propagates in the $z-$direction and oscillates in the $x-$direction
G_{xz}	Stiffness measured using a shear wave that propagates in the $x-$direction and oscillates in the $z-$direction

G_s	Specific gravities
G_c	Specific gravities of coarser grains
G_f	Specific gravities of finer grains
G_p^*	The equivalent shear stiffness for contacting particles
G_{p1}	Shear modulus of the contacting particle 1
G_{p2}	Shear modulus of the contacting particle 2
$G_{0,HM}^{EMT}$	Shear modulus obtained from an effective medium theory
HPC	High-performance computing
I	The moment of inertia of an individual grain
I_G	Index of grading
I_G^{active}	Index of grading based on the PSD of the active particles
I_G^{stress}	Index of grading based on the PSD of the stress distribution
k	Parameter used in the calculation of the equivalent void ratio
k^{ab}	Local stiffness matrix
K_N	Contact stiffness in the normal direction
K_T	Tangential contact stiffness
$\boldsymbol{l}_j^c$	Branch vector
l^c	Branch vector length
l_M^{pc}	Maximum branch vector length
L	Distance between the bottom and top bender
$L_x^{cluster}$	Length of the largest cluster of contacting particles in $x-$direction
$L_y^{cluster}$	Length of the largest cluster of contacting particles

	in y −direction
$L_z^{cluster}$	Length of the largest cluster of contacting particles in z −direction
L_x^{pcell}	Size of the periodic cell in x −direction
L_y^{pcell}	Size of the periodic cell in y −direction
L_z^{pcell}	Size of the periodic cell in z −direction
$LAMMPS$	Large-scale Atomic/Molecular Massively Parallel Simulator
$LVDT$	Linear Variable Differential Transformer
m	Mass of an individual grain
M	The cumulative mass of grains whose particle diameter is smaller than d_i^p
MD	The maximum deviation
M_i	Moment acting on an individual grain i
M_0	Small-strain constrained modulus
M_T	Total mass of the specimens
MT	Moist-tamping method
MPI	Message Passing Interface
n	Fitting parameter for Hardin's empirical equation
n_f	Proportion of nonactive finer particles
n_c	Proportion of nonactive coarse particles
n_p	Specimen porosity
N_c	Total number of contacts
$N_{c,a}$	Number of contacts involving particle a
N_p	Total number of particles
N_t	Total number of stress-transmitting particles
$N_{c,V}$	Total number of contacts in volume V

NCL	Normal compression lines
N_c^{CC}	Total number of coarse-coarse contacts in volume V
N_c^{CF}	Total number of coarse-finer contacts in volume V
N_c^{FF}	Total number of finer-finer contacts in volume V
N_c^k	Number of contacts within the specified partition
$N_{p,finer}$	Number of particles belonging to the finer fraction
$N_{p,coarse}$	Number of particles belonging to the coarse fraction
p_a	Atmospheric pressure
p^a	Mean normal stress for particle a
p'	Mean effective stress
p'_{finer}	Effective stress transferred by the finer fraction
p^*	Specified threshold stress in calculating e_G
PSD	Particle size distribution
PSD^{active}	Particle size distribution of active particles
PSD^{stress}	Cumulative distribution of the contribution of each particle to the overall stress
q	Deviatoric stress
r	A parameter for the calculation of the equivalent void ratio
r^a	Radius of particle a
REV	Representative element volume
$RMSD$	Root mean square deviation
R_1	Radius of contacting particle 1
R_2	Radius of contacting particle 2
R^*	Equivalent radius for contacting particles
R^2	Coefficient of determination

s_i	Particle size (non-dimensionalised) with respect to the maximum particle size d_{max}
$\bar{s}$	Geometric mean of the weight distribution
S^*	Threshold finer fraction
S	Strain-increment tensor proposed in Parkin (1965)
SR_{cf}	Size ratio between the coarser and finer grains, $D_{coarser}/D_{finer}$.
SR_{ci}	Size ratio between coarser and intermediate grains, $D_{coarser}/D_{int}$
SR_{if}	Size ratio between intermediate and finer grains, D_{int}/D_{finer}.
SR	Size ratio
SD	Slurry deposition method
Su_b	Fitting constant value in Suzuki et al. (1981)
TC	Transitional coarse-dominated behaviour
TF	Transitional fines-dominated behaviour
T^{max}	Maximum sliding tangential contact force
v_{phase}	Phase velocity in the frequency domain
v_{group}	Group velocity in the frequency domain
V	Total volume of the simulated specimen
V^a	Volume of particle a
V^f	Volume of finer particles with mean stress p', below a specified threshold, p^*
V^c	Volume of coarse particles with mean stress p', below a specified threshold, p^*
V^k	Volume of particle k
V_f	Volume of finer fraction
V_v	Volume of voids

V_a	Volume of active particles
V_{ina}	Volume of inactive particles
V_s	Shear wave velocity
V_p	Compression wave velocity
w_i	Weight retained at the sieve opening d_i
w_{tot}	Total weight of the specimen
WP	Water pluviation method
X_{dim}	Length in the x direction
Z	Coordination number
Z_{dim}	The length in the z direction
ψ	State parameter
v_s	Poisson's ratio of a specimen
v_p	Particle Poisson's ratio
v_{p1}	Poisson's ratio for contacting particle 1
v_{p2}	Poisson's ratio for contacting particle 2
μ	Inter-particle friction coefficient
α	Stress-reduction factor
α_{ff}	The proportion of the stress transferred by the finer-finer contacts
α^a	Contribution of an individual particle, a, to the overall stress
β	Stress-reduction factor when $\alpha \geq 1$
β_p^{ff}	Proportion of the stress transferred by finer-finer contacts
β_p^{cf}	Proportion of the stress transferred by coarse-finer contacts
β_p^{cc}	Proportion of the stress transferred by coarse-coarse contacts

σ'_{ij}	Effective overall stress tensor for the specimen
$\boldsymbol{\sigma'}$	Effective confining pressure
σ'_3	Minor principal stress
σ'_2	Intermediate principal stress
σ'_1	Major principal stress
σ'_{zz}	Mean normal stress in the $z-$ direction
σ'_{xx}	Mean normal stress in the $x-$ direction
σ'_{yy}	Mean normal stress in the $y-$ direction
σ'_{ii}	Mean normal stress in a certain direction
σ_{ij}^{k}	Stress tensor within the specified partition
σ_{ij}^{FF}	Overall effective stress tensor for finer-finer contacts
σ_{ij}^{CF}	Overall effective stress tensor for coarse-finer contacts
σ_{ij}^{CC}	Overall effective stress tensor for coarse-coarse contacts
$\bar{\sigma}_{ij}^{a}$	Average stress tensor for the particle a
$\bar{\sigma}_{ff}^{k}$	Mean stresses carried by the finer-finer contacts involving particle k
$\bar{\sigma}^{k}$	Mean stresses from all contacts acting on particle k
ρ	Bulk density of the specimen
ρ_m	Bulk density considering only active particles
ρ_α	Bulk density considering e_α
x_i^a	The displacement of particle a due to the global strain field
$\ddot{x}$	Acceleration of an individual grain
$\boldsymbol{x}_i^c$	branch vector connecting the centre of particle a

	to the contact point c
$\delta\varepsilon_q^e$	Increment in elastic deviatoric strain
$\delta\varepsilon_z^e$	Strain in the z direction
$\delta\varepsilon_x^e$	Strain in the x direction
$\delta\varepsilon_y^e$	Strain in the y direction
δq	Increment in deviatoric stress
δ_n	Normal overlap of the two contacting grains
δ	Particle scale displacement
δ_t	Tangential displacement
$\dot{\varepsilon}_{ij}$	Strain rate tensor applied to the periodic cell
ε_{ij}	Strain tensor applied to the periodic cell
Δs	Incremental tangential contact displacement
Δt	Timestep
$\boldsymbol{\Delta f}^{ab}$	Increment in the contact force vector induced by an increment in the displacement of the two grains
$\boldsymbol{\Delta x}^{ab}$	Incremental displacements of the two contacting particles
Δx_i^a	Incremental displacement of particle a due to the global strain field
$\Delta\varepsilon_{ij}$	Increment in strain
γ	Shear strain
φ	Degree change in phase-frequency relationship
$\ddot{\varphi}$	Angular acceleration of the grain

Chapter 1. Introduction

1.1. Background

While current understanding of sand behaviour is mainly based on physical experiments on well-graded soils which contain grains with a wide range of sizes, many sands of engineering interest such as those present in tailings dams, for example, are poorly graded soils. Gap-graded soils are a particular type of poorly graded soils, which have a deficiency of certain particle sizes. The simplest types of gap-graded soils are mixtures of finer and coarser grains. A schematic drawing of such a bimodal gap-graded soil is illustrated in Figure 1.1. The term "Fines" in geotechnical engineering normally refers to grains whose diameters are smaller than 0.075 mm (e.g. $ASTM\ D$ 2487-Standard Practice for Classification of Soils for Engineering Purposes) or 0.063 mm (e.g. DIN standard code etc). However, the finer grains considered in this thesis are not grains whose diameters are smaller than these specific diameters (i.e. 0.075 mm, 0.063 mm). Instead, these finer grains are cohesionless grains that have relatively small particle diameters, as shown in Figure 1.1. The term, "percentage finer fraction (F_{finer})" instead of "fines content (FC)" is therefore used in this thesis for clarity and consistency.

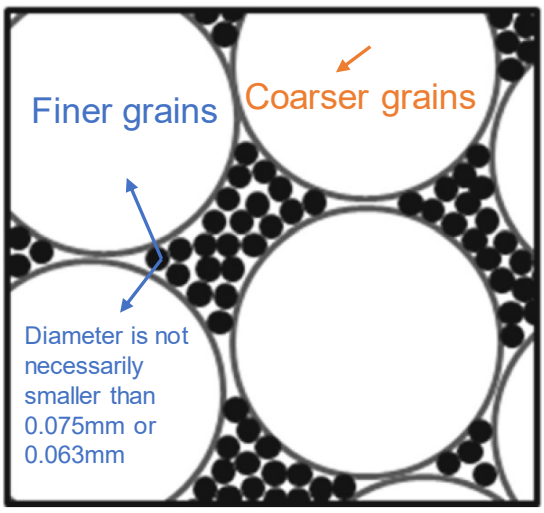


Figure 1.1: Schematic drawings of gap-graded soil fabric (Modified from Shire et al., 2016)

Bimodal, gap-graded soils can be described by two key characteristics: (1) the proportion, expressed as a percentage, of the finer fraction present (F_{finer}), that is the proportion of the overall mass that is made up of finer grains; (2) the size ratio (SR) between the finer fraction and the coarser fraction, which is the ratio of the median diameter of the coarser grains to the median diameter to the finer grains. A typical particle size distribution for a bimodal gap-graded soil is shown in Figure 1.2.

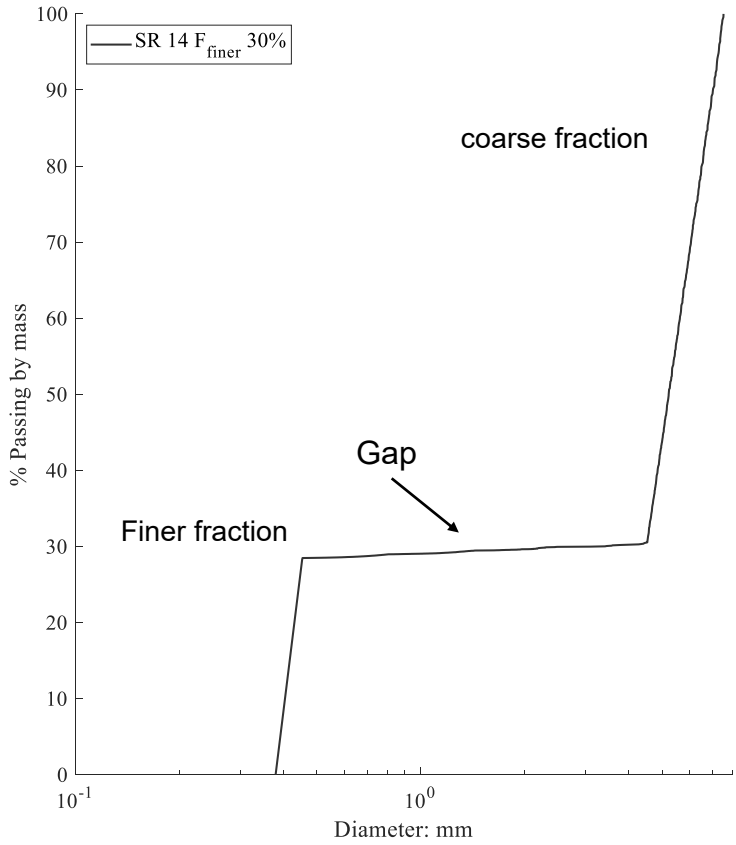


Figure 1.2: A typical particle size distribution for a bi-modal gap-graded soils with $SR = 14.0$, $F_{finer} = 30\%$

Gap-graded soils have drawn considerable interest in geotechnical engineering because the addition of cohesionless finer grains can significantly alter the mechanical behaviour of sands, for example, the shearing behaviour (e.g. Carraro et al., 2009) resistance to liquefaction (e.g. Thevanayagam et al., 2002), susceptibility to internal instability (e.g. Skempton & Brogan, 1994) and small-strain stiffness (G_0) (e.g. Yang & Liu, 2016).

The global void ratio, e, has been widely used as a state variable for natural clean soils. However, uncertainties and concerns have been expressed about the use of e to predict the behaviour of gap-graded soils. Prior studies (e.g. Thevanayagam et al., 2002) have postulated that the particles that make up the finer fraction may exist in the void spaces that form between the coarser grains without actually contacting these coarser grains. In other words, these finer particles do not contribute to the stress transmission of gap-graded soils. Following this proposition, various state variables, such as the skeleton void ratio, e_{sk}, the equivalent void ratio, e^*, and the granular void ratio, e_G, have been proposed to take into the existence of these inactive finer particles into account. However, contrasting conclusions have been proposed about what is the appropriate alternative state variable to adopt in the case of gap-graded soils.

Characterising the shear wave velocity, V_s, and the small strain shear modulus, G_0, of granular materials has long been of interest in soil mechanics and geotechnical engineering. Proper consideration of the elastic properties of a soil, including G_0, is necessary to design and evaluate the operational performance of geotechnical structures where displacement and deformation tolerances are small. Specifically, G_0 must be accurately known to accurately predict settlement. The values of V_s and G_0 are important in site response analyses which predict the likely accelerations that will occur at a particular site in the event of an earthquake. However, most previous research carried out to understand the links between soil characteristics and G_0 has considered natural clean sands. Concerns have been raised about the influence of cohesionless finer grains on the G_0 of gap-graded soils, and whether relationships between soil characteristics and G_0 developed for well-graded sands are applicable in the case of gap-graded soils.

The incomplete understanding of gap-graded soil behaviour may lead to issues with the design of geotechnical structures such as tailings dams, embankment dams and flood embankments. Gap-graded materials are also often encountered in industrial processes where size segregation can be an issue. Furthermore, advancing insight into the behaviour of these materials can inform understanding of geological processes and understanding of the fundamental particle-scale mechanisms, such as the relative contribution of finer and coarser grains to stress transmission. It is clear that most research within both geomechanics and the broader granular mechanics community has considered bimodal materials, i.e., mixtures of materials with two different sizes, and there is scope to look at a broader range of gap-graded materials.

1.2. Research questions

This doctoral research uses the discrete element method (DEM) to explore the nature of stress transmission in gap-graded materials including the consideration of the stress transmitting grains and the distribution of stress amongst different size fractions. Then a new approach to indirectly measure the proportion of stress-transmitting finer particles is developed using both DEM and experimental tests. In contrast to other studies that have considered gap-graded soils, this research considers both bimodal and trimodal mixtures and contextualizes any observations by carrying out parallel studies on materials with continuous gradings.

The effect of size ratio (between coarse and finer fraction)

Previous studies have used different SRs when studying the G_0 of soil mixtures, but the effect of SR on the observed response has received less detailed consideration. However, the SR effect may strongly affect stress transmission at the particle-scale and influence the macro-scale mechanical behaviour of gap-graded soils, including G_0. The conflicting views expressed

by previous researchers may be attributed to this SR effect. For instance, several studies (e.g. Yang et al, 2015) indicated that the global void ratio is the most appropriate state variable to capture the mechanical behaviour of soil mixtures; this suggests that finer fraction is active in stress transmission. Their conclusions may be limited in the extent of their applicability because Yang & Liu (2016) used a mixture with a SR of approximately 4, which is relatively small compared to SRs in other studies (e.g. Thevanayagam et al. (2002) used a SR of approximately 24). A schematic diagram of the fabric of a gap-graded material with SR = 4 is provided in Figure 1.3(a).

In contrast, other studies (e.g. Thevanayagam et al., 2002) have indicated that the equivalent void ratio (e^*) is capable of capturing the mechanical behaviour of soil mixture; this suggests that the finer fraction may be partially active in stress transmission. The results illustrated by Thevanayagam et al. (2002) may be explained by the fact that they used a SR of approximately 24, which is large compared to those reported in Yang et al. (2015). This case is illustrated in Figure 1.3(b), where the finer grains are not active. Figure 1.4 presents the SR used in several prior studies and it can be seen that the SR values applied vary from approximately 4 to 140. However, very few studies have considered the effect of SR on the mechanical behaviour.

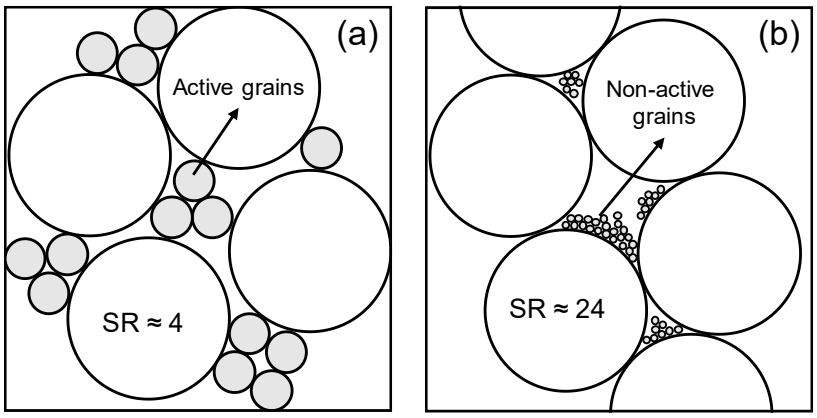


Figure 1.3: Evolution of fabric with two distinct SR values: (a) Small SR; (b) Large SR

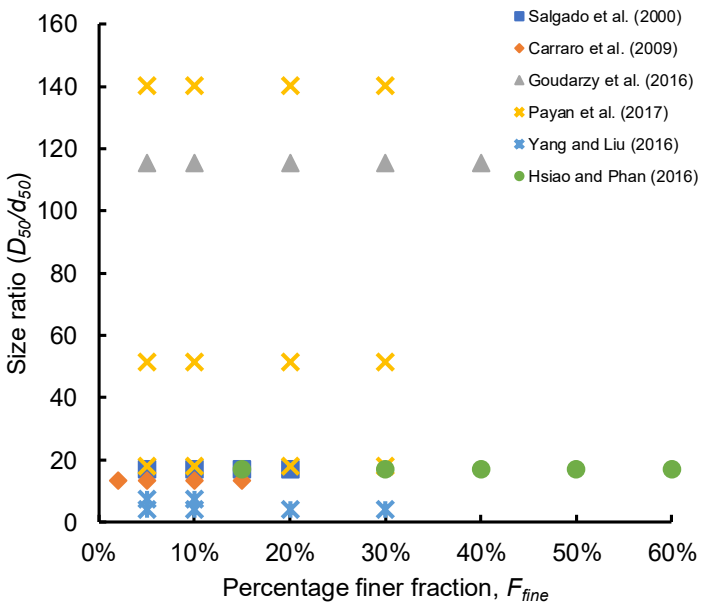


Figure 1.4: SR values reported in several prior studies

Study of traditional state measures (e.g. void ratio; bulk density)

To capture the mechanical behaviour of gap-graded soils, various state variables have been proposed in prior studies. However, there is little consensus on the selection of state variables that can be used to predict the mechanical behaviour of gap-graded soils. In addition, although the global void ratio has been considered an appropriate state variable for materials with continuous particle size distributions (e.g. linear), in-depth micromechanical analyses of the state of this type of material are relatively rare. This study investigates the applicability of these proposed state variables (e.g. e, e_{sk}, e^*, e_m) for both gap-graded soils and soils with a continuous grading.

An investigation into trimodal specimens

Restricting consideration to non-plastic cohesionless granular materials, it can be seen that there has been a large number of experimental studies looking at soil mixtures. In most cases, the finer grains were mixed with coarser grains so that those soil mixtures were almost bimodal. However, natural geological deposits of purely bimodal soil mixtures are rare. Therefore, a comprehensive

and relevant understanding of the stress distribution in materials needs to consider more complex particle size distributions. In a first step to developing this broader perspective, this study considers trimodal materials, with finer fraction, intermediate fraction and coarser fraction.

This study aimed to examine the mechanical behaviour of gap-graded soils from the perspective of DEM and experiments. The overall research methodology is shown in Figure 1.5. Considering the DEM component of this research, the characteristics of stress transmission in bimodal and trimodal gap-graded soils were investigated to identify key trends, followed by studies that quantified the G_0 of gap-graded soils. The conclusions obtained from the DEM analyses informed the experimental program design. In the experimental phase of this research, triaxial tests were carried out with bender elements and local transducers to measure G_0 values from both dynamic and static methods. The DEM simulations and associated analyses provided information on the fundamental mechanics behind overall response trends observed in the experimental study. At the same time, the experimental studies enabled an understanding of the extent to which the DEM simulations are generating physically meaningful data. In this way, a combination of physical experiments and numerical simulations were used to systematically study stress transmission and G_0 in gap-graded soils.

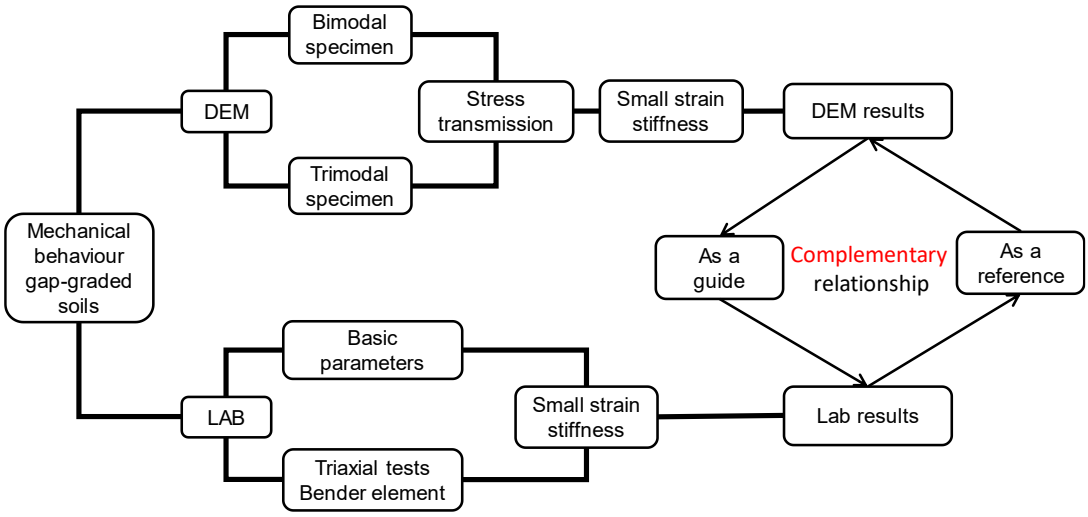


Figure 1.5: Research methodology

1.3. Scope of research

The current research investigated the mechanical behaviour of a broad range of sands, from continuous specimens to gap-graded soils. Where gap-graded materials are considered in DEM studies, very large specimen sizes are required to obtain representative data, particularly where large size ratios are considered (Shire et al., 2014, Sufian et al., 2021). Consequently, to limit the computational cost of the DEM simulations considered here, all specimens were generated with perfectly spherical particles to enable a large number of specimens with different $PSDs$ to be considered. Note that prior studies (e.g. Altuhafi & Coop, 2011) have shown that particle characteristics, such as particle shape and roughness are significant for studying soil behaviour. However, the materials considered are inherently ideal and the complexity and heterogeneity of real soil particle morphologies are neglected due to the fact that simulations with non-spherical particles are computationally more expensive. Besides, the use of non-spherical particles may introduce many more factors that would need to be considered. This approach allows the effect of particle size distribution to be isolated from any effects that might arise from variations in particle morphology. Furthermore, in the DEM simulations, ideal conditions are

simulated so that the fabric effects that would occur in any physical specimens are not reproduced.

All of the DEM simulations shown in this thesis were conducted using a modified version of the open-source $LAMMPS$ code (Plimpton, 1995), and exploiting the high-performance computing (HPC) facilities of Imperial College London (i.e. $CX1$, $CX2$) to carry out all the simulations. Care was taken to ensure that a representative element volume was attained in all specimens, and the maximum number of particles considered in the simulations was 1,002,541.

For the DEM simulations on specimens with periodic boundaries, the way stress is transmitted in the material was considered for specimens with a range of particle size distributions. These analyses have an advanced understanding of the influence of PSD shape on the percentage of active stress-transmitting particles and the consequent efficacy of traditional state variables to quantify the material state. The results indicate that a large number of relatively small grains may not be active in stress transmitting for soil mixtures, which, in principle, limits the potential to use e to quantify state and consequently mechanical behaviour.

The influence of the PSD shape on particle scale stress transmission was also investigated, and the results indicate that for continuous specimens, the cumulative distribution obtained by considering particle stresses has a very similar shape to the particle size distribution. In contrast, for soil mixtures, the relative contribution of the finer grains to the overall stress transmission is dependent upon SR, F_{finer} and the material density. The proportion of effective stress carried by the finer grains is normally lower than the percentage by mass of finer grains. For macro-scale behaviour of soil mixtures, small strain

probes were used to measure the small strain stiffness (G_0) of these specimens. A theoretical stiffness matrix method is developed which shows that this is a clear link between its particle size distribution and the stiffness distribution amongst the different size fractions for granular materials. The particle scale stress transmission may strongly affect the stiffness behaviour of soil mixtures, which leads to a semi-proposed state variable showing better performance to describe the stiffness of soil mixtures.

For the DEM simulations with mixed rigid boundaries and periodic boundaries, both static and dynamic methods were used to measure a static stiffness, G_{sta} and dynamic stiffness, G_{dyn}, respectively. The results show that when an appropriate state variable is used, the G_{sta} values are consistently larger compared to its G_{dyn} values. For all these granular materials, the difference between G_{sta} and G_{dyn} values may be strongly associated with the relative difference in bulk density. Experimental tests were then conducted using both static and dynamic methods to assess whether the macro-scale response which was seen in the simulation data accurately reflects the response of a physical specimen.

1.4. Outline of thesis

This thesis contains eight chapters in total. Chapter 1 has introduced gap-graded soils and the motivation for this doctoral research study. Chapter 2 provides an overview of recent research considering soil mixtures. Recent experimental research as well as research using DEM simulation data is synthesized. Prior research that has considered the small strain stiffness of gap-graded soils is also reviewed. Chapter 3 outlines the methodologies used for the DEM study; the verification of the DEM code used is briefly introduced.

Chapter 4 shows the effect of PSD shape on the proportion of stress-transmitting particles and implications for measures of soil state. A binary perspective was adopted, differentiating between active stress transmitting particles and particles that do not transfer stress and considering the implications for measuring void ratio. The potential limitations of the use of traditional state variables (i.e., void ratio, bulk density) are presented. Chapter 5 shows the influence of PSD shape on the nature of stress distribution in granular materials. The nature of stress distribution was analysed by considering the proportion of stress transmitted by particles of different sizes. For gap-graded materials, a particle scale perspective was also adopted to consider the stress transmission both within and between the different size fractions.

Chapter 6 considers the small strain stiffness of soil mixtures obtained via DEM simulations. Firstly, the small-strain probe method is used for the generated specimens with periodic boundaries (i.e. the same specimens considered in Chapter 5). Then new cuboidal specimens are created with rigid boundaries in the z direction and periodic boundaries in the x and y directions so that both dynamic and static methods can be used to measure G_0. Chapter 7 provides an overview of an experimental study in which both bender element and small strain shear probes were used to study the G_0 values. A direct comparison of the data obtained from both of these two approaches is then made.

Chapter 8 presents a summary of the research. The key findings of this study are presented and some recommendations for further studies are also presented.

Chapter 2. Literature review

2.1. Introduction

This research considers the mechanical behaviour of gap-graded soils. As discussed in Chapter 1, a gap-graded soil can be considered as a mixture of materials with distinct sizes or soil with a deficiency of particular sizes or size intervals. Hitherto most research that has considered gap-graded soils or gap-graded granular materials has considered bimodal mixtures, i.e., mixtures of finer and coarser grains. As explained in Chapter 1, these materials can be characterized by the proportion by mass of finer particles (F_{finer}) and the ratio of the diameters characterizing the size of the coarser and finer fractions (SR). Various definitions of SR have been used in prior studies; in this thesis, SR is taken to be the ratio of the median diameter of the coarse fraction ($D_{c,50}$) and the median diameter of finer fraction ($d_{f,50}$) i.e., $SR = D_{c,50}/d_{f,50}$.

It is important from the outset to highlight that amongst the experimental studies considered in this Chapter, the soil mixtures reported in some of these prior studies may not be strictly gap-graded. For instance, Murthy et al. (2007) studied the undrained monotonic response of mixtures of clean and silty sands, however, the gap between the coarser and finer grains is arguably not completely distinct, as illustrated in Figure 2.1(a). In contrast, Thevanayagam et al. (2002) studied the undrained fragility of soil mixture, and in that study, significant gaps between the coarser grains and the finer grains can be identified, as illustrated in Figure 2.1(b). In this Chapter, both research that has considered distinct size fractions as well as research where the size fractions are less distinct, are reviewed.

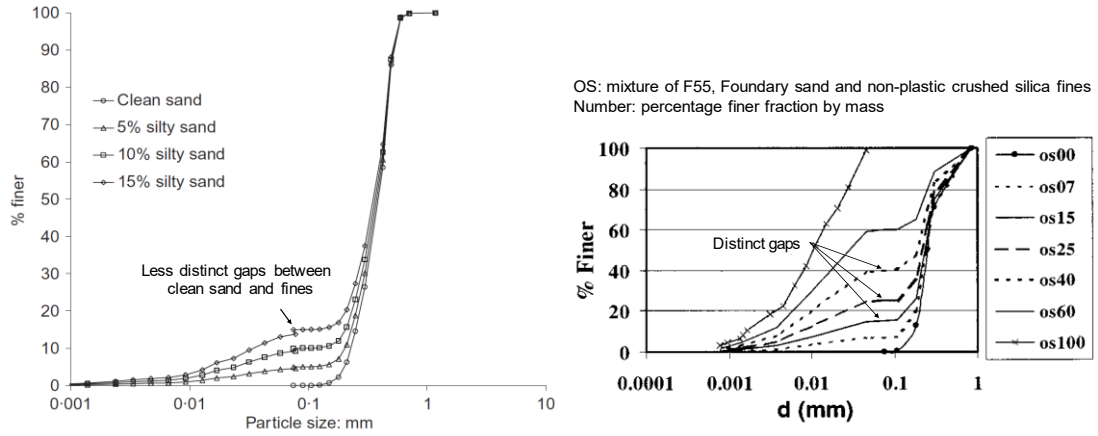


Figure 2.1: Soil mixtures considered in prior studies: (a) Particle size distributions considered by Murthy et al. (2007); (b) Particle size distributions considered by Thevanayagam et al. (2002)

This Chapter provides a review of research related to soil mixtures considering both experimental and DEM -based studies. Section 2.2 reviews prior experimental studies that have considered the packing characteristics and the mechanical behaviour of soil mixtures. Section 2.3 considers prior research that has used DEM to study the packing characteristics and the mechanical behaviour of soil mixtures. Section 2.4 provides the summary for the literature review and identifies key research gaps.

2.2. Mechanical behaviour of soil mixtures: an experimental perspective

2.2.1. The effect of specimen reconstitution methods on shearing behaviour

It is generally accepted that the way in which a sand specimen is constructed in the laboratory can affect the overall behaviour. The commonly used specimen reconstitution methods for granular materials include moist-tamping (MT), air pluviation (AP), dry deposition (DD), slurry deposition (SD) and water pluviation (WP). Each technique has its own particular strengths and limitations

and should be selected by considering the testing materials and the actual engineering application (i.e. the extent to which the specimen is representative of the in-situ environment of interest). The MT method has been used in several studies that considered soil mixtures (e.g. Yang et al., 2006; Yang & Wei, 2012; Ke & Takahashi, 2012; Papadopoulou & Tika, 2008) since this method allows specimens to be reconstituted with a wide range of densities. However, several research studies (e.g. Polito & Martin, 2001; Vaid et al., 1999; Carraro et al., 2009) have indicated that the MT method neither reproduces the real natural depositional process for soil mixtures in situ (i.e. underwater) nor produces a relatively uniform specimen.

Other studies (e.g. Kuerbis et al., 1988; Carraro & Prezzi, 2008; Carraro et al., 2009; Ventouras & Coop, 2009, etc) have found that although the WP method can be used to simulate the physical process of soil deposition in situ, it is not well-suited to form laboratory specimens comprising soil mixtures because of the segregation of finer particles that occurs. In contrast, AP method could be considered as an appropriate method used to simulate the physical process of soil deposition in situ. Besides, this AP method can also guarantee the uniformity of the specimens (Lade & Yamamuro, 1997; Zlatović & Ishihara ,1995). However, this AP may not be able to prepare the extremely loose specimens. Nevertheless, this method is applied in this study for experimental tests, which is discussed in Chapter 7 in details. By modifying the SD method, Carraro & Prezzi (2008) proposed a new slurry-based method that is capable of producing loose to dense specimens containing either plastic or non-plastic fines. In addition, this new slurry-based method avoids particle segregation, and the soil behaviour of reconstituted specimen resembles those of natural soil deposits formed underwater. Although this SD method has various advantages, this method requires many custom-made instrumentations,

which may not be accessible at this stage. Therefore, this method is not applied in this study.

There is not a consensus in the literature on the effect of specimen reconstitution methods on the mechanical behaviour of soil mixtures. Several studies (e.g. Yang et al., 2008; Naeini & Baziar, 2004; Sze & Yang, 2013) have shown that the specimen reconstitution methods have a measurable influence on the critical state of soil mixtures. This may be attributed to the inherent anisotropy arising from the particle orientation. However, the lack of rigorous analysis of e_{max}, e_{min} values and the uniformity of the specimens of soil mixtures considered in those studies gives rise to some concerns about the robustness of these conclusions. In contrast, several research studies (e.g. Carrera et al., 2011; Shipton & Coop, 2012; Nocilla et al., 2006) did not identify any significant effect of the specimen reconstitution methods on the critical state of soil mixtures. Murthy et al. (2007) also showed that although the initial specimen fabric has a strong effect on the undrained behaviour at the beginning of shearing (i.e. up until the phase transformation point), the effect of the initial fabric diminishes with increasing strain, so that there is a unique CSL in $e - lnp'$ space regardless of the specimen reconstitution methods. These contradictory opinions about the effect of the reconstitution methods used on the shearing behaviour may be attributed to differences in the particle characteristics or a deficit in the quality of the experimental protocols used, as discussed above. Murthy et al. (2007) therefore stated that the $CSLs$ of soil mixtures may be independent of the reconstitution methods when a material with relatively round particles is considered.

2.2.2. The concept of a threshold finer fraction

Previous experimental research has tended to systematically vary F_{finer} and consider the resultant variation in the overall response (e.g. Thevanayagam et

al., 2002). These studies have led to the classification of the behaviour of soil mixtures based on the F_{finer} into two categories (e.g. Thevanayagam & Mohan, 2000): (1) coarser grains-dominated behaviour, where the soil behaviour is assumed to be dominated by the coarser grains, this occurs when the percentage finer fraction F_{finer} is relatively low; (2) finer grains-dominated behaviour, where the soil behaviour is assumed to be determined by the finer grains; this occurs when F_{finer} exceeds a certain value. The F_{finer} delineating these two classes of soil mixtures is called the threshold finer fraction (S^*). Several studies (e.g. Lade et al., 1998) have systematically varied F_{finer}, measured e_{min} and e_{max} and used the minima on the plots of e_{min} or e_{max} versus F_{finer} to identify S^*; where e_{min} and e_{max} are the minimum void ratio and the maximum void ratio of the materials, respectively. However, Zuo & Baudet (2015) analysed existing methods used to determine S^*. They have shown that different, seemingly rational approaches yield different S^* values, as illustrated in Figure 2.2(b). Consequently, it can be concluded that the identification of a unique S^* remains an unresolved issue.

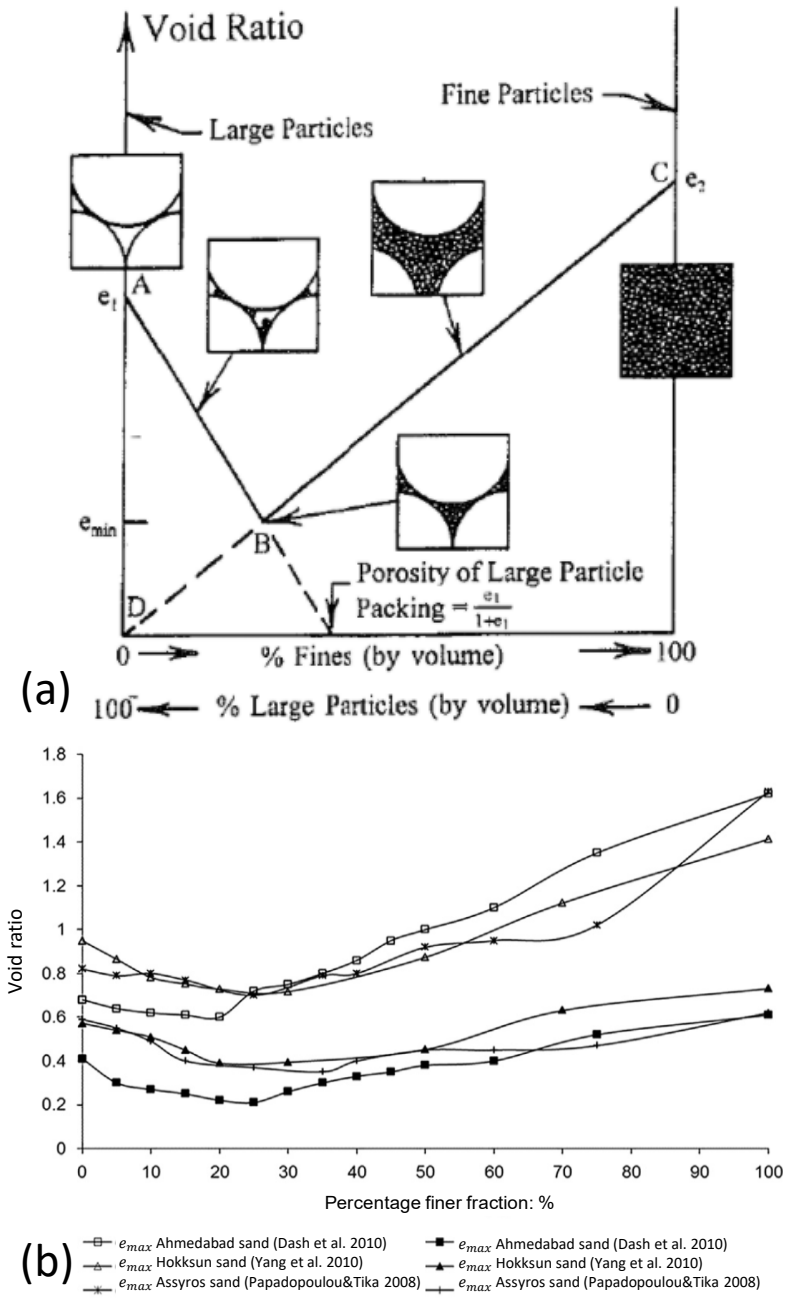


Figure 2.2: Variation in index properties, e_{min} and e_{max} with F_{finer}: (a) Modified from Lade et al., 1998; (b) Modified from Zuo & Baudet, 2015

Carrera et al. (2011) used the Stava tailings collected from a collapsed dam to study the behaviour of soil mixtures, the tailings contained sand and silt-sized particles with sub-angular or sub-rounded particle shapes. By studying this mixture, they indicated unique normal compression lines ($NCLs$) for particular values of F_{finer}. The intercept of these $NCLs$ in an $e - lnp'$ plot with $p' =$

$1\ kPa$ was found for each F_{finer} considered, where p' is the mean effective stress. As illustrated in Figure 2.3(a), for the soil mixtures considered, as F_{finer} increases, the NCL intercept values decrease and reach a minimum point when F_{finer} is about 50%. Carrera et al. (2011) proposed that F_{finer} at this minimum point may be taken to be S^*. Using a similar approach, Thevanayagam et al., (2002) by studying soil mixtures (natural sands and silica fines) have indicated that the location of the critical state line (CSL) also changes with F_{finer}. A set of parallel lines was also identified for different F_{finer}. As illustrated in Figure 2.3(b), the intercept of these $CSLs$ in an $e - lnp'$ plot with $p' = 1\ kPa$ can be identified and when these intercepts values are plotted against F_{finer}, the minima identified in Figure 2.3(b) are taken to give S^*.

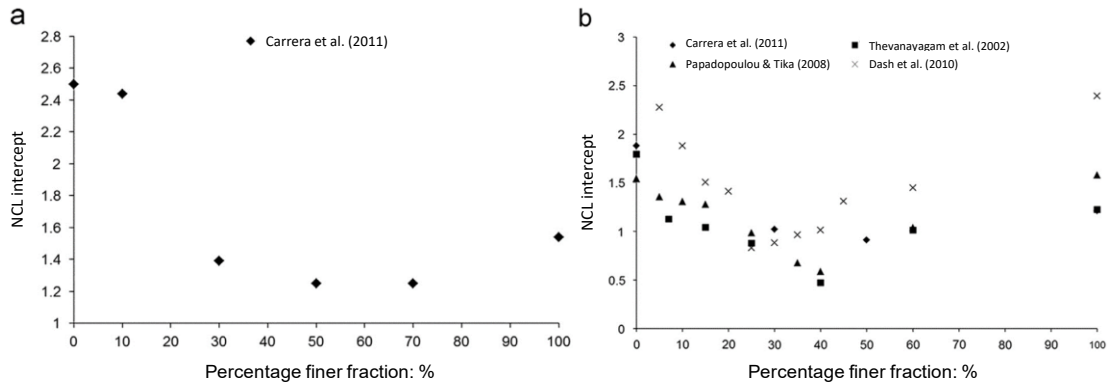


Figure 2.3: Variation in intercepts (a) The normal compression line (Carrera et al., 2011); (b) The critical state line with fines content (Zuo & Baudet, 2015)

Using a theoretical approach, Thevanayagam & Mohan (2000) and Thevanayagam et al. (2002) determined S^* as:

$$\frac{e}{S^*} = e_{max(finer)} \qquad 2.1$$

where $e_{\max(finer)}$ is the maximum global void ratio of the finer fraction. Following ideas developed in prior studies (e.g. Mitchell, 1976; Salgado et al., 2000), Zuo & Baudet (2015) proposed that S^* should be calculated as:

$$\frac{e + S^*}{1 - S^*} = e_{max(coarser)} \quad 2.2$$

where $e_{\max(coarser)}$ is the maximum global void ratio of the coarser fraction. Equations 2.1 and 2.2 indicate that S^* is not a constant value, but it depends on the global void ratio of the soil mixtures. Zuo & Baudet (2015) showed that, in principle, the intersection of Equation 2.1 and Equation 2.2, can be used to identify S^* as:

$$S^* = \frac{e_{\max(coarser)}}{1 + e_{\max(coarser)} + e_{\max(finer)}} \quad 2.3$$

Zuo & Baudet (2015) proposed that S^* may also be determined when using $e_{\min(finer)}$ and $e_{\min(coarser)}$:

$$S^* = \frac{e_{min(coarser)}}{1 + e_{min(coarser)} + e_{min(finer)}} \quad 2.4$$

where $e_{\min(finer)}$ is the minimum global void ratio of finer fraction, $e_{\min(coarser)}$ is the minimum global void ratio of coarser fraction. From an experimental standpoint, Zuo & Baudet (2015) observed that the S^* values determined when intercepts of the $NCLs$ or $CSLs$ (p' = 1 kPa) reach a minimum value show significant scatter. Amongst the theoretical methods, the S^* values obtained from Equation 2.3 and Equation 2.4 are consistent and slightly smaller than those obtained from $NCLs$ or $CSLs$. This may be attributed to the differences in the characteristics of the soils considered (e.g. particle shape). In addition, Zuo & Baudet (2015), amongst others, have indicated that S^* is highly dependent on SR. Rahman et al. (2014) also suggested that the concept of S^* is an idealisation of a transition zone rather than being a unique value.

2.2.3. State variables used for soil mixtures

From prior research studies, it can be seen that a key challenge when considering the behaviour of soil mixtures is to clearly understand the relative contribution of the finer and coarser fractions in soil mixtures. Various state

variables have therefore been proposed as an alternative to the global void ratio (e) to capture the contribution (or lack of contribution) of the finer grains to stress transmission and the overall strength and stiffness of the specimen.

Coarser grains-dominated behaviour

When F_{finer} is lower than S^*, prior studies (e.g. Mitchell, 1976) indicated that only a small fraction of the finer grains actively plays a role in stress transmission, i.e. the behaviour is dominated by the coarser grains. The intergranular void ratio, e_g, was therefore proposed by Mitchell (1976) to replace the global void ratio, e, by treating the volume occupied by all finer grains as if it were void space, as illustrated in Equation 2.5.

$$e_g = \frac{e\left(G_f - G_f F_{finer} + G_c F_{finer}\right) + G_c F_{finer}}{G_f\left(1 - F_{finer}\right)} \qquad 2.5$$

where G_f and G_c are the specific gravities of finer and coarser grains, respectively. By assuming that G_f equals G_c, Shen et al. (1977) introduced a skeleton void ratio (e_{sk}) (equation 2.6) to describe soil mixtures with finer and coarser fractions that have the same mineralogy:

$$e_{sk} = \frac{e + F_{finer}}{1 - F_{finer}} \qquad 2.6$$

However, several studies (e.g. Ni et al., 2004) indicated that it is not accurate to assume that the entire finer fraction does not transfer stress. Consequently, an equivalent void ratio (e^*) was proposed by Thevanayagam (2000) to describe the behaviour of soil mixtures by assuming that the finer fraction partially contributes to the stress transmission:

$$e^* = \frac{e + (1 - b)F_{finer}}{1 - (1 - b)F_{finer}} \qquad 2.7$$

where b is a variable that quantifies the relative contribution of the finer grains to the stress transmission. Rahman et al. (2008) used curve fitting to propose

an empirical expression for b:

$$b = \left\{ 1 - exp\left[-0.30 \frac{\left(\frac{F_{finer}}{S} * \right)}{k} \right] \right\} \times \left(r \frac{F_{finer}}{S*} \right)^{r} \quad 2.8$$

where $r = \left(\frac{D_{c,10}}{d_{f,50}} \right)^{-1}$, $k = (1 - r^{0.25})$, $D_{c,10}$ is 10th percentile diameter of the coarser fraction, and $d_{f,50}$ is the median diameter of the finer fraction. As indicated by the form of Equation 2.8, they concluded that the relative contribution of the finer grains depends upon $D_{c,10}$, $d_{f,50}$, F_{finer} and S^*.

While a number of studies (e.g. Rahman et al., 2008) have shown that e^* is capable of predicting the mechanical behaviour of their soil mixtures with non-plastic finer grains, other studies (e.g. Carrera et al., 2011; Yang et al., 2015) have indicated that this value of b is hypothetical, lacks a scientific basis, and the estimation of b is based on an empirical equation that has no physical meaning. Yang et al. (2015) argued that neither e_{sk} nor e^* are capable of predicting consistently the mechanical behaviour of soil mixtures with non-plastic finer grains. They highlighted the need to investigate the complex particle scale interaction between coarser and finer grains. Yang et al. (2015) argued that the global void ratio, e, remains an appropriate state variable for soil mixtures. However, their conclusions cannot be considered to be definitive. The SR of the soil mixtures they considered is only approximately 4, which may not be large enough to enable conclusions relevant to larger SR values.

Finer grains-dominated behaviour

When the F_{finer} exceeds S^*, the mechanical behaviour of the soil mixture considered is considered to be strongly affected or dominated by the finer fraction. The interfines void ratio (e_f) (equation. 2.9) can be used instead of e.

$$e_f = \frac{e}{F_{finer}} \qquad 2.9$$

Use of e_f assumes that the coarser grains float with the assembly of finer grains with little contribution to the overall stress transmission (Thevanayagam et al., 2002).

2.2.4. Shearing and compression behaviour

The shearing behaviour in both drained and undrained conditions is influenced by F_{finer}. Continuing to restrict consideration to non-plastic finer grains, the addition of finer grains may lead to an increase in strain-softening as observed in undrained triaxial tests (e.g. Yang & Wei, 2012). For the data presented in Figure 2.4(a), the coarser grains are clean Toyoura sand, and the finer grains are crushed silica. They stated that for specimens with similar post-consolidation void ratios, the peak deviatoric stress significantly decreases as F_{finer} increases from 0% to 15% and there is also a significant increase in the amount of strain softening. Furthermore, the addition of finer grains leads to a significant downward shift in the critical state lines in the $e - logp'$ plane; representative data are given in Figure 2.4(b).

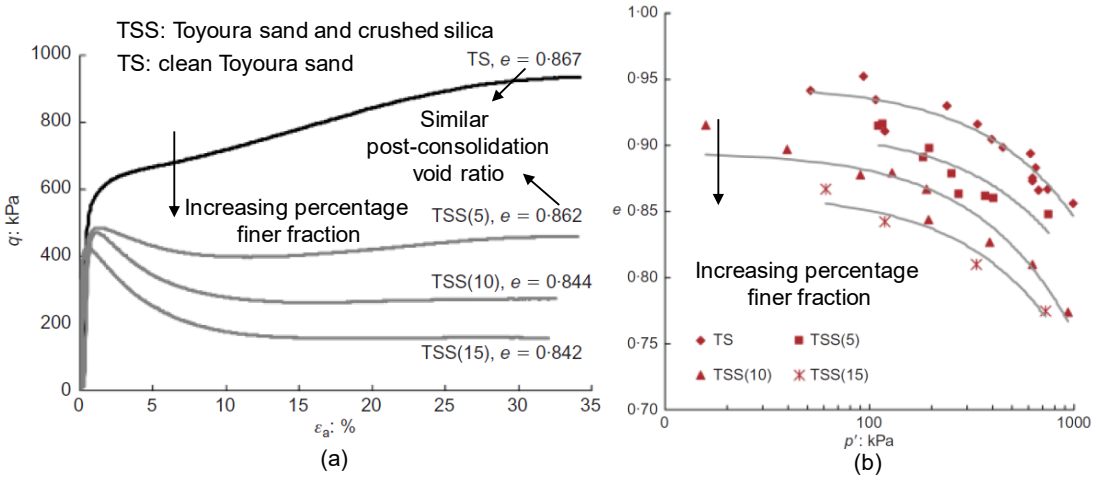


Figure 2.4: The effect of the addition of finer grains on the shearing behaviour of gap-graded soils (Modified from Yang & Wei, 2012): (a) Undrained stress-strain behaviour (q is the deviator stress, ε_a is the axial strain); (b) Critical state lines

To unify the mechanical behaviour of soil mixtures, various alternative state variables (e.g. e^*) have been used to interpret shearing behaviour with satisfactory results. Data from Rahman et al. (2008) are presented in Figure 2.5, where e^* was calculated from Equations 2.7 and 2.8.

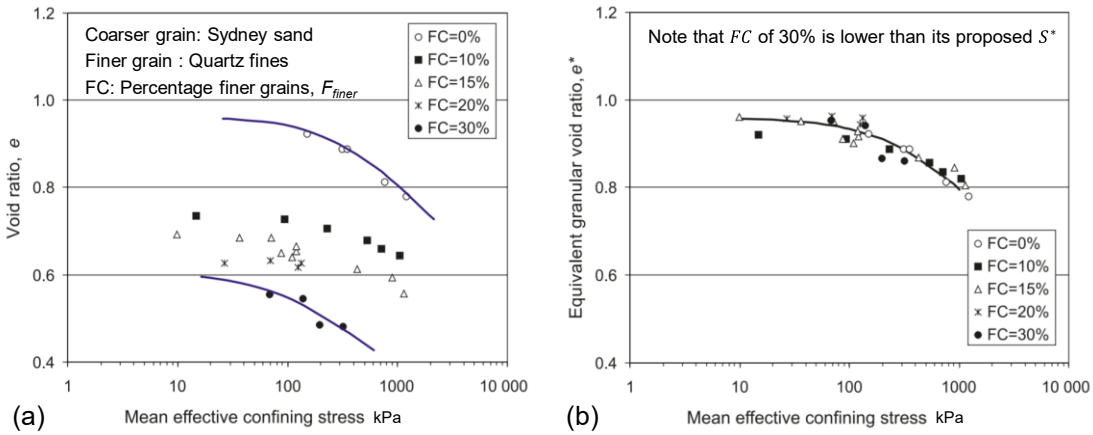


Figure 2.5: The introduction of equivalent void ratio, e^*, to interpret the in shearing behaviour of soil mixtures; (a) CSL data presented in terms of the global void ratio, e; (b) CSL data presented in terms of the equivalent void ratio, e^*, calculated using equation 2.7 (Rahman et al., 2008)

Considering Figure 2.5(a), the $CSLs$ in the $e - logp'$ plane shift downwards with increasing F_{finer}, however, no single CSL can be identified to describe the mechanical behaviour of all these specimens when e is used. In contrast, in the $e^* - logp'$ plane, when the equivalent void ratio (e^*) is used, a single CSL can be drawn to unify the responses of specimens with increasing F_{finer} values.

For each considered experimental study mentioned above, the tabular summary is presented in Table 2.1, which indicates, the specimen preparation method, the reported S^* and the state variables used. For those studies whose SR values were not specifically reported, the SR values provided were determined by digitizing the particle size distribution provided. It is clear that a range of SR have been used in prior studies, however, S^* in many of these

studies of several studies were not specifically stated.

Table 2.1: The summary of several prior experimental studies for shearing behaviour

Reference	Preparation method	SR	Reported S^*	Selected state variable
Zlatović & Ishihara (1995)	MT, AP, WP	18.3	30%-40%	e
Lade et al. (1998)	N/A	1.76 -30	Appr. 30%	$e,\ e_{sk}$
Salgado et al. (2000)	SD	17.0	N/A	e
Polito & Martin II (2001)	MT	6; 14.3	25%	e
Thevanayagam et al. (2002)	AP, MT	24.1	25%	$e,\ e_f,\ e^*,\ (e_f)_{eq}$
Naeini & Baziar (2004)	MT, WP	7.6	30%	e
Ni et al. (2004)	MT	4.4; 16.7	N/A	$e;\ e^*$
Yang et al. (2005)	MT	13.8	30%	e
Carraro & Prezzi (2007)	SD	13.6; 303.9	N/A	e
Papadopoulou & Tika (2008)	MT	15.0	35%-40%	e
Carraro et al. (2009)	SD	13.6; 303.9	N/A	e
Cabalar (2010)	MT	6.8	6.1%- 12.8%	e
Dash et al. (2010)	AP	10.1	20%	e
Carrera et al. (2011)	MT, AP	7.4	25%-45%	e
Rahman et al. (2012)	MT	67.7	35%	$e;\ e^*$
Yang & Wei (2012)	MT	4.0; 5.0; 7.4; 9.1	40%	e
Ke & Takahashi (2012)	MT	10.75	N/A	e
Wei & Yang (2014)	MT	6.2; 11.4	40%	e
Shipton & Coop (2015)	SD, WP	19.6	N/A	e
Ponzoni et al. (2017)	WP, MT	3.25	N/A	e

Following Shire et al. (2016), when the SR is lower than 6, the finer grains cannot exist easily in the voids without actively contacting other particles; a SR

of 6 then can be considered as a high threshold value in studies of gap-graded soils. The mechanical behaviour of gap-graded soils is expected to show different characteristics when the SR is larger than 6 in comparison to cases where the SR is lower than 6. Lade et al. (1998) concluded that a SR of approrixamtely 7 can be considered as a threshold, which is similar to that identified in Shire et al. (2016). In contrast, Shire et al. (2016) also indicated that a SR of 2 should be considered as the lower threshold for gap-graded soils. Between $SR = 2$ and $SR = 6$, there could exist an intermediate type of gap-graded behaviour.

For gap-graded soils, prior studies (e.g., Zhang & Baudet, 2013; Zhang et al., 2020) have considered the importance of particle breakage of gap-graded soils during compression behaviour. As illustrated in Zhang & Baudet (2013), the breakage behaviour was identified as its particle size distribution changed with increasing stress levels. Besides, the amount of small particles created during compression is strongly associated with its finer fraction. Zhang & Baudet (2013) also stated that in contrast to what is usually identified, the gap-graded specimens did not tend towards a fractal grading cruve. Zhang et al. (2017) also stated that the particle size distribution of gap-graded soils tends to retain a memory of their initial grading shape. Their probability density functions of the particle sizes evolve from a bimodal to a multi-modal distribution before and after shearing. It can be seen that the particle breakage is significant for gap-graded soils, especially for the effect on their particle size distributions. However, this thesis did not consider the effect of particle breakage at the current stage due to the potential limitations of computational resources and it would introduce many other factors which may affect the key objectives of this thesis. Further studies may foucs on the effect of particle breakage.

2.2.5. Small-strain stiffness

The small-strain or elastic stiffness G_0, is important in geotechnical engineering design and interpretation of geophysical seismic test data. Based on studies of clean, natural quartz sands. Hardin & Richart (1963) and their colleagues proposed the following empirical expression to describe the relationship between G_0, the global void ratio, e and the mean effective confining pressure (p'):

$$G_0 = AF(e)\left(\frac{p'}{p_a}\right)^n \qquad 2.10$$

where p_a (i.e. atmospheric pressure) is reference stress, $F(e)$ is a function of e. A and n are fitting parameters. For clean well-graded sands, $F(e)$ maybe estimated by Equation 2.11 (Hardin & Richart 1963).

$$F(e) = \frac{(c-e)^2}{1+e} \qquad 2.11$$

where c is empirically assessed to be 2.97 for angular sands and 2.17 for rounded sands. Prior studies (e.g. Mitchell & Soga, 2005) have also proposed a summary of the available expressions for $F(e)$.

In experiments, the G_0 of granular materials can be quantified through dynamic wave propagation tests including bender element tests and resonant column tests (e.g. Hardin & Richart, 1963). The resonant column device is capable of identifying the fundamental resonant mode of specimens. To adhere to this assumption and get reliable experimental results, the effects of boundary conditions and equipment stiffness need to be considered carefully. In a resonant column test, a soil specimen is subjected to torsional excitation typically at increasing frequencies, and the shear stiffness (G_0) is then estimated from the measured resonant frequency.

The other widely used dynamic method is bender element testing, which was proposed by Shirley (1978). In comparison with the resonant column test, an advantage of this method is that this method requires fewer resources and it may be installed into commonly used conventional equipment including oedometers and triaxial cells. In a bender element test, two piezoceramic elements are installed at opposite sides of the specimen. A voltage is applied to one of the elements (i.e. the transmitter element) which causes the bender to displace and generate a small amplitude stress wave propagating through the specimen. When this stress wave reaches the second transducer, i.e. the receiver element, that transducer is in turn displaced and the voltage generated can be recorded. While there has been a lot of discussion about the interpretation of bender element test data, the simple peak-peak method is generally accepted to give reasonably accurate results (e.g. Otsubo, 2016; Yang & Liu, 2016). As illustrated in Yang & Liu, (2016), in the peak-to-peak method, the inserted or input signal is sinusoidal in form and the travel time is taken to be the difference between the peak in the input signal and the peak in the output signal recorded at the receiver element. When the tip of the transmitter element translates horizontally so the element bends, the shear wave velocity is recorded. These elements can also work in extension mode so that the compression wave velocity can also be determined (Lings, 2001). When the elements bend, the shear wave velocity (V_s) is calculated based on the distance between the two tips of bender elements. Then G_0 can be calculated as:

$$G_0 = \rho(V_s)^2 \qquad 2.12$$

where ρ is the bulk density of the specimen. In addition, the other elastic moduli can also be calculated as illustrated below assuming an isotropic soil state:

$$M_0 = \rho\left(V_p\right)^2 \quad 2.13$$

$$\nu_s = \frac{M_0 - 2G_0}{2(M_0 - G_0)} \quad 2.14$$

$$E_0 = 2G(1 + \nu_s) = \frac{G_0(3M_0 - 4G_0)}{M_0 - G_0} \quad 2.15$$

where the M_0 is the small-strain constrained modulus, V_p is the compression wave velocity, the ν_s is the Poisson's ratio of the specimen, and E_0 is the small-strain Young's modulus of the specimen.

Soil is anisotropic and strictly speaking, the stiffness values should be associated with a particular plane, as indicated in several prior studies (e.g. Lings, 2001; Gasparre et al., 2007; Powell et al., 2016). Typically, subscripts are added to G that indicate the direction of propagation and the direction of oscillation of the shear wave to determine a particular G value. For example, G_{zx} indicates the stiffness measured using a shear wave that propagates in the $z-$ direction and oscillates in the $x-$direction. Some studies have shown that G_{zx} may not always equal G_{xz}. For example Pennington et al. (1997) observed this tendency for very stiff over-consolidated clays. Besides, Lings (2001) also indicates that the G_{sta} values obtained in triaxial tesing are not equivalent to the exactly G_{zx} for the dynamic method. In the current study, only G_{zx} from the dynamic method is considered.

A number of studies have compared the G_0 values determined using bender elements and resonant column tests. Yang & Gu (2013) studied the effect of the testing method on G_0 (i.e. for glass beads using a custom-designed apparatus). Their apparatus can measure G_0 using both bender elements and resonant column method on the same specimen at the same state. As illustrated in Figure 2.6, the G_0 values obtained from the resonant column tests

are similar to those identified from the bender element tests. The maximum difference between these two methods is approximately 10%. However, Yang & Gu (2013) highlighted that the G_0 values obtained from the bender element method are consistently larger than the G_0 values obtained from the resonant column tests. Yang & Gu (2013) attributed this tendency to the fact that the resonant column method is capable of quantifying the overall G_0 for the whole specimen. In contrast, the bender element method measures the G_0 considering the central line of the specimen from the transmitter to the receiver. Yang & Gu (2013) attributed this relatively high G_0 value to the fact that the contact forces in the centre of the specimen tend to be higher (Figure 2.7), this may lead to a relatively high G_0 value. As illustrated in Figure 2.7, the contact forces of the central line are stronger. They also acknowledged that the density of the specimen will be lower close to the boundaries; this may also contribute to the discrepancy in data.

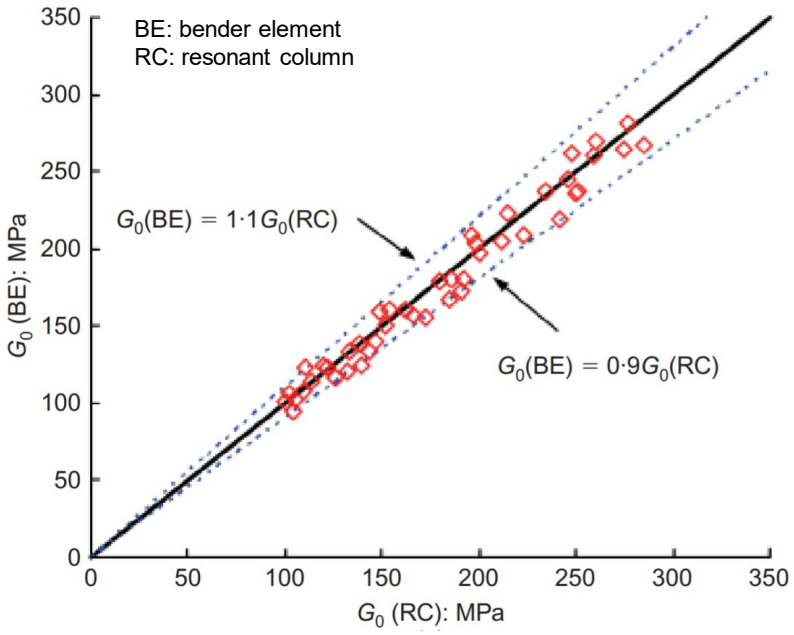


Figure 2.6: Comparisons of shear stiffness measurements from bender element tests and resonant column tests (Yang & Gu, 2013)

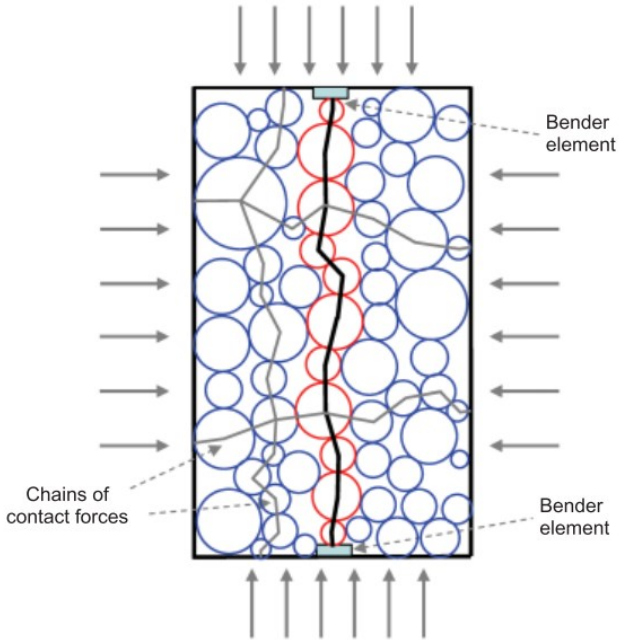


Figure 2.7: Schematic illustration of wave paths and force chains in bender element tests (Yang & Gu 2013)

For soil mixtures, Yang & Liu (2016) also indicated that both bender element tests and the resonant column method are capable of acquiring similar G_0 values, as shown in Figure 2.8. However, it can be seen that the maximum difference between the stiffness values from these two methods is approximately 20%.

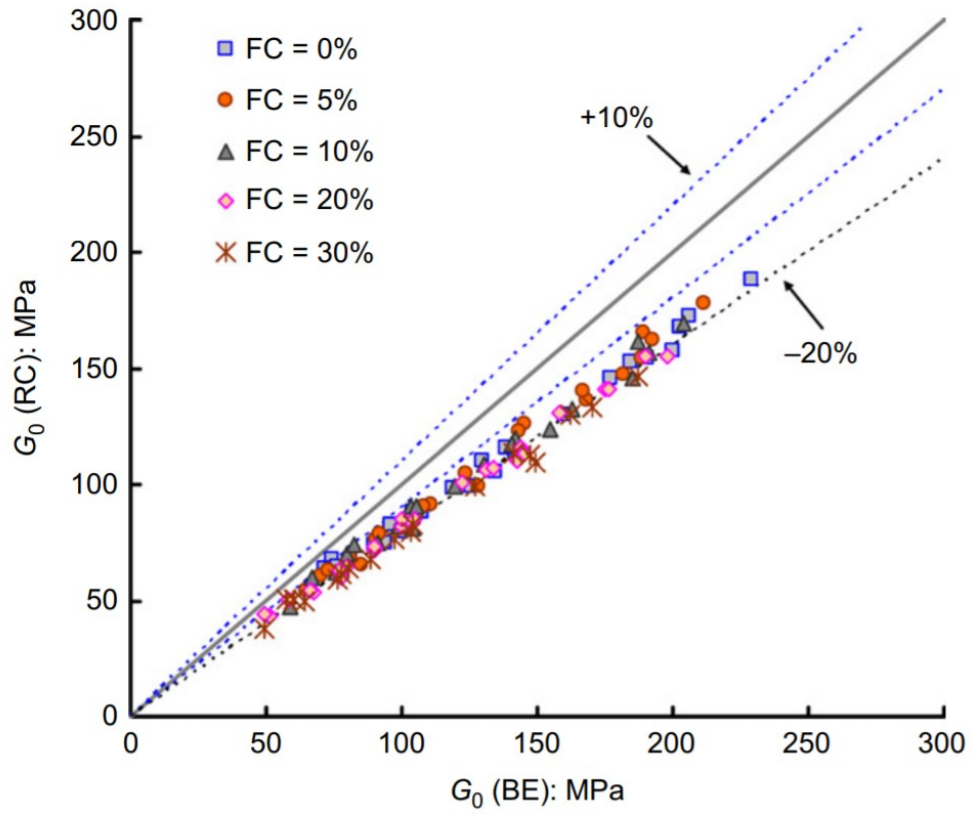


Figure 2.8: Comparison of shear modulus measurements from the resonant column and bender element tests (Yang & Liu, 2016)

Zuo & Baudet (2020) also presented the normalised behaviour of soil mixtures from small-strain stiffness to large strain shearing behaviour. They stated that once a unique relationship between volume and pressure for both pure sand and soil mixtures is built, they can be successfully normalised for composition and volume, and the effect of finer particles on the index properties, compressibility and density could be cancelled. Carraro et al. (2009) presented a systematic laboratory investigation of the static behaviour of soil mixtures containing various amounts of either non-plastic or plastic finer grains. The results showed that G_0 is affected by both F_{finer} and nature of the finer grains. At a similar mean effective stress and relative density (D_r), adding non-plastic silt resulted in a larger decrease in G_0 when compared to the G_0 of mixtures of sands containing plastic finer grains. For given F_{finer}, the G_0 increases with increasing relative density. As illustrated in Figure 2.9, both in the case of non-

plastic finer particles and plastic fines (i.e. kaolin clay), G_0 increases with increasing mean effective stress and decreasing relative density. Most importantly, their data suggested that none of the parameters proposed in the literature (i.e. e^* or D_r, e_g, e_{sk}, e^*) could properly predict the mechanical response (i.e. stiffness behaviour) of the soils they tested.

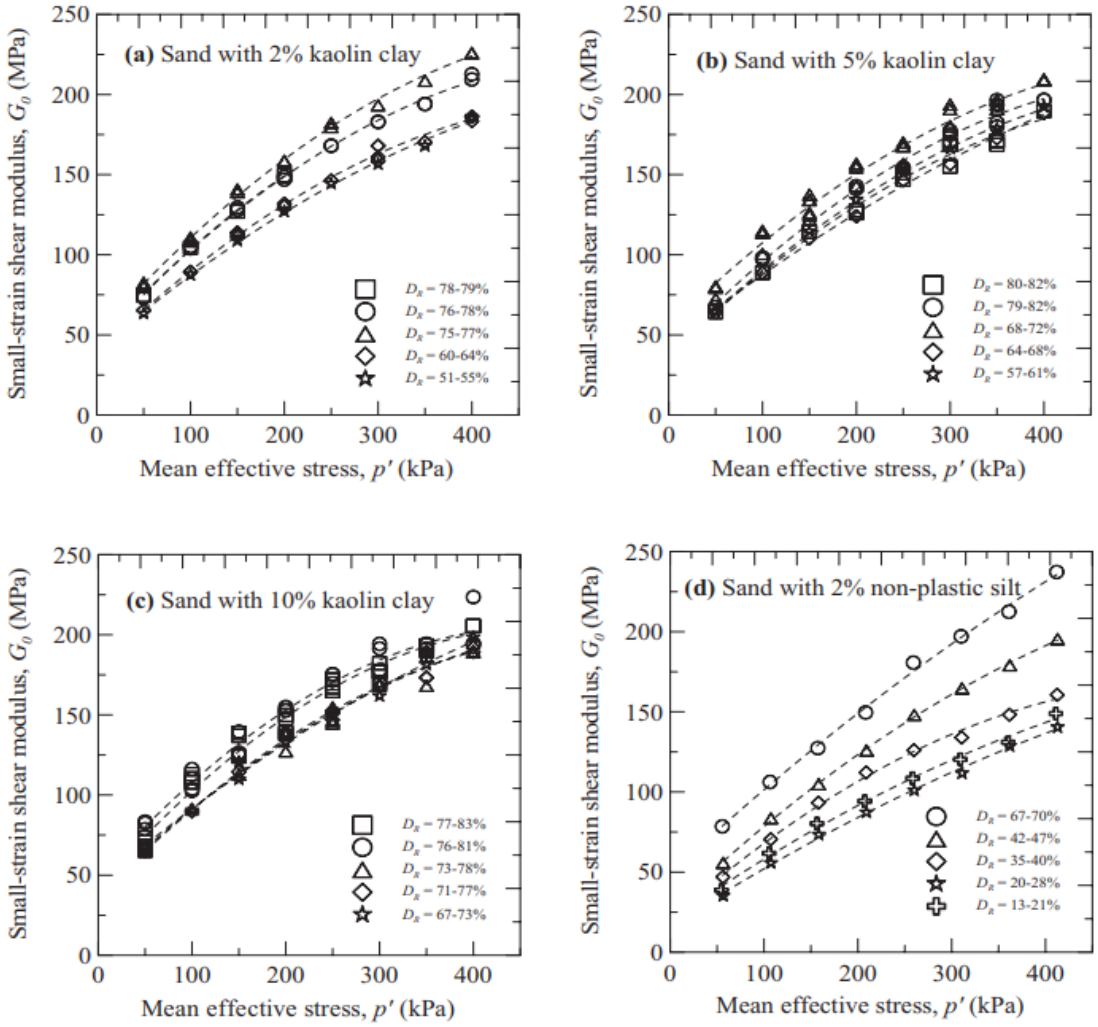


Figure 2.9: Variation of the small-strain shear modulus with soil state for sands with (a) 2% kaolin clay; (b) 5% kaolin clay; (c) 10% kaolin clay; and (d) 2% non-plastic silt (Carraro et al., 2009)

Wichtmann et al. (2015) used a resonant column apparatus to study the G_0 of soil mixtures and highlighted that F_{finer} has a significant effect on G_0 by comparing specimens with a similar value of e and consistent mean effective confining stresses. Wichtmann et al. (2015) considered a number of specimens,

all with a F_{finer} of 10.8%, with the diameter of finer grains varying from 0.01 mm – to 0.063 mm. With various coarse fractions gradations and $D_{c,50}$ values (specimen F7 to F12), similar results are observed as shown in Figure 2.11. In contrast, when the diameter of finer grains varies from 0.04 mm – to 0.063 mm, specimen F13 with the same F_{finer} of 10.8% (i.e. shown in red line in Figure 2.10) shows a distinct stiffness behaviour compared to these of specimens F7 to F12. This result shows that soil mixtures with same F_{finer} may show distinct behaviour if the gradation of the finer fraction changes, this suggests that the PSD shape can significantly influence the impact of F_{finer} on soil behaviour.

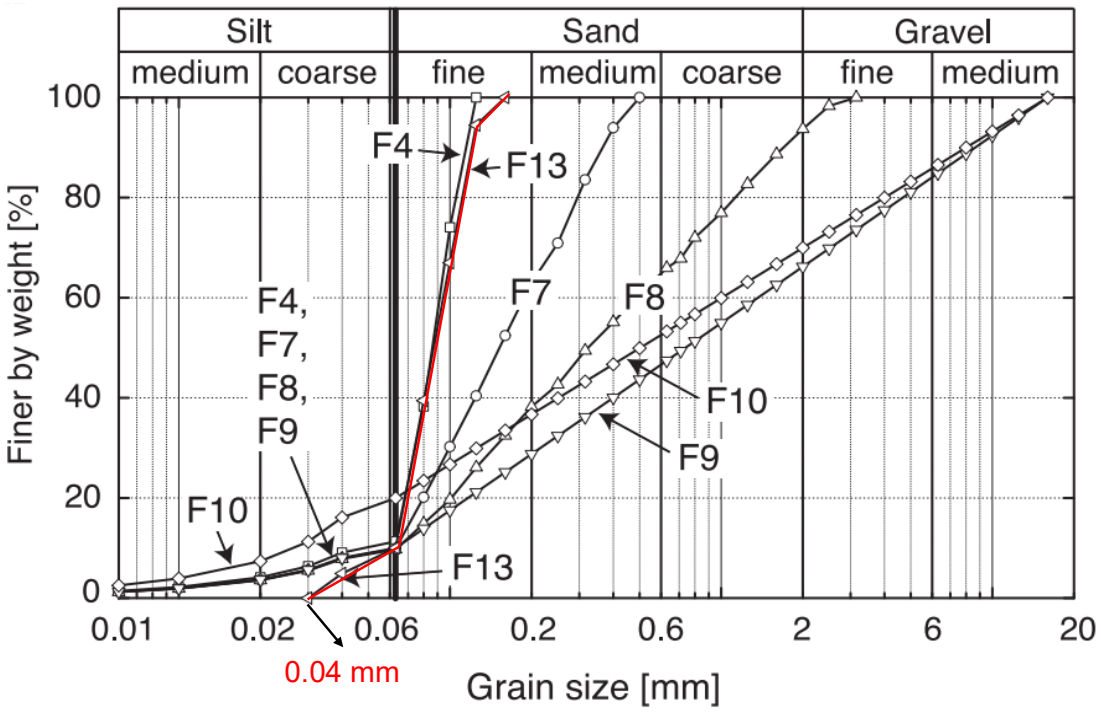


Figure 2.10: Particle size distribution of the soil mixtures considered by Wichtmann et al. (2015)

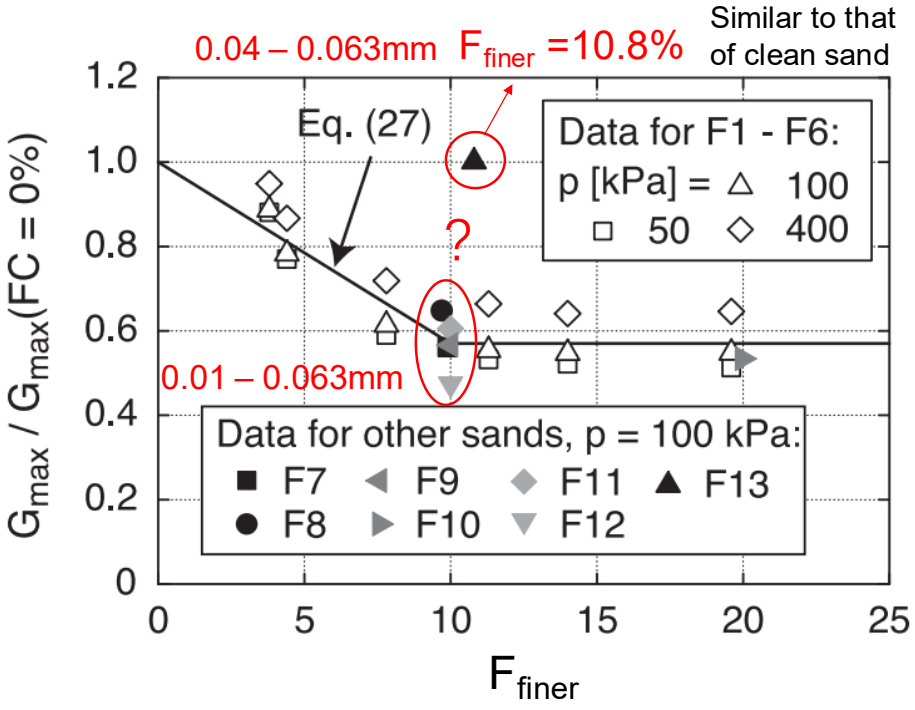


Figure 2.11: Shear stiffness of the soil mixtures considered by Wichtmann et al. (2015)

Several studies (e.g. Goudarzy et al., 2016; Goudarzy et al., 2017; Gong et al., 2019) have used e^* rather than e to express the relationship between density and G_0, modifying equation 2.10 and as below:

$$G_0 = AF(e^*)\left(\frac{p'}{p_a}\right)^n \qquad 2.16$$

Their results show that this modified empirical function is capable of predicting G_0 for their gap-graded materials with satisfactory accuracy when F_{finer} is lower than their reported S^* (i.e. $F_{finer} < 30\%$). As illustrated in Figure 2.12(a), when e is used, no clear relationship can be estimated between e and G_0. In contrast, when e^* is used to replace the e, a unique relationship is identified across the range of F_{finer} values considered.

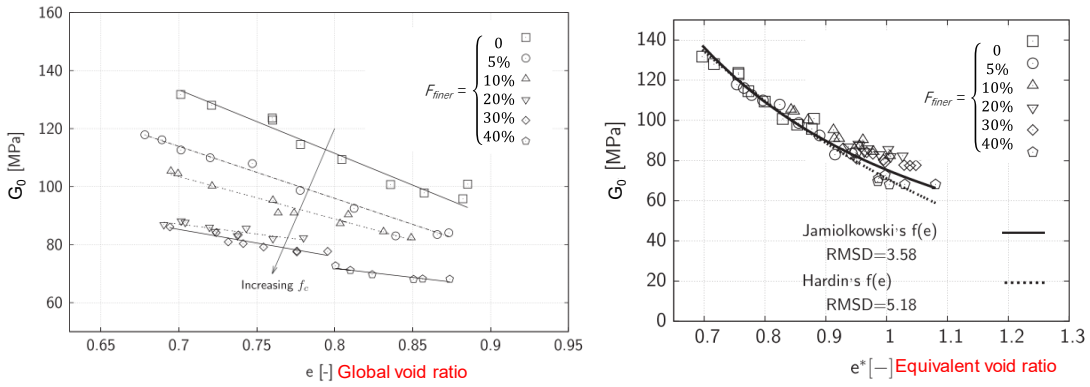


Figure 2.12: Comparison between global void ratio and the equivalent void ratio at effective confining stress of 200 kPa: (a) The effect of F_{finer} on the variation in G_0 with e; (b) The effect of F_{finer} on the variation in G_0 with e^* (Goudarzy et al., 2017)

The state parameter ψ was also proposed by Yang & Liu (2016) as an alternative to e, ψ is the difference between the global void ratio at the current state and the global void ratio at the critical state when subjected to same mean effective confining stress (Ken Been & Jefferies, 1985). This parameter has been widely used to predict the shearing behaviour of granular materials. Yang & Liu (2016) have used both resonant column and bender element tests to study the effect of F_{finer} on G_0 and developed a modified version of Equation 2.1 which includes the state parameter ψ, as shown in equation 2.17.

$$G_0 = AF(\psi)\left(\frac{p'}{p_a}\right)^n = A\frac{(c-\psi)^2}{1+\psi}\left(\frac{p'}{p_a}\right)^n \qquad 2.17$$

Yang & Liu (2016) proposed a new approach that allows a unified characterisation of G_0 for clean sands and soil mixtures. As illustrated in Figure 2.13, for four different mean effective stress (i.e. 100 kPa, 200 kPa, 400 kPa, 500 kPa), for all the F_{finer} values considered, a unique relationship is observed between ψ and G_0 for their soil mixtures.

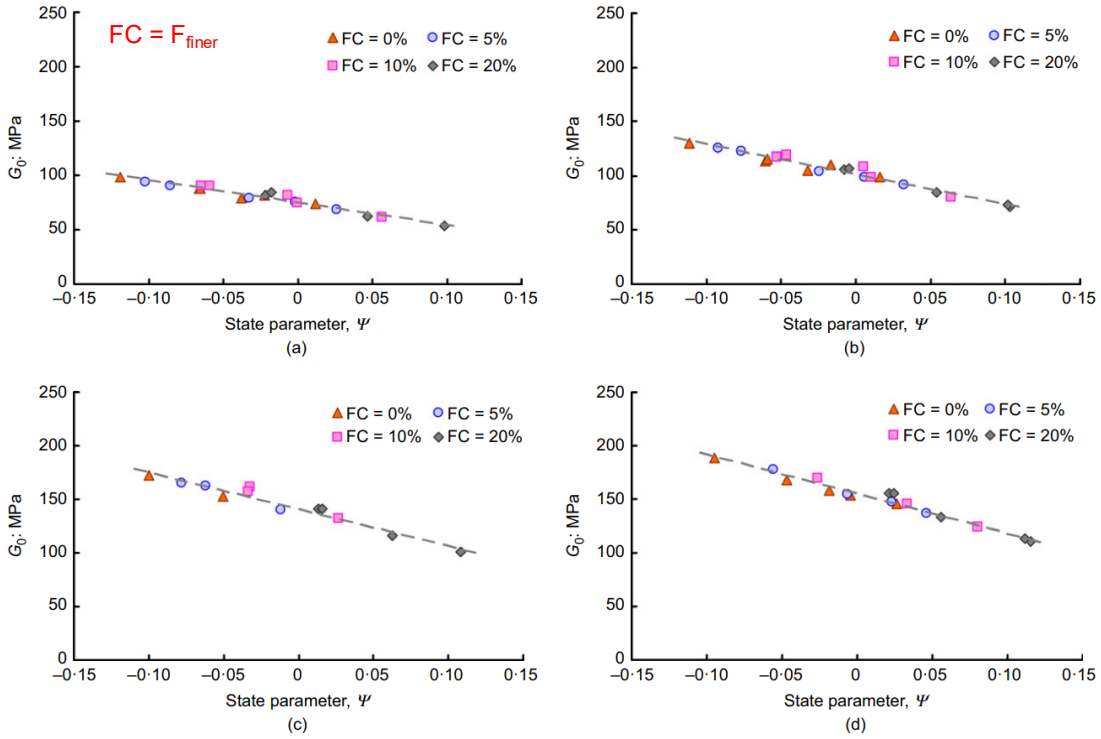


Figure 2.13: Variation in shear modulus with state parameter at different confining stresses: (a) p' = 100 kPa; (b) p' = 200 kPa; (c) p' = 400 kPa; (d) p' = 500 kPa (Yang & Liu, 2016)

Although Yang & Liu (2016) proposed a correlation between ψ and G_0, there is not a strong fundamental basis for using ψ to estimate G_0. In contrast to Yang and Liu (2016), Hsiao and Phan (2015) found no clear relation between G_0 and the state parameter. They argued that G_0 is measured when the material is subjected to a small strain (i.e. < 10^{-5}). While, to quantify the state parameter, a relatively large strain (i.e. >25%) is required to identify the critical state. Although in soil mechanics, the ψ quantified from knowledge of the critical state line position is considered to be a useful parameter which is capable of capturing both the effect of e and the mean effective stress, Hsiao and Phan raised a fundamental concern as to whether a parameter quantified based upon critical state conditions can be linked to small-strain measured G_0. It is widely accepted that the soil fabric of small strain (i.e. < 10^{-5}) is significantly distinct compared to its fabric at a critical state.

Prior research has shown that equation 2.10 (which is empirical) may be modified to predict the G_0 for soil mixtures. However, contrasting views on the selection of appropriate state variables suggest that studies on G_0 of soil mixtures remains an area of great uncertainty. In addition, most prior studies have focused on G_0 of gap-graded soils with lower F_{finer} (<30%). A different result may be drawn when referring to large F_{finer} (>30%). In general, these prior studies are summarised as illustrated in Table 2.2.

Table 2.2: Summary of prior research that has considered the stiffness of gap-graded materials with a non-plastic finer fraction

Reference	Method	Preparation method	Reported SR	Reported S^*	Selected state variable
Salgado et al. (2000)	Resonant column	SD	17.0	N/A	e
Goudarzy et al. (2016)	Resonant column	MT	10	30%	e; e^*
Yang & Liu (2016)	Resonant column Bender element	MT	4; 7.35	40%	e
Hsiao & Phan (2016)	Bender element	MT	17.0	40%	e
Goudarzy et al. (2017)	Resonant column	DD	140.0	30%	e; e^*
Payan et al. (2017)	Resonant column	DD	18.0; 51.5; 140	20%	e; ψ

2.3. Mechanical behaviour of soil mixtures: DEM perspective

2.3.1. Compression behaviour of gap-graded soils

There have been contradictory opinions and significant discussion in the literature, as to which is the most appropriate state variable to predict stiffness and how to account for finer grains that do not transfer stress (e.g. Yang et al., 2018). The lack of consensus in the literature arises because the relative contribution of finer and coarser fractions to stress transmission cannot be directly measured in laboratory experiments on $3D$ particulate materials. An alternative way of investigating the mechanical behaviour of gap-graded soils is to use computer simulation techniques. The discrete element method (DEM) is now well accepted as a geotechnical research tool. An advantage of DEM is that it is capable of capturing an average stress and the contact force for each grain and each contact, respectively. Consequently, DEM can be used to investigate the relative contribution of the finer and coarser fractions to stress transmission through the material.

For DEM, one of the significant points is to make sure that a representative element volume of the specimen is prepared so that reliable results can be obtained. Various DEM studies have used different particle numbers. For instance, Liu et al. (2020) employed a maximum of 9,944 particles to study the suffusion behaviour of gap-graded soils. Gong et al. (2019) used a maximum of 59,802 particles to simulate the stiffness behaviour of gap-graded soils. Zhang et al. (2019) used a maximum of 106,901 particles to simulate the shearing behaviour of gap-graded soils, the particles used in these studies are restricted within a small range (i.e. $<$ 100,000). They stated that such a small specimen may be large enough to be representative. In contrast, Shire et al. (2014) employed a maximum of 304,205 particles to study the stress transmission of gap-graded soils, and Otsubo et al. (2021) used a maximum of

2,286,346 particles to study the shear wave propagation of gap-graded soils. Besides, Sufian et al. (2021) employed a maximum of 3,287,256 particles to simulate the large strain shearing behaviour of gap-graded soils. These studies all highlighted the importance to prepare such large specimens for gap-graded soils, especially for the large strain shearing behaviour. In this study, the specimen size was therefore carefully selected so that the representative specimens were used for all simulations, this is illustrated in the following Chapter 4.

Using DEM, Shire et al. (2014) considered stress transmission in ideal gap-graded soils when subjected to isotropic compression. Following an idea proposed by Skempton & Brogan (1994), a stress-reduction factor (α) was proposed by Shire et al. (2014) to quantify the effective stress transferred by the finer fraction. Following Potyondy and Cundall (2004), the overall mean effective stress in a volume, V, can be related to the mean stress of the individual grains as:

$$p' = \frac{1}{V}\sum_{a=1}^{N_p}(p^a V^a) \qquad 2.18$$

where V^a is the volume of particle a, p^a is the mean stress in particle a, and N_p is the total number of particles in the system. Adapting this equation, Shire et al. (2014) proposed that the stress in the finer fraction can be calculated as:

$$p'_{finer} = \frac{(1-\mathrm{n}_p)}{\sum_{N_{p,finer}} V^a}\sum_{a=1}^{N_{p,finer}}(p^a V^a) \qquad 2.19$$

where $N_{p,finer}$ is the number of finer particles in the system and n_p is the porosity. The proportion of the overall stress transferred by the finer particles is then given as:

$$p'_{finer} = \alpha p' \qquad 2.20$$

where p'_{finer} is the effective stress transferred by the finer fraction and p' is the overall effective stress applied. The particle size distributions used by Shire et al. (2014) are shown in Figure 2.14.

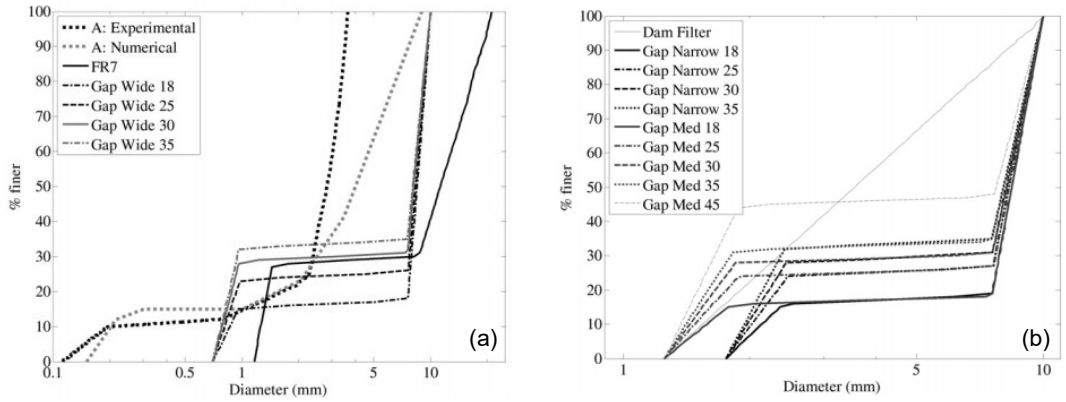


Figure 2.14: $PSDs$ of specimens analysed: (a) Wider gradations; (b) Narrower gradations (modified from Shire et al., 2014)

As illustrated in Figure 2.15, Shire et al. (2014) considered three classifications based on F_{finer}: (1) coarser grains-dominated, when F_{finer} is lower than 24%; the coarser fraction dominates the behaviour, the α value of these specimens is lower than 0.4, and the resulting fabric is termed “underfilled”. (2) Transitional, density dependant behaviour, when F_{finer} varies from 24% to 35%. In the loose condition, the α values are lower than 0.4, in contrast, these α values increase to approximately 1.0 when referring to the dense condition. (3) Finer grains-dominated, when F_{finer} is larger than 35%, the finer fraction dominates stress transmission. As illustrated in Figure 2.15, in the latter case the α values are larger than 0.8 and the resulting soil fabric is termed “overfilled”.

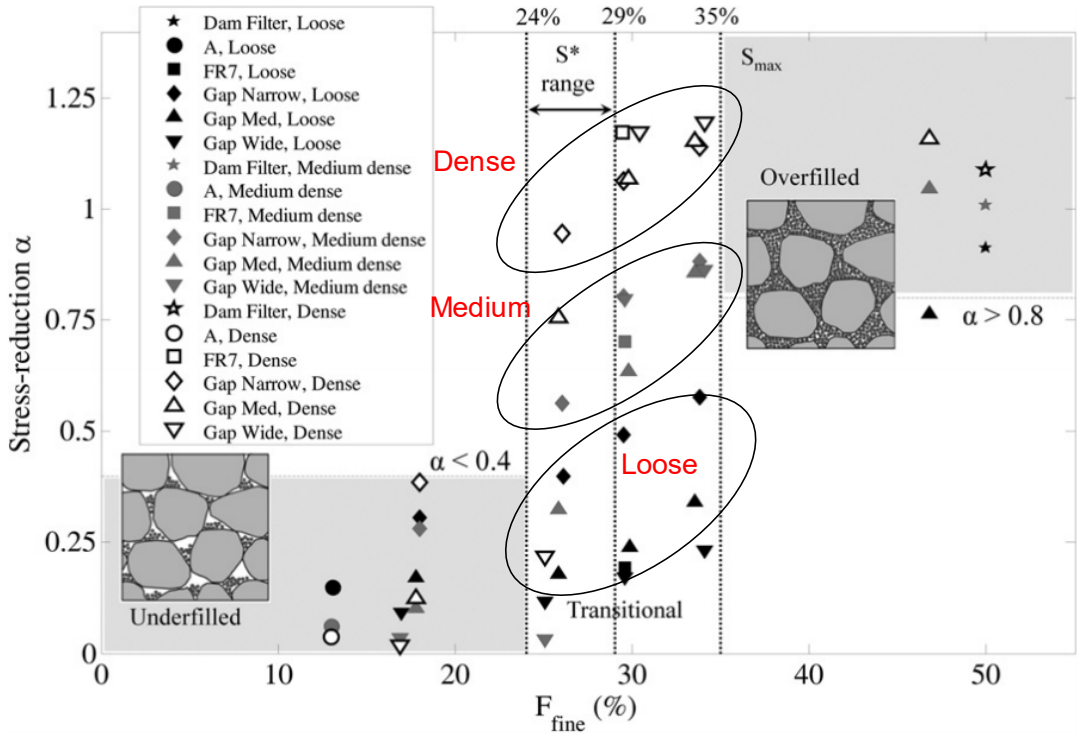


Figure 2.15: Variation of stress-reduction factor α with F_{finer} (Shire et al., 2014)

Minh & Cheng (2013) studied the effect of $PSDs$ (with various continuous gradings) on the 1D compressive behaviour of granular materials using DEM with spherical particles. Their results indicate that well-graded materials are less compressible compared to these uniformly graded materials. They also indicated that the compressibility of materials is strongly associated with these particles carrying large contact forces. Their results highlighted that there is a larger proportion of inactive particles in the loose cases compared to the denser cases. This work highlighted the significant effect of $PSDs$ on soil behaviour even for materials with continuous gradings. Materials with $PSDs$ that lie between linear and gap-graded distributions may have distinct features and this is explored in this thesis.

2.3.2. Shearing behaviour

Numerical studies of bimodal graded soils are relatively rare compared to the number of experimental studies since the simulation of gap-graded soils is

computationally expensive. A large number of particles were required to create a representative volume for DEM simulation. Furthermore, the mass of the smaller grains controls the critical time step for the simulations. Amongst the limited studies, Artigaut et al. (2019) conducted a series of constant p' DEM triaxial compression simulations in a dense condition to study stress heterogeneity in gap-graded soils under shearing. The simulations results illustrate that the value of α can vary from a relatively high value (α >1, indicating that finer grains transfer a large proportion of stress) to a lower value (α <1, indicating that finer grains transfer a small proportion of stress) with shear induced-dilation. Artigaut et al. (2019) highlighted this could lead to an increased risk of seepage-induced internal instability.

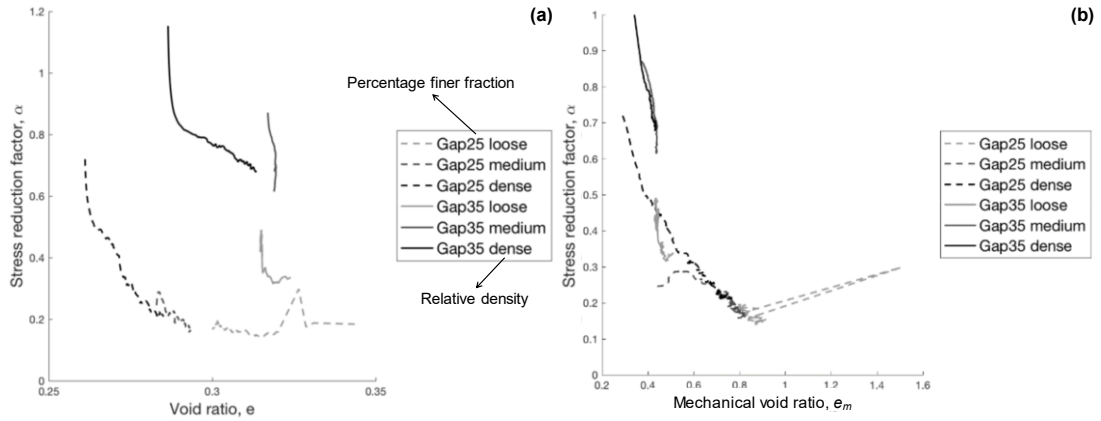


Figure 2.16: Stress reduction factor (α) and mechanical void ratio (e_m) (modified from Artigaut et al., 2019)

Given that DEM enables tracing of the stress and forces acting on each grain during shearing, an alternative state variable, the mechanical void ratio (e_m) was proposed by Otsubo (2016) to capture the behaviour of gap-graded soils. This mechanical void ratio is calculated by treating these grains with 0 or 1 contact point as part of the void volume (the gravity effect was neglected in their simulations). The mechanical void ratio is conceptually similar to the skeleton void ratio (e_{sk}). As illustrated in Figure 2.16, Artigaut et al. (2019) explored relationships between α and the global void ratio, e (Figure 2.16a), and

between α and the mechanical void ratio, e_m (Figure 2.16b). These data show that α varies during shearing, particularly for the dense specimens.

Sufian et al. (2021) conducted a series of constant mean stress triaxial compression for gap-graded soils using DEM, several SRs and F_{finer} values were considered with the maximum axial strain approximately being 5%. This study showed that the S^* cannot be identified. An evolution of the stress distribution amongst finer and coarse particles is observed, and it is seen to be strongly associated with SR, F_{finer} and fabric anisotropy. Sufian et al. (2021) also proposed a granular void ratio, e_G as shown below:

$$e_G = \frac{e + n_f}{1 - n_f - n_c} \quad 2.21$$

where n_f is the proportion of nonactive finer particles, which can be calculated:

$$n_f = \frac{V^f(p' \leq p^*)}{V} \quad 2.22$$

where V^f is the volume of finer particles with mean stress p', below a specified threshold, p^*, and V is the volume of all particles. The proportion of non-active coarser particles, n_c, is given as:

$$n_c = \frac{V^c(p' \leq p^*)}{V} \quad 2.23$$

Where V^c is the volume of coarser particles with $p' < p^*$. Sufian et al. (2021) considered a range of p^* values from 1 Pa to 1000 Pa to calculate e_G. It can be seen from Figure 2.17, that while the e_G values increase with increasing p^*, the influence of p^* is not significant. It can be seen that when F_{finer} is 30%, a measurable difference can then be observed for e_G with increasing p^*. When compared to e_m, the advantage of e_G is that it can capture the significant difference between the participation of the coarse and finer fraction in the stress transmission and recognizes that many finer particles may transfer a non-zero, but negligible stress.

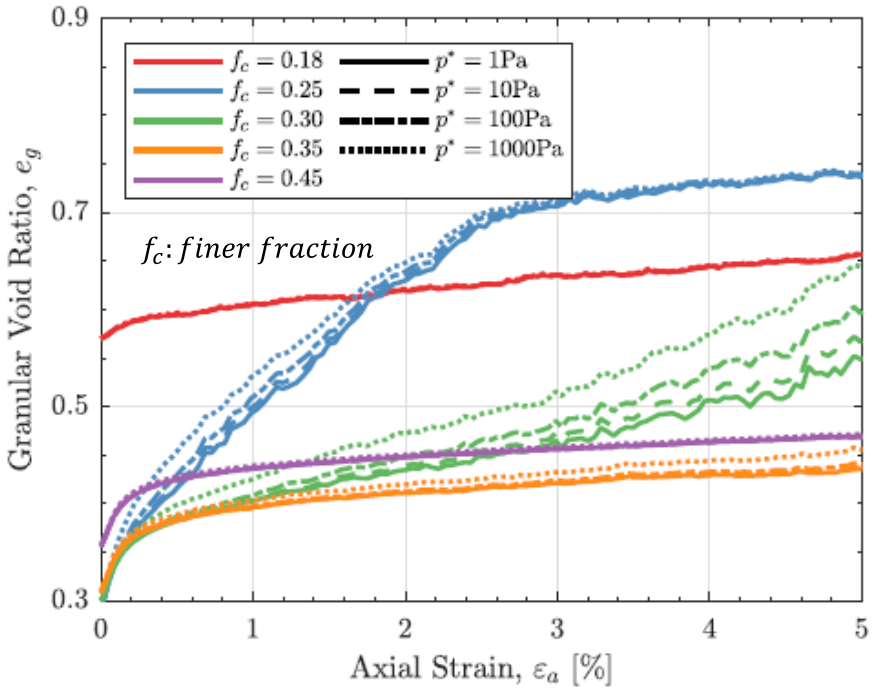


Figure 2.17: The granular void ratio calculated using different threshold mean stress values, p^* (Sufian et al., 2021).

By analysing the interparticle contact network, Sufian et al. (2021) considered the stress heterogeneity from the perspective of the contacts. Sufian et al. (2021) calculated the stress tensor using the contact information as follows:

$$\sigma_{ij}^{k} = \frac{1}{V}\sum_{\mathrm{n}=1}^{N_c^k}(f_i^c l_j^c) \qquad 2.24$$

where N_c^k is the number of contacts within the specified partition, such as the coarse-coarse contacts, $\boldsymbol{f}_i^c$ is the contact force vector; $\boldsymbol{l}_j^c$ is the branch length vector; V is the total volume of the specimen. Equation 2.24 allows the mean stress transferred to be divided into three partitions: (1) the proportion of the stress transferred by finer-finer contacts, β_p^{ff}; (2) the proportion of the stress transferred by coarse-finer contacts, β_p^{cf}; (3) the proportion of the stress transferred by coarse-coarse contacts, β_p^{cc}.

As illustrated in Figure 2.18, by using β_p, Sufian et al. (2021) proposed four categories of bimodal granular material fabric: (1) $\beta_p^{cc} \geq \beta_p^{cf} \geq \beta_p^{ff}$: coarse-dominated (C); (2) $\beta_p^{cf} \geq \beta_p^{cc} \geq \beta_p^{ff}$: transitional coarse-dominated (TC); (3) $\beta_p^{cf} \geq \beta_p^{ff} \geq \beta_p^{cc}$: transitional fines-dominated (TF); (4) $\beta_p^{ff} \geq \beta_p^{cf} \geq \beta_p^{cc}$: fines-dominated (F):

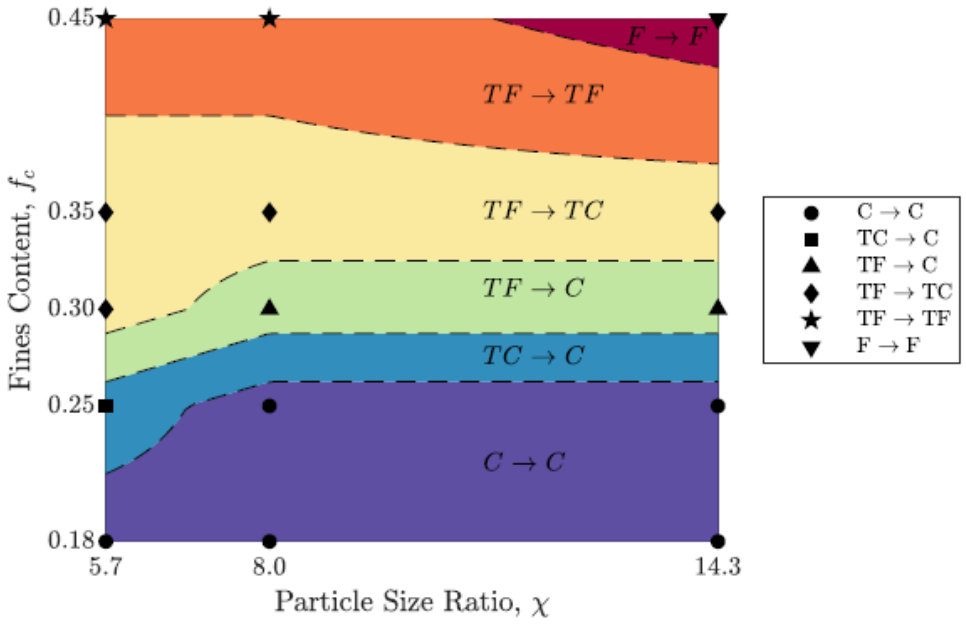


Figure 2.18: Stress distribution for gap-graded soils during shearing from the perspective of contacts. Note that only dense cases are considered in developing the contour. This contour represents approximate delineation (hence, the dashed lines) based on linear interpolation from the available data points shown by the markers (Sufian et al., 2021).

Sufian et al. (2021) also showed that the distribution of stress amongst the two-size fractions in gap-graded soils may change with increasing axial strain, especially for the denser specimens they considered, where the stress transferred by the finer fraction gradually decreases during shearing. For instance, as shown below, as shearing progresses, the stress transferred by fine-fine (β_p^{ff}) and fine-coarse (β_p^{cf}) contacts increases with increasing F_{finer}.

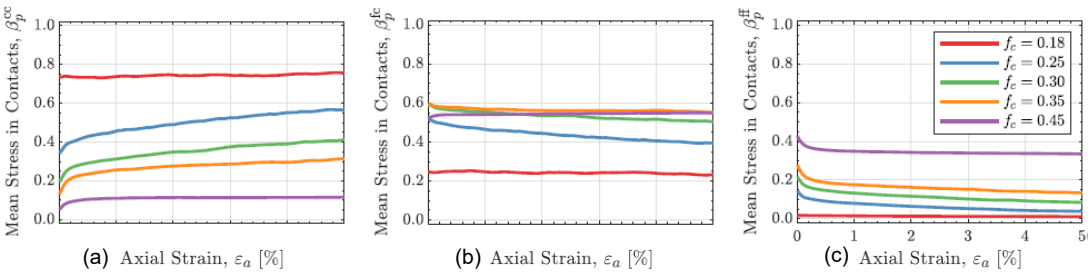


Figure 2.19: Proportion of the stress transferred by different groups of contacts during shearing: (a) Mean stress in coarse-coarse contacts versus axial strain; (b) Mean stress in coarse-fine contacts versus axial strain; (c) Mean stress in fine-fine contacts versus axial strain (modified from Sufian et al., 2021)

Zhu et al. (2020) used relatively small DEM specimens (particle number < 100,000) to study the variation in the shearing behaviour of gap-graded soils with increasing F_{finer} and SR by DEM. They showed that when $20\% \leq F_{finer} \leq 50\%$, the peak friction angle increases with increasing SR. And they stated that neither F_{finer} nor SR affect the critical friction angle. They also showed that the contribution of coarse-coarse, coarse-finer and finer-finer contacts to the peak and critical shear stress is strongly associated with F_{finer} and SR. In general, they stated that the percentage contributions of coarse-coarse and finer-finer contacts to the peak stress are significantly larger than those to the critical state stress. However, the percentage contribution of coarse-finer contacts to the peak stress is normally lower than the contribution of these contacts to the critical state stresses.

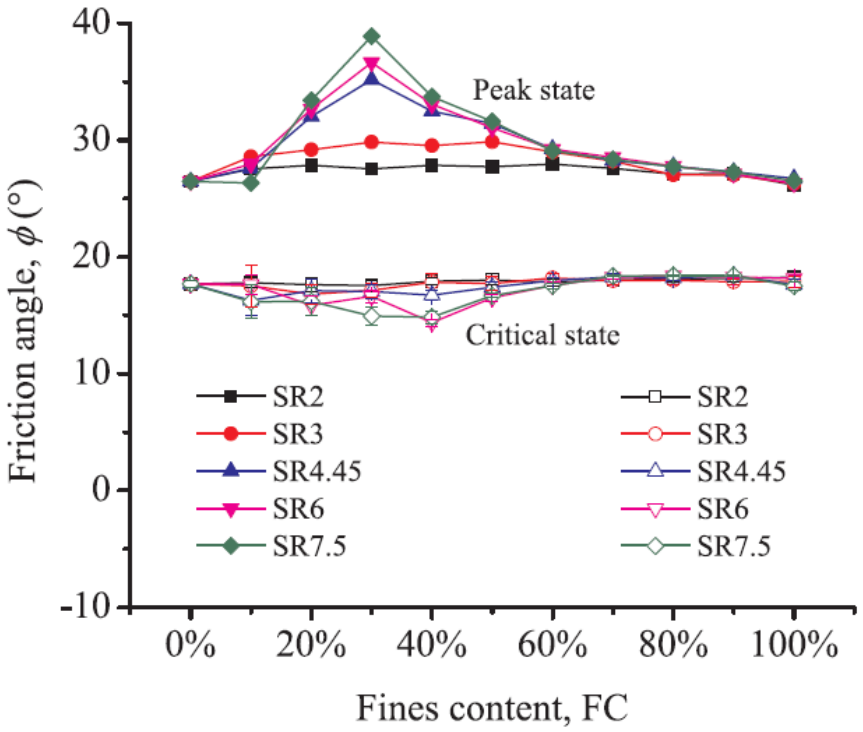


Figure 2.20: Relationship between the friction angle and F_{finer} (Zhu et al., 2020)

2.3.3. Small-strain stiffness

Gong et al. (2019) studied the G_0 of gap-graded soils using DEM simulations. They estimated G_0 from the initial elastic stage of drained triaxial tests. The state-dependency of G_0 for their gap-graded soils is reflected in the dependency of G_0 on F_{finer}. Their studies also highlighted the significant effect of Z on G_0. In general, at a given effective confining pressure, they found that G_0 decreases with increasing F_{finer} (Figure 2.21). This tendency is similar to that observed in experimental tests (e.g. Yang & Liu, 2016). They proposed that finer grains start to provide significant contributions to the force chain and G_0 with increasing F_{finer}.

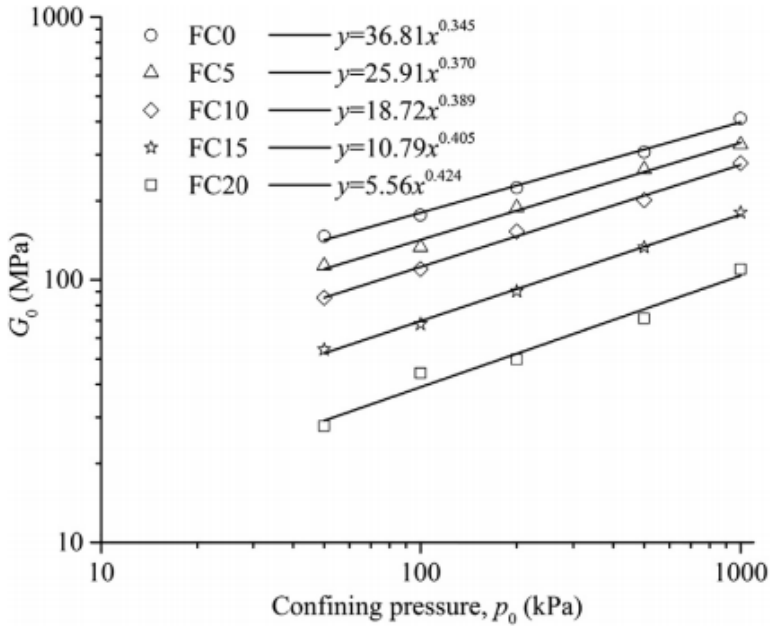


Figure 2.21: The G_0 of various specimens at a similar initial void ratio (e = 0.577) versus the confining pressure on a double log scale (Gong et al., 2019)

Otsubo et al. (2019) studied the G_0 of gap-graded soils using DEM simulations and laboratory experiments where they systematically varied F_{finer}. Both their DEM and their experimental data indicated that at low F_{finer} (<30%), the G_0 of gap-graded specimens decreases with increasing F_{finer}, as illustrated in Figure 2.22. The $G_{sta}/F(e)$ values they reported were quantified through small strain triaxial probes, while the $G_{dyn}/F(e)$ data were obtained through bender element tests. As F_{finer} increased from 30% to 35%, a substantial increase in G_0 was identified, as illustrated in Figure 2.22.

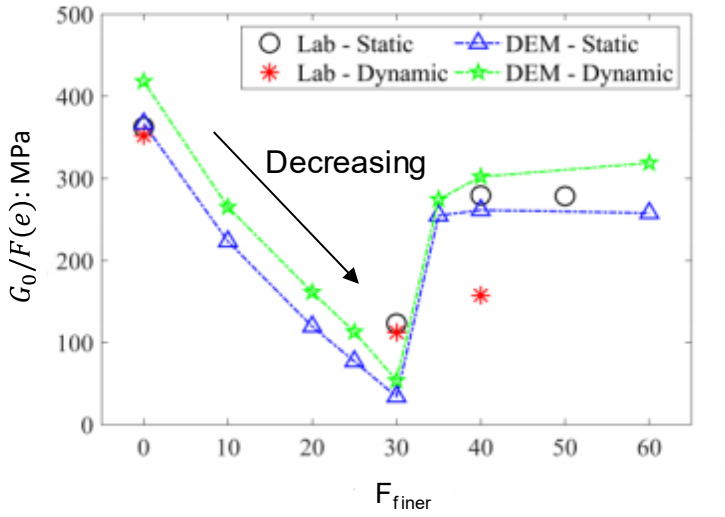


Figure 2.22: The effect of F_{finer} on G_0 for soils mixtures (Otsubo et al., 2019)

Otsubo et al. (2021) also studied the small-strain stiffness G_0 of soil mixtures using both experiments and DEM simulations. They explored whether the percentage of active finer particles could be identified using laboratory geophysics by using the phenomenon that granular materials act as a filter that removes the high-frequency components of applied seismic waves. The low-pass frequency (f_{lp}) is the maximum frequency that can be transferred by granular material. They recognised that this f_{lp} is dependent upon particle size, void ratio and confining pressure. They also found that when the proportion of active finer particles is increased, the low-pass frequency (f_{lp}) increases suddenly since a significant amount of stress is transferred by those finer particles (Otsubo et al., 2021). The relationship between f_{lp} and F_{finer} observed by Otsubo et al. (2021) is shown in Figure 2.23. They considered two SR values (GN and GW) and three different packing density levels. Their data showed that f_{lp} tends to increase with increasing F_{finer}.

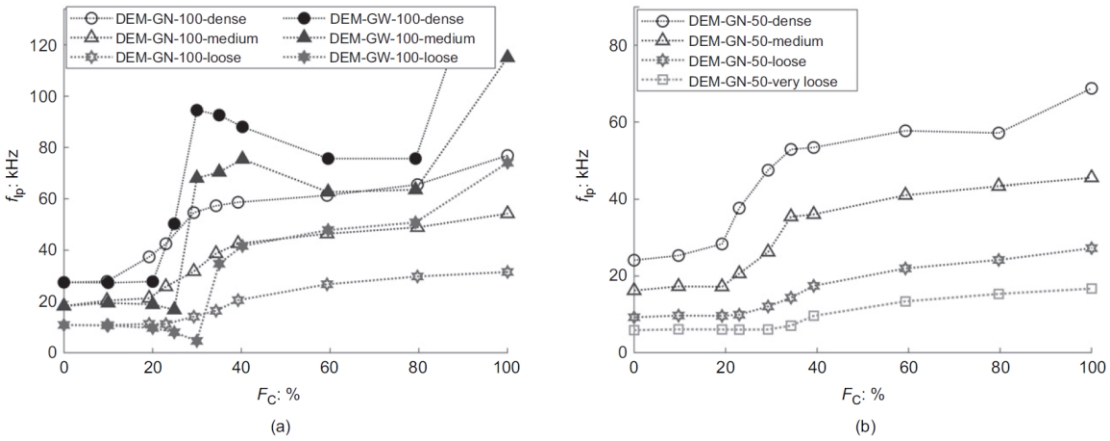


Figure 2.23: Relationship between f_{lp} and F_{finer}: (a) $p' = 100\ kPa$; (b) $p' = 50\ kPa$

Otsubo et al. (2021) employed their DEM observations and propose a method where the experimental data can be used to identify the contribution of the finer particles to stress transmission within the specimen. Figure 2.24 shows the link between f_{lp} and V_s as well as the nature of the material fabric.

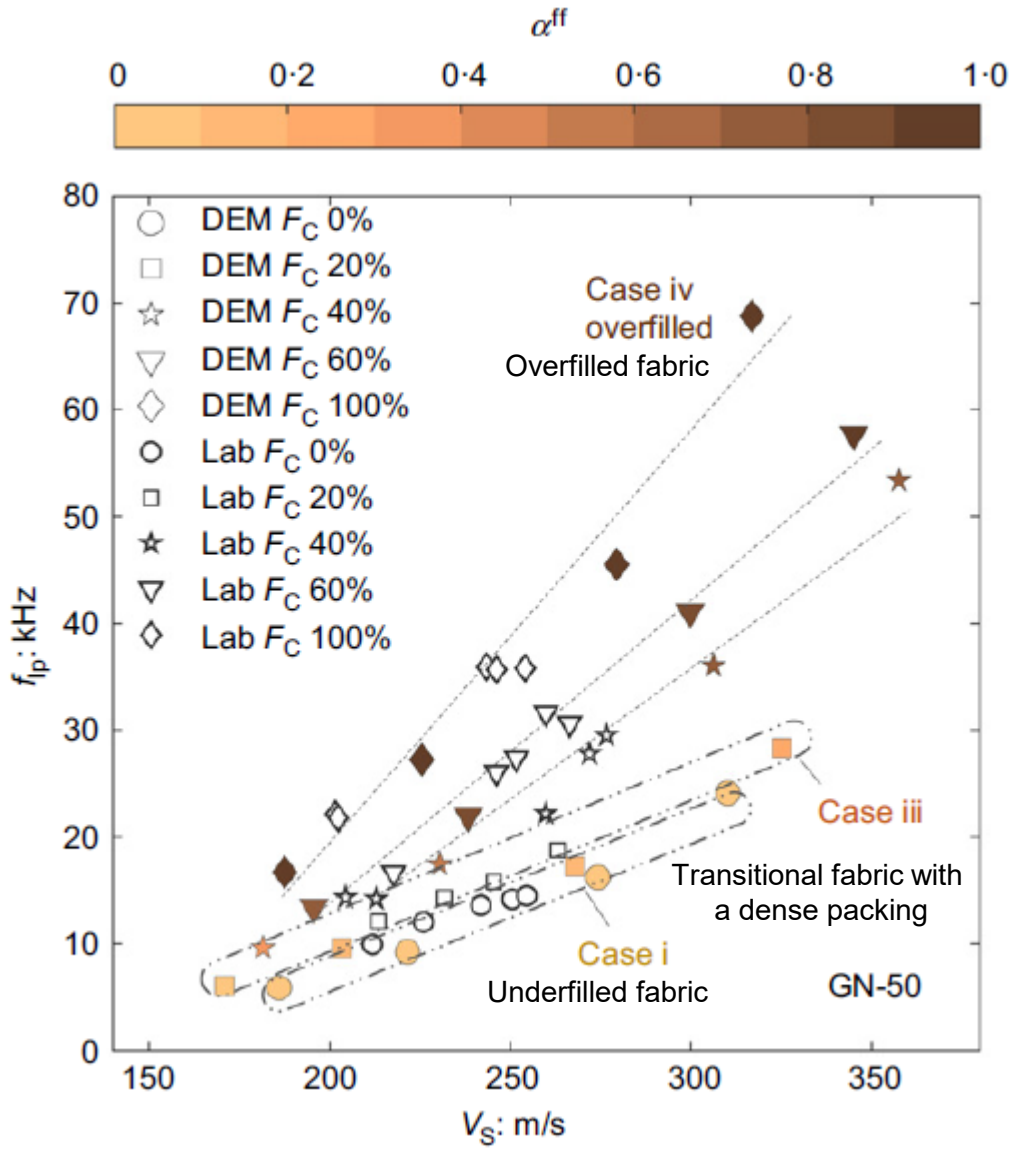


Figure 2.24: Relationship between f_{lp} and V_s for combined DEM and experimental data for GN samples at $p' = 50\ kPa$

The α_{ff} values proposed by Otsubo et al. (2021) are shown in Figure 2.24, which represents the proportion of the stress transferred by the finer-finer contacts:

$$\alpha^{ff} = \frac{V}{V_f} \frac{\sum_{k=1}^{N_{p,finer}} (\bar{\sigma}_{ff}^{k} V^{k})}{\sum_{k=1}^{N_p} (\bar{\sigma}^{k} V^{k})} \qquad 2.25$$

where V^k is the volume of particle k, V_f is the volume of finer fraction, V is the total volume. $N_{p,finer}$ is the total number of finer particles and N_p is the

total number of particles. $\bar{\sigma}_{ff}^{k}$ is the mean stresses carried by the finer-finer contacts involving particle k. $\bar{\sigma}^{k}$ is the mean stresses from all contacts acting on particle k. Otsubo et al. (2021) showed that the $f_{lp} - V_s$ relationship is strongly dependent on α_{ff}, which in turn depends on both packing densities and F_{finer}.

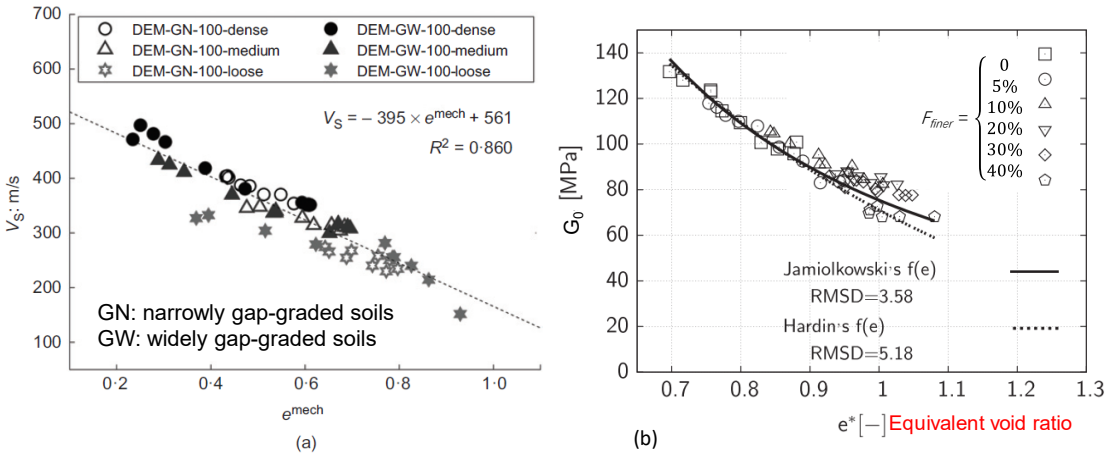


Figure 2.25: Relationship between V_s and packing properties observed in DEM simulations: (a) Mechanical void ratio; (b) The equivalent void ratio (modified from Otsubo et al., 2021 and Goudarzy et al., 2017)

Referring to the selection of appropriate state variables, Otsubo et al. (2021) showed that there is a strong correlation between V_s and e_m (Figure 2.25(a)), indicating that it is more appropriate to use e_m to describe the mechanical behaviour of gap-graded soils than e. They proposed that although e^* (Figure 2.25(b), Equation 2.7), does not directly correspond to e_m, the idea of using new effective state variable to replace the global void ratio, e is appropriate for gap-graded soils.

Prior DEM studies (e.g. Yang & Liu, 2016; Otsubo, 2016) have shown that the G_0 of granular materials is strongly associated with their coordination number, Z. However, it is difficult to directly measure the Z values in experimental tests. In contrast, e is generally used in practice as the state variable to describe the

mechanical behaviour of granular materials. Therefore, some studies have tried to establish a relationship between Z and e, followed by estimation on G_0 from this relationship. However, even for a monodisperse and uniform packing, several different relationships between Z and e exist (Otsubo, 2016). For instance, Gotoh (1978) used mathematical considerations to build a relationship between Z and e:

$$\mathrm{Z} = 20.7\left(\frac{1}{1+e}\right) - 4.35 \; (0.429 < e < 1.13) \qquad 2.26$$

Ouchiyama & Tanaka (1980) used an analytical method to derive an expression between Z and e, as illustrated:

$$\mathrm{Z} = \frac{32}{13}\left[7 - 8\left(\frac{1}{1+e}\right)\right] \qquad 2.27$$

By studying a mono-sized random packing, Suzuki et al. (1981) proposed a relationship between Z and e with an introduction of fitting constant value Su_b.

$$Z = 2.828\frac{(1+e)^{1/3}}{\left(\frac{Su_b}{d^p}\right)^2\left\{1+\left(\frac{Su_b}{d^p}\right)^2\right\}} \qquad 2.28$$

where d^p is the grain diameter. Using DEM simulations, Zhang et al. (2001) simulated several specimens with various initial states by changing simulation parameters such as the damping coefficient. They proposed the following expression:

$$\mathrm{Z} = \left[0.183 - 659.2\left(\frac{1}{1+e}\right)^{20.96}\right]^{-1} \qquad 2.29$$

It can be seen that these studies did not include the effect of effective confining stress in their analysis. In contrast, Makse et al. (2000) focused on the effect of

effective confining stress on the $Z-e$ relationship and indicated a complex effect of stress level on this relationship. Barreto & O'Sullivan (2012) studied the evolution of $Z-e$ relationship for a true-triaxial loading condition and they showed that there is not a unique relationship between Z and e even in the case of monodisperse materials. For soil mixtures, the interaction amongst coarser and finer grains is much complex compared to these uniformly sized materials. A unique correlation between Z and e for soils mixtures is not likely. In addition, although several studies (e.g. Gu et al., 2013) have indicated that the G_0 of their continuously graded packing is determined by its corresponding Z value, this proposed relationship may not be appropriate for soil mixtures. In the case of soil mixtures, different contact types can be identified such as the contact between coarser grains and coarser grains and the contact between finer grains and finer grains. While each of these types of contact have the same contribution to the material's Z value, the contribution of each contact type to G_0 remains uncertain.

Apart from soil mechanics, DEM is also used within broader granular mechanics communities for gap-graded materials. For instance, Tunuguntla et al. (2017) employed DEM to compare the efficiency of several theoretical continuum models which are used to predict particle segregation in the size-based bidisperse granular flows over inclined channels. Petit et al. (2020) applied the DEM method to study the jamming transition at packing fraction in granular matter and proposed that an addition discontinuous transition, upon compression, inside the jammed regime for an asymmetric bidisperse granular packing. It can be seen that this DEM has been widely used in a large range of subjects.

2.4. Summary

This Chapter has presented a review of experimental and DEM studies of the

mechanical behaviour of gap-graded materials. The experimental studies considered have studied the shearing behaviour and the small-strain behaviour of soil mixtures. The key challenge which emerges from all of the experimental studies is how to capture or quantify the relative contribution of different grains in a soil mixture to the overall behaviour. Several state variables such as, e_{sk} and e_m have been proposed as summarized in this Chapter. This Chapter has also considered the methods used to quantify the G_0.

The DEM studies considered here focused on isotropic compression, shearing behaviour and small-strain behaviour of soil mixtures. Due to the fact that simulating the mechanical behaviour of soil mixtures requires much more computational resources. DEM studies of gap-graded soils are rare in comparison with studies of materials with uniform particle size.

Chapter 3. Methodology and research methods

3.1. Background to DEM

The discrete element method (DEM) is a numerical method that can simulate the mechanical behaviour of assemblies of particles by explicitly considering the particles and their interactions and this method is now widely applied in a number of research fields. As shown by O'Sullivan (2019) and O'Sullivan et al. (2021) for Figure 3.1(a) and (b), respectively, since the mid-1990s there has been a rapid increase in the number of published papers whose keyword includes DEM. In addition, there is also a high rate of growth in DEM-related research in scientific research in general (Figure 3.1(b)). The DEM algorithm was proposed by Cundall & Strack (1979) and the paper outlining this algorithm has become the most highly cited paper in Géotechnique.

This study employs an in-house modified version of the Large-scale Atomic/Molecular Massively Parallel Simulator ($LAMMPS$) code (Plimpton, 1995), the main features of this code are introduced in this Chapter.

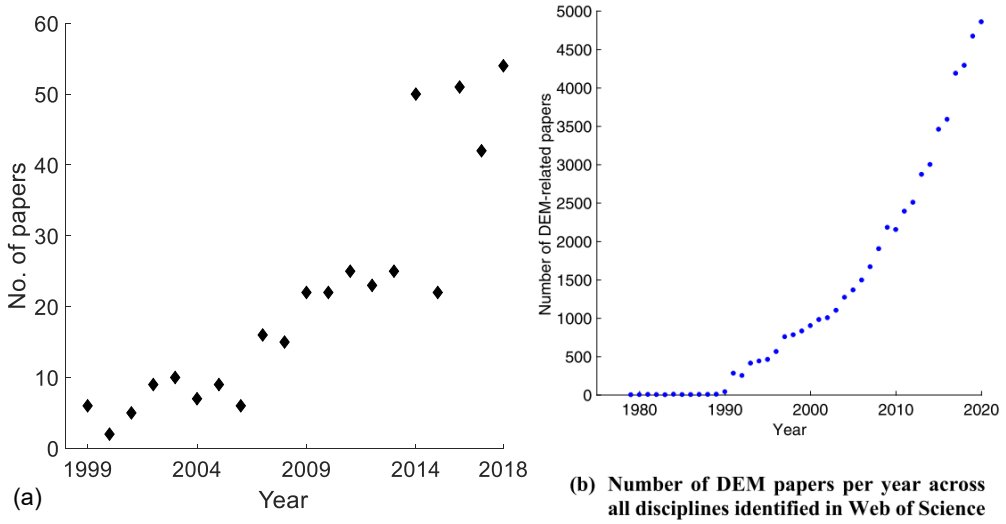


Figure 3.1: Number of DEM-related papers per year (O'Sullivan, 2019; O'Sullivan et al., 2021)

$LAMMPS$ was originally developed as a molecular dynamics (MD) code. Molecular dynamics is a numerical method that can simulate the interaction of atoms and molecules. $LAMMPS$ was released and is maintained by staff at the Sandia National Laboratories in the US. One of the key characteristics of the $LAMMPS$ code is the capability to run simulations on distributed or shared-memory, multi-processor computers. The parallel implementation of LAMMPS is achieved through the Message Passing Interface (MPI). MPI is a standardized means of exchanging messages between multiple computers and running a parallel program across distributed memory. $LAMMPS$ therefore can be used on both massively parallel high-performance machines and multi-core desktop computers. Furthermore, $LAMMPS$ can also run on just one core.

As outlined in prior studies (e.g. Huang, 2014; Otsubo, 2016), a spatial-decomposition technique is adopted when a $LAMMPS$ simulation is run on multiple processors. As illustrated in Figure 3.2, the whole simulation domain can be divided into several subdomains (4 subdomains in Figure 3.2a and 16 subdomains in Figure 3.2b). Each of the subdomains is assigned to a single processor (node). Key characteristics such as the contact force calculation and integration of motion of particles within these subdomains are calculated by the relevant assigned processor. The key information about atoms on the border of two adjacent subdomains is communicated between the corresponding processors. The communication time between the corresponding processors can significantly influence the simulation time. The communication time increases as the number of subdomains increases. The computing capability of the individual processors also determines the simulation time.

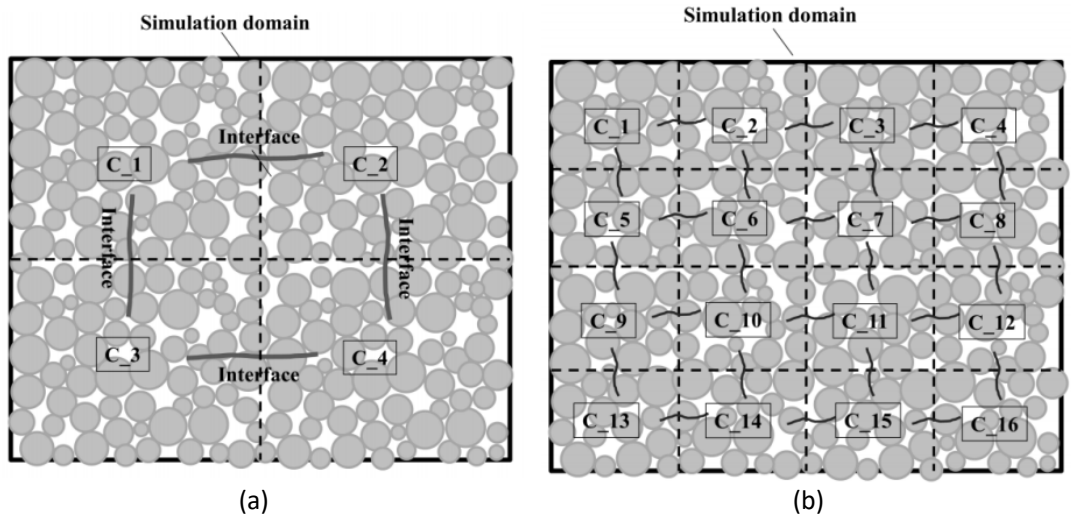


Figure 3.2: Schematic of the spatial-partition parallel technique for a $2D$ problem: The simulation domain is divided into (a) Four subdomains; (b) 16 subdomains (C denotes core) (modified after Huang, 2014)

A scaling test documented in O'Sullivan (2015) is presented here (Figure 3.3) as a reference to aid the understanding of readers. As illustrated in Figure 3.3, several scaling tests were conducted using the version of $LAMMPS$ used in this research on two UK national HPC machines. It can be seen that the simulation time for the same test does not linearly decrease with increasing number of processors; this is attributed to the fact that the communication time required to transfer amongst the neighbouring processors significantly increases as the number of processors increases. In this study, scaling tests were also conducted before actual studies, a representative example is illustrated in Figure 3.4 for a specimen of 82,598 spheres with a linear grading and a C_u of 4.5, subject to isotropic compression. All simulations were conducted on the high-performance computing facilities, $CX1$ at Imperial College London. The simulations were terminated after 50,000 timesteps. The time spent on the simulation and the ideal time cost (assuming that communication time is 0) were recorded as illustrated in Figure 3.4. These results agree with the scaling test illustrated in Figure 3.3. For instance, when 48 cores were applied, approximately 25.43 s is required to complete these

50,000 timesteps. In contrast, the ideally estimated time assuming linear scaling is approximately 6.7s, which is significantly lower compared to that of the actual simulation time. The influence of communication time is observed in this study. Additional scaling tests were also conducted for the following simulations so that the HPC facilities were efficiently used. As illustrated in Huang (2014), for maximum of 4 nodes with 48 cores, the currently used code is effective for parallel processing simulations, and the accumulated round-off errors caused by the communications are negligible. A direct comparison of serial and parallel simulations of the code found a negligible effect of partitioning effect on the overall response.

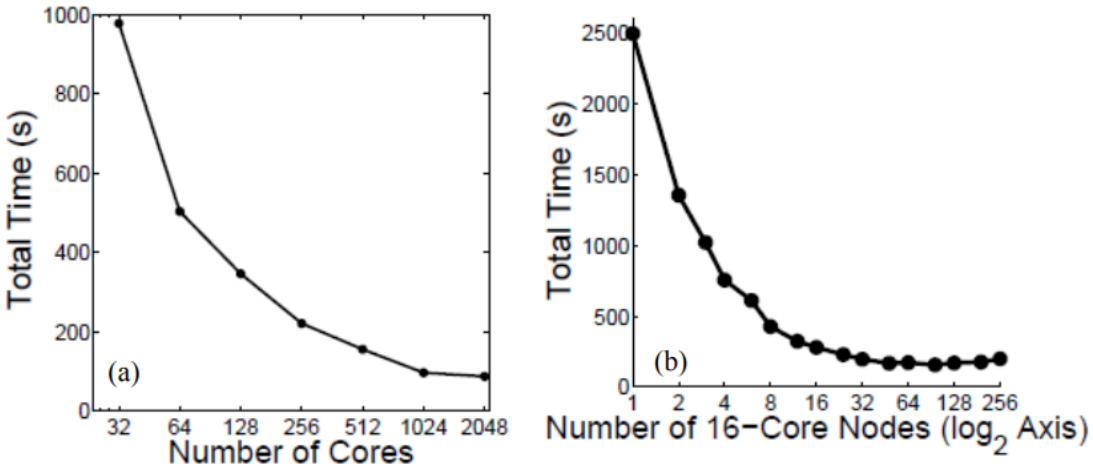


Figure 3.3: Scaling tests of the modified $LAMMPS$ code on the UK's national high-performance computing (HPC) facilities: (a) Triaxial compression simulation on a face-centred-cubic sample composed of 125,000 uniform spheres, run for 100,000 timesteps on HECToR Phase 3; (b) Constant volume simulation on a polydisperse sample comprising 351,248 spheres, run for 100,000-time steps on Hartree Blue Joule (O'Sullivan, 2014)

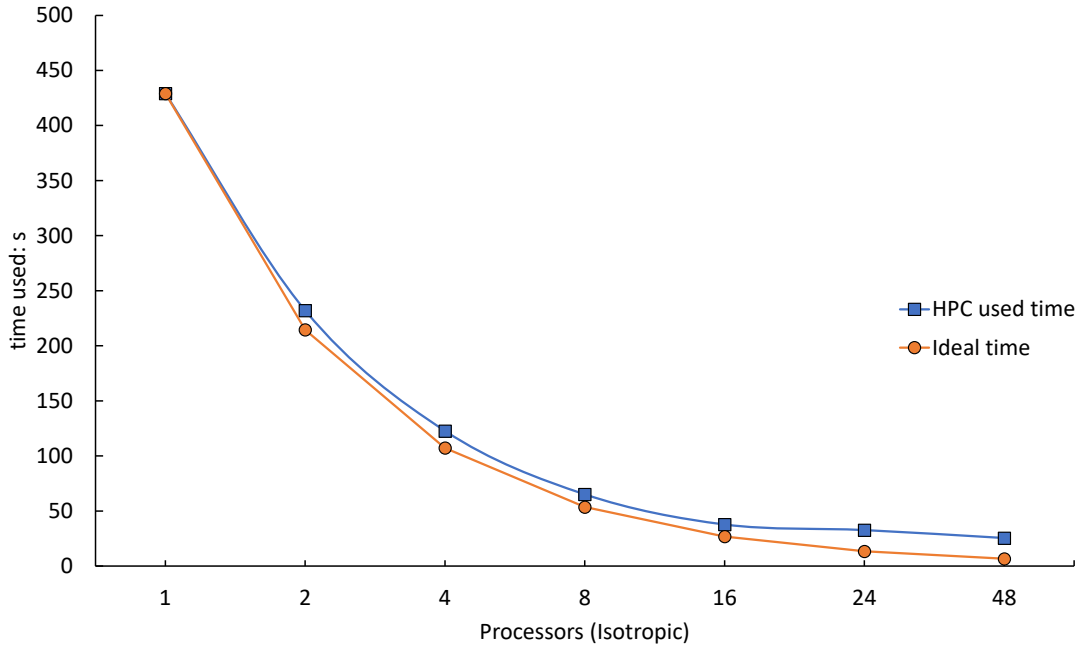


Figure 3.4: Scaling tests for a specimen with a linear grading considered in the current study (C_u of 4.5)

3.2. Introduction to DEM

In the DEM algorithm, Newton's second law is used to calculate the motion of each grain:

$$F_p = m(\ddot{x} - g) \quad 3.1$$

$$M_i = I\ddot{\varphi} \quad 3.2$$

where F_p is the force applied on an individual grain, m is the mass of an individual grain, $\ddot{x}$ is the acceleration of an individual grain, g is the gravitational acceleration (i.e. 9.8 m/s^2), M_i is the moment acting on an individual grain, I is the moment of inertia of an individual grain and $\ddot{\varphi}$ is the angular acceleration of the grain.

The DEM algorithm is presented in Figure 3.5. Pairs of contacting grains are identified; these rigid grains can overlap with each other. These overlaps simulate the deformation that occurs at the contacts between real, physical particles. In a DEM analysis the contact forces between contacting grains are

calculated in each timestep. At each contact point, the normal force (F_n) is calculated from the normal overlap (δ_n) of the two contacting grains and the stiffness in the normal direction (K_N):

$$F_n = K_N \delta_n \quad 3.3$$

In contrast to the calculation of normal contact forces, the tangential contact force (F_t) is calculated incrementally. The incremental tangential contact force (ΔF_t) is the product of the incremental tangential contact displacement (Δs) and the incremental tangential contact stiffness (K_T), as is illustrated below:

$$\Delta F_t = K_T \Delta s \quad 3.4$$

The tangential force is a summation of these increments. Note that maximum tangential contact force is limited to be the maximum sliding tangential contact force (i.e. $T^{max} = \mu F_n$). The rotations of the individual grains need to be considered when tangential contact forces are included in DEM, the moment applied is the product of F_t and lever arm.

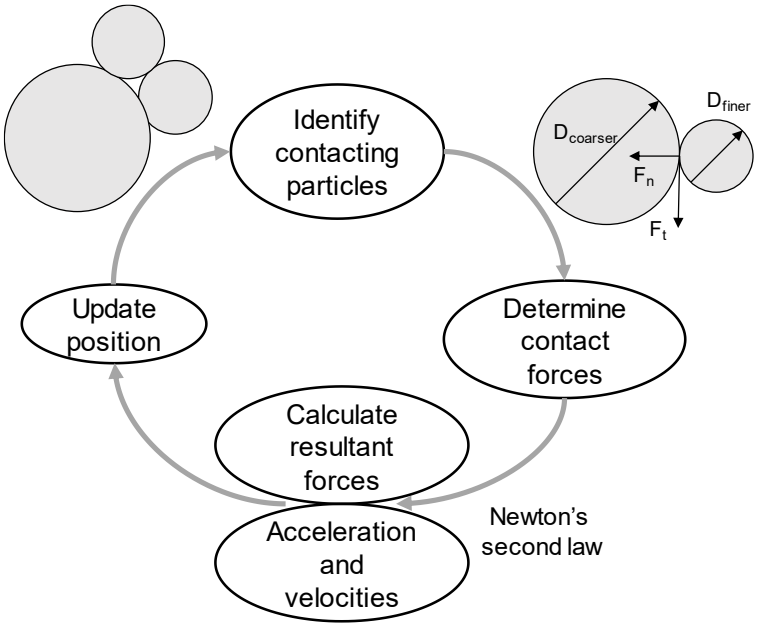


Figure 3.5: Calculation in each time step

Referring to Equations 3.1 and 3.2. the resultant forces and moments acting on the particles are used to calculate the translational and rotational accelerations,

followed by the updating of the grain positions for the next timestep. This process is also illustrated in Figure 3.5. As outlined in Hanley & O'Sullivan (2017), the second-order velocity-Verlet integration scheme has been adopted in this DEM code. This method is conditionally stable when the time increment used is less than a threshold value, which is called the critical timestep. As illustrated in Otsubo et al. (2017), several approaches such as the oscillation period of a single degree of freedom system, the Rayleigh wave speed and Gerschgorin's theorem have been introduced to determine the critical time step. However, in this study, the timestep is set up as auto, which is only related to the mass of the particle and is considered to be very conservative.

Hertz-Mindlin contact model

A simplified Hertz-Mindlin contact model was used in all the simulations presented in this study. In the contact normal direction, the simplified Hertz-Mindlin contact model calculates the normal force as:

$$F_n = \frac{4}{3} R^{*0.5} E^* {\delta_n}^{3/2} \tag{3.5}$$

where F_n is the contact normal force, δ_n is the normal displacement, i.e. the overlap at the contact point, R^* is given by $1/R = 1/R_1 + 1/R_2$, and R_1 and R_2 are the radius of the contacting particles, respectively. The relative Young's modulus, E_p^*, is given by

$$E_p^* = \left(\frac{1 - v_{p1}^2}{E_{p1}} + \frac{1 - v_{p2}^2}{E_{p1}} \right)^{-1} \tag{3.6}$$

where v_{p1} and v_{p2} are the Poisson's ratio for the two contacting particles, respectively. E_{p1} and E_{p1} are Young's modulus values for the two contacting particles.

The tangential forces are given as:

$$F_t = 8G_p^*\sqrt{R^*\delta_n}\delta_t \quad 3.7$$

where δ_t is the tangential displacement, G_p^* which is given as:

$$G_p^* = \left(\frac{2-v_{p1}}{G_{p1}} + \frac{2-v_{p2}}{G_{p2}}\right)^{-1} \quad 3.8$$

where G_{p1} and G_{p2} are the shear modulus of the two contacting particles.
The normal (incremental) stiffness (K_N) depends on the diameters of the contacting particles and the contact force, as follows:

$$K_N = 2E_p^*{R^*}^{0.5}{\delta_n}^{0.5} \quad 3.9$$

This contact model has been widely used in prior DEM studies (e.g. Otsubo et al., 2021; Sufian et al., 2021) and has proven to be effective in simulating the state-dependent soil behaviour of granular materials. The particle shear modulus, G_p, for all particles was 29.17 GPa and the particle Poisson's ratio, v_p, for all particles was 0.2, which follows prior studies and are similar to these experimental identified values (e.g. Huang et al., 2014).

Many of the simulations described in this thesis were carried out using periodic boundaries. Where a periodic boundary is used, the coordinates of particles close to a given periodic boundary are remapped to an equivalent position just outside the opposite periodic boundary. In this way, ideal boundary-free simulations can be carried out. When the system is deformed the periodic boundary positions are adjusted according to the global strain applied. Furthermore, the position of each particle in the system is adjusted according to the global strain field.

Referring to Thornton (2000), in a periodic cell, if the strain rate tensor applied

to the periodic cell is given by $\dot{\varepsilon}_{ij}$, then in a timestep Δt the incremental displacement of particle a due to the global strain field, Δx_i^a is $\Delta x_i^a = \dot{\varepsilon}_{ij} x_i^a \Delta t$, where x_i^a is the vector describing the location of particle a. This displacement Δx_i^a is added to the displacement calculated from consideration of the resultant force acting on each particle.

3.3. Verification of the DEM code used

As discussed above, the version of $LAMMPS$ used in this study was modified and maintained by Dr Kevin Hanley. Some of the key features of the currently used code were summarised in Huang (2014): (1) New control algorithms were added for periodic boundaries to apply both stress and strain-controlled simulations; (2) Particle rotations can be fixed by controlling the angular velocities before the calculation of the contact forces and moments. With these modifications, the verification of this code is important and therefore illustrated in this section. Note that most of the simulations conducted in this study consider only isotropic compression and small strain shearing (i.e. axial strain $\approx 5 \times 10^{-5}$). The large strain shearing simulations described in this section serve as a general validation for the code.

Several methods can be used to validate a DEM code. One of the most used validation methods is the analytical method proposed by Itasca Consulting Group (2007). In this study, the DEM code used was validated by an analytical solution derived for a face-centred cubic (FCC) packing of uniform spheres by Thornton (1979).

Figure 3.6 introduces the FCC packing, as illustrated in Figure 3.6(d), there are six contact points for a typical rigid grain in a FCC packing. Each contact is

matched on a contact located diametrically opposite it, as a result, a grain has a total of 12 contact points. Thornton (1979) showed that the most conservative failure mechanism of an FCC packing is identified by the loss of two sets of contacts at contact point T_P and U for triaxial loading. For the plane-strain loading, the failure mechanism of an FCC packing can be identified by the loss of either the T_P or U contacts.

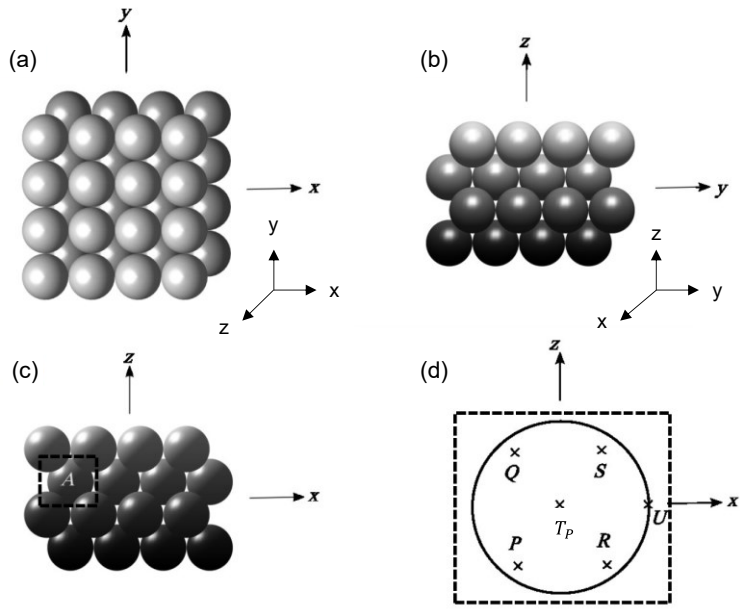


Figure 3.6: FCC packing of uniform spheres: (a) Plan view; (b) View from the x −direction; (c) View from the y −direction; (d) Contact distribution for a single grain (modified from Huang, 2014)

To estimate the stress tensor at failure for this FCC packing, Parkin (1965) proposed a strain-increment tensor S (Equation 3.10), which is used to calculate the stress tensor associated with the failure mechanism.

$$S = \begin{bmatrix} d\varepsilon_{xx} & d\varepsilon_{xy} & d\varepsilon_{xz} \\ d\varepsilon_{yx} & d\varepsilon_{yy} & d\varepsilon_{yz} \\ d\varepsilon_{zx} & d\varepsilon_{zy} & d\varepsilon_{zz} \end{bmatrix} = \begin{bmatrix} -2a_F & 0 & 0 \\ 0 & -2b_F & 0 \\ 0 & 0 & a_F + b_F \end{bmatrix} \qquad 3.10$$

Where $a_F + b_F = 1$, as shown in Parkin (1965), the term $(a_F + b_F)$ is the major principal strain increment at failure. The values of a_F and b_F indicate the ratio of the other two principal strain increments. Therefore, in triaxial compression conditions with $\sigma_2' = \sigma_3'$, a_F = b_F = 0.5. In a plane strain loading condition, a_F

= 0 or b_F = 0. In this study, both the triaxial loading condition and the plane strain loading condition were studied.

Based on the strain-increment tensor in Equation 3.10, Parkin (1965) calculated the average stress tensor of FCC packing for a triaxial loading condition and a plane strain loading condition. For a triaxial loading condition, the peak stress ratios are calculated as given in Equation 3.11 and Equation 3.12.

$$\frac{\sigma'_{zz}}{\sigma'_{xx}} = \frac{2 + \frac{2\mu}{F_{Pa}}}{1 - \frac{2a_F\mu}{F_{Pa}}} \qquad 3.11$$

$$\frac{\sigma'_{yy}}{\sigma'_{xx}} = \frac{1 - \frac{2b\mu}{F_{Pa}}}{1 - \frac{2b_F\mu}{F_{Pa}}} \qquad 3.12$$

where $F_{Pa}=\sqrt{\frac{3}{2}\left(\mathrm{a_F}^2+\mathrm{b_F}^2\right)+\mathrm{a_F b_F}}$, μ is the inter-particle friction coefficient of the FCC packing. For a plane strain loading condition, the peak stress ratios can be calculated as given in equation 3.13.

$$\frac{\sigma'_1}{\sigma'_3} = \frac{2 + \frac{2\mu}{F_{Pa}}}{1 - \frac{2\mu}{F_{Pa}}} \qquad 3.13$$

where $F_{Pa} = 3/2$, σ'_1 and σ'_3 are the major and minor principal effective stresses, respectively. Analytical solutions show that the peak stress ratios for the FCC packing depend upon the inter-particle friction μ and the combination of a_F and b_F (i.e. the loading conditions, triaxial or plane strain).

For both plane strain and triaxial loading conditions, an FCC packing of 7776 rigid spherical grains (Figure 3.7) was compressed to an isotropic mean effective confining pressure (i.e. 500 kPa), followed by shearing simulations. For the plane strain loading condition, the position of one pair of the horizontal

boundaries normal to the x axis was fixed and the stress in the y direction was maintained constant. For the triaxial loading condition, the normal stresses in the x and y directions were fixed and kept equal, a constant strain rate was applied in z direction to simulate shearing. Various μ values were used to systematically verify the DEM code.

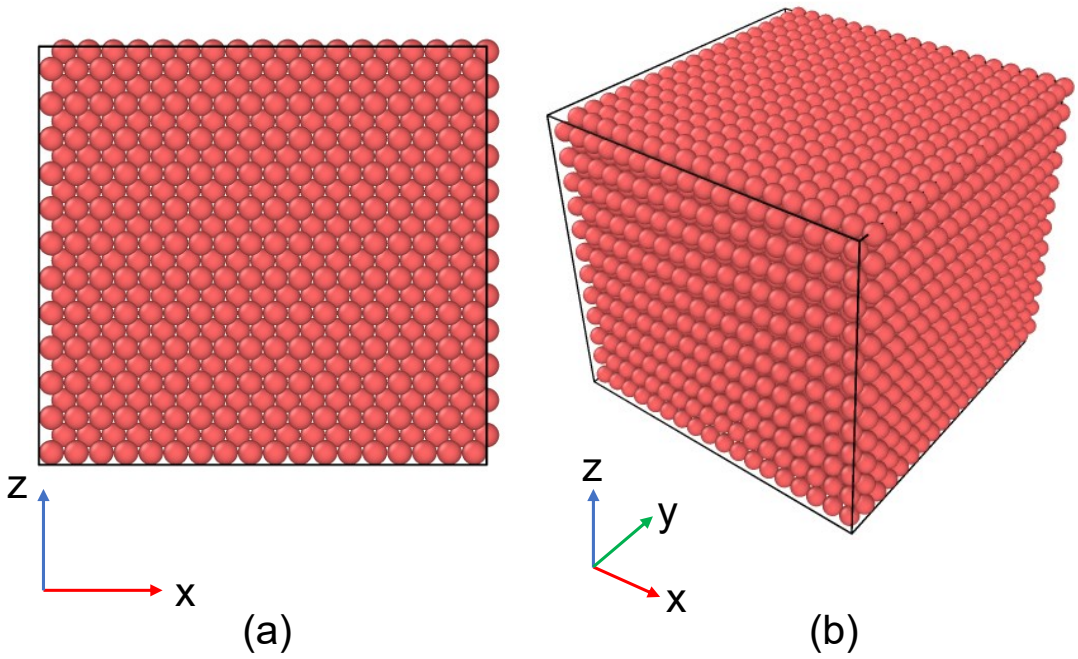


Figure 3.7: Schematic drawing of a FCC packing of 7776 spherical grains: (a) Front view; (b) $3D$ view

3.2.1. Plane strain loading condition

One typical set of data for shearing of the FCC packing under plane strain conditions is shown in Figure 3.8 for the case with μ equal to 0.2. Figure 3.8(a) illustrates the evolution of stresses in x, y, z direction, the stress in the $x-$direction is 500 kPa, whereas the stresses in the y and z directions increased gradually with increasing axial strain (displacement in z direction). When the axial strain was approximately 0.093%, both the stresses in y and z directions reached a maximum value and failure was judged to occur. This failure is associated with a decrease in the coordination number (Z), these

failure points are close to the peak points. Figure 3.8 (b) shows the evolution of stress ratios (i.e. σ_{zz}/σ_{xx}), the peak stress ratio is approximately 3.45, which is same as the analytical solution calculated based on equation 3.13. Figure 3.8(c) illustrates the evolution of coordination number (Z). Z decreases from 12 to 10 suddenly when the axial strain is approximately 0.093%, this point can be identified as the failure point for this FCC packing. Figure 3.8(d) and Figure 3.8(e) illustrate plan views of the contact force network before and after failure, respectively. Each line illustrated in Figure 3.8(d) and Figure 3.8(e) is a link between two contacting grains, and the thickness of the line is proportional to the magnitude of the normal contact forces normalised by the average normal contact forces. The results show that two contacts are lost when this FCC packing reaches the failure point, which is also the same as the analytical solution. Note that this FCC packing may not be representative of real sand behaviour because of the uniform, lattice packing. This packing is studied to verify that this DEM code is capable of getting the same results as those predicted from theoretical calculations.

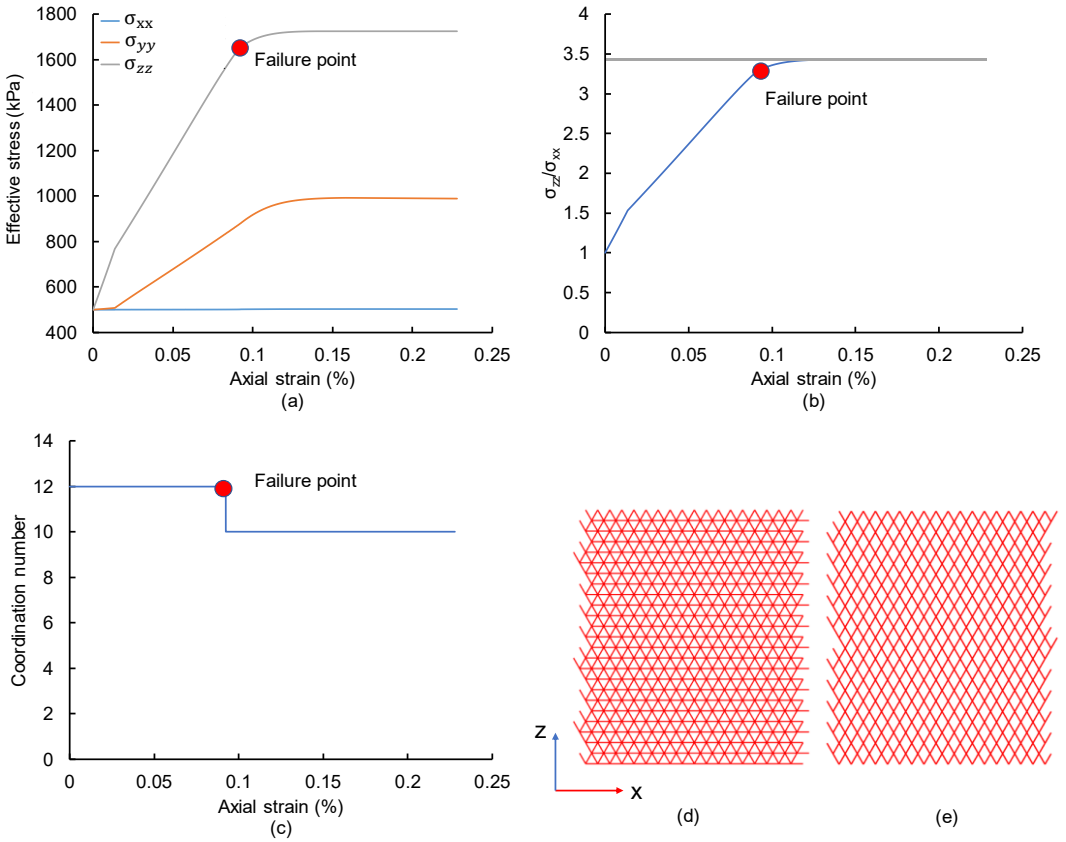


Figure 3.8: FCC validation simulation for a plane strain loading condition (μ = 0.2) (against theoretical solution): (a) Principal stresses; (b) Stress ratio; (c) Coordination number; (d) Contact force network before failure; (e) Contact force network after failure of another slice

3.2.2. Triaxial loading condition

Figure 3.9 illustrates typical shearing behaviour for the FCC packing under a triaxial loading condition compression along z direction with μ equal to 0.2. Figure 3.9(a) shows that both stresses in x and y direction are constant, and the stress in z direction increases gradually and attains a peak when the axial strain is approximately 0.92%. Figure 3.9(b) illustrates that the measured stress ratio (i.e. σ_{zz}/σ_{xx}) is approximately 3, which is same to that of analytical solution. Figure 3.9(c) illustrates that Z drops from 12 to 8, which is also same as is given by the analytical solution. In order to systematically verify the DEM code, various μ (i.e. 0.1, 0.2, 0.3, 0.4, 0.5, 0.6) were used in DEM simulations to compare the simulated results to those of analytical solutions. Figure 3.10 illustrates that simulation results are same to analytical solutions for different μ.

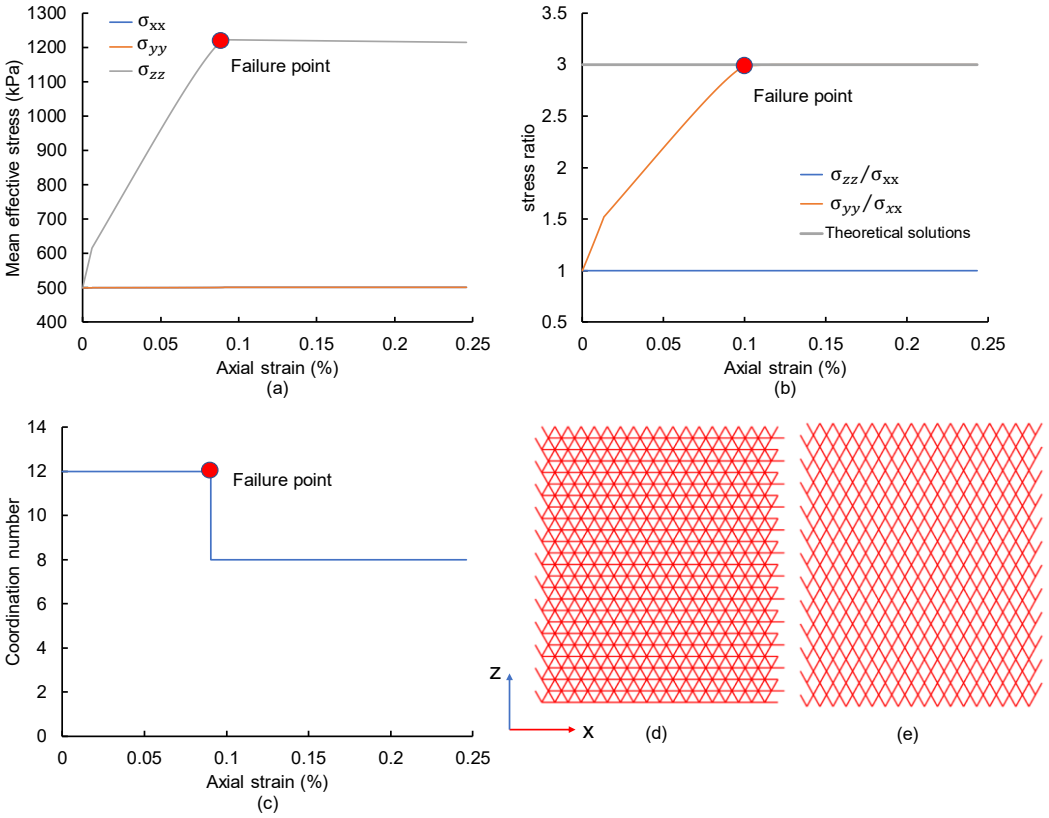


Figure 3.9: FCC validation simulation for a triaxial loading condition (μ = 0.2) (against theoretical solution): (a) Principal stresses; (b) Stress ratio; (c) Coordination number; (d) Contact force network before failure; (e) Contact force network after failure of another slice

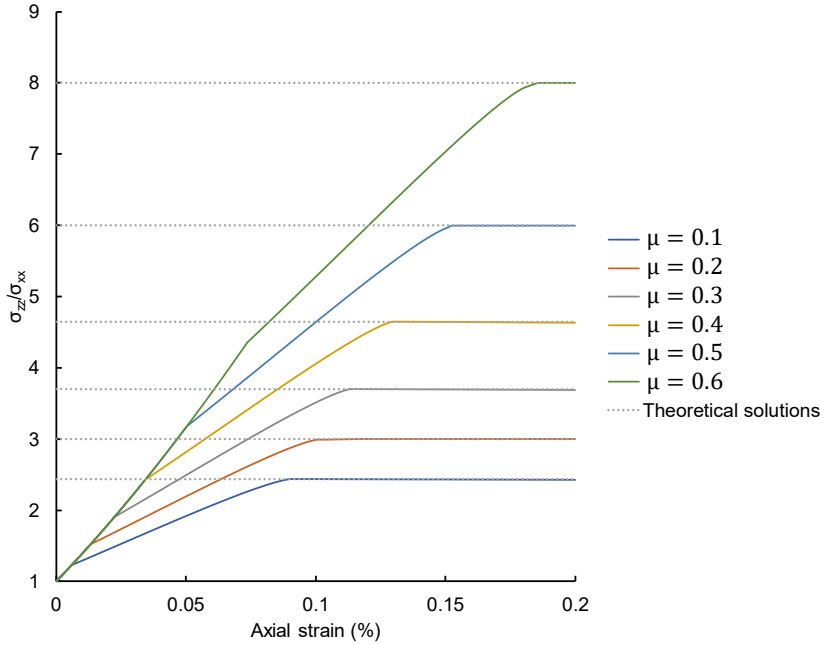


Figure 3.10: Validation simulations of triaxial loading conditions with various μ

3.4. DEM setup

For the simulations conducted in this study, two sets of boundary conditions were applied depending on the simulation objectives. In all cases, the numerical specimens were subjected to isotropic compression, followed by either shear wave propagation simulations or small strain shearing simulations. Specimens with a range of $PSDs$ were created depending on the requirement of the particular research question. Therefore, in this section, the details of the particular particle size distributions considered in each parametric study are described in the relevant chapters. Here general features, common to all or any of the simulations are presented.

The particles were initially placed randomly in diffuse (non-contacting) positions through an in-house placement code, then the generated specimens were subject to isotropic compression to the specified mean effective stress p'. For the isotropic compression stage, to make sure that the simulations reached a point where they were stable, the coordination number, Z (the average value of contacts per grain) was confirmed to be constant (i.e. any variation was less than 0.001) for approximately 500,000 simulation cycles before termination. Then, data were extracted for analysis or further simulations (e.g. small strain probe tests).

Following Shire et al. (2014), to investigate the effect of packing density, three inter-particle friction coefficients (μ) were used during isotropic compression: (1) “dense” specimens were created with μ = 0.001; (2) “medium-dense specimens” were created with μ = 0.1; (3) “loose” specimens were created with μ = 0.3. it is common practice for people to control the packing densities by this method for DEM study. This method allows for a consistent creation of different packing configurations. However, the “loose” and “dense” specimens created

in this program do not directly correspond to experimental lab specimens with relative packing densities of 0% and 100%, respectively. In addition, the "medium-dense" specimens also cannot be associated with a specific relative density. The method used here is highly idealized, so that the complexity and heterogeneity of real soil particle morphologies are neglected and fabric effects which occur in any physical experimental tests are not considered. For instance, it is widely accepted that particle shape has a significant effect on granular material packing density (e.g. Cho et al., 2006; Youd, 1973; Zhao et al., 2018a; Zhao et al., 2018b). This study focused on spherical particles to enable a large number of specimens with different $PSDs$ to be considered as simulations with non-spherical particles are computationally more expensive. Consequently, the range of attainable void ratios is narrower than is the case for a natural sand with more irregular particle morphologies, e.g. Cho et al. (2006), and varies with specimen PSD. This study also has excluded from consideration the effect of other factors, such as the particle roughness which certainly affect the mechanical behaviour of a granular material. In addition, all simulations involve isotropic compression, followed by either shear wave propagation simulations or small-strain behaviour (i.e. shear strain $< 10^{-5}$) simulation, therefore the effects of the evolution of soil fabric when subject to relatively large shear deformation were not be considered in this program. Chapter 4 and 5 present the results following the compression stage only, while Chapter 6 shows the results of the shear wave propagation and small-strain shearing behaviour.

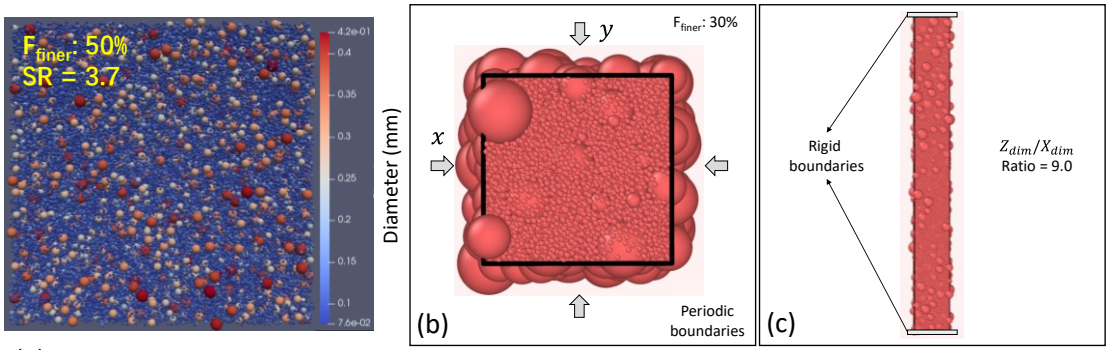
3.4.1. Numerical simulation approach (purely periodic boundaries)

In some of the simulations, all the boundaries to the virtual specimens were periodic, and the specimens were cubic. Periodic boundary conditions were employed in the x, y and z directions to remove boundary effects (e.g. Thornton, 2000; Shire et al., 2014). The dimensions in the x, y and z

directions are similar for these specimens. An example of created specimen (F_{finer} of 50%, SR = 3.7) is illusrated in Figure 3.11(a)

3.4.2. Numerical simulation approach (mixed boundaries)

For the specimens with mixed boundaries, the same version of $LAMMPS$ was used with the simplified Hertz-Mindlin contact model and the same particle parameters (e.g. G_p = 29.17; ν_p = 0.2). To enable both G_{dyn} and G_{sta} to be obtained on identical specimens, the numerical specimens considered had a cuboidal shape. The lateral boundaries, i.e. the $x-$ and $y-$ directions were periodic, rigid boundary boundaries were used at the top and bottom of the specimens to enable shear wave velocity measurements, as illustrated in Figure 3.11(b&c), the length in the z direction, Z_{dim} is approximately 9 times the length in the x direction, X_{dim}. The specimen elongation was required to ensure the specimen dimensions exceeded the wavelength of the propagating shear waves and was selected following Otsubo (2016). The in-house placement code referred to above was used to create all the mixed boundary specimens. As before, three inter-particle friction coefficients, μ (i.e. 0.001; 0.1; 0.3) were used to prepare the “dense”, “medium-dense” and “loose” specimens. After the compression stage, either small-strain shearing simulations or shear wave propagation simulations were conducted to obtain both G_{sta} and G_{dyn}, respectively.



(a)

Figure 3.11: Examples of specimens created under periodic boundaries and mixed boundaries: (a) Periodic boundary; (b) Mixed boundary (periodic boundaries in x and y directions); (c) Mixed boundary (rigid boundaries in the z direction)

3.5. Summary

This Chapter introduced the DEM code used. An overview of a verification study was presented. For both plane strain and triaxial loading conditions, the theoretical solutions were employed to verify the simulation results for FCC packings. The simulated stress ratios σ_{zz}/σ_{xx} for all simulations agree with these estimated from theoretical solutions. For the setup of DEM, the key features, such as the selected boundary conditions, the used inter-particle frictions and the particle parameters were also introduced.

Chapter 4. Influence of inactive particles on quantifying the state of granular materials

4.1. Introduction

It is widely accepted that the use of the global void ratio, e and bulk density, ρ as measures of state may not be effective in frameworks to predict the mechanical behaviour of gap-graded soils since the finer fraction may not transfer any stress. However, few studies have systematically explored this issue for a wide range of gradings. Developing upon ideas put forward in the prior studies which have explored the idea of an effective void ratio for gap-graded soils, this Chapter examines this issue for a broad range of particle size distributions through DEM.

The global void ratio, e, and the bulk density, ρ, are measures of granular materials state that are routinely used to interpret data and predict soil behaviour. Considering the conceptual diagrams of soil presented, for example, in undergraduate textbooks, there is an implicit understanding that the entire particle phase of the soil is engaged in stress transmission and that changes in packing density relate to variations in the way contacting particles are arranged.

When interpreting laboratory geophysics tests the shear wave velocity, V_s, and the small-strain (elastic) shear stiffness, G_0, are related as

$$G_0 = \rho V_s^2 \qquad 4.1$$

Equation 4.1 was derived assuming a homogeneous elastic continuum material. Using discrete element method (DEM) simulation data. Nguyen & O'Sullivan (2019) compared dynamic shear stiffness values deduced from simulations of wave propagation tests with static shear stiffness values obtained from stress probes. For the ideal isotropic, monodisperse specimens they considered the

two stiffness values should be similar if equation 4.1 is valid, however, this agreement was only observed for the denser specimens they considered. Experimental verification of equation 4.1 is non-trivial; Lings (2001) showed that the shear stiffnesses obtained from a small-strain probe in a triaxial cell, G_{sta}, does directly not correspond to either G_{zx} or G_{xz}. Using horizontally mounted piezoceramic shear plates, Dutta (2019) experimentally noted that the extent to which static and dynamic measurements agree seems to depend on the specific material considered.

Various so-called void ratio correction functions $F(e)$ have been proposed in the literature to describe the expected variation of G_0 with packing density. Amongst other expressions, $F(e)$ may be estimated by equation 4.2 (Hardin and Black, 1966).

$$\mathrm{F(e)} = \frac{(\mathrm{c} - \mathrm{e})^2}{1 + \mathrm{e}} \qquad 4.2$$

where c is empirically assessed to be 2.97 for angular sands and 2.17 for rounded sands. This expression and the other expressions documented in the literature, are empirical and lack a fundamental mechanical basis. As outlined in Mitchell & Soga (2005) and Otsubo (2016), effective medium theory, whether adopting a static or kinematic hypothesis, indicates that density effects should be accounted for by considering both e and coordination number, Z, (i.e. the average number of contacts per particle) (e.g. Chang & Liao, 1994). Moreover, this relationship may be significantly affected by particle size distributions (e.g. Zhao et al., 2020). Based on empirical analysis of stiffness data obtained from discrete element method (DEM) simulations on virtual specimens of soil, Nguyen et al. (2018) highlighted the challenge of developing a correction function including e and Z that can be applied for a range of anisotropic stress states.

While DEM simulations consider ideal model soils, the data generated can include the individual particle stresses and the forces between contacting particles. Consequently, DEM can be used to directly quantify the relative contribution of each particle to stress transmission and so inform the general understanding of stress transmission in soil. Numerous DEM studies have identified the existence of particles that do not transmit stress (often referred to as inactive particles) and suggested that analysis of the mechanical behaviour should exclude consideration of these particles from the solid phase of the material, e.g. Thornton (2000). Using DEM data, an alternative state variable, the mechanical void ratio, e_m, can be determined (Otsubo, 2016). In the case of gravity-free DEM simulations, this mechanical void ratio is calculated by considering grains with 0 or 1 contact points, which do not transfer stress, to be part of the void volume. Furthermore, fundamental studies of granular material stiffness (Yimsiri & Soga, 2000; Otsubo 2016) have indicated that there is a stronger correlation between G_0 and e_m than there is between G_0 and e.

Gap-graded soils are poorly graded soils that have a deficiency of certain particle sizes. The simplest gap-graded soils which have been considered in prior research are almost bimodal mixtures of non-plastic finer and coarser grains. Restricting consideration to non-plastic finer particles, these prior studies have often focused on the sensitivity of the mechanical behaviour to the proportion by mass of finer grains in the material (F_{finer}).

The possibility that some particles might not transmit stress has been explicitly recognised amongst experimental researchers in the case of gap-graded soils. Various state variables have been proposed to replace the conventional global void ratio, e, to capture the contribution (or lack of contribution) of finer grains to stress transmission. As discussed in Chapter 2, various state variables were proposed, such as skeleton void ratio, e_{sk}, equivalent void ratio e^*, mechanical

void ratio, e_m, granular void ratio, e_G.

While some studies (e.g. Rahman & Lo, 2008, Otsubo, 2016) have shown that their proposed state variables (e.g. e_m, e^*) may be more appropriate to describe the mechanical behaviour of gap-graded soils, others studies (e.g. Carrera et al., 2011; Yang et al., 2015) have indicated that e is still the most appropriate state variable for gap-graded soils. In particular, Yang et al. (2015) argued that neither e_{sk} nor e^* are effective, they highlighted the lack of investigations to account for complex particle scale interaction between coarser and finer grains and concluded that e remains an appropriate state variable for gap-graded soils.

Throughout the discussion on effective void ratio, prior research has exclusively considered gap-graded soils. This Chapter extends consideration to a broader range of particle size distribution (PSD) shapes to better understand the extent to which this issue is unique to, or particularly significant for gap-graded / bimodal soils. This approach recognizes that naturally geological deposits of purely bimodal soils are rare, and so a comprehensive and relevant understanding of stress distribution in soil needs to consider a broader range of particle size distributions. Initially continuous gradings (linear and fractal $PSDs$) are investigated in Sections 4.4.1 and 4.4.2 before considering both bimodal and trimodal gap-graded specimens in Sections 4.4.3 and 4.4.4.

4.2. Overview of DEM simulations

The absence of gravity means that some grains may have a connectivity value of 0. The connectivity value is the number of contacts per grain. A connectivity value of 0 or 1 indicates this grain is not active in stress transmission when periodic boundaries are used. As with the other simulations presented in this

thesis, the samples had an ideal isotropic fabric, and the particles were perfectly spherical. An overview of the DEM simulations approach adopted here was presented in Chapter 3. However, details specific to the simulations presented in this Chapter are provided here for clarity. The DEM simulations presented in this Chapter were conducted with periodic boundary conditions. A simplified Hertz-Mindlin contact model was used. A stress-controlled algorithm was used to obtain the desired isotropic stress of $p' = 500\ kPa$. Three packing densities were applied as presented in Chapter 3. A total of 201 DEM specimens were considered in this Chapter. The number of spherical particles included in the virtual specimens ranged between 16,715 and 636,871, as detailed in Section 4.3 below.

4.3. $PSDs$ considered

In this thesis, the $PSDs$ applied for each Chapter are not 100% the same, therefore, for clarity, the $PSDs$ of the simulations presented in each Chapter are given within the relevant Chapter. In this Chapter, to contrast the way stress is distributed in soil mixtures with the way stress is transmitted in specimens with continuous gradings, various particle size distribution (PSD) curves were used. For all these specimens, as discussed in previous research (e.g. Shire et al., 2016; Shire et al., 2014; Sufian et al., 2020; Otsubo, 2016), it is important to create large specimens so that a representative element volume (REV) can be obtained, especially for the bimodal gap-graded soils. Therefore, data confirming that a REV was achieved for the linear, bimodal and trimodal $PSDs$ considered here are presented along with the PSD data.

4.3.1. Continuous particle size distribution

Linear specimens

In the case of the continuous $PSDs$, one of the simplest shapes that can be envisioned is a perfectly linear PSD (albeit on a semi-logarithmic scale). In this study, various linear $PSDs$ with different uniformity coefficients (C_u) were studied under three distinct states which were attained by varying the inter-particle friction coefficient, μ as detailed in Chapter 3. A total of 6 linear gradings were created with the C_u increasing from 1.5 to 6.0.

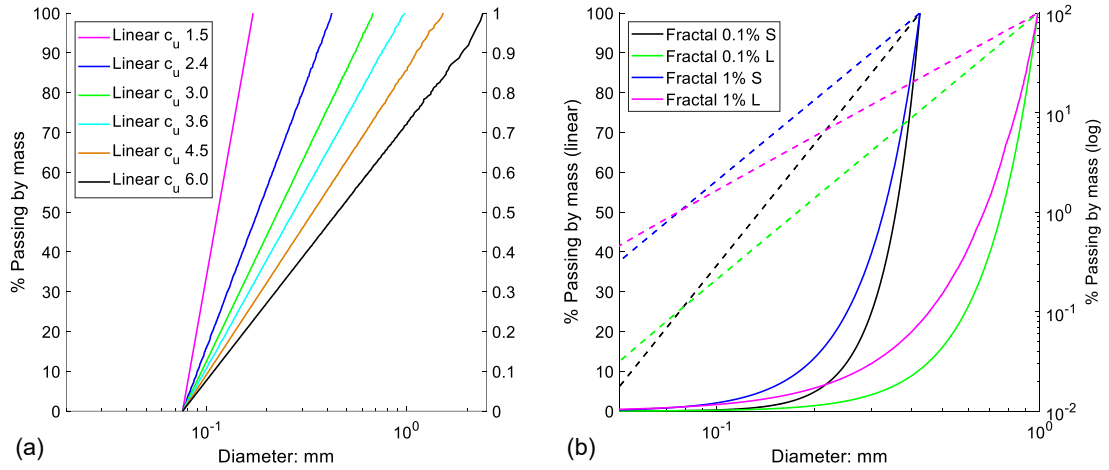


Figure 4.1: Particle size distribution for specimens with continuous gradings: (a) Linear specimens; (b) Fractal specimens (dashed lines are to be read on log-log space, solid lines are to be read in log-linear space)

As illustrated in Figure 4.1(a), the minimum particle diameters d_{min}^{p} used in each linear specimen are 0.076 mm and the maximum particle diameters d_{max}^{p} increased with increasing C_u. Consequently, when C_u is approximately 2.4, the maximum diameter is 0.425 mm, when C_u is 3.6, the maximum diameter increases to 0.985 mm. For the highest C_u considered (i.e. C_u of 6.0), the volume of the larger particles is significantly large compared to these of smaller particles. Therefore, a large number of particles is required when the volume differences amongst these particles are significant. The maximum C_u considered is C_u = 6.0 due to the limitation of the computational resources required for simulations.

Specimen size effect of a liner specimen

In any DEM study, it is important to make sure that the specimen size is large enough to be representative. In this study, to ensure that the specimen sizes considered were sufficient to generate representative data for the linear specimens, two linear specimens were created with same the particle size distribution but distinct specimen sizes, i.e. 9,045 grains and 42,896 grains for C_u = 2.4.

As illustrated in Figure 4.2(a), the distributions of connectivity data for these two specimens are presented, the x-axis is the particle connectivity and the y-axis is the cumulative distribution of connectivities by volume. A particle's connectivity is the number of contacts that it participates in, the average connectivity of a specimen equals the coordination number Z. Almost same curve can be observed for these two specimens with distinctive sizes. Figure 4.2(b) also indicates that the proportions of inactive grains are very similar at all three packing densities considered. It can be seen that a specimen with 9,045 grains is large enough to be representative of linear specimens. The dimension of the larger specimen (i.e. 42,896 grains) of the specimen preparation is approximately $3.5 \times 10^{-3}\, m$. Therefore, the dimensions of the other linear specimens were determined relative to this size of $3.5 \times 10^{-3}\, m$, as summarized in Table 4.1. Table 4.1 also lists the number of grains, the C_u and the coefficient of curvature (C_z) of each specimen are listed. It is clear that the number of grains increased with increasing C_u. Note that these specimens are larger than similar samples discussed in Shire & O'Sullivan (2016). In this earlier study, Shire & O'Sullivan (2016) used 9,313 particles for a C_u of 1.5 and 59,183 for a C_u of 6.0; here 33,306 particles were considered for C_u of 1.5 and 147,316 particles were considered for C_u of 6.0.

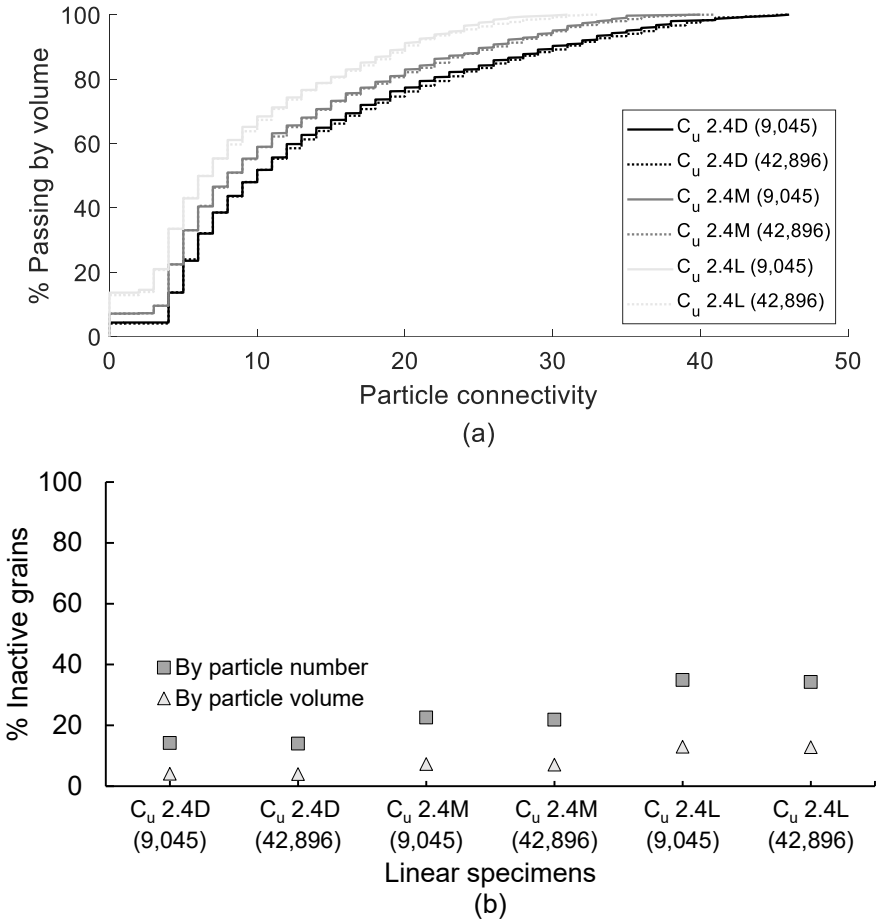


Figure 4.2: Specimen size effect for linear specimens (i.e. C_u 2.4): (a) Cumulative distribution of connectivities by volume; (b) Percentage of inactive grains

Table 4.1: Key data for linear specimens

Specimens	No. particles	C_u	C_z	Dimensions (m)
Linear C_u 1.5	33,306	1.5	0.92	3.5×10^{-3}
Linear C_u 2.4	42,896	2.4	0.84	4.5×10^{-3}
Linear C_u 3.0	41,168	3.0	0.8	4.8×10^{-3}
Linear C_u 3.6	58,634	3.6	0.78	5.5×10^{-3}
Linear C_u 4.5	82,598	4.5	0.74	6.5×10^{-3}
Linear C_u 6.0	147,316	6.0	0.70	8.0×10^{-3}

Fractal specimens

Another relatively simple type of continuous PSD is fractal specimens. Some researchers have proposed that fragments generated by weathering always satisfy a fractal PSD (Tyler & Wheatcraft, 1992). In this study, 4 different specimens with fractal grading were created based on the fractal model proposed by Tyler & Wheatcraft (1992):

$$\frac{M(d^p < d_i^p)}{M_T} = (\frac{d_i^p}{d_{max}^p})^{3-D^*} \quad 4.3$$

where d^p is the particle diameter, $M\ (d^p < d_i^p)$ is the cumulative mass of grains whose particle diameter is smaller than d_i^p, M_T is the total mass of the specimen, D^* is the fractal dimension and d_{max}^p is the maximum particle diameter. Note that Equation 4.3 is a particular case where the minimum particle diameter d_{min}^p is 0. These fractal gradings are linear in double-logarithmic space.

Two d_{max}^p values (0.425 mm and 0.985 mm) were used to create fractal specimens comparable to the linear specimens. The fractal specimen with the smaller maximum diameter, i.e. d_{max}^p of 0.425 mm is denoted S, while the specimen with the larger d_{max}^p of 0.985 mm is denoted L. As illustrated in Figure 4.1(b), the particle diameter of 0.076 mm was associated with both the 0.1% volume percentile and the 1% volume percentile for both values of d_{max}^p considered. For instance, the specimen 'Fractal 0.1% L' has a d_{max}^p of 0.985 mm and the diameter of the 0.1% volume percentile is 0.076 mm. The grading curves for the fractal specimens are plotted in both semi-logarithmic and double-logarithmic coordinate axes, as illustrated in Figure 4.1(b). The generated fractal specimens are summarised, as illustrated in

Table 4.2. The number of grains, the fractal dimension, the C_u and the C_z of

each specimen are listed. Note that the fractal dimensions given in Table 4.2 were estimated by curve fitting Equation 4.3 to the $PSDs$, as illustrated in Figure 4.1(b). Note that for "Fractal 0.1% S", the D^* is fitted to -1.0. It can be seen that both the fractal and linear specimens are continuous specimens, the C_u of fractal specimens ranges from 1.6 to 2.8. Based on the study of the specimen size effect for the linear specimens, it is reasonable to assume that a minimum number of particles of 59,698 (i.e. the dimension $\approx 10.0 \times 10^{-3}$) is large enough to be representative.

Table 4.2: Key data for fractal specimens

Specimens	No. particles	D^*	C_u	C_z	Dimensions (m)
Fractal 0.1% S	59,698	-1.0	1.6	1.1	10.0×10^{-3}
Fractal 0.1% L	66,806	0.3	1.9	1.2	13.0×10^{-3}
Fractal 1% S	66,886	0.3	1.9	1.2	7.0×10^{-3}
Fractal 1% L	102,978	1.2	2.8	1.3	8.0×10^{-3}

4.3.2. Gap-graded specimens

For the gap-graded soils, both bimodal and trimodal specimens were created in this study, as illustrated in Figure 4.3.

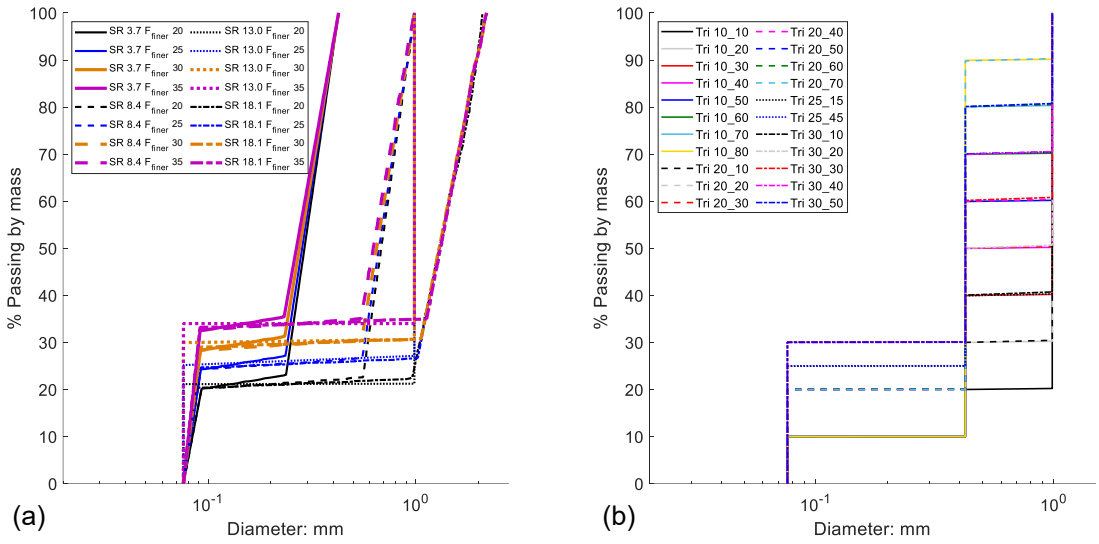


Figure 4.3: Particle size distributions for gap-graded soils: (a) Bimodal specimens; (b) Trimodal specimens

Bimodal specimen

In the case of bimodal gap-graded specimens, various SR (i.e. D_{50}/d_{50}) values were considered: 3.7, 8.4, 13.0 and 18.1, where D_{50} is the median diameter of the coarser fraction and d_{50} is the median diameter of the finer fraction. In all cases, there was a slight polydispersity in the two fractions within each specimen. The d_{min}^{p} was the same as that used in the linear specimens (i.e. 0.076 mm), while d_{max}^{p} increased with increasing SR. For the bimodal specimens, 8 values of F_{finer} were used to systematically study the bimodal mixtures (i.e. 5%, 10%, 15%, 20%, 25%, 30%, 35%, 50%). Typical bimodal particle size distributions are illustrated in Figure 4.3(a). Each specimen is identified by its SR and F_{finer}. For instance, 'SR 8.4 F_{finer} 35' indicates a bimodal material with $SR = 8.4$ and $F_{finer} = 35\%$. When considering bimodal, gap-graded soils, it is important to consider the size ratio at which the finer particles plausibly can exist unstressed within the void space. Shire et al. (2016) found that in three dimensions the largest sphere which can fit within the void body of the densest face-centred cubic packing of uniform spheres $(e = 0.35)$ occurs at $SR \approx 4.45$ through the theoretical considerations. However, most

experimental studies have shown that a clear indication of bimodal behaviour occurs for SR values ≥ 6. In the case of the SRs of 8.4, 13.0 and 18.1, these SRs are larger than the SRs of 6, which suggests that for all of these specimens, the finer grains are able to fill in the void of the coarser grains.

Specimen size effect of a bimodal specimen

As illustrated in Section 4.3.1, following the prior studies (Shire et al., 2016; Shire et al., 2014; Sufian et al., 2020; Otsubo, 2016), the bimodal specimens considered should all be $REVs$, an example to confirm that $REVs$ were attained is therefore illustrated here. For SR 8.4 F_{finer} 25, two specimens were generated with distinct sizes (i.e. 40,020 particles and 100,871 particles). The comparison of key data is presented in Figure 4.4; for all packing densities, the observed key metrics are similar for both specimens. Similar verifications were conducted for other specimens (e.g. SR 3.7 F_{finer} 50, SR 13.0 F_{finer} 25). The dimensions of the specimen during specimen preparation stage (SR 8.4 F_{finer} 25 of 40,020 particles) is approximately $4 \times 10^{-3}\ m$, then the other specimens were therefore created relative to this dimension of $4 \times 10^{-3}\ m$. The details of all these created specimens are presented from Table 4.3 to Table 4.6.

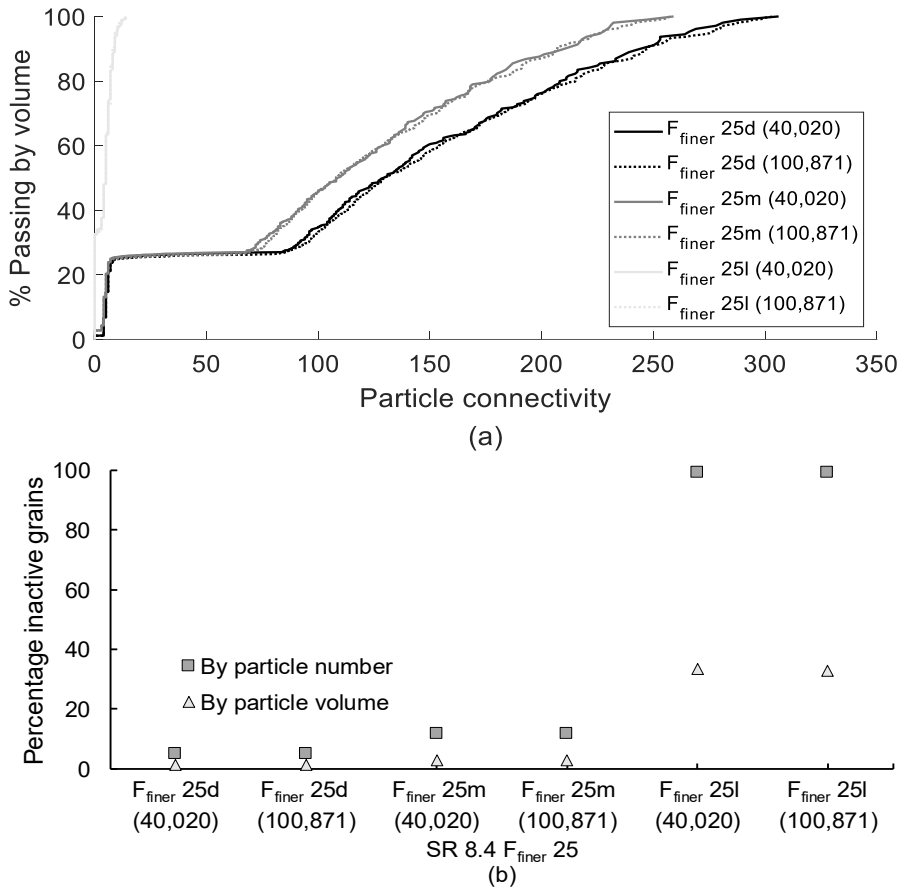


Figure 4.4: Specimen size effect for bimodal specimens: (a) Cumulative distribution of connectivities by volume; (b) Percentage of inactive grains (d, m and l denote dense, medium and loose specimens, respectively).

Table 4.3: Key data for bimodal gap-graded specimens with SR = 3.7

Specimens	F_{finer}: %	No. particles	No. finer particles	No. coarser particles	C_u	C_z	Dimensions (m)
SR 3.7 F_{finer} 5	5	16,715	11,455	5,260	1.5	0.9	5.50×10^{-3}
SR 3.7 F_{finer} 10	10	38,925	31,698	7,227	2.0	1.2	6.00×10^{-3}
SR 3.7 F_{finer} 15	15	53,960	47,025	6,935	3.6	2.2	6.00×10^{-3}
SR 3.7 F_{finer} 20	20	60,906	56,151	4,755	3.6	2.2	5.50×10^{-3}
SR 3.7 F_{finer} 25	25	72,610	68,030	4,580	3.6	2.2	5.50×10^{-3}
SR 3.7 F_{finer} 30	30	84,307	80,001	4,306	3.6	1.0	5.50×10^{-3}
SR 3.7 F_{finer} 35	35	72,126	69,007	3,119	3.6	0.4	5.00×10^{-3}
SR 3.7 F_{finer} 50	50	94,686	92,539	2,147	3.6	0.4	5.00×10^{-3}

Table 4.4: Key data for bimodal gap-graded specimens with SR = 8.4

Specimens	F_{finer}: %	No. particles	No. finer particles	No. coarser particles	C_u	C_z	Dimensions (m)
SR 8.4 F_{finer} 5	5	18,446	17,742	704	1.5	0.9	6.50×10^{-3}
SR 8.4 F_{finer} 10	10	36,166	35,498	668	2.3	1.4	6.50×10^{-3}
SR 8.4 F_{finer} 15	15	53,879	53,278	601	8.5	5.1	6.50×10^{-3}
SR 8.4 F_{finer} 20	20	84,205	83,594	611	8.5	5.2	6.50×10^{-3}
SR 8.4 F_{finer} 25	25	102,149	101,579	570	8.4	5.2	6.50×10^{-3}
SR 8.4 F_{finer} 30	30	120,049	119,503	546	8.5	1.7	6.50×10^{-3}
SR 8.4 F_{finer} 35	35	108,428	108,036	392	8.4	0.2	6.00×10^{-3}
SR 8.4 F_{finer} 50	50	104,355	104,155	200	8.4	0.2	5.20×10^{-3}

Table 4.5: Key data for bimodal gap-graded specimens with SR = 13.0

Specimens	F_{finer}: %	No. particles	No. finer particles	No. coarser particles	C_u	C_z	Dimensions (m)
SR 13.0 F_{finer} 5	5	17554	17069	485	1	1	5.00×10^{-3}
SR 13.0 F_{finer} 10	10	11183	11084	101	13.0	13.0	5.00×10^{-3}
SR 13.0 F_{finer} 15	15	45359	45117	242	13.0	13.0	4.80×10^{-3}
SR 13.0 F_{finer} 20	20	59681	59377	304	13.0	13.0	4.60×10^{-3}
SR 13.0 F_{finer} 25	25	79284	79074	210	13.0	13.0	4.60×10^{-3}
SR 13.0 F_{finer} 30	30	99767	99192	575	13.0	0.1	4.60×10^{-3}
SR 13.0 F_{finer} 35	35	129287	128996	291	13.0	0.1	4.80×10^{-3}
SR 13.0 F_{finer} 50	50	225517	225413	104	13.0	0.1	5.20×10^{-3}

Table 4.6: Key data for bimodal gap-graded specimens with SR = 18.1

Specimens	F_{finer}: %	No. particles	No. finer particles	No. coarser particles	C_u	C_z	Dimensions (m)
SR 18.1 F_{finer} 5	5	148535	147593	942	1.7	0.9	10.5×10^{-3}
SR 18.1 F_{finer} 10	10	159607	159146	461	2.0	1.0	9.00×10^{-3}
SR 18.1 F_{finer} 15	15	227586	227192	394	17.9	9.1	9.00×10^{-3}
SR 18.1 F_{finer} 20	20	176653	176487	166	17.7	9.2	7.00×10^{-3}
SR 18.1 F_{finer} 25	25	289726	289531	195	18.3	9.2	8.00×10^{-3}
SR 18.1 F_{finer} 30	30	253540	253415	125	18.2	9.2	7.20×10^{-3}
SR 18.1 F_{finer} 35	35	257919	257798	121	17.8	0.1	7.00×10^{-3}
SR 18.1 F_{finer} 50	50	481611	481453	158	18.1	0.1	8.00×10^{-3}

Trimodal specimens

The $PSDs$ of the trimodal specimens considered here are presented in Figure 4.3(b), to systematically study the key features of trimodal materials. This study considered three fixed size ratios: (a) the size ratio between coarse and finer particles, $SR_{cf} = 13.0$; (b) the size ratio between intermediate and finer particles, $SR_{if} = 5.6$; (c) the size ratio between coarse and intermediate particles, $SR_{Ci} = 2.3$. Note that SR_{cf}, SR_{if} are same to those of bimodal studies (i.e. 13.0 and 5.6). In a series of parametric studies, for a given, fixed F_{finer}, F_{int} was systemically increased. PSD data for trimodal materials with F_{finer} values of 10%, 20%, 25% and 30% are illustrated in Figure 4.3(b). Each trimodal specimen considered had the same d^p_{min} of 0.076 mm, an intermediate grain diameter, d^p_{int}, of 0.425 mm and a d^p_{max} of 0.985 mm. For clarity, each of those specimens is named as $Tri\ \ A\_B$, where A represents a F_{finer} by mass and B represents the F_{int} by mass. For example, '$Tri\ 10\_60$' indicates a trimodal specimen with F_{finer} of 10% and the F_{int} of 60%.

Specimen size effect for a trimodal specimen

As discussed above for the linear and bimodal gap-graded specimens, it is important that $REVs$ were attained when creating the trimodal specimens. The influence of specimen size on key data was investigated for a typical gradation (i.e. Tri 10_70) by comparing data for two specimens: a small specimen with 83,069 grains and a larger specimen with 636,871 grains. Both the distribution of connectivities (Figure 4.5(a)) and the proportion of inactive particles (Figure 4.5(b)) are very similar, showing that a specimen of approximately 80,000 grains with a generated dimension of approximately $6.5 \times 10^{-3}\, mm$ is sufficient to get representative results. Then other trimodal specimens were created with particles number larger than 80,000 and specimen dimensions relative to $6.5 \times 10^{-3}\, mm$. The details of these created trimodal specimens were summarised from Table 4.7 to Table 4.9.

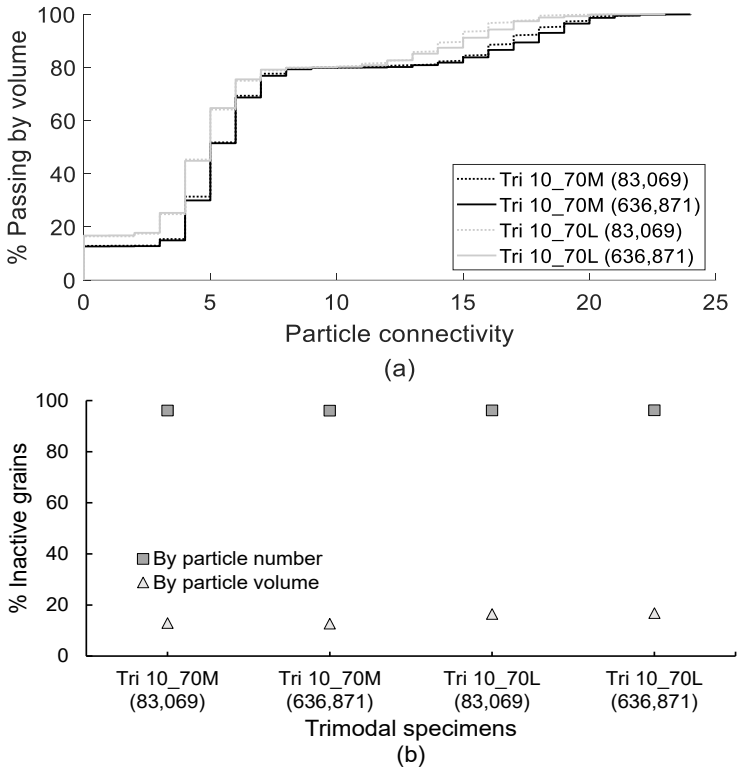


Figure 4.5: Influence of specimen size on particle-scale data generated for a representative trimodal gradation, Tri 10_70: (a) Cumulative distribution of connectivities by volume; (b) Percentage of inactive grains.

Table 4.7: Key data for bimodal gap-graded specimens with F_{finer} = 10%

Specimens	Number of particles	F_{int}:%	$F_{coarser}$: %	No. finer particles	No. intermediate particles	No. coarser particles	C_u	C_z	Dimension (m)
Tri 10_10	102,204	10	80	101239	591	374	13.0	13.0	7.0×10^{-3}
Tri 10_20	93,118	20	70	91764	1057	297	13.0	2.4	7.0×10^{-3}
Tri 10_30	90,878	30	60	89102	1529	247	13.0	2.4	7.0×10^{-3}
Tri 10_40	94,083	40	50	91772	2099	212	13.0	2.4	7.0×10^{-3}
Tri 10_50	90,063	50	40	87402	2499	162	5.6	5.6	7.0×10^{-3}
Tri 10_60	92,282	60	30	89101	3057	124	5.6	5.6	7.0×10^{-3}
Tri 10_70 S	83,069	70	20	79727	3265	77	5.6	5.6	7.0×10^{-3}
Tri 10_70 L	636,871	70	20	617,066	19,805	500	5.6	5.6	13.0×10^{-3}
Tri 10_80	97104	80	10	92814	4246	44	5.6	5.6	7.0×10^{-3}

Table 4.8: Key data for bimodal gap-graded specimens with F_{finer} = 20%

Specimens	Number of particles	F_{int}:%	$F_{coarser}$:%	No. finer particles	No. intermediate particles	No. coarser particles	C_u	C_z	Dimension (m)
Tri 20_10	99363	10	70	98914	288	161	13.0	2.4	5.5×10^{-3}
Tri 20_20	111343	20	60	110400	788	155	13.0	2.4	5.5×10^{-3}
Tri 20_30	111634	30	50	110558	948	128	13.0	2.4	5.5×10^{-3}
Tri 20_40	105707	40	40	104416	1194	97	5.6	5.6	5.5×10^{-3}
Tri 20_50	100403	50	30	98846	1486	71	5.6	5.6	5.5×10^{-3}
Tri 20_60	95630	60	20	93896	1688	46	5.6	5.6	5.5×10^{-3}
Tri 20_70	91312	70	10	89234	2056	22	5.6	5.6	5.5×10^{-3}

Table 4.9: Key data for bimodal gap-graded specimens with F_{finer} = 25%, 30%

Specimens	Number of particles	F_{finer}: %	F_{int}: %	$F_{coarser}$: %	No. finer particles	No. intermediate particles	No. coarser particles	C_u	C_z	Dimension (m)
Tri 25_15	149907	25	15	60	146508	3233	166	13	2.4	5.8×10^{-3}
Tri 25_45	150848	25	45	30	149030	1732	86	5.6	5.6	5.8×10^{-3}
Tri 30_10	96242	30	10	60	95867	285	90	13.0	0.1	4.8×10^{-3}
Tri 30_20	102424	30	20	50	101939	405	80	13.0	0.1	4.8×10^{-3}
Tri 30_30	102602	30	30	40	101666	869	67	5.6	0.2	4.8×10^{-3}
Tri 30_40	102781	30	40	30	101956	777	48	5.6	0.2	4.8×10^{-3}
Tri 30_50	102960	30	50	20	101826	1099	35	5.6	0.2	4.8×10^{-3}

4.4. Results and discussion

4.4.1. Linear specimens

Dense condition

Figure 4.6 schematically illustrates how the connectivity of the darker, central grain increases from 1 to 4 as the number of other particles it contacts increases. Specimens with 0 contact with other particles or only one contact cannot transfer stress and are considered to be inactive here.

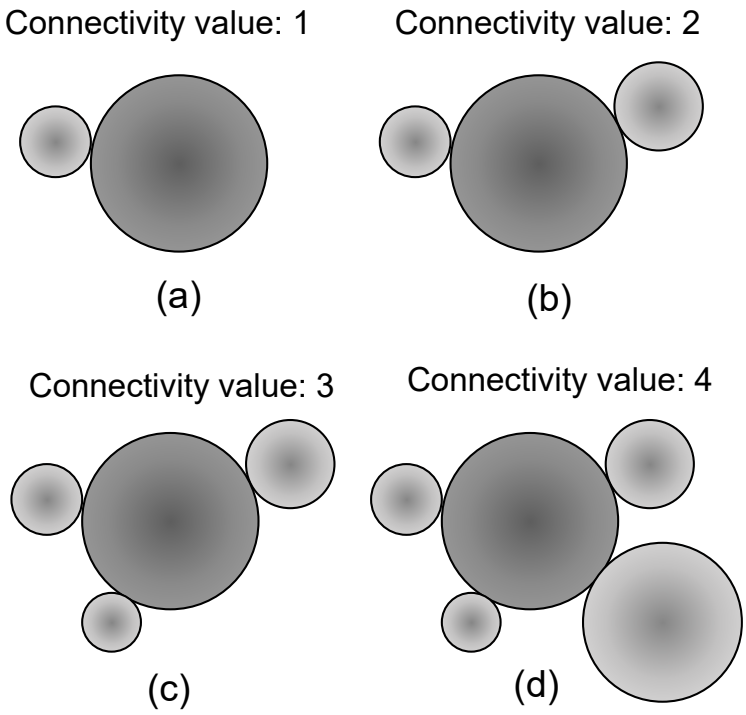


Figure 4.6: Schematic drawing of connectivity value for the darker particle: (a) connectivity value of 1; (b) connectivity value of 2; (c) connectivity value of 3; (d) connectivity value of 4

Key data quantifying the proportion of stress transmitting particles for the dense specimens with linear $PSDs$ are presented in Figure 4.7. Figure 4.7(a) illustrates the cumulative distribution of the particle connectivity values by the number of particles. Referring to Figure 4.7(a) it is clear that, for the linear specimens, many grains have connectivity values lower than 2, these grains are not active in transferring stress. These data indicate that, even in the case of specimens with continuous gradations, the smaller particles in a granular material may not be active in stress transmission. The proportion by number of inactive grains increases with increasing C_u from approximately 5% where C_u = 1.5, to approximately 24% where C_u = 6.0. In contrast, Figure 4.7(b) presents data for the cumulative distribution of the grain connectivity values by particle volume. The volumetric percentage of inactive grains is rather small compared to the percentage by number of inactive particles. These data indicate that the inactive grains tend to have relatively small diameters. For example, for the

dense specimen with C_u = 6.0, approximately 24% of grains by number are inactive, and these inactive particles comprise only 4% of the total particle volume.

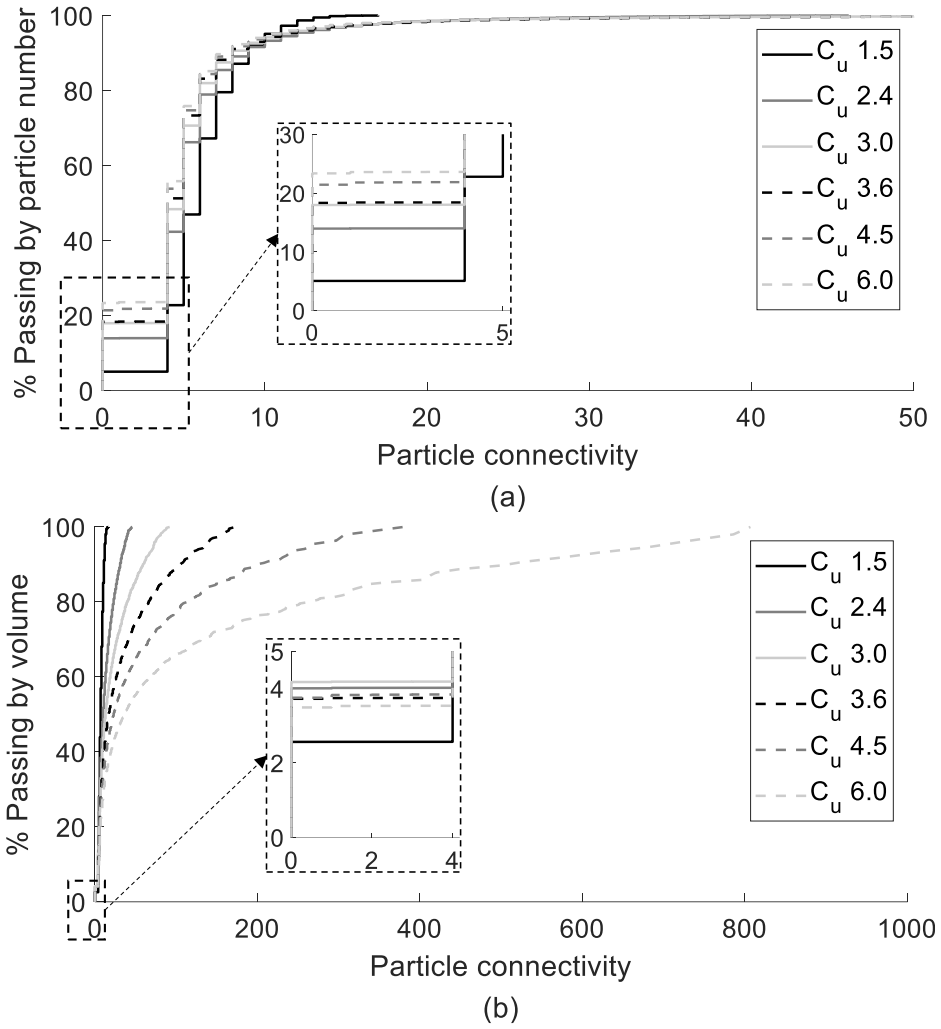


Figure 4.7: Cumulative distribution of connectivities for linear specimens in the dense condition: (a) distribution by number; (b) distribution by volume

The size-dependency of the inactive grains is confirmed in both Figure 4.8(a) and (b). For instance, as illustrated in Figure 4.8(a) in the dense condition, for all 6 C_u values considered here, the median diameter (D_{50}) of the inactive grains is lower than the specimen D_{50}. Furthermore the D_{50} of the inactive grains remains at approximately 0.088 mm for all C_u values considered. In contrast, the D_{50} of the active grains increases with increasing C_u. Besides, it

can be seen that the similar tendency can be observed for the loose condition, as illustrated in Figure 4.8(b).

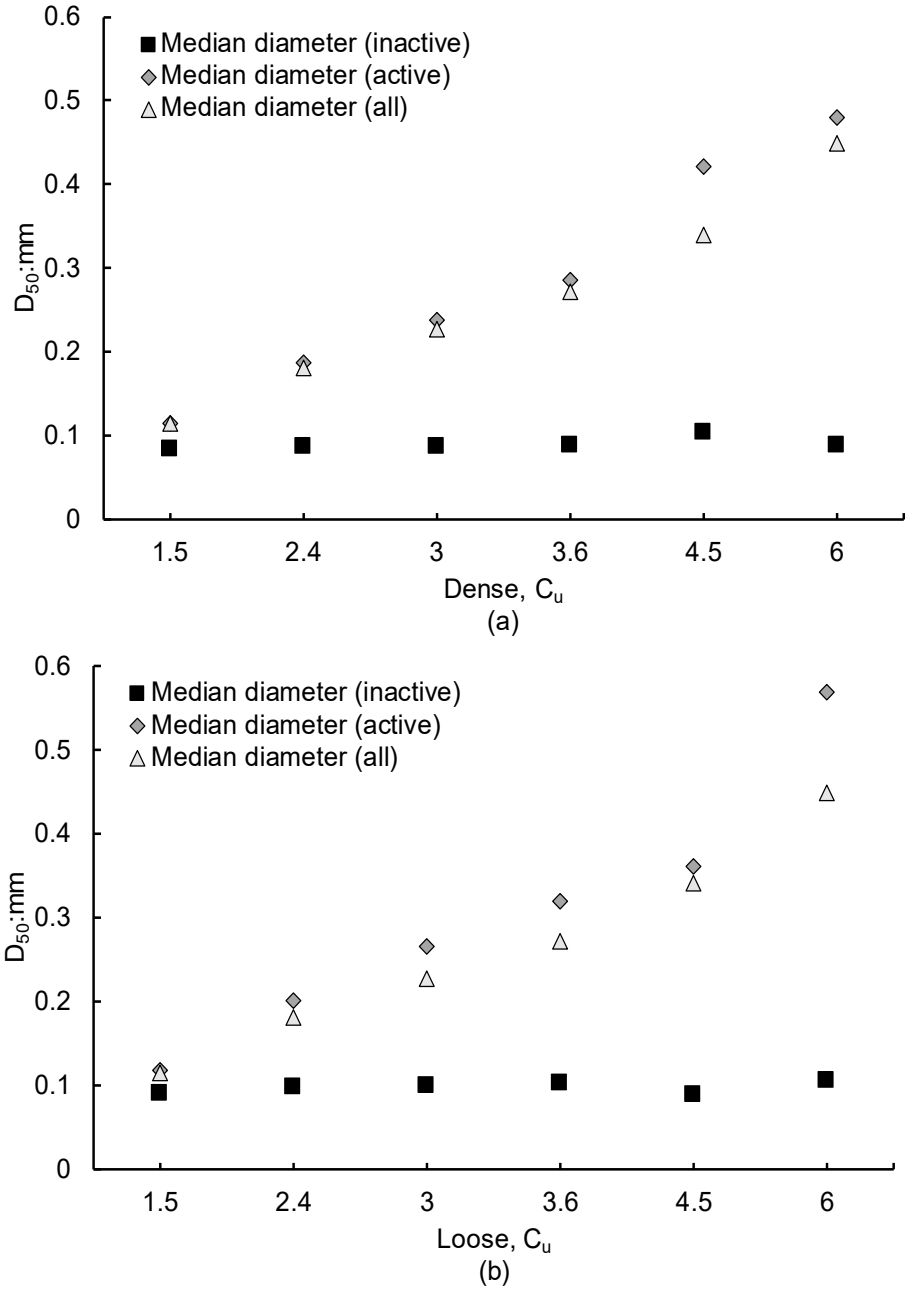


Figure 4.8: Percentage of inactive grains versus C_u for linear specimens: (a) D_{50} of inactive, active and all particles for dense specimens; (b) D_{50} of inactive, active and all particles for loose specimens

Medium and loose condition

Trends observed for the dense specimens were also observed in both medium

and loose conditions. The data in Figure 4.9 and Figure 4.10 indicate that the proportion of inactive grains also increases with increasing C_u in both the medium and loose conditions. As before, the volumetric percentage of inactive grains is much smaller than the percentage by number of inactive grains. In addition, the data in Figure 4.9 and Figure 4.10 show that the maximum particle connectivity value significantly increases with increasing C_u in both the medium and loose conditions.

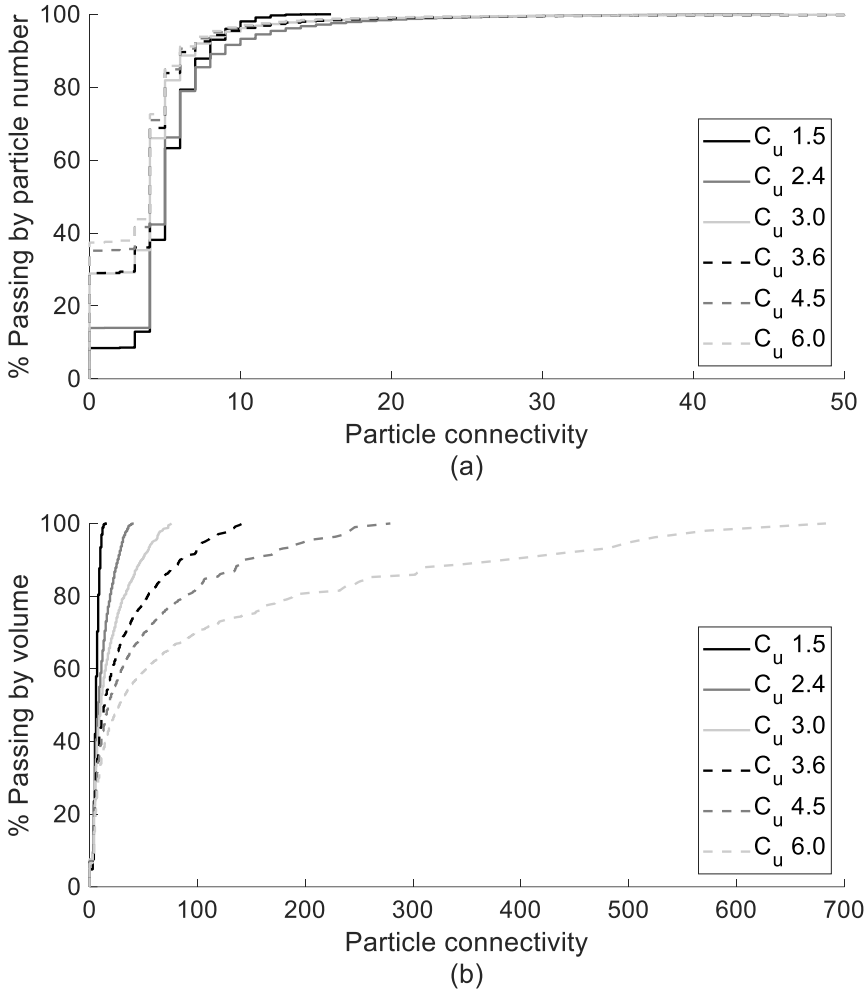


Figure 4.9: Cumulative distribution of connectivities for linear specimens in the medium density: (a) distribution by number; (b) distribution by volume

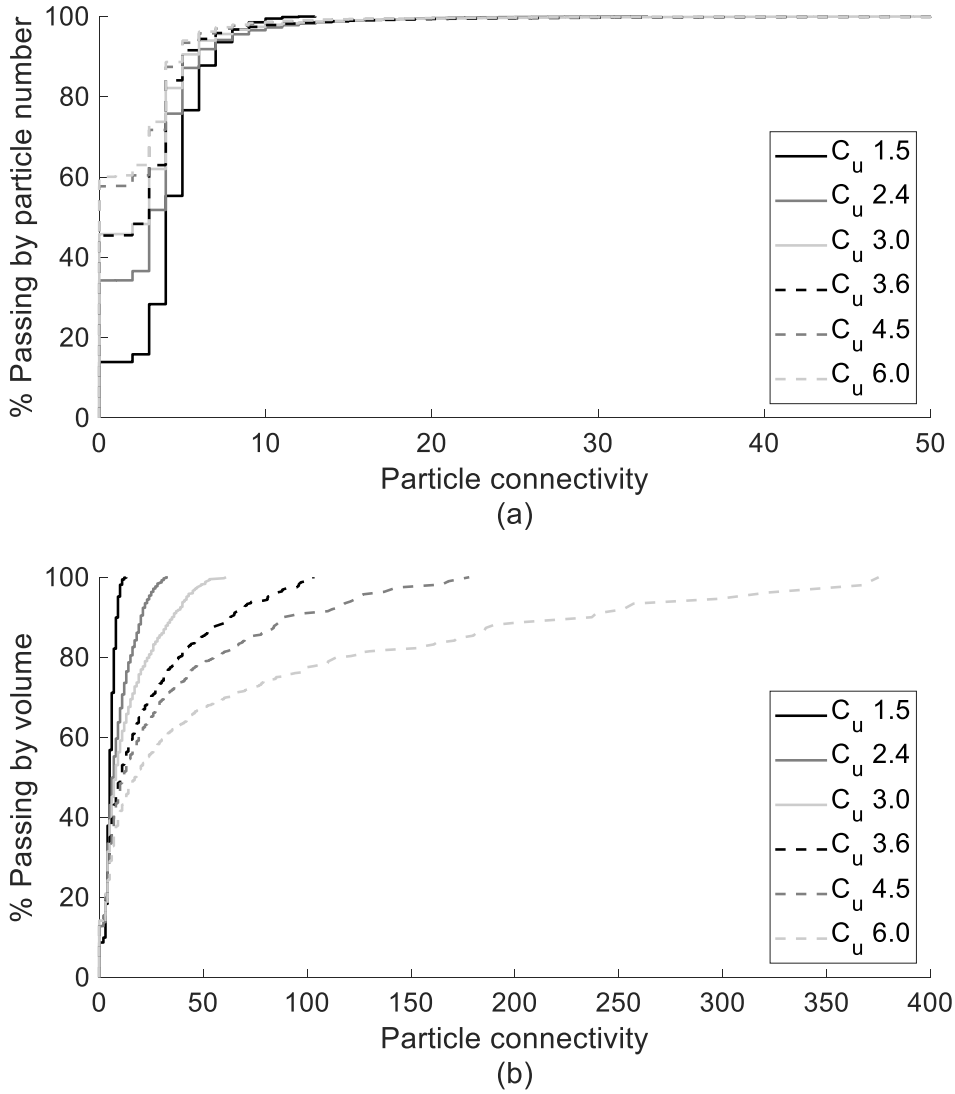


Figure 4.10: Cumulative distribution of connectivities for linear specimens in the loose density: (a) distribution by number; (b) distribution by volume

Density effect in linear specimens

Three representative C_u values (i.e. C_u of 1.5, 3.6, and 6.0) were selected to illustrate the influence of packing density on the cumulative distribution of the particle connectivity values. As illustrated in Figure 4.11, when C_u is 1.5, a limited density effect is identified, for the loosest case, approximately 9% of the particles by volume are inactive. While approximately 3% of the particles by volume are inactive in the densest case. Figure 4.11 shows that for this small C_u value, the maximum particle connectivity values are similar (i.e. 17) in the dense, medium and loose cases.

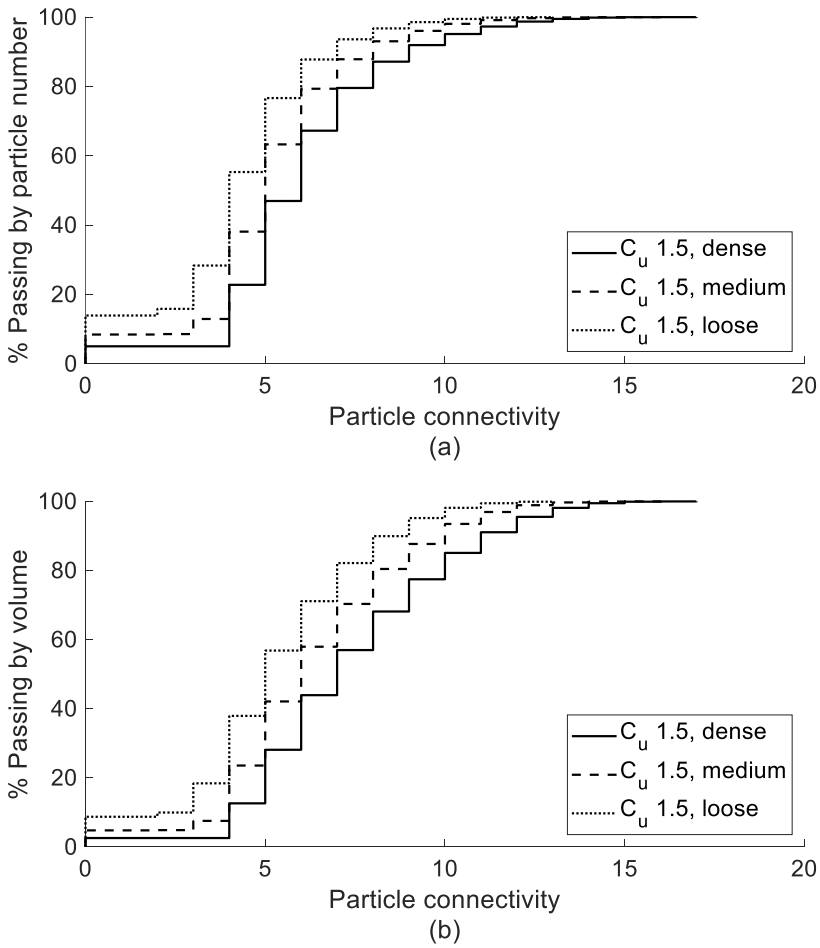


Figure 4.11: Effect of density on cumulative distribution of connectivities for linear specimens when C_u = 1.5: (a) distribution by number; (b) distribution by volume

The data for $C_u = 3.6$ are illustrated in Figure 4.12. In this case, the proportion by number of inactive grains is more clearly density-dependent (Figure 4.12(a)). In the loose case, approximately 45% of the total number of grains are inactive, while approximately 19% of grains in the dense condition are inactive. As before, the volumetric proportion of inactive grains is smaller than the proportion by number of inactive grains (Figure 4.12(b)). However, for the loosest specimen considered, the volumetric proportion of inactive grains is relatively large (13.5%). The maximum connectivity values increase from approximately 100 to 175 when the packing densities change from the loosest to the densest condition.

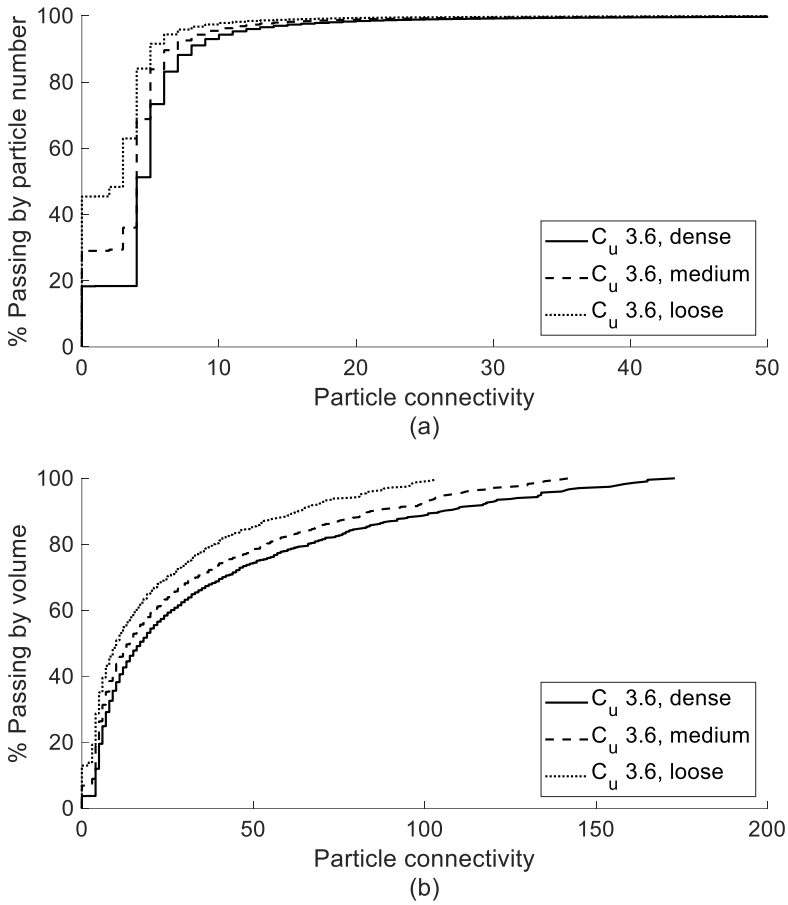


Figure 4.12: Effect of density on cumulative distribution of connectivities for linear specimens when C_u = 3.6: (a) distribution by number; (b) distribution by volume

When C_u = 6.0, similar trends were identified in comparison with the case of C_u = 4.5, as illustrated in Figure 4.13, so that a finite density effect is observed. The maximum connectivity values significantly increase from approximately 380 to 800 when densities change from the loose to the dense. The data from Figure 4.11 to Figure 4.13 suggest that the effect of packing density on linear specimens increases with increasing C_u.

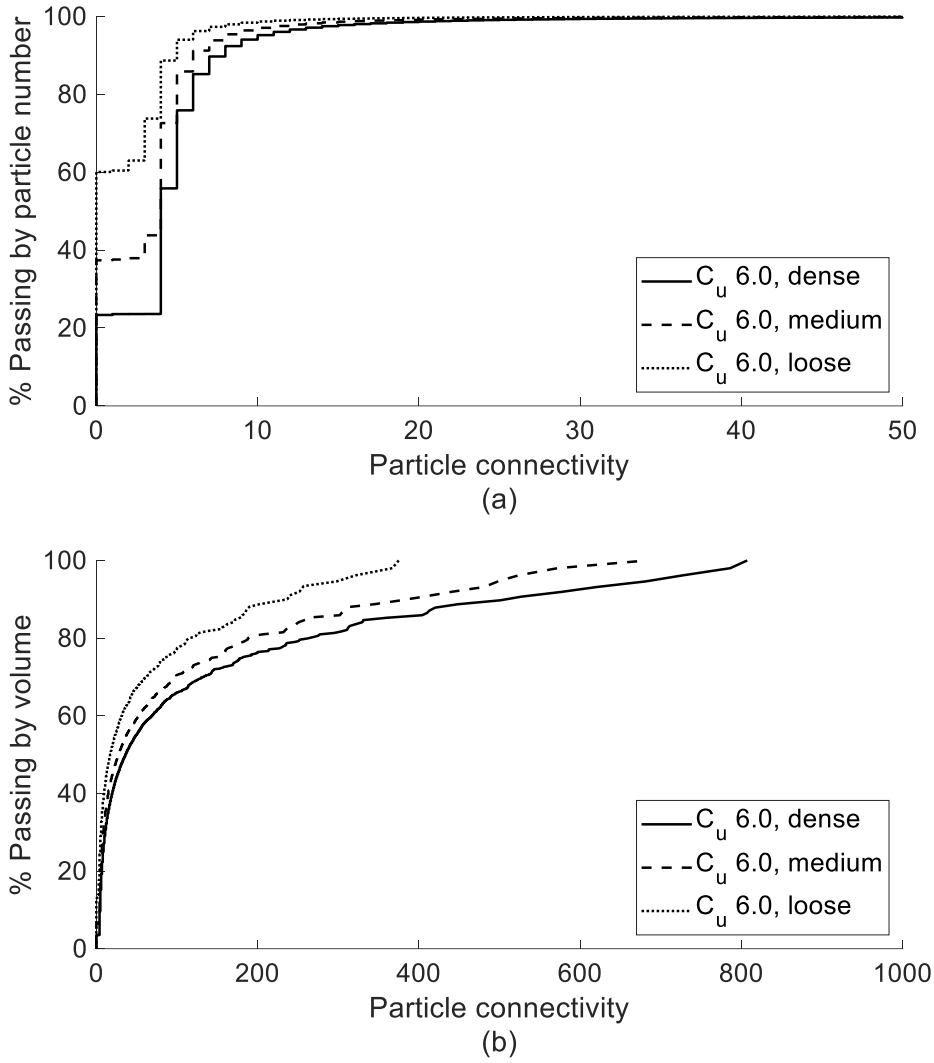


Figure 4.13: Effect of density on cumulative distribution of connectivities for linear specimens when C_u = 6.0: (a) distribution by number; (b) distribution by volume

Figure 4.14 considers the variation in the proportion of inactive particles with C_u for all of the linear specimens, considering both the proportion by number of particles (Figure 4.14(a)) and the proportion by particle volume (Figure 4.14b)). In general, the proportion by number of inactive grains increases with increasing C_u. There is a less significant increase in the volumetric proportion of inactive grains with increasing C_u. For the ideal scenarios considered here, a finite proportion of the grains may be inactive, and the proportion of inactive grains increases with increasing C_u and is density-dependant.

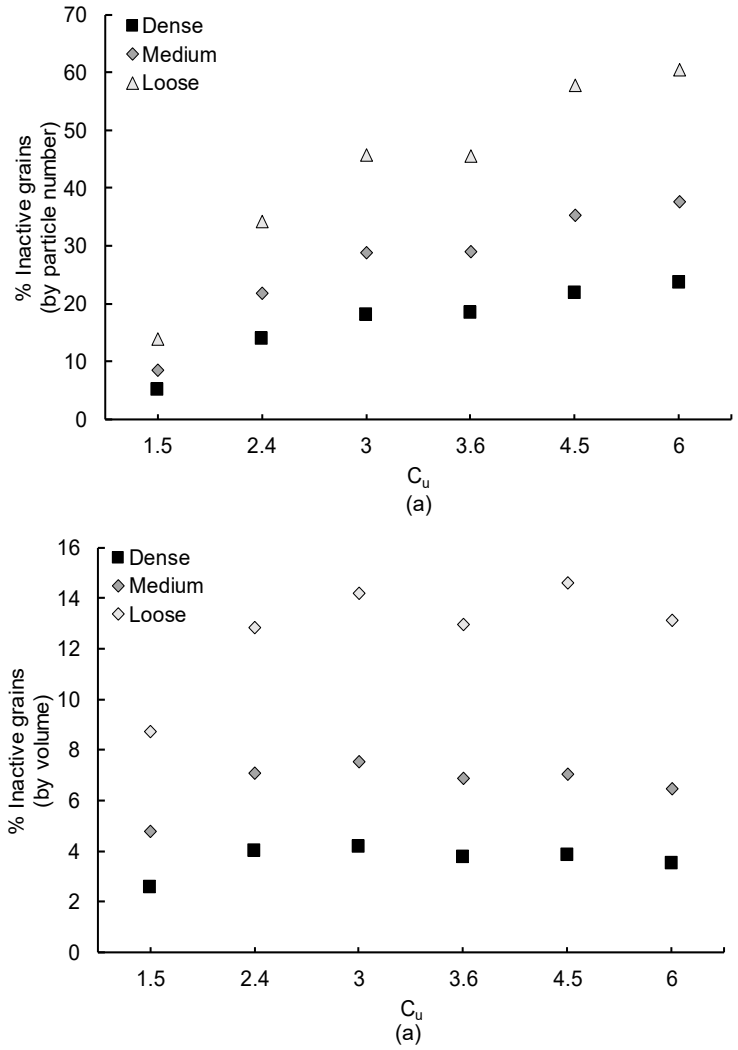


Figure 4.14: Percentage of inactive grains versus C_u for linear specimens: (a) percentage of inactive grains by number (b) percentage of inactive grains by volume

Relative differences in state variables

Developing upon the ideas that have hitherto been put forward for gap-graded soils and outlined in Chapter 2, Figure 4.15 compares e_m and e for the linear specimens at all three levels of density considered. As discussed in Section 4.1, e_m is calculated by considering these grains whose connectivity values are lower than 2 as part of the void space. As expected, the e_m values are consistently larger than their corresponding e values. In the dense condition, these e values are close to their corresponding e_m. However, a significant difference between e and e_m can be observed in the loosest condition.

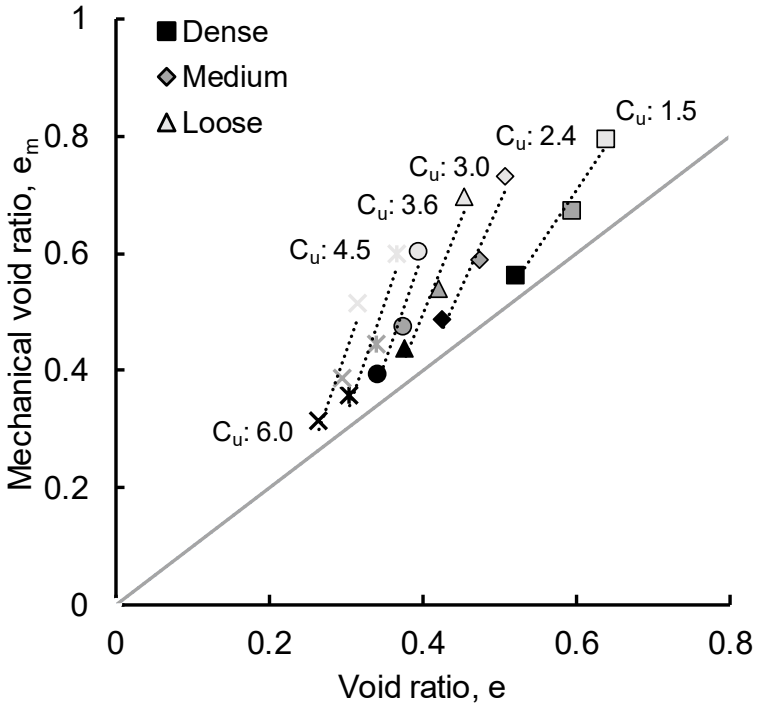


Figure 4.15: Comparison of measures of packing density for linear specimens, e versus e_m

To quantify the effect of these inactive particles on the traditional measures of state, the relative differences for void ratio and bulk density were compared for the cases where these particles are considered part of the solid or void phases of the material. Figure 4.16(a) considers the variation in $(e_m - e)/e$ with C_u, it is clear that the magnitude of this difference is finite relative to e for all the specimens considered and relatively large in the case of the loosest specimens. For C_u values exceeding 2, the difference $(e_m - e)/e$ is less sensitive to variations in C_u than it is to variations in density and no systematic variation with C_u is observed. Figure 4.16(b) considers specimen bulk density by calculating the relative difference $(\rho - \rho_m)/\rho$ and again, considering the data from this perspective, there are measurable differences, particularly when the loosest specimens are considered. In the loose condition, the relative difference $(\rho - \rho_m)/\rho$ can reach approximately 14%. It is widely accepted that the bulk density is significant in estimating the stiffness values of granular materials, $G_0 = \rho V_s^2$, as illustrated in Chapter 2. Then the overestimation of bulk density

may lead to the overestimation of the stiffness values. This issue is then discussed in detail in Chapter 6. The data presented in Figure 4.16 indicate that using the global void ratio,e, to quantify state may have limitations even in the case of specimens with a continuous grading.

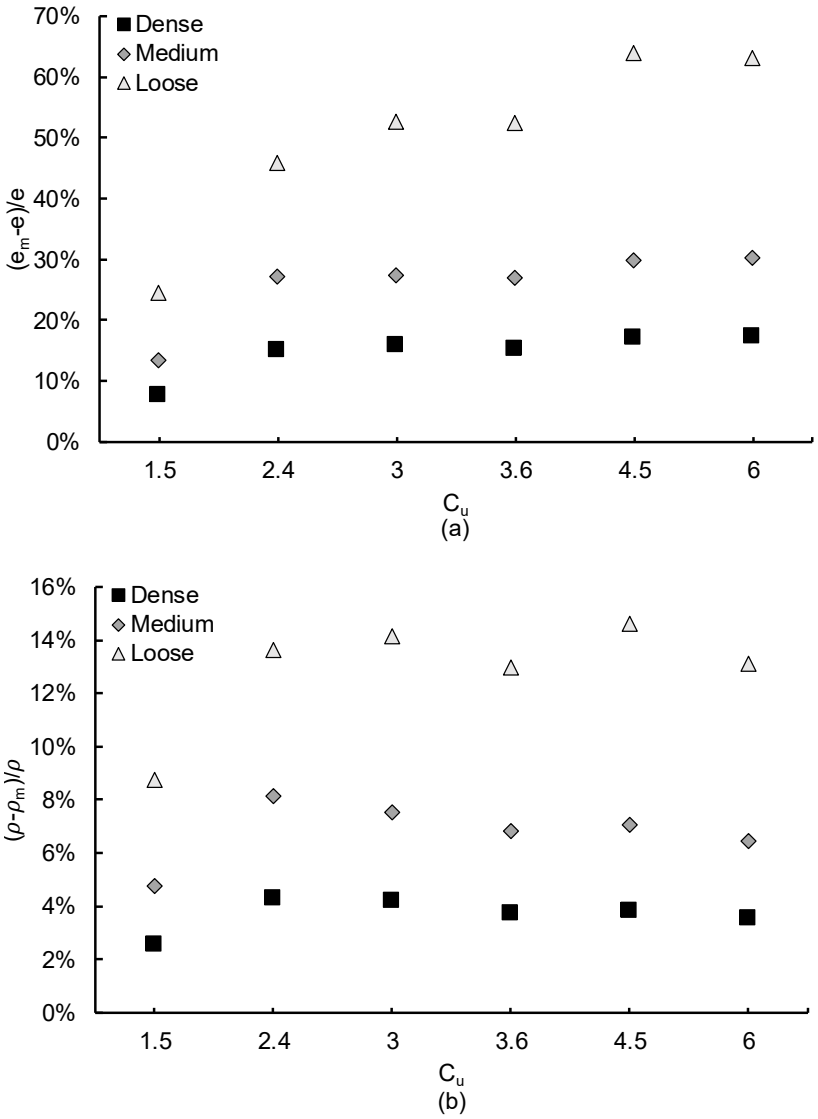


Figure 4.16: Comparison of measures of packing density for linear specimens: (a) $(e\text{-}e_m)/e$ versus C_u; (b) $(\rho - \rho_m)/\rho$ versus C_u

4.4.2. Fractal specimens

Figure 4.17(a) presents the cumulative distribution by number of particle connectivities for the dense fractal specimens. Figure 4.17(b) is the cumulative distribution of connectivities by particle volume. For these fractal specimens, a

large proportion by number of grains does not transfer stress. For instance, for Fractal 1% L, more than 90% of the total number of particles are inactive. In these fractal specimens there is a large number of particles with a diameter $<$ 0.076 mm, most of these grains are inactive. As before, the volumetric proportion of inactive particles is lower, but still finite (approximately 8%) (Figure 4.17(b)), which suggests that these inactive grains have a relatively small diameter.

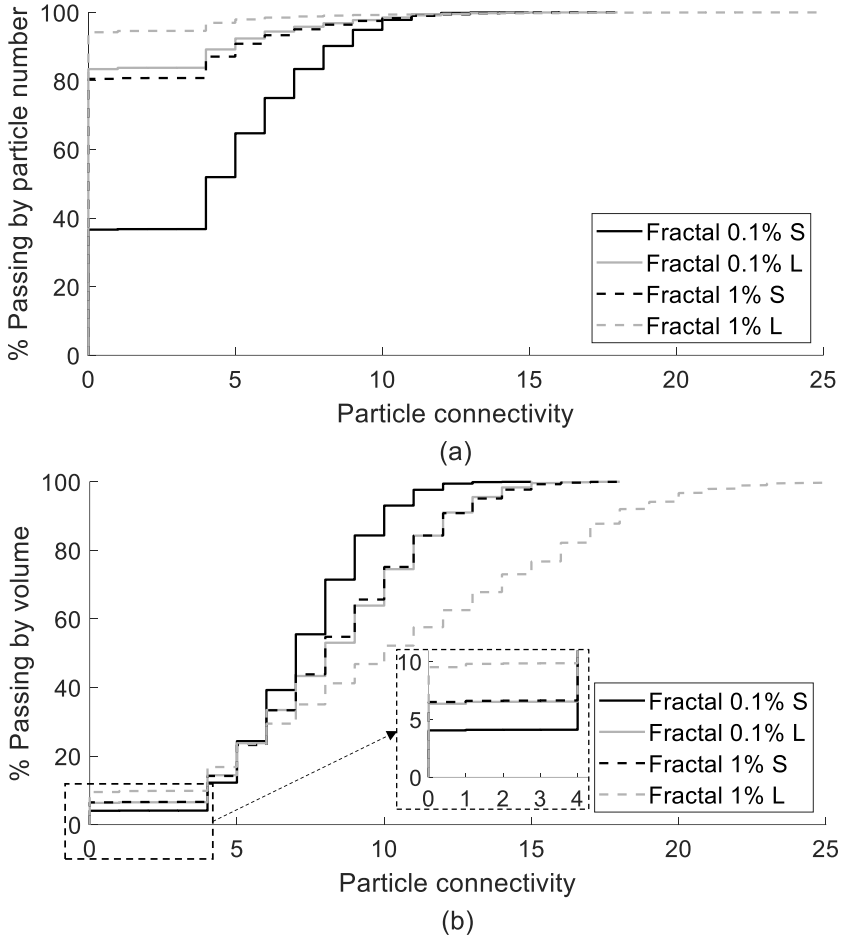


Figure 4.17: Cumulative distribution of connectivities for dense fractal specimens: (a) distribution by number; (b) distribution by volume

The data in Figure 4.18(a) and (b) confirm that the D_{50} values of the inactive grains are significantly smaller than those of the active grains, which is similar to the tendency observed for linear specimens. Figure 4.19(a) and (b) show the effect of density on stress transmission in a representative fractal specimen

(Fractal 0.1% L), and it is clear that this density effect is less marked than these for the linear specimens considered above. For instance, the maximum connectivity values for these three densities are similar, and all approximately 17.

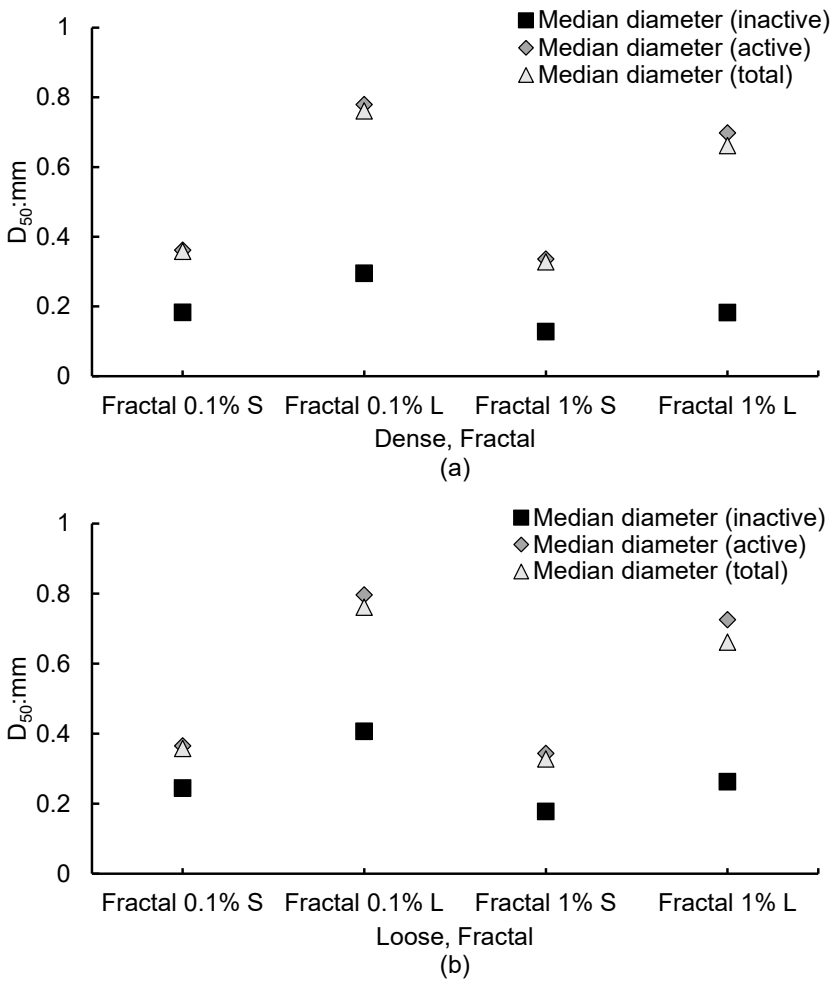


Figure 4.18: (a) D_{50} of inactive, active and all particles for dense specimens; (b) D_{50} of inactive, active and all particles for loose specimens.

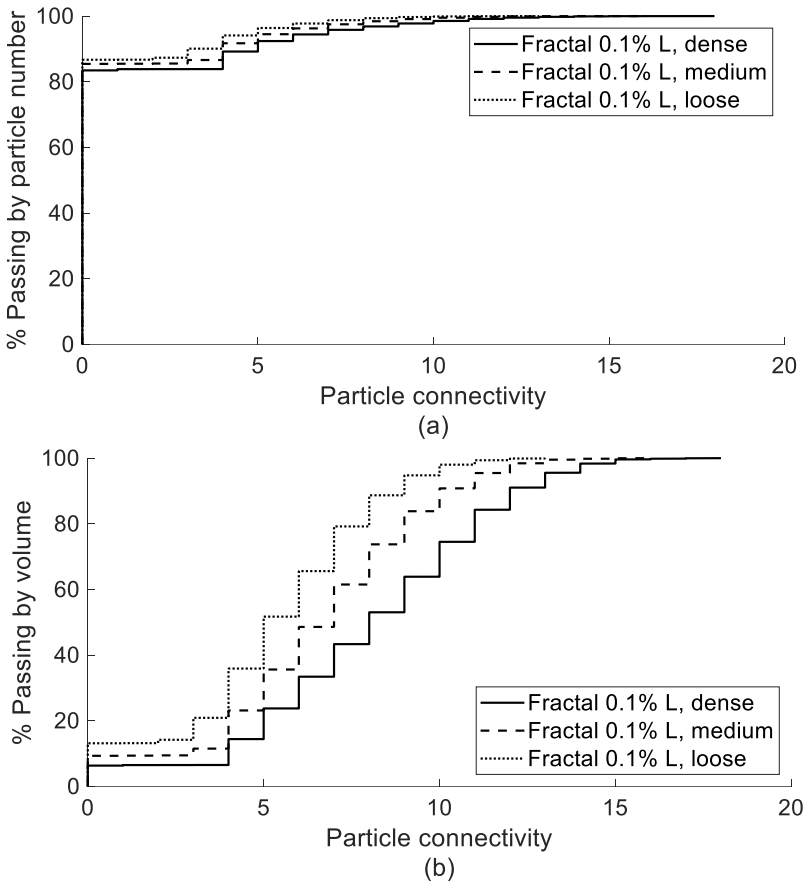


Figure 4.19: Effect of density on cumulative distribution of connectivities for a fractal specimen: (a) distribution by number for Fractal 0.1% L; (b) distribution by volume for Fractal 0.1% L

Figure 4.20(a) and (b) summarize the proportion of inactive particles in these four fractal specimens, considering both the proportion by number of particles (Figure 4.20(a)) and the proportion by particle volume (Figure 4.20(b)). Figure 4.20(a) indicates that there is a relationship between C_u and the proportion of inactive grains. The proportion of inactive grains by particle number and volume increases with increasing C_u. Figure 4.20(b) shows that the volumetric proportion of inactive grains is sensitive to density. In particular, a relatively large proportion of inactive particles is observed for the loosest case.

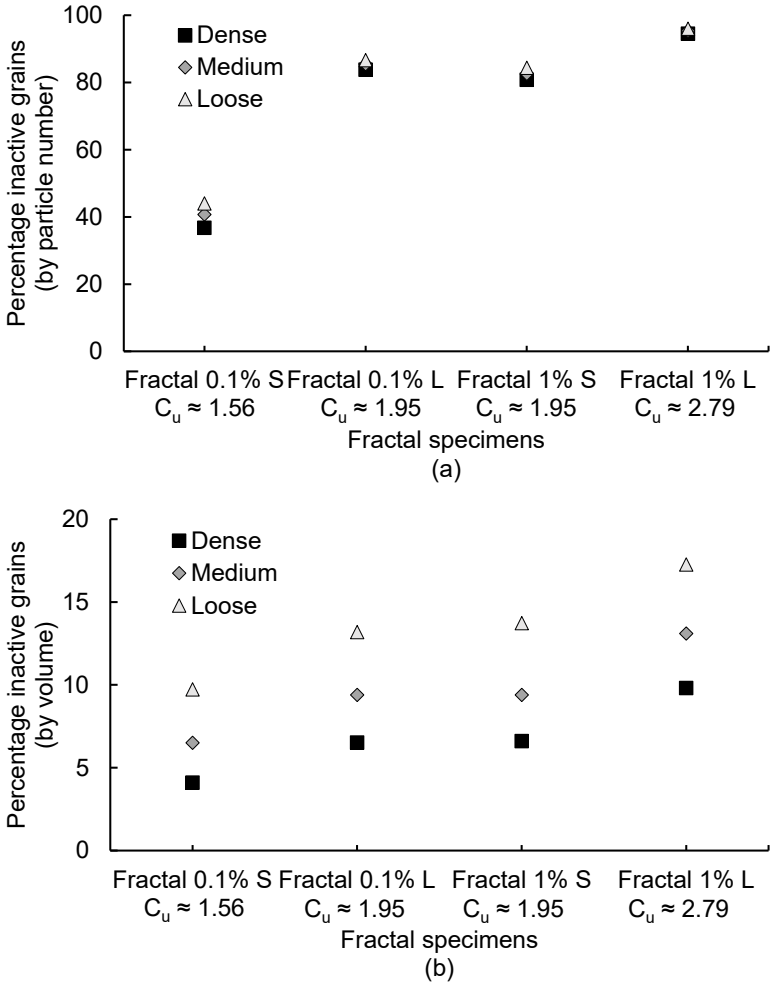


Figure 4.20: Variation in the percentage of inactive grains with C_u for fractal specimens: (a) percentage of inactive grains by number (b) percentage of inactive grains by volume

Relative differences in state variables

Referring to Figure 4.21, it can be seen that e_m is consistently large compared to the corresponding e for the fractal specimens. In particular, a relatively large difference can be observed for the loosest condition.

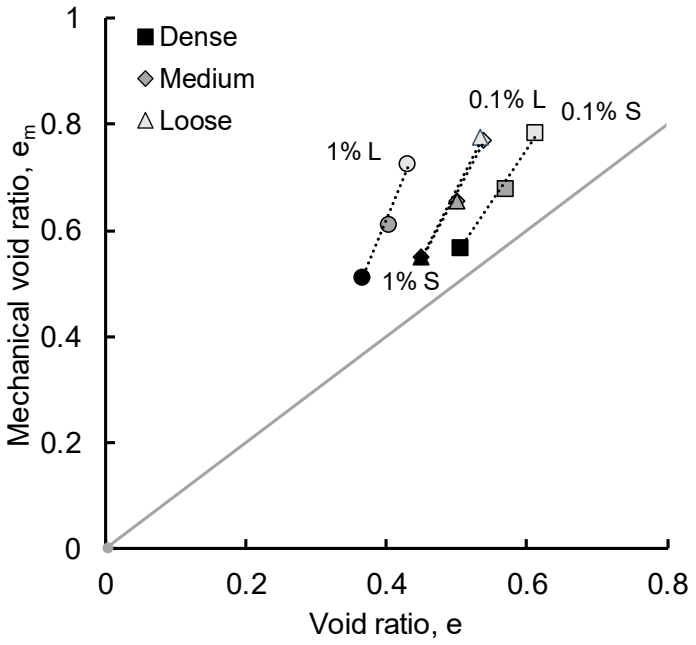


Figure 4.21: Comparison of measures of packing density for fractal specimens, e versus e_m

Figure 4.22 presents the relative differences in the state variables, void ratio and bulk density. For instance, Figure 4.22(a) shows that, for Fractal 1% L, the relative differences in void ratio, quantified as $(e_m - e)/e$ are approximately 41% and 70% in the densest and loosest conditions, respectively. The relative bulk density difference is also quantified, the maximum relative difference can be observed for Fractal 1% L in the loosest case, $(\rho - \rho_m)/\rho$ is approximately 16%.

Although the shapes of the $PSDs$ differ in the linear cases, the results shown in Figure 4.22 further indicate the limitation of e as a metric that can quantify the proportion of stress transmitting contacts and particles even where the PSD shape is continuous. As before the data indicate that the effect is more pronounced in looser specimens.

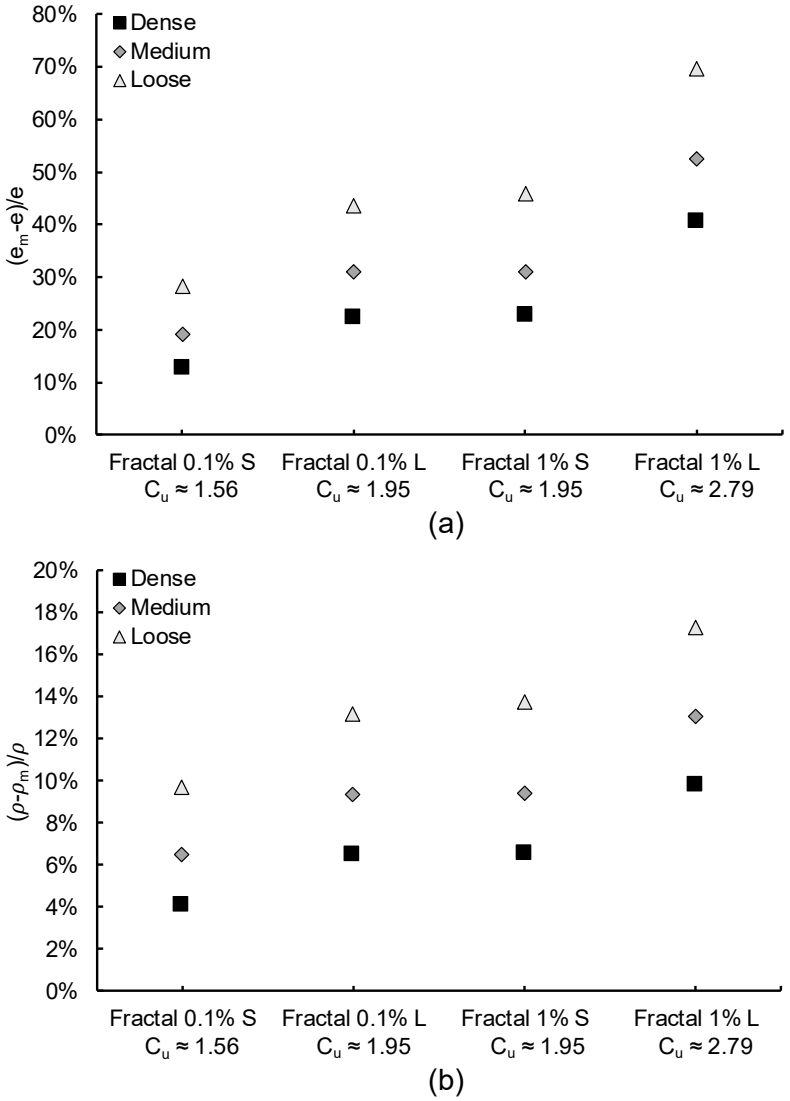


Figure 4.22: Comparison of measures of packing density for fractal specimens: (a) (e -e_m)/ e versus C_u; (b) (ρ-ρ_m)/ ρ versus C_u

4.4.3. Bimodal specimens

The size ratio of 3.7

The first set of data considered for the bimodal specimens are for the case where the SR = 3.7. Recalling the discussions in Section 4.3.2, for this SR, it is very unlikely that the finer particles can sit within the voids between the coarser grains without contacting the coarser grains. SR = 3.7 is the smallest SR considered for the bimodal specimens considered in this study. Figure 4.23(a) illustrates the relationship between F_{finer} and global void ratio, e for the loose and dense bimodal samples with SR = 3.7. Note that these densest

and loosest void ratios were acquired for a specific isotropic state (i.e. p' = 500 kPa) using μ = 0.001 or 0.3, respectively. As clarified in Chapter 3, these densest and loosest void ratios are not directly equivalent to those measured in laboratory tests based on particular standards (e.g. $ASCE\ D4253$; $ASCE\ D4254$). However, these void ratio data capture key trends of void ratio variation with F_{finer} that has been reported in several experimental studies including Lade et al. (1998). It can be seen that the minima of the densest void ratio is reached when F_{finer} is 20%, while the minima of the loosest void ratio is observed when F_{finer} is 25%. This result agrees the findings proposed in Zuo & Baudet (2015), as illustrated in Chapter 2, that the minima points of the loosest and densest void ratios do not occur at the same F_{finer}. Following Zuo & Baudet (2015), the threshold finer fraction S^* seems to be located between F_{finer} values of 20% and 25%.

Figure 4.23(b) illustrates the relationship between e_m and F_{finer}; for both the densest and loosest void ratios, the e_m gradually decreases with increasing F_{finer}. No threshold point which one might associate with S^* can be identified in Figure 4.23(b).

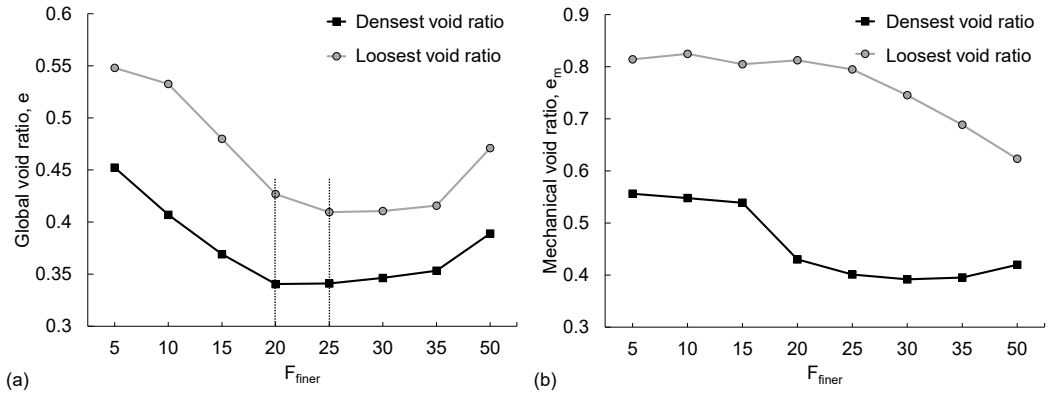


Figure 4.23: Influence of F_{finer} on global void ratio and mechanical void ratio when SR = 3.7: (a) e versus F_{finer}; e_m versus F_{finer}

Data giving the cumulative distribution of connectivity for the underfilled soil

fabric (i.e. F_{finer} = 10%) where $SR = 3.7$ is illustrated in Figure 4.24. These data indicate that for all three packing densities considered, more than 80% of finer grains are inactive in the stress transmission from the perspective of either the particle number or the particle volume. In contrast, more than 80% of coarser grains are active, these data confirm that the coarser particles dominate the soil behaviour at such a small F_{finer} value even though the SR is relatively low.

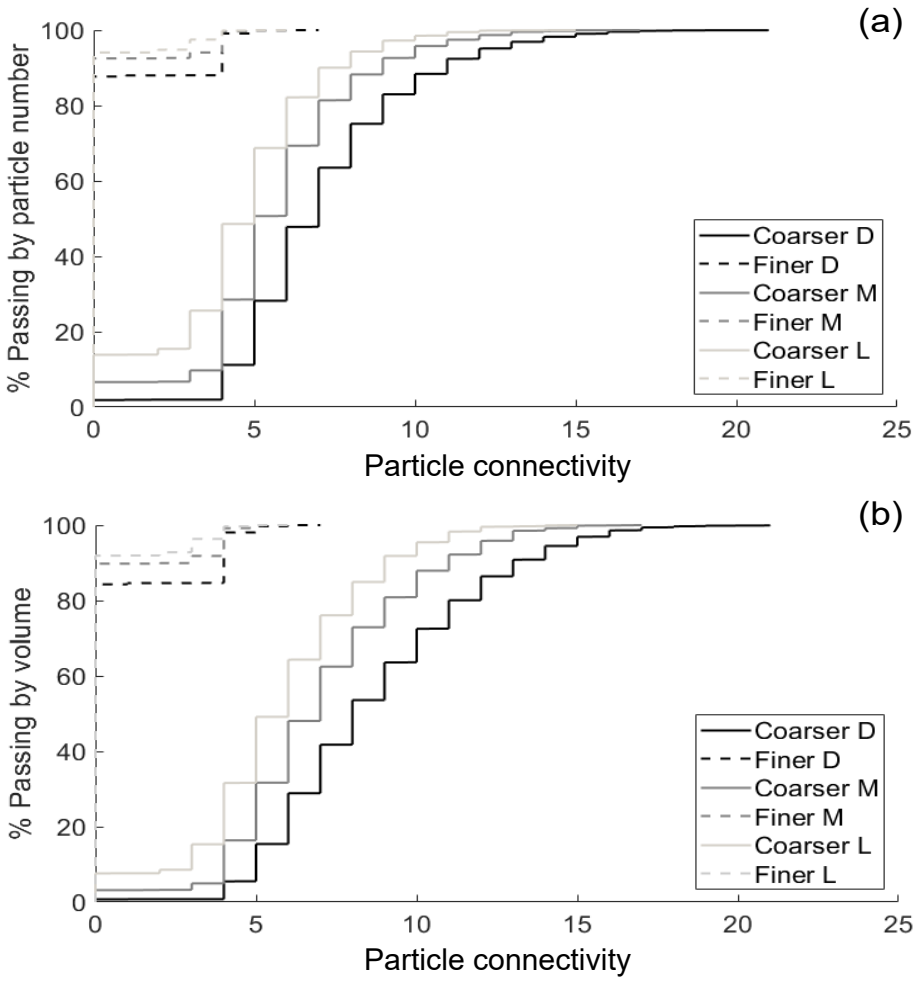


Figure 4.24: Cumulative distribution of connectivities for bimodal specimens with F_{finer} = 10% (SR 3.7): (a) distribution by number; (b) distribution by volume (D, M and L denote dense, medium-dense and loose specimen respectively)

For F_{finer} = 25%, The distribution of connectivities is markedly different when compared to the data for F_{finer} = 10%. As illustrated in Figure 4.25, from the

perspective of particle volume, the proportions of inactive finer grains are approximately 19%, 45% and 79% in the densest, medium and loosest conditions, respectively. For this F_{finer}, the effect of density on the soil behaviour is significant.

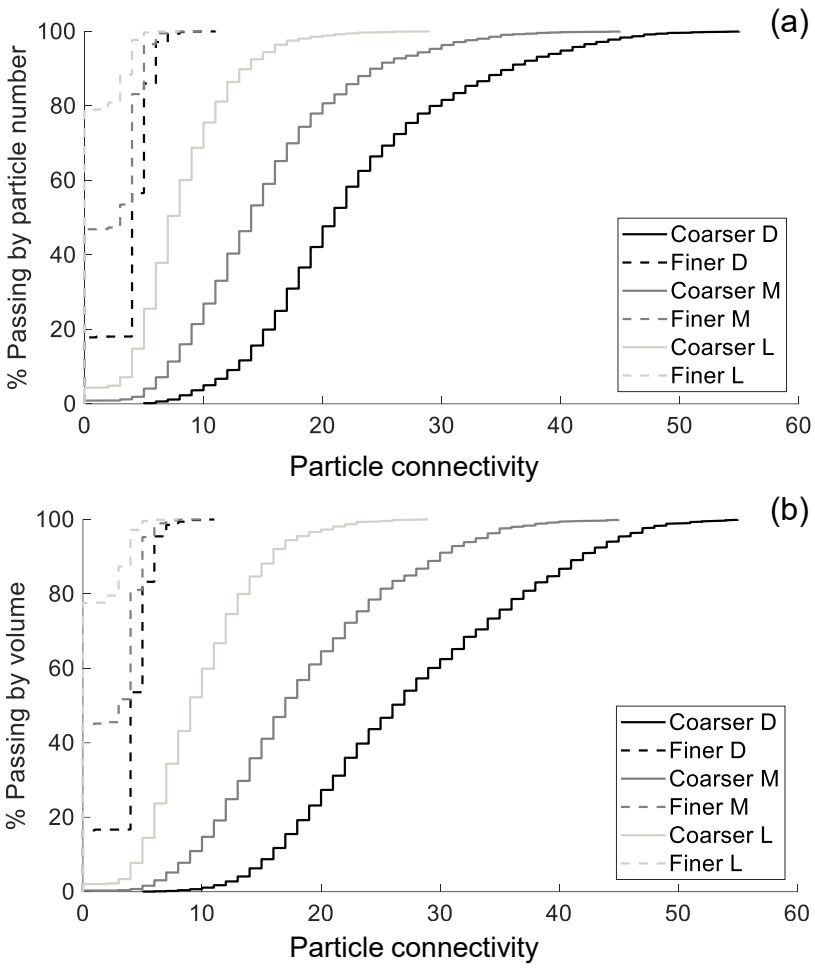


Figure 4.25: Cumulative distribution of connectivities for bimodal specimens with F_{finer} = 25% (SR 3.7): (a) distribution by number; (b) distribution by volume (D, M and L denote dense, medium-dense and loose specimen respectively)

The data in Figure 4.26 show that when F_{finer} increases to 50%, more than 80% of the finer grains by volume become active in stress transmission. Compared to the trend identified in Figure 4.25 for the specimens with F_{finer} = 25%, the effect of packing density is less evident at this higher F_{finer} of 50%.

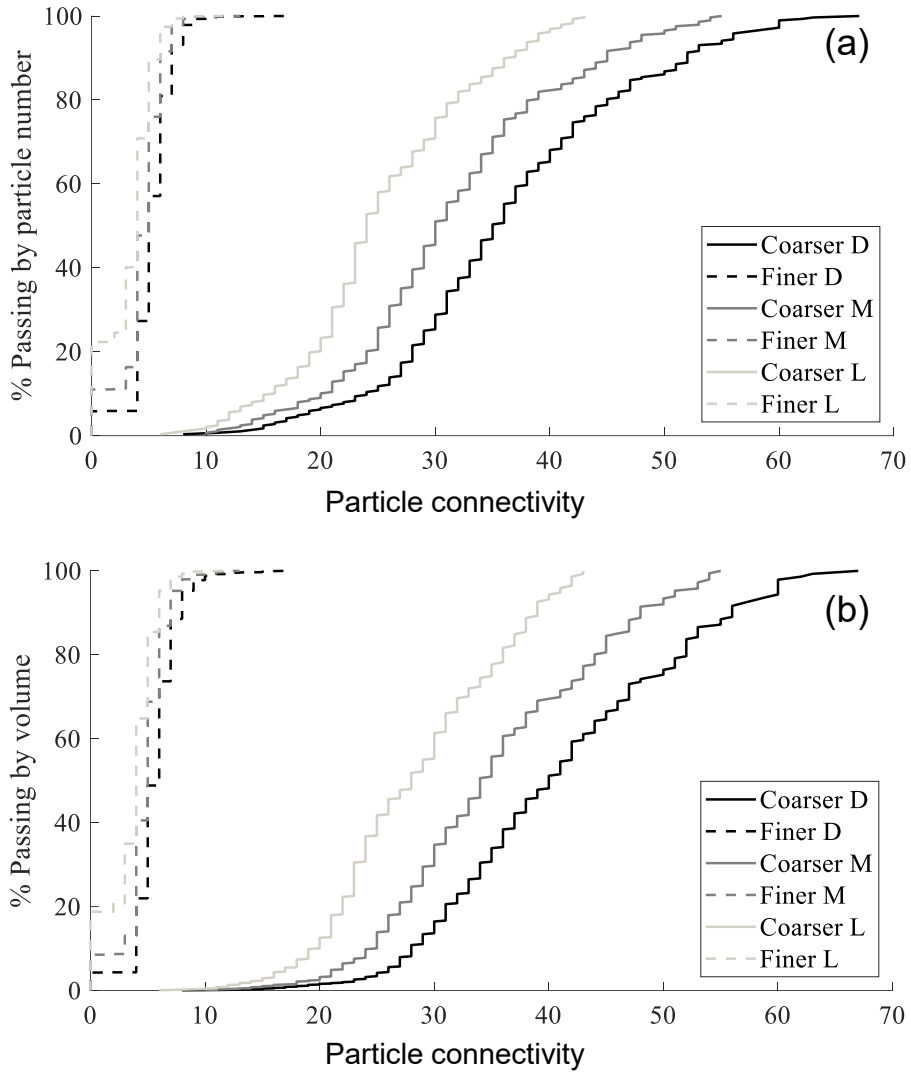


Figure 4.26: Cumulative distribution of connectivities for bimodal specimens with F_{finer} = 50% (SR 3.7): (a) distribution by number; (b) distribution by volume (D, M and L denote dense, medium-dense and loose specimen respectively)

To better understand how the material fabric varies with F_{finer}, the percentages of inactive grains in these bimodal specimens are illustrated in Figure 4.27. As illustrated in Figure 4.27(a), in the dense condition, the percentage of inactive grains gradually increases when F_{finer} varies from 5% to 10%, followed by a gradual decrease when F_{finer} increases from 10% to 50%. A significant decrease in the proportion of inactive grains can be identified between F_{finer} of 15% and 20%. When referring to the medium and loose condition, a similar trend is identified compared to that observed in the dense condition.

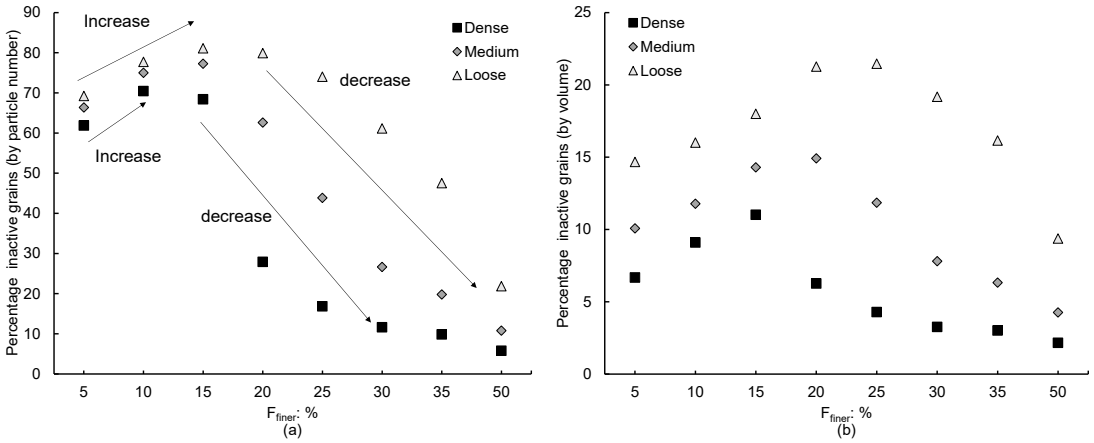


Figure 4.27: Percentage of inactive grains versus F_{finer} for bimodal specimens with SR = 3.7: (a) percentage of inactive grains by number (b) percentage of inactive grains by volume

To study this significant change in the proportion of active particles between F_{finer} of 15% and 20%, the connectivity distributions for samples with these two F_{finer} values in the dense condition are illustrated in Figure 4.28. Figure 4.28 indicates a significant difference in the proportion of active finer grains when F_{finer} is varied from 15% to 20%. When F_{finer} is 15%, approximately 80% of the finer grains are inactive in the stress transmission, while only approximately 30% of finer grains are inactive when F_{finer} is 20%. This significant difference in the proportion of inactive particles reflects a significant change in the fabric of the material.

Figure 4.28 also indicates that the maximum particle connectivity in the sample with F_{finer} = 20% is large (approximately 54) compared to that observed for the sample with F_{finer} = 15% (approximately 34). Figure 4.29 shows two-dimensional projections of the particles along with a thin slice through the centre of the sample for each of two specimens (i.e. F_{finer}= 15% and F_{finer} = 20%) at the end of isotropic compression. The slice considered had a thickness of 0.038 mm. The grains in coloured grey are inactive grains, and the thickness of the line between the centroid of two individual grains represents the magnitude of the contact normal force. These plots illustrate the marked change

in the material fabric when F_{finer} increases from 15% to 20%.

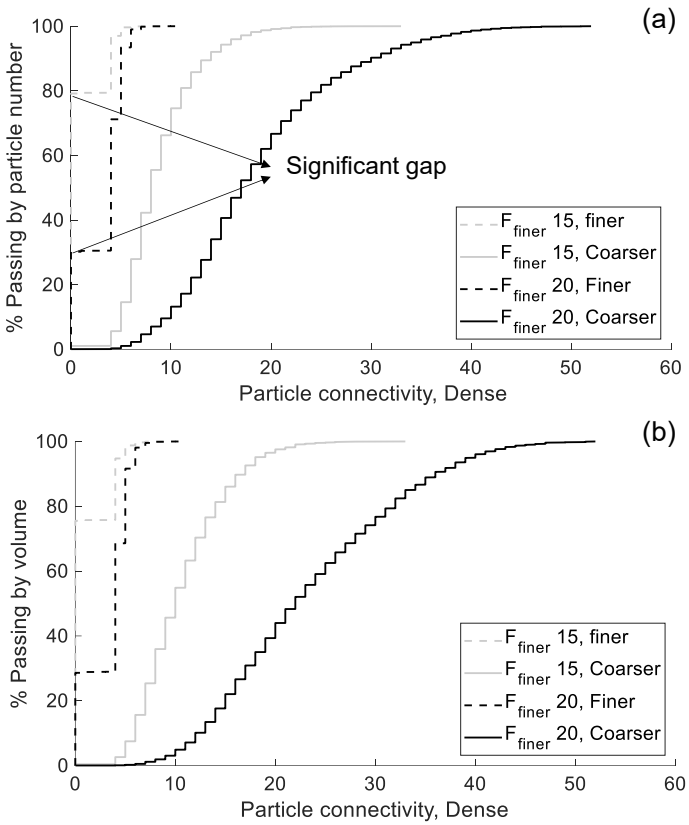


Figure 4.28: Comparison between the F_{finer} of 15% and 20%: (a) by particle number; (b) by volume

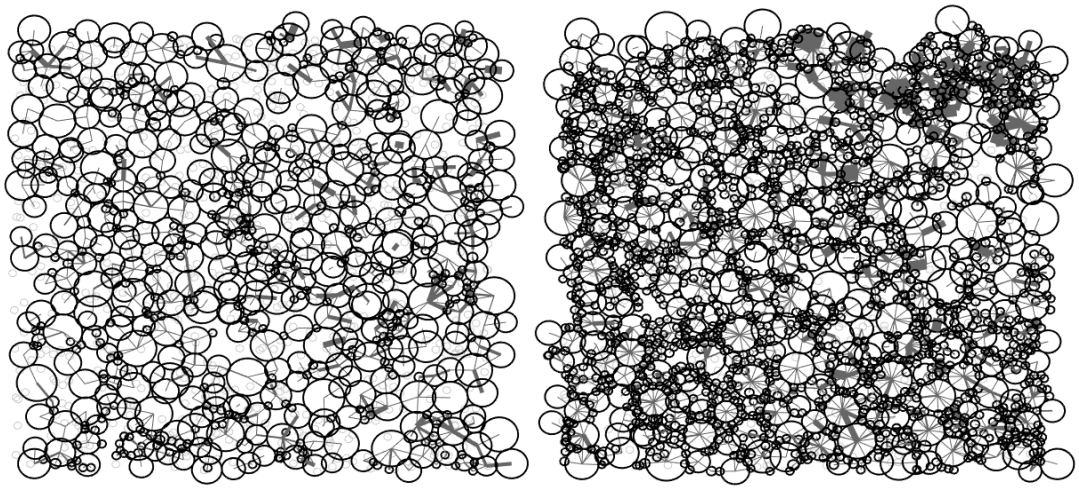


Figure 4.29: Comparison between the F_{finer} of 15% and 20% in contact force network in the densest condition: (a) F_{finer} = 15%; (b) F_{finer} = 20%

Figure 4.30 illustrates the relationship between e and e_m for all the bimodal samples considered with SR = 3.7. The trend is similar to those observed in the linear and fractal specimens, i.e. the e_m values are consistently above their corresponding e values. The difference between e and e_m increases as the sample density decrease.

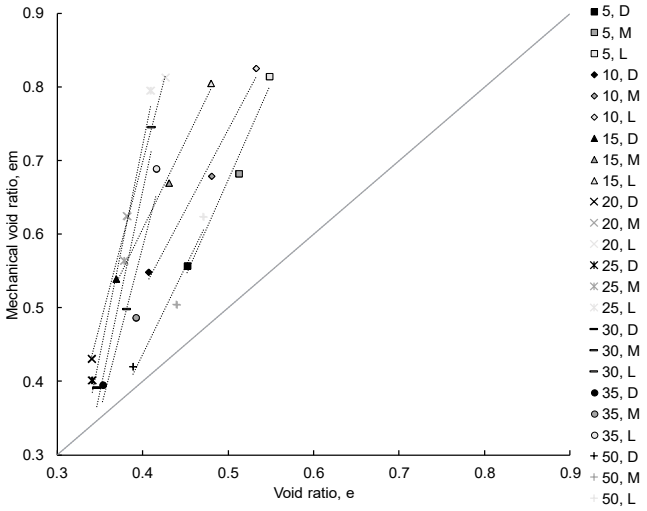


Figure 4.30: Comparison of measures of packing density for bimodal specimens (SR = 3.7), e versus e_m (numbers in legend indicates the F_{finer} from 5% to 50%. D, M and L denote dense, medium-dense and loose specimen, respectively)

Figure 4.31 illustrates the relative difference in the measures of state, i.e. *(e - e_m)/ e* and *(ρ - ρ_m)/ ρ* for these bimodal specimens. The relative differences for the loose specimens are higher than these of the case in the dense and medium conditions. The maximum relative differences are approximately 21% which is large compared to the maximum relative difference observed in the linear specimens (approximately 13%).

Similar trends can be observed in the measure of differences in bulk density. In the dense condition, these relative differences increase with increasing F_{finer} until F_{finer} attains 15%, followed by a decrease with F_{finer} up to 50%. The maximum relative difference in the bulk density is approximately 10%. In contrast, in the loose condition, the relative differences in bulk density increase

until F_{finer} is 25%, and there is a subsequent monotonic decrease with additional increments in F_{finer}; in this case, the maximum relative difference is approximately 20%.

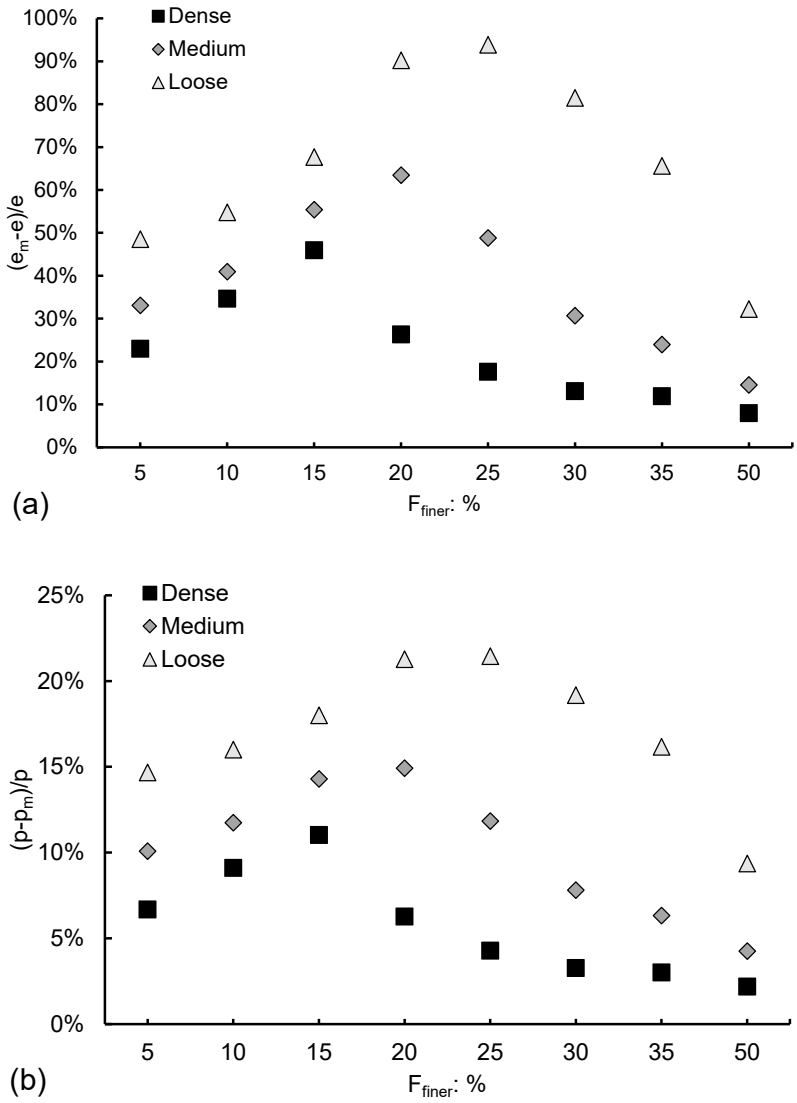


Figure 4.31: Comparison of measures of packing density for bimodal specimens (SR = 3.7): (a) (e - e_m)/ e versus F_{finer}; (b) (ρ - ρ_m)/ ρ versus F_{finer}

As discussed in Chapter 2, different state variables (i.e. e, e_m, e_{sk}, e^*) have been proposed to enable the prediction of the behaviour of gap-graded soils. The variation in each of these state variables with F_{finer} is presented here. The b values used in calculating the equivalent void ratio, e^*, were determined using the empirical equation proposed in Rahman et al. (2008). The specimens

with F_{finer} values of up to 25% were considered.

In the dense condition, as illustrated in Figure 4.32(a) when F_{finer} is 5% and 10%, the three alternative state variables (i.e. e_m, e_{sk}, e^*) have similar values. This suggests that the assumption that finer grains have limited contribution seems reasonable with a lower F_{finer} (i.e. 5%, 10%). In contrast, when F_{finer} is 15%, clear differences can be identified amongst these three state variables. The data indicate that e_{sk} may not be an appropriate state variable to capture the soil behaviour of gap-graded soils since in this F_{finer}, the finer grains start to provide a finite contribution to the structure. When F_{finer} is 20% and 25%, the e_{sk} measure is no longer effective when compared to e_m. While e_m and e^* are similar for all F_{finer} values considered.

In the medium-dense condition, as illustrated in Figure 4.32(b), e_{sk} increases as F_{finer} increases. The e_m values are larger than the e^* and e_{sk} values when F_{finer} is 5% and 10%. This may be because, at this medium density level, not all of the coarser grains are active in the stress transmission. When F_{finer} is larger than 15%, clear differences are observed among these state variables.

In the loose condition, as illustrated in Figure 4.32(c), the e_m values are larger than the e^* and e_{sk} values when F_{finer} is lower than 25%. For these specimens, a relatively large proportion of coarser grains are inactive, for instance, more than 18% of coarser grains by number are inactive when F_{finer} is 5%. In addition, the differences amongst these state variables are significant when F_{finer} is larger than 5%. In general, it can be seen that only e_m has captured the effect of packing density, while the other state variables do not include the effect of density which is rather significant.

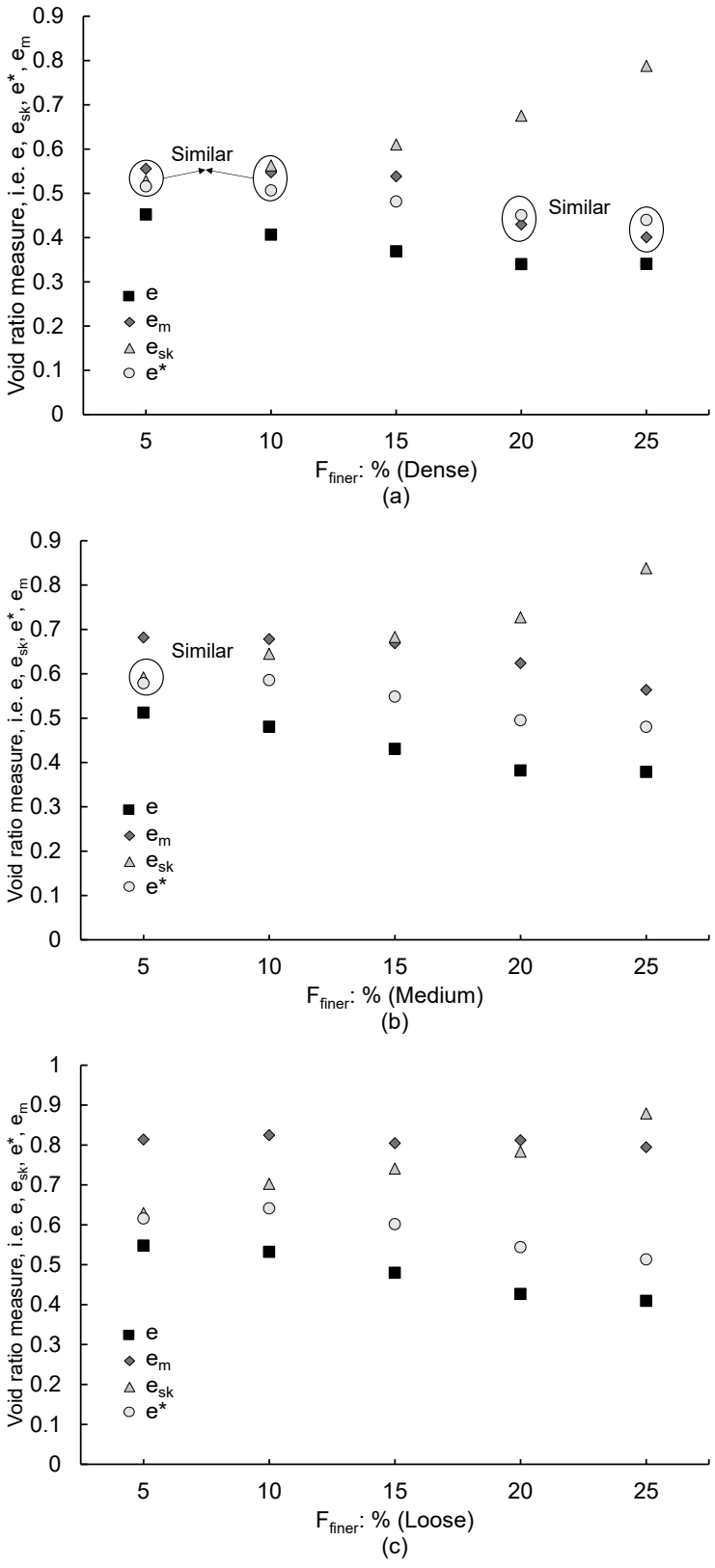


Figure 4.32: Different state variables for bimodal gap-graded soils (SR = 3.7): (a) Dense condition; (b) Medium condition; (c) Loose condition

The size ratio of 8.4

As discussed before, a SR value of 8.4 is sufficiently large that a finer particle can fit within a void formed between the coarser grains without contacting any of the coarser grains forming the void. Figure 4.33 illustrates the variation in void ratio with F_{finer} for the loosest and densest packings for the specimens with SR = 8.4. Considering the densest specimens, which give data analogous to the densest void ratio obtained in a laboratory test, the minimum value of e is attained when F_{finer} is 20%, while the minimum point is reached when F_{finer} is 30% for the loosest packings considered (i.e. analogous to the loosest void ratio e_{min}). Figure 4.33(b) shows the relationship between F_{finer} and e_m for both the loosest and densest packings considered. For the dense specimens, a sudden drop in e_m is observed when F_{finer} increases from 20% to 25%. This drop indicates that soil fabric changes in this case. In contrast, for the loosest specimens, a comparable change of soil fabric is identified when F_{finer} increases from 30% to 35%.

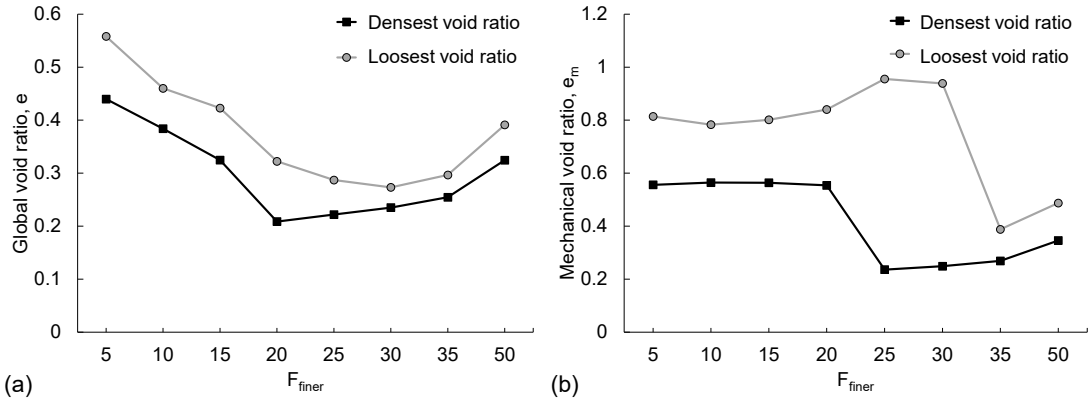


Figure 4.33: Influence of F_{finer} on e and e_m ($SR = 8.4$): (a) e versus F_{finer}; e_m versus F_{finer}

Figure 4.34 shows the cumulative distribution of connectivities for the bimodal specimens with SR = 8.4 when F_{finer} = 10%; these data show that more than 98% of finer grains by volume are inactive at all three density levels considered. In contrast, more than 90% of the coarse grains by volume are active in

transferring stress. This case can be considered to be coarse-dominant behaviour.

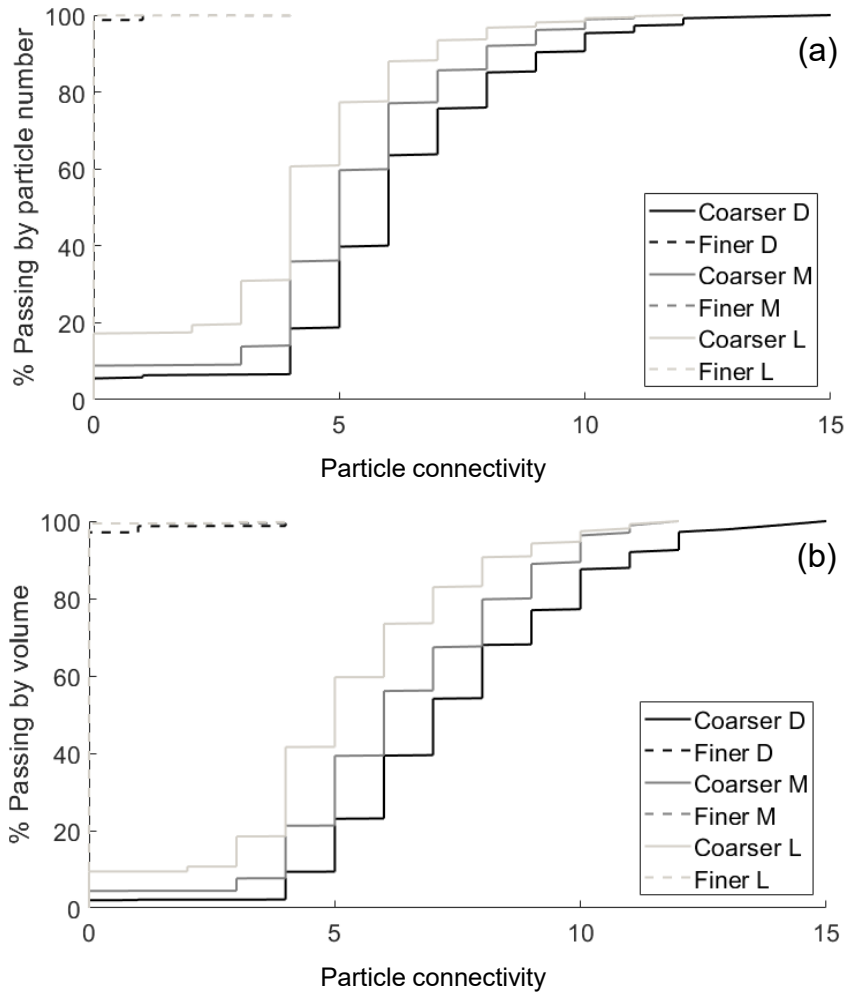


Figure 4.34: Cumulative distribution of connectivities for bimodal specimens with F_{finer} = 10% (SR 8.4): (a) distribution by number; (b) distribution by volume (D, M and L denote dense, medium-dense and loose specimen, respectively)

Figure 4.35 shows the cumulative distribution of connectivities for bimodal specimens with SR = 8.4 when F_{finer} = 25%; the key finding is that the effect of density on the cumulative distribution of connectivities is significant in this case. In the dense condition, the connectivity values of the coarser grains can be as high as 300, while the maximum connectivity values of the coarser grains decrease to a value of approximately 20 in the loose condition.

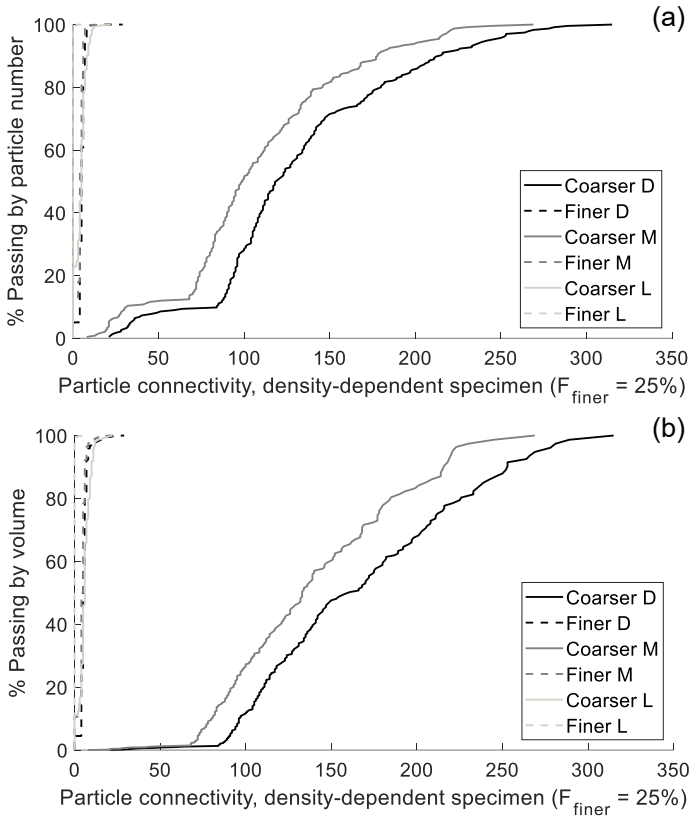


Figure 4.35: Cumulative distribution of connectivities for bimodal specimens with F_{finer} = 25% (SR 8.4): (a) distribution by number; (b) distribution by volume (D, M and L denote dense, medium-dense and loose specimen respectively)

Figure 4.36 shows the cumulative distribution of connectivities for bimodal specimens when F_{finer} = 50%. For all three density conditions considered, the connectivity values of these coarser grains are large with median values between 125 and 175, this is indicative of an overfilled fabric.

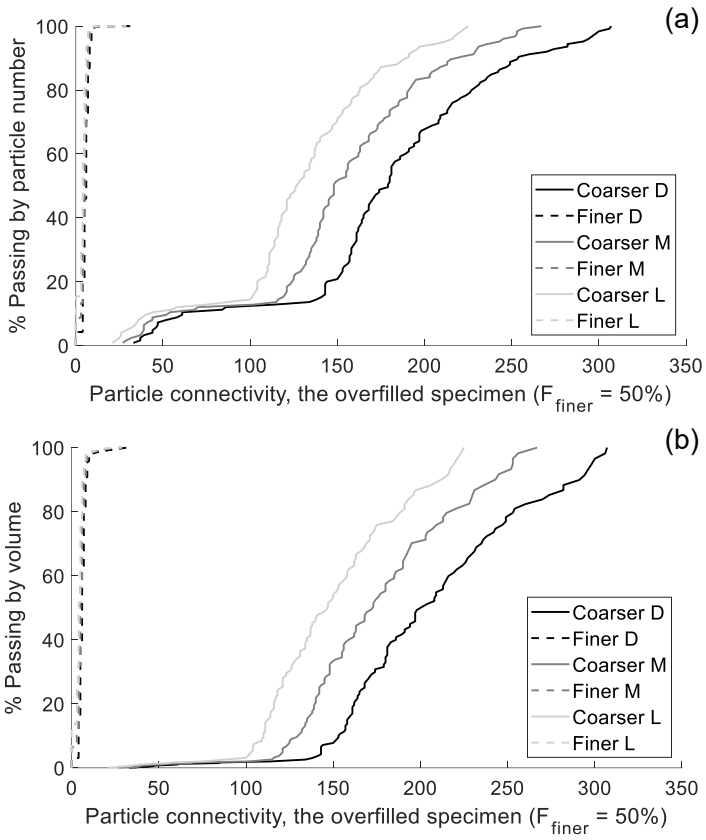


Figure 4.36: Cumulative distribution of connectivities for bimodal specimens with F_{finer} = 50% (SR 8.4): (a) distribution by number; (b) distribution by volume (D, M and L denote dense, medium-dense and loose specimen respectively)

The percentages of inactive grains in the bimodal specimens with SR = 8.4 are presented in Figure 4.37. Figure 4.37(a) illustrates the percentages of inactive grains by particle number for all three density levels, it can be seen that more than 98% of particles are inactive when F_{finer} varies from 5% to 20%, when F_{finer} ranges from 25% to 30%, a significant difference is observed when comparing the data for the dense and loose conditions. When $F_{finer} \geq 35\%$, most particles are active irrespective of the density level. Besides, Figure 4.37(b) shows that the percentage of inactive grains by volume gradually increases when F_{finer} varies from 5% to 20%, which may suggest that these finer grains are filling in the voids without transferring stress. However, this tendency is not observed in Figure 4.37(a) since the number of inactive particles is significantly large compared to the number of active particles.

When F_{finer} is exceeds 20% in the dense condition, as illustrated in Figure 4.37(b), the percentage of inactive grains decreases to approximately 3%, which suggests that almost all of the finer grains transfer stress. In contrast, in the loose condition, the percentage of inactive grains attains a maximum when F_{finer} is 30%. These results differ from the data for SR = 3.7 illustrated in Figure 4.27, reflecting the significant size ratio effect when SR is increased from 3.7 to 8.4.

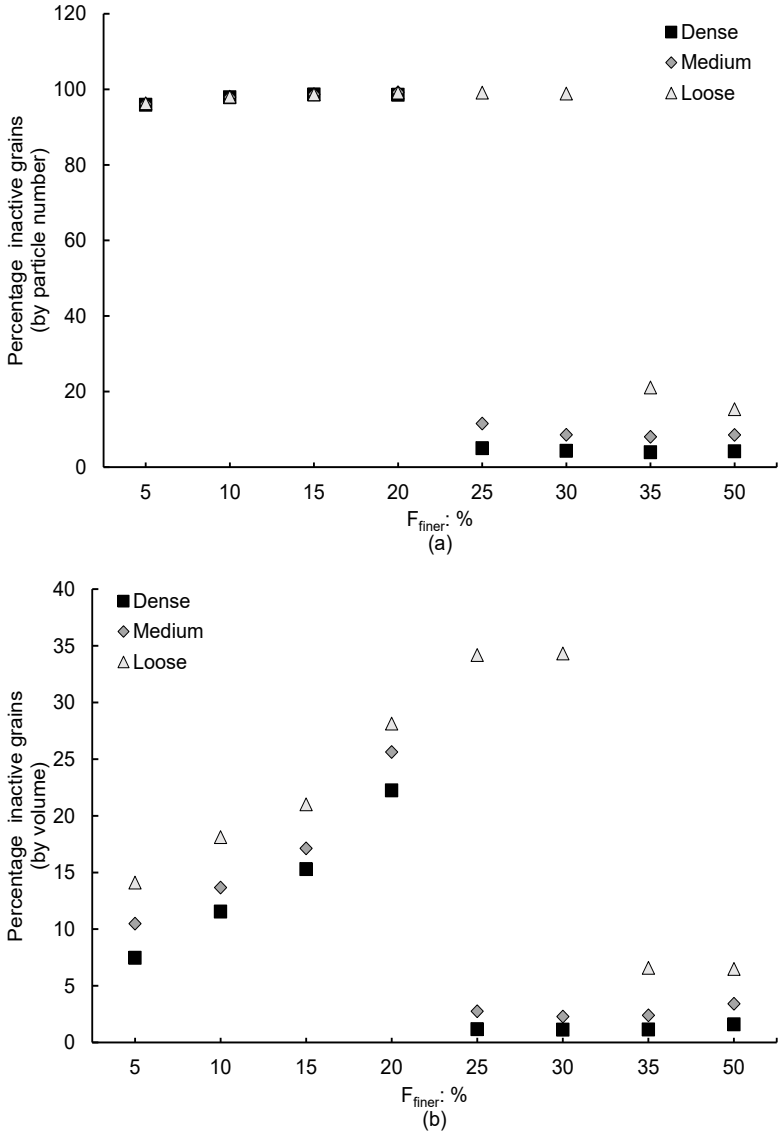


Figure 4.37: Percentage of inactive grains versus F_{finer} for bimodal specimens (SR = 8.4): (a) percentage of inactive grains by number (b) percentage of inactive grains by volume

To investigate the significant change in the soil fabric as a function of specimen

density when F_{finer} is 25%, the e, e_m and Z data for this case at the three density conditions considered are illustrated in Figure 4.38(a). These data clearly show that both e_m and Z change significantly as the packing density reduces. Figure 4.38(b) and Figure 4.38(c), illustrate the projections of segments through the centre of two of these specimens (i.e. dense; loose) at the end of isotropic compression. The grains illustrated in grey are the inactive grains, and the thicknesses of the lines between the centroids of pairs of grains represent the magnitude of the contact normal force. It can be seen that the fabric of the dense specimen can be considered to be overfilled while the fabric of the loose specimen is underfilled. In addition, Figure 4.38(c) shows that the small Z in the loose case can be attributed to the reduction in the number of finer-finer contacts and coarser-finer contacts.

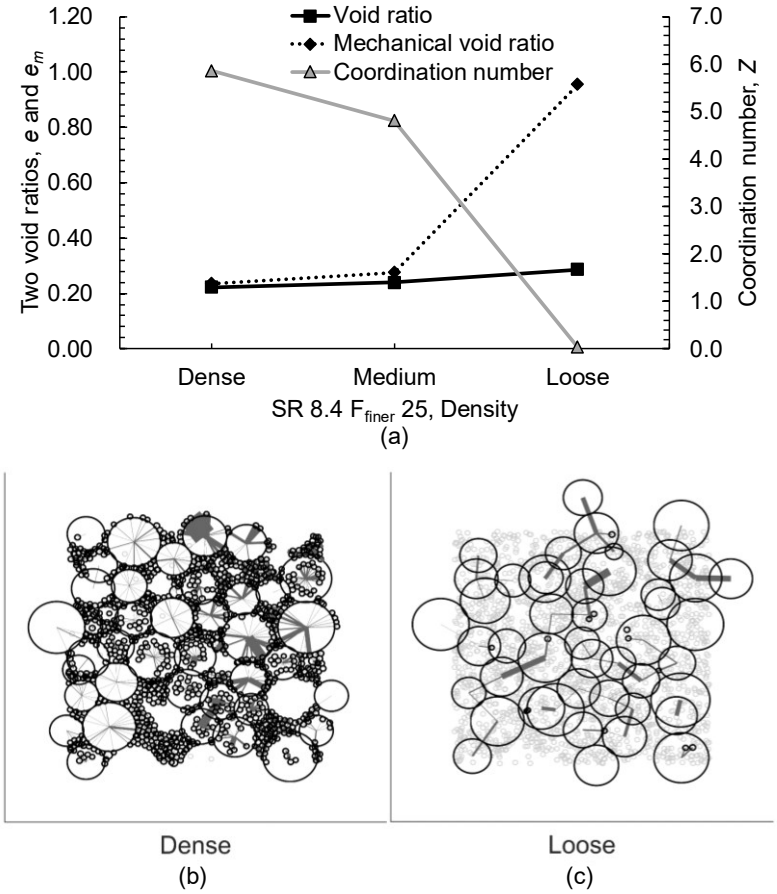


Figure 4.38: Comparison between the dense and loose condition of F_{finer} of 25% in contact force network (SR = 8.4): (a) macro scale; (b) dense; (c) loose

Figure 4.39 compares e and e_m when SR is 8.4 for all F_{finer} and density values considered. For F_{finer} values between 5% and 20%, the trends are similar, and the e_m values of all these specimens are above their corresponding e values. The lines defining the relationship between e_m and e are almost parallel for F_{finer} values from 5% to 20%. When F_{finer} increases to 25% and 30%, a more significant density effect can be observed. In the loose condition, the e_m values for these specimens are much larger than their corresponding e values. In contrast, in the dense condition, the e_m values are similar to their e values. For F_{finer} values from 35% to 50%, the e_m values are similar to the e values irrespective of the density condition.

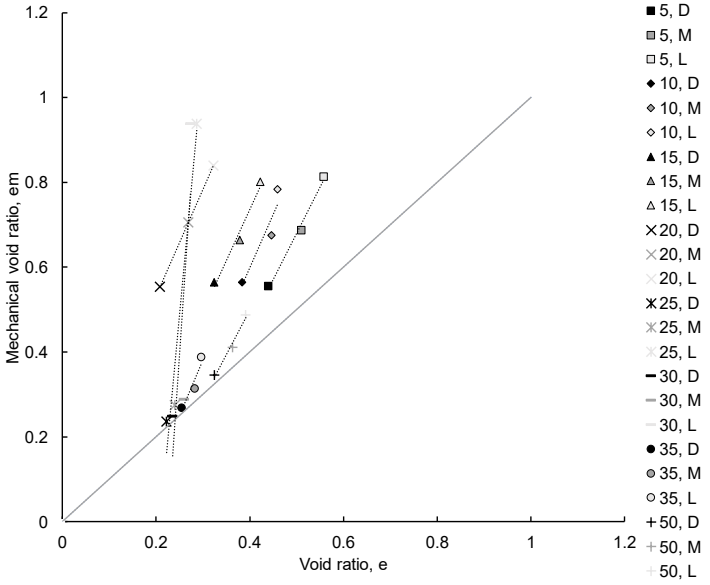


Figure 4.39: Comparison of measures of packing density for bimodal specimens (SR = 8.4), e versus e_m (the numbers in the legend indicate the F_{finer}. D, M and L denote dense, medium-dense and loose specimen respectively)

Figure 4.40 illustrates the relative differences in the measures of state $(e - e_m)/e$ and $(\rho - \rho_m)/\rho$ for these bimodal specimens. In general, the relative differences in both measures of state for these specimens are significantly higher than those identified when SR = 3.7. For the case where SR = 3.7 the maximum difference in $(e - e_m)/e$ is approximately 92%, in contrast when SR = 8.4, the void ratio measures can differ by up to 240%. In addition, Figure

4.40(b) shows that the relative difference in bulk density is also significant, especially in the loose condition. The maximum normalized difference is approximately 35% when F_{finer} is 25% and 30%.

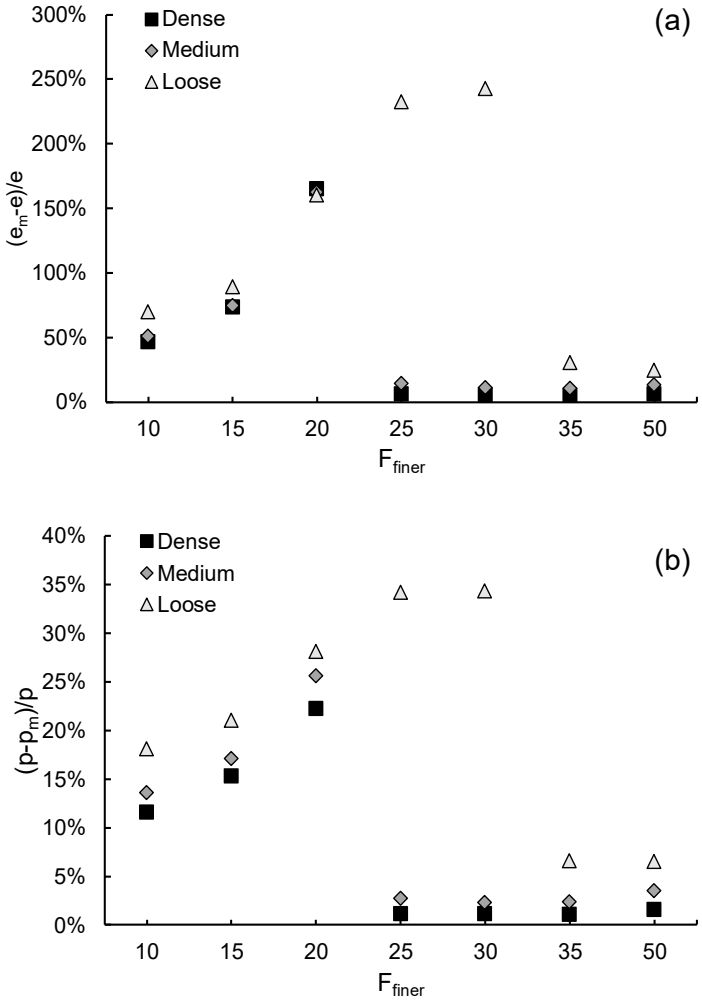


Figure 4.40: Comparison of measures of packing density for bimodal specimens (SR = 8.4): (a) $(e - e_m)/e$ versus F_{finer}; (b) $(\rho - \rho_m)/\rho$ versus F_{finer}

Figure 4.41 compares the four different void ratio measures considered in this study (i.e. e, e_m, e_{sk}, e^*) for the bimodal specimens with SR = 8.4. F_{finer} values between 5% and 25% were considered and the divergence amongst these four state variables increases with increasing F_{finer}. In contrast, for the loosest specimens, the e_m data are significantly larger than the e values, which indicates an underfilled case. Again, it can be seen that only e_m can capture the variation in the state with specimen density.

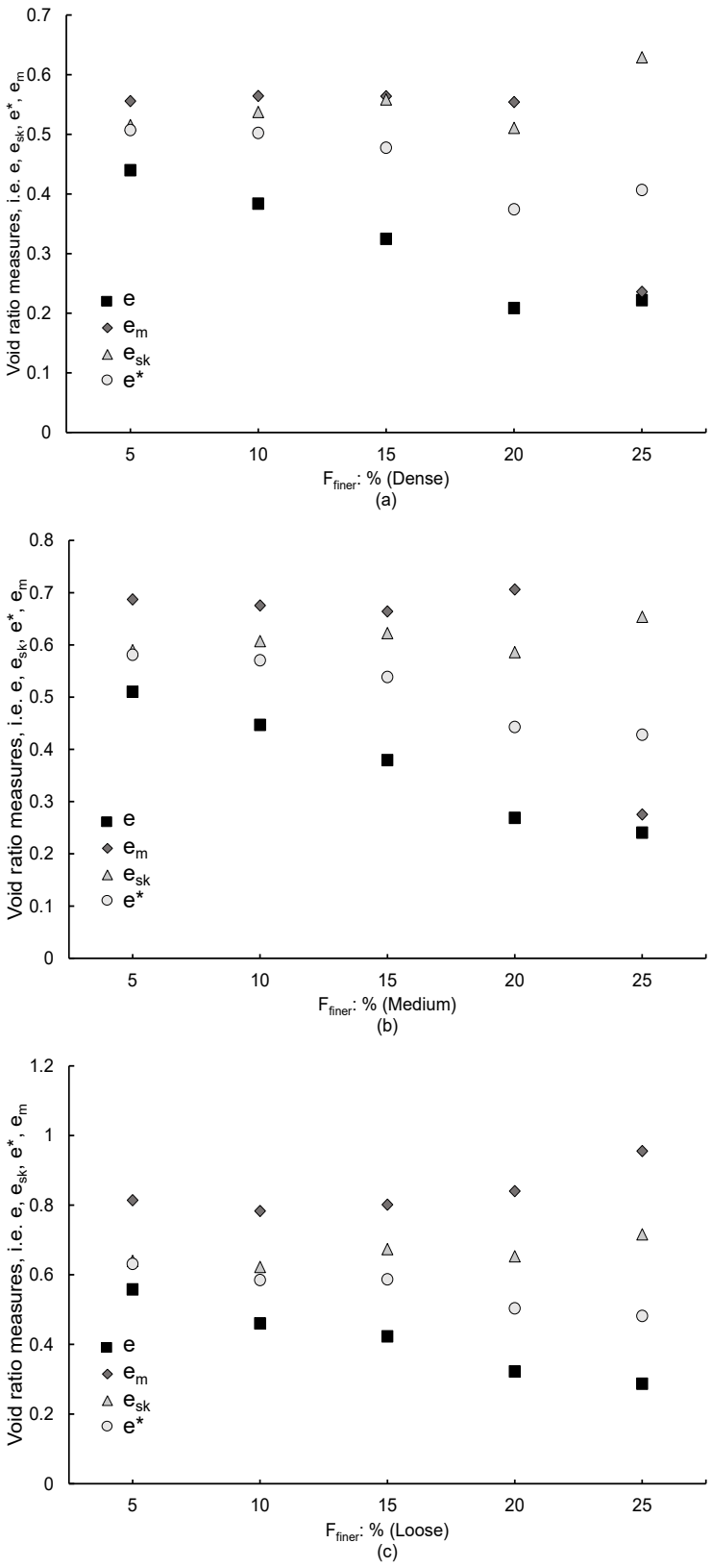


Figure 4.41: Different state variables for bimodal gap-graded soils (SR = 8.4): (a) Dense condition; (b) Medium condition; (c) Loose condition

The size ratio of 18.1

The largest size ratio considered in this Chapter was SR = 18.1, For this SR, the maximum diameter was 2.260 mm. Such a large size ratio has rarely been considered in prior DEM studies since the computing resources required are very large. The maximum number of particles used in the simulations considering this large SR was 481,611, which is also rather large compared to the most prior DEM studies.

Figure 4.42(a) illustrates the variation in void ratio, e, with F_{finer} for the bimodal gap-graded soils with SR = 18.1, For the dense specimens, a minimum point is attained when F_{finer} = 25%. For the loose specimens, a minimum point is reached when F_{finer} is 30%. Figure 4.42(b) shows the relationship between F_{finer} and e_m for the loosest and the densest packings considered here. For the dense specimens, a sudden drop is observed when F_{finer} increases from 20% to 25%. In contrast, for the loosest specimens, a similar change in soil fabric is identified when F_{finer} increases from 30% to 35%. In general, the variation in void ratio with F_{finer} for these bimodal gap-graded soils with SR = 18.1 is similar to that identified for the specimens with SR = 8.4. No strong size ratio effect can be observed when the SR is increased from 8.4 to 18.1. In contrast, a significant size ratio effect was identified when SR was increased from 3.7 to 8.4. For instance, when SR = 3.7 the densest void ratio is approximately 0.34 when F_{finer} is 20%. In contrast, for SR = 8.4 and 18.1 the densest void ratios $\approx$ 0.19 in both cases.

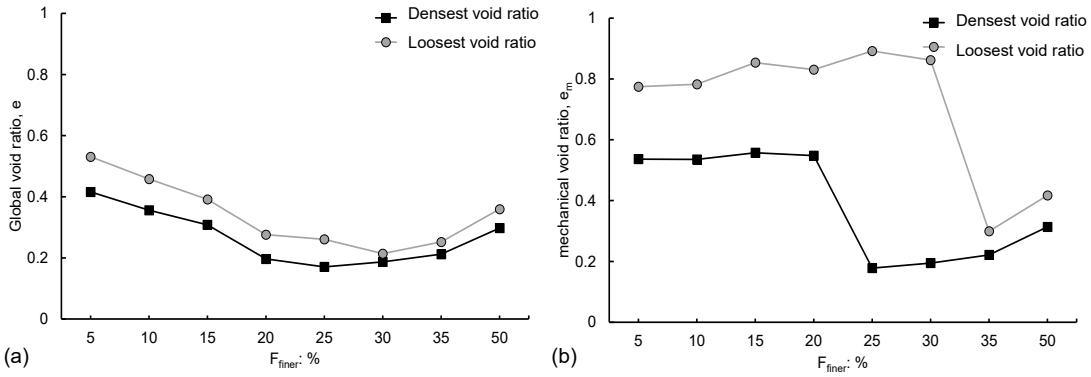


Figure 4.42: Influence of F_{finer} on global void ratio and mechanical void ratio (SR = 18.1): (a) e versus F_{finer}; (b) e_m versus F_{finer}

Figure 4.43 shows the cumulative distribution of connectivities for the bimodal specimens with SR = 18.1 when F_{finer} = 10%; these data show that more than 99% of the finer grains are inactive irrespective of the specimen density, this behaviour is also similar to that observed with SR = 8.4. The maximum connectivity value is approximately 18, which is also similar to that identified for the SR of 8.4. Since all these active particles are coarse particles, this case can be considered a coarse-dominant behaviour.

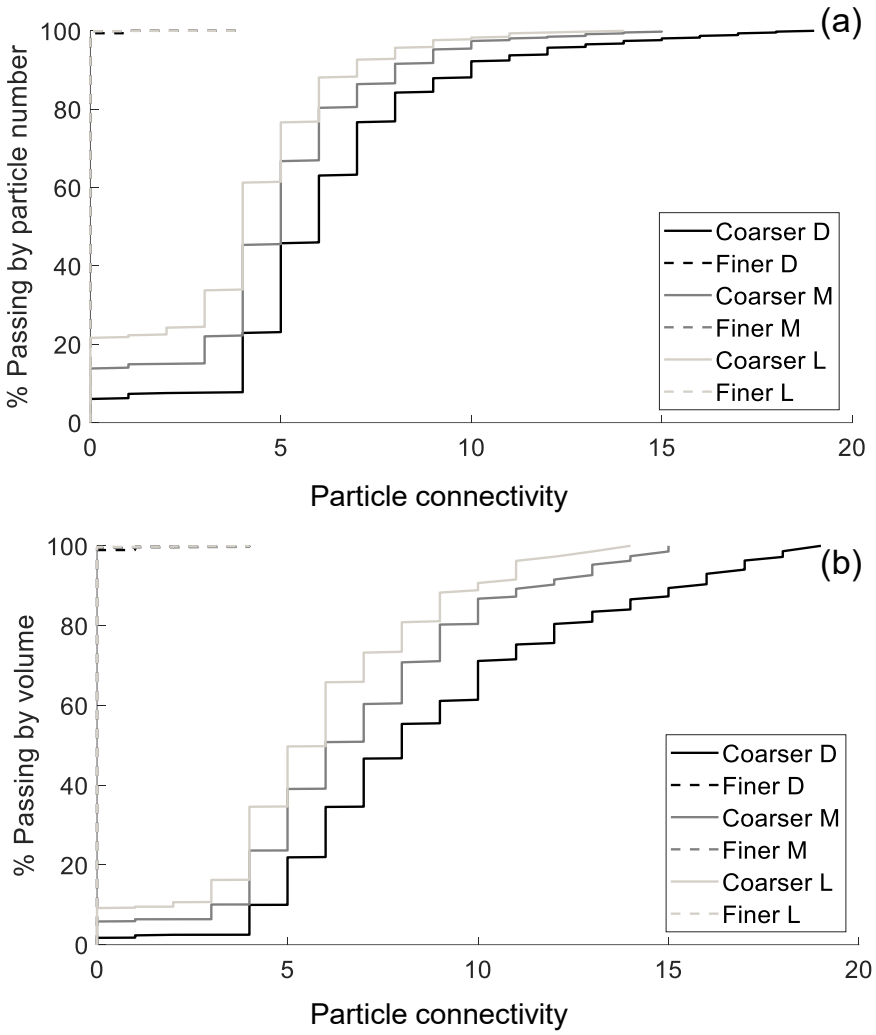


Figure 4.43: Cumulative distribution of connectivities for bimodal specimens with F_{finer} = 10% (SR 18.1): (a) distribution by number; (b) distribution by volume (D, M and L denote dense, medium-dense and loose specimen respectively)

Figure 4.44 shows the cumulative distribution of connectivities for bimodal specimens with SR = 18.1 when F_{finer} = 25%. For this size ratio, in the dense condition, the maximum connectivity value for the coarser grains is approximately 1700, which is significantly larger compared to that identified when size ratios are 8.4 (approximately 325). A strong density effect can also be observed. As the maximum connectivity value for the coarser grains decrease to approximately 20 in the medium and loose conditions. This significant decrease in connectivity values suggests that the soil fabric changes from being overfilled to an underfilled fabric.

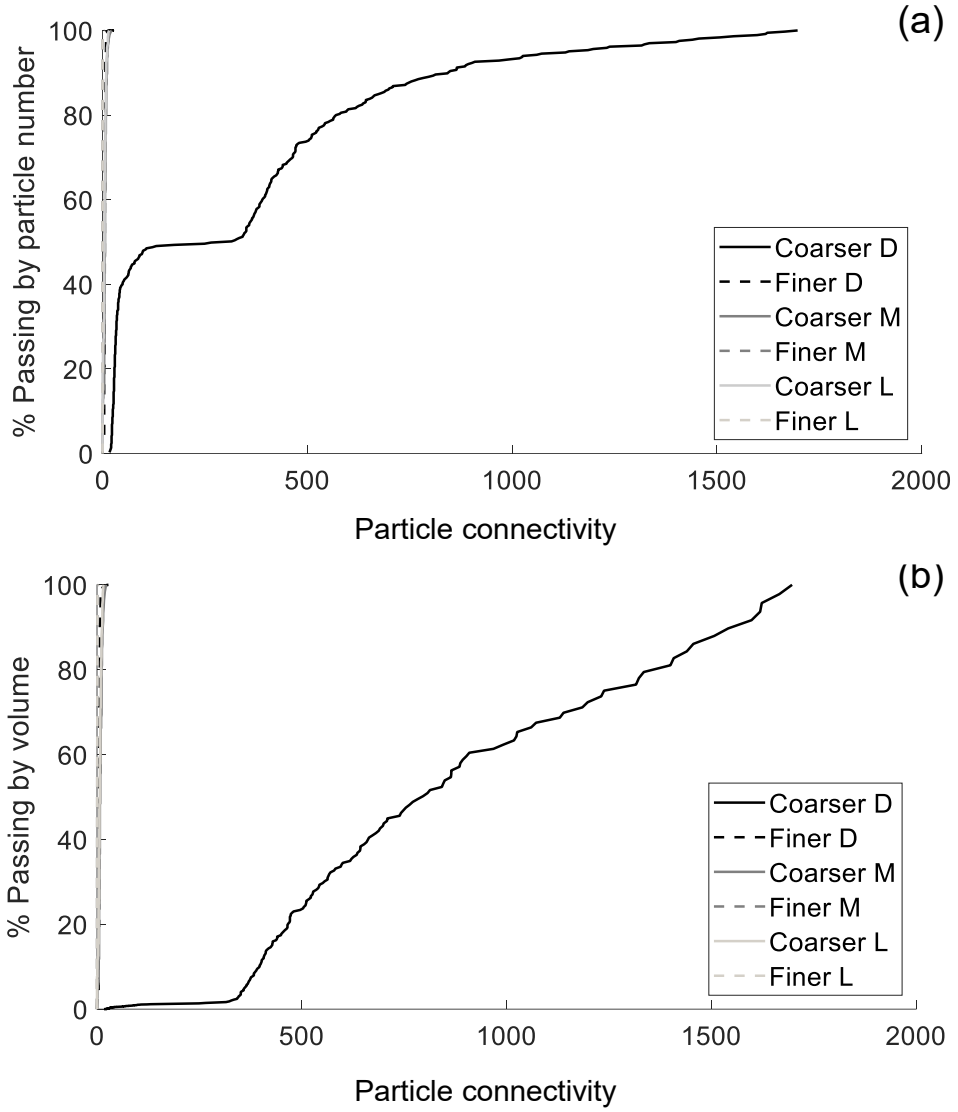


Figure 4.44: Cumulative distribution of connectivities for bimodal specimens with F_{finer} = 25% (SR 18.1): (a) distribution by number; (b) distribution by volume (D, M and L denote dense, medium-dense and loose specimen respectively)

Figure 4.45 shows the cumulative distribution of connectivities for the bimodal specimens with SR = 18.1 when F_{finer} = 50%. For all three density conditions considered, the maximum connectivity values of the coarser grains are large, which is indicative of an overfilled soil fabric. Moreover, the connectivity values of each particle also significantly increased to approximately 1700 compared to that observed for the SR of 8.4 (i.e. approximately 350).

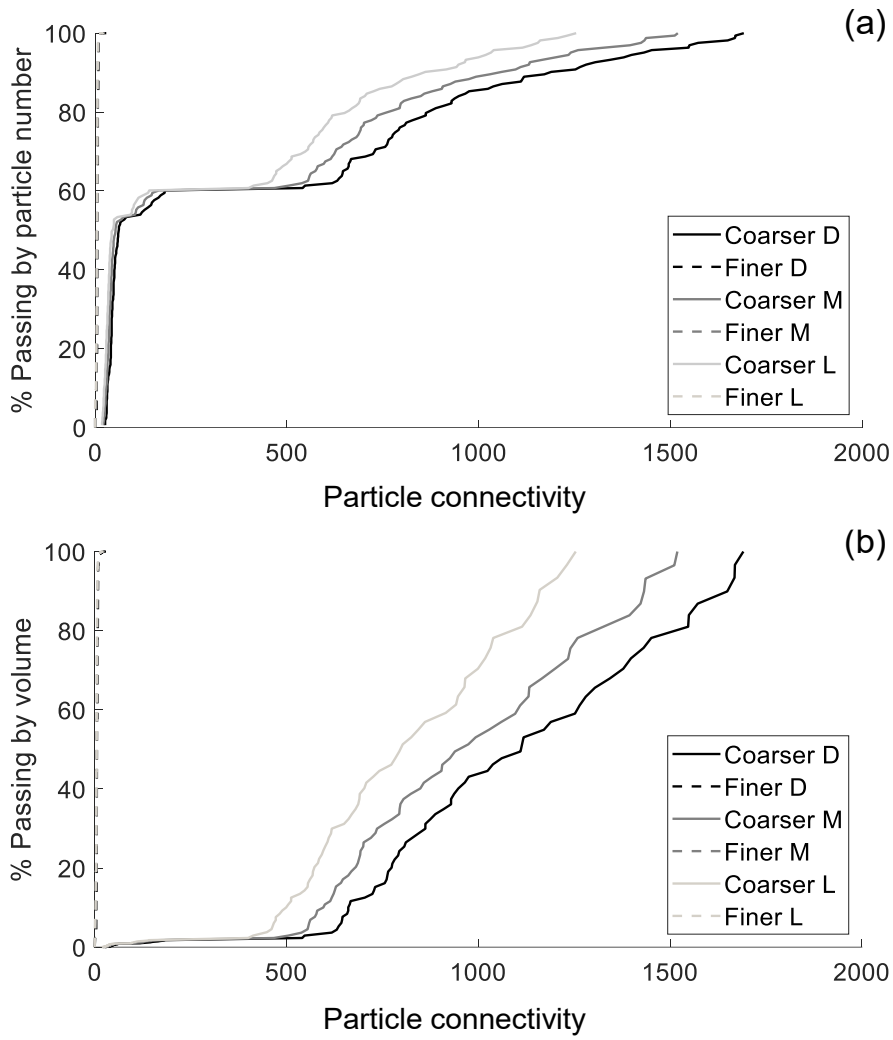


Figure 4.45: Cumulative distribution of connectivities for bimodal specimens with F_{finer} = 50% (SR 18.1): (a) distribution by number; (b) distribution by volume (D, M and L denote dense, medium-dense and loose specimen respectively)

The percentages of inactive grains in the bimodal specimens with SR = 18.1 are presented in Figure 4.46. For the three densities considered, the percentage of inactive grains by volume gradually increases when F_{finer} increases from 5% to 20%, which indicates that these finer grains are filling in the void without significant stress. In the dense condition, when $F_{finer} \geq$ 20%, the percentage of inactive grains decreases to approximately 2%, which indicates that almost all the finer grains start to transfer stress. In contrast, in the medium and loose conditions, the percentage of inactive grains reaches a peak value when F_{finer} is 30%. These results are similar to the data for SR =

8.4 (i.e. Figure 4.46). Changes in density do not have a marked influence on the proportion of inactive grains for the samples with $SR \geq 8.4$ considered here.

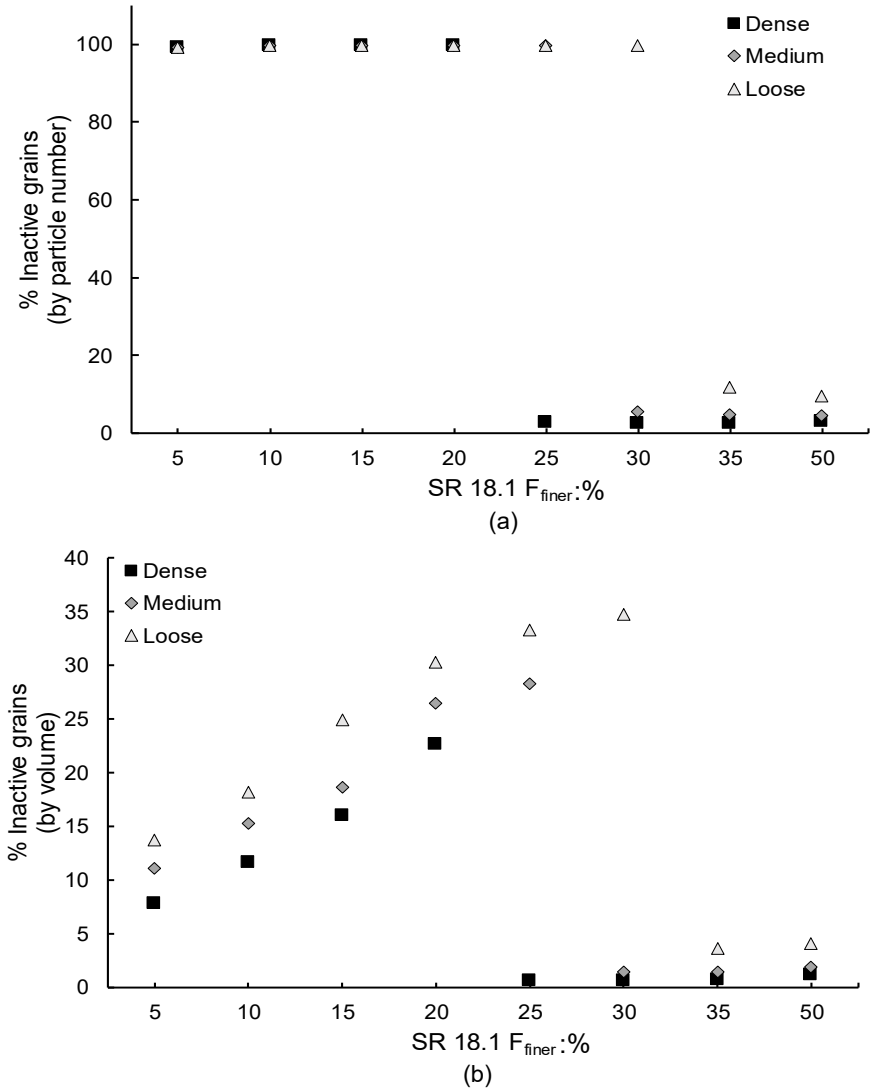


Figure 4.46: Percentage of inactive grains versus F_{finer} for bimodal specimens (SR = 18.1): (a) percentage of inactive grains by number (b) percentage of inactive grains by volume

Figure 4.47 compares e and e_m when SR = 18.1. In general, a similar trend is observed compared to that identified when SR = 8.4. For F_{finer} values between 5% and 20%, the e_m values are above their corresponding e values. In the case of F_{finer} values of 25% and 30%, a significant density effect can be observed. For the loosest specimens, the e_m values are much larger than the corresponding e values. In contrast, in the dense condition, the e_m values are similar to the e values. For F_{finer} values from 35% to 50%, the e_m values

are similar to the e values irrespective of the density condition.

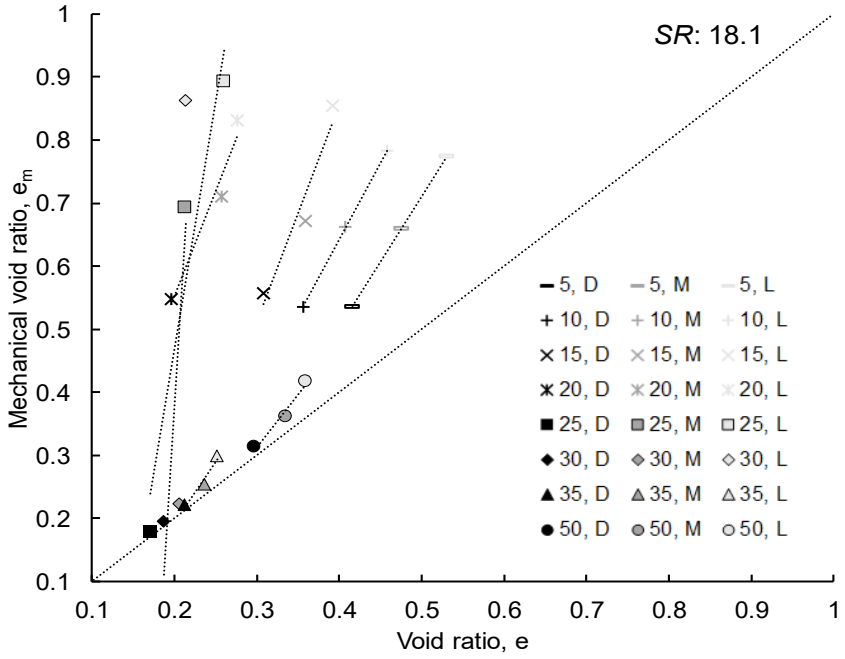


Figure 4.47: Comparison of limiting measures of packing density for bimodal specimens (SR = 18.1), e versus e_m (numbers in legend indicates the F_{finer} from 5% to 50%. D, M and L denote dense, medium-dense and loose specimen respectively)

Figure 4.48 illustrates the relative difference in the key measures of state $(e - e_m)/e$ and $(\rho - \rho_m)/\rho$ for the bimodal specimens with SR = 18.1. In general, the relative differences in both bulk density and void ratio for these specimens are significantly higher than those calculated for SR = 3.7, while similar trends are observed for SR = 8.4 and SR = 18.1. The maximum relative difference in the void ratio is approximately 280%. Figure 4.48(b) shows that the relative difference in bulk density can be significant, especially in the loose condition. The maximum difference in bulk density is approximately 33% when F_{finer} is 30%.

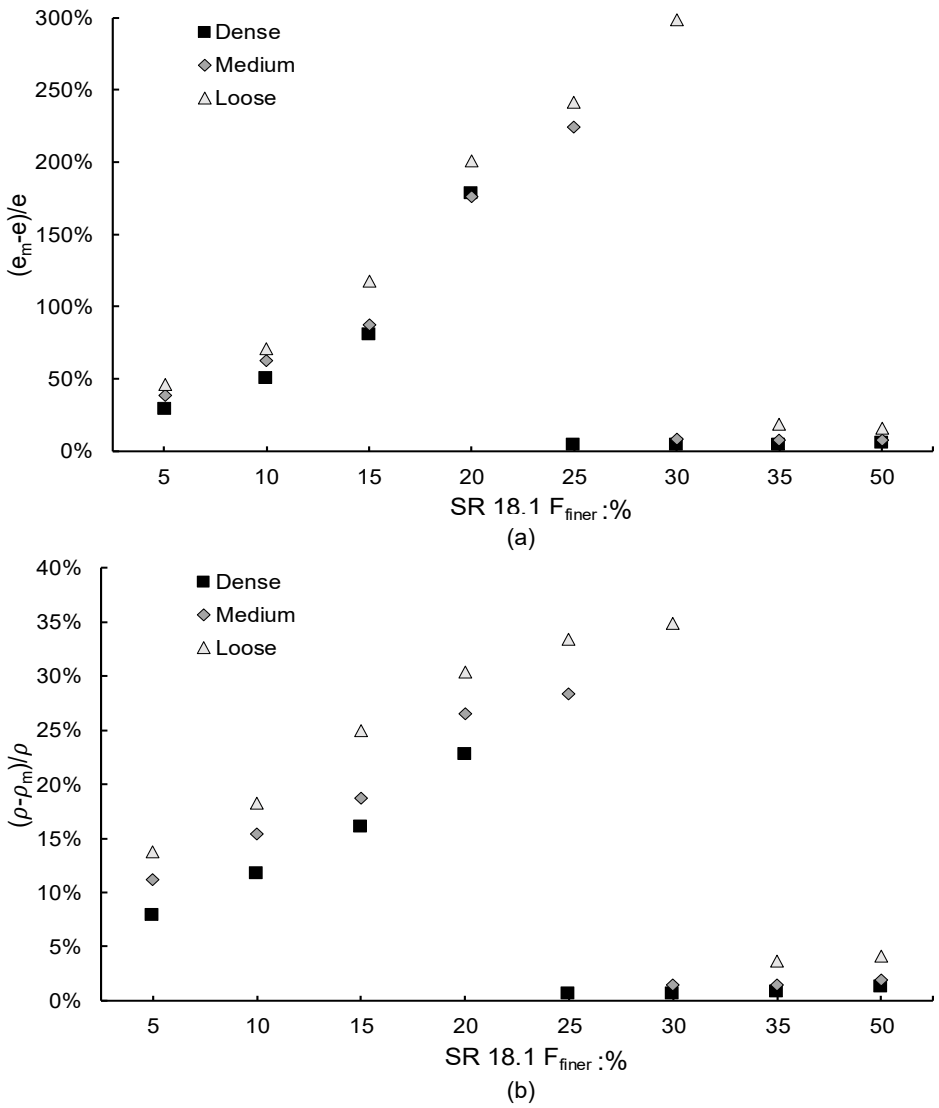


Figure 4.48: Comparison of limiting measures of packing density for bimodal specimens (SR = 18.1): (a) $(e - e_m)/e$ versus F_{finer}; (b) $(\rho - \rho_m)/\rho$ versus F_{finer}

Figure 4.49 compares the four different measures of void ratio analysed in this study (i.e. e, e_m, e_{sk}, e^*) for the bimodal gap-graded soils with SR = 18.1. F_{finer} values of 5% to 30% were considered. In general, the divergence amongst these four state variables increases with increasing F_{finer}. In the dense condition, as illustrated in Figure 4.49(a), similar values can be identified for these different state variables when F_{finer} is 5% and 10% and most of the finer particles are inactive. In contrast, when F_{finer} is between 15% and 30%, these state variables start to diverge. The calculated e_{sk} is significantly larger than e_m and e^* because the finer grains become active in the stress

transmission. In the medium and loose conditions, even when F_{finer} is 5% and 10%, a finite difference is observed amongst the values of e_m, e^* and e_{sk}. Again, the data also indicate a significant density effect that is not captured or considered in the calculation of e^* and e_{sk}. In particular, considering the loose specimens, the e_m values are large compared to the values of these of e_{sk} and e^*. This result may be attributed to the fact that not all coarser grains are active in the stress transmission, especially in the looser condition.

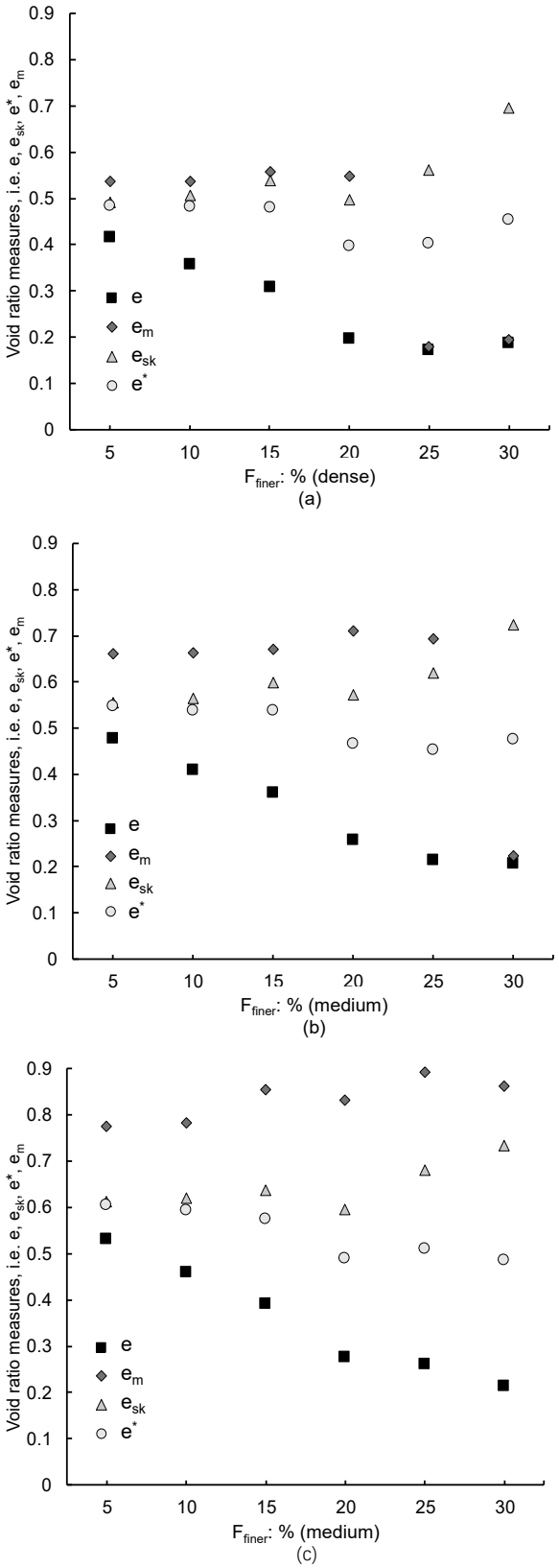


Figure 4.49: Different state variables for bimodal gap-graded soils (SR = 18.1): (a) Dense condition; (b) Medium condition; (c) Loose condition

Size ratio effect

In general, for the SRs considered in this Chapter (SR = 3.7, 8.4, 18.1), the size ratio has a clear effect, with increasing SR, the particle connectivity values increase significantly. For instance, for a SR with 3.7, the maximum connectivity value is approximately 70, while the maximum connectivity value increases to approximately 1,700 when SR increases to 18.1.

For the specimens with SR = 3.7, the proportion of inactive grains (either by number or by volume) increases gradually when F_{finer} is low (i.e. F_{finer} < 25%), followed by a smooth decrease when F_{finer} increases to a value exceeding 25%. In contrast, for SR values of 8.4 and larger, the proportion of inactive grains may drop significantly with increasing F_{finer}. For instance, for SR = 18.1 in the densest specimens, the proportion of inactive grains decreases from 22.7% to 0.62% when F_{finer} increases from 20% to 25%. These data confirm the earlier observation by Shire et al. (2016) that when one considers bimodal materials, the size ratio must be carefully considered. There are clear differences in response when the finer particles can fit completely within the void space formed by the coarser particles and the case where the finer particles may be larger than the voids formed between the coarser grains.

Considering the relative differences in the state variables e and ρ, the difference $(e - e_m)/e$ is generally low for the specimens with SR = 3.7. This relative difference initially increases with increasing SR, however, there is a little variation amongst SR values of 8.4 and larger. In the case of the specimens with SR larger than 8.4, the most significant differences are observed in the case of the underfilled specimens with F_{finer} = 25% or F_{finer} = 30%.

4.4.4. Trimodal specimens

F_{finer} = 10%

For the trimodal specimens with F_{finer} = 10%, simulation results for two representative gradations, Tri 10_30 and Tri 10_60, are presented in Figure 4.50(a) and Figure 4.50(b), which illustrate cumulative distributions of connectivity by particle number and by volume, respectively. Figure 4.50(a) indicates that more than 99% of particles by number are inactive, which indicates an underfilled soil fabric. A limited density effect can be observed for specimens Tri 10_30 and Tri 10_60, for instance, for Tri 10_60, approximately 96.2% and 96.6% particles are inactive for both specimens, the maximum particle connectivity values observed in the dense condition is slightly larger than the values identified for the medium and loose conditions.

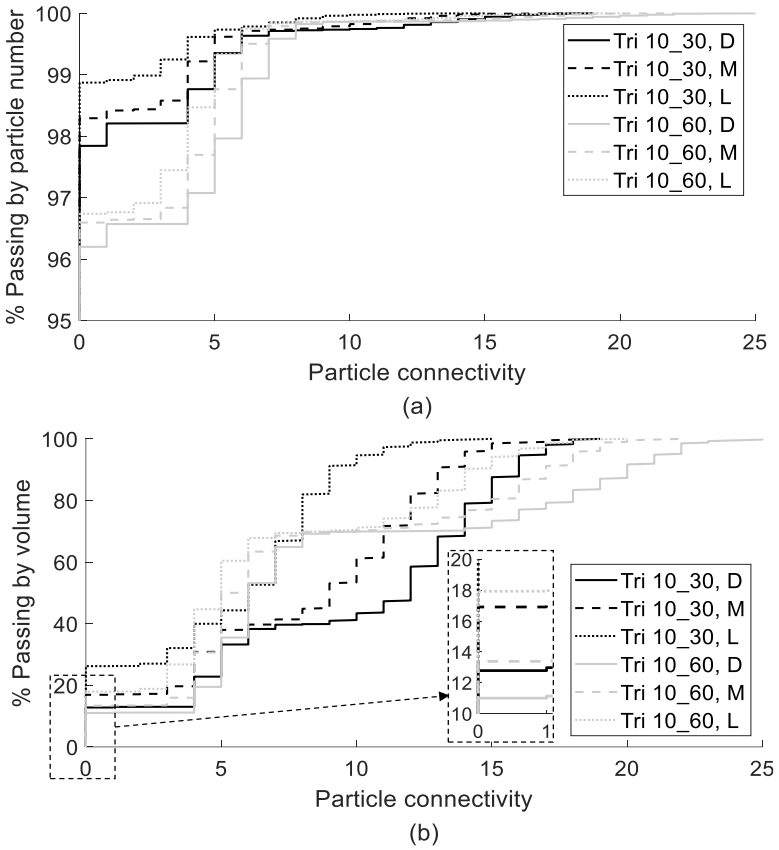


Figure 4.50: Cumulative distribution of connectivities for typical trimodal specimens (F_{finer} = 10%): (a) by particle number; (b) by particle volume (D, M and L denote dense, medium-dense and loose specimen respectively)

The two measures of void ratio e and e_m are compared in Figure 4.51 for the trimodal specimens. When F_{finer} is 10%, a finite difference can be observed for all mixtures and there is a clear packing density effect.

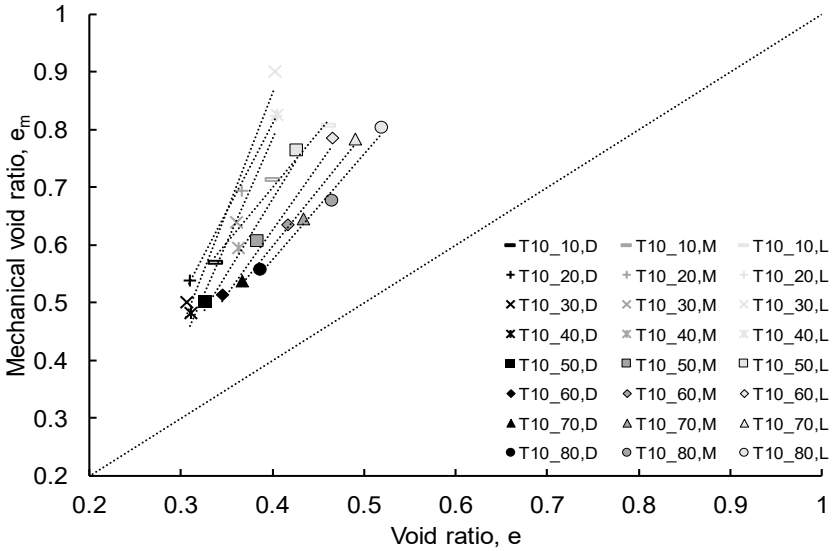


Figure 4.51: e versus e_m for trimodal specimens for F_{finer} of 10% (D, M and L denote dense, medium-dense and loose specimen respectively)

Figure 4.52 shows the percentage of inactive grains in the trimodal specimens when F_{finer} is 10% by both particle number and particle volume. As illustrated in Figure 4.52(a), the percentage of inactive grains by particle number slightly decreases with increasing F_{int}. Considering the percentage of inactive grains by volume, approximately 20% grains are inactive. When F_{finer} is 10%, a finite density effect can be observed.

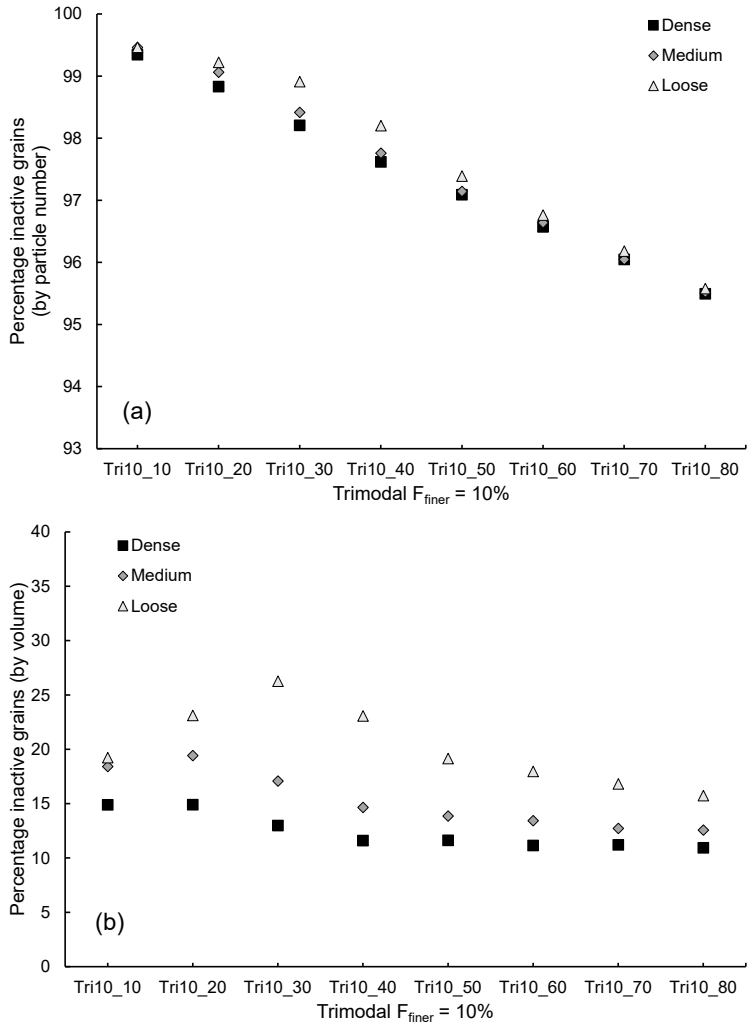


Figure 4.52: Percentage of inactive grains for trimodal specimens (F_{finer} = 10%): (a) by particle number; (b) by particle volume

Figure 4.53 shows the relative differences in void ratio and bulk density for the trimodal specimens with F_{finer} = 10%. As F_{int} increases, the relative differences in void ratio increase from approximately 75% and reaches a maximum value of 120% when F_{int} is 30%, followed by a slight decrease to 50% until F_{int} is 80%. A similar trend can also be observed in the bulk density data, the maximum relative difference in bulk density is approximately 26% when F_{int} is 30%. A measurable density effect can be observed, especially when F_{int} is 30% and 40%.

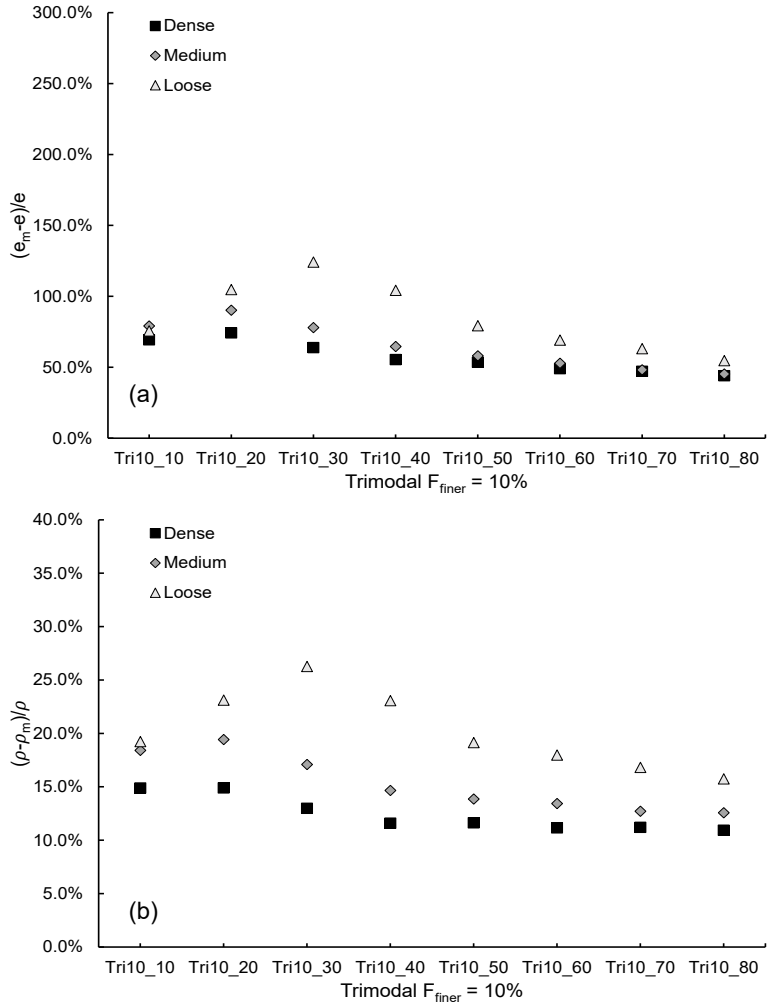


Figure 4.53: Comparison of traditional measures for trimodal specimens (F_{finer} = 10%): (a) e and e_m; (b) ρ and ρ_m

F_{finer} = 20%

Connectivity distribution data for specimens Tri 20_20 and Tri 20_40 are presented in Figure 4.54, both the cumulative distributions of connectivity by particle number and by volume are presented. These data show that when F_{finer} is 20%, a significant change in the nature of stress transmission starts to be observed as F_{int} increases. For instance, in the dense condition, for Tri 20_40, approximately 4% of the grains by particle number are inactive. In contrast, for the medium and loosest conditions, more than 98% of the particles are inactive.

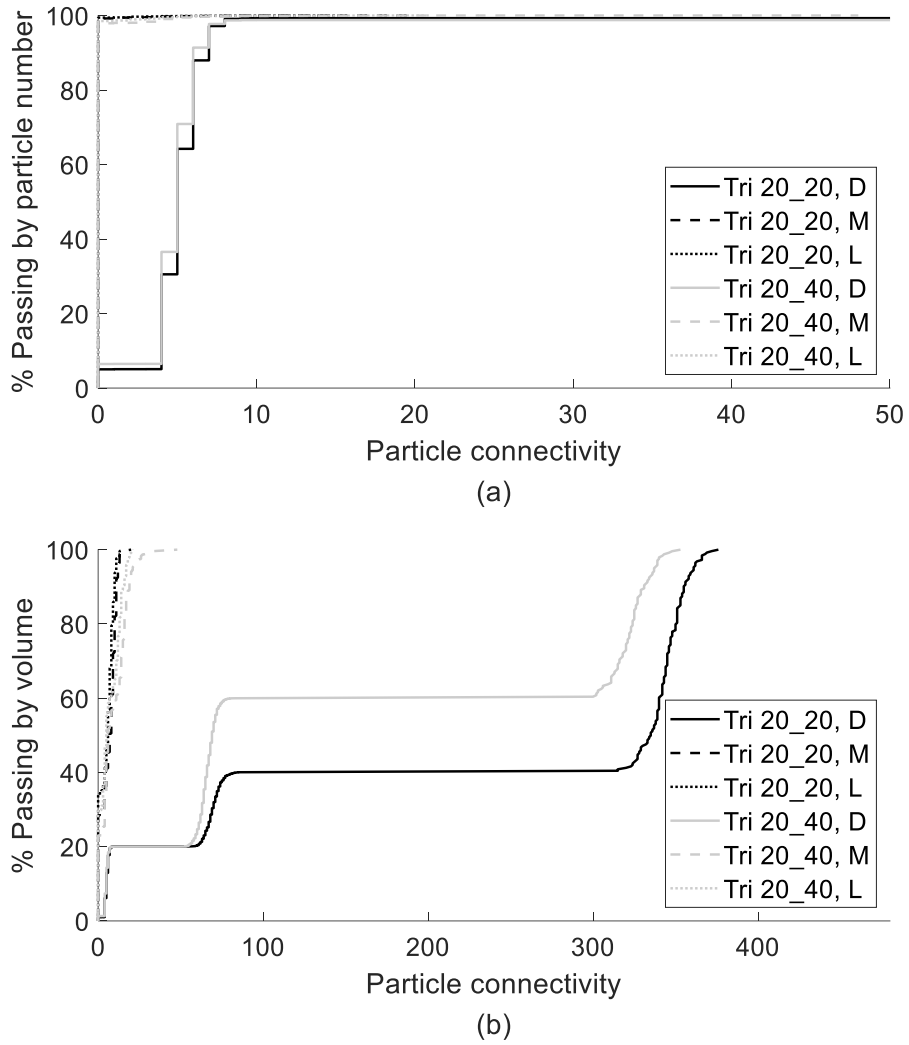


Figure 4.54: Cumulative distribution of connectivities for typical trimodal specimens (F_{finer} = 20%): (a) by particle number; (b) by particle volume (D, M and L denote dense, medium-dense and loose specimen respectively)

The difference between e and e_m for the trimodal specimens with F_{finer} = 20% is also illustrated in Figure 4.55 for various values of F_{int}. In general, when referring to the dense condition, most of these specimens (except for $Tri\,20\_10$, $Tri\,20\_60$, $Tri\,20\_70$) show similar values between e and its corresponding e_m. In contrast, for the medium and loose conditions, a significant gap between e and e_m can be identified when F_{finer} = 20%.

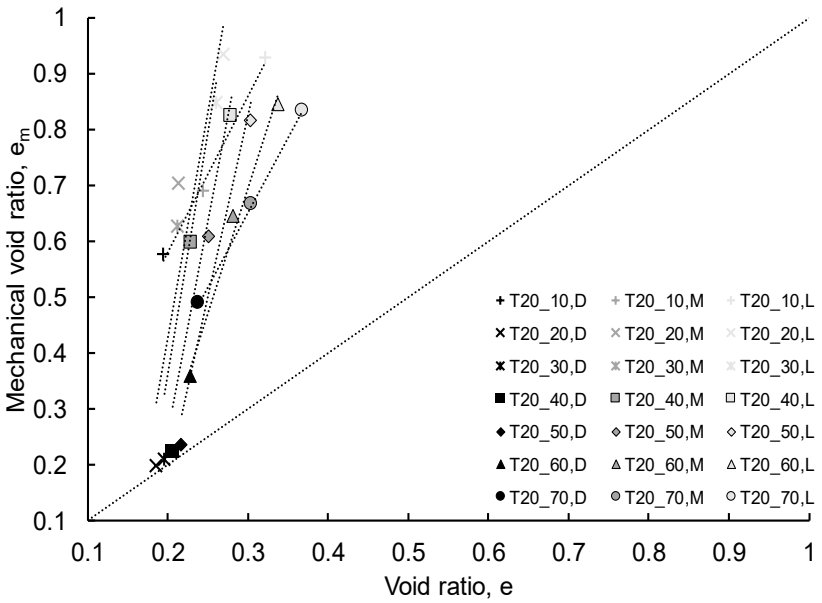


Figure 4.55: e versus e_m for trimodal specimens of a F_{finer} of 20% (D, M and L denote dense, medium-dense and loose specimen respectively)

Figure 4.56 shows the percentage of inactive grains in the trimodal specimens with F_{finer} = 20%. As illustrated in Figure 4.56(a) and (b), the percentage of inactive grains by either particle number or volume is strongly dependent on F_{int} and their packing density. When F_{int} is 10%, more than 98% of the grains are inactive irrespective of the packing density. For F_{int} values between 20% and 50%, a strong density effect can be observed, in the densest condition, more than 90% of grains start to be active, while more than 98% of grains are inactive in the medium and the loosest condition. When F_{int} is 60% and 70%, it can be seen that the density effect starts to decrease.

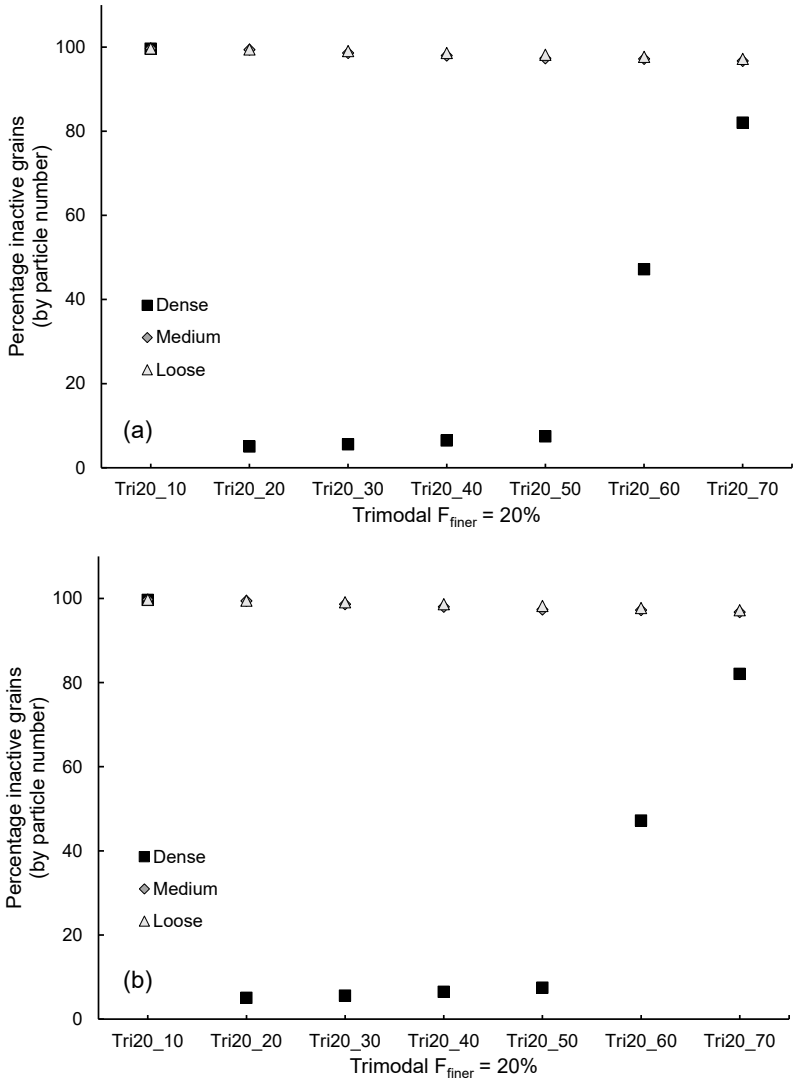


Figure 4.56: Percentage of inactive grains for trimodal specimens (F_{finer} = 20%): (a) by particle number; (b) by particle volume

Figure 4.57 shows the relative differences in bulk density and void ratio for the trimodal specimens when F_{finer} is 20%. A density effect can be observed for some specimens (e.g. Tri 20_20, Tri 20_30). For instance, for Tri 20_30, the relative difference in bulk density is approximately 1% in the dense condition. In contrast, a much higher relative difference (i.e. 32 %) can be identified for this Tri 20_30 in the loose condition. The extent to which the observed stress transmission patterns are stress-dependent varies with PSD; for instance, a significantly greater density dependence is observed for Tri 20_20 or Tri 20_30 than in the case of Tri 20_10 or Tri 20_70.

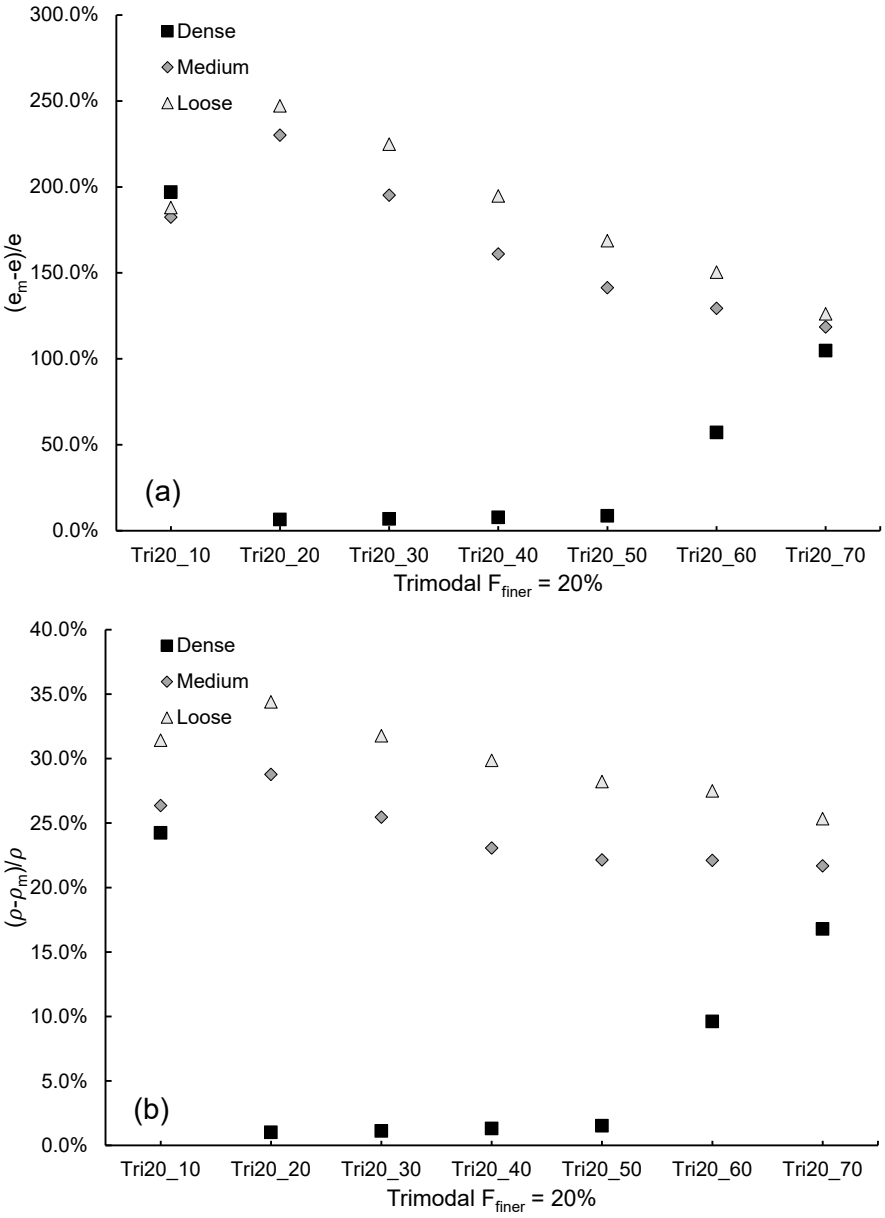


Figure 4.57: Comparison of traditional measures for trimodal specimens (F_{finer} = 20%): (a) e and e_m; (b) ρ and ρ_m

F_{finer} of 25% and 30%

Connectivity distribution data for specimens Tri 25_15 and Tri 25_45 are presented in Figure 4.58(a) and Figure 4.58(b), these give the cumulative distributions of connectivity by particle number and by volume, respectively. These data show that when F_{finer} is 25%, a significant change in the nature of stress transmission can be identified. For instance, in the dense condition, for

Tri 25_45, approximately 5% grains by particle number are inactive. In contrast, For the loosest condition, more than 98% of particles are inactive.

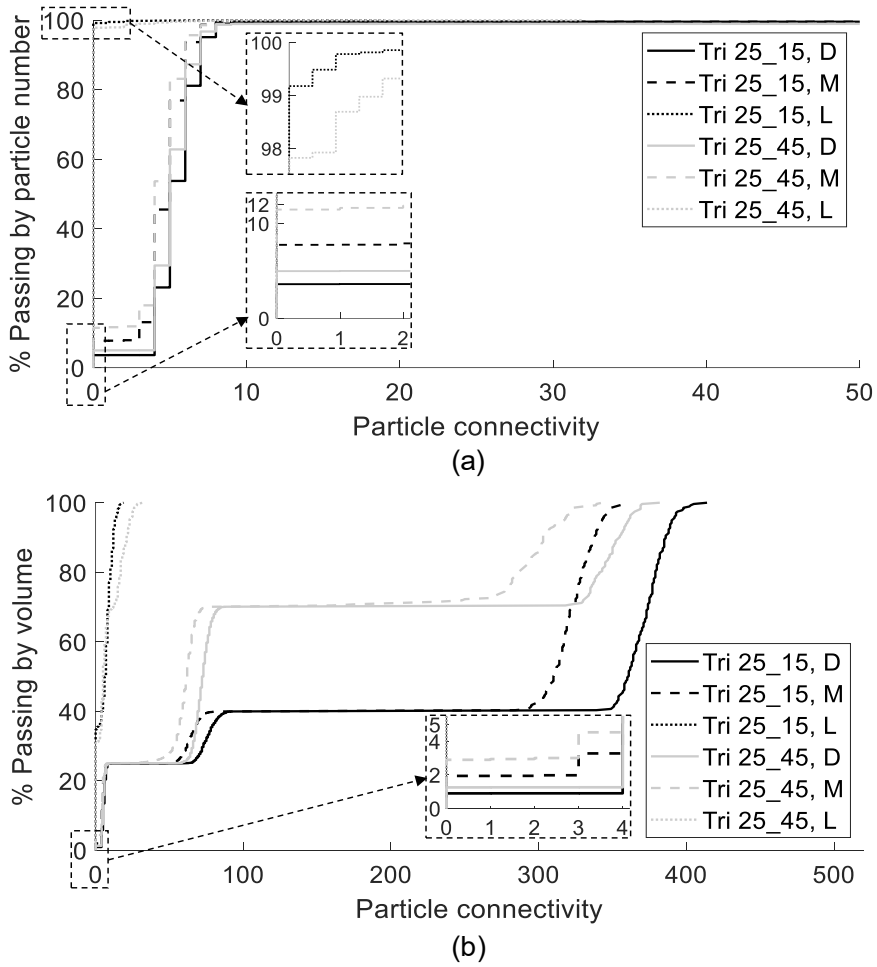


Figure 4.58: Cumulative distribution of connectivities for typical trimodal specimens (F_{finer} = 25%): (a) by particle number; (b) by particle volume (D, M and L denote dense, medium-dense and loose specimen respectively)

Connectivity distribution data for specimens Tri 30_20 and Tri 30_40 are presented in Figure 4.59(a) and Figure 4.59(b), these give the cumulative distributions of connectivity by particle number and by volume, respectively. These data show that when F_{finer} is 30%, approximately 95% of the particle by volume are active in stress transmission. It can also be observed that the density effect is smaller when compared to that identified when F_{finer} is 25%. For instance, in the dense condition, for Tri 30_40, approximately 2% of the

grains by particle volume are inactive. For the loose condition, approximately 5% of particles by particle volume are inactive.

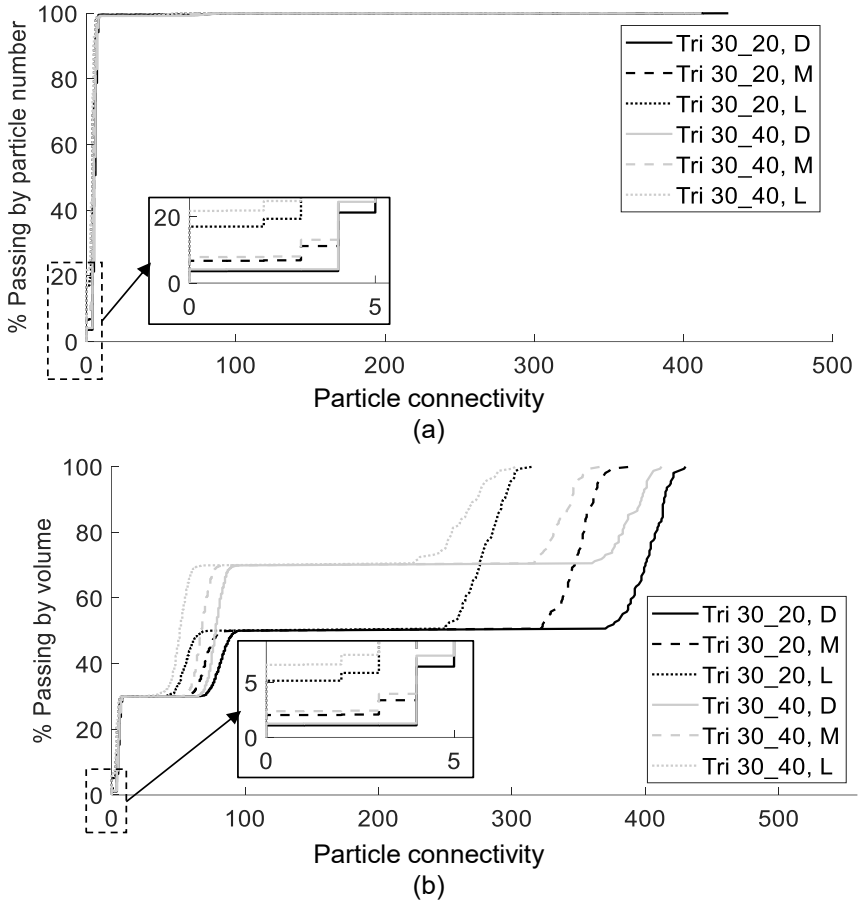


Figure 4.59: Cumulative distribution of connectivities for typical trimodal specimens (F_{finer} = 30%): (a) by particle number; (b) by particle volume (D, M and L denote dense, medium-dense and loose specimen respectively)

Figure 4.60 presents the comparison between e and e_m when F_{finer} is 25% and 30%. The difference between e and e_m can be significant in the case of the loose specimens when F_{finer} is 25%. When F_{finer} is 30%, the difference between e and e_m reduces as the finer particles become active in stress transmission.

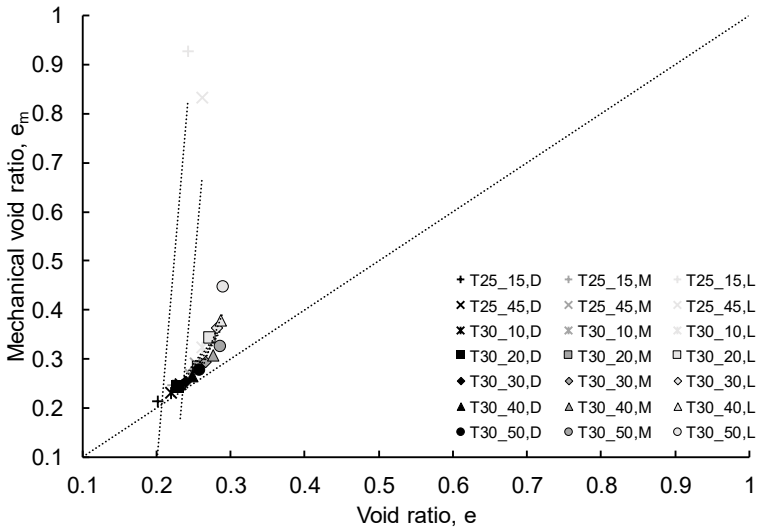


Figure 4.60: e versus e_m for trimodal specimens for a F_{finer} of 25% and 30% (D, M and L denote dense, medium-dense and loose specimen respectively)

Figure 4.61 presents the percentage of inactive grains for trimodal specimens when F_{finer} is 25% and 30%, when F_{finer} is 25%, strong density effect can be observed. When F_{finer} is 30%, only small difference can be observed, which suggests that these finer particles start to transfer stress for all the density conditions considered. In general, the tendency identified in these specimens suggests that trimodal gap-graded soils are more sensitive to the effect of density than bimodal gap-graded soils.

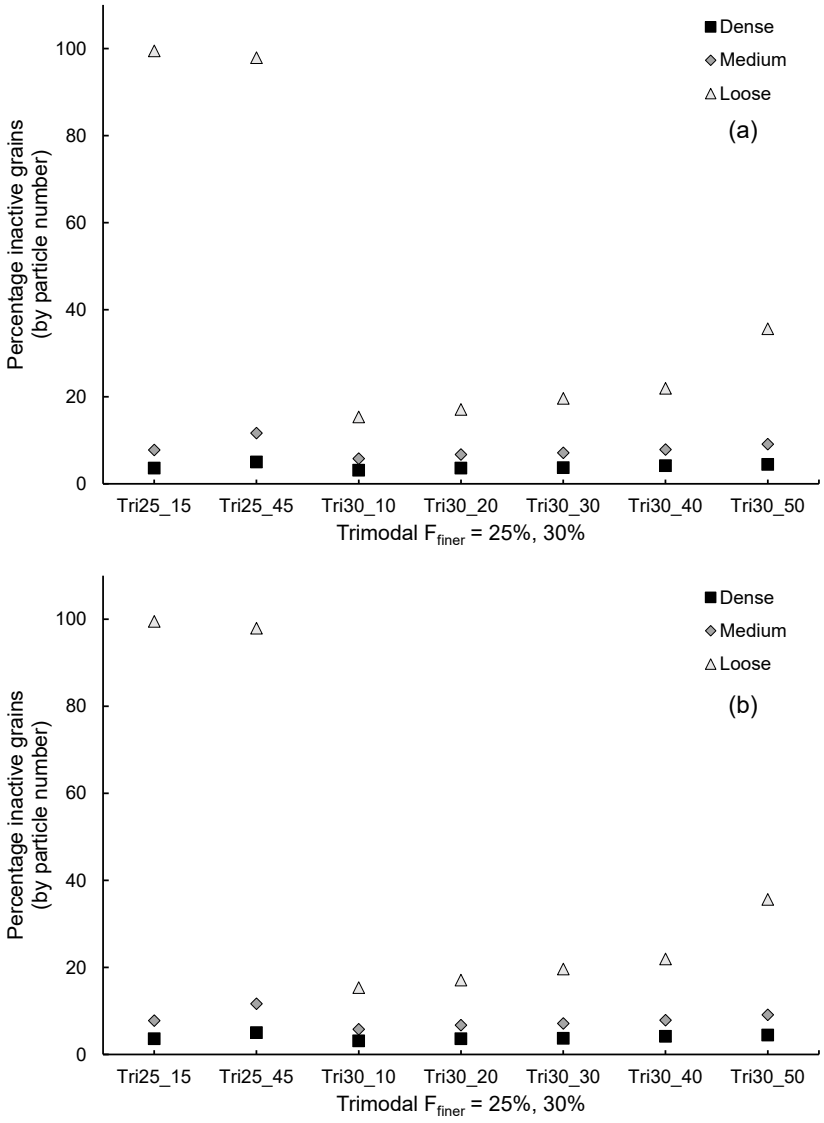


Figure 4.61: Percentage of inactive grains for trimodal specimens (F_{finer}= 25%; 30%): (a) by particle number; (b) by particle volume

Figure 4.62 presents the relative difference of these traditional measures for trimodal specimens when F_{finer} is 25% and 30%, significant relative difference can be observed when F_{finer} is 25% in the loosest condition. For instance, for Tri 25_15 and Tri 25_45, the relative difference $(\rho - \rho_m)/\rho$ could be approximately 35% when referring to the loosest condition.

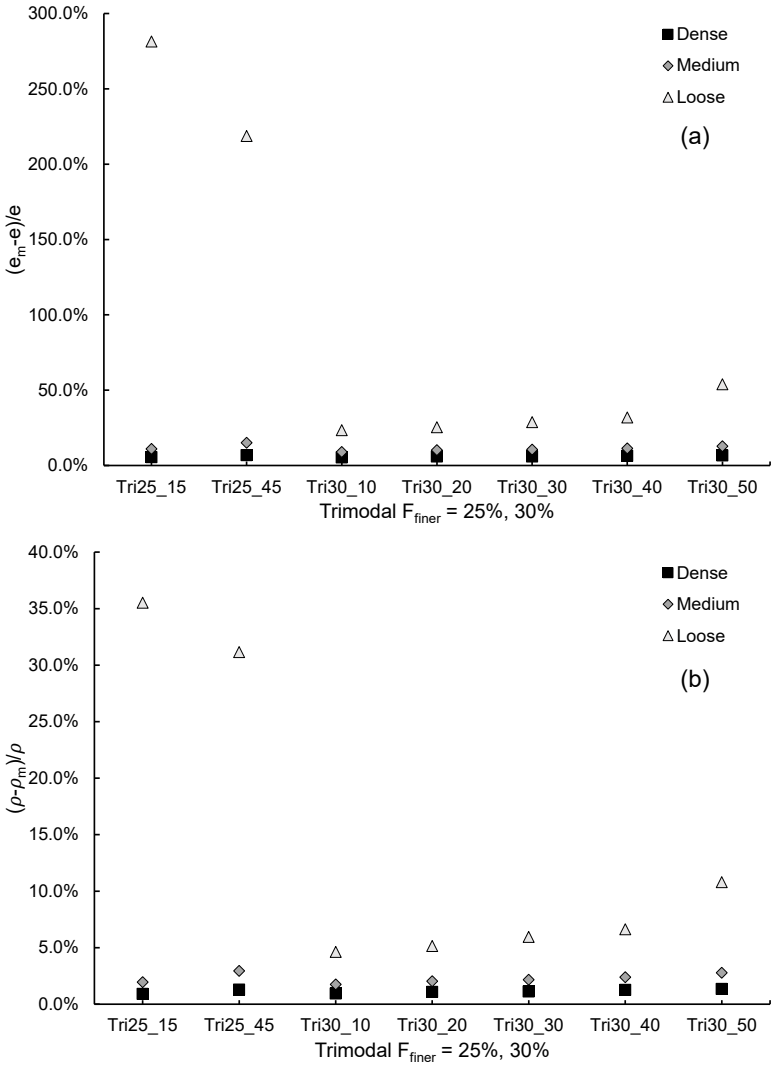


Figure 4.62: Comparison of traditional measures for trimodal specimens (F_{finer} = 25, 30%): (a) e and e_m; (b) ρ and ρ_m

4.5. Summary

This study has presented a comprehensive DEM investigation on stress transmission in specimens with different types of PSD to appraise, at a fundamental level, the extent to which void ratio and bulk density are appropriate measures of material state for non-plastic soils. The use of high-performance computing enabled 201 specimens to be created with up to 636,871 particles. An in-house specimen generation code ensured the distribution of particles within the specimen was not influenced by the periodic boundary locations. The significant idealizations in the modelling approach,

namely the spherical particle geometries and the use of friction to control packing density, have been adopted in several prior geomechanics studies using DEM. The study has taken a rather simplistic binary approach, by considering the connectivity and the proportion of inactive grains so that distribution or variations in the contribution made by the stress-transmitting were not considered. i.e. the proportion of the contribution made by each of those grains that are actively engaged in stress transmission is not captured. A more in-depth analysis of the distribution of stress amongst the active, stress-transmitting particles is presented in Chapter 5.

The data presented have shown that even for continuous $PSDs$ (i.e. linear and fractal specimens), a finite number of relatively small grains may not be active in transferring stress. While these inactive grains are small, in some cases the proportion of the overall specimen volume they occupy is finite so that when they are considered to be part of the void space to quantify the material state, there is a finite effect on both void ratio and density. The difference between the void ratio, e, that considers the mass/volume of all grains, and the mechanical void ratio, e_m, that considers only stress transmitting grains in the solid volume, is highly density-dependent. This poses a problem: we know at a fundamental level that stiffness, in particular, is closely correlated to e_m. The accuracy with which we can approximate e_m by considering e varies with density and the difference is most pronounced for loose specimens. This must compromise the use of e in empirical expressions to predict soil behaviour.

The shortcomings of using e as a predictor of soil behaviour have long been recognised with gap-graded or bimodal soils. The current contribution has shown that the range of materials for which e is a measure with limitations of the state is broader than has hitherto been appreciated. The large discrepancy between e and e_m in the case of loose materials is particularly significant as

these materials have the greatest susceptibility to liquefaction. This Chapter indicates that research programs that have explored these in gap-graded soils should also be extended to a broader range of soils. In general, similar strong density-dependent behaviour can be observed for both bimodal and trimodal specimens, while these trimodal specimens may be more sensitive to the change of packing density.

Chapter 5. The effect of particle size distribution on stress transmission

5.1. Introduction

As discussed in Chapter 4, plotting the particle size distribution (PSD) is one of the most basic ways to characterize a soil in both geotechnical research and practice. Chapter 4 which shows the effects of the shape of the PSD on traditional measures of state have taken a rather simplistic, binary approach. These studies have typically considered gap-graded soils and identified particles as either stress transmitting (i.e. active) or non-stress transmitting (i.e. inactive). However, there may be merit in looking at the heterogeneity of stress transmission in the active grains using a more nuanced approach that considers the extent to which the particles are engaged in stress transmission. This is the focus of the analyses presented in this Chapter.

The particle size distribution is sometimes termed an intrinsic material property (e.g. Been et al., 1991). Hight & Leroueil (2003) identified the complete grading as one of the factors that determine the character of geomaterials, while Cubrinovski & Ishihara (2002) stated that the nature of the material is described by properties that include the PSD. Miura et al. (1997) classify the PSD as a primary physical property. It is acknowledged that the PSD can influence packing. Mitchell & Soga (2005) noted that uniformly grained soils tend to have a narrower range of possible densities compared to well-graded soils. Mitchell & Soga (2005) cited the work of Youd (1973) who demonstrated a systematic relationship between C_u and both the maximum and minimum void ratios, e_{max} and e_{min}, respectively. Cubrinovski & Ishihara (2002) concluded that the void ratio extent $e_{max} - e_{min}$ is indicative of the overall PSD, and particularly, the fines content, FC. Miura et al. (1997) observed that the void ratio extent

($e_{max} - e_{min}$) is an index of the the degree of possible change in the soil structure; for the specimens they considered with continous gradings there was no obvious link between C_u and $e_{max} - e_{min}$.

Miura et al. (1997) stated that the mechanical properties of soil must be attributed to its primary characteristics (which include the PSD). Considering large strain responses, recent studies on internal erosion and particle acknowledge that if the grading of a soil changes as a result of particle breakage or erosion then there is a change in the material's mechanical behaviour. For example, the position of the critical state line in $e\ log - p'$ shape can shift (Wood & Maeda, 2008). Considering the small strain and dynamic responses, Rollins et al. (2020) used regression analysis to develop expressions for the damping ratio and modulus degradation curves for gravels that include C_u, recognizing that as C_u increases, the G_0/G_{max} versus γ curves shift downwards and to the left as the reference strain reduces. Senetakis et al. (2012) and Payan et al. (2017) also studied the effect of grading on soil behaviour and proposed empirical correlations to quantify the effect of PSD (i.e. C_u; d_{50}) on the small-strain stiffness of sands.

As acknowledged by Salgado et al. (2000), much of our understanding of soil behaviour has come through tests on "clean" sands and it is important to establish whether the frameworks established by studying these materials can be used to describe the mechanical behaviour of a broader range of sands. In the analyses presented in Chapter 4, all particles are classified either as being stress-transmitting (i.e. active) or not involved in stress transmission (i.e. inactive) without considering the proportion of stress transmitted by individual particles or by groups of particles in a particular size fraction. The analyses presented in this Chapter recognise that this binary classification of particles

provides only limited insight and so the fundamental mechanics that underlie the link between the PSD shape and the engineering behaviour is investigated by considering the distribution of stresses amongst the particles of different sizes.

5.2. Overview of DEM approach

The simulation approach used for this Chapter has been described in Chapter 3. The key points to highlight are that the DEM simulations were conducted with periodic boundary conditions. A simplified Hertz-Mindlin contact model was used and three inter-particle friction coefficients (μ) were used during isotropic compression so that three packing densities could be considered for each gradation. Refer to Section 3.4 for a more detailed description of the simulation approach.

5.3. $PSDs$ considered

The $PSDs$ considered in this Chapter are similar to those shown in Chapter 4, additional bimodal specimens with a SR of approximately 14.5 were generated to provide additional data to study the size ratio effect. For the continuous specimens and trimodal specimens, the $PSDs$ are shown in Figure 4.1 and Figure 4.3(b), respectively. The representative bimodal gap-graded specimens are shown in Figure 5.1. Again, each of these specimens is defined by the SR and F_{finer}, for instance, 'SR 14.5 F_{finer} 50' indicates a bimodal specimen with SR = 14.5 and F_{finer} = 50%.

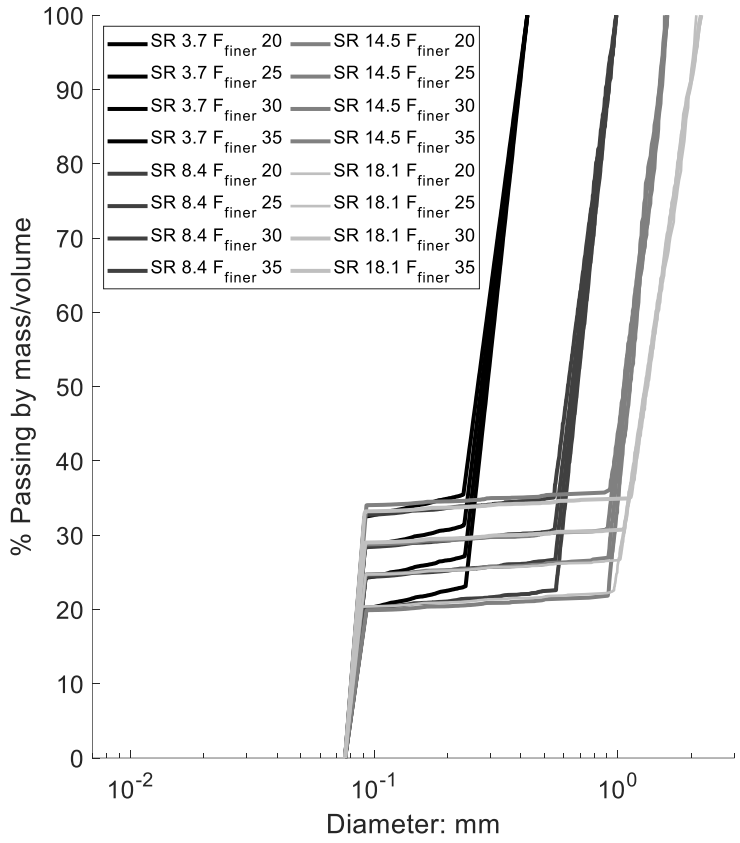


Figure 5.1: Particle size distributions of bimodal gap-graded soils in Chapter 5

5.3.1. Quantifying shape of the particle size distribution: the introduction of the index of grading, I_G

In this Chapter, the index of grading, I_G proposed in Guida et al. (2018) is employed to describe the shape of all $PSDs$ considered. In soil mechanics, the shape of a PSD is often described using the coefficient of uniformity, $C_u = D_{60}/D_{10}$. This parameter has proved to be useful in classifying soils. However, as noted by Guida et al. (2018), while C_u can differentiate well-graded and poorly graded soils, it may not be able to quantify or describe the shape of the entire PSD. The C_u only considers two points on the PSD (i.e. D_{60} and D_{10}). Consequently, it cannot capture the key trends of the entire distribution, especially for gap-graded soils. For instance, for the bimodal specimens discussed in this Chapter, they have similar C_u values but distinct F_{finer}. The coefficient of curvature (C_z) also shows similar problems compared to those of

C_u, the C_z is also unable to differentiate these bimodal gap-graded soils. Therefore, Guida et al. (2018) have considered several other measures of PSD shapes, and proposed an index of polydispersity, the index of grading, I_G, to overcome the limitations of C_u & C_z. This I_G metric considers the entire distribution instead of only two or three points:

$$I_G = \exp\sqrt{\sum_i \frac{w_i}{w_{tot}}(lns_i - ln\bar{s})^2} \quad 5.1$$

where w_i is the weight retained at the sieve opening d_i, w_{tot} is the total weight of the specimen, s_i is the particle size (non-dimensionalised) with respect to the maximum particle size d^p_{max}, $s_i = d_i/d^p_{max}$ and $\bar{s}$ is the geometric mean of the weight distribution calculated as below:

$$\bar{s} = \exp\left[\sum_i \frac{w_i}{w_{tot}} \ln(s_i)\right] \quad 5.2$$

Guida et al. (2018) argued that in comparison to C_u, this index I_G can better capture the characteristics of gap-graded soils. The I_G values of all considered $PSDs$ are therefore calculated as discussed in the following.

Linear specimens

The calculated I_G values for the linear specimens are illustrated in Figure 5.2 and Table 5.1, for the linear specimens, the I_G values increase monotonically with increasing C_u. This observation agrees with the trends observed in Guida et al. (2018).

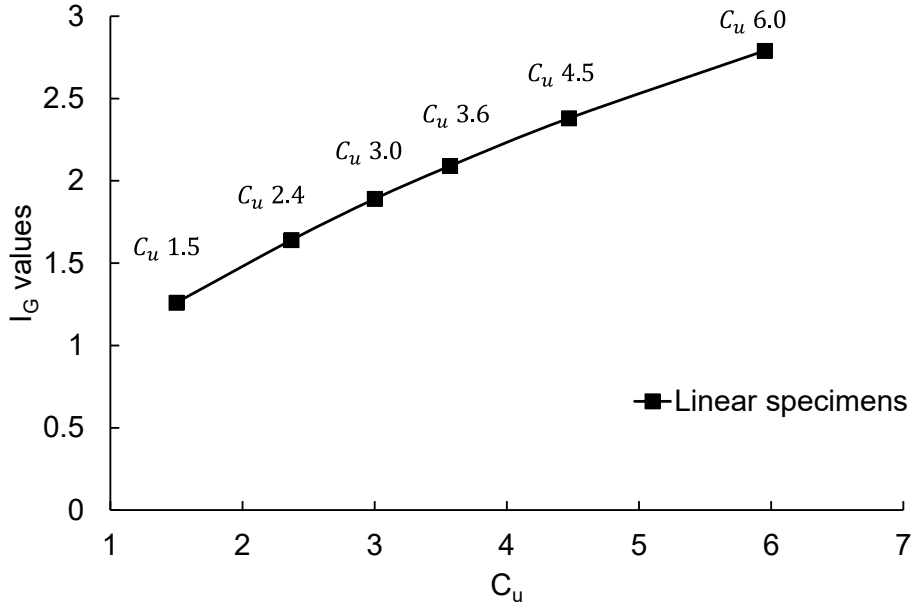


Figure 5.2: Variation in the I_G values for the linear specimens with C_u

Table 5.1: Measures of PSD shape for the linear specimens

Specimen	C_u	C_z	I_G
C_u 1.5	1.50	0.92	1.26
C_u 2.4	2.37	0.84	1.64
C_u 3.0	3.00	0.80	1.89
C_u 3.6	3.57	0.78	2.09
C_u 4.5	4.47	0.74	2.38
C_u 6.0	5.95	0.70	2.79

Fractal specimens

For fractal specimens, the I_G values are illustrated in Figure 5.3 and Table 5.2, the I_G values of fractal specimens also increase monotonically with increasing C_u. Note that Fractal 0.1% L and Fractal 1% S have similar C_u and I_G values. In general the data here indicate that for continuous specimens a clear relationship can be established between C_u and I_G.

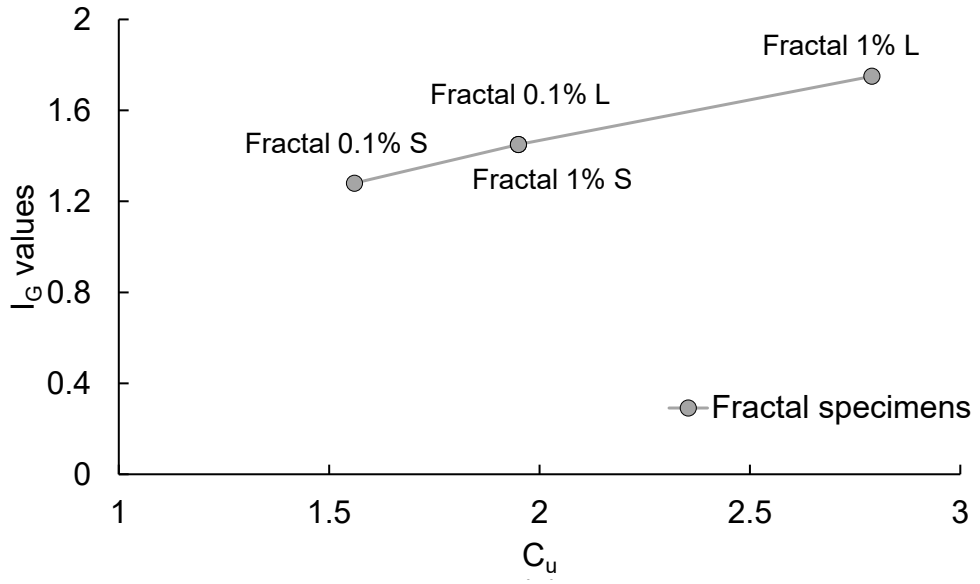


Figure 5.3: Variation in the I_G values for the fractal specimens with C_u

Table 5.2: Measures of PSD shape for the fractal specimens

Specimens	C_u	C_z	I_G
Fractal 0.1% S	1.56	1.11	1.28
Fractal 0.1% L	1.95	1.16	1.45
Fractal 1% S	1.95	1.16	1.45
Fractal 1% L	2.79	1.26	1.75

Bimodal specimens

The I_G values of the bimodal specimens are presented in Figure 5.4 with the specimens being grouped by SR. The limitation of using C_u and C_z to describe gap-graded soils is clear from the data presented in Table 5.3, Table 5.4, Table 5.5 and Table 5.6 for SR values of 3.7, 8.4, 14.5 and 18.1, respectively. For instance, for bimodal specimens with SR = 14.5, it can be seen that neither C_u nor C_z can differentiate the gap-graded specimens with different F_{finer} values. For the bimodal specimens with SR = 14.5, the C_u values of these specimens are 14.31, 14.22, 14.28 and 14.46 when $F_{finer} \approx$ 15%, 20%, 25% and 35%, respectively. The C_u clearly cannot distinguish these bimodal specimens with markedly different F_{finer} values. In contrast, the

I_G values are 2.12, 2.96, 3.20 and 3.61 for these four bimodal specimens (i.e. 15%, 20%, 25%, 35%), showing that I_G is able to capture the variation in the PSD shape as F_{finer} increases. For all the SR values considered the I_G values of the specimens increase monotonically with increasing F_{finer}. In addition, the slope of the curve of I_G versus F_{finer} increases with increasing SR, and the I_G values increase with increasing SR. These data indicate that the I_G is better suited as a measure of PSD shape than either C_u or C_z in the case of gap-graded soils.

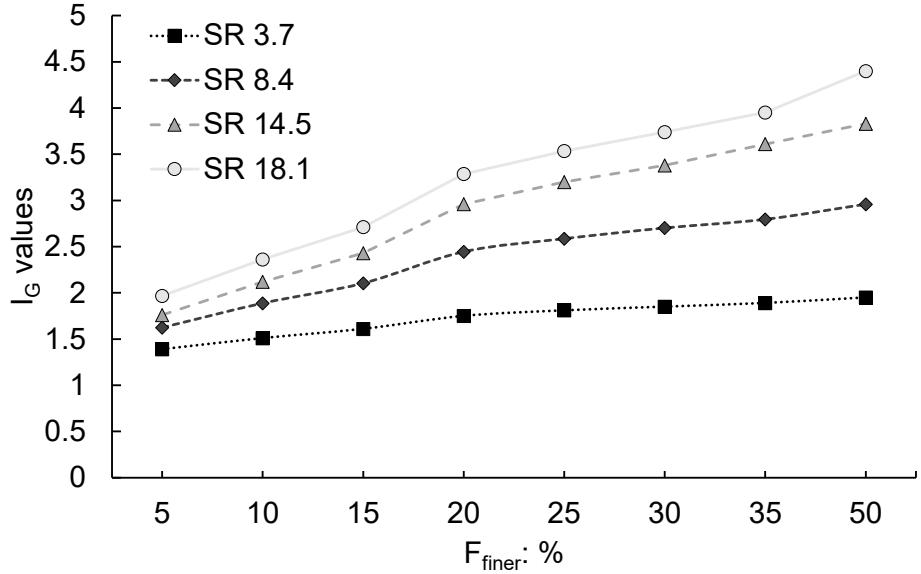


Figure 5.4: Variation in the I_G values with increasing F_{finer} for the bimodal specimens with different size ratios (SR)

Table 5.3: Measures of PSD shape for the bimodal specimens with SR = 3.7

Specimen	C_u	C_z	I_G
SR 3.7 F_{finer} 5	1.37	0.94	1.39
SR 3.7 F_{finer} 10	1.81	1.21	1.51
SR 3.7 F_{finer} 15	3.67	2.40	1.61
SR 3.7 F_{finer} 20	3.73	2.37	1.75
SR 3.7 F_{finer} 25	3.74	2.30	1.81
SR 3.7 F_{finer} 30	3.70	1.03	1.85
SR 3.7 F_{finer} 35	3.64	0.35	1.89
SR 3.7 F_{finer} 50	3.29	0.36	1.95

Table 5.4: Measures of PSD shape for the bimodal specimens with SR = 8.4

Specimen	C_u	C_z	I_G
SR 8.4 F_{finer} 5	1.37	0.94	1.62
SR 8.4 F_{finer} 10	1.58	1.06	1.89
SR 8.4 F_{finer} 15	8.59	5.67	2.10
SR 8.4 F_{finer} 20	8.75	5.59	2.44
SR 8.4 F_{finer} 25	8.75	5.44	2.59
SR 8.4 F_{finer} 30	8.67	1.95	2.70
SR 8.4 F_{finer} 35	8.49	0.15	2.79
SR 8.4 F_{finer} 50	7.74	0.15	2.96

Table 5.5: Measures of PSD shape for the bimodal specimens with SR = 14.5

Specimen	C_u	C_z	I_G
SR 14.5 F_{finer} 5	1.39	0.93	1.76
SR 14.5F_{finer} 10	1.40	0.94	2.12
SR 14.5 F_{finer} 15	14.31	9.21	2.43
SR 14.5 F_{finer} 20	14.22	9.43	2.96
SR 14.5 F_{finer} 25	14.28	9.02	3.20
SR 14.5 F_{finer} 30	14.17	2.24	3.38
SR 14.5 F_{finer} 35	14.46	0.09	3.61
SR 14.5 F_{finer} 50	13.16	0.09	3.83

Table 5.6: Measures of PSD shape for the bimodal specimens with SR = 18.1

Specimen	C_u	C_z	I_G
SR 18.1 F_{finer} 5	1.74	0.90	1.97
SR 18.1 F_{finer} 10	1.96	1.02	2.36
SR 18.1 F_{finer} 15	17.85	9.15	2.71
SR 18.1 F_{finer} 20	17.66	9.20	3.29
SR 18.1 F_{finer} 25	18.28	9.18	3.53
SR 18.1 F_{finer} 30	18.20	9.24	3.74
SR 18.1 F_{finer} 35	17.78	0.08	3.95
SR 18.1 F_{finer} 50	18.06	0.07	4.40

Trimodal specimens

For the trimodal gap-graded soils, the I_G values are presented in Figure 5.5. The variations measures of PSD shape for the trimodal specimens are presented in Table 5.7, Table 5.8 and Table 5.9. The index C_u again cannot effectively differentiate amongst these trimodal specimens, for instance, the C_u values are the same and equal to 5.59 for Tri 20_40, Tri 20_50, Tri 20_60 and Tri 20_70. In contrast, for the same F_{finer} value, the I_G values decrease

monotonically with increasing F_{int}. The data presented on Figure 5.5 support the use of I_G as a measure of the shape of PSD that is capable of differentiating trimodal gap-graded soils.

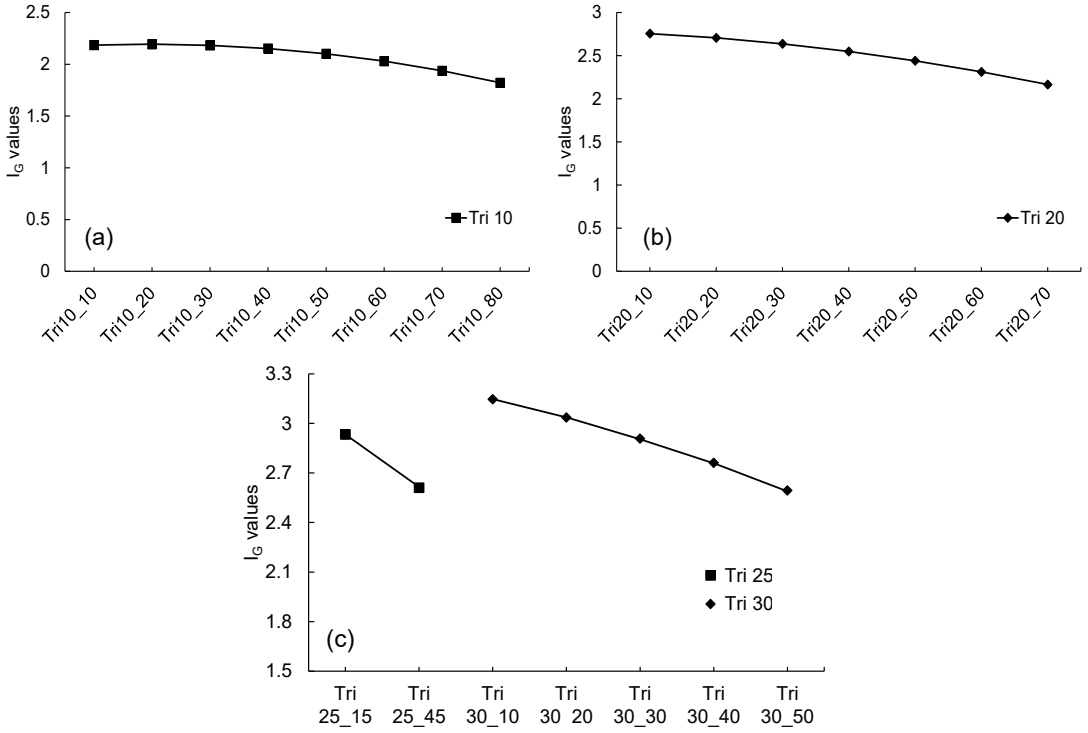


Figure 5.5: Variation in the I_G values for the trimodal specimens: (a) F_{finer} of 10%; (b) F_{finer} of 20%; (b) F_{finer} of 25% and 30%

Table 5.7: Measures of PSD shape for the trimodal specimens ($F_{finer} = 10\%$)

Specimens	C_u	C_z	I_G
Tri 10_10	12.96	12.96	2.19
Tri 10_20	12.96	2.41	2.19
Tri 10_30	12.96	2.41	2.18
Tri 10_40	12.96	2.41	2.15
Tri 10_50	5.59	5.59	2.10
Tri 10_60	5.59	5.59	2.03
Tri 10_70	5.59	5.59	1.94
Tri 10_80	5.59	5.59	1.82

Table 5.8: Measures of PSD shape for the trimodal specimens ($F_{finer} = 20\%$)

Specimens	C_u	C_z	I_G
Tri 20_10	12.96	2.41	2.76
Tri 20_20	12.96	2.41	2.71
Tri 20_30	12.96	2.41	2.64
Tri 20_40	5.59	5.59	2.55
Tri 20_50	5.59	5.59	2.44
Tri 20_60	5.59	5.59	2.31
Tri 20_70	5.59	5.59	2.17

Table 5.9: Measures of PSD shape for the trimodal specimens ($F_{finer} = 25\%,\ 30\%$)

Specimens	C_u	C_z	I_G
Tri 25_15	12.96	2.41	2.93
Tri 25_45	5.59	5.59	2.61
Tri 30_10	12.96	0.08	3.15
Tri 30_20	12.96	0.08	3.04
Tri 30_30	5.59	0.18	2.91
Tri 30_40	5.59	0.18	2.76
Tri 30_50	5.59	0.18	2.59

5.4. Stress analysis approaches adopted

In this Chapter, two approaches were employed to study the relationship between stress transmission and particle size distributions. The first approach (outlined in Section 5.4.1) considered the average stress of individual particles, while the second approach (outlined in Section 5.4.2) considered the stress transmitted by individual contacts.

Particle-based perspective

Following Potyondy & Cundall (2004) and referring to Shire et al. (2014), the overall stress tensor can be calculated from the stress tensors for the individual particles as

$$\sigma'_{ij} = \frac{1}{V}\sum_{a=1}^{N_t}\left(\bar{\sigma}^a_{ij}V^a\right) \tag{5.3}$$

where σ'_{ij} is the effective overall stress tensor for the specimen, N_t is the total number of stress-transmitting particles, $\bar{\sigma}^a_{ij}$ is the average stress tensor within the particle a, V^a is the volume of the particle a. The contribution of an individual particle, a, to the overall stress is then given by

$$\alpha^a = \frac{\bar{\sigma}^a_{ij}\,V^a}{V} \tag{5.4}$$

Equation 5.4 indicates a link between α^a and V^a. However, following Potyondy & Cundall (2004), Equation 5.5 can be expanded so that the V^a dependency is no longer evident:

$$\alpha^a = \frac{\frac{1}{V^a}\sum_{N_{c,a}}\boldsymbol{x}_i^c\boldsymbol{F}_j^c\,V^a}{V} = \frac{\sum_{N_{c,a}}\boldsymbol{x}_i^c\boldsymbol{F}_j^c}{V} \tag{5.5}$$

where $N_{c,a}$ is the number of contacts involving particle a, $\boldsymbol{x}_i^c$ is the branch vector connecting the centre of particle a to the contact point c and $\boldsymbol{F}_j^c$ is the force (vector) applied at contact c. For the spherical particles considered in this study, $|\boldsymbol{x}_i^c| \approx r^a$, where r^a is the radius of particle a reflecting the fact that some measure of size (length) is inherent to any definition of average particle stress.

Contact-based perspective

The contact force data extracted at the end of the isotropic compression were used to calculate the stresses in the virtual specimen so that the $3D$ stress tensor is given by:

$$\sigma'_{ij} = \frac{1}{V}\sum_{C=1}^{N_{c,V}} \boldsymbol{f}_i^c \boldsymbol{l}_j^c \qquad 5.6$$

where $N_{c,V}$ is the total number of contacts in volume V, $\boldsymbol{f}_i^c$ is the force vector for contact c and $\boldsymbol{l}_j^c$ is the branch vector. In this case, the branch vector is the vector joining the centroids of the particles which contact at c. The contribution of contact c to the overall stress is:

$$\frac{\boldsymbol{f}_i^c \boldsymbol{l}_j^c}{V} \qquad 5.7$$

In each case, whether Equation 5.3 or Equation 5.6 is adopted, the mean effective stress is calculated from the trace of the stress tensor, i.e. $p' = \sigma'_{ii}/3$.

5.5. Analysis of stress distribution within the specimens

5.5.1. Specimens with continuous gradings

Linear specimens

The data for the specimens with linear $PSDs$ are presented in Figure 5.6. Figure 5.6(a) illustrates the $PSDs$ for all grains. The horizontal axis for the plot in Figure 5.6(a) considers the normalised diameters d^p / d^p_{Max} since the absolute diameter of grains in these DEM simulations will not influence the data generated. Figure 5.6(b) shows the particle size distribution of the active particles, PSD^{active} in the dense specimens at the end of the simulations when the material has attained an isotropic stress of 500 kPa. As discussed in Chapter 4, this study considers these particles with 0 or 1 connectivity values to be inactive particles. The particles which have contact points with contact force > 0 are capable of transferring the stress. Comparing Figure 5.6(a) and (b), it is evident that for the dense specimens, the $PSDs$ for the active particles are similar to the overall $PSDs$, which illustrates that most of the grains are capable of transferring stress.

By adopting Equation 5.3, Figure 5.6 (c) shows the cumulative distribution of the contribution of each particle to the overall stress. In this study, this distribution is termed the PSD^{stress}. It can be seen that the shape of the $PSDs$ in Figure 5.6(a) and the shape of the PSD^{stress} in Figure 5.6(c) are very similar. These data indicate that for the dense specimens with a continuous grading, the fraction of the overall stress transferred by each grain is proportional to its particle mass. For instance, as identified in Figure 5.6 for specimen Linear C_u $1.5(D)$, the 20% percentiles on both the overall and active PSD curves (Figure 5.6(a) & (b) respectively) occur at d^p/d^p_{Max} = 0.53 (Points A & B). The 20% percentile on the PSD^{stress} plot for this specimen also occurs at d^p/d^p_{Max} = 0.53 (Point C, Figure 5.6 (c)).

By applying Equation 5.6, the stress transmission can also be analysed from the perspective of contact points. Figure 5.6(d) shows the cumulative distribution of the contribution of each contact point to the overall stress as a function of the normalised branch vector length (i.e. branch vector length divided by the maximum branch vector, $|l^c|/|l^{pc}_M|$). This distribution is therefore denoted as CSD^{stress} in this study. Although the shape of CSD^{stress} is not perfectly linear (Figure 5.6(d)), the overall shape of the curve is close to those identified in Figure 5.6(a) and Figure 5.6(b). For instance, the 20% percentile on the CSD^{stress} curve for this specimen Linear C_u $1.5(D)$ occurs at $|l^c|/|l^{pc}_M|$= 0.57 (Point D, Figure 5.6(d)).

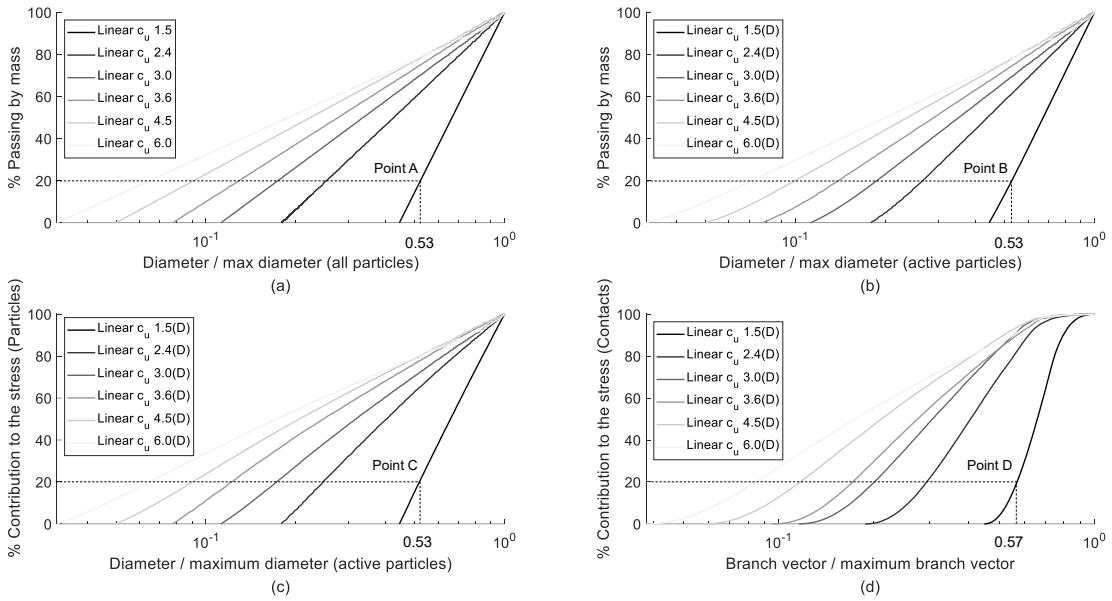


Figure 5.6: Typical results for linear specimens in the densest condition: (a) PSD plots considering all particles; (b) PSD plots considering active particles; (c) PSD^{stress} plots; (d) CSD^{stress} plots, "D" denotes the densest case

For both the medium and the loose conditions, as illustrated in Figure 5.7 and Figure 5.8, respectively, a similar tendency can be observed compared to that identified in the densest condition. In general, the shape of PSD^{active}, PSD^{stress} and CSD^{stress} are similar to their PSD for the dense, medium and loose conditions.

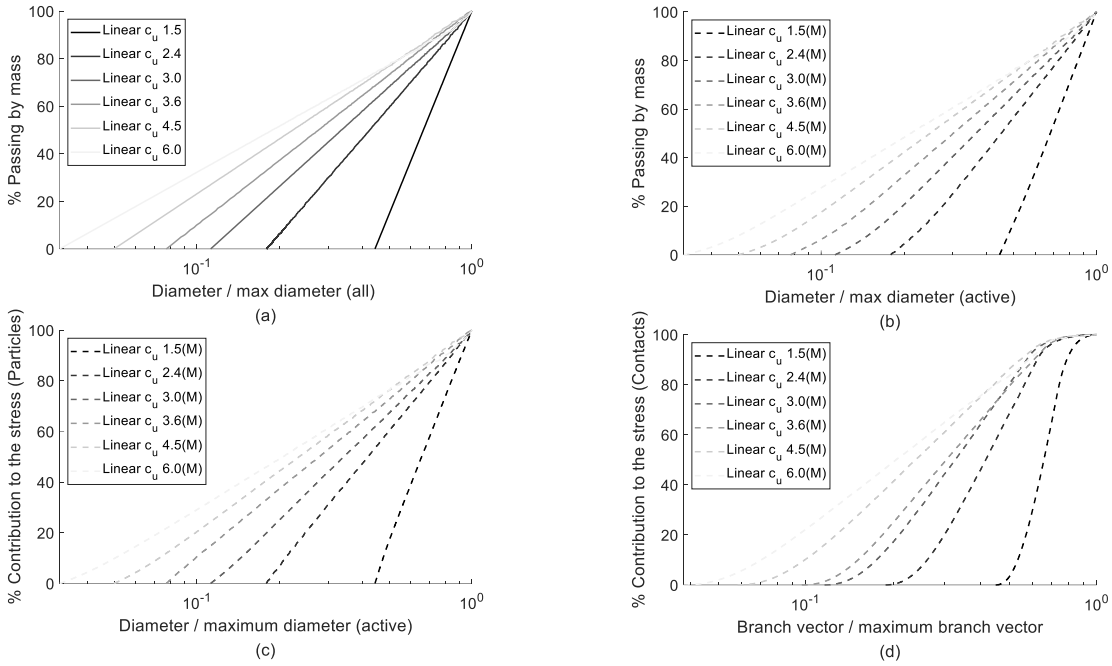


Figure 5.7: Typical results for linear specimens in the medium-dense condition: (a) PSD plots considering all particles; (b) PSD plots considering active particles; (c) PSD^{stress} plots; (d) CSD^{stress} plots, "M" denotes the medium-dense case

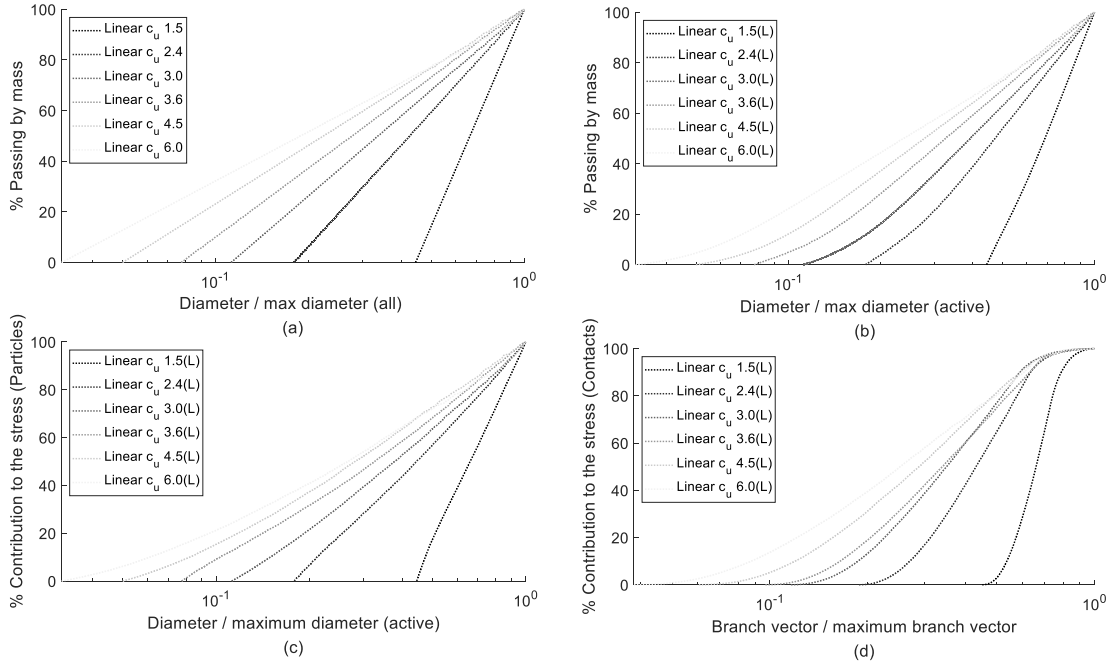


Figure 5.8: Typical results for linear specimens in the loosest condition: (a) PSD plots considering all particles; (b) PSD plots considering active particles; (c) PSD^{stress} plots; (d) CSD^{stress} plots, "L" denotes the loosest case

The effect of packing density on the linear specimens is considered in Figure 5.9. two representative gradings (i.e. the smallest C_u of 1.5 and the largest C_u of 6) were studied following the template used in Figure 5.6. The $PSDs$ for all the particles in the simulations are illustrated in Figure 5.9(a). Figure 5.9(b) shows the PSD^{stress} plots for all packing densities. For the smaller C_u of 1.5, it can be seen that the effect of packing density on the PSD^{stress} is negligible. In contrast, a finite density effect is observed for the larger C_u of 6. For instance, as illustrated in Figure 5.9(a), the 20% percentile values for the $PSDs$ for the specimens with C_u = 6 occur at d^p/d^p_{Max} = 0.065. When considering only the active particles, the d^p/d^p_{Max} values associated with the 20% percentile are approximately 0.094 and 0.071 for the loosest and densest conditions, respectively (Figure 5.9(b)). These data indicate that it is the smaller particles that tend to be less likely to be active at lower density values. In general, the effect of packing density increases with increasing C_u. Figure 5.9(c) and (d) support this conclusion. For the specimens with C_u = 1.5, the effect of density on the PSD^{stress} data is not significant. In contrast, for the specimens with C_u = 6, a finite density effect can be observed considering both the PSD^{stress} data and the CSD^{stress} data; in the case of PSD^{stress}, the d^p / d^p_{Max} values associated with the 20% percentile data are 0.096 and 0.065 for the loosest and densest conditions, respectively.

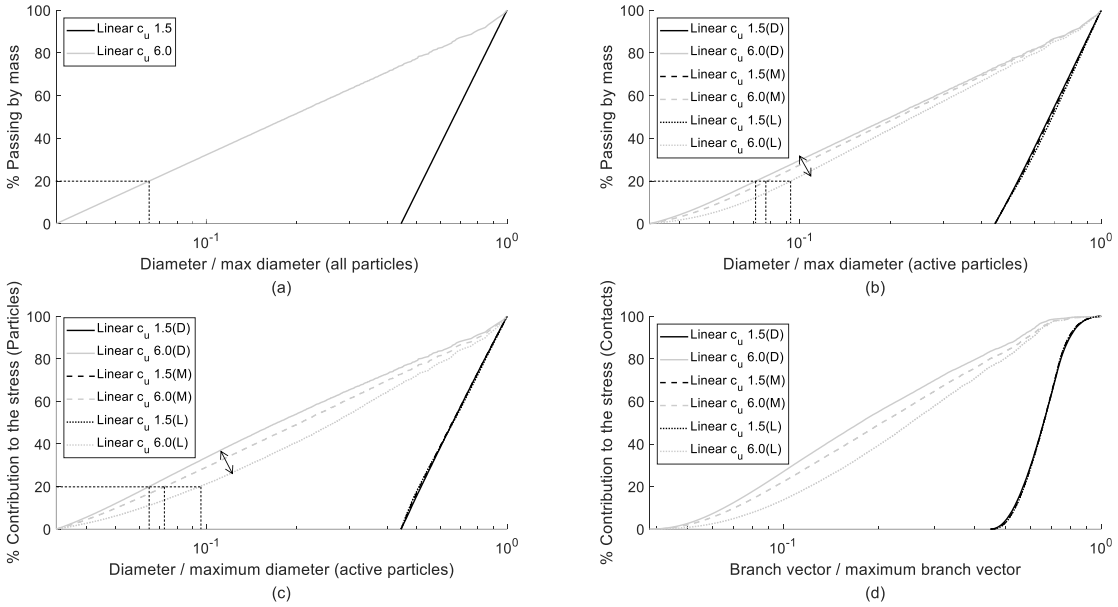


Figure 5.9: The effect of density on stress distribution for two linear gradations (i.e. C_u 1.5, 6.0): (a) PSD plots considering all particles; (b) PSD plots considering active particles; (c) PSD^{stress} plots; (d) CSD^{stress} plots, "D" denotes the densest case, "M" denotes the medium-dense case, "L" denotes the loosest case.

A summary or overview of the linear specimens is obtained by quantifying the shapes of these cumulative distributions. The I_G^{active} values based on the PSD of the active particles were calculated so that the w_i and w_{tot} in Equation 5.1 are determined by only considering the active grains. Figure 5.10 shows that the I_G^{active} values are very similar to the I_G values obtained considering the entire PSD, particularly for the densest specimens. There is, however, a slight density–dependency; for the loosest specimens I_G^{active} is clearly less than I_G and the difference between the two measures increases with increasing C_u. The I_G^{stress} values were calculated by taking w_i and w_{tot} in Equation 5.1 (refering to Equation 5.3) as $\frac{(1-\mathrm{n}_p)}{\sum_{a=1}^{N_t} V^a} p^a V^a$ and $\frac{(1-\mathrm{n}_p)}{\sum_{a=1}^{N_t} V^a} \sum_{a=1}^{N_t} (p^a V^a)$. It is reasonable to state that for the densest specimens $I_G \approx I_G^{active} \approx I_G^{stress}$; while the agreement is not as close for the loosest specimens. However, it still can be observed that the values of I_G and I_G^{stress} are similar, particularly for the specimens with lower C_u values. Thus, for each of the specimens with a narrow continuous linear grading considered here, the distribution of stress

amongst the constituent particles is very similar to its particle size distribution.

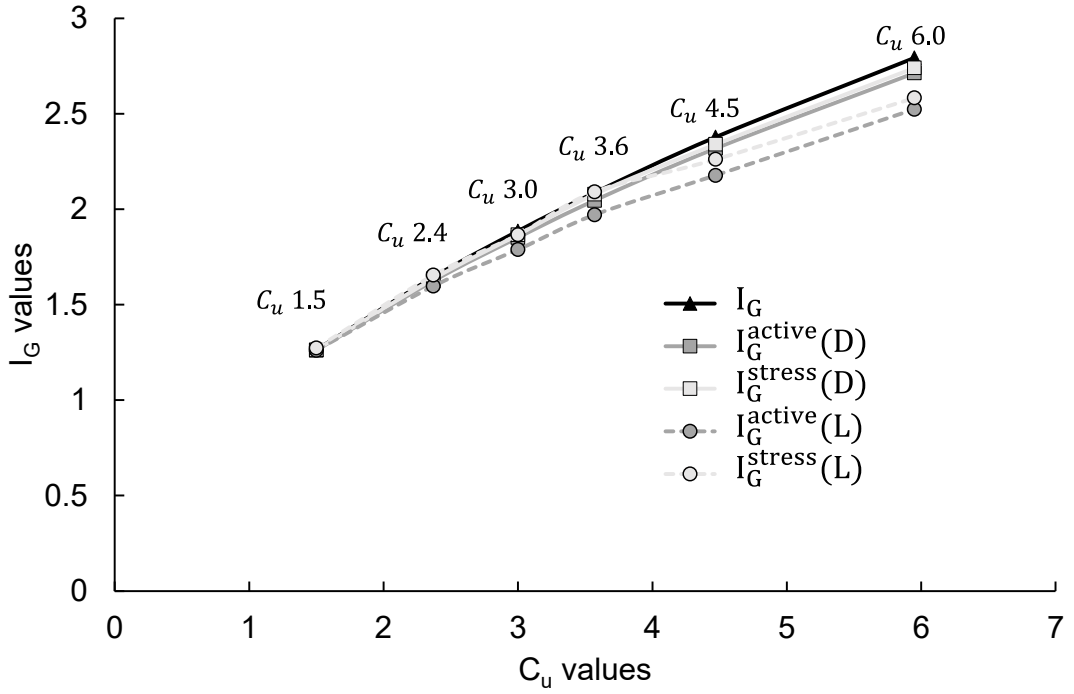


Figure 5.10: Comparison of I_G, I_G^{active} and I_G^{stress} data for linear gradations, "D" denotes the densest case, "L" denotes the loosest case

Fractal specimens

Results for two representative fractal specimens are shown in Figure 5.11. Figure 5.11(a) illustrates the $PSDs$ for specimen 'Fractal 0.1% S' and 'Fractal 0.1% L'. The effect of packing density on stress transmission in those fractal specimens can be observed from the plots shown in Figure 5.11(b), (c) and (d). Figure 5.11(c) and (d) indicate that the effect of density on the stress transmission within the fractal specimens is negligible from either the perspective of the particles or the contacts. In addition, the PSD^{stress} (Figure 5.11(c)) and CSD^{stress} (Figure 5.11(d)) plots are similar to the corresponding $PSDs$. For instance, for the PSD considering all particles in Figure 5.11(a), the 20% percentile point occurs at $d^p/d^p_{Max} \approx 0.55$; considering the PSD^{stress} data, the d^p/d^p_{Max} values associated with the 20% percentile are 0.568, 0.561 and 0.561 for the loosest, medium and densest conditions, respectively (Figure

5.11(c)). The fraction of the mean stress transferred by each particle is proportional to its particle mass. This result shows a similar behaviour compared to that of linear specimens with C_u of 1.5. The data support the finding that a similarity between the PSD and the PSD^{stress} may be a characteristic of specimens with a continuous grading particularly where the C_u is relatively low.

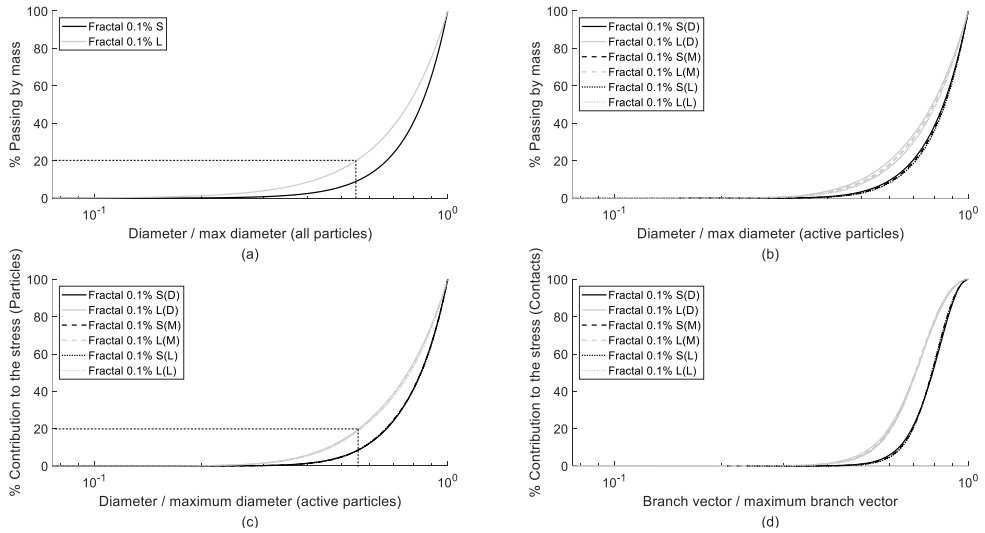


Figure 5.11: Typical results for fractal specimens: (a) PSD plots considering all particles; (b) PSD plots considering active particles; (c) PSD^{stress} plots; (d) CSD^{stress} plots , "D" denotes the densest case, "M" denotes the medium case, "L" denotes the loosest case.

This effect of density can also be quantified through consideration of I_G, I_G^{active} and I_G^{stress}. Figure 5.12 illustrates that for these fractal specimens, the I_G^{active} and I_G^{stress} values identified in the densest condition are similar to those observed in the loosest condition. In general, the I_G^{active} and I_G^{stress} values are similar to the corresponding I_G values.

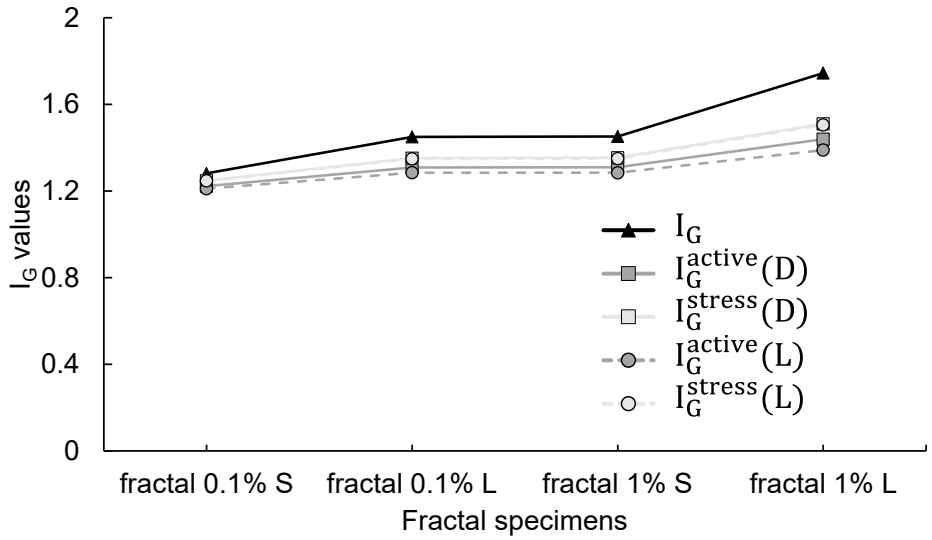


Figure 5.12: Comparison of I_G, I_G^{active} and I_G^{stress} data for fractal gradations, "D" denotes the densest case, "L" denotes the loosest case

5.5.2. Specimens with bimodal gradings

Distribution of stress amongst particles

Following the template used for the specimens with continuous gradings, Figure 5.13 considers the influence of F_{finer} on the bimodal specimen data by considering the dense specimens with SR = 14.5. Figure 5.13(a) and (b) present the PSD and the PSD^{active}, respectively. Figure 5.13(c) shows the evolution of PSD^{stress} with increasing F_{finer} while Figure 5.13(d) presents the CSD^{stress} data. The longest branch vectors are associated with contacts between the coarser grains, while the contacts between the finer grains have the shortest branch vectors. It is clear that the contribution of the finer particles to the overall stress transmitted is negligible when $F_{finer} \leq$ 20% and the finer particles only start to measurably transfer stress when $F_{finer} \geq$ 25%. There are clear differences between the shape of the PSD plots and the PSD^{stress} plots. It is only for F_{finer} > 30% that it can be reasonably said that the plots are similar.

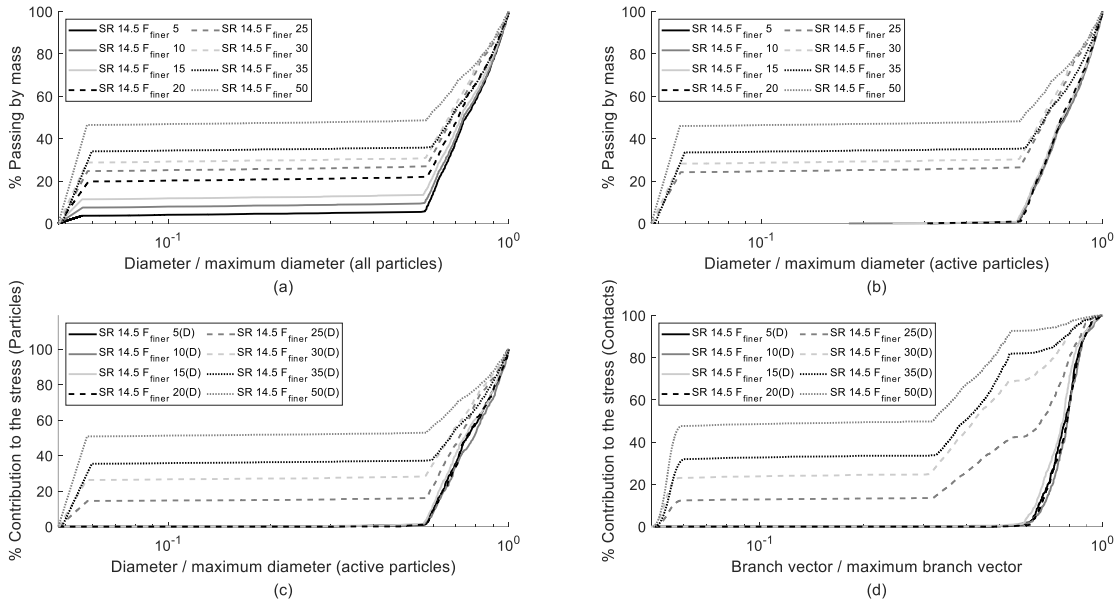


Figure 5.13: Representative results for the bimodal specimens with SR = 14.5 in the densest condition: (a) PSD plots considering all particles; (b) PSD plots considering active particles; (c) PSD^{stress} plots; (d) CSD^{stress} plots , "D" denotes the densest case

Figure 5.14 considers the effect of density on the PSD^{stress} and CSD^{stress} data by considering three representative F_{finer} values (10%, 30% and 50%) with SR of 14.5. For F_{finer}= 10%, density has a negligible effect on the number of active particles (Figure 5.14(b)) as well as the PSD^{stress} and CSD^{stress} data (Figure 5.14(c) and (d)). When F_{finer} increases to 30% and 50%, changes in density have a finite effect on the data. The PSD^{stress} and CSD^{stress} data are more sensitive to density (Figure 5.14(c) and (d) respectively) than the PSD of the active particles (Figure 5.14(b)).

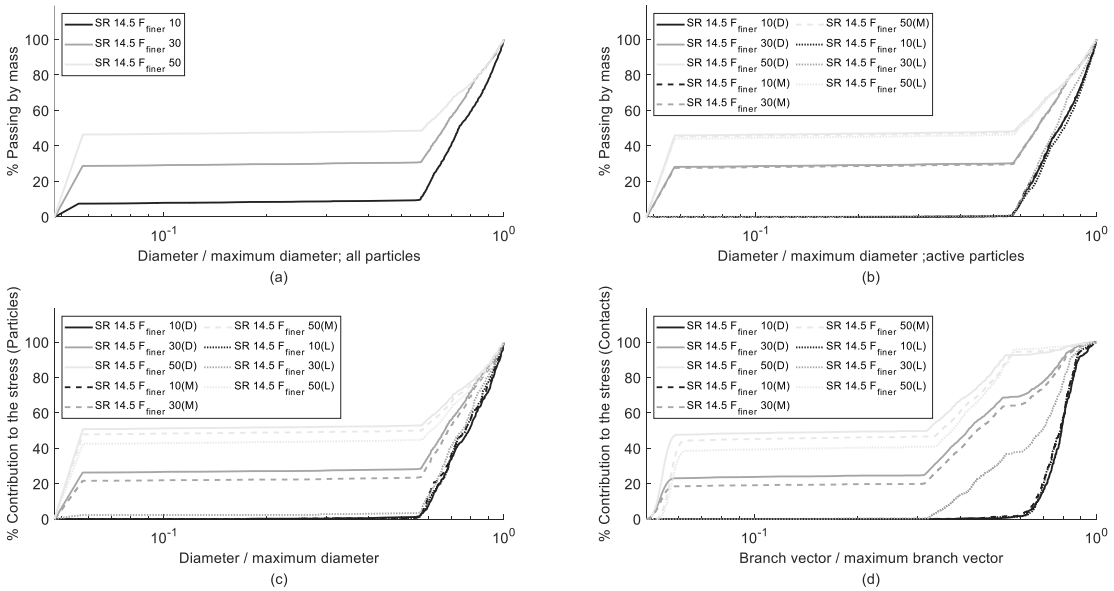


Figure 5.14: Representative results for the bimodal specimens, the effect of density: (a) PSD plots considering all particles; (b) PSD plots considering active particles; (c) PSD^{stress} plots; (d) CSD^{stress} plots , "D" denotes the densest case, "M" denotes the medium-dense case, "L" denotes the loosest case.

The data presented in Figure 5.15 enable direct comparison of the PSD (upper plots) and PSD^{stress} data (lower plots) for representative bimodal specimens with increasing SRs under the densest packing case. At the densest packing density, when $SR \geq 8.4$, the PSD^{stress} (Figure 5.15(d)/(f)) data for a given specimen exhibit a distinctly different shape when compared to its corresponding PSD (Figure 5.15(c)/(e)) when $F_{finer} \leq 20\%$, while a sudden shift is observed when $20\% \leq F_{finer} \leq 25\%$. The shape of the PSD and PSD^{stress} plots are similar when $F_{finer} \geq 25\%$. In addition, the data obtained for the case when $SR = 3.7$ differ from the other SR values considered; as illustrated in Figure 5.15(b), for SR = 3.7 the PSD^{stress} plots shift upwards with increasing F_{finer} for all F_{finer} considered. In contrast, for the other SR values (SR > 3.7) the finer fraction has a limited contribution to the PSD^{stress} data for $F_{finer} \leq 20\%$.

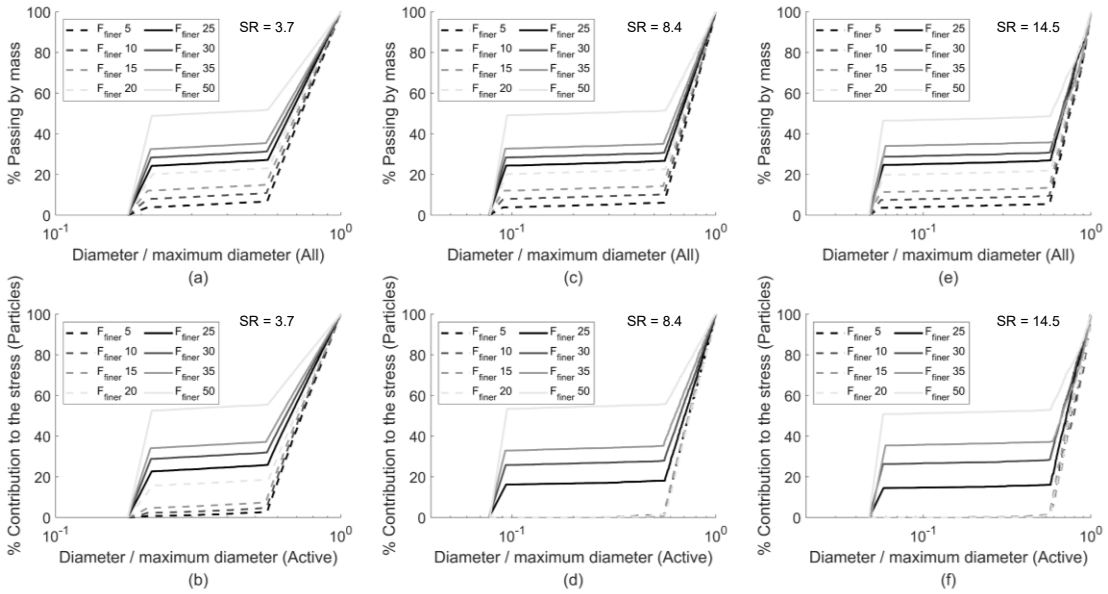


Figure 5.15: Representative results for the bimodal specimens in the densest condition, the effect of SR: (a) PSD plots, SR = 3.7; (b) PSD^{stress} plots, SR = 3.7; (c) PSD plots, SR = 8.4; (d) PSD^{stress} plots, SR = 8.4; (e) PSD plots, SR = 14.5; (f) PSD^{stress} plots, SR = 14.5

To understand the variations in the relative contributions of the coarse and finer fractions with SR, F_{finer} and density, Figure 5.16 shows the proportion of the mean stress transferred by the coarser and finer grains for the three packing densities considered and four SR values. Figure 5.16(a) shows that for a SR of 3.7, the finer particles have a measurable contribution to the overall stress for all density levels and F_{finer} values considered. This can be attributed to the fact that for $SR < 6$, the finer grains cannot exist easily in the voids without actively contacting other particles, as previously discussed in Chapter 4. For the densest case, the proportion of stress transferred by the finer fraction approaches their F_{finer} (i.e. the dashed line) once F_{finer} > 20%.

For the SRs of 8.4, 14.5 and 18.1, the finer particles have a negligible contribution to the stress when $F_{finer} \leq 20\%$ and the finer particles start to transfer stress only when $F_{finer} \geq 25\%$. Density affects the proportion of stress transferred by F_{finer} in all cases. Moreover, the density effect is most

significant when F_{finer} is approximately 25% and 30%. When F_{finer} is 50%, it can be seen that the coarse and finer particles transfer approximately equal proportions of the overall stress, which shows that these coarse particles are still significant in terms of stress transmission at this F_{finer}, i.e., it is a misnomer to term the materials “fines dominated”. When compared to the continuous packings, using the same consistent approach to vary density, the effect of density on stress transmission is more significant for the bimodal specimens. In general, it is clear that the contribution of the finer particles to the overall stress tensor is proportionally less than the mass of finer grains in the system for $F_{finer} < 50\%$.

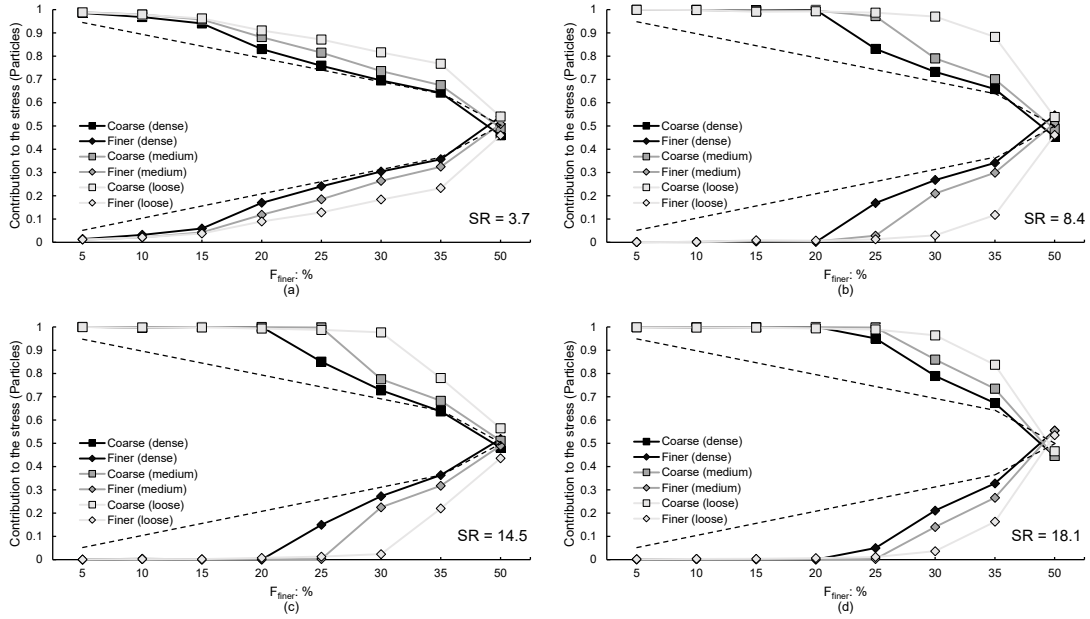


Figure 5.16: Stress contribution of finer and coarser particles, the effect of SR: (a) SR = 3.7; (b) SR = 8.4; (c) SR = 14.5; (d) SR = 18.1

From the perspective of a single contact point

To understand the nature of stress distribution in the bimodal specimens it is also useful to investigate this issue from the perspective of a single contact point. Specimens with a size ratio of 14.5 with three typical F_{finer} values (i.e. 5%, 30%, 50%) were selected to cover a broad range of F_{finer} values. The evolution of interactions amongst different contact types within increasing

F_{finer} is considered.

In a bimodal specimen, there are three contact types: contacts between two coarser grains ($C-C$), contacts between two finer grains ($F-F$) and contacts between a coarser and a finer grain ($C-F$). To quantify the contribution of each contact type to the overall stress, the overall stress tensor was decomposed into $F-F$ (σ_{ij}^{FF}), coarser-finer (σ_{ij}^{CF}), and coarser-coarser (σ_{ij}^{CC}) contributions, so that, for example:

$$\sigma_{ij}^{FF} = \frac{1}{V}\sum_{C=1}^{N_c^{FF}} f_i^c l_j^c \qquad 5.8$$

where N_c^{FF} is the total number of $F-F$ contacts in volume V.

To illustrate the relative proportion by number of the different types of contacts as well as the magnitude of their contributions to the overall stress, a series of pie charts are considered in the following discussion. For a F_{finer} value of 10%, the CSD^{stress} data are not measurably sensitive to density (Figure 5.17(a)). For this F_{finer} = 10%, the upper sets of pie charts in Figure 5.17(b) illustrate the number of contacts for the three packing densities considered, and the lower set of pie charts illustrate the stress transmission from the perspective of contacts. It can be seen that the $C-C$ contacts transfer about 99% of the stress irrespective of packing density, i.e. their contribution exceeds their corresponding proportion by number in the specimens. The insensitivity to density reflects the underfilled nature of the fabric, i.e. the finer grains can rest in the void space between the coarse grains with sufficient space around them that they do not engage in load-transmitting contacts.

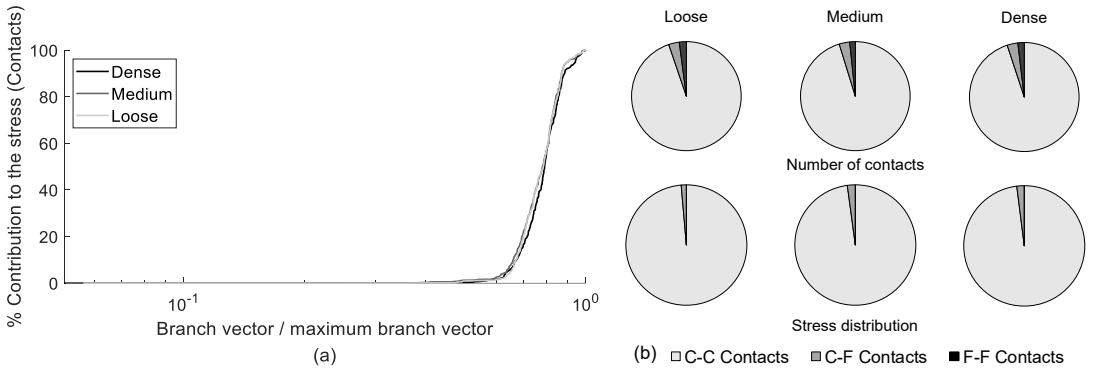


Figure 5.17: Data for bimodal specimens with $SR = 14.5$ and F_{finer} = 10%: (a) CSD^{stress}; (b) Pie charts illustrating the numeric proportion of different contacts in the samples and the stress distribution amongst the different contacts

Where F_{finer} is 30%, the CSD^{stress} data exhibit a clear density sensitivity (Figure 5.18); the contribution of the $F-F$ and $C-F$ contacts which have relatively short branch vectors are measurably larger in the medium and dense packing in comparison with the loose case. Considering the pie chart plots in Figure 5.18(b), and again comparing the upper and lower rows, it is clear that in the loosest case, the proportion of stress transferred by the $C-C$ contacts is markedly larger than the proportion by number of $C-C$ contacts in the specimen. It is important to note when looking at the pie chart plots that the coordination number, Z of this specimen changes from approximately 0.016 to 6.03 when the density increases from the loosest to the densest case, reflecting a significant change in the soil fabric.

As illustrated in Figure 5.18(b), in the loose condition, approximately 63% of stress is carried by the $C-C$ contacts, the $C-F$ contacts transfer approximately 37% of the overall stress, while the $F-F$ contacts account for a negligible proportion (i.e. 0.2%) of stress transmission. In the dense condition, the $C-C$ contacts account for approximately 31% of the stress transmission whereas the $F-F$ contacts which account for approximately 86% of contacts by number transfer only approximately 24% of the stress.

Previous studies (e.g. Shire et al., 2016) have shown that the fabric evolves from being underfilled to filled and overfilled with increasing F_{finer}. A similar tendency is observed in this study. Furthermore, these data confirm the observation of Shire et al. (2014) that the soil fabric may also evolve with changes in density for certain F_{finer} values. The stress distribution illustrated in Figure 5.18(b) also indicates that the relative contribution of finer grains increases when density conditions change from the loose to the dense condition.

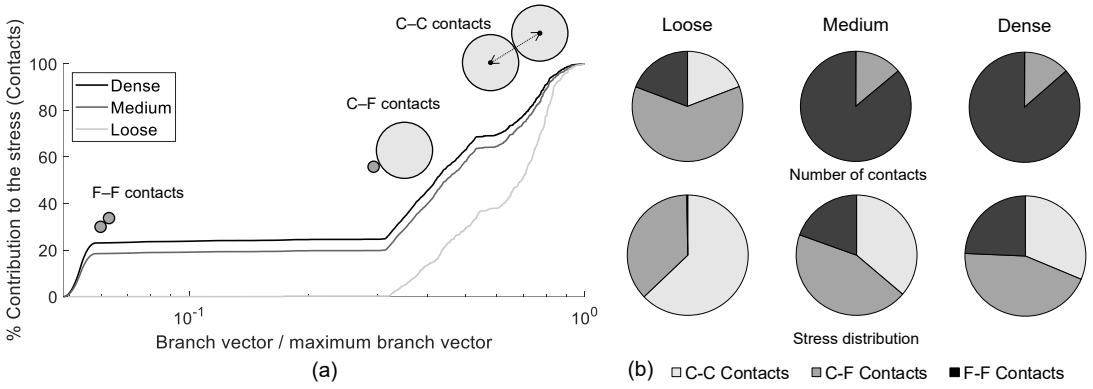


Figure 5.18: Data for bimodal specimens with $SR = 14.5$ and F_{finer} = 30%: (a) CSD^{stress}; (b) Pie charts illustrating the numeric proportion of different contacts in the samples and the stress distribution amongst the different contacts

The data presented in Figure 5.19 show that when F_{finer} increases to approximately 50%, an overfilled soil fabric is identified, and density has a less marked effect. For instance, as illustrated in Figure 5.19(a), plots for the contact contributions of each contact to the overall stress are similar for the three density conditions considered. Figure 5.19(b) illustrates that the density effect becomes small when referring to the number of contacts of each type. Figure 5.19 (b) illustrates that the $F-F$ contacts transmit a large proportion of the stress, however, it can be seen that the $C-F$ contacts and $C-C$ contacts still are capable of making a significant contribution to the overall stress

transmitted, for instance, in the loose condition, the $C-F$ contacts transfer approximately 56% stress. This result highlights that the relative contribution of coarser grains is significant even when F_{finer} is approximately 50%.

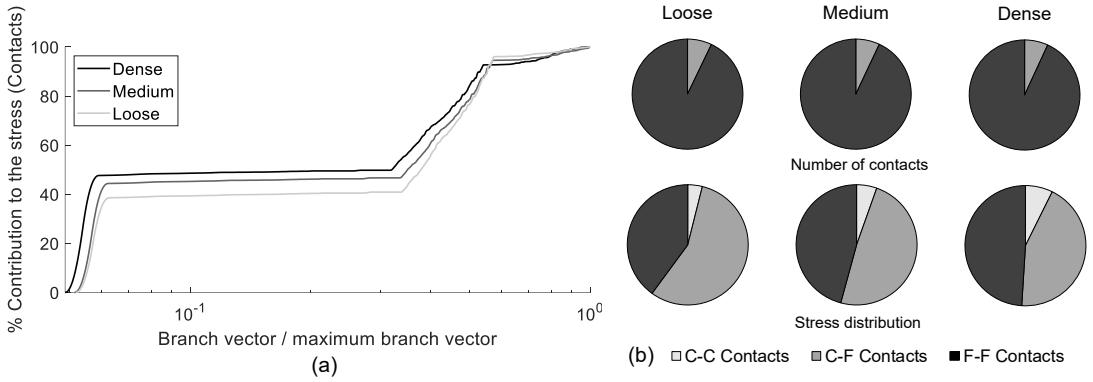


Figure 5.19: Data for bimodal specimens with $SR = 14.5$ and F_{finer} = 50%: (a) CSD^{stress}; (b) Pie charts illustrating the numeric proportion of different contacts in the samples and the stress distribution amongst the different contacts

Figure 5.20 shows how the contribution of each contact type to the overall mean stress varies with F_{finer} for the specimens with SR of 3.7 for the three packing densities considered here.

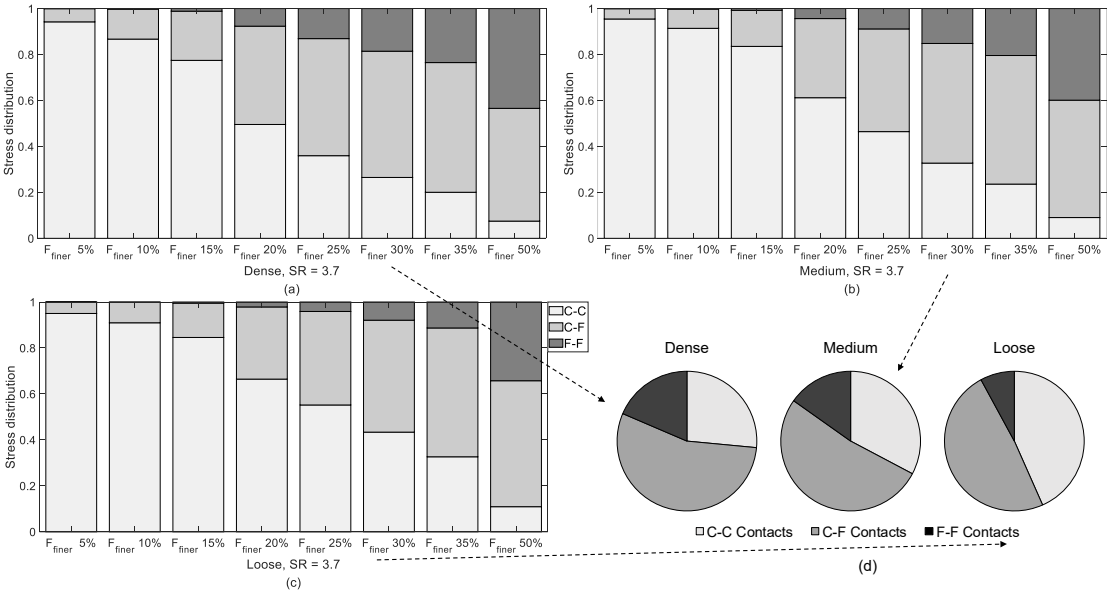


Figure 5.20: Variation in the proportion of stress transmitted by each of the three sets of contact with increasing F_{finer} when $SR = 3.7$: (a) Dense specimens; (b) Medium-dense specimens; (c) Loose specimens; (d) Example pie chart with equivalent data for F_{finer} of 30%

The data in Figure 5.20 show that when SR = 3.7, there is no clear threshold separating the coarse-dominant behaviour, transitional behaviour, and fines-dominant behaviour. The contribution of $C-F$ contacts and $F-F$ contacts to the overall stress gradually increases with increasing F_{finer}. The effect of density is most evident for $20\% \leq F_{finer} \leq 35\%$. As illustrated in Figure 5.20(d), when F_{finer} is 30%, the stress distribution of these specimens is strongly associated with the packing density. In the densest condition, the $F-F$ contacts transfer approximately 18.5% of the overall stress, while the $F-F$ contacts only transfer approximately 7.8% of the overall stress in the loosest condition.

The data for the specimens with SR = 8.4 are presented in Figure 5.21, which show that when the size ratio increases from 3.7 to 8.4, there is a different pattern to the variation in the distribution of stress amongst the different contact types with F_{finer}. For SR = 8.4, when $F_{finer} \leq 20\%$, the $C-F$ and $F-F$ contacts transfer a small fraction of stress compared to the $C-C$ contacts irrespective of packing density. In contrast, when the size ratio is 3.7, both $C-F$ and $F-F$ contacts transfer a significant amount of the overall stress when $F_{finer} \leq 20\%$.

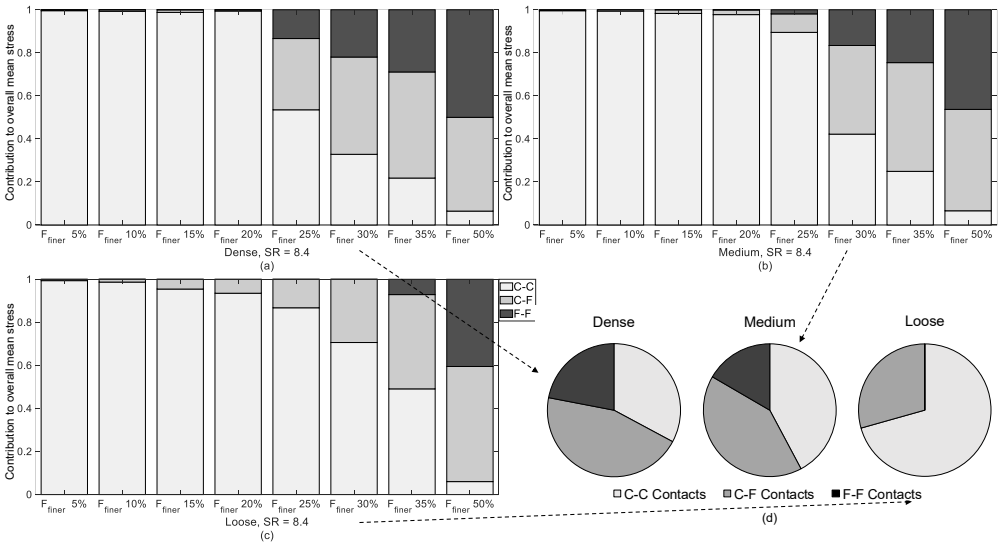


Figure 5.21: Variation in the proportion of stress transmitted by each of the three sets of contact with increasing F_{finer} when $SR = 8.4$: (a) Dense specimens; (b) Medium-dense specimens; (c) Loose specimens; (d) Example pie chart with equivalent data for F_{finer} of 30%

For SR = 8.4, when F_{finer} is 25% and 30%, the distribution of stress amongst the different contact types is very sensitive to the packing density. In contrast, when $F_{finer} \geq$ 30%, the density effect is diminished. When F_{finer} is 50%, the $C-F$ contacts and $F-F$ contacts start to transfer almost all of the overall stress (approximately 90%).

Data for SR = 14.5 are illustrated in Figure 5.22. When these data are compared to the results for SR = 8.4, no clear differences can be observed, the effect of SR start to decrease when $SR \geq 8.4$.

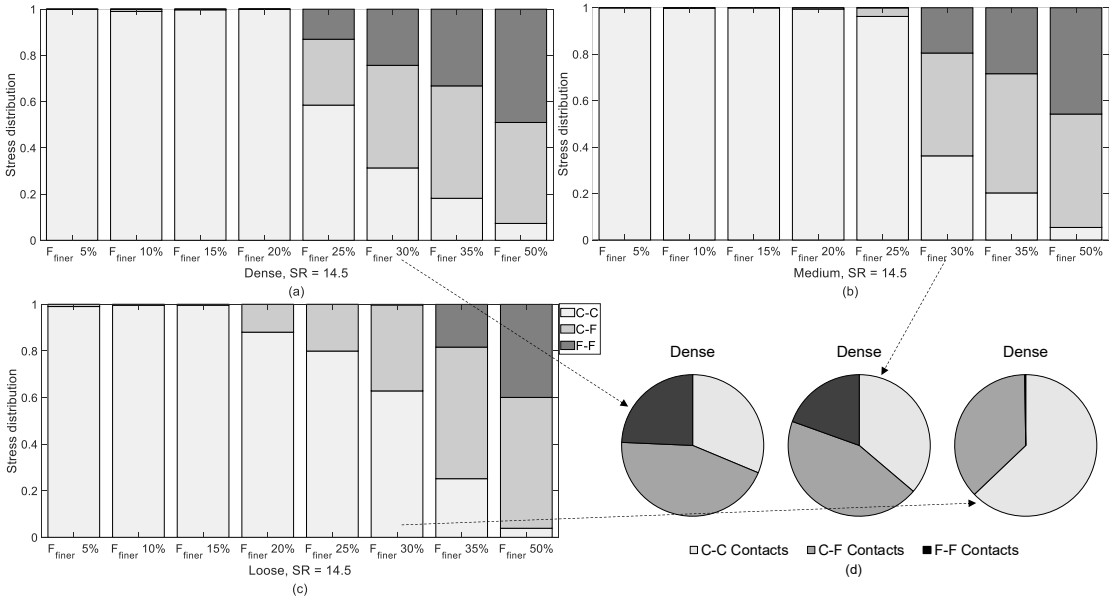


Figure 5.22: Variation in the proportion of stress transmitted by each of the three sets of contact with increasing F_{finer} when $SR = 14.5$: (a) Dense specimens; (b) Medium-dense specimens; (c) Loose specimens; (d) Example pie chart with equivalent data for F_{finer} of 30%

The effect of size ratio on the stress distribution in the bimodal specimens

Figure 5.23 directly compares the distribution of stress amongst the three contact types for all the SR values considered. When $F_{finer} \leq$ 20%, the specimens with $SR = 3.7$ differ from the specimens with $SR \geq 8.4$. For the specimens with $SR = 3.7$ at these low F_{finer} values, the trapping of individual finer grains between coarse particles is evident, $C - F$ contacts make a relatively large contribution to the overall stress transferred, and the $F - F$ contacts are also capable of transferring stress. In contrast, for SR values of 8.4, 14.5 and 18.1 for $F_{finer} \leq$ 20%, the $C - F$ and $F - F$ contacts make an almost negligible contribution to the overall stress. When $F_{finer} \geq$ 25%, for all the SRs considered, the $C - F$ contacts and $F - F$ contacts play an increasingly significant role in transferring the overall stress, as F_{finer} increases. However, when F_{finer} is 50%, for all these SRs, the combined stress transferred by the $C - C$ and $C - F$ contacts > 50%, which provides further evidence that the coarse grains are still significant contributors to the

overall stress transmitted even at F_{finer} = 50%.

The lack of consensus amongst previous studies on the selection of an appropriate state variable (i.e. void ratio) to predict the mechanical response of gap-graded soils may be partially attributed to this SR effect. The results presented in Figure 5.23(a) and Figure 5.23(b) clearly show that the mechanics of the response of specimens with low SR values is measurably different from the mechanics of specimens with SR values exceeding 6.5. Amongst the previous studies, Yang et al. (2015) concluded that the global void ratio is the most suitable state variable to capture the soil behaviour of the soil mixtures they tested. However, they used a SR of approximately 4 in their experimental work. In contrast, the SRs used in Thevanayagam et al. (2002) and Goudarzy et al. (2016) are rather large (i.e. approximately 24 and 140). Therefore, the global void ratio may not be an appropriate state variable to capture this soil behaviour in this case.

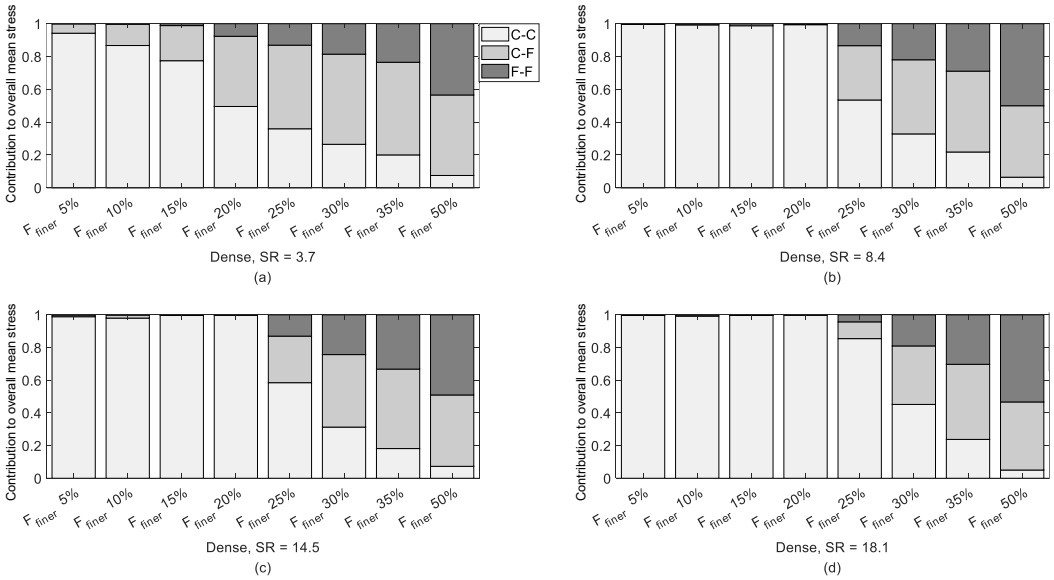


Figure 5.23: Variation in the proportion of stress transmitted by each of the three sets of contact with increasing F_{finer} in the dense condition with four distinct SRs: (a) SR = 3.7; (b) SR = 8.4; (c) SR = 14.5; (d) SR = 18.1

The graph and network algorithms study for bimodal specimens

When considering whether a particular size fraction dominates the material response, it is interesting to explore whether the contact network formed only amongst particles in that size fraction is sufficient to transfer stress through the specimen. Therefore, it is useful to assess the extent to which the connections amongst each contact type ($C-C$, $C-F$ or $F-F$) form a percolating, stress transmitting network. Here the graph and network algorithms in $MATLAB$ (MathWorks, 2019) were used to analyse the undirected graphs that can be formed by considering separately the contact networks formed by the $C-C$, $C-F$ and $F-F$ contacts. For each network, the lengths of the largest clusters of contacting particles in the direction of each of the three cartesian axes ($L_x^{cluster}$, $L_y^{cluster}$ and $L_z^{cluster}$) were normalised by the size of the periodic cell containing the specimen in the same direction (L_x^{pcell}, L_y^{pcell} and L_z^{pcell}). The averages of these three normalized lengths, $\langle\frac{L_i^{cluster}}{L_i^{pcell}}\rangle$, are presented in Figure 5.24. Figure 5.24(a) shows that when F_{finer} is 5%, for the $C-C$ contacts, $\langle\frac{L_i^{cluster}}{L_i^{pcell}}\rangle \approx 1$, and so the largest cluster formed by the $C-C$ contact network traverses the specimen and the $C-C$ contacts form a percolating network in this specimen. In contrast, $\langle\frac{L_i^{cluster}}{L_i^{pcell}}\rangle$ for the $F-F$ contacts is only $\approx$ 2.5%, confirming the insignificant role of the $F-F$ contacts in stress transmission. For a SR of 3.7, (Figure 5.24(a)) shows that both the $C-C$ and $C-F$ contact networks span the entire specimen when $F_{finer} > 5\%$. It is only when $F_{finer} \geq 20\%$ that the $F-F$ contacts form a percolating network in the specimen. Figure 5.24(b), (c) and (d) consider the variation in $\langle\frac{L_i^{cluster}}{L_i^{pcell}}\rangle$ for the three contact networks for specimens F_{finer} for SR = 8.4, 14.5 and 18.1, respectively. For these three SRs, the $C-C$ contacts form percolating networks in the specimens for all F_{finer} values considered. For $5\% \leq$

$F_{finer} \leq 20\%$, $\langle \frac{L_i^{cluster}}{L_i^{pcell}} \rangle$ values for the $C-F$ contacts are consistently ≈ 0.2, and there is little evidence of cluster formation in the $F-F$ network. When $F_{finer} \geq 25\%$, the $\langle \frac{L_i^{cluster}}{L_i^{pcell}} \rangle$ values for these three contacts ≈ 1.

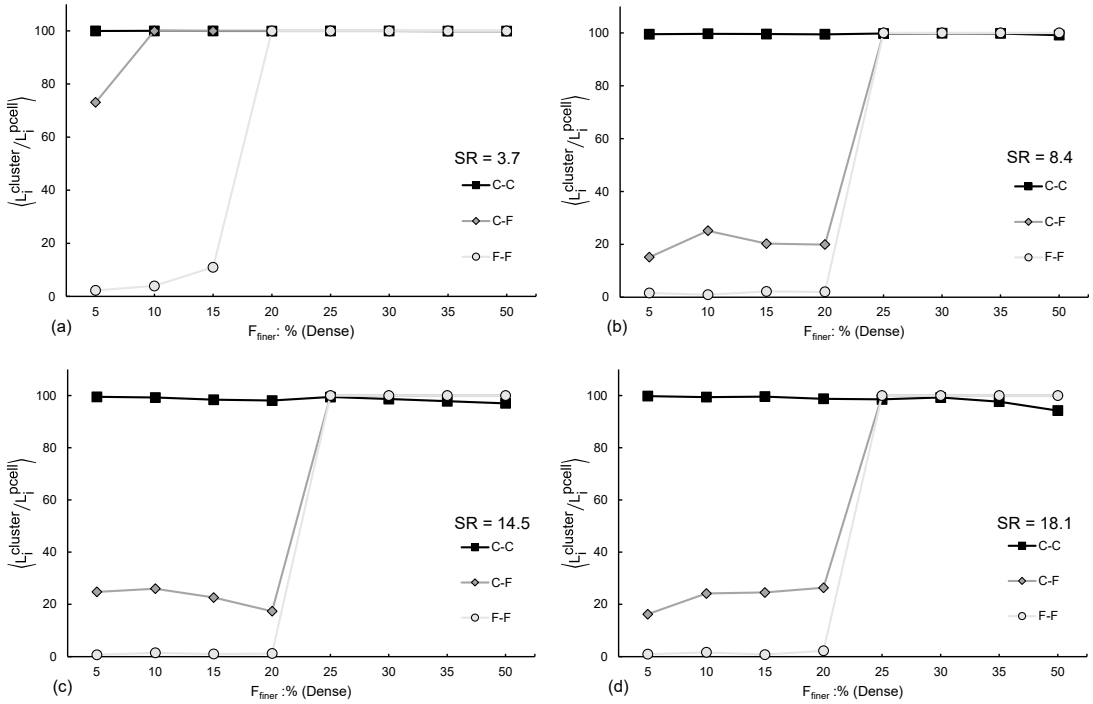


Figure 5.24: The averages values of these three normalized lengths for the three sets of contact in the densest condition: (a) SR = 3.7; (b) SR = 8.4; (c) SR = 14.5; (d) SR = 18.1

Using the index of grading to analyze stress distribution in the bimodal specimens

Figure 5.25 shows the I_G values for the bimodal gap-graded specimens for SR = 3.7, 8.4, 14.5 and 18.1 with increasing F_{finer}. It can be seen that the data for the specimens with SR = 3.7 show trends when compared to the larger SR values considered. When SR is 3.7, the I_G values for the $PSDs$ gradually increase with increasing F_{finer}. Both the I_G^{active} and I_G^{stress} values are clearly dependant on the packing densities and the F_{finer}. In the densest condition for SR = 3.7, significant differences can be observed when $F_{finer} \leq 20\%$, while $I_G \approx I_G^{active} \approx I_G^{stress}$ when $F_{finer} \geq 20\%$, which suggests that for these

samples the finer particles are capable of transferring a proportion of the overall stress that is broadly in line with the proportion by mass of these particles in the specimens. In the loosest condition, the I_G^{active} and I_G^{stress} values of these gap-graded soils are smaller compared to the corresponding I_G values, a strong density effect is evident when $F_{finer} = 20\%$, and then this effect gradually decrease with increasing F_{finer}.

When the SR values are 8.4, 14.5 and 18.1, the I_G values of the $PSDs$ also gradually increase with increasing F_{finer}. Both I_G^{active} and I_G^{stress} are also strongly associated with the F_{finer} and packing density. The I_G^{active} and I_G^{stress} values of these gap-graded soils differ from the I_G values when F_{finer} $\leq$ 20% for all density levels When $F_{finer} \leq 20\%$. I_G^{active} and I_G^{stress} maintain relatively stable and low values. A strong density effect is clear in the I_G^{active} and I_G^{stress} data when F_{finer} is 25% and 30%. For these F_{finer} values in the densest specimens, the I_G^{active} and I_G^{stress} values are similar to the corresponding I_G, while in the loosest specimens there are significant differences amongst between I_G, I_G^{active} and I_G^{stress}, This observed density effect gradually decreases when F_{finer} $\geq$ 35%.

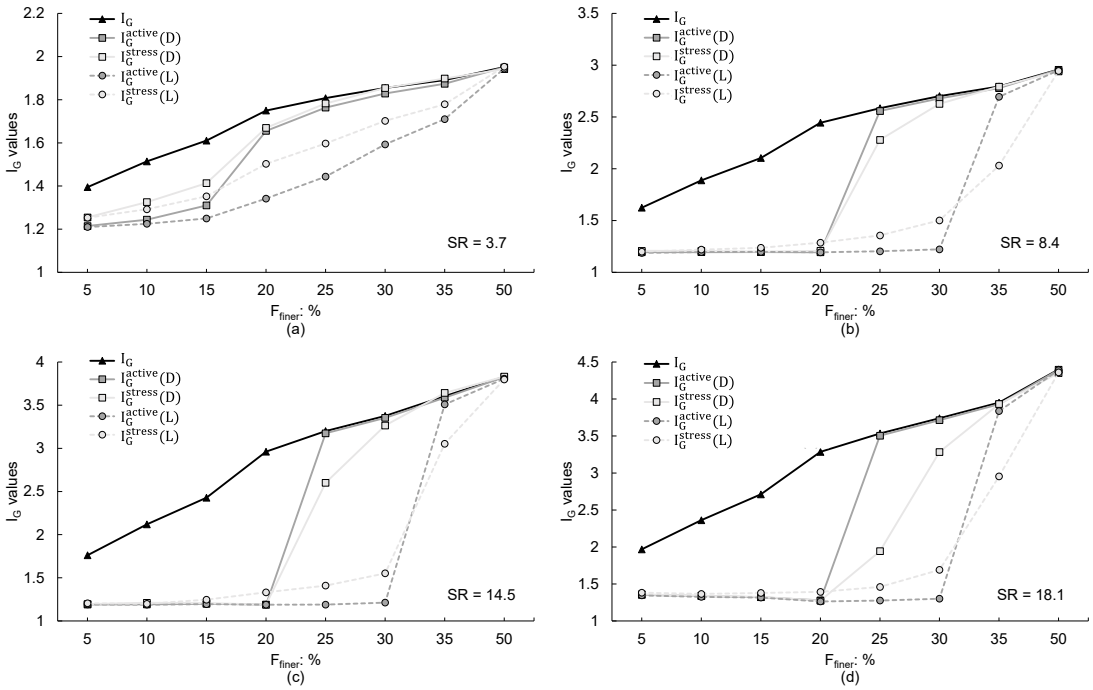


Figure 5.25: Comparison of I_G, I_G^{active} and I_G^{stress} data for bimodal gradations: (a) SR = 3.7; (b) SR = 8.4; (c) SR = 14.5; (d) SR = 18.1, "D" denotes the densest case, "L" denotes the loosest case.

5.5.3. Specimens with trimodal gradings

Density effect

Following the template used to discuss the bimodal specimens above. Figure 5.26 presents key data for two typical trimodal specimens (i.e. Tri 25_15; Tri 25_45). Figure 5.26(b) illustrates that the packing density measurably affects the $PSDs$ of the active particles. Similar to the bimodal specimens, the distribution of stress in the trimodal specimens can also be studied from the perspective of both the particle and the contacts. For the trimodal specimens, there are three particle types: (i) coarser fraction; (ii) intermediate fraction; (iii) finer fraction. As illustrated in Figure 5.26(b), for both specimens, the PSD^{active} for the loose specimen lies well below the dense PSD^{active}. This shows that a significant proportion of the finer particles can be inactive in the case of mixtures of more than two size fractions, supporting an extension of the discussion on gap-graded soil behaviour to soils with more complex mixtures of particle sizes.

For the trimodal specimens, six contact types exist: (i) coarser-coarser contacts ($C-C$ contacts), (ii) coarser-intermediate contacts ($C-I$ contacts), (iii) intermediate-intermediate contacts ($I-I$ contacts), (iv) intermediate-finer contacts ($I-F$ contacts), (v) coarser-finer contacts ($C-F$ contacts) and (vi) finer-finer contacts ($F-F$ contacts). As illustrated in Figure 5.26(d), the CSD^{stress} data provides additional evidence of a significant effect of packing density on the stress distribution amongst the different contact types and confirm the negligible role of the finer grains in the looser packing states.

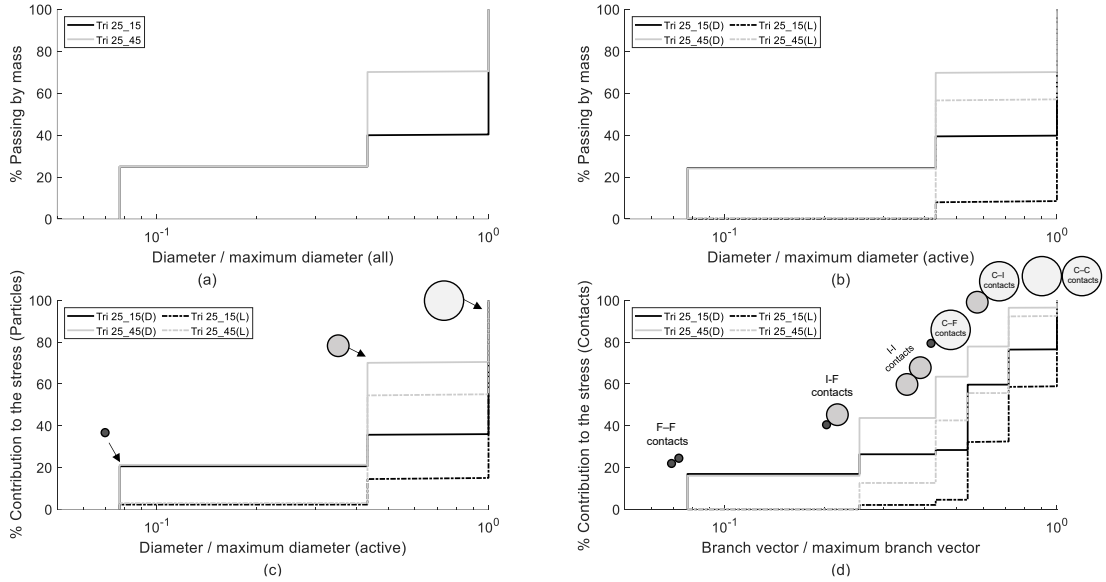


Figure 5.26: Representative results for trimodal specimens, the effect of density: (a) PSD plots considering all particles; (b) PSD plots considering active particles; (c) PSD^{stress} plots; (d) CSD^{stress} plots , "D" denotes the densest case, "L" denotes the loosest case.

Figure 5.27(a) and (b) illustrates the stress distribution from the perspective of the contacts for Tri 25_15 and Tri 25_45 using pie charts. These results illustrate that the stress transferred by $F-F$ contacts and $I-F$ contacts decreases when the packing density decreases. The $F-F$ contacts transfer negligible stress in the loose specimens. In contrast, the stress transferred by $C-C$ contacts, $C-I$ contacts increases when the density reduces. The finer grains have a relatively large contribution to the overall stress transmitted in the

dense specimens, which is similar to the trends identified for the bimodal specimens. This strong density effect is evident in Figure 5.27(c) and (d); for Tri 25_15, and Tri 25_45, the stress transferred by the coarse particles certainly decreases when packing density reduces from the dense to the loose case. However, there is a more significant reduction in the amount of stress transmitted by the intermediate particles as the packing density reduces. These data highlight the sensitivity of stress transmission in trimodal gap-graded specimens to the specimen packing density.

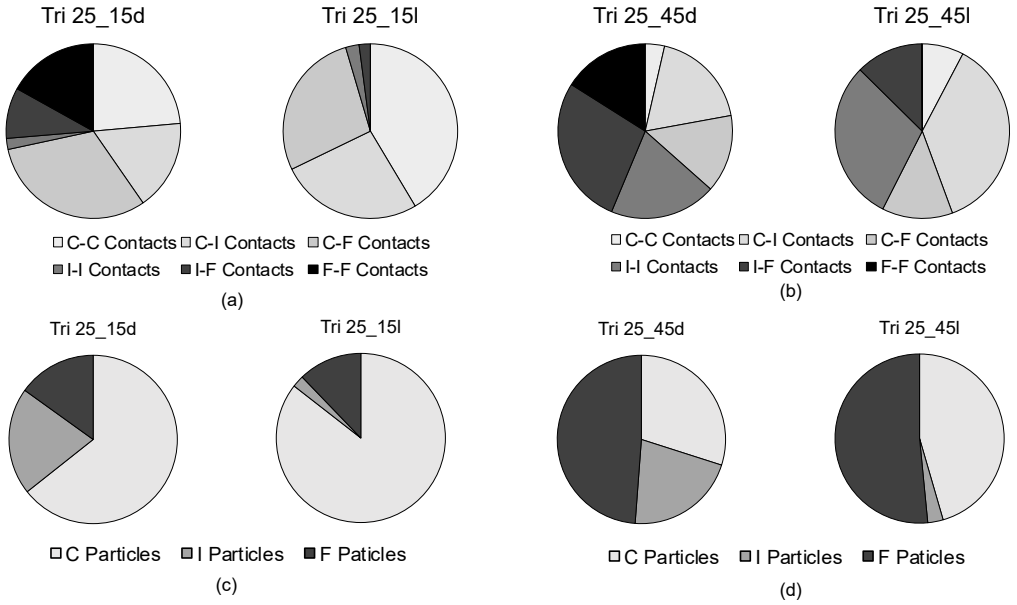


Figure 5.27: Representative pie chart results for trimodal specimens, the effect of density: (a) PSD plots considering all particles; (b) PSD plots considering active particles; (c) PSD^{stress} plots; (d) CSD^{stress} plots , "d" denotes the densest case, "l" denotes the loosest case.

The coordination number Z of Tri 25_45 changes from 5.88 (in the densest condition) to 0.089 (in the loosest condition), which reflects a significant change in the soil fabric. This trend is similar to that identified for the bimodal specimens. Considering the two-dimensional projections of the particles along with a thin slice through the centre of the sample for each of the two specimens presented in Figure 5.28. It can be seen that the soil fabric changes from a filled fabric (i.e. Figure 5.28(a)) to an underfilled fabric (i.e. Figure 5.28(b)) when the packing

density reduces from the densest to the loosest condition. In addition, both Figure 5.28(a) and Figure 5.28(b) also illustrate that the number of $F-F$ contacts, $C-F$ contacts and $I-F$ contacts significantly decreases when the packing density reduces from the densest to the loosest condition.

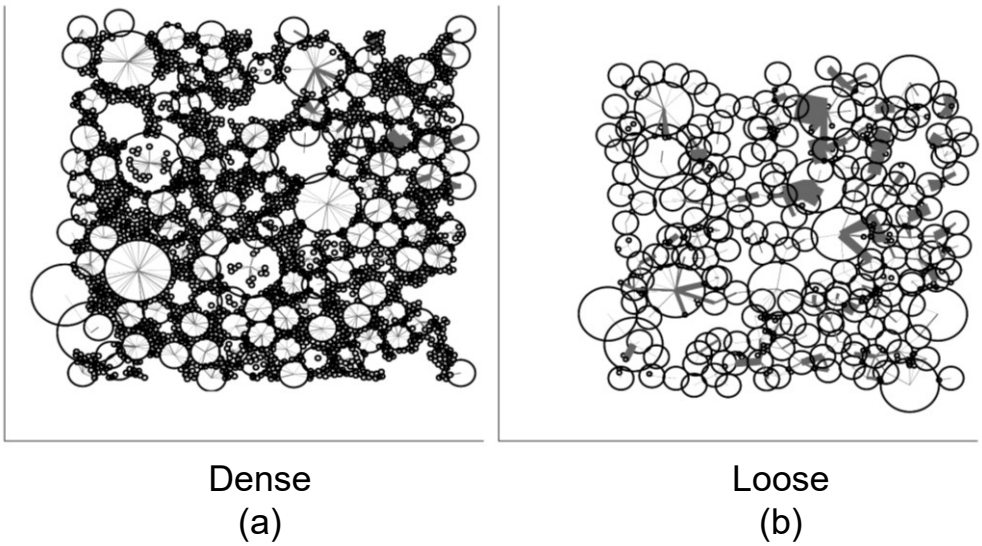


Figure 5.28: Comparison between the dense and loose conditions for Tri 25_45 in two-dimensional projections of contact force network: (a) Dense; (c) Loose

Figure 5.29 shows the I_G values for the trimodal gap-graded soils. Referring to Figure 5.29(a) for the specimens named Tri 10_X, where F_{finer} is 10%, in all cases the I_G^{active} and I_G^{stress} values are significantly lower than the I_G values, indicating a high proportion of inactive grains, irrespective of packing density. The data in Figure 5.29(b) and (c) show that when F_{finer} is 20% and 25%, the I_G^{active} and I_G^{stress} exhibit a similar pattern in their variation with the F_{int}, reflecting the presence of a finite proportion of inactive particles, whose actual value depends on the specimen density and the F_{int} value. Figure 5.29(c) shows that for F_{finer} = 30%, the proportion of inactive particles is not significant, irrespective of F_{int} and specimen density. Overall, the data on Figure 5.29 show that the concerns around the suitability of the using global void ratio, e, as a measure of state in the case of bimodal gap-graded mixtures

are also applicable to more complex mixtures with more than two size fractions. Multiple factors influence the distribution of stress amongst the different size fractions and identifying whether or not a material with a mixture of size fractions may have inactive finer particles is not straightforward.

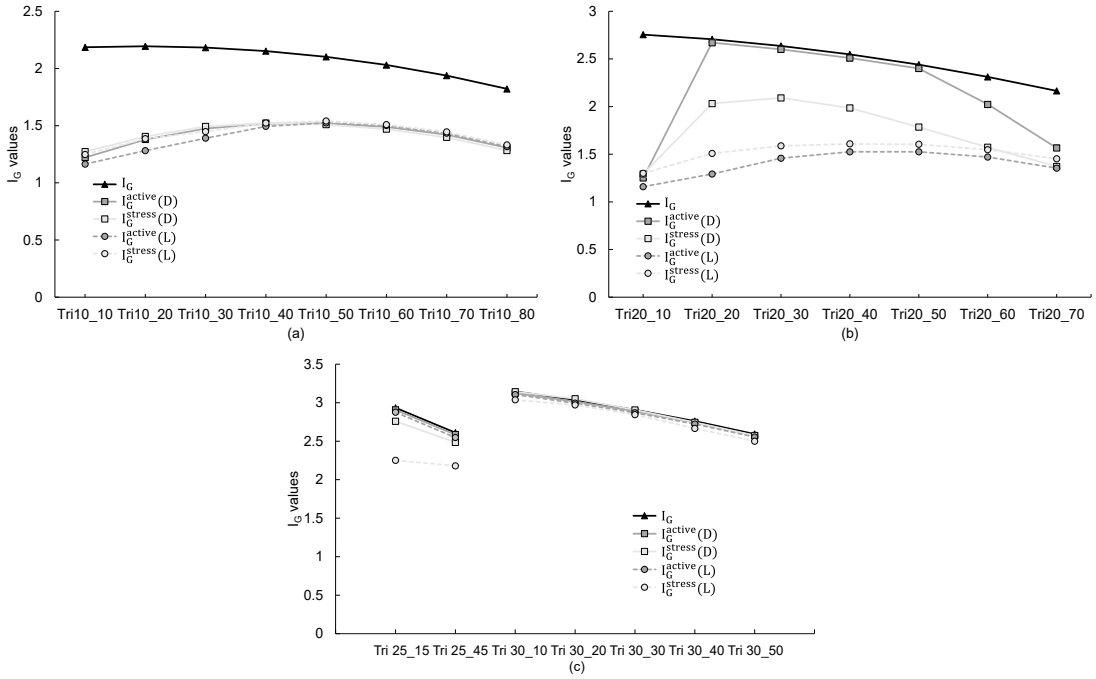


Figure 5.29: Comparison of I_G, I_G^{active} and I_G^{stress} data for trimodal specimens: (a) F_{finer} = 10%; (b) F_{finer} = 20%; (c) F_{finer} = 25%, 30%, "D" denotes the densest case, "L" denotes the loosest case.

5.6. Summary

This Chapter has presented a DEM investigation on the nature of stress transmission in granular materials. Specimens with a continuous grading as well as bimodal and trimodal gap graded specimens, comprising two and three size fractions respectively, were considered. The DEM simulations exploited high-performance computing capabilities to achieve representative element volumes and used periodic boundaries to ensure homogeneous specimens. The inherently ideal nature of the models created (spherical particles, isotropic stress state, isotropic fabric) enabled the influence of PSD to be isolated from

other factors that might influence stress transmission in granular materials. The following main points can be made based upon the data presented:

1. For specimens with a linear grading, there is a clear link between the particle size distribution and the distribution of stress amongst the different size fractions. The cumulative distribution obtained by considering particle stresses has a very similar shape to the particle size distribution. The agreement is observed using both C_u as well as the newer I_G measure that uses more information to quantify the distribution shape. The extent of the agreement reduces with increasing C_u and a finite difference can be observed for the largest C_u considered (i.e. C_u = 6).

2. For the bimodal gap-graded specimens, it is clear that the proportion of stress carried by the finer grains is significantly lower than the percentage by mass of finer grains in the specimen for all SR values considered for $F_{finer} < 50\%$. Use of the I_G metric enabled a comparison of the distribution of particle sizes with the distribution of stress and revealed a clear contrast between the bimodal and continuous gradings. The current results show that the relative contribution of finer grains in stress transmission is dependent upon SR, F_{finer} and density conditions. The data also indicate a fundamental difference between the nature of stress transmission in the specimens with the lowest SR considered (3.7) and the remaining three specimen types with SR = 8.4, 14.5 and 18.1. In the case of SR = 3.7, in contrast to the other SR values, the large size of the finer particles relative to the voids means that the finer particles are involved in stress transmission even at low F_{finer} values.

3. For the trimodal specimens, it is clear that for some combinations of F_{finer}, F_{int} and packing density, a measurable proportion of the finer particles are

inactive. This supports an extension of the recent discussions on the unsuitability of global void ratio as a measure of state in bimodal gap graded materials to include more complex mixtures. Identifying whether a trimodal material might have inactive grains is not straightforward. The use of I_G also enabled a comparison between PSD and PSD^{stress}, showing that, for the gradations considered here, the likelihood of the finer fraction being inactive is greatest in the specimens with $F_{finer} \leq 20\%$. For $F_{finer} = 25\%$, the extent to which the finer particles are inactive is density dependent; for $F_{finer} = 30\%$, there is no evidence of large volumes of inactive finer particles. However, the 26 specimens considered here represent only a very small subset of the possible size combinations and it is not possible with these limited data to draw general conclusions as to when finer particles are likely to be inactive in soils comprising mixtures of distinct size fractions.

4. For the bimodal gap-graded specimens, the stress distribution can be partitioned into three different contact types ($C-C$, $C-F$, $F-F$). A basic network analysis enabled assessment as to whether the force network formed by each of these size fractions was sufficient to transmit stress across the entire specimen.

Chapter 6. Examining the small-strain stiffness of gap-graded soils

6.1. Introduction

The key characteristics of the small-strain behaviour of gap-graded soils have been provided in Chapter 2. Therefore, only a brief review is provided in this Chapter. The small-strain stiffness, G_0, is a significant parameter for geotechnical engineering design, as it can predict deformation and it is used in site response analysis. The following empirical expression (originally proposed by Hardin & Richart 1963) was developed from studies of clean, natural quartz sands:

$$G_0 = AF(e)(p')^n \quad 6.1$$

where $F(e)$ is a function of e, and A and n are fitting empirical parameters. For smooth elastic spheres, n can be taken to be 0.33 following Hertzian theory (Otsubo & O'Sullivan, 2018); the larger n values observed in experiments on sands may be attributed to finite surface roughness and non-spherical particle geometry (Goddard, 1990; Otsubo & O'Sullivan, 2018). Referring to Mitchell & Soga (2005), a number of expressions for $F(e)$ have been proposed in the literature. For both uniform and well-graded sands, experimental data support the use of the functional form proposed by Hardin & Richart (1963):

$$\mathrm{F(e)} = \frac{(\mathrm{c} - \mathrm{e})^2}{1 + \mathrm{e}} \quad 6.2$$

Based upon their experimental data, Hardin & Richart (1963) suggested $c = 2.97$ for angular sands and $c = 2.17$ for rounded sands. In Equation 2.11, e is taken as a measure of the material state. A number of researchers have highlighted a link between the PSD and the parameters adopted in Equations

6.1 and 2.11. For example, Payan et al. (2016), Menq (2003), Wichtmann & Triantafyllidis (2009) and Senetakis et al. (2012) have all proposed relationships between A and C_u, the coefficient of uniformity.

As discussed in Chapter 2, it has long been accepted that in gap-graded soils, finer particles may exist in the void space formed by the coarse fraction without transferring stress. Prior research on the mechanical behaviour of soil mixtures comprising coarse and finer fractions with distinct sizes have demonstrated the inadequacy of e as a descriptor of state when G_0 is considered. A number of studies have found that if a relatively small proportion of non-plastic grains (finer grains) are added to clean sand, the G_0 value is affected (e.g. Carraro et al., 2009; Wichtmann et al., 2015; Yang & Liu, 2016). Recent experimental research has highlighted the challenges of directly applying Equations 6.1 and 2.11 to gap-graded soils. Wichtmann et al. (2015) proposed correlations amongst c, n, A and F_{finer}. Yang & Liu (2016) highlighted the limitations of using Equation 6.1 with gap-graded materials and proposed a relationship between A and F_{finer}, i.e. $A = 95.39e^{-F_{finer}}$. Payan et al. (2017) also observed a systematic variation in A with F_{finer} (noting that they use a different functional form for $F(e)$). Liu & Yang (2018) indicated that curve fitting should be used to find A for a given F_{finer}, and that the value of A depends on the difference in size between the coarser and finer particles.

Recognising the challenges of considering the response of gap-graded soils within established frameworks of soil behaviour, as already presented in Chapter 2, several variables have been proposed to describe the state of gap-graded soils. These include e_g (Mitchell, 1976), e^* (Thevanayagam, 2000), e_m (Otsubo, 2016), ψ (Yang & Liu, 2016) and e_G (Sufian et al., 2021). In general, these prior studies illustrates that particles may not be active in stress

transmission.

A number of theoretical approaches have been applied to derive expressions for G_0. As illustrated in Chapter 2, Chang & Liao (1994) proposed an Effective Medium Theory (EMT), which developed a relationship between G_0 and both the granular material properties and the stress level by assuming a uniform strain field (kinematic assumption). Also adopting the kinematic assumption proposed by Chang & Liao (1994), Otsubo (2016) proposed that the stiffness of a granular material is strongly associated with $Z/(1+e)$ so that:

$$G_{0,HM}^{EMT} = \frac{(5-4v_p)}{5(2-v_p)}\left[\frac{\sqrt{3}}{\sqrt{2}\pi(1-v_p)}\right]^{2/3} G_p^{2/3}\sigma'^{1/3}\left[\frac{Z}{(1+e)}\right]^{2/3} \quad 6.3$$

where v_p and G_p are the particle Poisson's ratio and particle shear modulus, respectively. The coordination number, Z, is the average number of contacts per particle. Otsubo et al. (2021) found that for bimodal soil mixtures, the shear wave velocity, V_s correlates more strongly with the ratio $Z_m/(1+e_m)$ rather than $Z/(1+e)$. As noted in Chapter 2, Z_m, the mechanical coordination number, is the average number of contacts for particles with more than one contact and e_m is the void ratio calculated by assuming the inactive particles form part of the void space. Equation 6.3 is based upon a mean response of the material and does not consider the details of the distribution of force amongst the different contacts. Following Hertzian contact mechanics, the stiffness of individual contacts is determined by the contact force and the radii of the contacting particles. In Equations 6.3, for gap-graded soils, both active coarse and finer particles are considered equivalent in the calculation of Z_m and e_m. However, recent studies (e.g. Sufian et al., 2021) and the analysis presented in Chapter 5 have shown that active coarse and finer particles do not make equivalent contributions to the overall stress transmission.

In practice, as illustrated in Chapter 2, the G_0 of granular materials is often quantified through dynamic wave propagation tests including bender element tests or resonant column tests (e.g. Hardin, 1965; Shirley, 1978). For a homogeneous elastic continuum, G_0 is estimated as follows:

$$G_0 = \rho(V_s)^2 \qquad 6.4$$

where the V_s is the shear wave velocity, and ρ is the bulk density of the solid. As illustrated in Chapter 4, there can be a measurable difference between the bulk density ρ of a gap-graded specimen and the mechanical bulk density calculated considering only the active particles, ρ_m. As pointed out above, it is widely accepted that the finer fraction and coarse fraction provide different contributions to the overall stress transmitted. Consequently, it is reasonable to question the applicability of Equation 6.4 to gap-graded soils.

Prior research has generated contrasting views on what is the appropriate state variable to consider in the case of gap-graded soils. Furthermore, the fundamental mechanisms that underlie the link between the PSD shape and the stiffness properties remain uncertain. This Chapter firstly aims to (1) study the ability of different state variables to capture the variation in stiffness amongst granular materials with different gradings, stress levels and packing density; (2) study the contribution of the different size fractions within the material to the overall stiffness.

The second section of this Chapter explores the implications of the observations in the DEM simulations for the interpretation of laboratory test data. As discussed in Chapter 2, although the DEM method is capable of identifying inactive particles directly, it is not possible to identify inactive

particles in conventional laboratory experiments. However, it may be possible to use the results from DEM simulations to develop indirect approaches to quantify the proportion of inactive particles in experimental studies. The results presented in Chapter 4 underpin an idea that is explored in this Chapter. The data from Chapter 4 show that the bulk density calculated considering all particles, ρ, may differ significantly from the bulk density calculated considering only the active particles, ρ_m. This difference could potentially influence the G_{dyn} values, since $G_{dyn} = \rho(V_s)^2$. In contrast, we do not explicitly consider the density when using a static approach to determine G_0, i.e. the value of G_{sta} does not rely on selecting an appropriate bulk density. It is also reasonable to assume that G_{sta} value is similar to its G_{dyn} value if all particles are equivalent in stress transmission.

The hypothesis explored in this Chapter is that the comparison of G_{sta} and G_{dyn} estimated by e, denoted here $G_{dyn}(e)$, enables assessment of the differences between e and e_m and between ρ and ρ_m. Consequently, we may be able to use the differences between G_{sta} and $G_{dyn}(e)$ to infer or indirectly quantify, the proportion of inactive particles in the tested specimen. This hypothesis is firstly developed using DEM with idealized isotropic specimens with mixed boundaries comprising spherical particles and using planar shear waves in the wave propagation simulations. Then the practical application of the concept is tested in a programme of laboratory experiments in a triaxial cell, which is detailed in Chapter 7.

6.2. Overview of DEM approach

An overview of DEM approach adopted in this research has been provided in Chapter 3, therefore, only a brief introduction to the setup of the DEM

simulations considered in this Chapter is presented in this Section. In general, the DEM simulations employed in this Chapter are divided into two categories based on the boundary conditions adopted: (1) periodic boundaries; (2) mixed boundaries. Therefore each of these two cases is presented separately.

6.2.1.Specimens with periodic boundaries only

For the specimens which only had periodic boundaries, the DEM simulations were conducted on cubic specimens using a modified version of the open-source molecular dynamics code Granular $LAMMPS$ (Plimpton, 1995). No gravitational body force was applied. As outlined in Chapter 3, a simplified Hertz-Mindlin contact model was used with a particle shear modulus of G_p = 29.17 GPa and a particle Poisson's ratio of v_p = 0.2. These parameters are similar to the experimental values for quartz sands.

The grains were initially placed randomly in diffuse (non-contacting) positions through an in-house placement code and then subjected to periodic isotropic compression to desired mean effective stress following Cundall (1988). In this chapter, to capture key characteristics of the state-dependent behaviour of granular materials, three mean effective stresses (i.e. 100 kPa, 500 kPa, 1000 kPa) were applied. For each simulation presented here, it was confirmed that the coordination number, Z (the average number of contacts per grain), remained stable (i.e. any variation was less than 0.001) for approximately 500,000 simulation cycles before terminating the compression stage.

As illustrated in Chapter 3, three inter-particle friction coefficients (μ) were used during isotropic compression: (1) "dense" specimens were generated using μ = 0.001; (2) "medium-dense" specimens were generated using μ = 0.1; (3) "loose" specimens were generated using μ = 0.3. Once the desired

mean effective mean stress was obtained, a μ of 0.3 was used for additional equilibration cycles, followed by constant σ_3' triaxial shearing simulations. To ensure a fully elastic response, i.e. with no interparticle sliding during these small-amplitude stress probes, the coefficient of friction, μ, was increased to 0.33. The desired axial strain is approximately 5×10^{-6}, which is considered appropriate to study the small-strain behaviour of granular materials (e.g. Kuwano & Jardine, 2002).

6.2.2. Specimens with mixed rigid and periodic boundaries

For the second set of simulations, the same version of $LAMMPS$ was used with the same simplified Hertz-Mindlin contact model and same particle parameters (e.g. G_p = 29.17; υ_p = 0.2). To enable both G_{dyn} and G_{sta} to be obtained on identical specimens, in this case, the numerical specimens considered had a cuboidal shape. The lateral boundaries, i.e. the vertical boundaries in the $x-$ and $y-$ directions were periodic. Horizontal, rigid boundary boundaries were used at the top and bottom of the specimens to enable shear wave velocity measurements. The specimen length in the z direction, Z_{dim} was approximately 9 times the length in the x direction, X_{dim}. This ratio between Z_{dim} and X_{dim} has proven to be effective in shear wave propagation simulations (Otsubo, 2016). The in-house placement code mentioned above was used to create all the mixed boundary specimens. The same three inter-particle friction coefficients, μ (i.e. 0.001; 0.1; 0.3) were used to prepare the "dense", "medium-dense" and "loose" specimens. After the compression stage, either small strain shearing simulations or shear wave propagation simulations were conducted to obtain G_{sta} and G_{dyn}, respectively on identical specimens.

6.3. $PSDs$ considered

6.3.1. Cubic specimen with periodic boundaries only

Figure 6.1 summarizes the gradings considered here. To investigate the effect of PSD on the stiffness of granular materials, a broad range of gradings were considered in this Chapter. Five linear $PSDs$ with C_u increasing from 1.5 to 4.8 are presented in Figure 6.1(a), The minimum particle diameter used in each linear specimen was 0.076 mm,while the maximum particle diameter increased with increasing C_u.

The bimodal gap-graded specimens presented in Chapter 5 were used for the small amplitude in drained shearing tests. For the bimodal gap-graded specimens, four distinct SRs (i.e. $D_{c,50}/d_{f,50}$) values were considered: 3.7, 8.4, 14.5 and 18.1; $D_{c,50}$ and $d_{f,50}$ are the median diameters of the coarse and finer fractions, respectively. A range of F_{finer} values were considered (i.e. F_{finer} = 5%, 10%, 15%, 20%, 25%, 30%, 35%, 50%). While the same specimens were provided in Chapter 5, for completeness, the $PSDs$ of the bimodal gap-graded soils are shown in Figure 6.1(b).

The trimodal specimens are also gap-graded materials, these specimens have the F_{finer}, the $F_{coarser}$ and an additional F_{int} (Figure 6.1(c)). All the trimodal specimens had the same minimum diameter of 0.076 mm, an intermediate grain diameter of 0.425 mm and a coarser particle diameter of 0.985 mm. These gradations are the same as those used in Chapters 4 and 5 for trimodal specimens, again, for completeness, the $PSDs$ of the trimodal gap-graded soils are shown in Figure 6.1(c).

For the linear specimens, the number of particles ranges from 33,306 to 147,316 with increasing C_u. For the bimodal-graded soils, the number of

particles ranges from 16,715 to 481,611 depending on the $PSDs$. For the trimodal specimens, the number of particles ranges from 83,069 to 636,871.

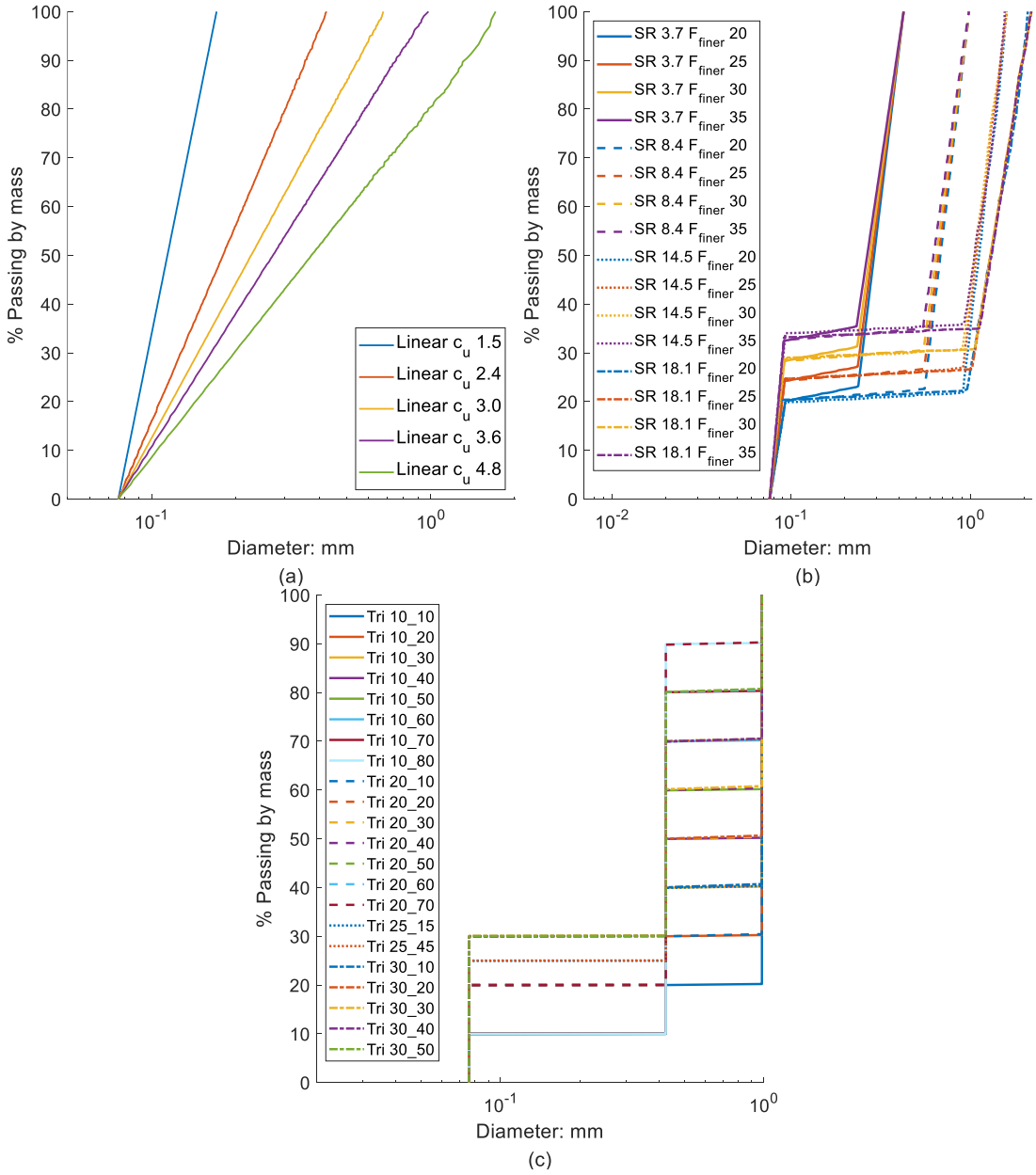


Figure 6.1: Particle size distributions (periodic boundaries): (a) Linear specimens; (b) Bimodal gap-graded specimens; (c) Trimodal gap-graded specimens

6.3.2. Cuboidal specimen with mixed boundaries

The particle size distributions considered in the DEM specimens with mixed rigid-periodic boundaries are presented in Figure 6.2. As illustrated in Figure 6.2(a), these included several “linear” specimens with coefficients of uniformity (C_u) between 1.2 and 4.8. As illustrated in Figure 6.2(b), two sets of gap-graded

materials with SRs (i.e. $D_{c,50}/D_{f,50}$) of 8 and 14 were considered, as before, $D_{c,50}$ and $D_{f,50}$ are the median particle diameters of the coarser and finer fractions, respectively. The F_{finer} values varied between 5% and 50%. In all cases, the minimum particle diameter was 0.38 mm. The minimum particle size used in the cubic and cuboidal specimens differed. Iniitally the value of 0.076 mm was selected to represent a finer sand. However, the larger size of the cuboidal samples had implications for computational cost. Increasing the minimum particle diameter increased the inertia of the smallest particle, thereby increasing the critical time step for numerical stability. In all cases, the simulations neglected surface interaction forces and so it is the relative particle sizes, rather than the absolute sizes that determine the material response. While the maximum particle diameter increased with increasing SR. Note that the number of particles in each specimen varies depending on the PSD, to ensure that the generated specimens were representative. For the linear specimens, the number of particles increased from 13,380 to 147,779 as C_u increased. For the bimodal gap-graded specimens, the number of particles ranged from 20,622 to 1,002,541.

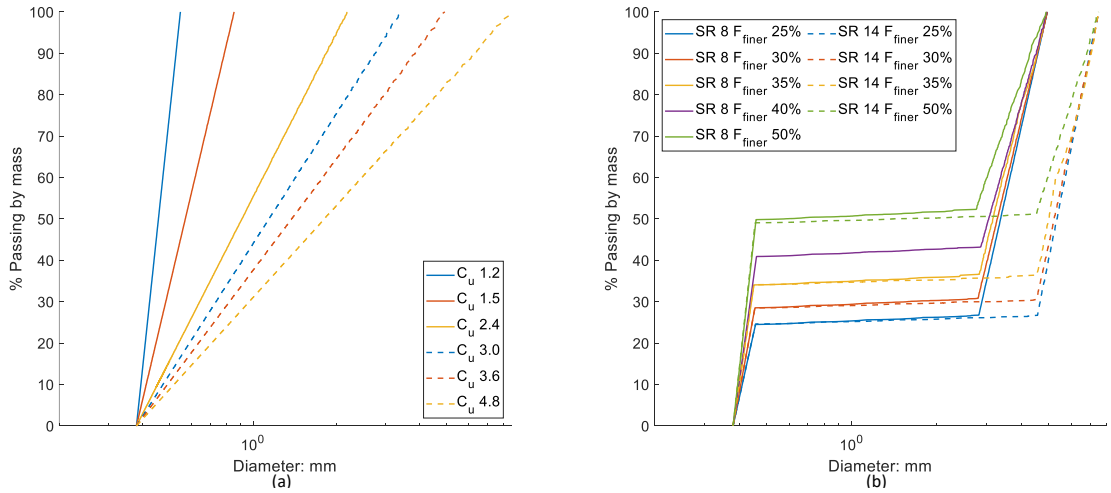


Figure 6.2: Particle size distributions (mixed boundaries): (a) Linear specimens; (b) Bimodal gap-graded specimens

6.4. Analysis approaches adopted

6.4.1. Stress analysis approaches

Following the analyses presented in Chapter 5, approaches to analysing the stress within specimens simulated were used in this Chapter. A brief overview is given here.

The particle-based perspective of stress heterogeneity

The overall stress tensor can be calculated from the stress tensors for the individual particles as:

$$\sigma'_{ij} = \frac{1}{V}\sum_{a=1}^{N_t}\left(\bar{\sigma}_{ij}^{a}V^{a}\right) \quad 6.5$$

where σ'_{ij} is the effective overall stress tensor for the specimen, N_t is the total number of stress-transmitting particles, $\bar{\sigma}_{ij}^{a}$ is the average stress tensor within particle a and V^a is the volume of particle a. The contribution of the individual particle, a, to the overall stress is then given by:

$$\alpha^a = \frac{\bar{\sigma}_{ij}^{a}\,V^a}{V} \quad 6.6$$

The contact-based perspective of stress heterogeneity

The contact force data extracted at the end of the isotropic compression were used to calculate the stresses in the virtual specimen so that the $3D$ stress tensor is given by:

$$\sigma'_{ij} = \frac{1}{V}\sum_{C=1}^{N_{c,V}} f_i^c l_j^c \quad 6.7$$

where $N_{c,V}$ is the total number of contacts in volume V, f_i^c is the force vector for contact c and l_j^c is the branch vector. In this case, the branch vector is the vector joining the centroids of the particles which contact at c. The contribution of contact c to the overall stress is

$$\frac{f_i^c l_j^c}{V} \quad 6.8$$

In each case, the mean effective stress is calculated from the trace of the stress tensor, i.e. $p' = \sigma'_{ii}/3$.

6.4.2. Static method to determine shear stiffness

The static shear stiffness is measured using simulations of drained triaxial shearing tests keeping the material behaviour within the elastic regime (i.e. shear strain $\gamma \leq 10^{-5}$). The notation G_{sta} is used to denote measures of elastic shear stiffness obtained from static probes. The shear stiffness, G_{sta}, is calculated following the equation:

$$G_{sta} = \frac{\delta q}{3\delta\varepsilon_q^e} \tag{6.9}$$

where $\delta\varepsilon_q^e$ is the increment of elastic deviatoric strain, δq is the increment of deviatoric stress. The deviatoric strain, $\delta\varepsilon_q^e$ is calculated as:

$$\delta\varepsilon_q^e = \frac{2}{3}\left[\delta\varepsilon_z^e - 0.5\left(\delta\varepsilon_x^e + \delta\varepsilon_y^e\right)\right] \tag{6.10}$$

Where $\delta\varepsilon_z^e$ is the normal strain in the z direction, in other words, the axial strain of the specimens. $\delta\varepsilon_x^e$, and $\delta\varepsilon_y^e$ are the normal strains in the x and y directions, respectively. Kuwano & Jardine (2002) used this approach experimentally to investigate the anisotropy of G_0 and found that an effectively linear behaviour can be identified at very small strains (approximately 10^{-5}).

6.4.3. Dynamic method to determine shear stiffness

For the dynamic method, a signal is applied to one of the rigid boundaries (i.e. the transmitter element) which causes it to displace (i.e. translate) a small amplitude stress wave propagates through the specimen. While there has been a lot of discussion about the interpretation of bender element test data, the simple peak-peak method is generally accepted. Where the peak-peak method is adopted, the time between the maximum in the inserted signal and the maximum in the received signal is taken to be the time for the wave to travel from the transmitter element to the receiver element. Although prior studies (e.g.

O'Donovan, 2013) observed an effect of input signal frequencies on the results and different results can be acquired when using different methods, Otsubo (2016) showed that consistent results can be obtained for both time and frequency domain approaches to data interpretation when a high-quality input sinusoidal pulse is applied for the shear wave propagation stage. The planar shear waves considered in the current study can be considered to be high quality in the context of Otsubo's work (Otsubo, 2016). However, in the interests of being complete, two different methods were applied to analyse the response recorded at the receiver wall and estimate the shear wave velocity, these are summarized here.

(1) Time domain

For the time domain analysis, as discussed previously in Chapter 2, the peak-peak method is one of the most widely used methods to estimate the shear wave velocity. This method was also used in this study, the variations in stresses at both the bottom and top walls were recorded. The local maxima in the incremental shear stresses recorded at these two walls were recorded, the time difference between these two peak points is defined as the propagation time. Based on the $z-$ dimension, i.e. the length of the specimen in the $z-$ direction, the shear wave velocity V_s can be easily determined.

(2) Frequency domain

A Fast Fourier Transform can be used to analyse the stress response of both the bottom and the top walls. The "fft" function available in $MTALAB$ (MathWorks, 2019) was used to get the frequency domain responses of the signals recorded at the transmitter and the receiver walls. The phase shift between these two signals can be used to capture the relationship between the frequency and the stacked phase (Viggiani & Atkinson, 1995; Alvarado & Coop,

2012; Greening & Nash, 2004). The "$phase$" and "$unwrap$" functions in MATLAB (MathWorks, 2019) were used to obtain the phase shift. Then the phase and group velocities and their corresponding V_s can be established from this phase-frequency relationship:

$$v_{phase} = 2\pi L \frac{f}{\varphi} \quad 6.11$$

$$v_{graph} = 2\pi L \frac{df}{d\varphi} \quad 6.12$$

For each specimen, the optimal frequency was identified in a parametric study. The frequencies of the inserted waves considered here ranged from 3 kHz to 20 kHz. G_{dyn} can be estimated by either ρ and ρ_m; as ρ_m<ρ, $G_{dyn}(e)$ is consistently larger than $G_{dyn}(e_m)$.

6.4.4. An example analysis of simulation data to obtain G_{sta} and G_{dyn}

To illustrate how the static and dynamic test simulation data were processed, a representative specimen (In this case a dense sample with SR = 8.0 and $F_{finer} = 50\%$ subject to a σ_3' of 500 kPa) is considered here in Figure 6.3. Figure 6.3(a&b) illustrates the estimation of G_{sta}. The linear stress-strain behaviour on Figure 6.3(a) indicates an elastic behaviour, so that G_{sta} can be calculated from Equation 6.9. The tangent stiffness data in Figure 6.3(b) confirm that the stiffness does not vary with strain during this probe. Figure 6.3(c) illustrates the estimation of V_s in the time domain, note that there is no attenuation of the signal in DEM. The lack of any evidence of a near field effect means that the peak-peak method can easily be applied to estimate the travel time of the shear wave through the sample. Figure 6.3(d) then illustrates the phase velocity, group velocity and also its corresponding V_s in the frequency domain. Consistent V_s values (i.e. approximately 513 m/s) are observed considering both the time and frequency domain data, which suggests that a

good quality signal has been attained in this simulation.

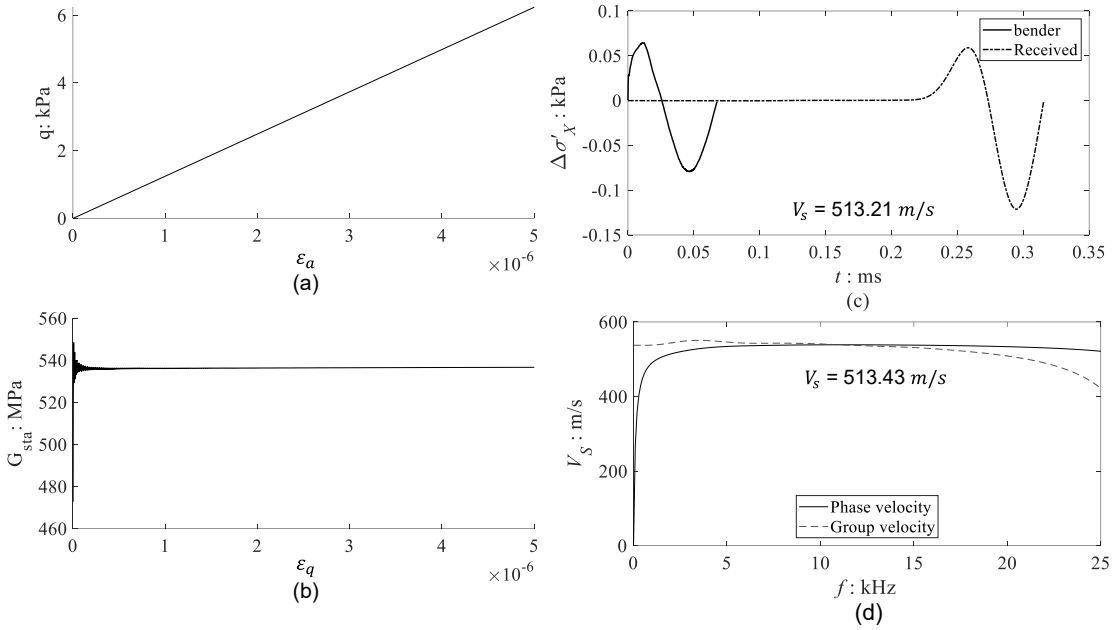


Figure 6.3: The quantification of G_{sta} and G_{dyn} in DEM: (a) $q-\varepsilon_a$ relationship; (b) $G_{sta}-\varepsilon_q$ relationship; (c) V_s in time domain; (d) V_s in frequency domain

6.4.5. Distribution of contact stiffnesses

A discussion on contact stiffness has already been presented in Chapter 3, therefore only a brief review is presented in this Section for the reader's convenience. For the relatively simple smooth frictional spheres with uniform elastic properties that are considered here, the contact stiffness depends upon the force transmitted and the radii of the two transmitting particles (Hertz, 1882; Johnson, 1985). A Hertzian contact model is used here and so the tangent (incremental) normal stiffness depends on the diameters of the contacting particles and the contact force, as follows:

$$k_N = \frac{dF_n}{d\delta} = 2E_p^* R^{*0.5}\delta^{0.5} = 2E_P^* A_c \qquad 6.13$$

The equivalent Young's modulus of two contacting particles, E_p^* can be illustrated:

$$E_p^* = \left(\frac{1 - v_{p1}^2}{E_{p1}} + \frac{1 - v_{p2}^2}{E_{p2}} \right)^{-1} \quad 6.14$$

where E_{p1} and E_{p2} are Young's modulus of contacting particles, and v_{p1} and v_{p2} are the Poisson's ratios of the contacting particles. The circular contact area (A_c) is $\sqrt{R^* \delta}$. The R^* is calculated $R^* = (1/R_1 + 1/R_2)^{-1}$.

The tangent or shear contact stiffness is:

$$k_T = 8 G_p^* A_c \quad 6.15$$

Where the equivalent shear modulus of two contacting particles is calculated as:

$$G_p^* = \left(\frac{2 - v_{p1}}{G_{p1}} + \frac{2 - v_{p2}}{G_{p2}} \right)^{-1} \quad 6.16$$

6.4.6. Stiffness matrix method

While Chapter 5 has presented the distribution of stress amongst the different contacts, these results cannot be directly related to the contribution of these contacts for the overall shear stiffness. The contacts in a physical granular material form a relatively complex network and the properties of the network edges depend upon the contact orientations, the effective radii, and the transmitted contact forces. To further advance our understanding, a stiffness-matrix based approach was developed and used in this Chapter. This new approach considers the contribution of each contact to the global stress field when a uniform strain field is assumed to describe the motion of all the particles. In this approach, following the procedure outlined in Itasca Consulting Group (2007), a local stiffness matrix k^{ab} is defined for the contact between particles a and b. For clarity, a representative 12 $\times$ 12 element stiffness matrix in the case where the contact normal is orientated along the $x-$ axis is given here as:

$$k^{ab,nx} = \begin{bmatrix} K_N & & & & & & & & & & & \\ 0 & K_T & & & & & & & & & & \\ 0 & 0 & K_T & & & & & & & & & \\ 0 & 0 & 0 & 0 & & symmetry & & & & & & \\ 0 & 0 & -R^*K_T & 0 & R^{*2}K_T & & & & & & & \\ 0 & R^*K_T & 0 & 0 & 0 & R^{*2}K_T & & & & & & \\ -K_N & 0 & 0 & 0 & 0 & 0 & K_N & & & & & \\ 0 & -K_T & 0 & 0 & 0 & -R^*K_T & 0 & K_T & & & & \\ 0 & 0 & -K_T & 0 & R^*K_T & 0 & 0 & 0 & K_T & & & \\ 0 & 0 & 0 & 0 & 0 & 0 & 0 & 0 & 0 & 0 & & \\ 0 & 0 & R^*K_T & 0 & R^{*2}K_T & 0 & 0 & 0 & R^*K_T & 0 & R^{*2}K_T & \\ 0 & R^*K_T & 0 & 0 & 0 & R^{*2}K_T & 0 & -R^*K_T & 0 & 0 & 0 & R^{*2}K_T \end{bmatrix} \quad 6.17$$

The increment in the contact force vector induced by an increment in the displacement of the two grains is given by:

$$\boldsymbol{\Delta f}^{ab} = k^{ab}\boldsymbol{\Delta x}^{ab} \quad 6.18$$

Where the incremental displacements of the two contacting particles are given by $\boldsymbol{\Delta x}^{ab} = [\Delta x_1^a \quad \Delta x_2^a \quad \Delta x_3^a \quad \Delta\theta_1^a \quad \Delta\theta_2^a \quad \Delta\theta_3^a \; \Delta x_1^b \quad \Delta x_2^b \quad \Delta x_3^b \quad \Delta\theta_1^b \quad \Delta\theta_2^b \quad \Delta\theta_3^b]$, and the vector $\boldsymbol{f}^{ab}$ gives both the forces and moments acting on particles a and b arising from this interaction, and hence the contact force.

Referring to Thornton (2000), in a periodic cell, if the strain rate tensor applied to the periodic cell is given by $\dot{\varepsilon}_{ij}$, then in a timestep Δt the incremental displacement of particle a due to the global strain field, Δx_i^a is $\Delta x_i^a = \dot{\varepsilon}_{ij} x_i^a \Delta t$, where x_i^a is the vector describing the location of particle a. In a similar manner, if an increment of strain $\Delta\varepsilon_{ij}$ is applied to the system, the incremental displacement is given by:

$$\Delta x_i^a = \Delta\varepsilon_{ij} x_i^a \quad 6.19$$

For simplicity, suppose that deformation is small and assuming that $\Delta l_j \approx 0$ (i.e. there is no change to the branch vector edges), $\Delta V \approx 0$ (i.e. the overall volume does not change), and there are no newly generated contacts. If each contact experiences an incremental force, Δf_i^c, then the resulting overall increment in stress is given by:

$$\Delta\sigma_{ij} = \frac{1}{V}\sum_{c=1}^{N_c} \Delta f_i^c \, l_j^c \qquad 6.20$$

The output from a DEM simulation can be used to determine stiffness matrices for each contact. The particle displacements due to the global strain field can be determined by applying an increment of strain $\Delta\varepsilon_{ij}$ and the increment in force for each contact can then be determined using Equation 6.18 before applying Equation 6.21 to determine the increment in stress and hence elements of the stiffness matrix. In engineering or Voigt notation the elasticity tensor C_{ij} is given by:

$$\begin{bmatrix}\Delta\sigma_{11}\\ \Delta\sigma_{22}\\ \Delta\sigma_{33}\\ \Delta\sigma_{23}\\ \Delta\sigma_{31}\\ \Delta\sigma_{12}\end{bmatrix} = \begin{bmatrix} C_{11} & C_{12} & C_{13} & C_{14} & C_{15} & C_{16} \\ & C_{22} & C_{23} & C_{24} & C_{25} & C_{26} \\ & & C_{33} & C_{34} & C_{35} & C_{36} \\ & & & C_{44} & C_{45} & C_{46} \\ & & & & C_{55} & C_{56} \\ & & & & & C_{66} \end{bmatrix} \begin{bmatrix}\Delta\varepsilon_{11}\\ \Delta\varepsilon_{22}\\ \Delta\varepsilon_{33}\\ 2\Delta\varepsilon_{23}\\ 2\Delta\varepsilon_{13}\\ 2\Delta\varepsilon_{12}\end{bmatrix} \qquad 6.21$$

This is a symmetric tensor and only the upper right-hand side of the tensor is given here. Note that $\sigma_{11} = \sigma_{xx}$, $\sigma_{22} = \sigma_{yy}$, $\sigma_{33} = \sigma_{zz}$, $\sigma_{23} = \sigma_{yz}$, $\sigma_{31} = \sigma_{xz}$, $\sigma_{12} = \sigma_{xy}$. $\varepsilon_{11} = \varepsilon_{xx}$, $\varepsilon_{22} = \varepsilon_{yy}$, $\varepsilon_{33} = \varepsilon_{zz}$, $\gamma_{23} = 2\varepsilon_{23} = 2\varepsilon_{yz}$, $\gamma_{13} = 2\varepsilon_{13} = 2\varepsilon_{xz}$, $\gamma_{12} = 2\varepsilon_{12} = 2\varepsilon_{xy}$. The stiffness matrix is normally used when all of the strains are known and the values of the stresses are to be determined.

Based on the uniform strain approach assumption, the relative contributions of the different contact types to the stiffness can be estimated. Firstly, the overall stiffness C_{ij}^{all} is estimated, then the contribution of each of the networks is given by: CC contribution: $\frac{C_{\mathrm{ij}}^{CC}}{C_{\mathrm{ij}}^{all}}$; CF contribution: $\frac{C_{\mathrm{ij}}^{CF}}{C_{\mathrm{ij}}^{all}}$; FF contribution: $\frac{C_{\mathrm{ij}}^{FF}}{C_{\mathrm{ij}}^{all}}$;
Based upon the Love-Weber formula:

$$\sigma_{ij}^{all} = \frac{1}{V}\sum_{c=1}^{N_c} f_i l_j = \frac{1}{V}\left(\sum_{c^{CC}=1}^{N_c^{CC}} f_i l_j + \sum_{c^{CF}=1}^{N_c^{CF}} f_i l_j + \sum_{c^{FF}=1}^{N_c^{FF}} f_i l_j\right) \qquad 6.22$$

Still assuming that the deformation is small and that $\Delta l_j \approx 0,\ \Delta V \approx 0$, and there are no newly generated contacts:

$$\Delta\sigma_{ij}^{all} = \frac{1}{V}\left(\sum_{c^{CC}=1}^{N_c^{CC}} \Delta f_i l_j + \sum_{c^{CF}=1}^{N_c^{CF}} \Delta f_i l_j + \sum_{c^{FF}=1}^{N_c^{FF}} \Delta f_i l_j\right) \qquad 6.23$$

To obtain the stiffness matrix a strain increment was imposed on the assembly. The relative displacement for each contact pair was determined assuming a uniform strain field to get $\boldsymbol{\Delta x}^{ab}$ in Equation 6.18. Then Equation 6.18 was used to calculate the increment in force for each contact pair where the stiffnesses were given as per Equation 6.17. The increment in stress was determined by inputting the force increments into equations 6.22 and 6.23. Then $\Delta\varepsilon_{\mathrm{ij}} > 0,\ \Delta\varepsilon_{other} = 0$ is imposed on the system,

$$C_{ij}^{all} = \frac{\Delta\sigma_{ij}^{all}}{\Delta\varepsilon_{ij}} \qquad 6.24$$

in this case, based on the theory of elasticity and assuming a linear elastic isotropic material, which suggests that the properties do not change with direction. The shear modulus can be expressed as $G_0 = E/2(1+\nu)$, the following relationship between the stress tensor and the strain tensor can be expressed as $\varepsilon_{xx} = [\sigma_{xx} - \nu(\sigma_{yy} + \sigma_{zz})]/E$, $\varepsilon_{yy} = [\sigma_{yy} - \nu(\sigma_{xx} + \sigma_{zz})]/E$, $\varepsilon_{zz} = [\sigma_{zz} - \nu(\sigma_{xx} + \sigma_{yy})]/E$ and also $\gamma_{xy} = 2\varepsilon_{xy} = \sigma_{xy}/G_0$, $\gamma_{xz} = 2\varepsilon_{xz} = \sigma_{xz}/G_0$, $\gamma_{yz} = 2\varepsilon_{yz} = \sigma_{yz}/G_0$. For this particular case, the input strain can be set as $[0\ 0\ 1;\ 0\ 0\ 0;\ 1\ 0\ 0]$, which suggests a case of shear in $xz-$ direction. Then the $G_0 = \sigma_{xz}/2\varepsilon_{xz}$, note that $\sigma_{xz} = \sigma_{13} = \sigma_{31}$ and the value of σ_{xz} equals to C_{13} and C_{31} when the input strain is set as $[0\ 0\ 1;\ 0\ 0\ 0;\ 1\ 0\ 0]$ since $\varepsilon_{xz} = \varepsilon_{13} = \varepsilon_{31} = 1$. Therefore, the shear stiffness G_0 can be directly estimated as from Equation 6.21. After that, the stiffness contribution of each fraction (i.e. coarse and finer fractions) can also be estimated.

6.5. Analysis of data for cubic specimens

6.5.1. Void ratio and coordination number

The variations in the e, e_m, Z and Z_m data for the linear specimens with C_u are presented in Figure 6.4. As illustrated in Figure 6.4(a), similar to the observation by Youd (1973), who considered experimentally measured maximum and minimum void ratios, the void ratios of the loose and dense specimens decrease with increasing C_u, and a similar trend can be observed for e_m. The offsets between the e and e_m data show that even for specimens with a continuous grading, a finite proportion of the particles may not be active in stress transmission; the offset is greater for the loose specimens and increases with increasing C_u. Figure 6.4(b) indicates that Z decreases with increasing C_u, while, for a given approach to specimen preparation (i.e. a given density level), Z_m is not sensitive to C_u.

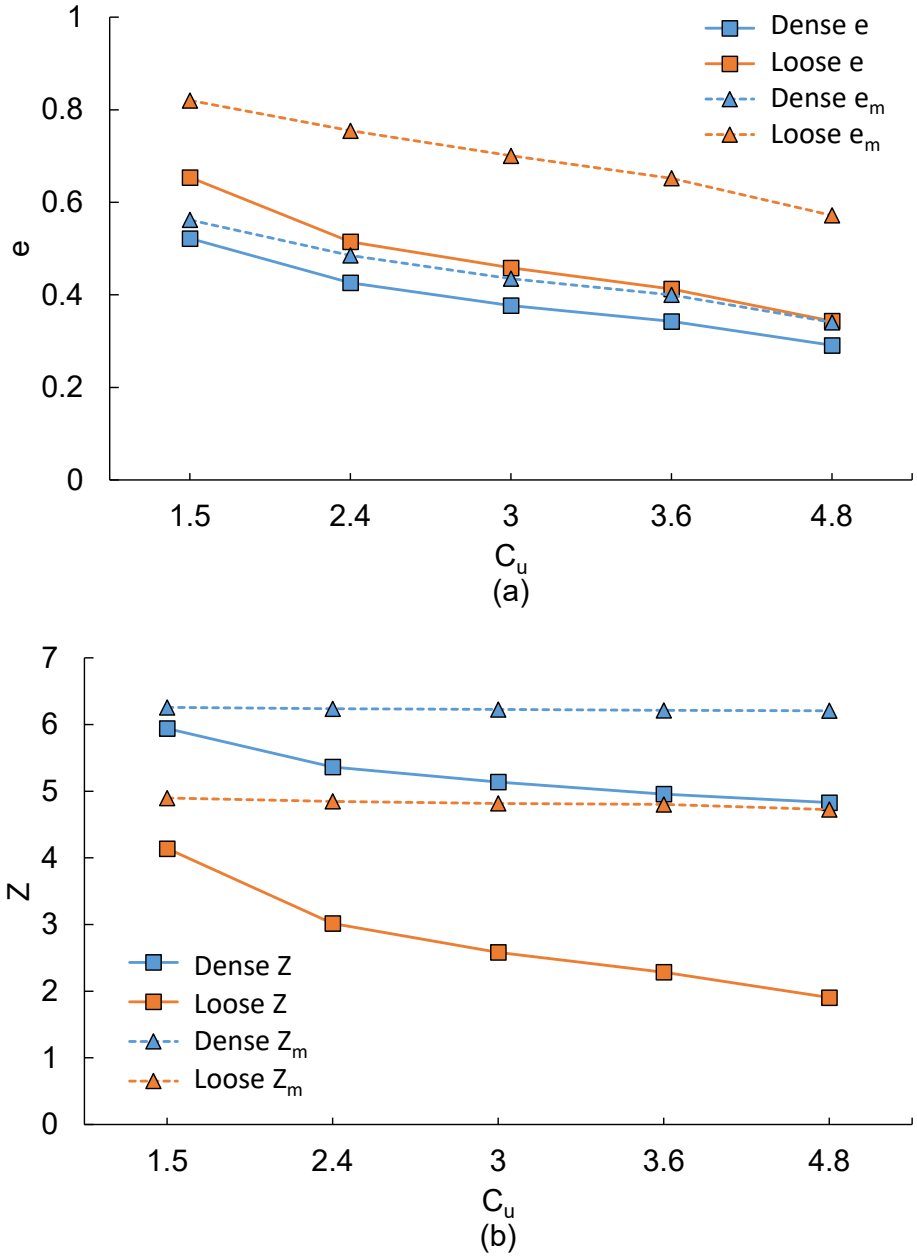


Figure 6.4: Variation of void ratio and coordination number for linear specimens: (a) e, e_m versus C_u; (b) Z, Z_m versus C_u

Figure 6.5 presents the e, e_m, Z and Z_m data for the bimodal gap-graded specimens. The observed trends in the variation of e and e_m with F_{finer} differ for the case of SR = 3.7 in comparison to the data for SR of 8.4 and 18.1; this can be explained by the fact that only when the SR > 6.5, can the finer grains in a purely bimodal material fit inside the voids formed by the coarse grains. Referring to Figure 6.5(a), for SR = 3.7, both the loose and dense e values

initially decrease with increasing F_{finer} and achieve a global minimum when $F_{finer} \approx 20\%$. When $F_{finer} \geq 20\%$, both the loose and dense e values exhibit a slight increase with increasing F_{finer}. The offset between the e and e_m values reduce with increasing F_{finer}. Different trends are observed when $SR \geq 8.4$, Figure 6.5(b&c) show that the loose and dense e values initially reduce with increasing F_{finer} to attain a global minimum and then subsequently increase with increasing F_{finer}. These data agree with prior experimental observations (e.g. Zuo & Baudet, 2015). In contrast, the e_m values initially increase with increasing F_{finer} before exhibiting a sharp drop indicating a marked change of soil fabric; subsequently e_m increases with increasing F_{finer}.

The variation in Z with F_{finer} for SR = 3.7 is distinct from the trends observed for the other SR values. For SR = 3.7, Z decreases to attain a local minimum when $F_{finer} \approx 15\%$, and subsequently increases with further increases in F_{finer} (Figure 6.5(d)). However, for a given packing density level, there is little variation in Z_m with F_{finer}. Figure 6.5(e&f) show that when $SR \geq 8.4$ initially, the Z values reduce to a very low value, so that $Z \approx$ 0.05, indicating that a large number of inactive particles. Contrasting the Z values in Figure 6.5(e) and (f), with the e values in Figure 6.5(b) and (c), the change in Z is much steeper than the change in e once the finer grains start to engage in stress transmission. For all these SR values considered, the Z_m values show little variation with F_{finer} in either the dense or loose specimens. These data clearly show that there is not a simple relationship between e and Z or between e_m and Z_m.

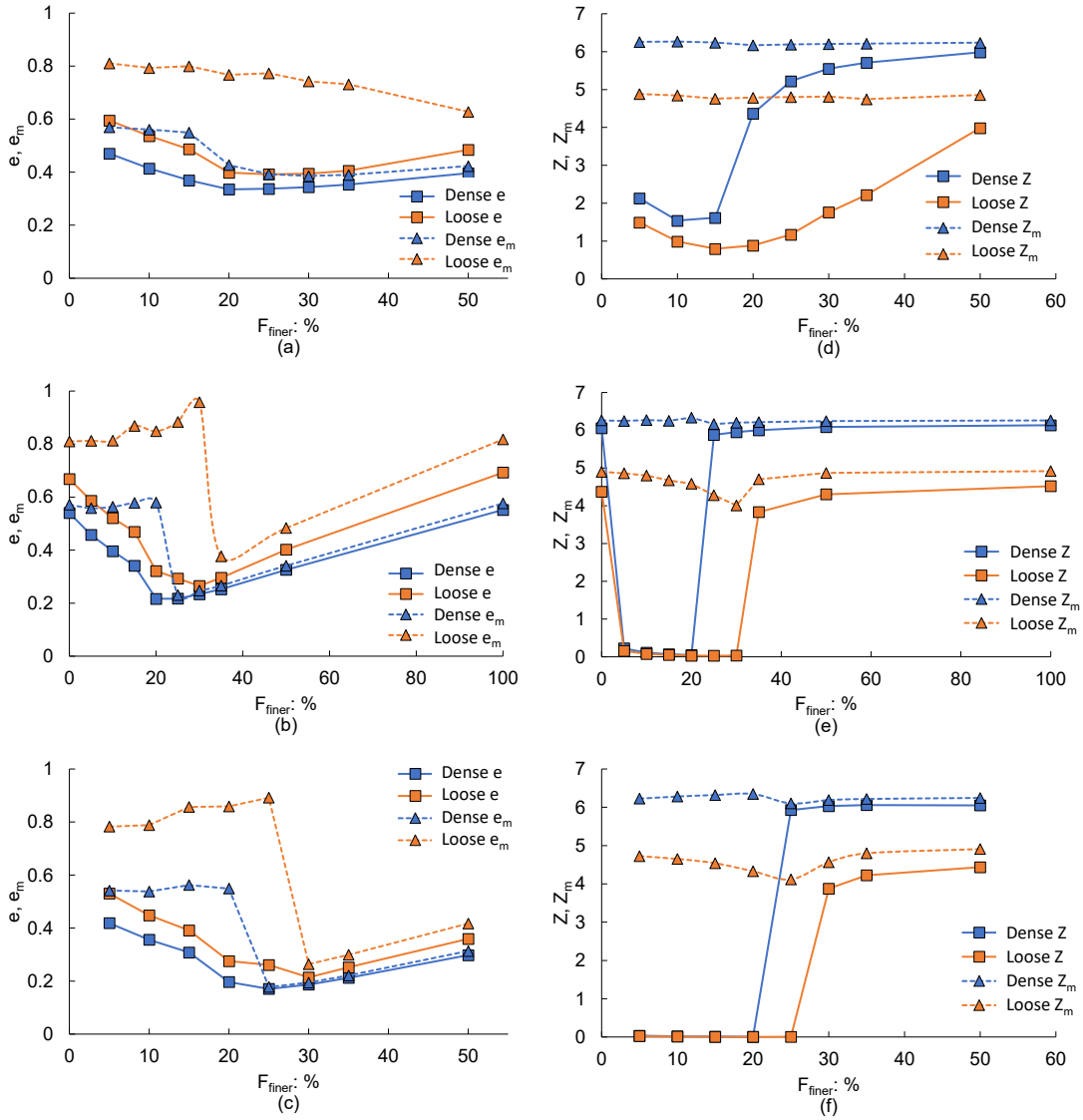


Figure 6.5: Variation in void ratio and coordination number with F_{finer} for bimodal specimens: (a) e and e_m data for SR = 3.7; (b) e and e_m data for SR = 8.4; (c) e and e_m data for SR = 18.1; (d) Z and Z_m data for SR = 3.7; (e) Z and Z_m data for SR = 8.4; (f) Z and Z_m data for SR = 18.1

6.5.2. Analysis of results for linear specimens

Figure 6.6(a) shows the relationship between G_0 and e for the linear specimens when $\sigma_3' = 500\ kPa$. A state-dependant behaviour is evident; for a given C_u, G_0 decreases systematically with increasing e. In line with the experimental research highlighted above, the data indicate that the relationship between G_0 and e is dependent upon C_u; the datasets for each C_u are distinct and the data points shift to the left as C_u increases. There is not a

unique overall relationship between G_0 and e. In contrast, Figure 6.6(b) shows a relatively good linear correlation between e_m and G_0, unifying the data for all 5 C_u values considered. Figure 6.6(c) shows that, in line with EMT, a weak correlation exists when G_0 is plotted against $Z/(1+e)$. Instead, Figure 6.6(d) shows that $Z_m/(1+e_m)$ can be used as an appropriate state variable to capture the variations in G_0 amongst the linear specimens, confirming the observation by Otsubo et al. (2021).

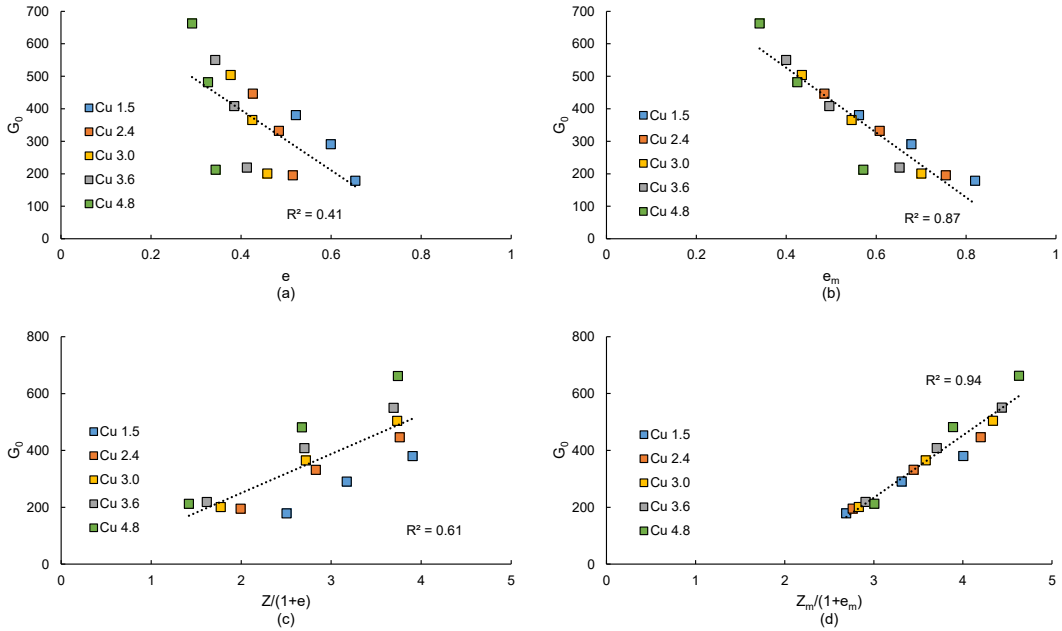


Figure 6.6: Exploration of correlations between G_0 and various state variables for linear specimens (σ_3' = 500 kPa): (a) G_0 versus e; (b) G_0 versus e_m; (c) G_0 versus $Z/(1+e)$; (d) G_0 versus $Z_m/(1+e_m)$

The ability of Hardin's equation to describe the variation in the shear modulus with state and mean effective pressure for the linear specimens is explored in Figure 6.7(a). The void ratio is the measure of state and with n being taken to be 0.33 following Otsubo (2016) for similar spherical particles. The decision to take n = 0.33 is one of convenience, the number of free variables needed to be constrained to enable the optimization. While the data analysis is empirical, Hertzian contact mechanics was used to obtain the particle stiffness values in

the simulations, and an n value of 0.33 emerges from this contact model. These c and A values were obtained by least-squares optimization using $MATLAB$. The optimal fit has an R^2 value of only 0.72, indicating that the global void ratio may not be able to capture the stiffness behaviour of these linear specimens in a unified way. Figure 6.7(b) shows the surface fit obtained by considering e_m, and a better performance is obtained in this case, with the R^2 being 0.98. Figure 6.7(c) shows the performance where the state is quantified as $Z_m/(1+e_m)$ and again a very good fit can be obtained. In general, for the specimens with a linear PSD and C_u values between 1.5 and 4.8, these data indicate that e_m and $Z_m/(1+e_m)$ can both be used as state variables to describe or predict the stiffness in a unified way.

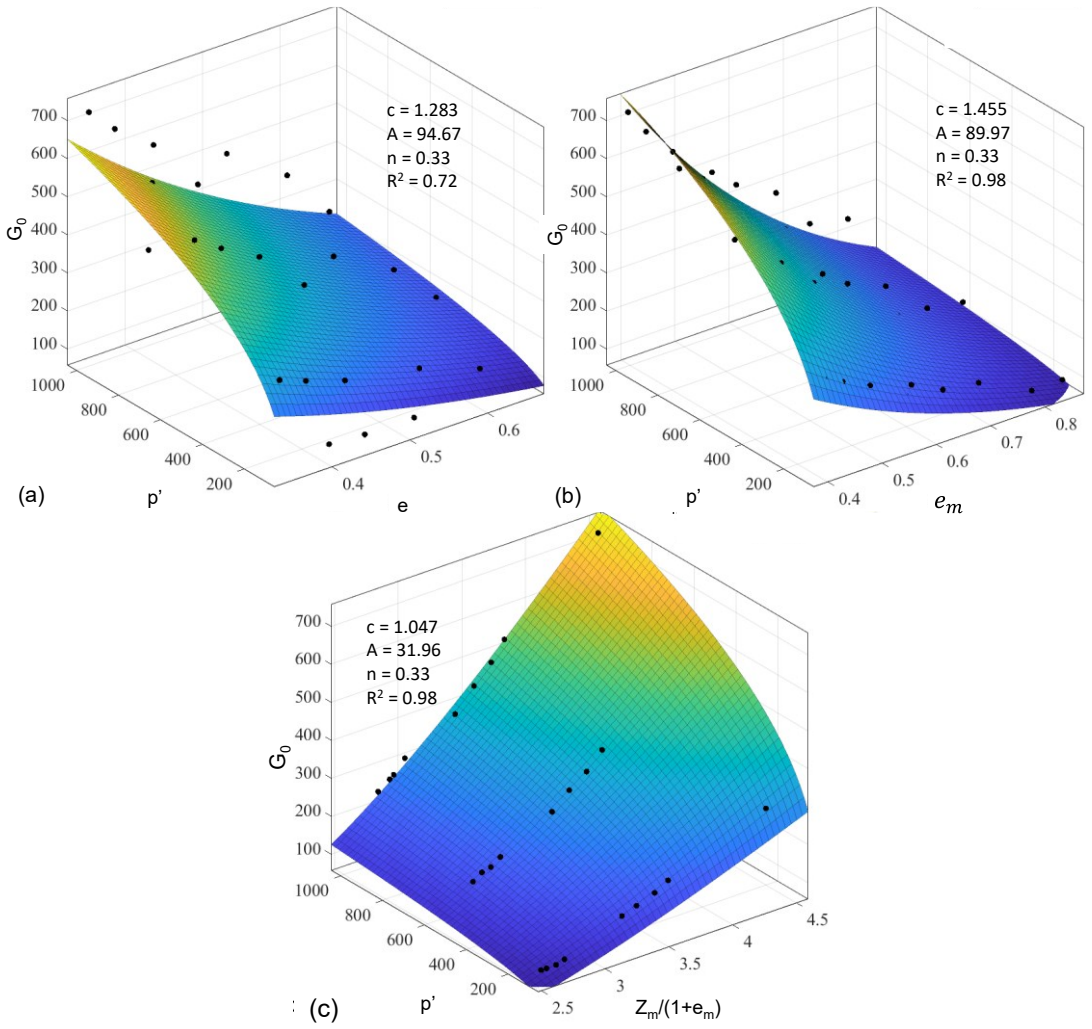


Figure 6.7: Performance of state variables for linear specimens in Hardin's equation: (a) The use of e; (b) The use of e_m; (c) The use of $Z_m/(1+e_m)$

6.5.3. Analysis of results for gap-graded specimens

Figure 6.8 presents the variation in G_0 with e for the four bimodal SRs (i.e. SR values of 3.7, 8.4, 14.5 and 18.1) when p' is 500 kPa. (Similar patterns are observed on the other p' values considered, i.e. 100 kPa and 1000 kPa). As before the trends observed when SR = 3.7 differ from the cases where SR = 8.4, 14.5 and 18.1. In all cases, the G_0 values vary with both e and F_{finer}. As F_{finer} increases, three distinct responses in G_0 can be observed. When $5\% \leq F_{finer} \leq 20\%$ (data plotted in blue), the G_0 values exhibit a similar sensitivity to changes in e and the data shift towards the left with increasing F_{finer}. When $20\% \leq F_{finer} \leq 35\%$, (data plotted in orange), the G_0 values are much more sensitive to changes in e. When F_{finer} is approximately 50%, there is a noticeable reduction in the sensitivity of G_0 to e. These three categories identified ($5 \leq F_{finer} \leq 20\%$, $20 \leq F_{finer} \leq 35\%$ and $F_{finer} > 35\%$) agree with the fabric classification boundaries proposed in Shire et al. (2014) (i.e. underfilled, transitional (density-dependent), and overfilled) who considered the distribution of stress amongst the finer and coarse fractions. The observed alignment with Shire's classification indicates that the distribution of stress amongst the different size fractions may have a significant influence on G_0 in the case of gap-graded soils.

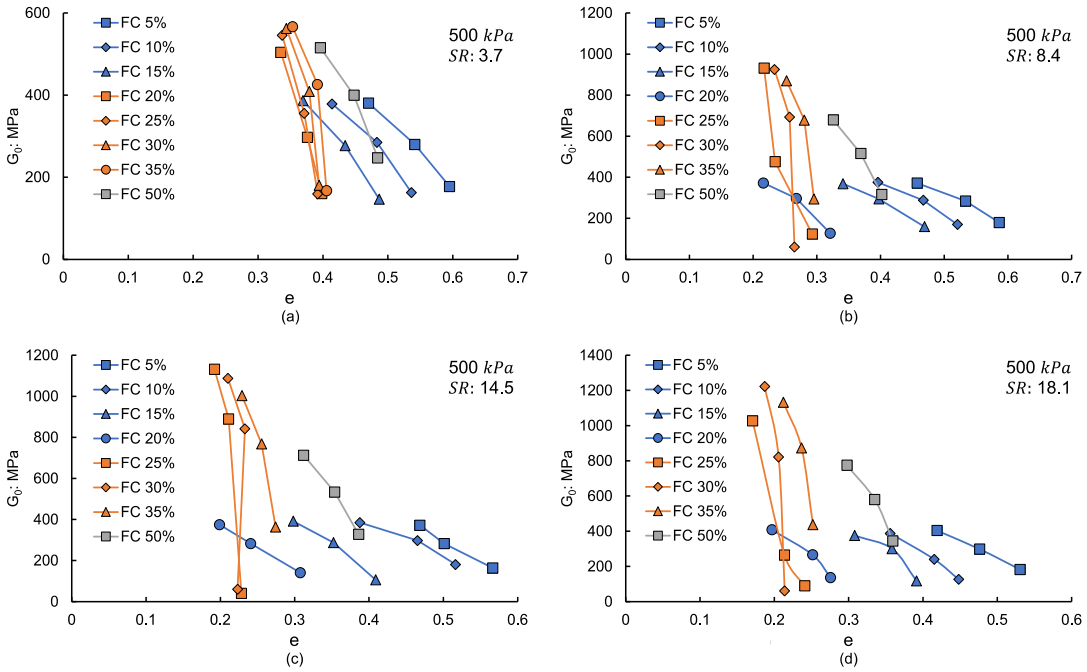


Figure 6.8: Variation in G_0 with e for bimodal specimens with various SR values (p' = 500 kPa): (a) G_0 versus e (SR = 3.7); (b) G_0 versus e (SR = 8.4); (c) G_0 versus e (SR = 14.5); (d) G_0 versus e (SR = 18.1)

Stiffness data for numerical specimens with a SR of 8.4 are shown in Figure 6.9. Data for the three values of effective confining pressure p' considered (i.e. 100 kPa, 500 kPa, 1000 kPa) are presented in Figure 6.9(a), (b) and (c), respectively. The typical state-dependent behaviour expected to occur in granular materials can be observed, both the void ratio and effective confining pressure influence the stiffness values of these specimens (note that the scale on the vertical axes differs for each of these three figures). In all cases, the distinct patterns in the variation of stiffness with e can be observed depending on the value of F_{finer}, in line with the observations made above in relation to the data in Figure 6.8.

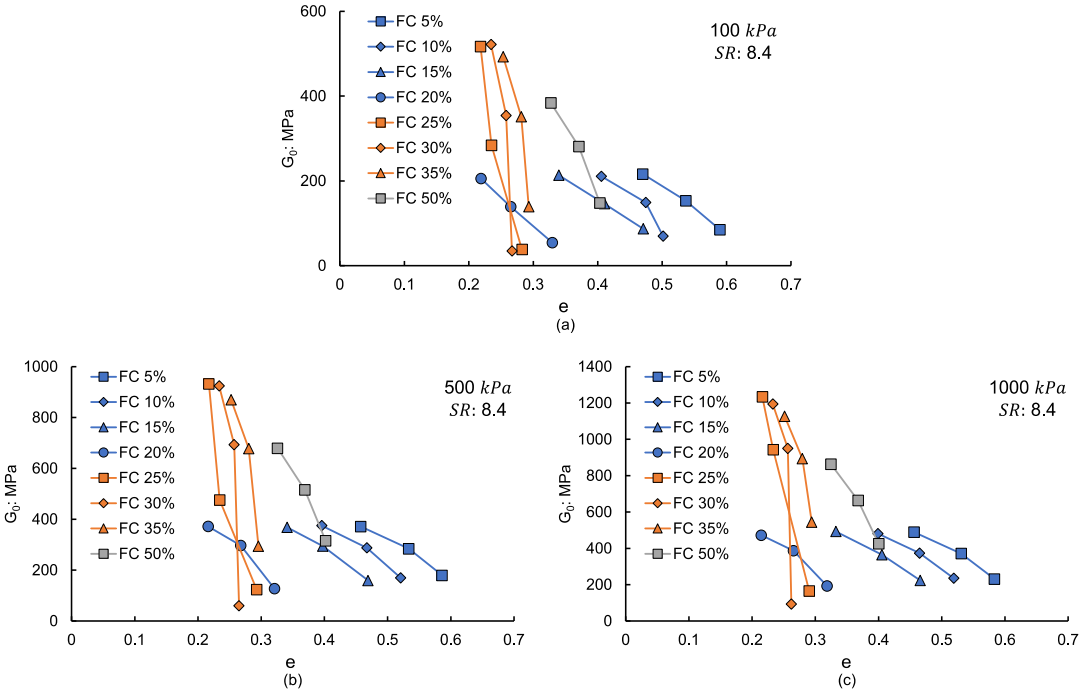


Figure 6.9: Variation in G_0 with e for bimodal specimens with SR = 8.4 and various p' values: (a) G_0 versus e (p' = 100 kPa); (b) G_0 versus e (p' = 500 kPa); (c) G_0 versus e (p' = 1000 kPa)

Figure 6.10 explores the existence of a correlation between G_0 and each of the four-state variables proposed for bimodal specimens considering the data for SR of 8.4 at $\sigma_3' = 500$ kPa. Figure 6.10(a) indicates no clear correlation between e and G_0 over the range of F_{finer} values considered. Figure 6.10(b) indicates some correlation between e_m and G_0, however the R^2 for this linear fit is only 0.80, this may be attributed to the inability of e_m to differentiate contributions by particles or contacts transmitting different amounts of stress. The correlation is also poor when the original EMT ratio, i.e. $Z/(1+e)$ is used (Figure 6.10(c)). In contrast, the ratio $Z_m/(1+e_m)$ gives a more reasonable linear correlation, with a R^2 of 0.87.

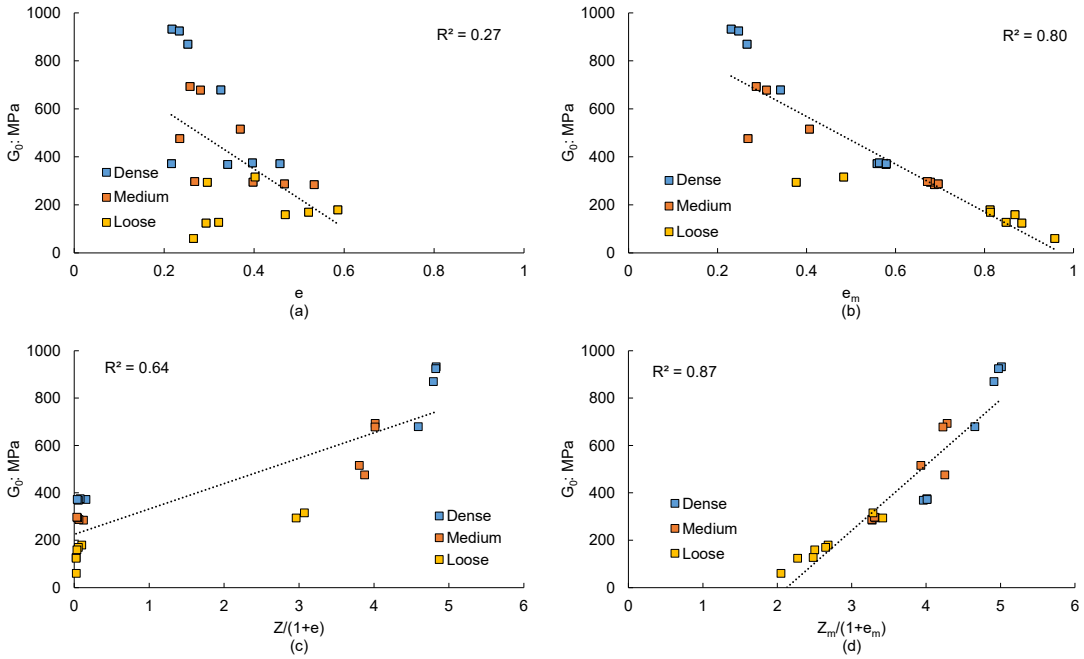


Figure 6.10: Performance of state variables for bimodal specimens (SR = 8.4; p'= 500 kPa): (a) G_0 versus e; (b) G_0 versus e_m; (c) G_0 versus $Z/(1+e)$; (d) G_0 versus $Z_m/(1+e_m)$

Figure 6.11 explores the applicability of Hardin's equation to all the data for the bimodal gap-graded soils with SR = 8.4. In Figure 6.11(a), the parameters A and c are determined by regression analysis using e, and taking n = 0.33; the correlation is very poor ($R^2 \approx$ 0.46). However, Figure 6.11(b) shows that if the ratio, $Z_m/(1+e_m)$ is used in lieu of e in Equation 2.11, (still assuming n = 0.33), a good fit to the data is attained, with $R^2 \approx$ 0.92. This result indicates that the ratio $Z_m/(1+e_m)$ may be a better state variable than e to predict G_0 for bimodal gap-graded soils.

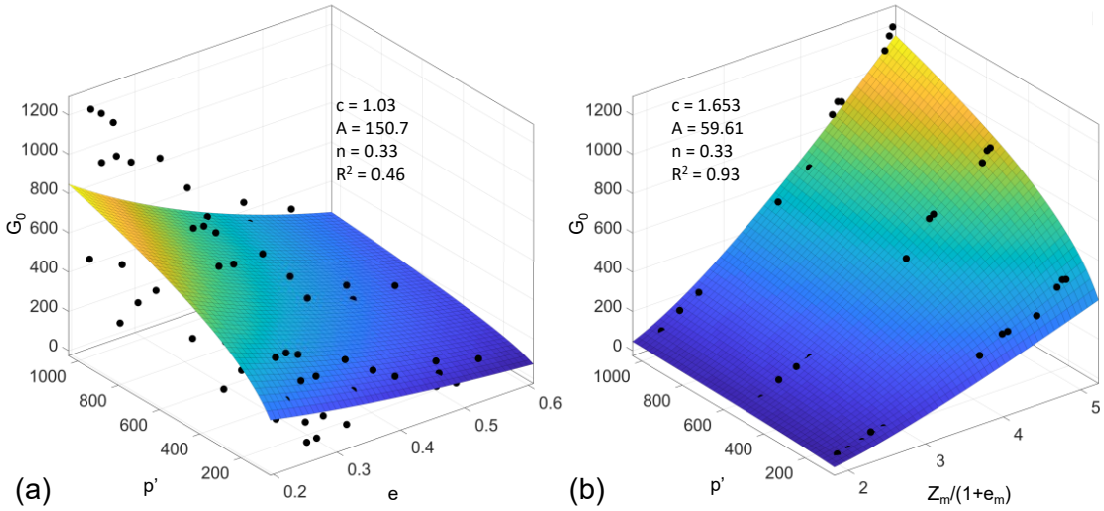


Figure 6.11: Performance of state variables for bimodal specimens in Hardin's equation (SR = 8.4): (a) The use of e; (b) The use of $Z_m/(1+e_m)$

Data for the trimodal specimens with $p' = 500\ kPa$ are presented in Figure 6.12. The data in Figure 6.12(a) show that for soil comprising a mixture of three distinct particle sizes, e does not correlate well with G_0. In contrast, Figure 6.12(b) shows a linear correlation between $Z_m/(1+e_m)$ and G_0 with $R^2 \approx 0.84$. However, comparing the data on linear specimens with the data on bimodal and trimodal specimens, the ratio $Z_m/(1+e_m)$ gives a measurably stronger correlation with G_0 for the linear specimens than for the bimodal and trimodal specimens (recalling that the R^2 value was 0.98, Figure 6.6(d)).

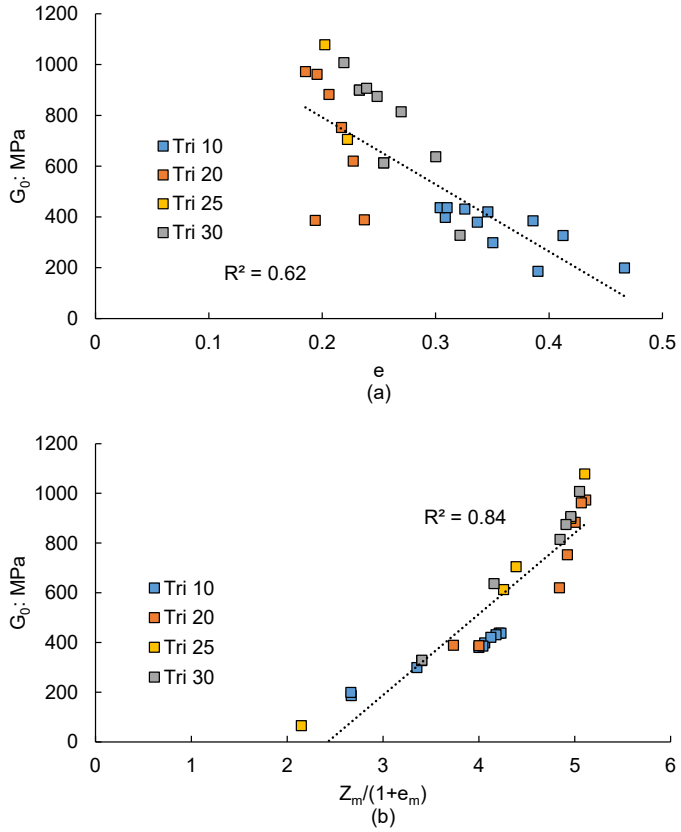


Figure 6.12: Performance of state variables for trimodal specimens (p'= 500 kPa): (a) G_0 versus e; (b) G_0 versus $Z_m/(1+e_m)$

A more comprehensive exploration of the extent to which G_0 correlates with the state variables considered here can be gained by considering all of the specimens in a unified way. The entire range of particle size distributions is considered in this study. Figure 6.13(a) shows the poor predictive capacity of Hardin's equation using e as the state variable when all the linear, bimodal and trimodal specimens are considered simultaneously. The use of the global void ratio e cannot effectively predict G_0, even when the optimal values of c and A are sought using least squares regression. Figure 6.13(b) presents the performance of Hardin's expression taking $Z_m/(1+e_m)$ as the state variable. In this case, an improved performance is observed with a R^2 value of being approxmately 0.90. This result shows that for this case where the particle elastic properties are constant, the use of the ratio $Z_m/(1+e_m)$ in the Hardin's equation enables accurate predictions of G_0 for a broader range of particle size

distributions. This good correlation does not negate the observations noted above, i.e. the effectiveness of the fit depends on the type of PSD considered, with the linear specimens showing a stronger correlation than the mixture specimens.

These data support the use of the functional forms presented by Hardin & Richart (1963), however, the controlled, ideal dataset generated here confirms that extrapolating the correlation of G_0 with e beyond the continuous $PSDs$ is not appropriate.

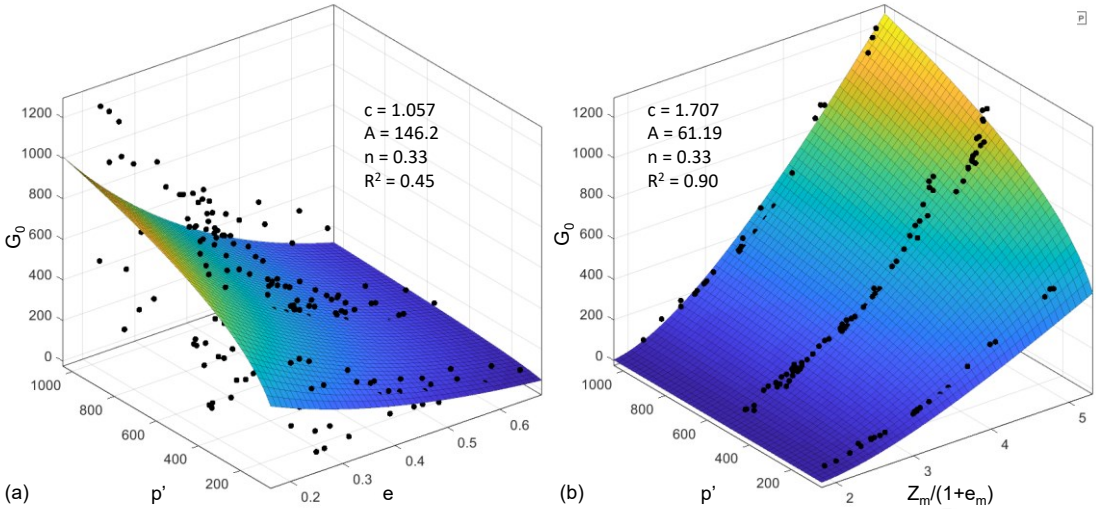


Figure 6.13: Correlation between G_0 and state variables for linear, bimodal and trimodal specimens in Hardin's equation: (a) The use of e as the state variable; (b) The use of $Z_m/(1+e_m)$ as the state variable

6.5.4. Heterogeneity of contributions to stiffness

If we accept the state variable that determines the stiffness of a soil is $Z_m/(1+e_m)$, we are not considering the fact, apart from the case of a lattice packing of uniform spheres, each contact has a different stiffness, and each particle transmits a different amount of stress. For the relatively simple smooth frictional spheres with uniform elastic properties that are considered here, the contact stiffness depends upon the force transmitted and the radii of the two transmitting particles (Hertz, 1882; Johnson, 1985). A measure of state such is

as $Z_m/(1+e_m)$ assumes either (i) each active contact and each particle have equal weight or (ii) that the average properties are representative. However, while these assumptions may be appropriate for linear specimens, it is hard to justify their application to gap-graded soils. This could partially explain the reason why the ratio $Z_m/(1+e_m)$ gives a measurably stronger correlation for the linear specimens than for the bimodal and trimodal specimens. Here we challenge the general applicability of any measure that considers only Z_m and e_m by exploring how the particle size distribution influences the distribution of stress amongst the active particles and the distribution of stiffness amongst the force-transmitting contacts, especially for gap-graded soils.

Figure 6.14 is a scatter plot of the k_N values against the normal force value for each contact point for the dense linear specimens. In all cases, the contact normal stiffness increases with increasing normal force, however, there is a wide range of stiffness values and there is no clear difference amongst the linear specimens considered here.

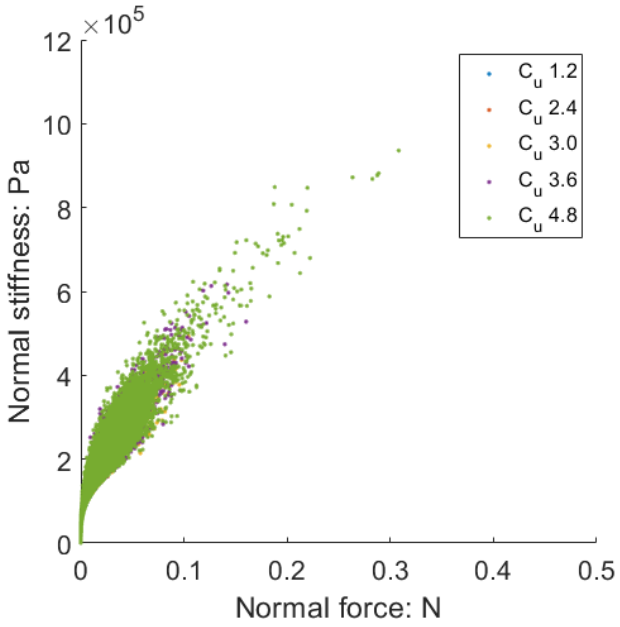


Figure 6.14: Normal stiffness versus normal force for linear specimens in the dense condition

Figure 6.15(a) shows the cumulative distribution of the normal stiffnesses, while

Figure 6.15(b) shows the same data normalised by the mean normal stiffness respectively. While no significant differences can be identified amongst these specimens, the range of k_N values increases with increasing C_u.

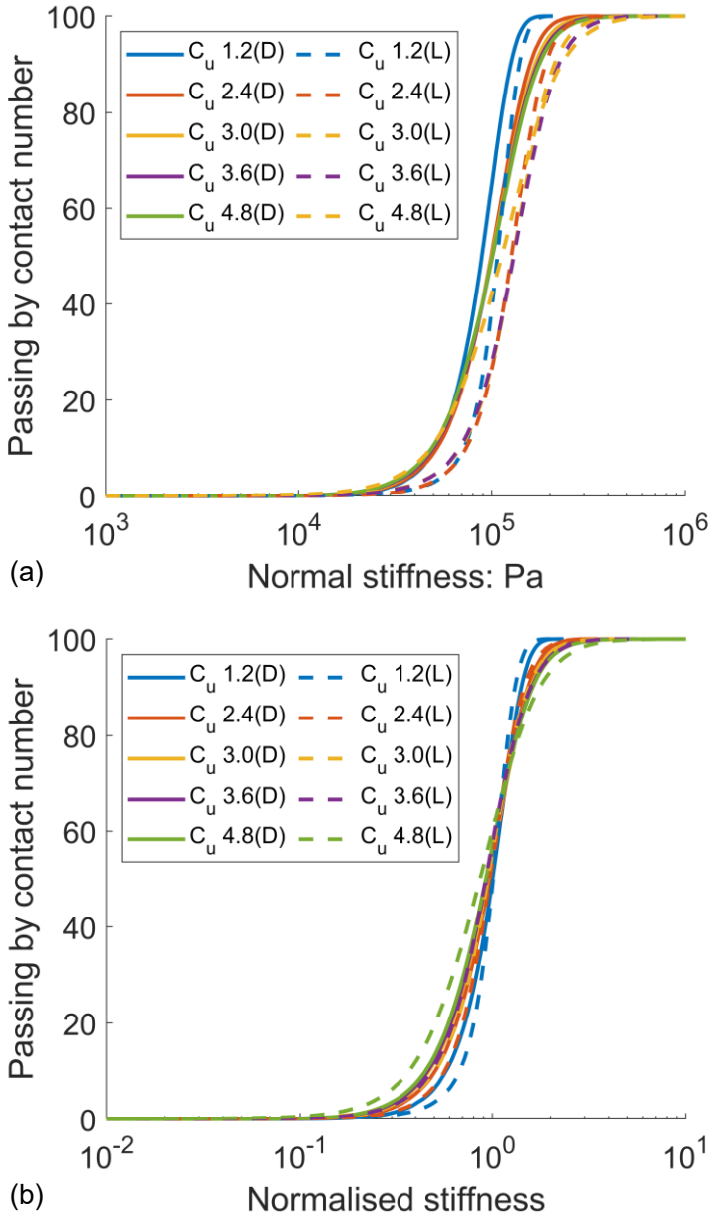


Figure 6.15: Normal stiffness characteristics for linear specimens: (a) Cumulative distribution of normal stiffness; (b) Cumulative distribution of normalised stiffness by average stiffness. "D" denotes the densest case, "L" denotes the loosest case

Figure 6.16 are scatter plots of the k_N values against the normal force for each contact point for representative bimodal gap-graded specimens with SR = 3.7 and 8.4 with F_{finer} = 10%, 25% and 50% respectively. Each class of contact,

i.e. coarse-coarse ($C-C$), coarse-finer ($C-F$) and fine-finer ($F-F$) is identified using a different colour. There is a clear difference between the three different contact types in these specimens. For all three F_{finer} values considered, the maximum contact force between two coarse particles ($C-C$) is significantly larger than the maximum contact force between a finer and coarser particle ($C-F$) which in turn is larger than the maximum contact force between two finer particles ($F-F$). At a given normal force, the $C-C$ contacts have the highest normal stiffness and the $F-F$ contacts have the lowest contact stiffness. This heterogeneity reflects a complex interdependency of force and stiffness; k_n depends upon on the effective radius. However, assuming that there is no generation and no loss of contacts when a small increment in uniform strain is applied, the increase in force at the stiffer contacts will be larger. These data highlight the fact that contacts between particles of different sizes have measurable differences in stiffness. In any system stiffer elements will attract load, adding to the complexity. This has not been explicitly considered in attempts to develop frameworks to predict G_0.

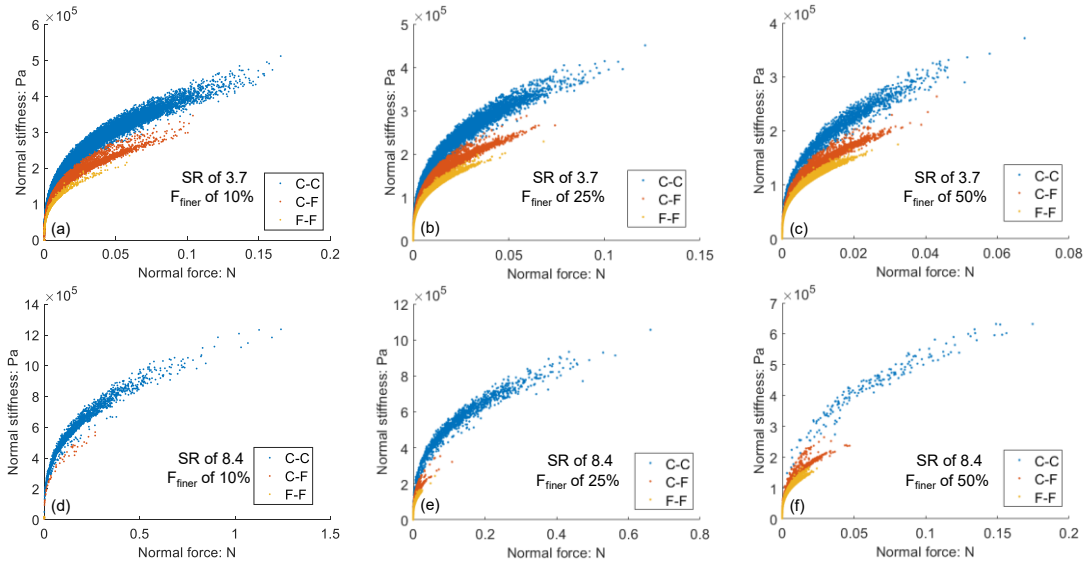


Figure 6.16: Normal stiffness versus normal force: (a) F_{finer} = 10%, SR = 3.7; (b) F_{finer} = 25%, SR = 3.7; (c) F_{finer} = 50%, SR = 3.7; (d) F_{finer} = 10%, SR = 8.4; (e) F_{finer} = 25%, SR = 8.4; (f) F_{finer} = 50%, SR = 8.4

Figure 6.17(a) presents the cumulative distribution, by number of contacts, of the normal stiffness for the dense bimodal specimens with SR = 8.4; a distinct behaviour can be observed between the underfilled specimens (i.e. F_{finer} of 5%, 10%, 15% and 20%) and overfilled conditions (F_{finer} of 25%, 30%, 35% and 50%). The significantly higher contact stiffness values when $F_{finer} < 20\%$, reflect the large stiffness values associated with the $C - C$ contacts. At $F_{finer} = 20\%$, the cumulative distribution indicates a mix of small contact stiffnesses and large contact stiffnesses. Referring to Figure 6.5 (e) when F_{finer} < 20%, the coordination number is very low, reflecting the low number of contacts. For a given macroscopic stress state, the average contact force will increase as the number of contacts reduces. Then for $F_{finer} > 20\%$, there is a more continuous distribution for the normal stiffness data. And the average contact stiffness is lower in this overfilled condition than it was in the underfilled case. Figure 6.17(b) presents the results for the loose condition and similar trends are evident. These data highlight that the finer fraction can significantly influence the range of stiffness values in the specimen and that there is also a density effect.

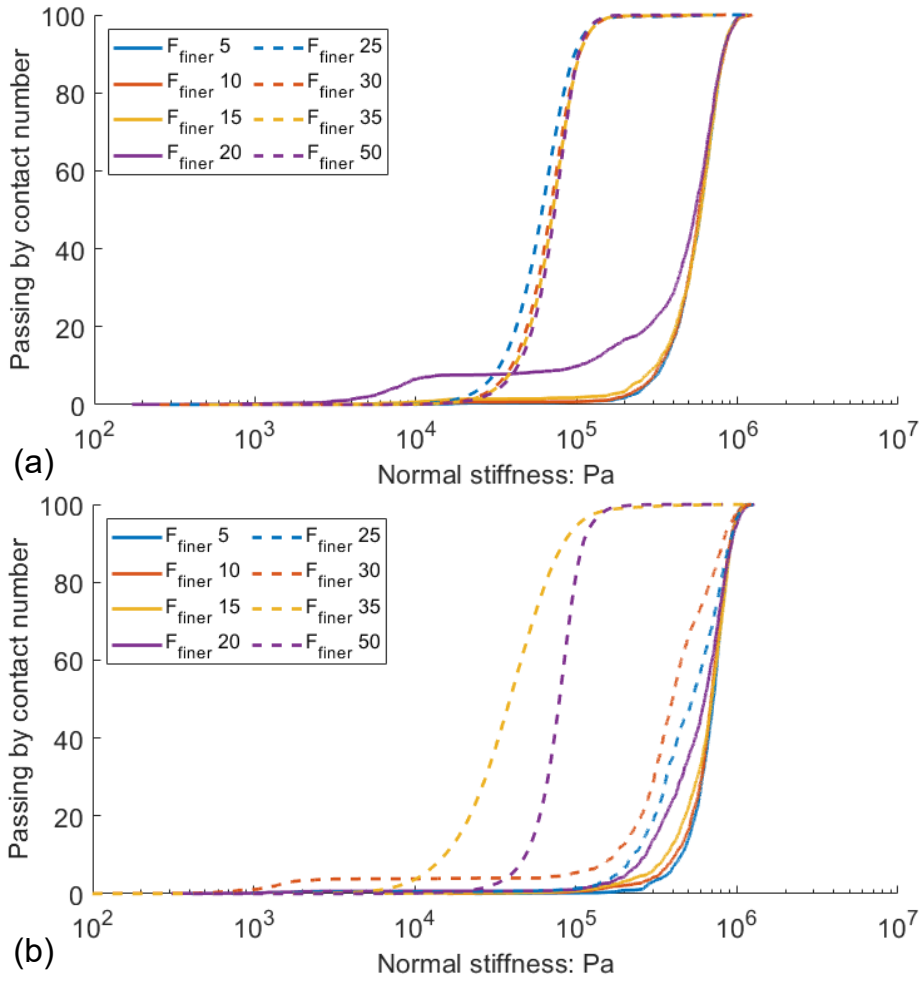


Figure 6.17: Variation in normal contact stiffness values for bimodal specimens: (a) Cumulative distribution of normal stiffness values for specimens in the dense condition; (b) Cumulative distribution of normal stiffness values for specimens in the loose condition

Figure 6.18 compares the stiffness values from the probe and the matrix method for the linear specimens. For the dense specimens, as shown in Figure 6.18(a), the probe and the matrix methods give similar trends when the variation in G_0 with C_u is considered. However, the stiffness values obtained from the matrix method consistently exceed those obtained from the probe method. This may be attributed to the uniform strain assumption underlying the stiffness matrix approach. Yimsiri & Soga (2000) and Magnanimo et al. (2008) amongst others have highlighted the inability of EMT to accurately predict stiffness. This maybe partially explained by the limitations of this kinematic assumption which also assumes a uniform strain field (Makse et al., 1999; La Ragione &

Magnanimo, 2012; Khalili et al., 2017). However, the stiffness matrix approach can accurately capture differences between specimens. Referring to Figure 6.18(b), if the G_0 data obtained using each approach are normalized by the G_0 for C_u = 1.2, a very similar trend is observed up to C_u = 3.6, while the data on Figure 6.18(c) show that if the data at 500 kPa are normalized by the data at 100 kPa, the responses are equivalent.

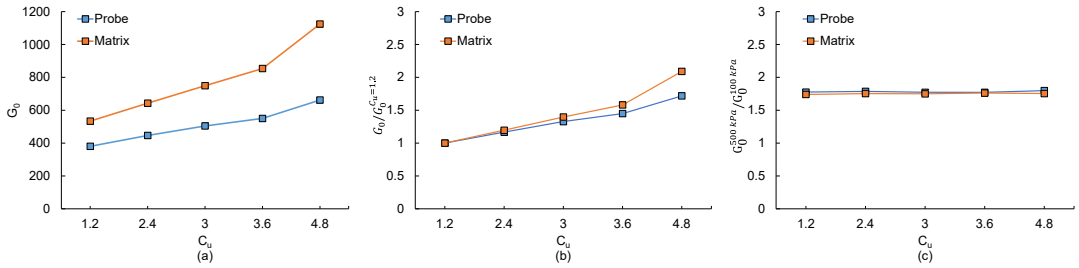


Figure 6.18: Comparison of G_0 values obtained in small strain probes and using the stiffness matrix method for dense linear specimens (p' = 500 kPa): (a) G_0 values versus C_u; (b) $G_0/G_0^{C_u=1.2}$ values versus C_u; (c) $G_0^{500\ kPa}/G_0^{100\ kPa}$ values versus C_u

To further support the ability of the matrix approach to provide insight into stiffness, the results of the medium-dense and loose linear specimens are also illustrated in Figure 6.19 and Figure 6.20, respectively. A similar tendency is observed in both medium and loose conditions. However, it can be seen that the difference between G_0 values obtained from the probe and G_0 values obtained from the stiffness matrix method may increase when packing density reduces from the dense to the loose condition.

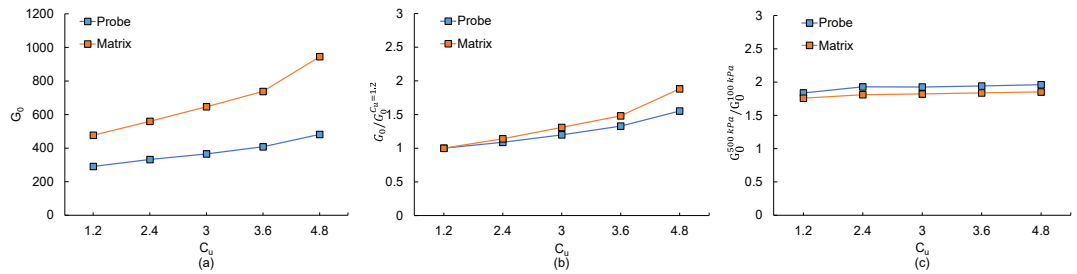


Figure 6.19: Comparison of G_0 values obtained in small strain probes and using the stiffness matrix method for medium linear specimens (p' = 500 kPa): (a) G_0 values versus C_u; (b) $G_0/G_0^{C_u=1.2}$ values versus C_u; (c) $G_0^{500\ kPa}/G_0^{100\ kPa}$ values versus C_u

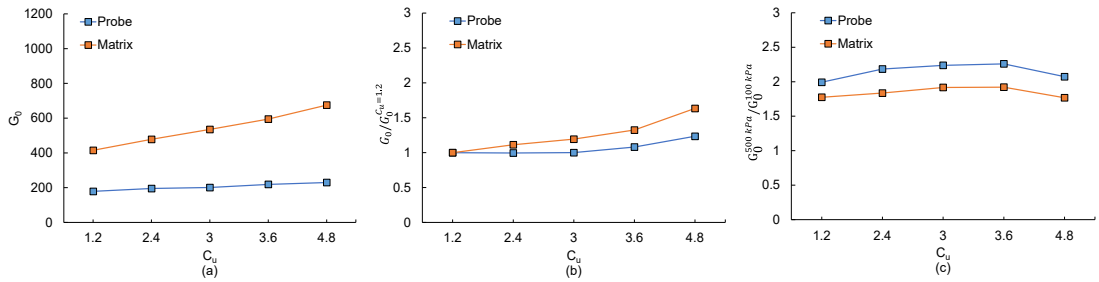


Figure 6.20: Comparison of G_0 values obtained in small strain probes and using the stiffness matrix method for loose linear specimens (p' = 500 kPa): (a) G_0 values versus C_u; (b) $G_0/G_0^{C_u=1.2}$ values versus C_u; (c) $G_0^{500\ kPa}/G_0^{100\ kPa}$ values versus C_u

Figure 6.21 shows the variation in the G_0 values obtained from both the probe (Section 6.4.2) and the stiffness matrix method (Section 6.4.6) with F_{finer} for the bimodal specimens. The data for specimens with SR = 3.7, 8.4 and 14.5 are shown in Figure 6.21(a), Figure 6.21(b) and Figure 6.21(c), respectively. The G_0 values predicted by the stiffness matrix method are consistently larger than those obtained using the probe method, just as was the case for the linear specimens.

However, both the probe-generated data and the G_0 values obtained using the stiffness matrix method show similar tendencies at a given packing density. For instance, for the SR = 8.4 in the dense condition, for both methods, the G_0 values maintain at a similar level when $5\% \leq F_{finer} \leq 20\%$ and reach a peak value when F_{finer} is approximately 30%, followed by a slight decrease when $F_{finer} \geq 30\%$. In addition, the SR = 3.7 data follow different trends when compared to the other SR values; again this can be explained by the fact that the finer particles in the specimens with SR = 3.7 cannot exist in the void space between the coarser particles without contacting the coarser particles.

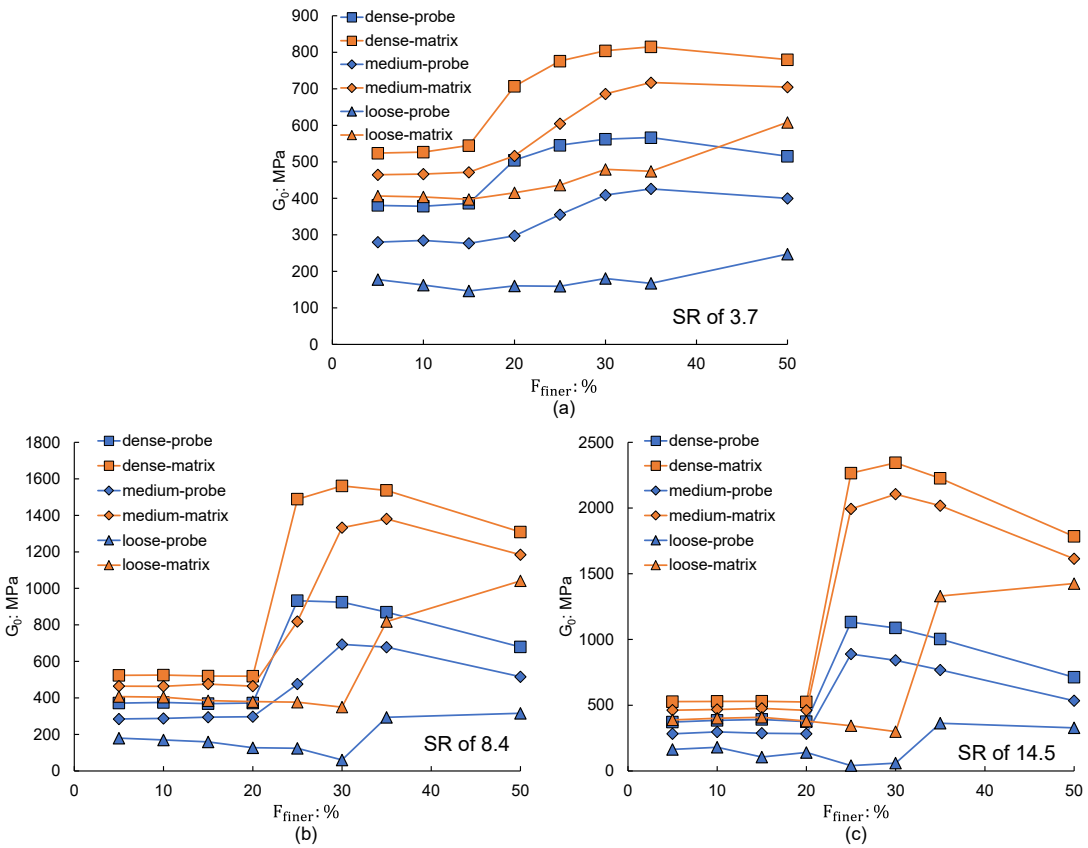


Figure 6.21: Variation in G_0 values obtained using the probe and stiffness matrix methods with F_{finer} for bimodal specimens with p'= 500 kPa: (a) SR = 3.7; (b) SR = 8.4; (c) SR = 14.5

In the dense condition, Figure 6.22(a) shows that at a given F_{finer}, the G_0 values at 500 kPa normalized by the G_0 values at 100 kPa, i.e. $G_0^{500\ kPa}/G_0^{100\ kPa}$, obtained using both methods are very similar. Figure 6.22(b) shows that, at a given stress level, if the G_0 values determined from each method at all F_{finer} values considered are normalized by the G_0 for F_{finer}= 5%, both approaches predict very similar trends. Overall, as before the stiffness matrix approach overestimates G_0, however, following appropriate normalization, it is capable of capturing the variation in G_0 with F_{finer} and stress level.

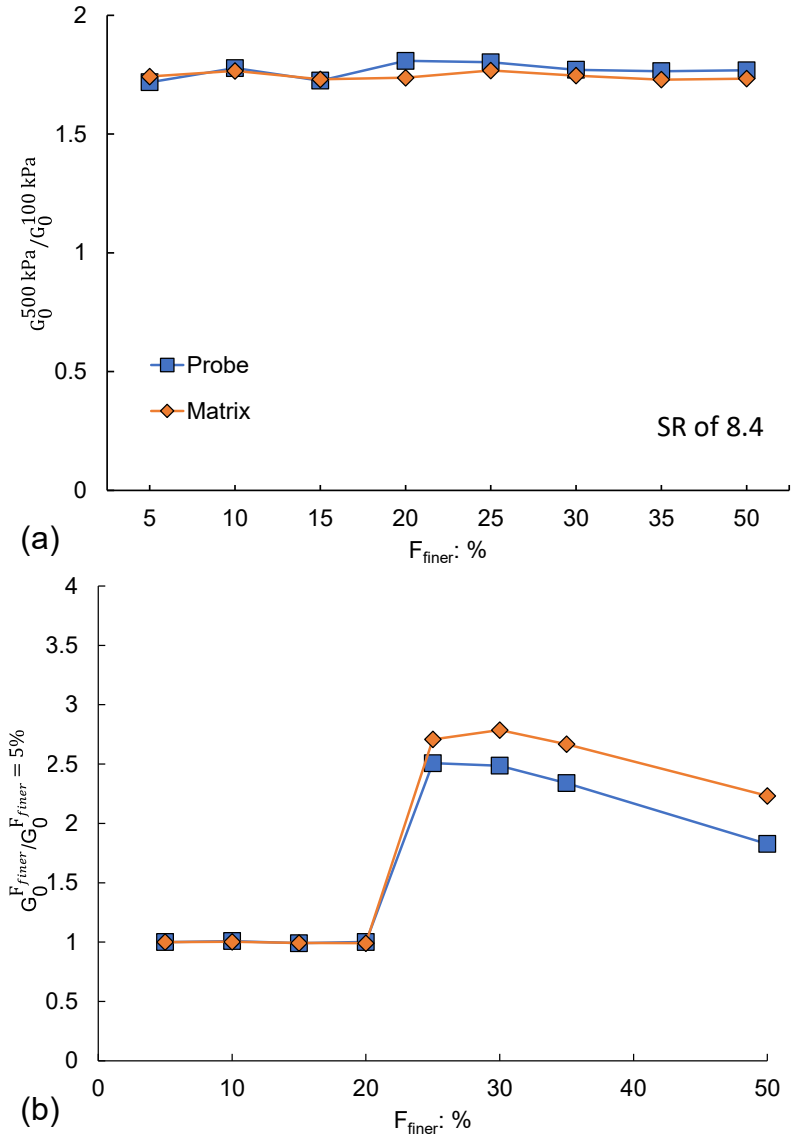


Figure 6.22: Comparison of G_0 values obtained using probes and using the stiffness matrix methods for bimodal gap-graded soils in the dense condition: (a) $G_0^{500\ kPa}/G_0^{100\ kPa}$ versus F_{finer}; (b) $G_0^{F_{finer}}/G_0^{F_{finer}=5\%}$ versus F_{finer}

The results observed in the medium and loose conditions are presented in Figure 6.23 and Figure 6.24, respectively. It can be seen that ratio $G_0^{500\ kPa}/G_0^{100\ kPa}$ obtained using both methods are relatively similar in the medium condition, while finite difference can be observed compared to that identified in the dense condition. As before, a larger difference can be observed for the ratio $G_0^{500\ kPa}/G_0^{100\ kPa}$ obtained using both methods in the loose condition. Furthermore, Figure 6.23(b) and Figure 6.24(b) shows a similar

tendency of ratio $G_0^{F_{finer}}/G_0^{F_{finer}=5\%}$ in the medium and loose conditions compared to that observed in the dense condition. While the stiffness matrix cannot accurately predict G_0 and while its ability to capture trends is somewhat dependant on the sample density, the normalized data are in sufficient agreement to allow the use of this method to gain some insight into the distribution of the contributions for the overall stiffness amongst the different contact types.

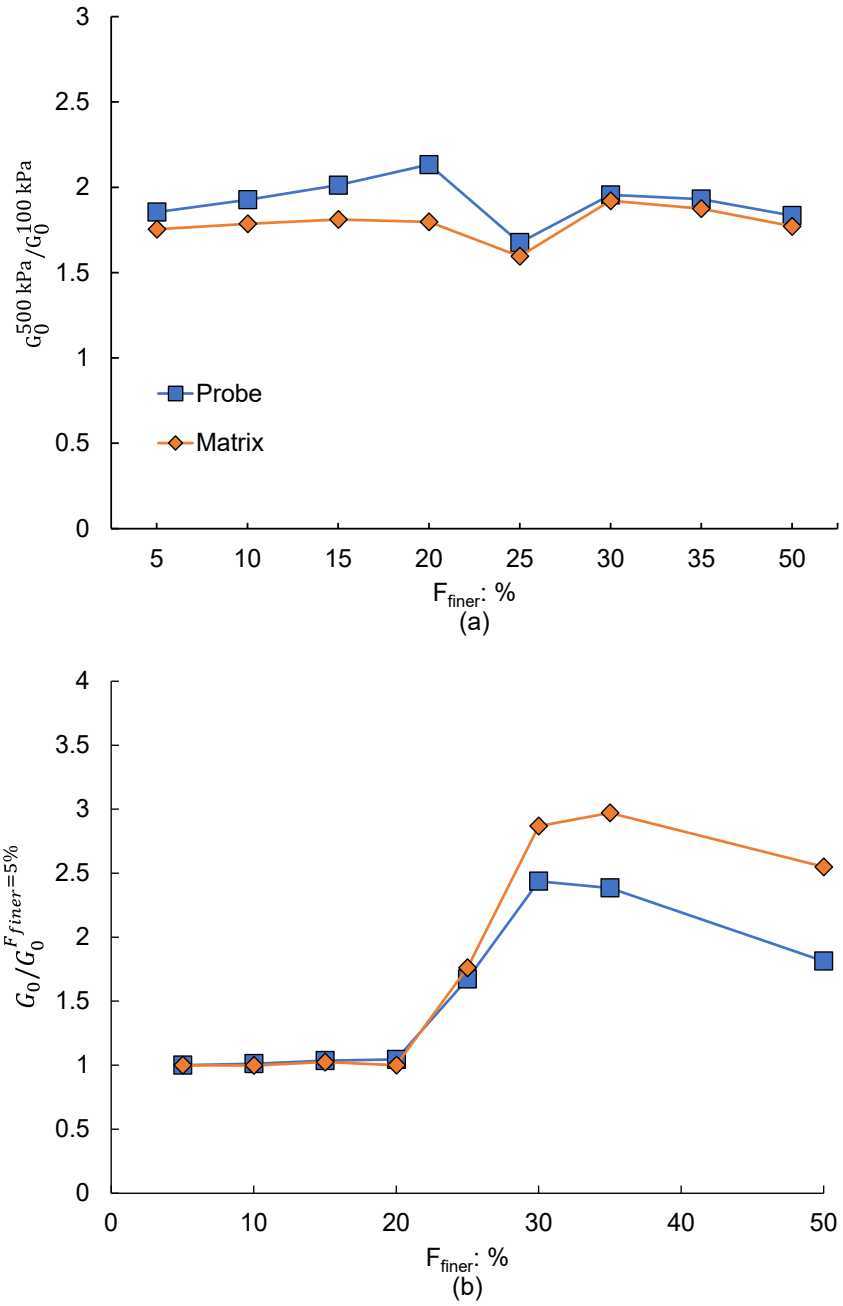


Figure 6.23: Comparison of G_0 values obtained using probes and using the stiffness matrix methods for bimodal gap-graded soils in the medium condition: (a) $G_0^{500\ kPa}/G_0^{100\ kPa}$ versus F_{finer}; (b) $G_0^{F_{finer}}/G_0^{F_{finer}=5\%}$ versus F_{finer}

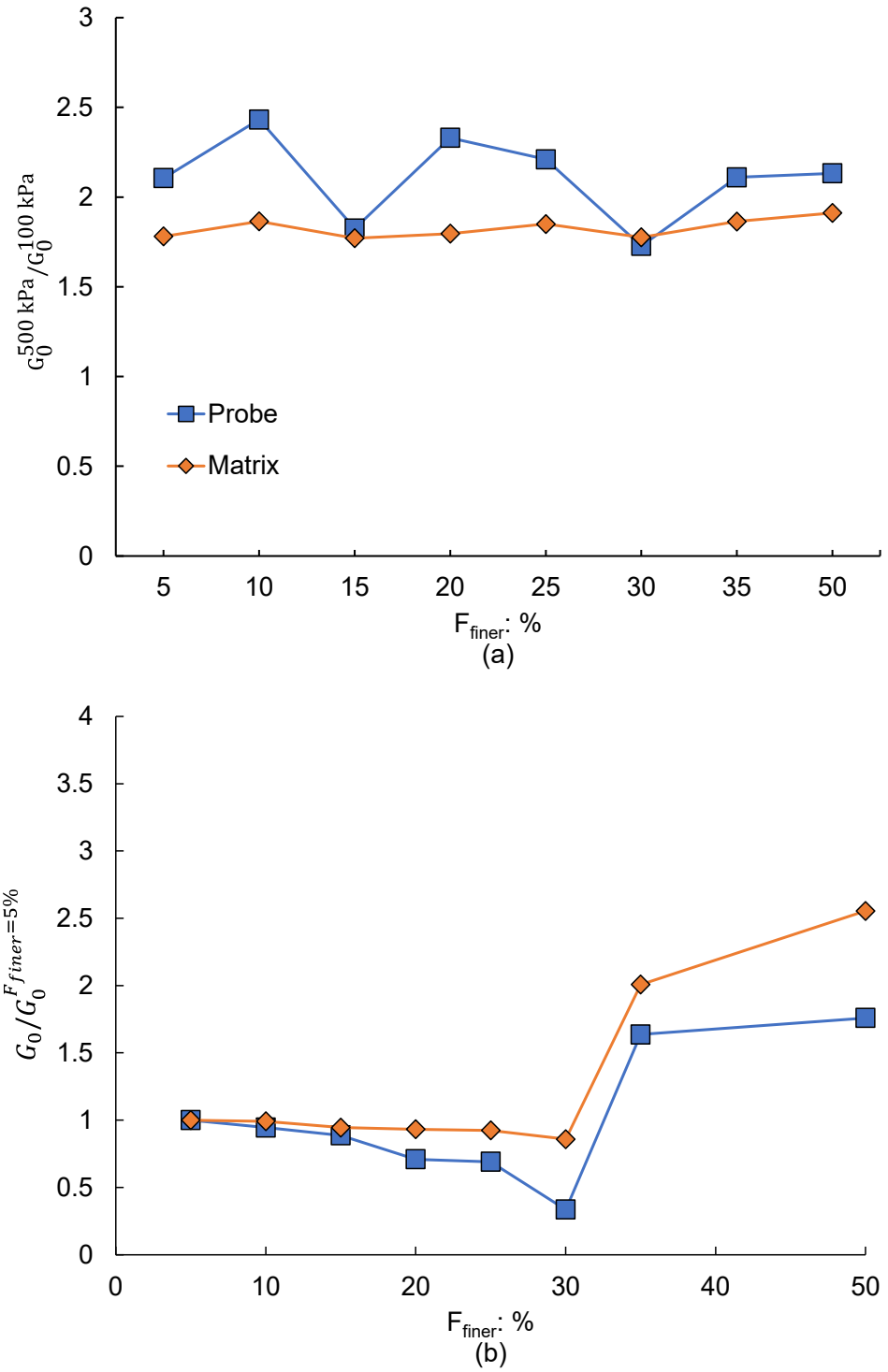


Figure 6.24: Comparison of G_0 values obtained using probes and using the stiffness matrix methods for bimodal gap-graded soils in the loose condition: (a) $G_0^{500\ kPa}/G_0^{100\ kPa}$ versus F_{finer}; (b) $G_0^{F_{finer}}/G_0^{F_{finer}=5\%}$ versus F_{finer}

6.5.5. Heterogeneity of stress amongst particles

Figure 6.25(a) shows the $PSDs$ for all the linear specimens considered, where the particle diameter is normalized by the maximum particle size, i.e. d^p/d^p_{Max}. Developed by adopting Equation 6.6, Figure 6.25(b) shows the cumulative distribution of the contribution of each particle to the mean macro-scope or overall effective stress, PSD^{stress}. The similarity in the shapes of the PSD^{stress} and the PSD suggests that the fraction of the overall effective stress transmitted by each individual grain is proportional to the particle volume. This result has already been presented and discussed in Chapter 5. Adopting Equation 6.8, Figure 6.25(c) presents the cumulative distribution of the contribution of each contact to the macro-scale mean effective stress (σ'_{ij}) as a function of the branch vector length normalised by the maximum branch vector identified for the relevant simulation, $|l^c|/|l^{pc}_M|$, CSD^{stress}. Again, the shape of the CSD^{stress} and the PSD is similar for each specimen considered here. Using Equation 6.23, the cumulative distribution of the contribution of each contact to the overall stiffness is presented in Figure 6.25(d), this distribution is denoted $CSD^{stiffness}$. It can be seen that the shape of the $CSD^{stiffness}$ is similar to the shape of the corresponding CSD^{stress}, which suggests that the contribution of each contact to the overall specimen stiffness is proportional to its contribution to the overall stress. These data also indicate that the contribution of each particle to the overall stiffness may be proportional to the proportion of the total volume of particles it occupies. This may be a feature of specimens with a continuous particle size distribution. Similar trends are observed in both the medium and loose conditions, respectively, as illustrated in Figure 6.26 and Figure 6.27. The effect of density is not evident for linear specimens.

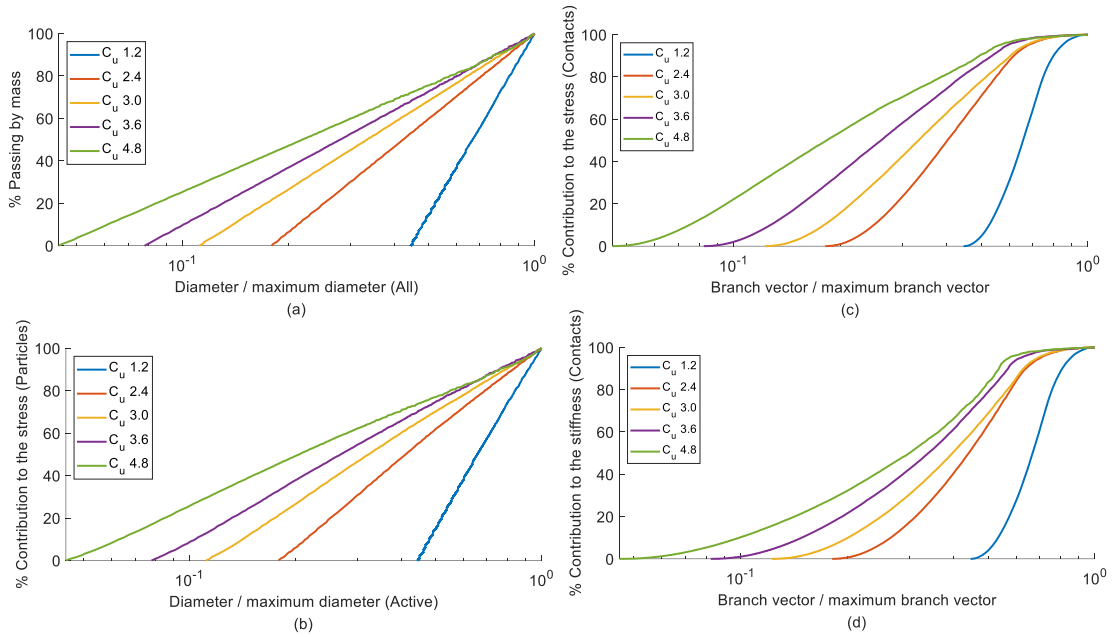


Figure 6.25: Key cumulative distribution data for linear specimens in the densest condition: (a) PSD plots; (b) PSD^{stress} plots; (c) CSD^{stress} plots; (d) $CSD^{stiffness}$ plots

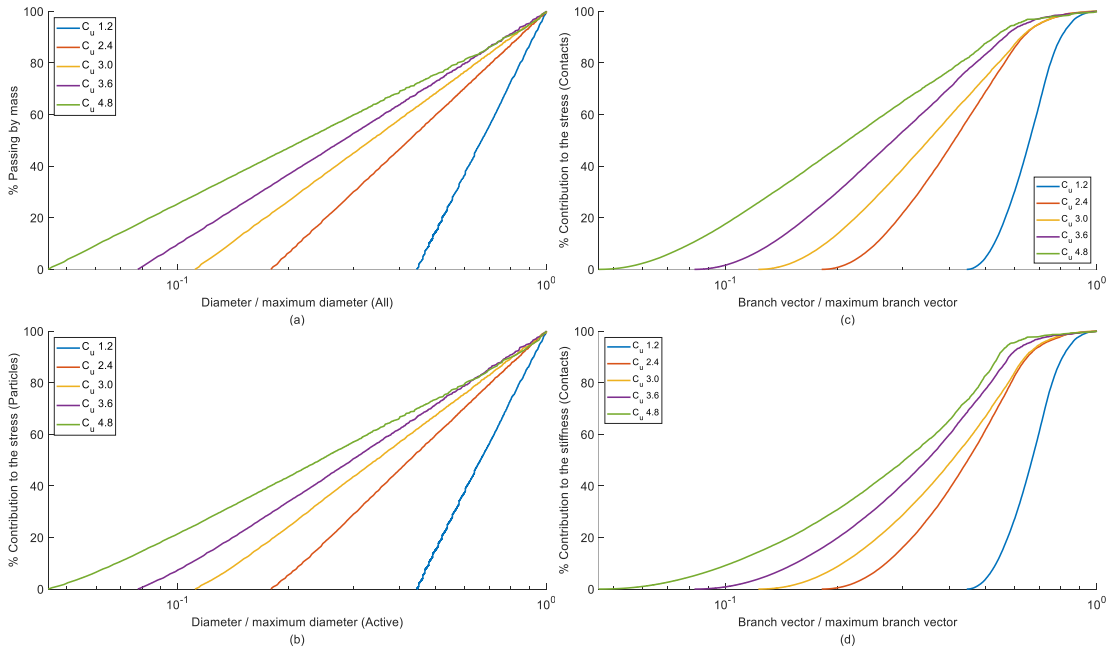


Figure 6.26: Key cumulative distribution data for linear specimens in the medium-dense condition: (a) PSD plots; (b) PSD^{stress} plots; (c) CSD^{stress} plots; (d) $CSD^{stiffness}$ plots

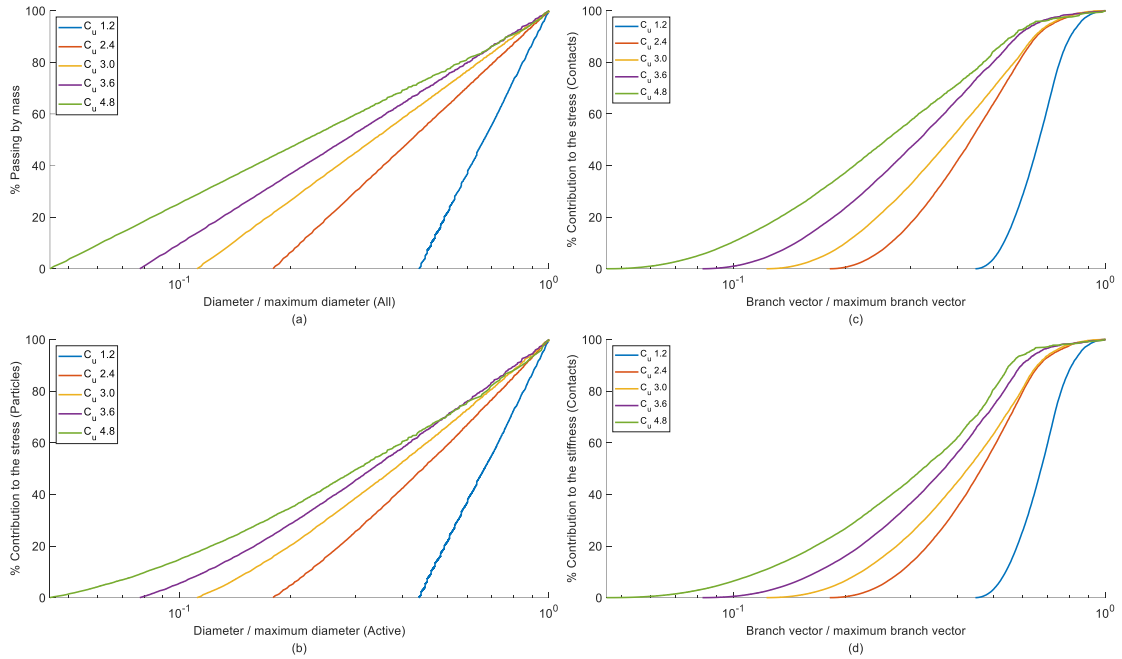


Figure 6.27: Key cumulative distribution data for linear specimens in the loosest condition: (a) PSD plots; (b) PSD^{stress} plots; (c) CSD^{stress} plots; (d) $CSD^{stiffness}$ plots

Data equivalent to those shown in Figure 6.25 are presented in Figure 6.28 for the gap-graded specimens in the dense condition. Figure 6.28(a, b, c&d) present the results for the SR of 3.7, while Figure 6.28(e, f, g&h) show the results for the SR of 8.4. The contribution of the contacts in each of the three sub-networks in a bimodal specimen can also be isolated. As illustrated in Figure 6.29, Figure 6.29(a) and (b) shows that for the SR of 3.7, the stiffness transferred by the $F-F$ contacts is negligble when $F_{finer} \leq 15\%$, and subsequently increases with increasing F_{finer}, while the stiffness transferred by the $C-C$ contacts decreases with increasing F_{finer}. In contrast, the stiffness transferred by the $C-F$ contacts increases significantly and reaches approxmately 65% when F_{finer} is 50%. For the SR of 8.4 (Figure 6.29(c&d)), a different behaviour can be observed when $F_{finer} \leq 20\%$, where both the $F-F$ contacts and the $C-F$ contacts have a negligible contribution to the overall stiffness at all packing densities. Figure 6.29(c) and (d) also indicates that the $C-F$ contacts have a contribution of 80% to the overall stiffness when F_{finer}

is approximately 50%. These stiffness distribution data clearly indicates that different contact groups make distinct contributions to the stiffness, which again supports the idea that the particle scale stress distribution may significantly affect the macro-scale stiffness of gap-graded soils. Therefore, these data support a critical analysis of whether Z_m and e_m are appropriate parameters to consider the stiffness of gap-graded soils, since these two parameters (Z_m and e_m) consider all active contacts and grains to be equivalent.

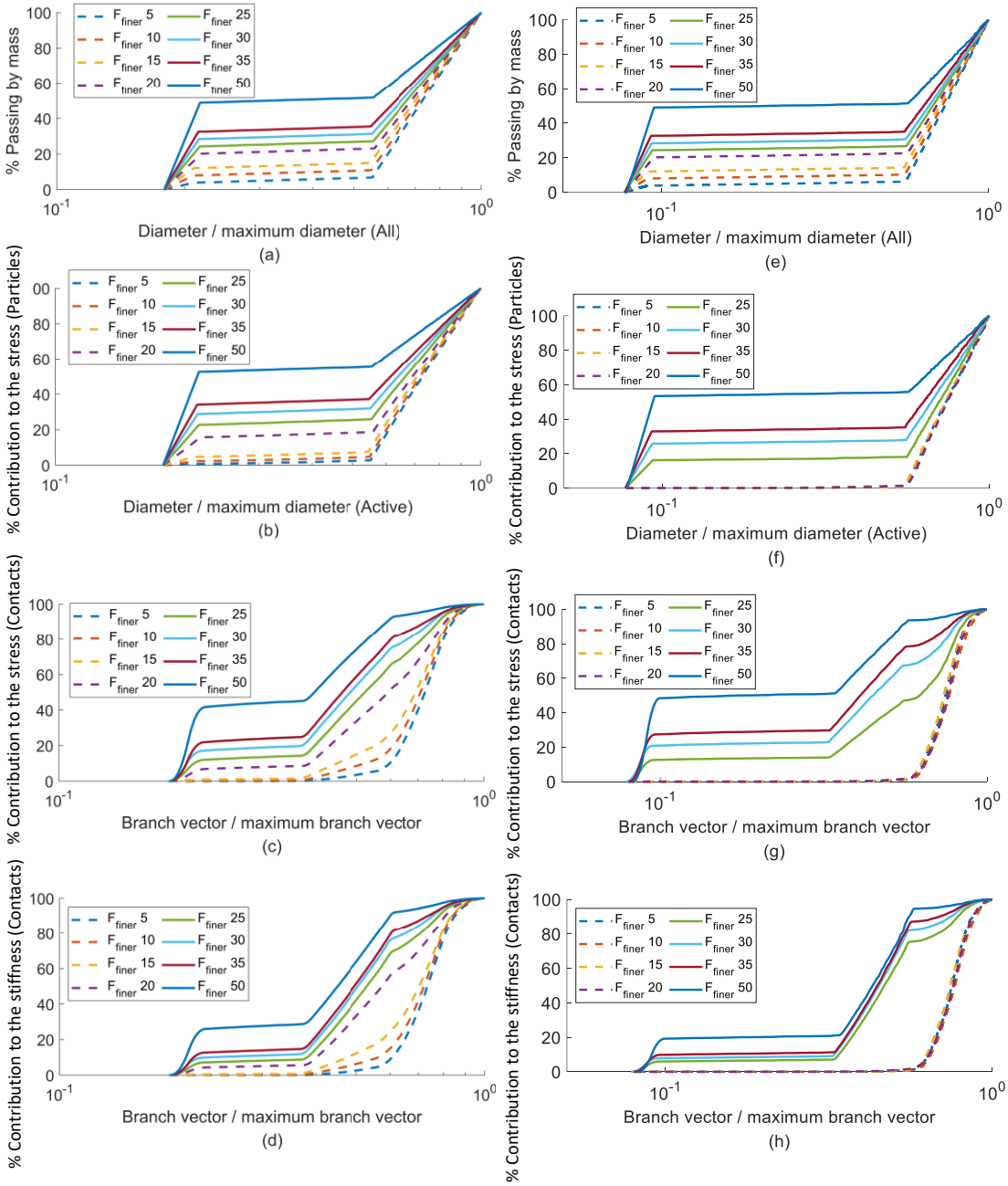


Figure 6.28: Typical results for bimodal specimens in the densest condition: (a) PSD plots considering all particles (SR = 3.7); (b) PSD^{stress} plots (SR = 3.7); (c) CSD^{stress} plots (SR = 3.7); (d) $CSD^{stiffness}$ plots (SR = 3.7); (e) PSD plots considering all particles (SR = 8.4);(f) PSD^{stress} plots (SR = 8.4);(g) CSD^{stress} plots (SR = 8.4); (h) $CSD^{stiffness}$ plots (SR = 8.4)

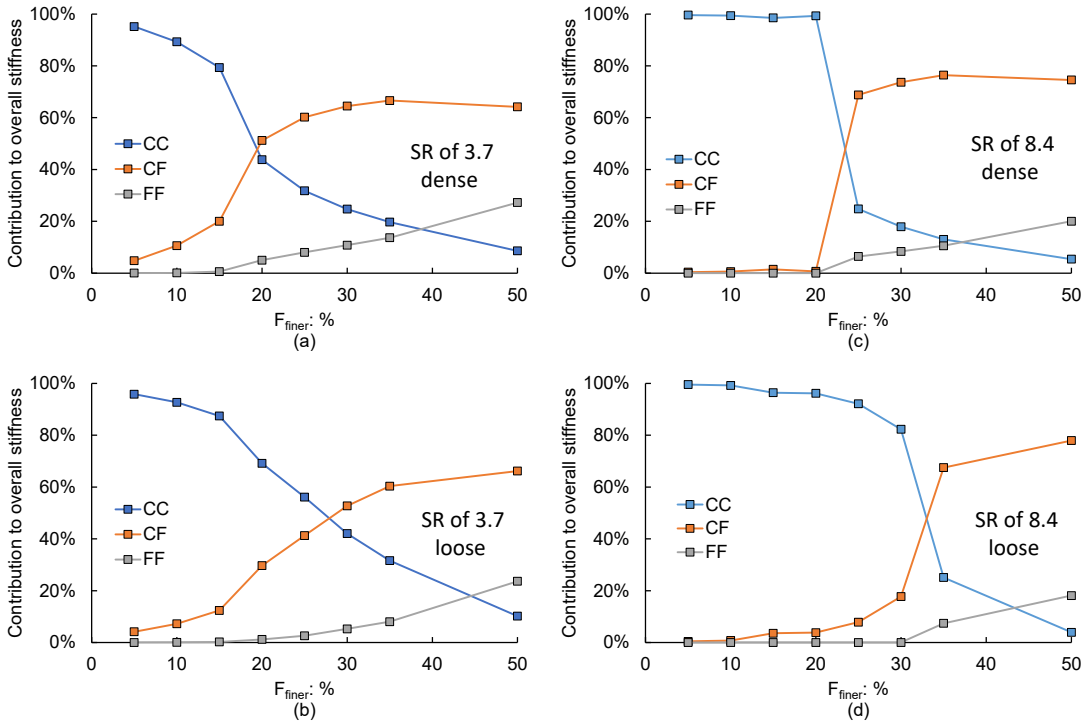


Figure 6.29: Variation in contribution of different contact types to overall stiffness for typical bimodal specimens when p' = 500 kPa: (a) SR = 3.7 in the dense condition; (b) SR = 3.7 in the loose condition; (c) SR = 8.4 in the dense condition; (d) SR = 8.4 in the loose condition

The results observed in the medium and loose conditions are also presented in Figure 6.30 and Figure 6.31, respectively. As previously reported in Chapter 5, the PSD^{stress} and CSD^{stress} data have a density dependence, especially for the F_{finer} of 20% and 25%. Moreover, it can be seen that $CSD^{stiffness}$ is also significantly affected by the effect of density. For instance, when F_{finer} is 25% in the dense condition, approximately 10% stiffness is carried by these $F-F$ contacts. In contrast, when referring to the loose condition, negligible stiffness is transferred by the $F-F$ contacts.

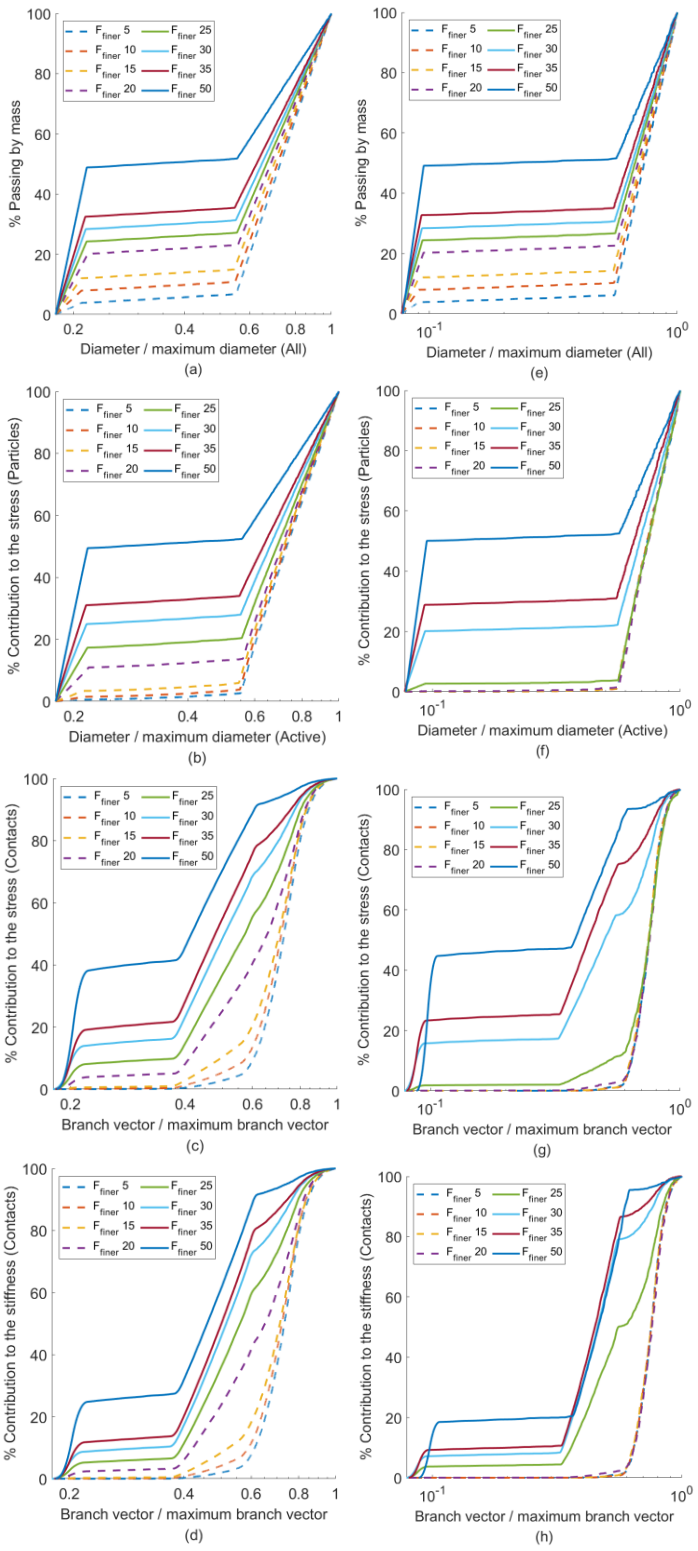


Figure 6.30: Typical results for bimodal specimens in the medium condition: (a) PSD plots considering all particles (SR = 3.7); (b) PSD^{stress} plots (SR = 3.7); (c) CSD^{stress} plots (SR = 3.7); (d) $CSD^{stiffness}$ plots (SR = 3.7); (e) PSD plots considering all particles (SR = 8.4);(f) PSD^{stress} plots (SR = 8.4);(g) CSD^{stress} plots (SR = 8.4); (h) $CSD^{stiffness}$ plots (SR = 8.4)

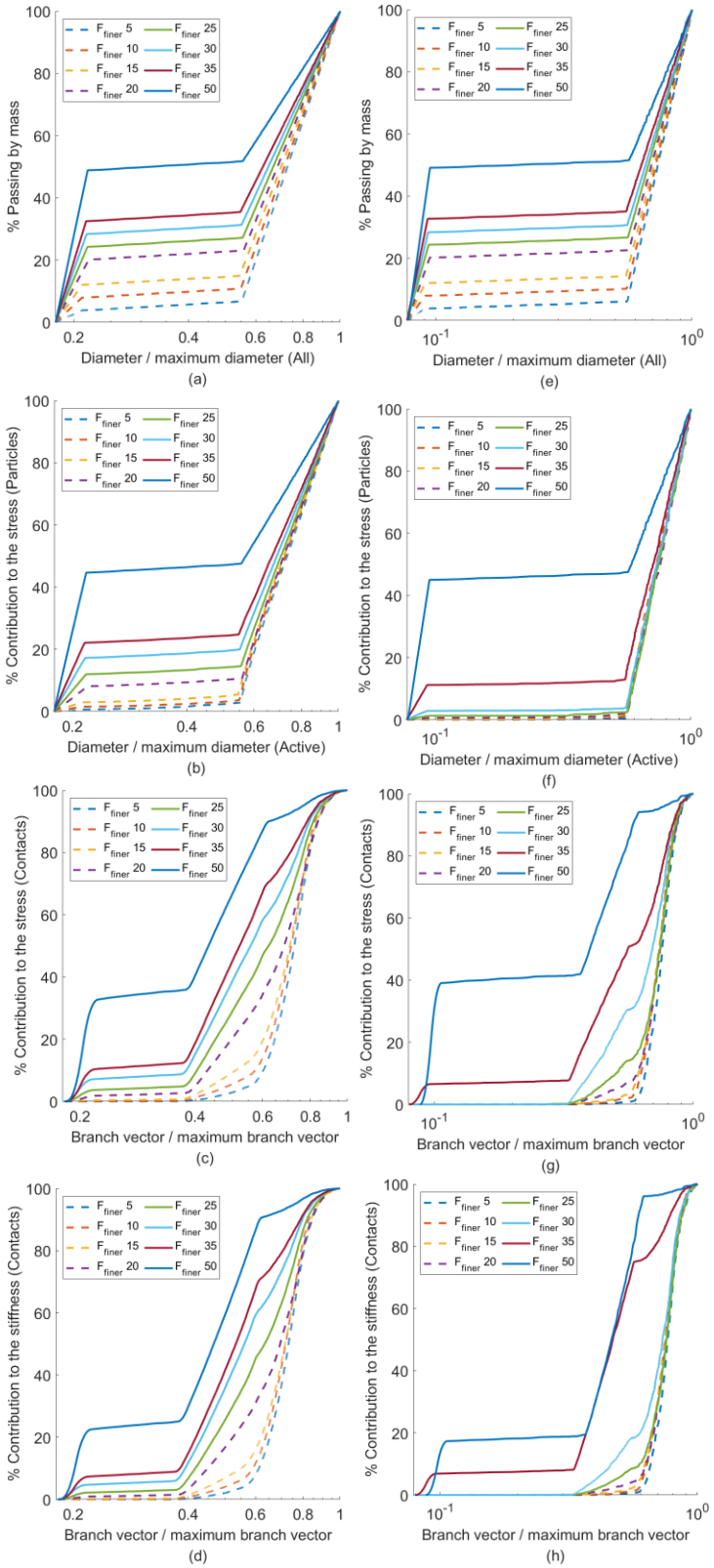


Figure 6.31: Typical results for bimodal specimens in the loosest condition: (a) PSD plots considering all particles (SR = 3.7); (b) PSD^{stress} plots (SR = 3.7); (c) CSD^{stress} plots (SR = 3.7); (d) $CSD^{stiffness}$ plots (SR = 3.7); (e) PSD plots considering all particles (SR = 8.4);(f) PSD^{stress} plots (SR = 8.4);(g) CSD^{stress} plots (SR = 8.4); (h) $CSD^{stiffness}$ plots (SR = 8.4)

6.5.6. A new measure of state that accounts for stress heterogeneity

As discussed before, active finer and coarse particles are considered equivalent in the calculation of e_m, and this approach may not be effective when predicting the stiffness of soil mixtures including bimodal materials. A semi-empirical method was therefore proposed to improve the performance of mechanical void ratio, e_m by weighting the contribution of each particle by the proportion of the overall stress it transmits. The stress reduction α proposed in Shire et al. (2014) was used to develop this weighting. This parameter α is detailed in Chapter 2. In general, when the contribution of the finer fraction is lower than its volume fraction, the α_f can be used to scale the contribution of the volume of the active finer fraction to the overall volume of active particles, as shown below:

$$p'_{finer} = \alpha_f p' \tag{6.25}$$

$$p'_{finer} = \frac{(1-n_p)}{\sum_{N_{p,finer}} V^a} \sum_{a=1}^{N_{p,finer}} (p^a V^a) \tag{6.26}$$

$$e_\alpha = \frac{V_t - (V_c + \alpha_f V_f)}{(V_c + \alpha_c V_f)} \tag{6.27}$$

The p'_{finer} is the effective stress transferred by the finer fraction, the n_p is specimen porosity, $N_{p,finer}$ is the number of active finer particles. p^a is the stress of the particle a, V^a is the particle volume of a. The V_t is the total volume of specimen, the V_c is the volume of active coarse grains, the V_f is the volume of active finer grains.

The e_α parameter acknowledges that the proportion of stress transferred by the finer fraction is smaller than its volume fraction when $\alpha_f \leq 1$. In contrast, when $\alpha_f \geq 1$, the stress contribution of coarse fraction is lower than its volume fraction as α_c can be calculated as:

$$p'_{coarse} = \alpha_c p' \quad 6.28$$

$$p'_{coarse} = \frac{(1-n_p)}{\sum_{N_{p,coarse}} V^a} \sum_{a=1}^{N_{p,coarse}} (p^a V^a) \quad 6.29$$

For this situation, α_c can be used to amend the volume of the active coarse fraction.

$$e_\alpha = \frac{V_t - (\alpha_c V_c + V_f)}{(\alpha_c V_c + V_f)} \quad 6.30$$

Figure 6.32(a) and (b) show the variation in α_f and α_c with F_{finer} for SRs = 3.7 and 8.4, respectively. When SR = 3.7, the α_f values remain approximately equal to 0.25 when $F_{finer} \leq 20\%$. In contrast, when SR is 8.4, the α_f values are close to 0 when $F_{finer} \leq 20\%$; this observation holds for SR values of 14.5 and 18.1. As F_{finer} increases, the α_f values increase slightly and reach a peak value of approximately 1 when F_{finer} is approximately 50%. The α_c values are also presented in Figure 6.32, for instance, in the dense condition, when F_{finer} is 35% and 50%, the stress transferred by the coarse fraction is lower than its volume fraction, the α_c rather than α_f is then presented.

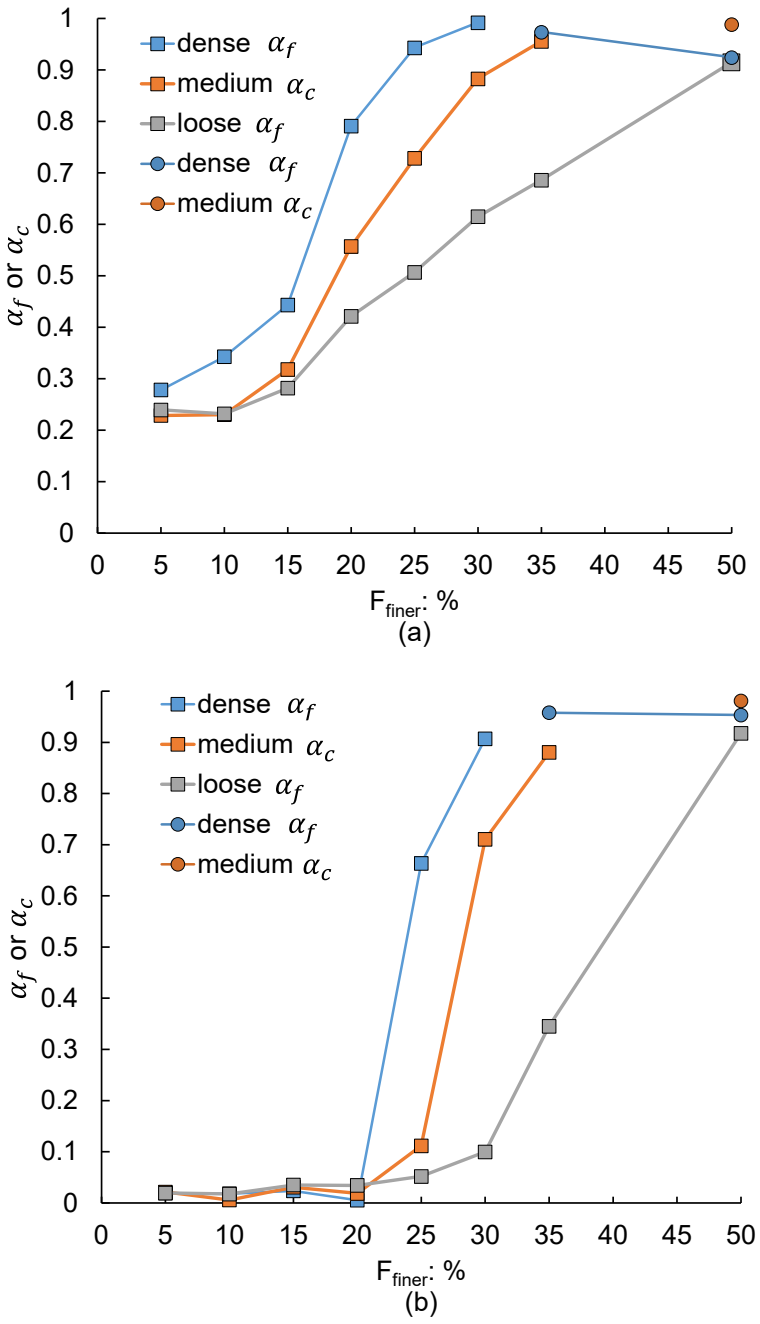


Figure 6.32: Particle scale stress distribution: (a) Stress reduction factors with increasing F_{finer} (SR = 3.7); (b) Stress reduction factors with increasing F_{finer} (SR = 8.4)

Figure 6.33 illustrates the variation in G_0 with e_α for all the specimens with SR = 8.4 at the σ_3' of 500 kPa, the correlation can be approximated relatively well by a straight line with $R^2 \approx 0.91$. In contrast, the correlations were relatively weaker when e ($R^2 \approx 0.27$) and e_m ($R^2 \approx 0.80$) were considered. Besides, the use of e_α shows better performance even compared to that when $Z_m/(1+$

e_m) is employed (i.e. $R^2 \approx 0.87$). Figure 6.33 also supports the assumption that the distribution of the overall stress amongst the different size fractions may directly affect the macro-scale stiffness of soil mixtures.

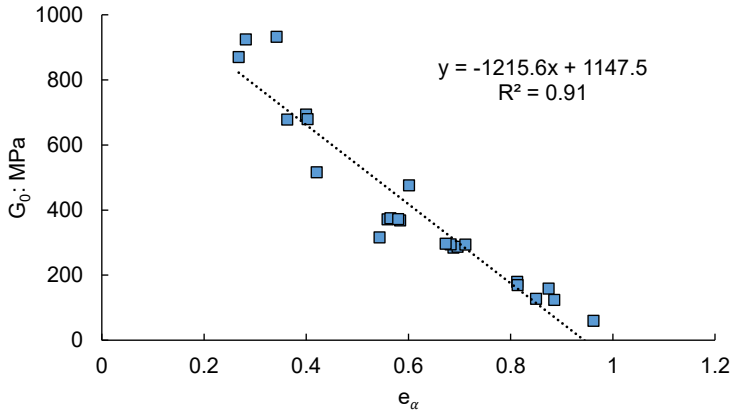


Figure 6.33: Performance of e_α for bimodal specimens (SR = 8.4; p'= 500 kPa)

Figure 6.34 presents the best fit surface defined using Hardin's equation and taking e_α as the measure of state when $SR = 8.4$; the R^2 value obtained was 0.95. As before, the n value is fixed to 0.33, based on the use of smooth elastic spheres. The e_α shows better performance and provides a potential way to find a unified characterisation of G_0 for soil mixtures.

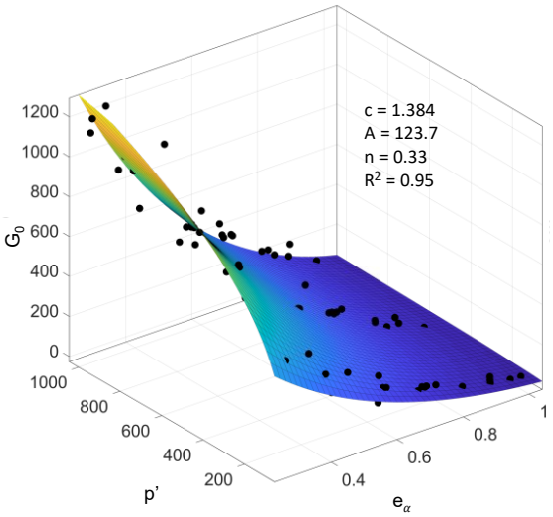


Figure 6.34: Optimal surface as described using Hardin's equation with e_α as the measure of state (SR = 8.4)

Data for all the bimodal specimens were also unified to assess whether a single set of parameters for Hardin's equation can be used to describe the variation in G_0 with both state and stress levels. The data presented in Figure 6.35 consider DEM specimens with four SR values (i.e. 3.7, 8.4, 14.5, 18.1) and three values of p'. Figure 6.35(a) shows that when a surface fit is attempted using e as the measure of state, no single, unified relationship is evident. This again confirms that the e cannot be used to predict G_0 for gap-graded soils. In contrast, Figure 6.35(b) presents the performance of e_α and it can be seen that relatively good performance is observed with the R^2 value being approximately 0.95. This result shows that e_α is a viable measure of state, which when variations in stress level are accounted for, correlates strongly with G_0.

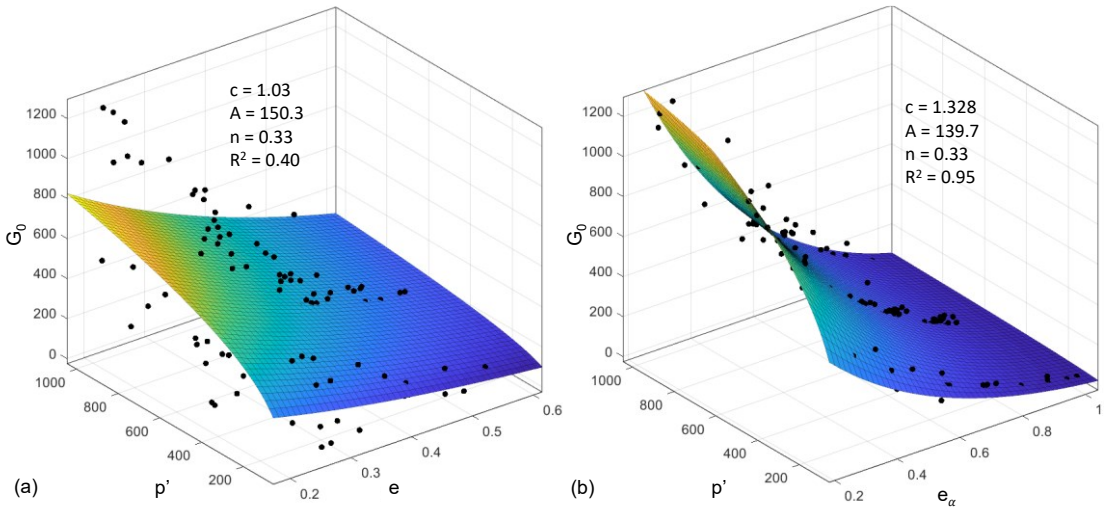


Figure 6.35: Performance of state variables as assessed by fitting the surface defined by Hardin's equation to all the bimodal specimen data: (a) Use of e as the measure of state; (b) Use of e_α as the measure of state.

Figure 6.36(a) presents the relationship between e_α and $Z_m/(1+e_m)$ for all the bimodal and trimodal specimens, a relatively linear fitting is identified with the R^2 value being approximately 0.92. To estimate e_α for the trimodal specimens, the volumes of the active coarse and intermediate fractions are combined. Although both Z_m and e_m do not weight the contribution of each

particle, the combination of $Z_m/(1+e_m)$ may restrain this limitation and then could be the potential state variable for gap-graded soils.

Figure 6.36(b) presents the surface fitting considering all the bimodal and trimodal gap-graded specimens using e_α as the state variable in Equation 2.11. Again, a relatively good performance can be identified, least squares regression can identify values of A and c that give a high R^2 value (i.e. 0.94), which again shows that e_α may allow a unified expression to be used to link state and stiffness across a range of $PSDs$ that are mixtures.

Although the parameters, e_m, Z_m, e_α cannot be directly quantified in conventional soil mechanics experiments, the current DEM simulations do have some implications for experimental studies of gap-graded soils. Firstly, the current results clearly illustrate that the global void ratio, e, cannot be considered as an appropriate state variable to study the soil mixtures in a unified way. A large number of inactive particles can be identified in soil mixtures. Furthermore, the efficiency of e decreases when density changes from the dense to the loose condition, which suggests correlations relating e and G_0 are less effective for loose specimens. Prior attempts to find a state variable to describe the behaviour of soil mixtures assumed that an appropriate state variable should be strongly associated with F_{finer} and SR, while the effect of packing density was always ignored. In contrast, this study indicates that the appropriate state variable should take the effect of packing density into account.

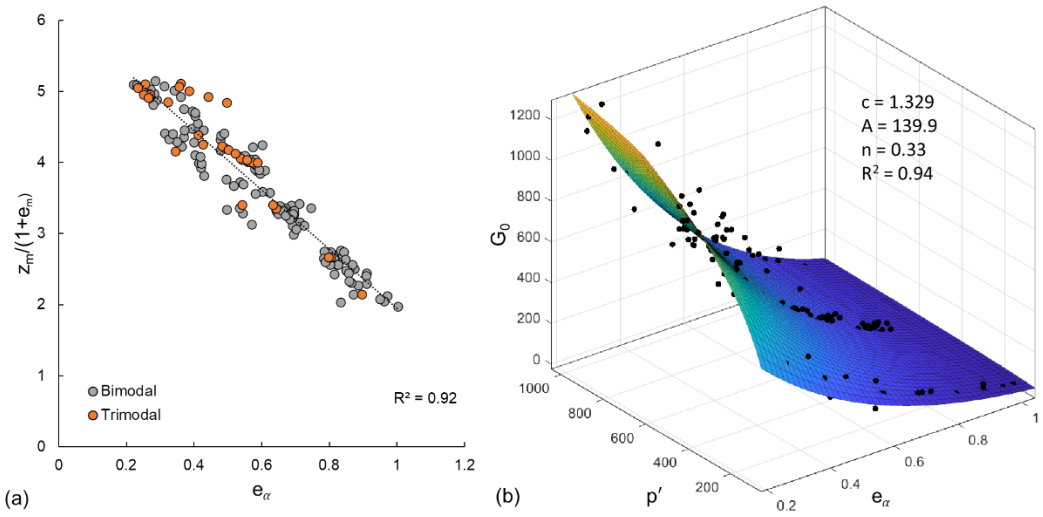


Figure 6.36: Performance of e_α for all bimodal and trimodal specimens: (a) $Z_m/(1+e_m)$ versus e_α (b) The use of e_α

6.5.7. Perspective

Although the current study indicates that the global void ratio, e is not able to describe the stiffness behaviour of a soil mixture in a unified way, it may be useful to examine the strength of a correlation with e for a specific F_{finer}, since only the global void ratio can be measured in experiments. For the specimens with SR = 8.4, the optimal value of A for use in Hardin's equations was determined using e as the measure of state for each F_{finer} value considered here. To constrain the optimization the value of c was fixed to be 1.28 following Otsubo & O'Sullivan (2018) for similar spherical particles. The fitted A values decrease with increasing F_{finer} until the $F_{finer} = 25\%$. This trend agrees with data presented in prior studies (e.g. Yang et al., 2018; Liu & Yang, 2018). However, the A values increase again when $F_{finer} > 25\%$. In addition, poor fitting performance can be observed when $25\% \leq F_{finer} \leq 35\%$, over this range of finer fractions, we know the nature of the distribution of stress between the coarse and finer fractions is highly sensitive to the density level. A clear soil fabric change can occur over this range of F_{finer} values so that an underfilled specimen can become overfilled when the packing density changes from being loose to being dense. The global void ratio cannot capture this soil fabric

change. However, the loose condition with underfilled soil fabric may not be easily identified in the experiments. For experimental tests, where only the global void ratio can be estimated, it may be feasible to employ Hardin's equation for changing F_{finer} with their corresponding A values.

Table 6.1: The fitting results within the Hardin's equation

F_{finer}	c	A	R^2
0	1.28	160.5	0.9524
5	1.28	98	0.908
10	1.28	79.32	0.86
15	1.28	66.11	0.8741
20	1.28	43.6	0.7357
25	1.28	88.49	0.4286
30	1.28	88.6	0.2673
35	1.28	105.8	0.6129
50	1.28	107.7	0.773

6.6. Analysis of data for cuboidal specimens

As shown in Chapter 4, the bulk density calculated considering all particles, ρ, may differ significantly from the bulk density calculated considering only the active particles, ρ_m. This difference may affect the estimation of G_{dyn}. If assuming that G_{sta} is strongly associated with G_{dyn} when all particles are equivalent in stress transmission, the comparison of G_{sta} and $G_{dyn}(e)$ may enable assessment of the difference between e and e_m, ρ and ρ_m and therefore the proportion of inactive stress-transmitting particles in the tested specimens. It can be seen that one of the advantages of this method is that the values required for quantifying these inactive particles (i.e. G_{sta} and $G_{dyn}(e)$) can be directly measured in the experimental study.

6.6.1. Void ratio and coordination number

Figure 6.37(a) and (b) illustrate the variation of e with the PSD for the dense

and loose specimens simulated in the mixed-boundary simulations considering linear and bimodal gap-graded soils (SR = 8.0), respectively. Both the e measured in the dense condition (i.e. the lowest e) and in the loose condition (i.e. the highest e) decrease with increasing C_u, which is similar to the observation identified in Youd (1973) and the results observed for periodic specimens. The minimum void ratio for randomly packed monodisperse spheres is 0.570 (Torquato et al., 2000), which is also close to the lowest e for the specimen with C_u = 1.2. Figure 6.37(b) shows that both the lowest and highest e decrease to a global minimum when F_{finer} is approximately 25%, followed by a gradual increase as F_{finer} increases. These trends agree with the experimental results summarized in Zuo & Baudet (2015) for bimodal gap-graded soils.

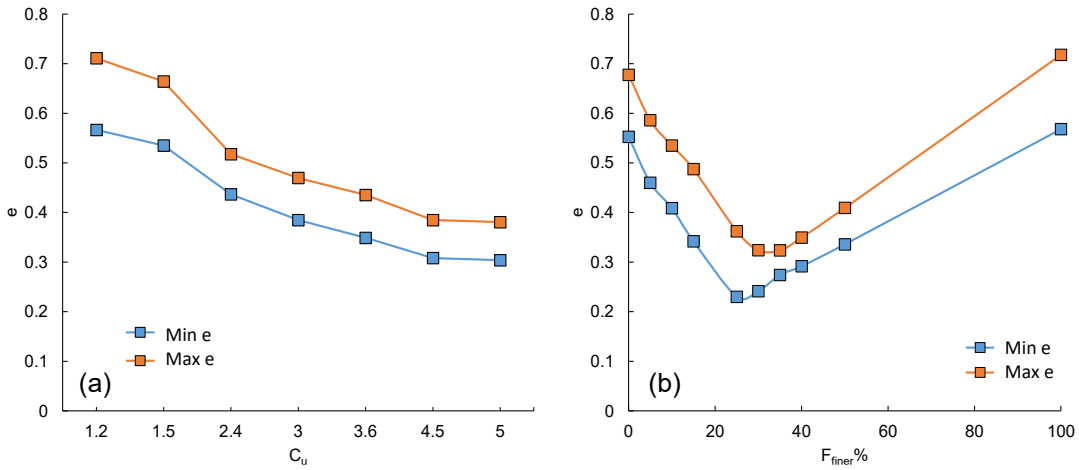


Figure 6.37: The variation of e (p' = 500 kPa): (a) e versus C_u; (b) e versus F_{finer} (SR = 8.0)

6.6.2. State-dependent soil behaviour

The state-dependent behaviour observed for the linear specimens is in line with our expectation of soil behaviour. Figure 6.38(a) shows that for each C_u considered, there is a correlation between G_{sta} and e and similar correlations are observed between $G_{dyn}(e)$ and e (Figure 6.38(b)). However, as before, no single correlation can be identified between all the G_{sta} or $G_{dyn}(e)$ and e.

In contrast, Figure 6.38(c) again indicates that the use of e_m unifies the data to give a single correlation between $G_{dyn}(e_m)$ and e_m, albeit with a R^2 value of approximately 0.73 for a best-fit linear regression. Similarly, for the gap-graded soils, the state-dependency of G_{sta} and $G_{dyn}(e)$ is clear; data for the specimens with $SR = 8$ are presented in Figure 6.38(d&e). Figure 6.38(f) shows that when $G_{dyn}(e_m)$ is plotted against e_m, there is a clearer correlation (R^2 value of 0.81 for linear regression). e_m shows better performance in describing the contribution of the soil state to the small-strain stiffness of gap-graded soils. While they are not presented here, the data for the specimens with $SR = 14$ are in agreement with the data for the specimens with $SR = 8$. Prior studies (e.g. Otsubo et al., 2021) also found that the correlation between G_0 (which they determined from the dynamic method) and e_m is not exactly linear. As outlined above in relation to the cubic specimens with periodic boundaries. Effective medium theory predicts that both e and Z (or e_m and Z_m) determine G_0. This may also be attributed to the fact that e_m considers that each particle and contact have an equivalent contribution to the overall response. However, this may not be true, especially for gap-graded soils, as shown in Section 6.5.

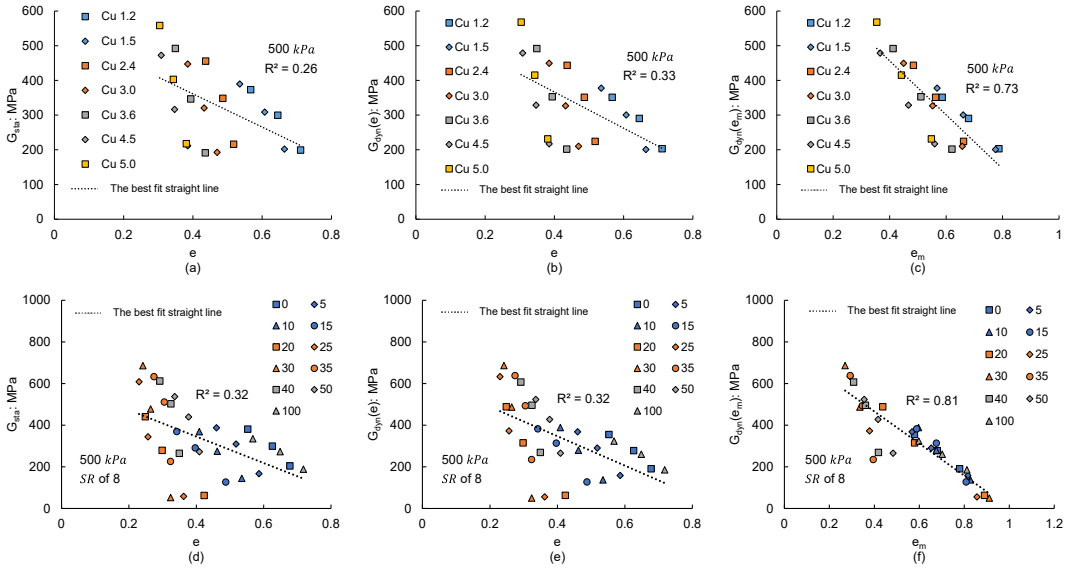


Figure 6.38: Assessment of the performance of various state variables (p' = 500 kPa): for linear specimens (a) G_{sta} versus e; (b) $G_{dyn}(e)$ versus e; (c) $G_{dyn}(e_m)$ versus e_m; for bimodal gap-graded specimens (SR = 8); (d) G_{sta} versus e; (e) $G_{dyn}(e)$ versus e; (f) $G_{dyn}(e_m)$ versus e_m

6.6.3. Comparison between G_{sta} and G_{dyn} and its implication

The G_{dyn} and G_{sta} data are directly compared in Figure 6.39. For the linear specimens (Figure 6.39(a&b)), for all C_u values considered, the $G_{dyn}(e)$ and G_{sta} values differ by less than 10%. The root mean square deviation ($RMSD$) from the 1:1 line was calculated to assess the strength of the proximity of these two calculated stiffnesses. Taking $\hat{y}_i$ to be the predicted value of the independent variable y_i where i indicates the data for a particular sample. If there are m observations of y_i, the square root of the mean of the squares of the deviations is given by $RMSD = \sqrt{\frac{\sum_{i=1}^{m}(\hat{y}_i - y_i)^2}{m}}$. For Figure 6.39(a) the $RMSD$ is approximately 10.7. The relative difference between G_{sta} and G_{dyn} normalised by G_{sta}, $abs(G_{sta} - G_{dyn})/G_{sta}$ is also calculated; the average of these values is approximately 4%, 5%, 8% and 9% for Figure 6.39(a), (b), (c) and (d), respectively. Figure 6.39(b) shows that for each specimen, at all states considered G_{sta} > $G_{dyn}(e_m)$ even though the differences between these two measures of stiffness are relatively small (approximately 5%). All of the data

generated for the gap-graded specimens with $SR = 8$ are presented in Figure 6.39(c&d). As illustrated in Figure 6.39(c), the normalised difference $(G_{sta} - G_{dyn})/G_{sta}$ is neither consistently positive nor negative and is about 10% in magnitude in most cases, however, a greater amount of scatter can be observed for some cases, such as F_{finer} values of 20% and 25%. When e_m is used (Figure 6.39(d)), the G_{sta} data tend to be consistently larger than the equivalent $G_{dyn}(e_m)$ data, which is similar to the linear specimens. However, it can be seen that even when relatively appropriate state variable is used (i.e. e_m), G_{sta} does not exactly equal to its corresponding $G_{dyn}(e_m)$. Both the $RMSD$ data and the $abs(G_{sta} - G_{dyn})/G_{sta}$ data quantitatively show that the G_{sta} and G_{dyn} data agree better for the linear specimens than for the bimodal specimens whether e or e_m is used.

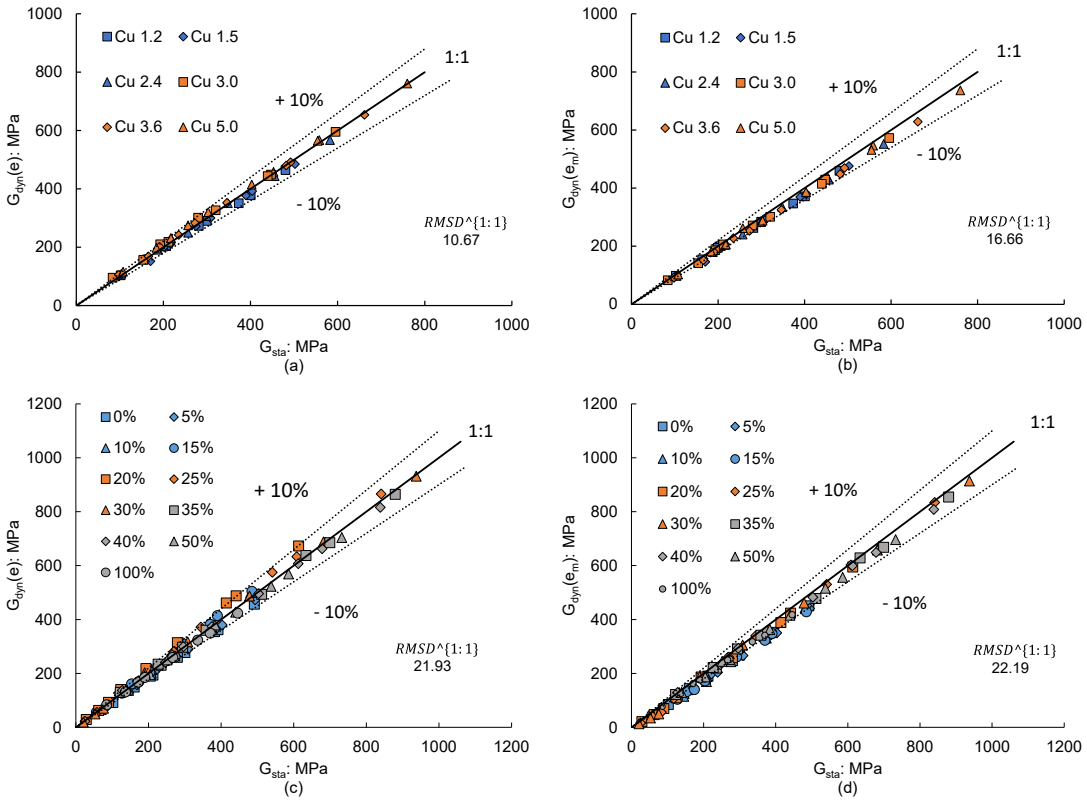


Figure 6.39: Comparison between G_{dyn} and G_{sta} values: for linear specimens (a) $G_{dyn}(e)$ versus G_{sta}; (b) $G_{dyn}(e_m)$ versus G_{sta}; for bimodal gap-graded specimens (SR = 8) (c) $G_{dyn}(e)$ versus G_{sta}; (d) $G_{dyn}(e_m)$ versus G_{sta}

Figure 6.40 considers the variation with C_u of the ratios $G_{sta}/G_{dyn}(e)$ (left vertical axis) and the ratios of e/e_m and ρ_m/ρ (right vertical axis). Figure 6.40(a) considers the dense specimens, while Figure 6.40(b) considers the medium-dense specimens. As C_u increases, both ρ_m/ρ and e/e_m decrease reflecting an increase in the proportion of inactive particles in the specimen. Interestingly, the ratio $G_{sta}/G_{dyn}(e)$ exhibits a similar trend, i.e. it reduces with increasing C_u. Only the $G_{dyn}(e)$ data estimated by global void ratio are considered here as these are the data that can be obtained in physical laboratory experiments.

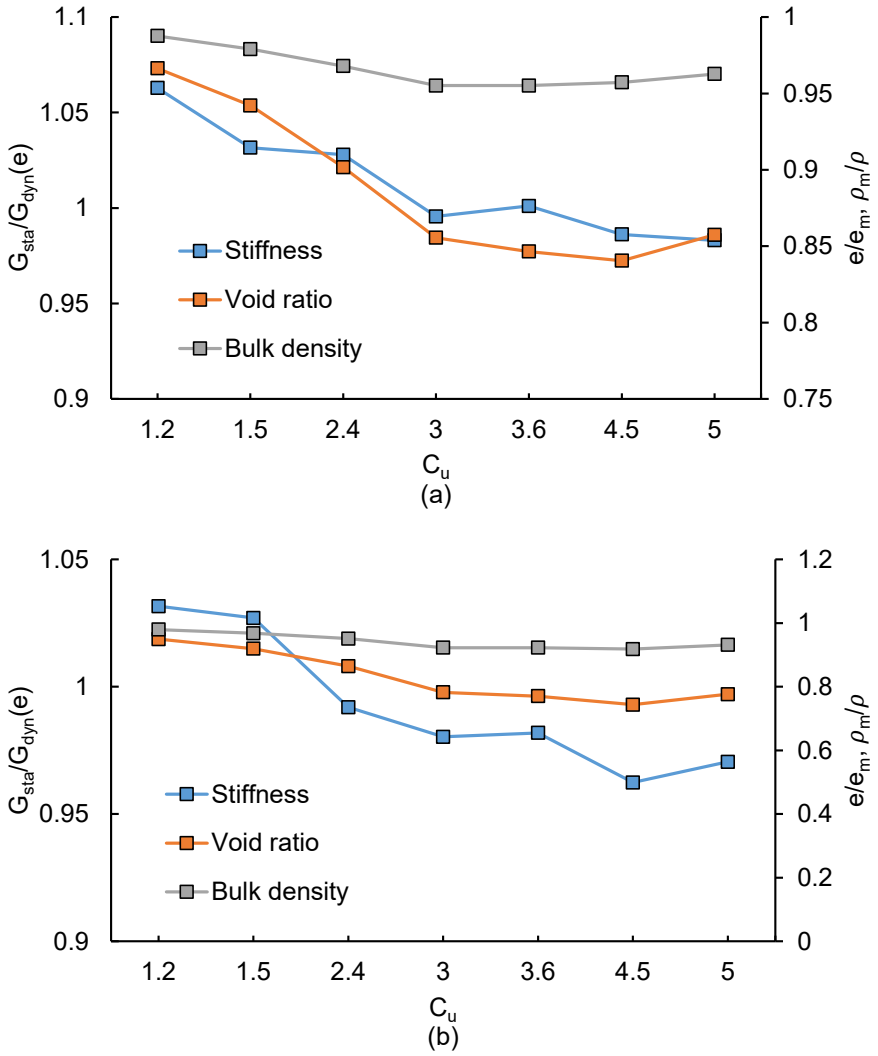


Figure 6.40: The variation of $G_{sta}/G_{dyn}(e)$ (left vertical axis) and e/e_m & ρ_m/ρ (right vertical axis) with increasing C_u: (a) Dense condition; (b) Medium-dense condition

For the linear specimens, the relationships between $G_{sta}/G_{dyn}(e)$ and e/e_m as well as ρ_m/ρ are explored in Figure 6.41(a) and (b), respectively. As e/e_m and ρ_m/ρ approach 1.0, indicating a small proportion of inactive particles, the G_{sta} values approach $G_{dyn}(e)$. The combination of the data in Figure 6.40 and Figure 6.41 support the possibility to use the ratio G_{sta}/G_{dyn} to quantify differences between e and e_m (or ρ and ρ_m) and hence to give an indication of the proportion of inactive stress-transmitting particles.

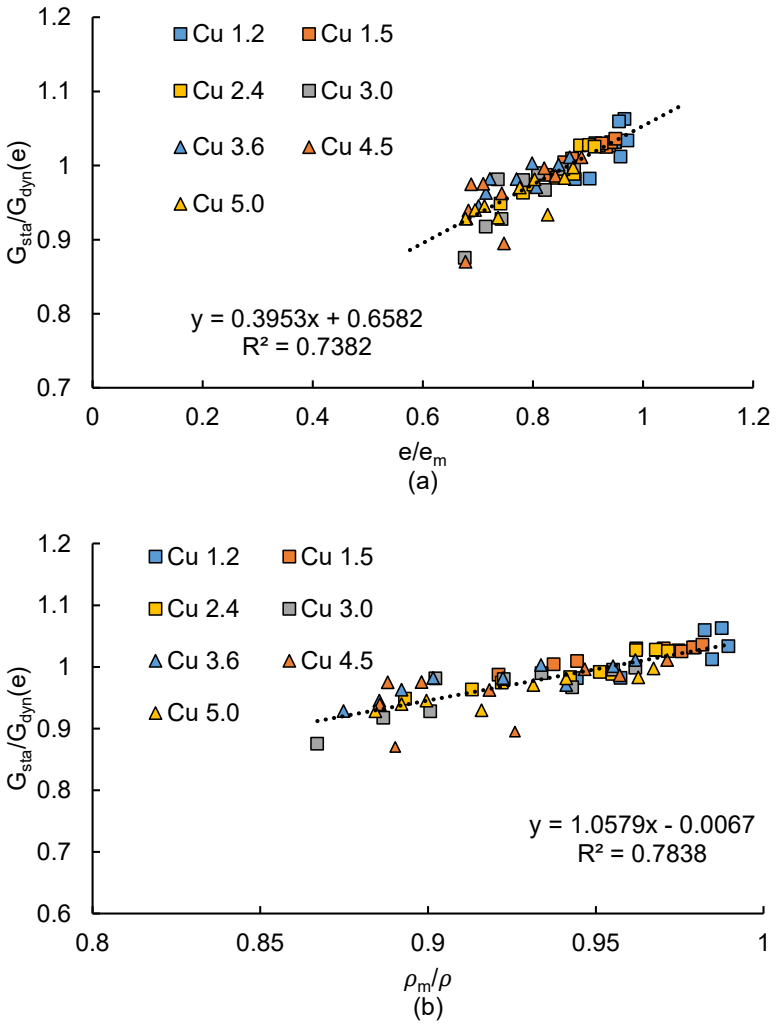


Figure 6.41: The relationship between $G_{sta}/G_{dyn}(e)$ and e/e_m & ρ_m/ρ for linear specimens: (a) $G_{sta}/G_{dyn}(e)$ versus e/e_m; (b) $G_{sta}/G_{dyn}(e)$ versus ρ_m/ρ

The data presented in Figure 6.42(a) and (b) for gap-graded mixtures with

$SR = 8$ (dense and medium-dense conditions) show that the ratio $G_{sta}/G_{dyn}(e)$ systematically varies with F_{finer}; the ratios e/e_m, ρ_m/ρ exhibit very similar trends when they are plotted against F_{finer}. Starting from a specimen comprising only coarse grains, as F_{finer} increases up to 20%, the ratios of e/e_m, ρ_m/ρ and $G_{sta}/G_{dyn}(e)$ all decrease. The differences between ρ and ρ_m suggests that a shortcoming in the use of $\rho(V_s)^2$ to determine G_{dyn} may explain the variation in $G_{sta}/G_{dyn}(e)$ with F_{finer}. As F_{finer} increases beyond 25%, the ratios e/e_m, ρ_m/ρ and $G_{sta}/G_{dyn}(e)$ all gradually increase to attain values that remain approximately constant for $F_{finer} \geq 50\%$.

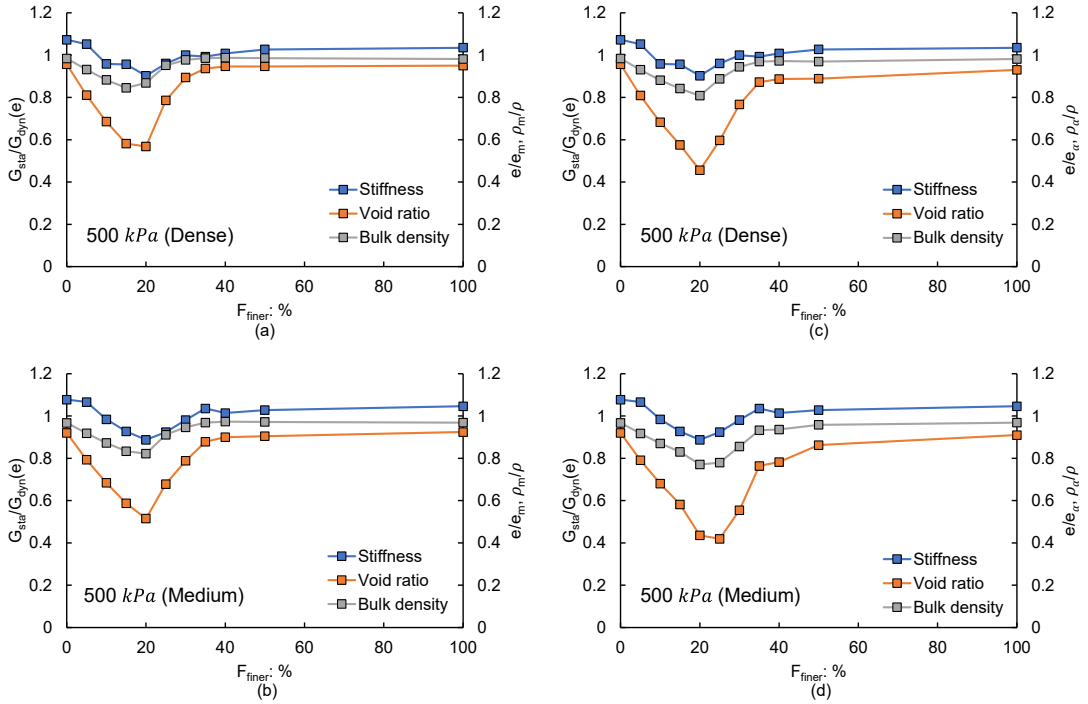


Figure 6.42: Variation in $G_{sta}/G_{dyn}(e)$ with F_{finer} ($SR = 8$; $500\ kPa$): (a) Dense samples, with right axes giving e/e_m and ρ_m/ρ; (b) Medium-dense samples, with right axis giving e/e_m and ρ_m/ρ; (c) Dense samples, with right axes giving e/e_α and ρ_α/ρ; (d) Medium-dense samples, with right axis giving e/e_α and ρ_α/ρ

Figure 6.42(c) and (d) also consider the use of the alternative, semi-empirical state variable e_α which weights the overall contribution of the finer fraction by the proportion of stress this fraction transmits, as presented in Section 6.5.1.

The parameter e_α acknowledges the fact that stress transferred by finer fraction may be significantly lower than its corresponding volume fraction. Figure 6.42(c) and (d) show that the use of e_α gives similar trends to those observed for e_m in Figure 6.42(a) and (b).

The data in Figure 6.43 show that the trends reported in Figure 6.42 for $SR = 8$ also hold for $SR = 14$. Furthermore, comparison of Figure 6.43(a) and (b) as well as comparison of Figure 6.43(c) and (d) show that the results are independent of p'; similar observations are made for p'= 500 kPa and p'= 1000 kPa, respectively.

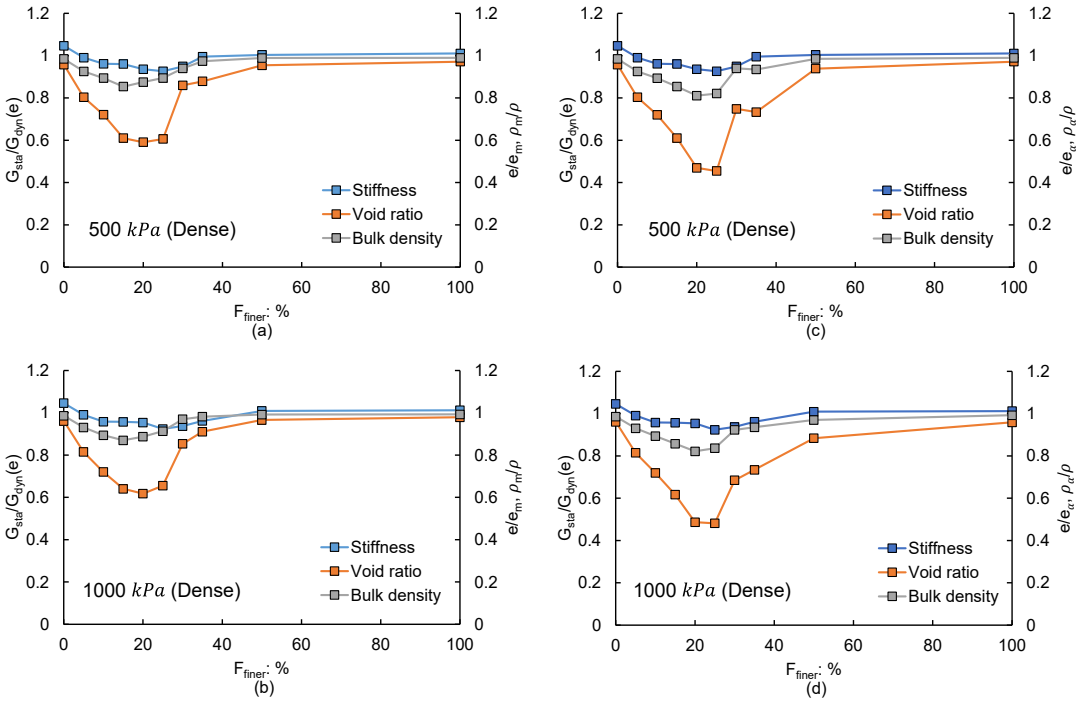


Figure 6.43: The trend of $G_{sta}/G_{dyn}(e)$ with increasing F_{finer} ($SR = 14$; dense): (a) p' of 500 kPa, with right axes giving e/e_m and ρ_m/ρ; (b) p' of 1000 kPa, with right axes giving e/e_m and ρ_m/ρ; (c) p' of 500 kPa, with right axes giving e/e_α and ρ_α/ρ; (d) p' of 1000 kPa, with right axes giving e/e_α and ρ_α/ρ

Figure 6.44 explores a relationship between $G_{sta}/G_{dyn}(e)$ and various ratios of the state variables presented above. As illustrated in Figure 6.44(a) and (b), for $SR = 8$, moderate linear correlations are identified between $G_{sta}/G_{dyn}(e)$

and e/e_m (R^2 = 0.68) and between $G_{sta}/G_{dyn}(e)$ and ρ_m/ρ (R^2 = 0.53). The use of e_m may overlook the fact that each contact has a different stiffness, and each particle transfers a different amount of stress. When e_α is used, a better performance can be observed with a larger R^2 values being obtained in both Figure 6.44(c) ($R^2 = 0.77$ for e/e_α) and Figure 6.44(d) ($R^2 = 0.73$ for ρ_α/ρ). The higher R^2 values suggest that e_α may be better correlated with the mechanical behaviour of gap-graded soils.

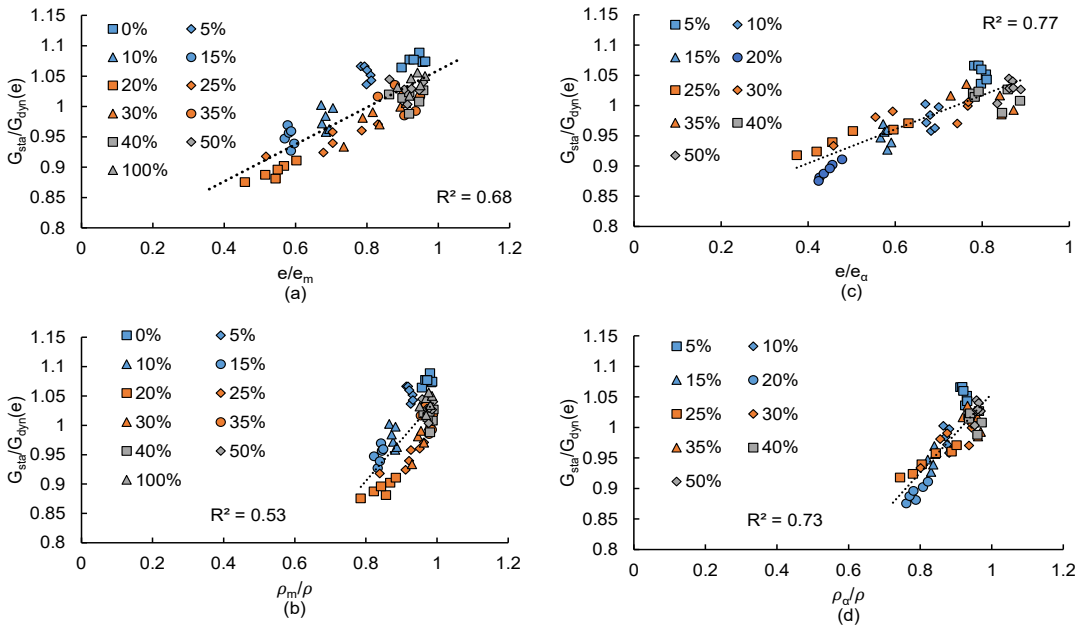


Figure 6.44: The relationship between $G_{sta}/G_{dyn}(\mathrm{e})$ and relative difference in state variables: (a) Ratio of e/e_m; (b) Ratio of ρ_m/ρ; (c) Ratio of e/e_α; (d) Ratio of ρ_α/ρ

In general, the DEM-generated data for both the linear and gap-graded specimens support the proposed hypothesis that the comparison of G_{sta} and $G_{dyn}(e)$ enables assessment of the difference between ρ and ρ_m. The ratio of $G_{sta}/G_{dyn}(e)$ gradually increases with the ratios of ρ_m/ρ, and in turn ρ_m/ρ depends on the proportion of inactive particles. A similar trend is identified when ρ_α is used.

6.7. Summary

This Chapter has presented a DEM investigation into the link between the small-strain stiffness and state for granular materials with both periodic boundaries and mixed boundaries. Specimens with linear gradings as well as bimodal and trimodal gap-graded specimens, comprising two and three size fractions respectively, were considered. The DEM simulations exploited high-performance computing capabilities to achieve representative element volumes. This Chapter has considered two types of specimens, the first with periodic boundaries and the second type of specimen had a combination of rigid wall and periodic boundaries. This summary section considers each sample type separately, as follows:

For periodic boundary specimens

A total of cubic 218 specimens bounded by three pairs of periodic boundaries were considered. The shear stiffness was determined via small-amplitude strain probes. The variation of shear stiffness with various measures of state was explored. The distribution of contact stiffness amongst the contacts in the specimens was considered from a particle-scale perspective. A theoretical stiffness-matrix method was used to analyse the contribution of each contact to the macro-scale stiffness. Even though the study is highly ideal (spherical particles and isotropic fabric and stress), the following main points can be made based upon the data presented:

(1) For specimens with a linear grading, there is a clear link between the particle size distribution and the distribution of stiffness amongst the contacts. While for gap-graded soils, the distribution of stiffness amongst the contacts is strongly associated with its F_{finer}, SR and density.

(2) For both linear and gap-graded specimens, the state variables e_m and $Z_m/(1+e_m)$ which relies upon particle-scale data, and can effectively describe the variations in G_0 amongst the specimens with greater accuracy than simply using e.

(3) A new stiffness-matrix approach was proposed to isolate the contributions of specified groups of particles to the overall stiffness. Based on this method and consideration of the distribution of contact stiffnesses, we showed that the $C-C$, $C-F$ and $F-F$ contacts each make measurably different contributions to the overall material stiffness.

(4) A new semi-empirical state variable e_α was proposed to account for the non-uniformity in stress and contact forces within granular materials. The distribution of stress amongst the different size fractions has a significant influence on G_0 in the case of gap-graded soils.

(5) It is not possible to measure e_m, Z_m or e_α experimentally. The current data support an empirical approach that uses regression analyses to determine the parameters in equation 6.1 for the particular material and specific particle size distribution under consideration.

For mixed boundary specimen

Section 6.6 has put forward a hypothesis that looking at the difference between the value of the small strain stiffnesses measured in static small strain probes (G_{sta}) and dynamic bender element tests (G_{dyn}) can indicate the proportion of inactive particles in a specimen of sand. The hypothesis was tested using data generated in DEM simulations. A total of 223 DEM test simulations were considered.

(1) Considering both the specimens with a continuous, linear particle size distribution as well as gap-graded specimens, a correlation is observed between the ratio $G_{sta}/G_{dyn}(e)$ and the ratios ρ_m/ρ and e/e_m where ρ_m and e_m are, respectively, the bulk density and void ratio considering only the active, stress transmitting particles. This correlation is approximately linear and in general, these data support the overall research hypothesis. The comparison of G_{sta} and $G_{dyn}(e)$ enables assessment of the difference between e and e_m and between ρ and ρ_m and therefore the proportion of inactive stress-transmitting particles in the tested specimens.

(2) For the gap-graded DEM specimens, a measure of void ratio that weights the finer fraction by the proportion of stress transmitted by the finer fraction (e_α) was considered and the linear correlation between $G_{sta}/G_{dyn}(e)$ and e/e_α is clearer in comparison with the correlation between $G_{sta}/G_{dyn}(e)$ and e/e_m. This observation highlights the limitation of binary classification of particles as inactive and active which has typically been adopted in the literature.

Chapter 7. Experimental investigation of the small-strain stiffness of uniform and gap-graded sands

7.1. Introduction

The small-strain stiffness of sand, G_0, has been introduced in Chapter 2 and Chapter 6 from the perspective of both numerical and experimental studies. It is widely accepted that e cannot be systematically used to capture or predict the behaviour of soil mixtures in the case where F_{finer} varies. As discussed in Chapter 6, the limitation of e as a predictor of G_0 in the case of gap-graded soils is attributed to the fact that many inactive particles may not be active in stress transmission; this phenomenon cannot be captured by the global void ratio. However, the identification of these inactive particles in experiments is rather difficult. Chapter 6, therefore, proposed a hypothesis that the comparison between G_{sta} and G_{dyn} estimated by e, $G_{dyn}(e)$ enables assessment of the differences between e and e_m, between ρ and ρ_m and therefore the proportion of inactive stress-transmitting particles in the tested specimen. This hypothesis was explored numerically in Chapter 6 and the numerical study provides a fundamental or theoretical basis that supports obtaining both static and dynamic measures of G_0 simultaneously to quantify the proportion of inactive particles in a specimen.

However, the DEM datasets generated and analysed in Chapter 6 are inherently ideal. The process used in the dynamic test simulations uses a planar shear wave which cannot easily be attained in the laboratory even when shear plates are used (Otsubo et al., 2019). Most laboratories use point source, and bender elements to determine V_s following Shirley (1978). In contrast to the DEM specimens, real physical sand specimens are inherently anisotropic, they would have larger heterogeneities compared to DEM simulations and

comprise non-spherical particles. Consequently, the feasibility of the proposed approach must be explored experimentally. In laboratory experiments, neither e_m/ρ_m nor e_α/ρ_α can be measured; the applicability of the proposed approach can only be tested by assessing whether the variation in $G_{sta}/G_{dyn}(e)$ with F_{finer} reported in Chapter 6 for DEM study is also observed in the experimental data.

This Chapter describes an experimental study that examines G_0 for gap-graded soils. The details of the experiments, as the setup of these apparatus are firstly documented, calibration of each part of the triaxial apparatus is firstly documented. The static and dynamic shear stiffness values are then determined. Finally, the variation in the difference between G_{sta} and G_{dyn} for gap-graded soils and their variation with F_{finer} is investigated.

7.2. Experimental methods

7.2.1. Soils tested

The sand samples tested in this study were available at the Geotechnical Laboratory at Imperial College London. The silica sand FRACTION A SA/1014/14-332 purchased from DavidBall Specialist Sands ($\rho = 2650\ kg/m^3$, $SiO_2 \geq 99.5\%, Fe_2O_3 \leq 0.015\%$) was selected as the coarse sands used to make up the soil mixtures. For the finer particles, the silica sand PML/0910/10-362, also purchased from DavidBall Specialist Sands ($\rho = 2650\ kg/m^3$,$SiO_2 \geq 99.5\%, Fe_2O_3 \leq 0.015\%$), was used. Images of these finer and coarse sands are presented in Figure 7.1(a) and (b), respectively.

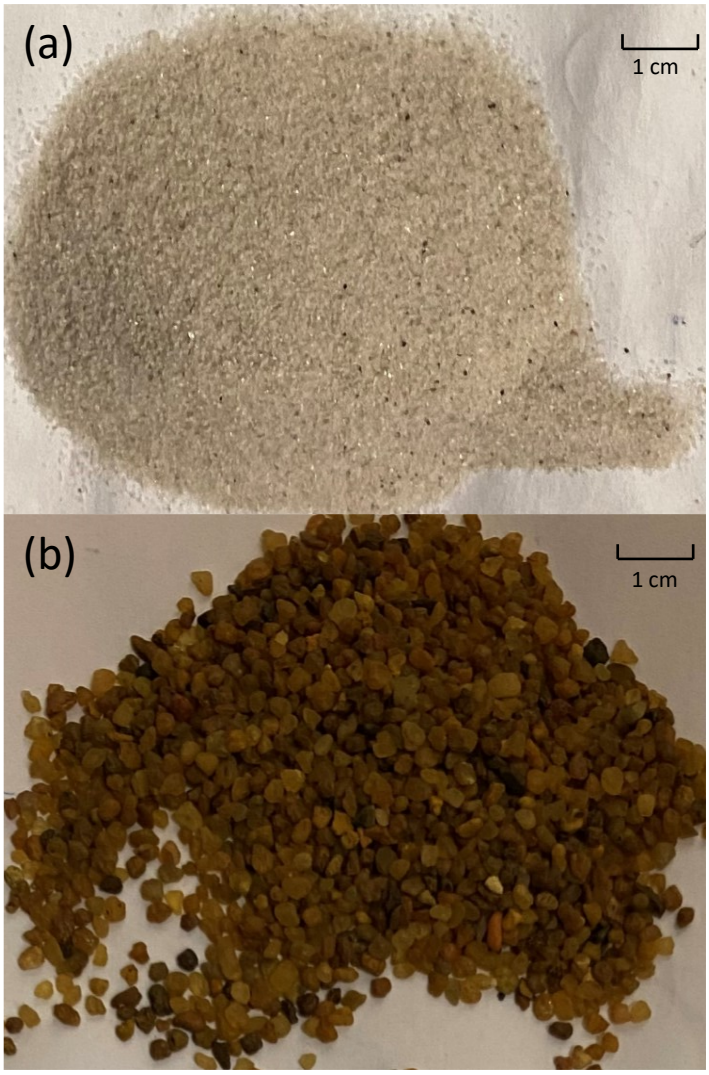


Figure 7.1: Images of sands used in experiments: (a) Finer sand; (b) Coarse sand

The particle size distributions ($PSDs$) for the finer and coarse sand, as well as the mixtures considered are presented in Figure 7.2(a). The particle size distributions of pure coarse and finer sands were analysed using a $QICPIC$ apparatus ($QICPIC/L$ Series from Sympatec Ltd, Germany) following Altuhafi et al. (2012) and Altuhafi et al. (2016). The particle size distributions of these gap-graded soils (i.e. $F_{finer} =$ 10%, 25%, 30%, 35% and 50%) are also synthetically calculated curves. That is these $PSDs$ of soil mixtures were inferred from the mix proportion. The median diameter of the coarse sand $D_{c,50}$ is 1.955 mm, while the median diameter of finer sand $d_{f,50}$ is approximately 0.245 mm. The SR ($D_{c,50}/d_{f,50}$) of the mixtures is therefore

calculated as approximately 8, which is similar to the SR values used in DEM simulations for mixed boundaries specimens (Considered in Section 6.6).

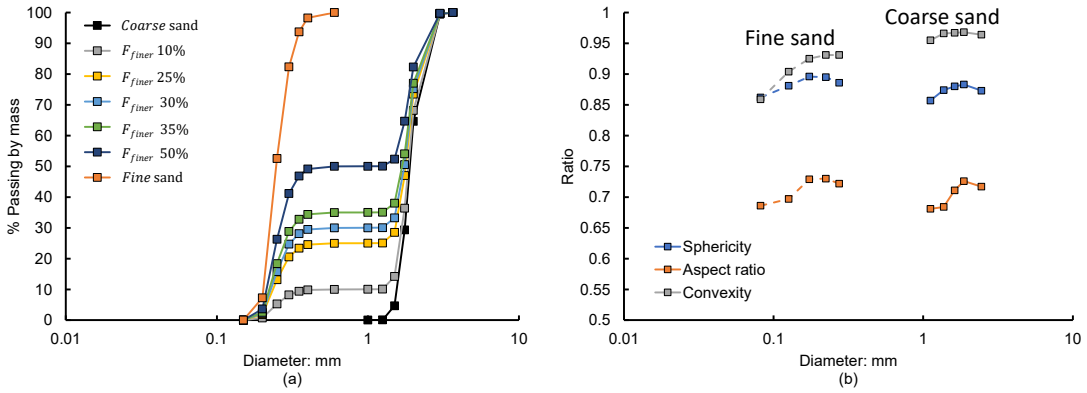


Figure 7.2: Particle characterization for the experimental specimens: (a) Particle size distributions; (b) Particle shape parameters

The particle-level characteristics of the finer and coarse sands were analysed using the $QICPIC$ apparatus, which is capable of quantifying the shape parameters (i.e. sphericity; aspect ratio; convexity) and particle size distributions of soils with particle sizes ranging from 0.55 μm to 33.792 mm. As illustrated in Figure 7.3, following Yang & Luo (2015), the aspect ratio is defined as the ratio between the minimum Feret diameter D^{Fmin} and maximum Feret diameter D^{Fmax}, the Feret diameter is a measure of an object size along a specified direction, as illustrated in Figure 7.3; the convexity is the area of the particle (A) divided by its area if any concavities within its perimeter were filled (A+B); the sphericity is defined as the ratio of the perimeter of a circle with the same area as the projected area of the particle to its actual perimeter.

For sphericity, aspect ratio and convexity parameters, five data points for both finer (i.e., for Feret diameters of 0.08172 mm; 0.12610 mm; 0.17321 mm; 0.22361 mm; 0.27386 mm) and coarse sand (i.e., for Feret diameters of 1.11803 mm; 1.36931 mm; 1.62019 mm; 1.87083 mm; 2.44949 mm) are presented in Figure 7.2b.

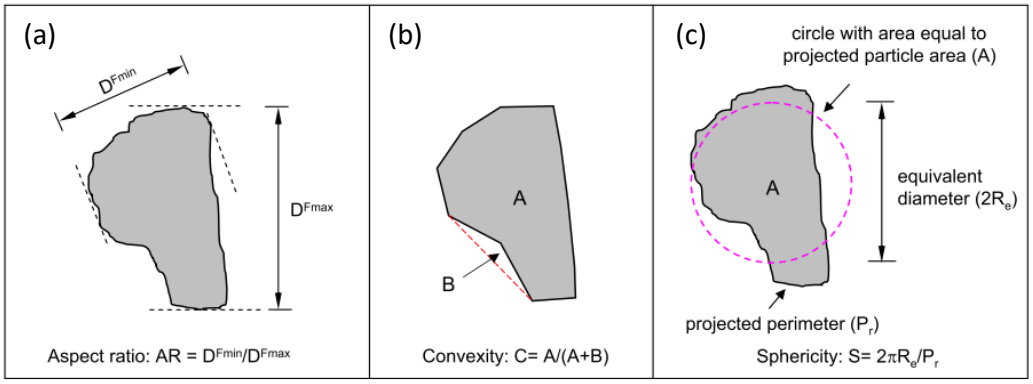


Figure 7.3: Schematic illustration of particle characterisation technique: (a) Aspect ratio; (b) Convexity; (c) Sphericity (modified from Yang & Luo, 2015)

The data in Figure 7.2b indicate that the shape parameters are similar for coarse and finer sands. For instance, the sphericity of the coarse particles is approximately 0.89, and the sphericity of the finer sand is approximately 0.90. These sphericity values show that the shape of the sand particles tested is relatively rounded following Altuhafi et al. (2012) and Altuhafi et al. (2016). It is clear that these sand particles are not perfectly spherical, unlike the particles used in DEM simulations. A summary of the size and shape measures of the mixtures is presented for each F_{finer} value considered on Table 7.1.

Table 7.1: Key size and shape measures for each sample presented as a function of F_{finer}

	Coarse sand	F_{finer} of 10%	F_{finer} of 25%	F_{finer} of 30%	F_{finer} of 35%	F_{finer} of 50%	Finer sand
D_{10} (mm)	1.554	0.600	0.236	0.229	0.224	0.214	0.203
$D_{30}(mm)$	1.755	1.678	1.520	0.6	0.315	0.262	0.225
$D_{50}(mm)$	1.896	1.857	1.778	1.742	1.686	0.6	0.247
$D_{60}(mm)$	1.967	1.936	1.873	1.846	1.815	1.655	0.258
C_u	1.27	3.23	7.94	8.06	8.10	7.73	1.27
e_{Low}	0.545	0.449	0.351	0.342	0.315	0.361	0.663
e_{High}	0.698	0.575	0.457	0.437	0.391	0.476	0.771
Sphericity	0.857	N/A	N/A	N/A	N/A	N/A	0.862
Aspect ratio	0.681	N/A	N/A	N/A	N/A	N/A	0.686
Convexity	0.955	N/A	N/A	N/A	N/A	N/A	0.91

Considering Table 7.1, the e_{Low} and e_{High} values are the lowest and highest void ratios identified in the relatively dense and loose specimens. Note that the processes used to generate the relatively loose and dense specimens here are not equivalent to the standard procedures that are followed to generate specimens with the relative densities of 0% and 100%, respectively. They were simply used to produce systematically different initial densities, as outlined in Section 7.2.3 below.

7.2.2. Equipment

Triaxial apparatus

The triaxial apparatus with local displacement transducers used in this study is illustrated in Figure 7.4. The nominal diameter and height of the test specimen are approximately 100 mm and 200 mm, respectively. Some of the local radial transducers and local vertical transducers are shown in Figure 7.4. These transducers were employed to measure the changes in specimen dimension throughout the tests, and therefore the volume change of the specimen. The

load cell used to measure the axial force applied to the specimen, as well as the cell and back pressure transducers can also be seen in Figure 7.4. Details about the calibration procedure used for all instrumentation are provided later in this Section.

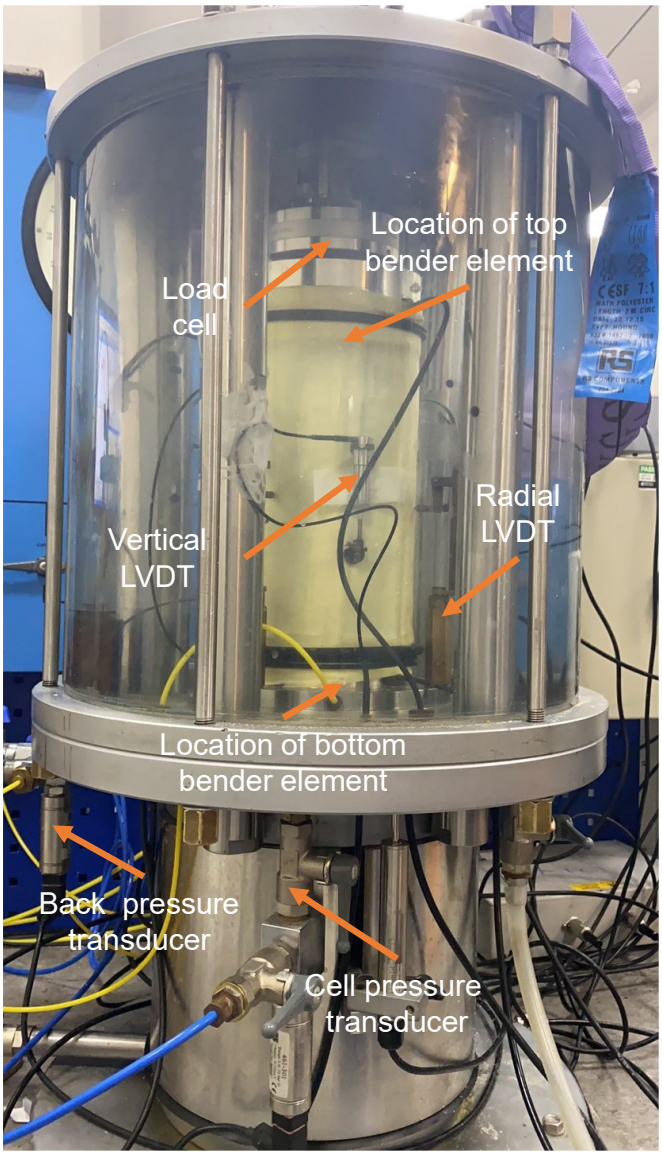


Figure 7.4: Triaxial apparatus indicating internal and external instrumentation

Bender element set-up

The bender element set-up used is schematically illustrated in Figure 7.5 following Alvarado & Coop (2012). Bender elements (10 mm long) were housed in the base pedestal and the top cap to enable the dynamic tests. The propagated wave which was generated by the movement of the top bender

element (transmitter) was then captured by the bottom bender element (receiver). The bottom bender element was connected to a signal amplifier. A function generator is sent to the top bender element (i.e., transmitter) to apply a shear disturbance at the top of the specimen, generating a shear wave. This shear wave propagated downwards through the specimen until a disturbance was recorded at the bottom element (i.e. the receiver). The received signal was then recorded by a personal computer (PC). For each specimen, a single period sine wave pulse was used, and the frequency applied to the transmitter varied from 3 kHz to 20 kHz so that a good quality received signal could be obtained following Otsubo (2016). Note that for each specimen, the optimum signals are distinct and are strongly associated with its F_{finer}, e, and p'. The travel distance used in the peak-peak method is taken to be the distance from the tip of the bottom to the tip of the top for the specimens. The determination of the optimal signal is discussed in Section 7.25.

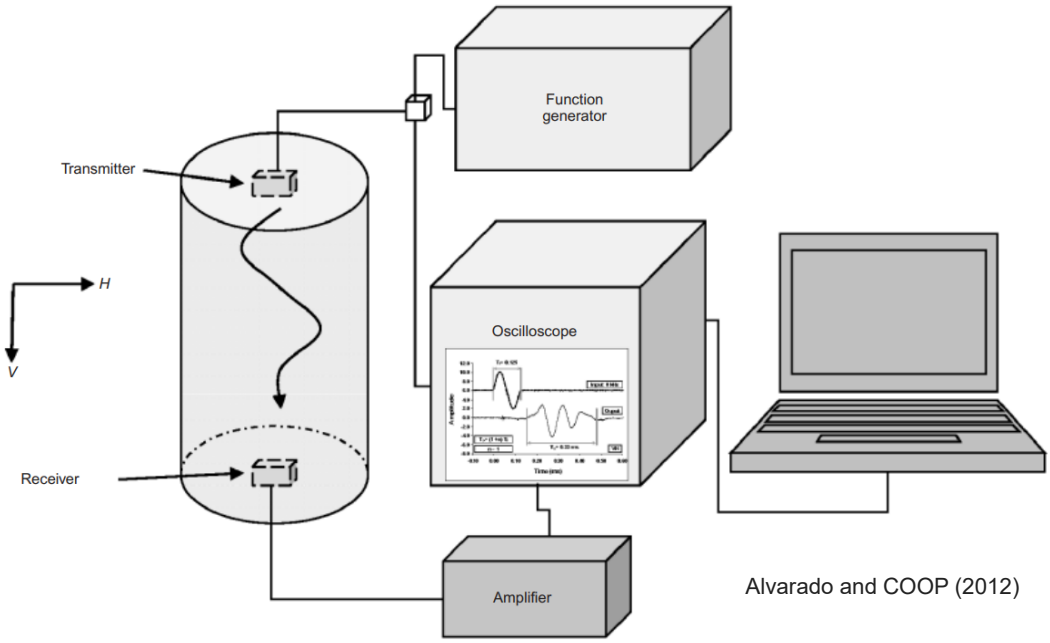


Figure 7.5: Schematic diagram of the bender element set-up (Alvarado & coop, 2012)

Figure 7.6 shows an example of a bender element test carried out in this study. Both the transmitted and received signals are recorded by the personal computer (PC) and the results of bender element tests are then subjected to further analysis.

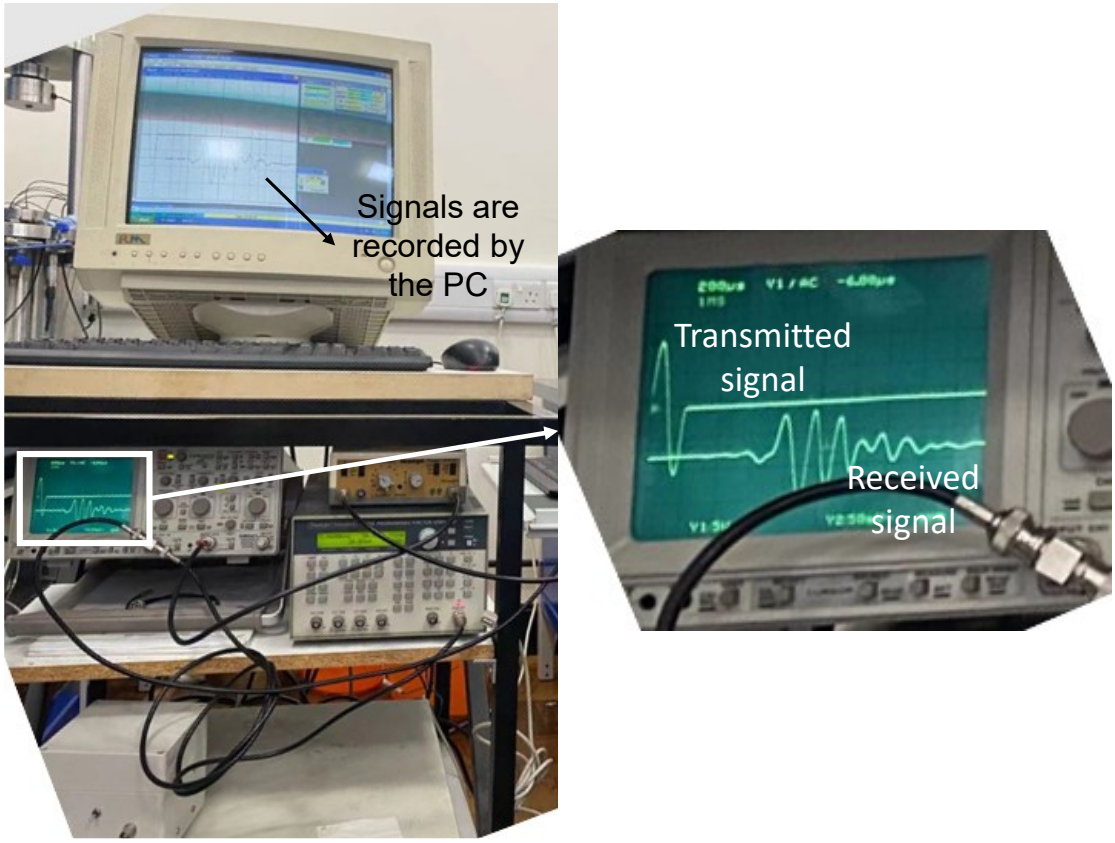


Figure 7.6: An example of a bender element test in this study

Calibration of the instrumentation used in the testing apparatus

Before the experimental programme started, the instrumentation used was calibrated to quantify the system precision and accuracy of all sensing components. The pressure, force and displacement transducers, as well as the volume gauge, were calibrated using appropriate standards. The calibration procedure applied to each one of the instruments included three loading-unloading cycles within the range of operation of each instrument. These calibration loops (instead of single-point checks) were carried out to fully

quantify typical but often overlooked errors such as those due to hysteresis and repeatability of the instruments when operated at constant lab room temperature ($\approx 20°C$).

(1) Pressure gauge

Both cell and back pressure transducers were calibrated using the Budenberg dead weight calibrator (serial number N2569) (Figure 7.7), whose calibration ranges from 103.43 kPa to 1034.25 kPa according to the manufacturer's manual. All values shown for this calibration dataset follow the resolution of the calibration standard system. For instance, for calibration of the pressure gauge, this instrument is readable to 0.01 mV, and this standard calibration instrument is readable to 0.01 kPa. The corresponding calibration results for the cell pressure transducer are shown in Figure 7.8.



Figure 7.7: Budenberg dead weight calibrator (Images from Budenberg Gauge Co Ltd; www.budenberg.co.uk)

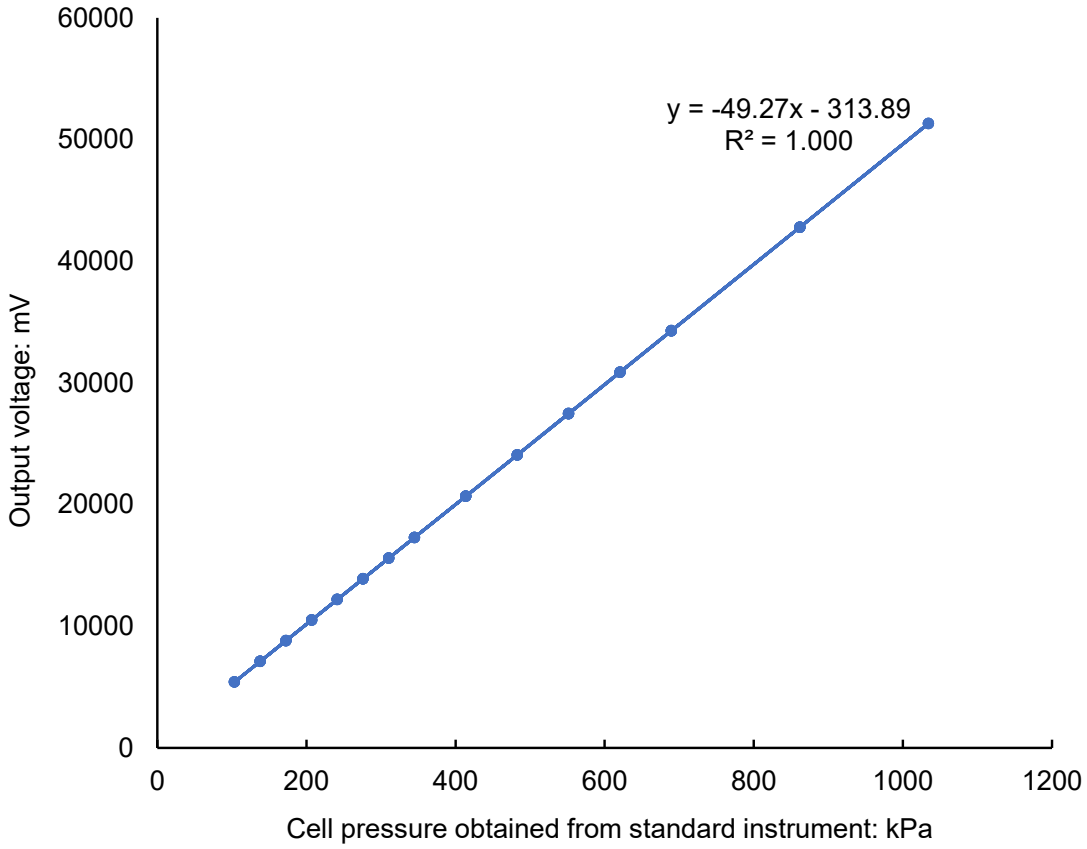


Figure 7.8: Best-fit calibration regression line for the cell pressure transducer

Referring to Figure 7.8, for the cell pressure, there is a linear relationship between voltage and displacement applied with R^2 being approximately 1.000. The fitted linear curve is obtained from the least-squares regression method, therefore for each datapoint, there is a difference between the pressure obtained from the standard instrument (i.e. this datapoint) and the estimated pressure from the fitting curve. The maximum value of this difference for each datapoint is defined as the maximum error. In this case, the maximum error of the system is 0.8 kPa. The maximum error divided by the calibration range is defined as the maximum percentage error, which is 0.1% in this case. The calibration of the back pressure transducer is the same as that for the cell pressure transducer, therefore, the detailed calibration data of the back pressure transducer is not shown with the key results being summarised in Table 7.2.

(2) Force transducer

The submersible load cell used (Applied Measurements Ltd, CBES, Capacity of 2000 N) was calibrated using the Budenberg dead weight calibrator (Figure 7.7). The calibration range used during load cell calibration varied from 165.29 N to 4846.55 N, referring to the manufacturer's manual. The calibration data produced at this stage is shown in Figure 7.9, which includes the best-fit linear regression curve obtained with this calibration dataset.

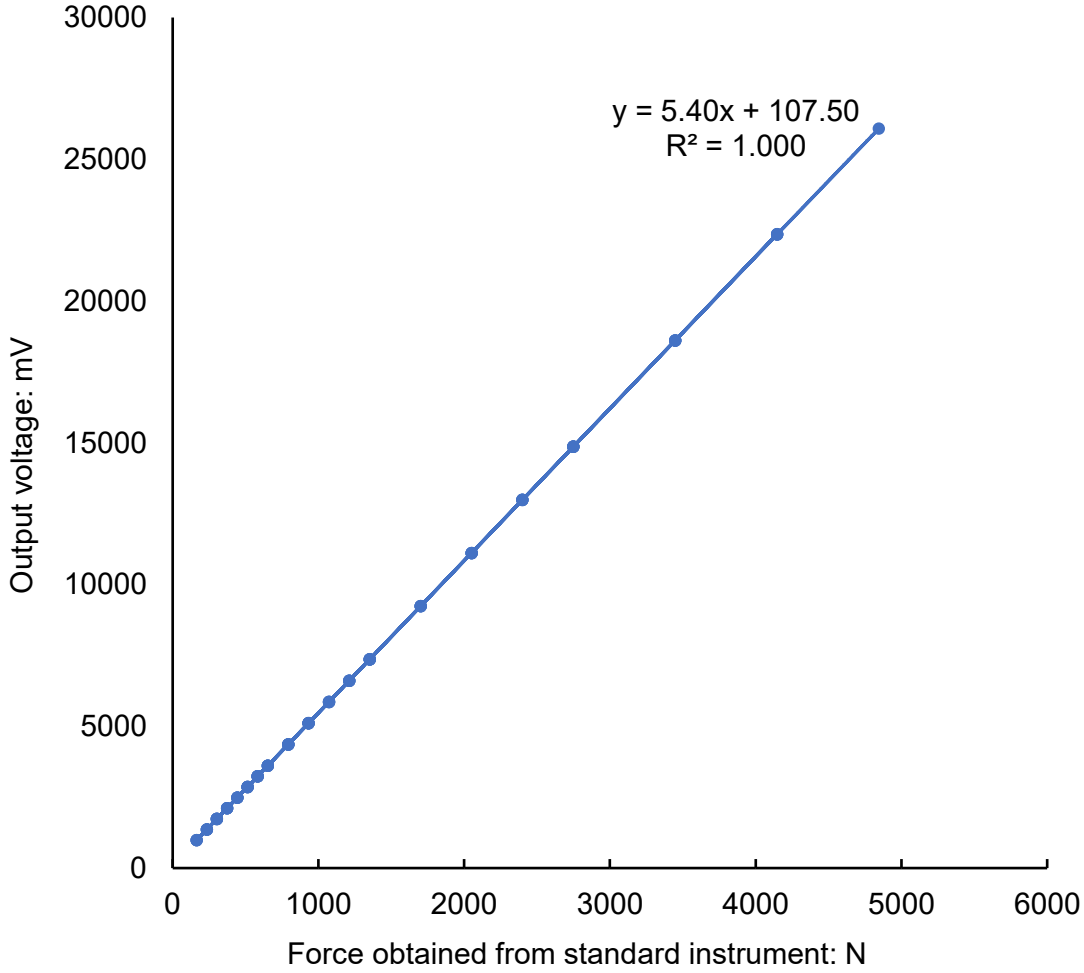


Figure 7.9: Best-fit calibration regression line for the load cell

Once the calibration regression curve was obtained, the values read by the load cell could then be calculated based on the calibration regression curve. Again, the difference between the calculated values read by the load cell and the values obtained by the standard instrument is defined as the system error of

the dataset. For this force transducer, the maximum error of these datasets was determined to be approximately 3.5 N. This corresponds to a maximum percentage error, which was determined as the ratio of maximum error to the measurement range, of approximately 0.1%.

(3) Displacement transducers

Three different types of displacement transducers were calibrated: (1) external displacement transducer (even though this external displacement transducer was not used in this study since all tests are restricted to small strain behaviour); (2) three vertical Linear Variable Differential Transformers ($LVDTs$), which were used to measure the axial displacement of the specimens; and (3) three radial $LVDT$s, which were used to measure the radial displacement of the specimens. All these displacement transducers were calibrated by a standard instrument (i.e. a standard micrometre). The resolution of this standard micrometre is 0.005 mm. Figure 7.10 presents one representative calibration dataset for a vertical $LVDT$ and Figure 7.12 provides one representative calibration dataset for a radial $LVDT$. When the desired displacement is 0 mm, the voltage is also approximately 0 mV. Key data for the $LVDTs$ are summarised in Table 7.2.

The regression curve for the vertical $LVDT$ 1 is presented in Figure 7.10. It can be seen that the R^2 value of the curve fitting is 1.0000. The resolution of this axial $LVDT$ is 0.00001 mm according to the manufacturer's manual. However, the manufacturers typically report the electronics resolution, this may not be sufficiently reliable for accurate measurement. Consequently, the standard calibration procedure was applied to study the system error for all these transducers. The maximum error of the $LVDT$ 1 system is 0.036 mm and the maximum percentage error is 0.6%. The variation in the error of this system with increasing calibration range is presented in Figure 7.11. The absolute error

of the $LVDT$ 1 gradually increases with increasing measure range. For instance, as illustrated in Figure 7.11, when the calibration range is from -1 to +1 mm, the maximum error of the system is lower than 0.006 mm. Besides, the system error approaches 0 when the working range is close to 0 mm (i.e. when the voltage is around 0 mV). In contrast, when the calibration range is around $\pm$ 3 mm, the maximum error is approximately 0.035 mm. This result indicates that the working range of displacement transducers should be close to 0 mm (i.e. 0 mV) to minimize the error compared to the measured vertical displacement during saturation, consolidation and shearing stage (i.e. $\approx$ 0.02 mm) (Figure 7.28 showing an example of the displacement of a vertical $LVDT$).

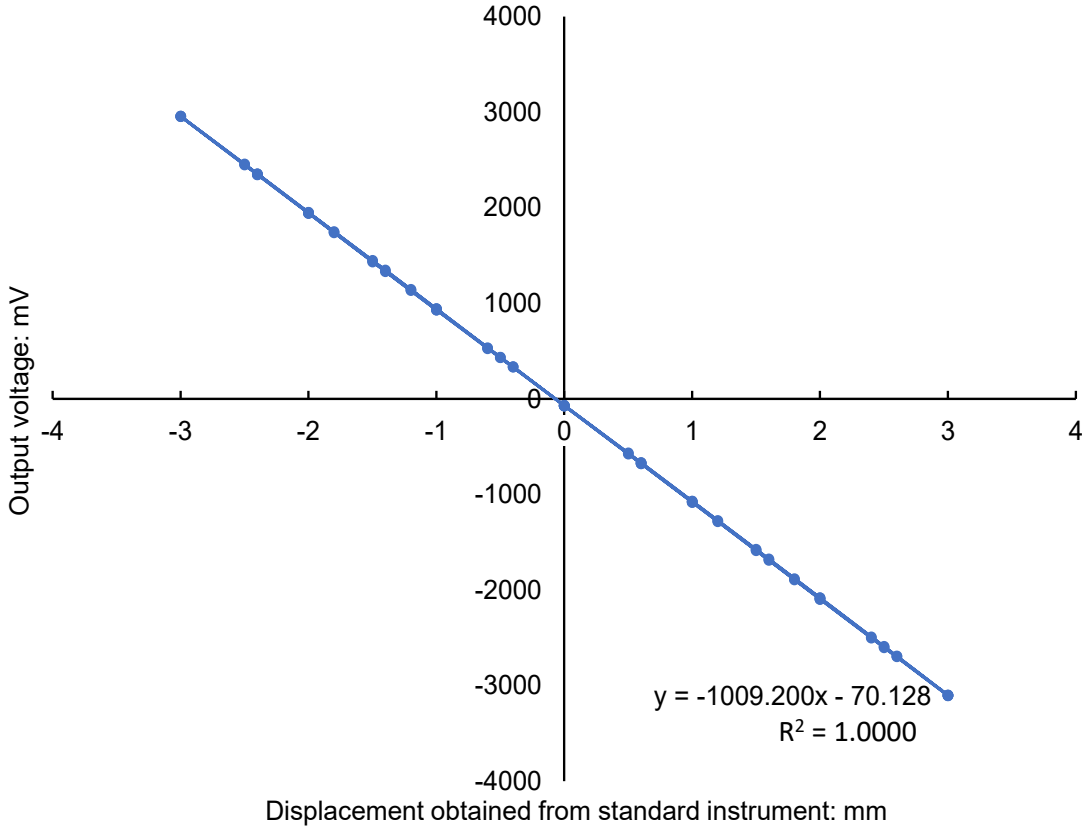


Figure 7.10: Best-fit calibration regression line for the vertical $LVDT$ 1

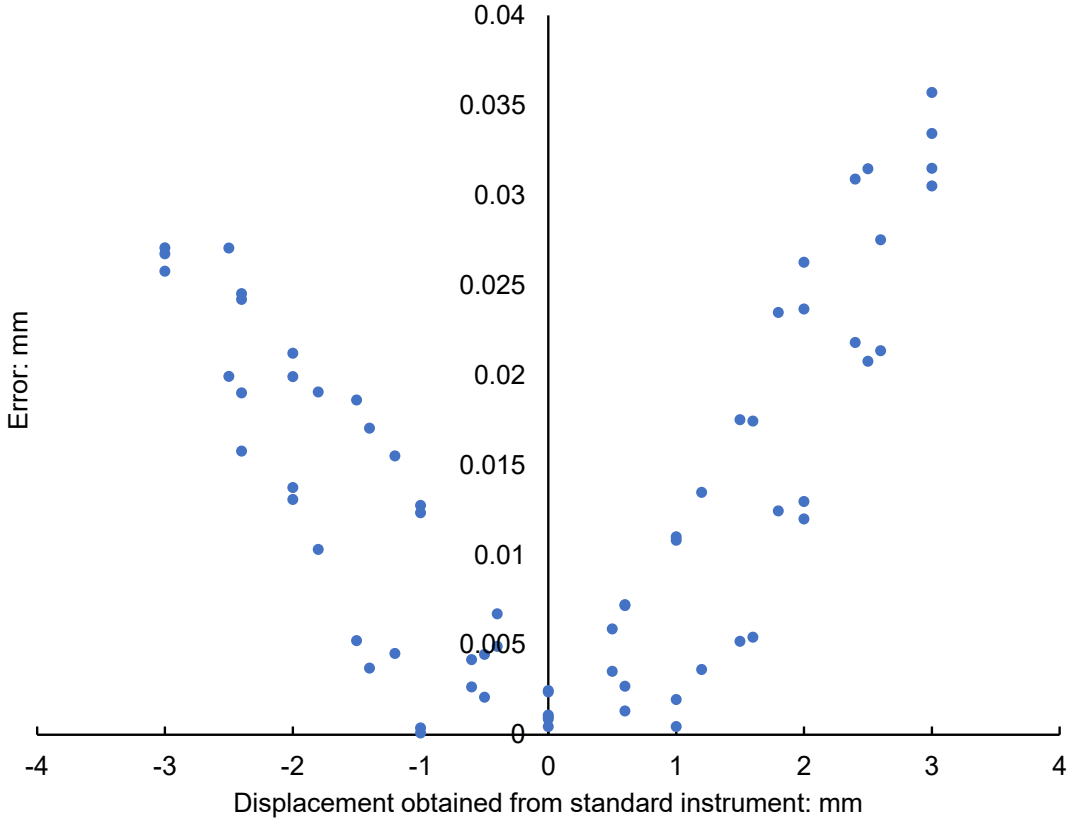


Figure 7.11: Error quantification for the vertical $LVDT$ 1

For the radial $LVDT$ 1, the calibration curve is shown in Figure 7.12. As illustrated in Figure 7.12, the best fit straight line obtained with linear regression has a R^2 value of 0.9998. The resolution of the radial $LVDT$ is 0.00001 mm according to the manufacturer's manual. In contrast, following the error calculation procedure described for the cell pressure transducer, the maximum error of this radial $LVDT$ system is calculated to be approximately 0.079 mm and the maximum percentage error is 1.3%. In addition, just as in the case of the axial $LVDTs$ transducers, the working range of these radial $LVDTs$ should be close to 0 mm (i.e. 0 mV) so that the error of the system minimized relative to the measured radial displacement during consolidation and shearing stage (i.e. $\approx 0.014\, mm$) (Figure 7.28 showing an example of the displacement of a radial $LVDT$). In general, when working range is from -3 mm to 3 mm, the standard calibration procedure employed showed that the average maximum

error of these six $LVDTs$ is approximately 0.089 mm. The average standard deviation of the error is approximately 0.021 mm. In contrast, when the working ranges of these $LVDTs$ were restricted (i.e. for instance, the working range of these $LVDTs$ was restricted within $\pm$ 1 mm), the maximum absolute error of these six $LVDTs$ was $<$ 0.007 mm. The average standard deviation of the error is 0.002 mm. The efficacy of these $LVDTs$ to measure strains within the region of elastic deformation was previously demonstrated in Cuccovillo & Coop (1997) and Kuwano & Jardine (2002). However, it is difficult to establish with confidence exactly how the measurements made in the actual tests (which involve mounting $LVDTs$ on different hardware/devices) relate to these calibration results.

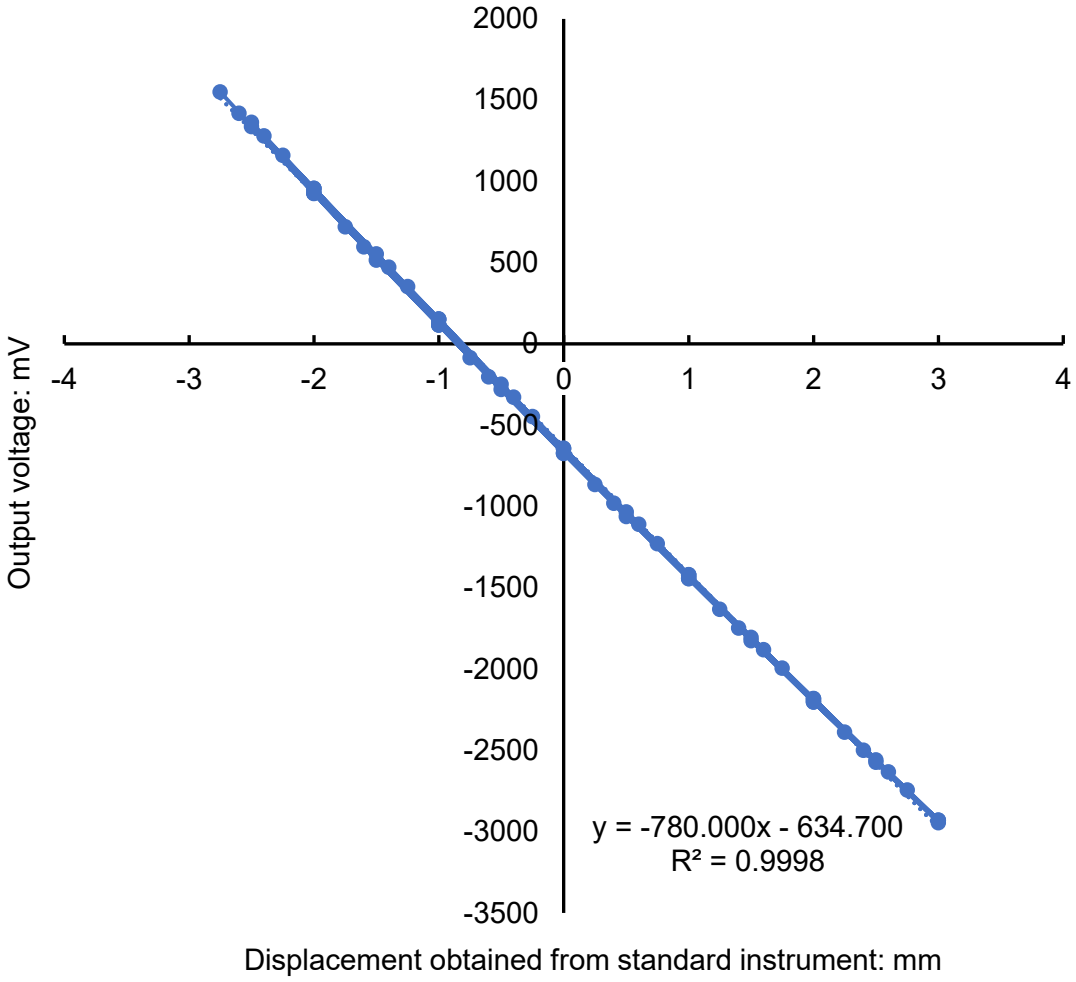


Figure 7.12: Best-fit calibration regression line for the radial $LVDT$ 1

(4) Volume gauge

The volume gauge was calibrated using a standard scale manufactured by Sartorius. By assuming that the density of de-aired water is $1.0\ g/cm^3$, the measured mass can be converted to volume. The capacity of this standard instrument is then 100 cc and the resolution of this instrument is 0.01 cc following the manufacturer's manual. This calibration was carried out under atmospheric conditions. The calibration data of this volume gauge is presented in Figure 7.13. The maximum error is 0.46 cc and the maximum percentage error is 0.57%. In some cases, de-aired water was added into the volume gauge during the saturation stage, which could lead to inaccuracies in the measurement of specimen volume. Therefore, the volume change of the specimen during a test was determined by the three vertical and radial transducers, not this volume gauge.

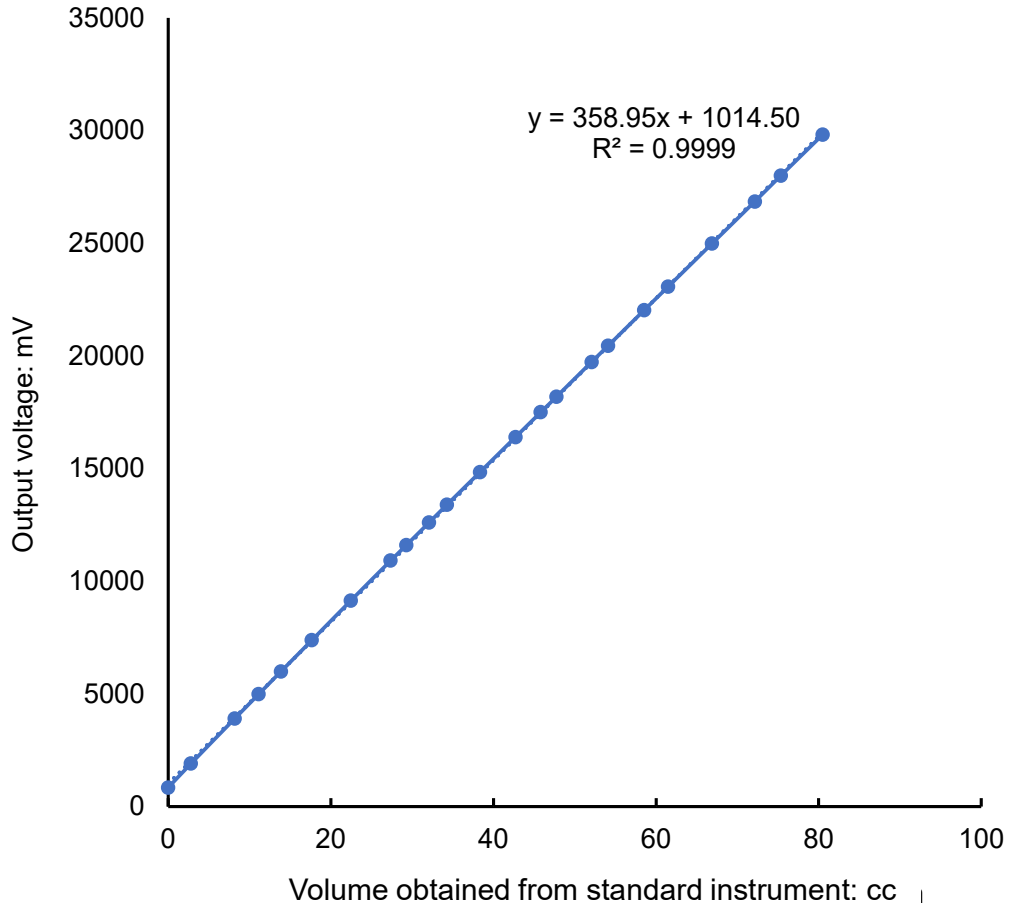


Figure 7.13: Best-fit calibration regression line for the volume gauge

A summary of the calibration results for all transducers used in this Chapter is presented in Table 7.2. Note that the estimated maximum error was calculated based on the calibration range. However, the calibration range is not necessarily the same as the desired working range. The maximum absolute errors of these transducers subjected to the desired working range are also presented in Table 7.2. To significantly reduce the system error effect, these transducers were carefully installed so that the working range was close to 0 mm to minimize the system errors.

Table 7.2: Summary of calibration results used in triaxial tests

Transducer	Type	Capacity	Calibrated against	calibration range	type of regression	R^2	Max error	Max error (desired working range)	Percentage maximum error (%)	Resolution
Load cell	Axial load	5000 N	Budenberg dead weight calibrator	165.29 N - 4846.55 N	Linear	1.0000	3.5 N	0.11 N (50-90 N)	0.1%	0.1 N
pressure gauge	Cell pressure	1034 kPa		103.43 kPa - 1034.25 kPa		1.0000	0.8 kPa	0.8 kPa (500-800 kPa)	0.1%	0.1 kPa
	Back pressure	1034 kPa		103.43 kPa - 1034.25 kPa		1.0000	1.0 kPa	0.6 kPa (400-700 kPa)	0.1%	0.1 kPa
Displacement	External displacement gauge	25 mm	Micrometre	0 -12 mm		1.0000	0.46 mm	N/A	2%	0.001 mm
	Axial $LVDT$ 1	12 mm		-3 mm to 3 mm		1.0000	0.036 mm	0.006 mm ($\pm$ 1 mm)	0.6%	0.00001 mm
	Axial $LVDT$ 2	12 mm		-3 mm to 3 mm		1.0000	0.070 mm	0.007 mm ($\pm$ 1 mm)	1.2%	0.00001 mm
	Axial $LVDT$ 3	12 mm		-3 mm to 3 mm		1.0000	0.048 mm	0.005 mm ($\pm$ 1 mm)	0.8%	0.00001 mm
	Radial $LVDT$ 1	12 mm		-3 mm to 3 mm		0.9998	0.079 mm	0.006 mm ($\pm$ 1 mm)	1.3%	0.00001 mm
	Radial $LVDT$ 2	12 mm		-3 mm to 3 mm		0.9998	0.087 mm	0.007 mm ($\pm$ 1 mm)	1.5%	0.00001 mm
	Radial $LVDT$ 3	12 mm		-3 mm to 3 mm		0.9998	0.089 mm	0.007 mm ($\pm$ 1 mm)	1.5%	0.00001 mm
Volume gauge	Volume change	100 cc	Weight scale	0 cc - 80.497 cc		0.9999	0.46 cc ($p*$)	N/A	0.6%	0.001 cc

7.2.3. Specimen preparation

As discussed in Chapter 2, various specimen preparation methods have been used in prior experimental studies. In this study, to minimise sample segregation and due to the limitations of experimental conditions, the dry deposition method was used for specimen preparation following Ishihara (1993). A simple sketch of the procedure is presented in Figure 7.14. After 24h of oven drying, the coarse and finer sand fractions were manually mixed to create a mixture with a desired F_{finer}. Then, the soil sample was poured into the mould with a funnel, as shown in Fig. 7.14. The inner diameter of the funnel was 10 mm, the length of funnel spout was 250 mm, the funnel top diameter was 100 mm. This funnel is not large enough to fill the mould in a single stage; each specimen needed to be filled in several steps (i.e. the process was repeated approximately 8 times). To achieve a loose density, specimens were prepared with care following Ishihara (1993) so that a relatively loose state could be obtained. The funnel spout was maintained at a zero height above the sand's surface.

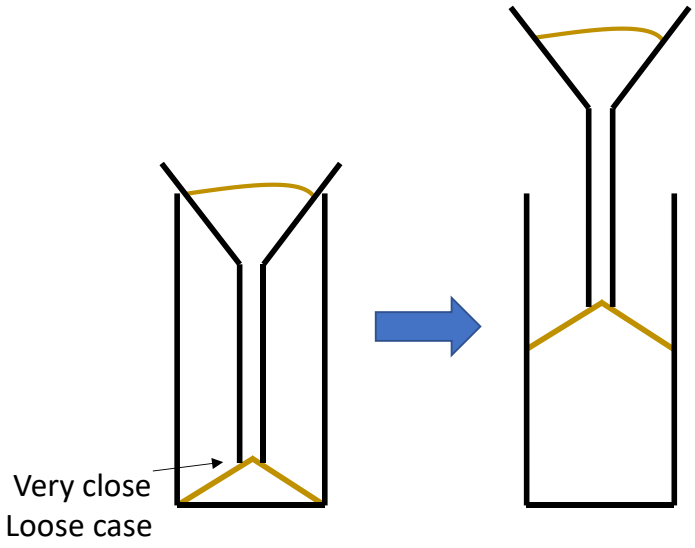


Figure 7.14: Simple sketch of specimen preparation for loose specimens

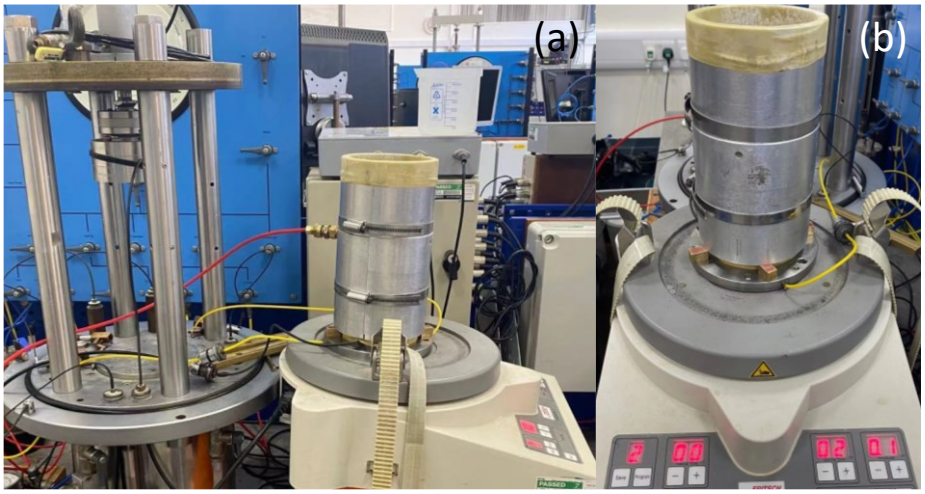


Figure 7.15: Specimen preparation of dense cases: (a) Side view; (b) Front view

To create the dense specimens, as illustrated in Figure 7.15, the mould containing the sample was placed. A vibratory table produced from $FRITSCH$ ($ANALYSETTE\ 3\ PRO$) was used for the entire specimen when the pouring illustrated in Figure 7.14 was completed. Figure 7.16 presents some simple sketches of the specimen preparation method used to create the dense specimens, illustrating the use of the vibratory table. Firstly, an extra extension mould (i.e. the diameter of 104 mm, height of 40 mm) was added to the original mould top and the funnel was used to place the soil sample into the mould with the drop height again being approximately 0 (Figure 7.16(b)). Then, the vibratory table ($ANALYSETTE\ 3\ PRO$) was turned on to densify the specimen with a cylindrical surcharge (i.e. length of 120 mm, width of 120 mm, height of 40 mm) of approximately 2 kg (Figure 7.16(c)). The vibration programme is set program 2 (i.e., frequency of 50-60 Hz), the vibration amplitude is 0.1 mm in vertical direction and the vibration time was fixed to be approximately 5 minutes. Following vibration, the soil in the extra mould and the extra mould itself was removed and the top surface of the specimen was levelled by a ruler using a process similar to that outlined in ASTM D4253 and D4254 (Figure 7.16(d)). The processes used to generate the relatively loose and dense specimens here are not equivalent to the processes that should be followed to

obtain the relative densities of 0% and 100%, respectively. They were systematically used to produce different initial densities.

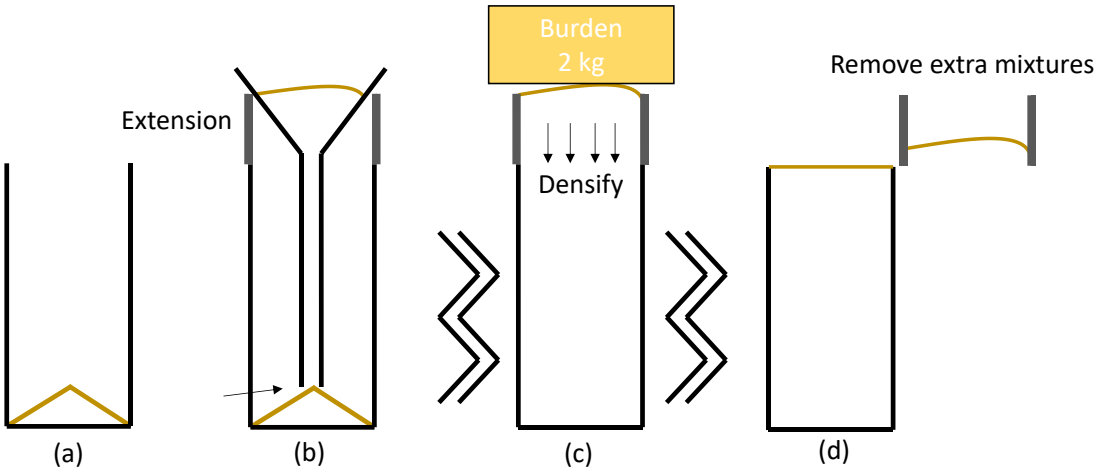


Figure 7.16: Simple sketch of specimen preparation for the desired dense state: (a) First step; (b) Second step; (c) Third step; (d) Fourth step

7.2.4. Analysis of specimen uniformity

To make sure that the specimen preparation method used produced uniform specimens, an analysis of specimen uniformity was carried out before any triaxial testing took place. In this analysis, a density gradient mould (Tastan & Carraro, 2013) was used to measure the characteristics of various layers in a given specimen. The density gradient mould used included several layer rings and was identical to the one developed by Dominguez-Quintans et al. (2019). The internal diameter and height of each layer ring were equal to 38 mm and 19 mm, respectively. The diameter and length of the specimens used in the triaxial programme were approximately 100 mm and 200 mm, respectively. This smaller density gradient mould was used since no larger apparatus was available at the time of this study.

To assess the loose specimens, as illustrated in Figure 7.17, four different layer rings were used (five layers for the creation of dense specimens). Firstly, the dry deposition method was used to prepare the loose state specimen as

presented in Figure 7.14. Then, a gelatine solution was used to solidify the soil specimen inside the density gradient mould. A dry gelatine powder produced by the food supply Dr. Oetker was initially mixed with pure boiled de-aired water (> 90°C) at a concentration of 5% (by weight) following Emery et al. (1973) and Dominguez-Quintans et al. (2019). Then, the gelatine solution ($\approx$ 90°$\mathbb{C}$) was permeated through the soil specimen under the pressure generated by the gravity effect (i.e. the gelatine solution was placed higher than the density gradient mould), which was applied from the bottom to the top of the specimen. This process normally was completed in less than 30 minutes until the top surface of the specimen was fully impregnated by the gelatine solution. Then the gelatine-filled specimen was allowed to solidify by waiting until the temperature of the specimen was close to the lab temperature. It normally took approximately an hour to finish this solidification (i.e. for the gelatine to solidify). Once the sample was sufficiently solid, the layer rings were then sliced carefully, layer by layer with the help of a saw, followed by further measurement (e.g. mass) and analysis (e.g. void ratio, density and F_{finer}). As illustrated in Figure 7.18, the saw had a wire thickness of approximately 1 mm, and it was capable of slicing the specimen while generating a smooth surface (Figure 7.19). A typical solidified soil layer is presented in Figure 7.19. The volume of each layer is assumed to be equal as calculated based on the height (i.e. 19 mm) and internal diameter (i.e. 38 mm) of each layer mould. The mass of any particles stuck to the inner side of the slice was also included in the assessment of the slice mass.

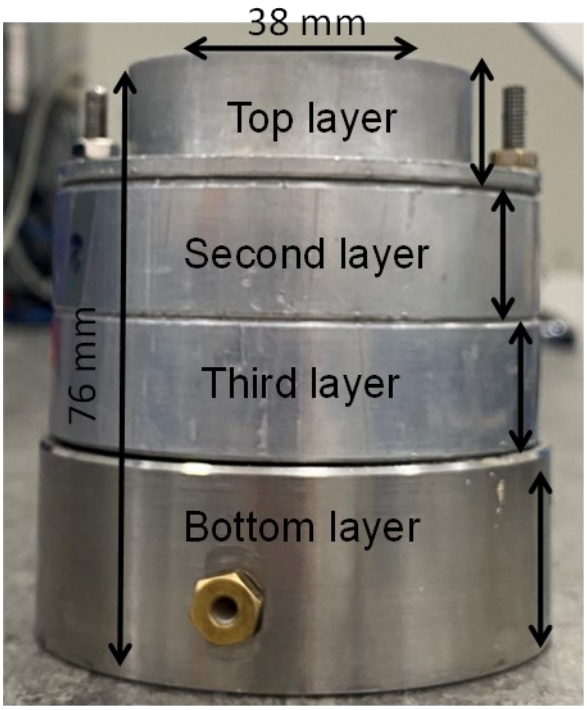


Figure 7.17: Separate moulds used to check specimen uniformity for the loose state (Dominguez-Quintans et al., 2019)



Figure 7.18: The saw used to cut the solidified specimen

For the dense specimens, as illustrated in Figure 7.21(a), an extension layer (i.e. extra mould) was added to the original four-slice stack shown in Figure 7.16. Figure 7.21(b) shows the vibratory table used to densify the specimens so that the uniformity of the dense specimens could be quantified. For this dense specimen, the same vibratory process was used compared to the main specimen.

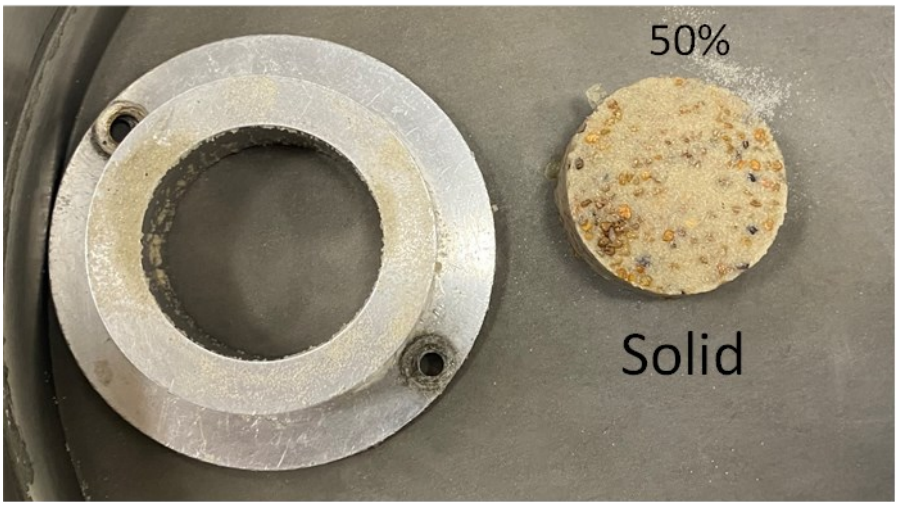


Figure 7.19: An example of the solidified soil mixture layer ($F_{finer} = 50\%$)

Each layered specimen slice was washed with hot water (> 90°C) to remove the gelatine over a sieve No. 100 (i.e. opening is 150 μm); the minimum particle diameter used in this study was approximately 300 μm, so that only water could go through this No 100 sieve. This process was repeated several times to ensure that all the gelatine material was washed out, as illustrated in Figure 7.20. After that, the layered soil samples, free of gelatine, were placed into the oven (≈ 60℃) for 24 hours for drying. Besides, the same values can be obtained after a certain number of readings. The constant dry mass (i.e. same value identified from the lab balance, readable to 0.001 g) could then be observed after 24 hours of drying.



Figure 7.20: The washing out of a solidified soil slice layer

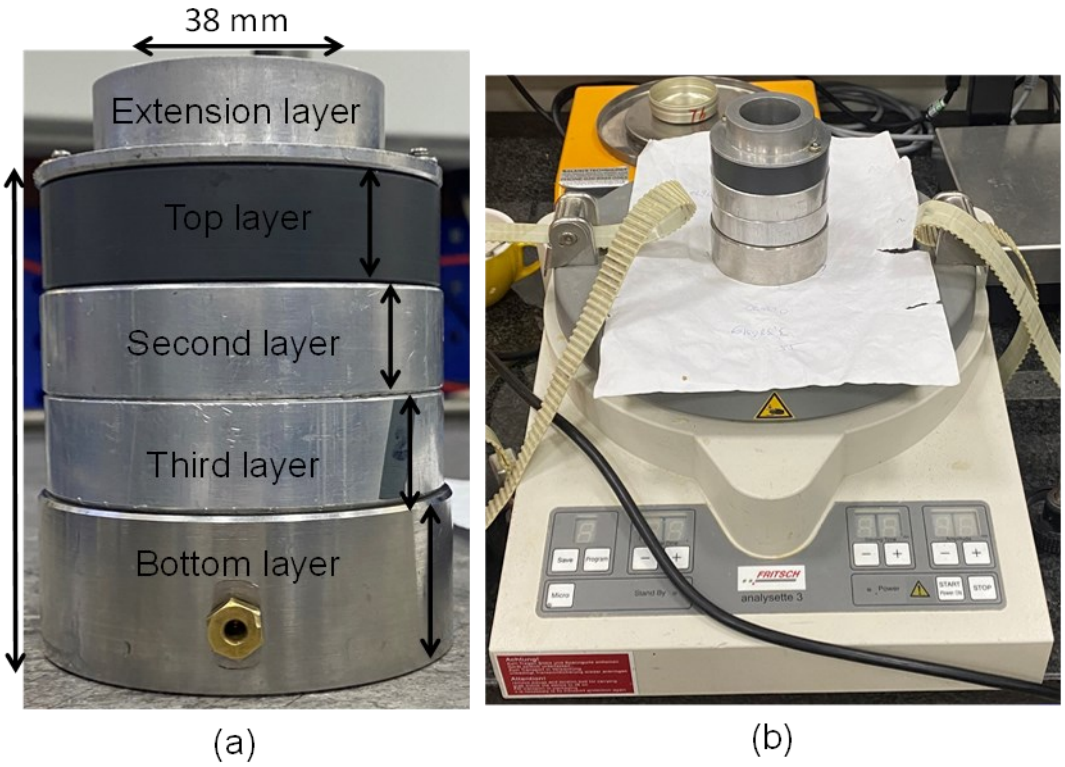


Figure 7.21: Specimen uniformity quantification for the dense state: (a) Density gradient mould used to check specimen uniformity for the dense state; (b) Vibration machine used for densifying the specimen (Dominguez-Quintans et al., 2019)

Once the dry mass of each layer was obtained, the corresponding void ratio

and density values for each layer were quantified. In this study of specimen uniformity, three representative F_{finer} were considered following Shire et al. (2014): (1) F_{finer} = 10%, which represents an underfilled state; (2) F_{finer} = 25%, which represents a state where we expect the proportion of inactive particles to depend on the specimen density; (3) F_{finer} = 50%, which represents an overfilled state. Both dense and loose cases are taken into account in these uniformity analyses.

The uniformity data for the dense specimen with F_{finer} of 10% are summarised in Table 7.3. As noted above, the balance is readable to 0.001 g, the volume of each slice is considered to be the same. Since the e is calculated from the mass and volume of the slice, the e values are shown with 3 decimal places. A small difference can be identified amongst the layers, for instance, for the first layer, the e is approximately 0.432, while the e of the second layer is approximately 0.453. To quantify the uniformity of each layer, the maximum deviation (MD) of each layer is calculated following Dominguez et al. (2019), which is also presented in Table 7.3. The MD of e can be calculated as $(e - e_{average})/e_{average} \times 100\%$, where e is the void ratio of the specific slice, while $e_{average}$ is the void ratio of the whole specimen. The variation in the MD with F_{finer} can be calculated based on the F_{finer} of each layer and the average F_{finer} of the whole specimen, (F_{finer} of each layer - F_{finer} of the whole specimen) / (F_{finer} of the whole specimen) $\times 100\%$. The coefficient of variation (COV) is also calculated following Carraro & Prezzi (2008). Table 7.3 shows that the MD of e for the top layer is maximum, approximately 3.80%.

Table 7.3: Quantifying uniformity of dense specimen with F_{finer} = 10%.

10% dense	mass (g)	density (g/cm^3)	e	F_{finer} (%)	MD (%) e	MD (%) F_{finer}
Top layer	39.886	1.851	0.432	9.5%	-3.8	-4.6
Second layer	39.300	1.824	0.453	9.2%	1.0	-7.5
Third layer	39.452	1.831	0.447	10.3%	-0.3	4.2
Bottom layer	39.034	1.811	0.463	10.7%	3.2	7.9
Average	**39.418**	**1.829**	**0.449**	**9.9%**	**N/A**	**N/A**
Coefficient of variation	**1%**	**1%**	**3%**	**7%**	**N/A**	**N/A**

The uniformity data for the loose specimens with F_{finer} = 10% are presented in Table 7.4. The void ratio of the loose specimens increased to approximately 0.745 compared to the dense specimens. The MD of e is greatest for the top layer which has an MD of approximately 1.6%. In addition, the MD identified in the loose specimen is smaller compared to the MD identified in the dense specimen.

Table 7.4: Quantifying uniformity of loose specimen with F_{finer} = 10%.

10% loose	mass (g)	density (g/cm^3)	e	F_{finer} (%)	MD (%) e	MD (%) F_{finer}
Top layer	32.498	1.508	0.757	10.0	1.6	0.8
Second layer	32.684	1.517	0.747	9.7	0.2	-1.3
Third layer	32.840	1.524	0.739	9.6	-0.9	-3.2
Bottom layer	32.842	1.524	0.739	10.2	-0.9	3.6
Average	**32.716**	**1.518**	**0.745**	**9.9**	**N/A**	**N/A**
Coefficient of variation	**0%**	**0%**	**1%**	**3%**	**N/A**	**N/A**

The results for the dense specimen with F_{finer} = 25% are shown in Table 7.5. A relatively good uniformity can also be observed, the void ratios for these four layers are approximately 0.358, 0.363, 0.365 and 0.352, respectively. Moreover, the largest MD for e is approximately 2.1% for the bottom layer.

Table 7.5: Quantifying uniformity of dense specimen with F_{finer} = 25%.

25% dense	mass (g)	density (g/cm^3)	e	F_{finer} (%)	MD (%) e	MD (%) F_{finer}
Top layer	42.058	1.952	0.358	25.0	-0.5	-0.6
Second layer	41.889	1.944	0.363	25.1	1.1	0.6
Third layer	41.840	1.942	0.365	25.1	1.5	0.3
Bottom layer	42.240	1.960	0.352	25.0	-2.1	-0.3
Average	**42.007**	**1.949**	**0.359**	**25.0**	**N/A**	**N/A**
Coefficient of variation	**0%**	**0%**	**2%**	**1%**	**N/A**	**N/A**

The results for the loose specimen with F_{finer} = 25% are shown in Table 7.6. Relatively good uniformity is observed for this loose condition, the void ratios for these four layers are approximately 0.603, 0.614, 0.610 and 0.612, respectively. Moreover, the largest MD for e is approximately -1.1% for the top layer.

Table 7.6: Quantifying uniformity of loose specimen with F_{finer} = 25%.

25% loose	mass (g)	density (g/cm^3)	e	F_{finer} (%)	MD (%) e	MD (%) F_{finer}
Top layer	35.616	1.653	0.603	25.4	-1.1	1.2
Second layer	35.374	1.642	0.614	25.1	0.7	0.0
Third layer	35.470	1.646	0.610	24.8	-0.0	-1.4
Bottom layer	35.420	1.644	0.612	25.1	0.4	0.9
Average	**35.470**	**1.646**	**0.610**	**25.1**	**N/A**	**N/A**
Coefficient of variation	**0%**	**0%**	**1%**	**1%**	**N/A**	**N/A**

The results for the dense specimen with F_{finer} = 50% are shown in Table 7.7. A relatively good uniformity can also be observed for this high F_{finer}, the void ratios for these four layers are approximately 0.371, 0.390, 0.377 and 0.394, respectively. The largest MD of e is approximately -3.0% for the top layer.

Table 7.7: Quantifying uniformity of dense specimen with F_{finer} = 50%.

50% dense	mass (g)	density (g/cm^3)	e	F_{finer} (%)	MD (%) e	MD (%) F_{finer}
Top layer	41.639	1.932	0.371	49.5	-3.0	-0.6
Second layer	41.081	1.906	0.390	50.3	1.8	0.9
Third layer	41.478	1.925	0.377	50.3	-1.7	0.8
Bottom layer	40.960	1.901	0.394	49.3	2.9	-1.1
Average	**41.290**	**1.916**	**0.383**	**49.9**	**N/A**	**N/A**
Coefficient of variation	**1%**	**1%**	**3%**	**1%**	**N/A**	**N/A**

The results for the loose specimen with F_{finer} = 50% are shown in Table 7.8. For this high F_{finer} in the loose condition, a relatively good uniformity is also

observed, the void ratios for these four layers are approximately 0.509, 0.512, 0.509 and 0.515, respectively. The maximum MD value for e is approximately 0.7%.

Table 7.8: Uniformity quantification of 50% loose specimen

50% dense	mass (g)	density (g/cm^3)	e	F_{finer} (%)	MD (%) e	MD (%) F_{finer}
top layer	37.850	1.757	0.509	50.5	-0.5	1.1
second layer	37.759	1.752	0.512	49.4	0.2	-1.0
third layer	37.839	1.756	0.509	50.4	-0.4	0.9
bottom layer	37.696	1.749	0.515	49.4	0.7	-1.0
Average	**37.786**	**1.754**	**0.511**	**49.9**	**N/A**	**N/A**
Coefficient of variation	**0%**	**0%**	**1%**	**1%**	**N/A**	**N/A**

In general, for all F_{finer} values considered in this study of uniformity, the obtained maximum MD value for e is a relatively large value for the dense specimens when compared to the loose specimen data. This suggests that relatively poor uniformity is always observed in the dense condition, this may be attributed to the use of the vibratory table for the dense specimens. In addition, the maximum MD value for e identified for all specimens $\approx$ 3.8% when F_{finer} = 10% in the dense condition. It is also reasonable to compare the results with the prior results reported in the literature review. For instance, Dominguez et al. (2019) showed a MD value for e $\approx$ 3.5%. Kuerbis & Vaid (1988) assessed their triaxial specimens and showed a MD value for e $\approx$ 5%. Carraro & Prezzi (2008) stated a MD value for e $\approx$ 3%. The maximum MD value for e of 3.8% obtained in this study therefore shows an acceptable level of uniformity when compared with prior research. Besides, for each specimen,

the estimated F_{finer} values are close to its desired F_{finer}. For instance, for $F_{finer} = 50\%$, loose condition, the measured finer fractions of each of the four layers are approximately 50.5%, 49.4%, 50.4% and 49.4%.

7.2.5. Experimental methods used to quantify stiffness

Test procedure

After preparing the specimen, the next step was to add de-aired water to the specimen. In this study, the de-aired water was introduced to the sample before the final assembly of the triaxial cell. As illustrated in Figure 7.22, a vacuum machine was used to generate de-aired water by applying the vacuum until no air bubbles could be identified. The volumetric gauge was firstly flushed with the de-aired water, and then the gauge was emptied, prior to adding more de-aired water. After that, the de-aired water was added to the specimen, as illustrated in Figure 7.22(b) where the path is identified in orange.

For the loose samples, the de-aired water was added into the specimen under a pressure gradient of approximately 7 kPa (i.e. gravity effect, the height difference between the de-aired water and the specimen). For the relatively dense specimens, it was not certain that the pressure gradient of 7 kPa (i.e. gravity effect, the height difference between the de-aired water and the specimen) was sufficient to fully saturate the specimen with de-aired water. Therefore, the back pressure transducer was increased to approximately 20 kPa to draw the de-aired water from the volumetric gauge into the specimen. When the de-aired water was visually observed to reach the top surface of the specimen, the specimen was then sealed with O-rings. After that, a suction of approximately 20 kPa was applied to this specimen and the efficacy of the seal achieved by the O-rings was checked at this stage. The use of suction is common practice in triaxial testing to hold the prepared specimens in place before the application of the cell pressure.

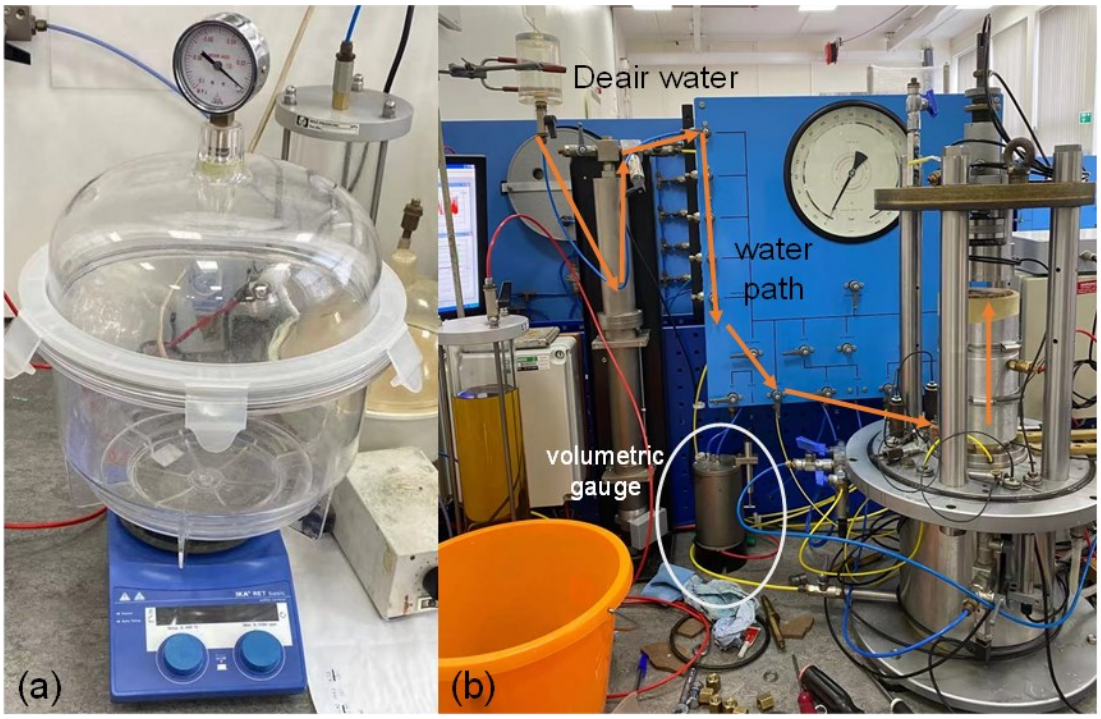


Figure 7.22: Adding of de-aired water into the specimen: (a) The vacuum machine used to generate de-aired water; (b) The procedure of adding de-air water

After the O-rings were put in place, the mould was dismounted, and the dimensions of the specimen were measured, as illustrated in Figure 7.23. For each specimen, the diameter of the top part, and the middle and bottom parts of the specimen were measured by a vernier calliper. The diameter at each location was measured twice. The digital vernier used is readable to 0.01 mm. Before testing, the thickness of the membrane was also measured six times (twice at the top, twice at the middle and twice at the bottom). For instance, for a representative prepared specimen (F_{finer} = 35%-1, relatively dense), the average measured thickness of the membrane was approximately 0.34 mm, the measured diameter of the specimen plus the average diameter of the membrane was 100.61 mm, so that the diameter of the specimen is 99.92 mm. For this specimen, the height was measured to be approximately 196.81 mm. Given that three dimensions of the specimen are measured, the initial volume of the specimen can be obtained, in this case, it was approximately 1543.27 cc.

After measuring the specimen diameter, the three vertical and radial transducers were mounted onto the specimens. Note that the initial readings of these transducers can be monitored using the computer at this stage. The data presented in Figure 7.11 are replotted in Figure 7.24 to illustrate how these data were used to inform the test setup. As illustrated in Figure 7.24, when the working range is close to 0 mm, the error of the system is just approximately 0.001 mm. Therefore, as illustrated in Figure 7.25, the position of the bases for these transducers was adjusted so that the initial measured value was close to 0 mm and to minimize the error.

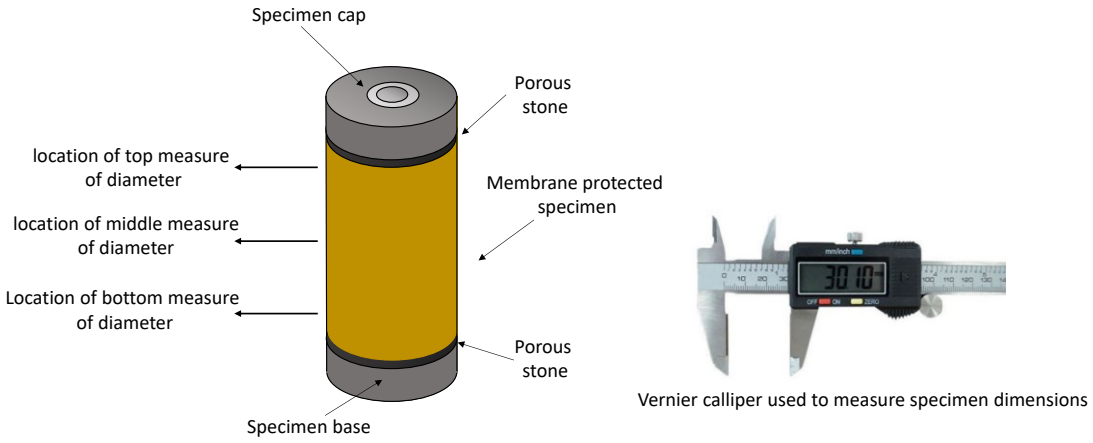


Figure 7.23: Quantifying the specimen dimensions: (a) Measurement of diameter at three locations; (b) The vernier calliper

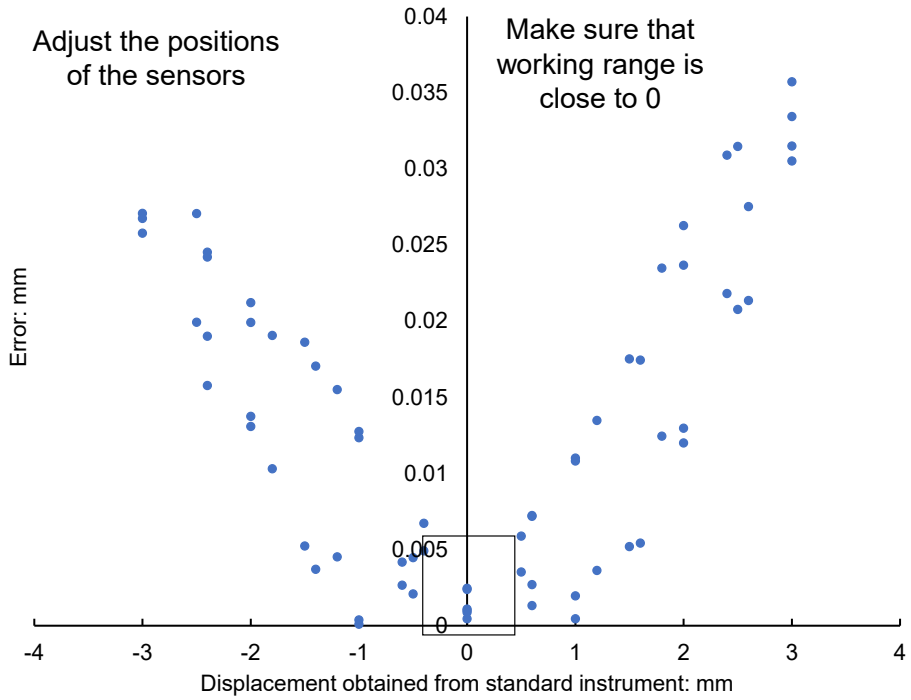


Figure 7.24: The relative error identified for a vertical transducer

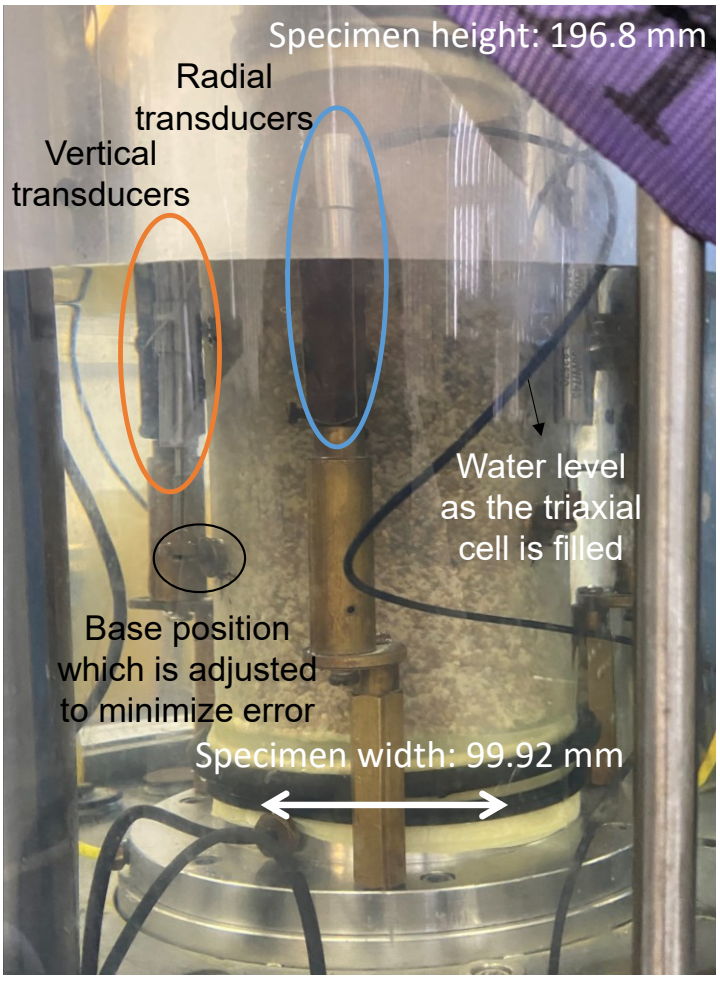


Figure 7.25: The instalment of transducers for a specimen

After the installation of the transducers, water was slowly added into the cell until the whole cell was filled with water. The raw test data were then recorded by a computer, as illustrated in Figure 7.26, the time interval selected for data acquisition was 1 s (i.e. the smallest time interval for the software), and the recording started when the cell was filled with water. Both initial cell and back pressures were approximately 12.3 and 10.8 kPa, note that these two values are just the initial transducer readings and are not controlled at this stage. The "internalstrain" shown in the Figure 7.26 is the recorded results of the vertical transducers. The "radialstrain" shown in the Figure 7.26 is the recorded results for the radial transducers. The initial recorded values are close to 0 mm to minimize the system error.

Time	Timer	load	cell	back	displacement	volumegauge	internalstrain1	internalstrain2	internalstrain3	radialstrain1	radialstrain2	radialstrain3
	min	N	kPa	kPa	mm	ml	mm	mm	mm	mm	mm	mm
15:16:13	583496.86	13.619	12.304	10.809	-0.0021	-10.7195	-0.19088	0.14160	0.28058	-0.33732	-0.39559	-0.19296
15:16:14	583496.88	13.817	12.317	10.834	-0.0025	-10.6948	-0.1906	0.14156	0.28058	-0.33727	-0.39544	-0.19297
15:16:15	583496.9	13.461	12.432	10.822	-0.0021	-10.6718	-0.19031	0.14160	0.28058	-0.33727	-0.39534	-0.19297
15:16:16	583496.91	13.58	12.407	10.822	-0.0025	-10.6542	-0.19011	0.14160	0.28062	-0.33722	-0.39524	-0.19292
15:16:17	583496.93	13.344	12.394	10.809	-0.0021	-10.6401	-0.18999	0.14164	0.28058	-0.33722	-0.39508	-0.19292

Interval 1s

No control of back and cell pressure

Vertical LVDT

Radial LVDT

Figure 7.26: An example of an originally recorded dataset

Then both the cell and back pressures were slowly increased to the desired stress with a rate of approximately 0.03 kPa/s. As illustrated in Figure 7.27, the back pressure was normally 400 kPa, which is considered large enough to obtain a saturated condition. There is no simple correlation between back pressure and B-value, However, BS 1377 states that the minimum back pressure should be approximately 300 kPa. It is reasonable to assume that a higher back pressure will yield a higher B-value. Therefore, a higher back pressure of 400 kPa was used in this study. The saturation was checked by considering the B-value. The average B-value was approximately 0.98 with a standard deviation $\approx$ 0.01. A summary of the B-values and the initial e values is presented in Table 7.9.

Table 7.9: B-values and initial e for the specimens

Specimens	B-values	Initial e
Pure coarse-1	0.98	0.55
Pure coarse-2	0.98	0.60
Pure coarse-3	0.96	0.62
Pure coarse-4	0.99	0.70
Pure fines-1	0.98	0.67
Pure fines-2	0.99	0.77
F_{finer}10%-1	0.97	0.57
F_{finer}10%-2	0.99	0.58
F_{finer}10%-3	0.98	0.46
F_{finer}10%-4	0.97	0.45
F_{finer}10%-5	0.98	0.45
F_{finer}25%-1	0.99	0.35
F_{finer}25%-2	0.98	0.37
F_{finer}25%-3	0.97	0.46
F_{finer}25%-4	0.98	0.47
F_{finer}30%-1	0.99	0.35
F_{finer}30%-2	0.97	0.38
F_{finer}30%-3	0.99	0.44
F_{finer}35%-1	0.99	0.32
F_{finer}35%-2	0.98	0.36
F_{finer}35%-3	0.97	0.39
F_{finer}50%-1	0.98	0.36
F_{finer}50%-2	0.97	0.37
F_{finer}50%-3	0.97	0.40
F_{finer}50%-4	0.95	0.41

F_{finer}50%-5	0.96	0.43
F_{finer}50%-6	0.98	0.48

The changes in dimension from the initial specimen setup to the end of the saturation were recorded by the six transducers so that the volume change could be tracked.

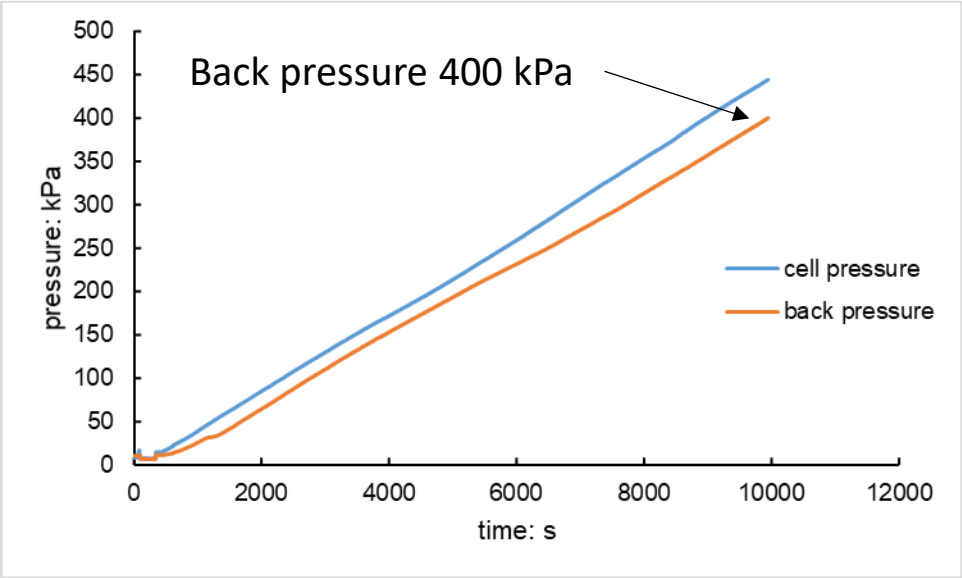


Figure 7.27: The increase in both cell and back pressures before the consolidation stage

After saturation was confirmed, a consolidation stage was conducted under a constant back pressure, while the cell pressure was increased to the desired target pressure. As discussed before, the rate of pressure increase was approximately 0.03 kPa/s. An example of this consolidation stage is presented below in Figure 7.28 for a dense specimen with F_{finer} = 50%. Figure 7.28(a) shows that the back pressure was maintained at 500 kPa during the consolidation, Figure 7.28(b) shows that the cell pressure increased to 600 kPa. The desired effective confining pressure is 100 kPa for this case. Figure 7.28(c) and (d) show $LVDT$ transducer data for one of these vertical and radial $LVDTs$, respectively. Figure 7.28(c) shows that the vertical displacement during this consolidation stage was approximately 0.02387 mm which is significantly

large compared to the system error shown in Figure 7.24 for a working range $\pm 0.5\ mm$ (i.e. 0.005 mm). In addition, the radial displacement during this consolidation stage is approximately 0.01371 mm, which is also large compared to the system error. These displacements correspond to a vertical strain of approximately $1.19 \times 10^{-2}\ \%$, and a radial strain of approximately $1.371 \times 10^{-2}\ \%$. A relatively similar strain can be observed for both the vertical and radial directions. Isotropic compression was targeted for all these samples. However, the anisotropic strain response could be a consequence of a slight anisotropy in stress due to gravity, or a specimen anisotropy due to the vertical pluviation of the specimens.

In general, Figure 7.28 shows that both vertical and radial transducers are capable of measuring changes in the specimen dimensions during this consolidation stage; these measurements can then be used to quantify the volume change during this consolidation stage. For all the tests, the mean vertical displacement was obtained by these three vertical transducers, the mean radial displacement was obtained in the same way. For these six transducers, if the readings were unreliable results, they were not used during this stage. Therefore, the mean volume changes were systematically recorded by these local transducers throughout the tests, from the initial specimen set up (including flushing and saturation) until the end of the test. The specimen dimensions were still slightly changing after the cell pressure has already reached its target value. Therefore, only when the specimen dimensions remained almost constant, could this consolidation stage be considered finished.

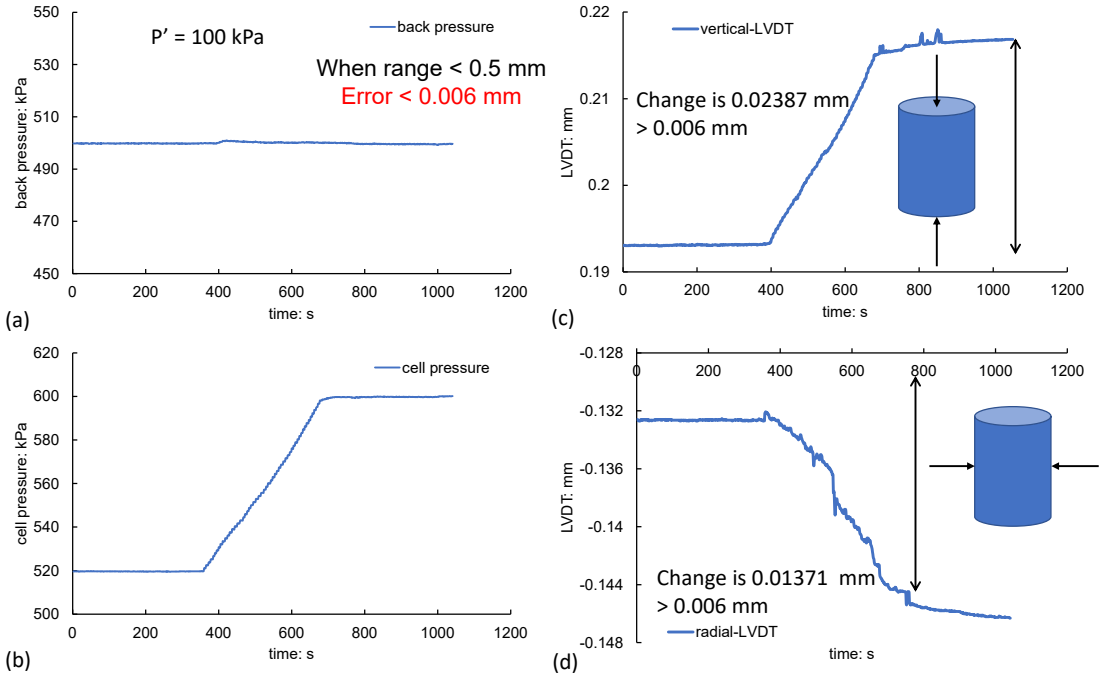


Figure 7.28: Key data recorded during the consolidation stage: (a) Change of back pressure; (b) Change of cell pressure; (c) Change of one of these vertical transducers; (d) Change of one of these radial transducers

Analysis approaches adopted

The method used to analyse the experimental data for the experiments is similar to that used in the DEM simulations, as illustrated in Chapter 6. Both dynamic and static methods were used to estimate the stiffness values.

(1) Bender element test (dynamic method)

Figure 7.29 presents an example for a specimen of the data analysis for the bender element test (i.e. F_{finer} 35%-1, relatively dense). The data were analysed in both the time domain and the frequency domain, using the same methods that were adopted to analyse the DEM simulation data. As illustrated in Figure 7.29(a), in the time domain, the peak-peak method was used to estimate the shear wave velocity. The travel distance used in the peak-peak method is taken to be the distance from the tip of the bottom bender element to the tip of the top bender element, and this gives a V_s of approximately 343.6 m/s. In contrast, Figure 7.29(b) presents the shear velocity estimated by

considering the frequency domain response, which is 343.8 m/s. For this specimen, the shear velocity identified in the time domain analysis is close to that identified in the frequency domain analysis. This consistency indicates that the quality of the generated signal is good enough to be representative, and then the estimated shear velocity can be considered as a reliable measure of the shear wave velocity. For each specimen, a single period sine wave pulse was used, and the frequency applied to the transmitter was varied from 3 kHz to 20 kHz (e.g. 3 kHz; 5 kHz; 7 kHz; 9 kHz; 11 kHz; 13 kHz etc.) so that a good quality received signal could be obtained following Otsubo (2016). For each specimen, the optimum frequency was distinct and strongly dependent upon F_{finer}, e and p'. For instance, for a specimen of certain soil state, for these increasing applied frequency (e.g. 3 kHz; 5 kHz; 7 kHz; 9 kHz; 11 kHz; 13 kHz etc.), the V_s obtained in time domain and frequency domain were also recorded, then the minimum difference between the V_s (time domain) and the V_s (frequency domain) for each applied frequency was identified, which is considered as the optimal frequency for this specimen and this V_s can be used for further calculation of G_0.

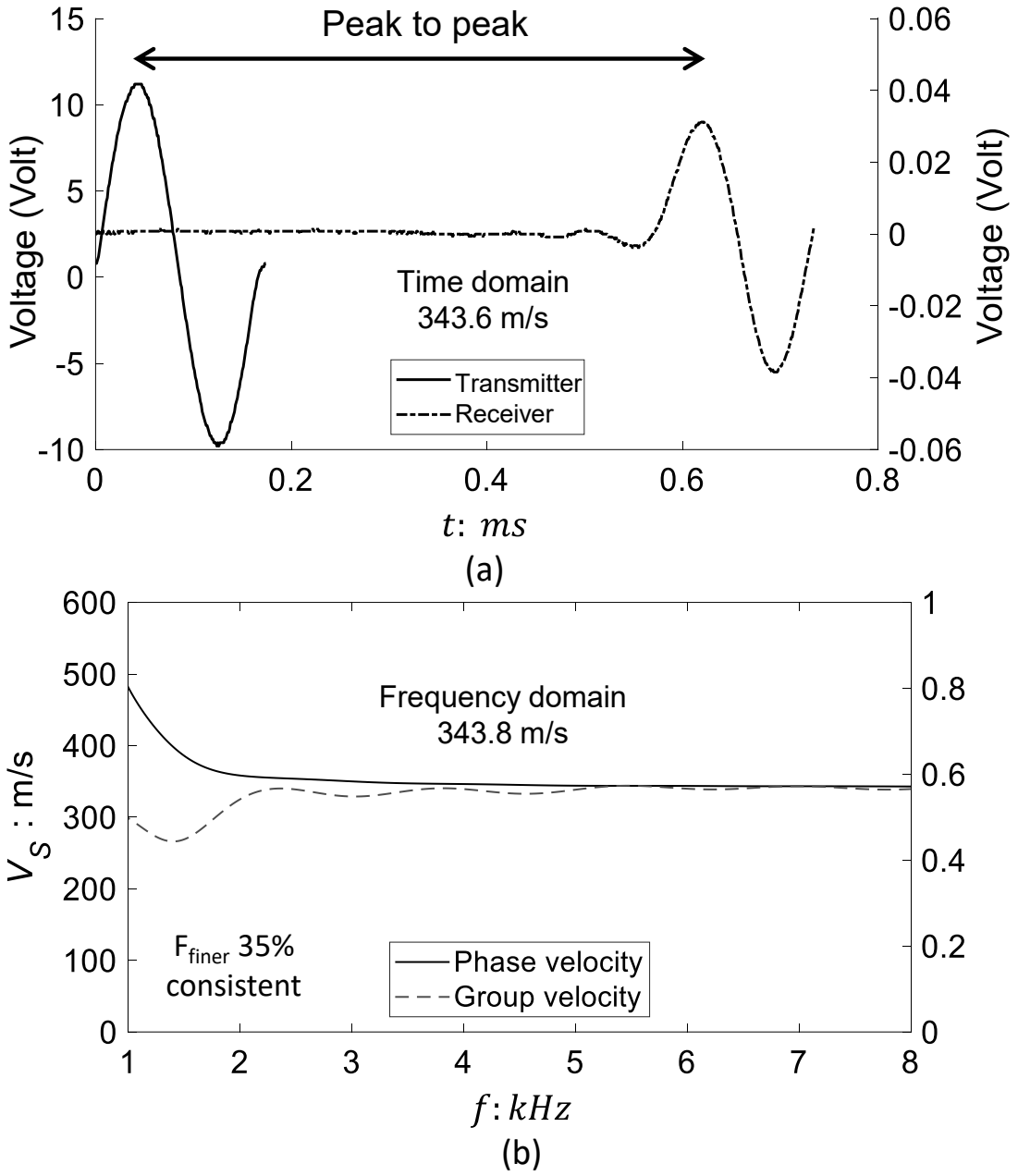


Figure 7.29: An example of data analysis for the bender element test: (a) V_s in time domain; (b) V_s in frequency domain (F_{finer} 35%-1, relatively dense)

(2) Triaxial apparatus with local transducers (static method)

For the static method, a drained axisymmetric compression test was conducted after the consolidation stage, where a small increment of axial strain ($\varepsilon_a \leq 5 \times 10^{-5}$) was applied so that the specimen response could be considered elastic (Kuwano & Jardine, 2002). As discussed above in relation to Figure 7.24,

when the initial transducer reading is close to 0 mm, the maximum system error for these transducers is minimized. However, the accuracy is still restricted by the apparatus used in this study, it can be improved with advanced equipment in the future.

The shear stiffness G_0 was calculated (assuming isotropic elastic media) following:

$$G_0 = \frac{\delta q}{3\delta \varepsilon_q^e} \quad 7.1$$

where δq is the increment in deviatoric stress, and $\delta \varepsilon_q^e$ is the incremental elastic deviatoric strain:

$$\delta \varepsilon_q^e = \frac{2}{3}[\delta \varepsilon_a^e - \delta \varepsilon_r^e] \quad 7.2$$

where $\delta \varepsilon_a^e$ is the applied incremental axial strain, which is also the incremental strain in the z direction, and $\delta \varepsilon_r^e$ is the incremental radial strains, which is also the incremental strain in the $x-$ and $y-$ directions respectively. This method is the same as that used in the DEM simulations. In this study, q was estimated from the measured force (from the load cell) and the area of the specimen. The area of the specimen was monitored using the radial transducers. As discussed before, the interval for all datapoints is 1 s, for each datapoint, the force, area and axial strain could be determined. For this static method, the $\delta \varepsilon_z^e$ and $\delta \varepsilon_x^e$ values were determined from the vertical and radial transducer measurements. The axial strain rate was approximately $6.25 \times 10^{-9}/s$ following Kuwano & Jardine (2002), which is slow enough to get stable measured data, particularly given the data logging frequency used.

An example data are illustrated in Figure 7.30 for a relatively dense specimen of F_{finer} of 35%, Figure 7.30(a) shows the stress-strain relationship, where the horizontal axis is the axial strain and the vertical axis is the deviatoric stress. A

relatively linear relationship can be observed during the elastic stage. Figure 7.30(b) shows the relationship between axial strain and shear time, similar results can also be identified for these three vertical transducers. For this case, the axial strain is then estimated by the average values of the three $LVDT$ transducers for further interpretation. The deformation was usually, but not always, taken to be the average of the three $LVDT$ measurements. The approach used to apply a quality check to the $LVDT$ data is described below.

Given the linear curves identified for the stress-strain relationship, it can be assumed that this specimen is within the elastic regime of deformation. The deformation was reversed so that the deviatoric stress decreased to 0 kPa and the sample returned to an isotropic stress state, returning to the consolidation stage. Then the cell pressure was increased by 100 kPa so that a p' of 200 kPa is obtained. Again, only when the dimensions of the specimen remained constant at the target stress level, was the consolidation stage considered to be over. After that, both static and dynamic methods were conducted again to quantify the specimen stiffness. Subsequently, measures of stiffness were obtained at p' of 300 kPa and 400 kPa following the same method. This method allows the comparison of the stiffness behaviour with similar post-consolidation void ratios (i.e. the same when considered correct to two decimal places) as p' increased.

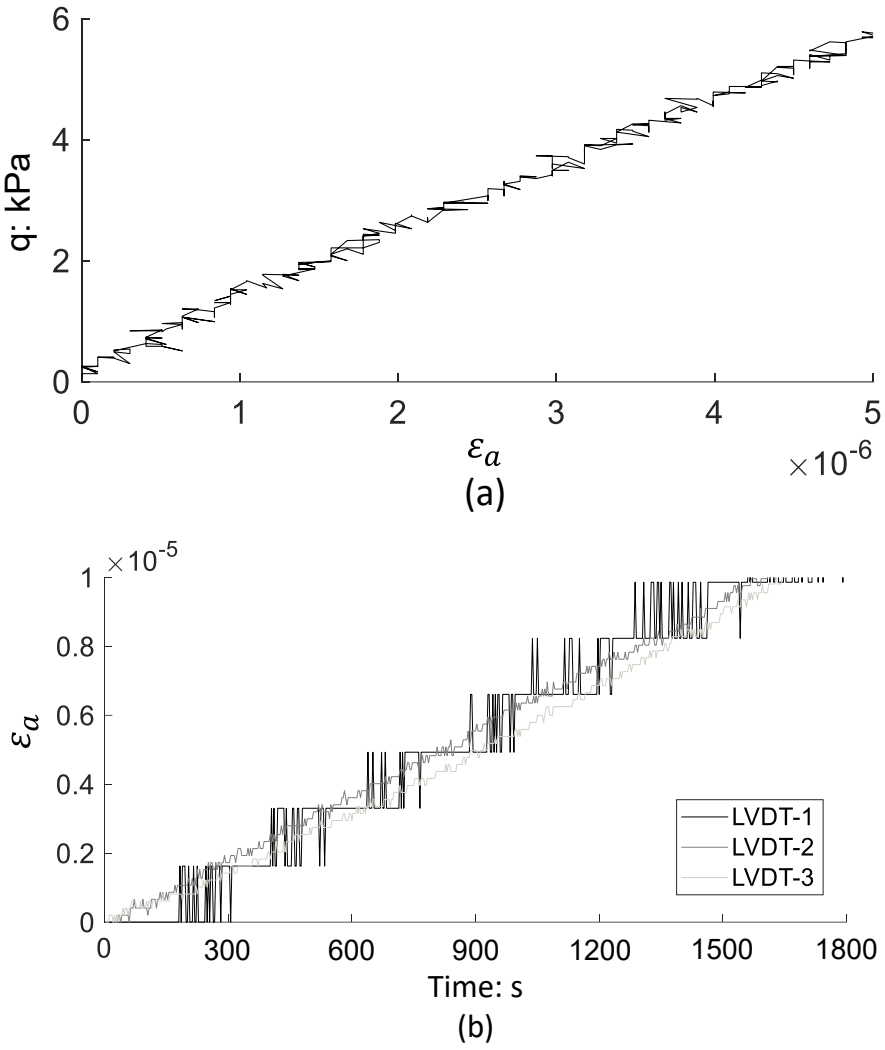


Figure 7.30: The quantification of stiffness values from the static method in experiments (relatively dense F_{finer} 35%-1): (a) $q - \varepsilon_a$ relationship; (b) $\varepsilon_a - time$ relationship

The relationship between deviatoric strain and small strain stiffness for this specimen is also presented in Figure 7.31. A relatively smooth and constant curve can be observed, which suggests that an appropriate shearing rate was applied for the data logging frequency used.

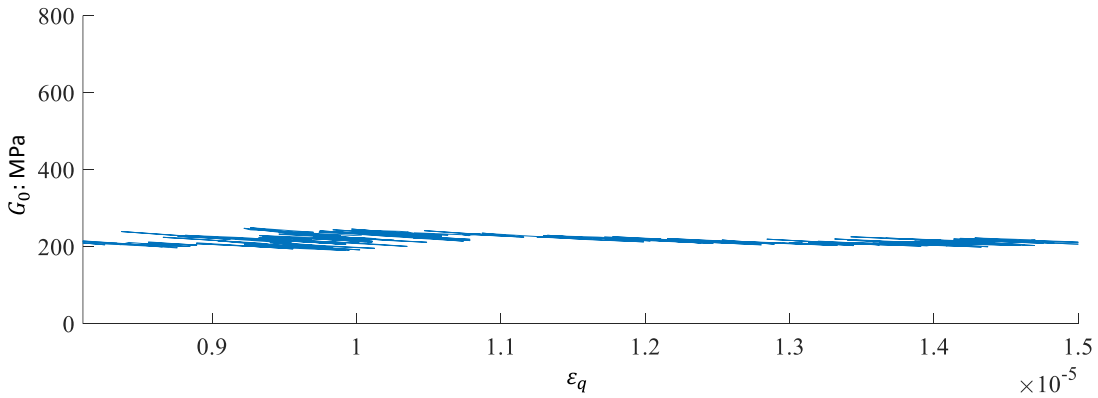


Figure 7.31: The relationship between ε_q and G_0

It is important to appreciate the limitations of this approach to measuring stiffness, the six transducers can only measure six points in the middle part of the specimen; this may not fully capture the changes in the specimen dimensions. Therefore, for some of the specimens, these transducers may not always give similar results, sometimes even distinct results, it may not be feasible to use the average values of these transducers for all tests. Besides, some errors could occur due to the transducers themselves and their operation, which are not relevant to specimen behaviour.

One example is illustrated in Figure 7.32, it can be seen that both vertical $LVDTs$ 1 and 2 show relatively consistent results, while vertical $LVDT$ 3 shows distinct results compared to those identified in transducers 1 and 2. In this case, it may not be appropriate to use the average values of these three transducers to quantify the axial strain of the specimen and so only the results for transducers 1 and 2 are considered in this case. It was therefore not appropriate to apply automatic interpretation procedures and apply the same rule to all data. Generally, if the relative differences amongst the three transducers were lower than 20%, the average values of these transducers were used. In contrast, if one of the transducers showed a divergent behaviour (i.e. the relative error between this transducer and the other two transducers was larger than 20%),

only the average values of those two similar transducers were used. The threshold of 20% used in this study was arbitrarily selected. If a transducer showed unreliable results, the data from this transducer were not used in the estimates of volume change.

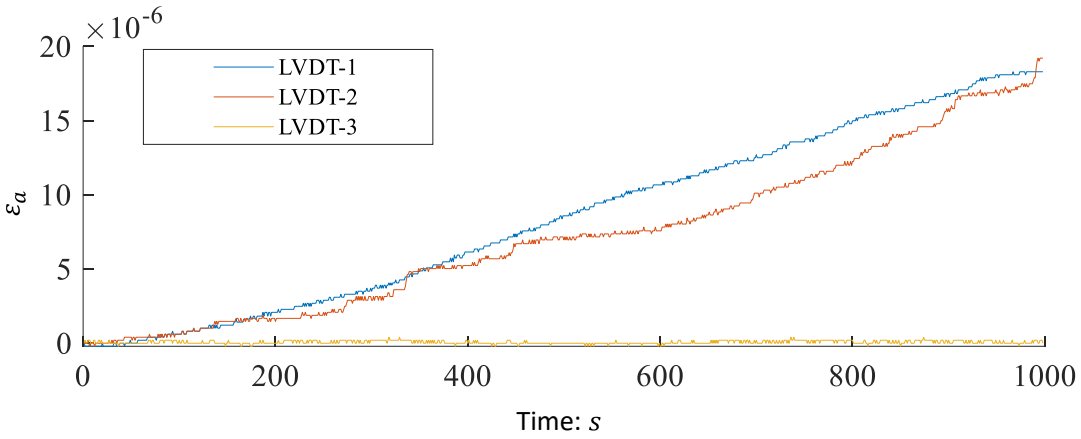


Figure 7.32: An example of divergent $LVDT$ responses that were sometimes observed (F_{finer} 50%-1, relatively dense)

7.3. Results and discussion

For the experimental program, as illustrated before, four effective stresses were applied (i.e. 100 kPa; 200 kPa; 300 kPa; 400 kPa). Based on the DEM simulations documented in Chapter 6, for this experimental study, F_{finer} values of 0%, 10%, 25%, 30%, 35%, 50% and 100% were selected, and for each F_{finer}, at least two packing densities were used.

7.3.1. Void ratio data

Figure 7.33(a) shows how the post-consolidation void ratio of the specimens varied with F_{finer} at $p' = 100\,kPa$. For both the relatively dense and loose specimens, the data agree with the trends presented in Lade et al. (1998) and Zuo & Baudet (2015); e gradually decreases with increasing F_{finer} until a $F_{finer} \approx 35\%$, then e increases with increasing F_{finer} when $F_{finer} \geq 35\%$.

The data on Figure 7.33(b) confirm that a similar trend is observed when p' is 400 kPa. In the DEM datasets (i.e. Figure 6.37(b) for SR = 8.0), the minimum points were associated with F_{finer} = 25% and 35% for the relatively dense and loose conditions, respectively. While for experimental data, the minimum void ratios are observed when F_{finer} = 35%. Clear differences between the simulations and the experiments may explain the different trends observed. For example, the samples were formed under gravity in the experiments and the particles were perfectly round in the DEM simulations.

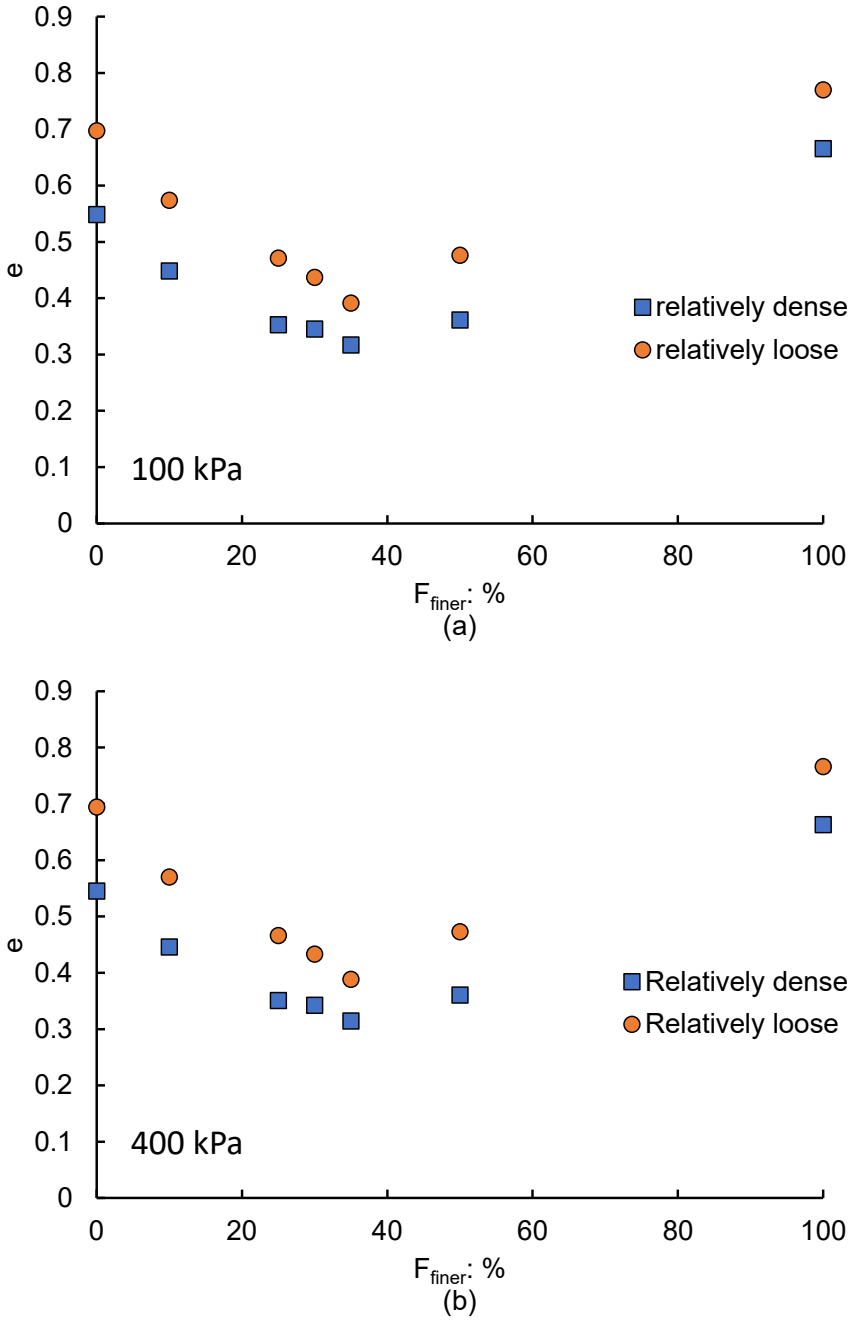


Figure 7.33: Variation in post-consolidation e with F_{finer}: (a) post-consolidation e versus F_{finer} (p' = 100 kPa); (b) post-consolidation e versus F_{finer} (p' = 400 kPa)

7.3.2. Shear wave velocity data

The variation in measured shear velocities with F_{finer} for the laboratory test specimens are illustrated in Figure 7.34 for two representative effective confining pressure values (i.e. 100 kPa; 400 kPa). In general, the trends observed are in agreement with the data shown in Otsubo et al. (2021). In the

dense condition, the shear wave velocities slightly decrease and reach a local minimum value when F_{finer} is approximately 20%, followed by slight increases until F_{finer} is approximately 35%. In the loose case, similar trends are observed.

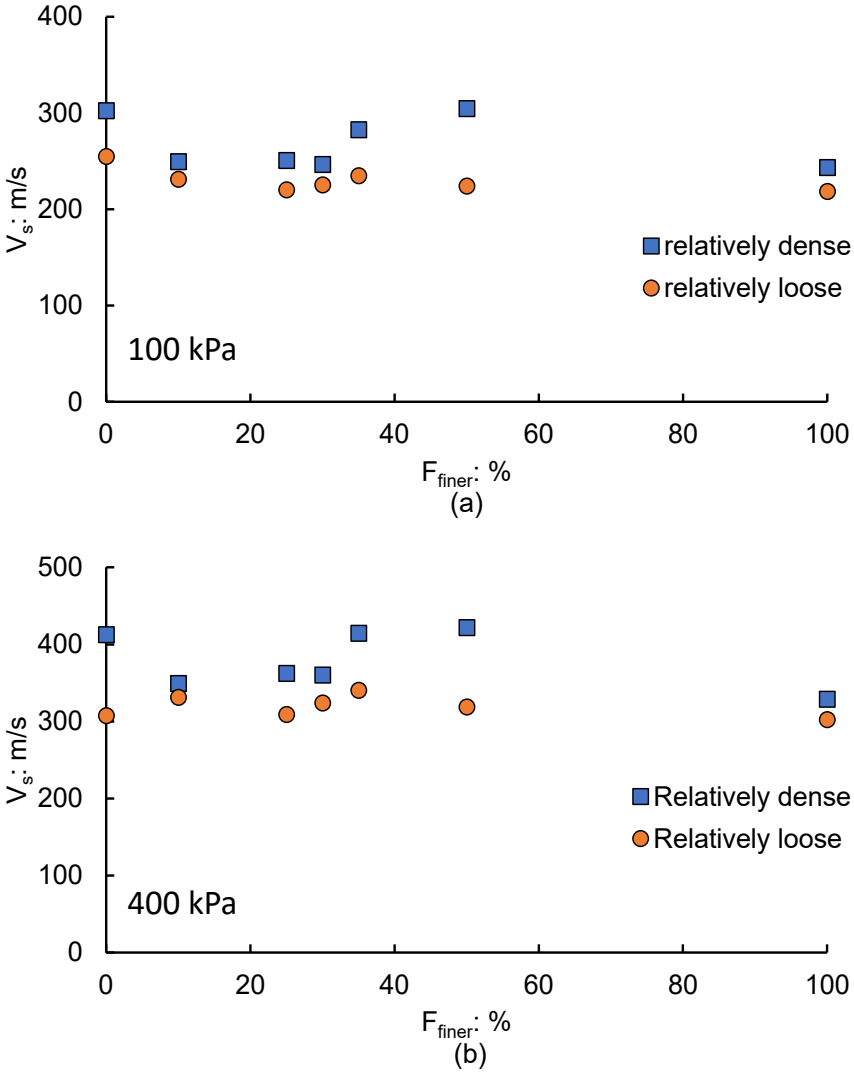


Figure 7.34: Quantification of the shear wave velocities with increasing F_{finer}: (a) V_s versus F_{finer} (p' = 100 kPa); (b) V_s versus F_{finer} (p' = 400 kPa)

The variation in shear wave velocity, V_s, with packing density (i.e. void ratio) is illustrated in Figure 7.35 for four effective confining pressure values. The state-dependent nature of the material behaviour is clear; both the void ratio and effective confining pressure simultaneously affect the specimen V_s. In general, when F_{finer} increases from 0 to 10%, the data shift to the left, for F_{finer} values

of 25% and 30%, similar trend lines are observed with a similar slope being identified. For F_{finer} values of 35% and 50%, similar trends are again observed with their slope being increased. When the F_{finer} is then increased to 100%, it can be seen that the data again shifts to the right.

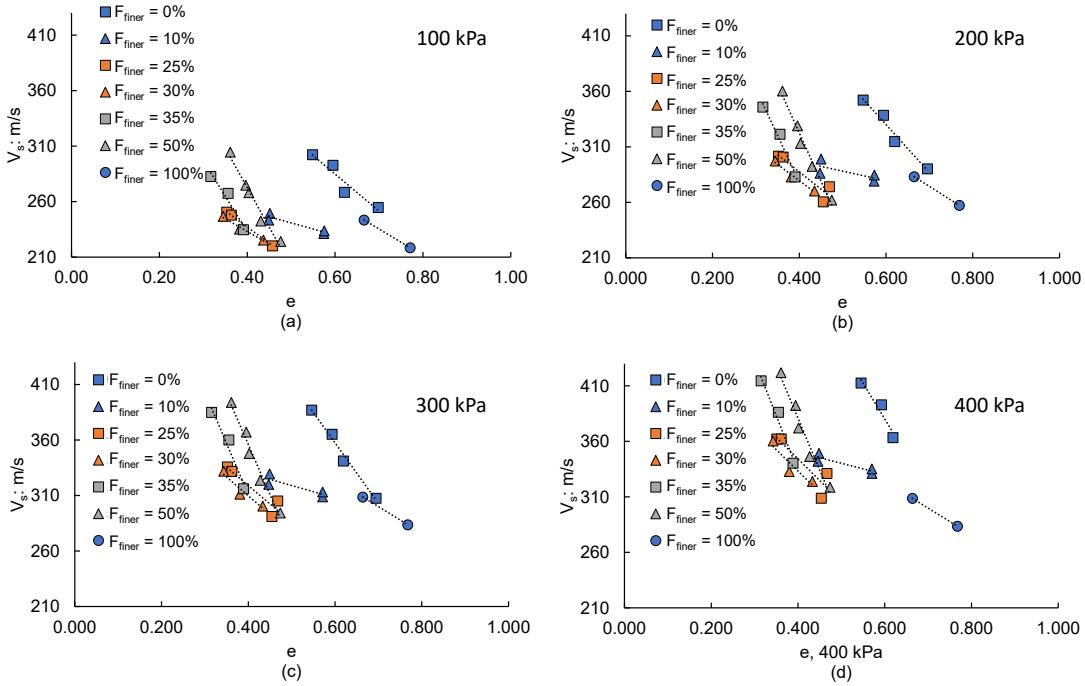


Figure 7.35: Relationship between V_s and e for four p' values: (a) $p' = 100\ kPa$; (b) $p' = 200\ kPa$; (c) $p' = 300\ kPa$; (d) $p' = 400\ kPa$

7.3.3. Shear stiffness data

The estimated dynamic stiffness values, G_{dyn} and the estimated static stiffness values, G_{sta} are presented in Figure 7.36 and Figure 7.37, respectively for the four confining pressure values considered. The trends observed are similar to those noted in relation to Figure 7.35. The state-dependent behaviour of gap-graded soils observed in the DEM dataset (i.e. Figure 6.38(d) & (e)) is replicated in the experiments as illustrated in Figure 7.36 & Figure 7.37. For instance, as F_{finer} increased from 0% to 10%, the $G_{dyn}(e) - e$ correlation shifts to the left as in the numerical simulations. When $25\% \leq F_{finer} < 35\%$, the correlations are close, again in agreement with the DEM data. When $35\% \leq F_{finer} \leq 50\%$, as described in grey colour, the trends

are similar, and they shift towards the right with increasing F_{finer}. In general, the key characteristics identified in the experimental dataset qualitatively agree with the DEM simulation data. Furthermore, these data clearly show that e cannot capture the variation in G_0 with state in a unified way.

The results presented here can be related to the prior studies for liquefaction resistance on non-plastic soil mixtures (Carraro et al., 2003). In particular, the trends observed is similar to the cyclic resistance ratio (CRR) behaviour presented in Carraro et al. (2003) (i.e. Figure 7.36(f)). As illusrated in Figure 7.36(e) and (f), when F_{finer} increases from 0% to 15%, the fitting curves shift to the left. This may suggest that the stiffness value may play a much more crucial role in CRR and in turn strongly affect the liquefaction response. This result shows that the stress-transmission may be the fundamental ingredient that strongly affects both of these aspects of the mechanical behaviour of soil mixtures.

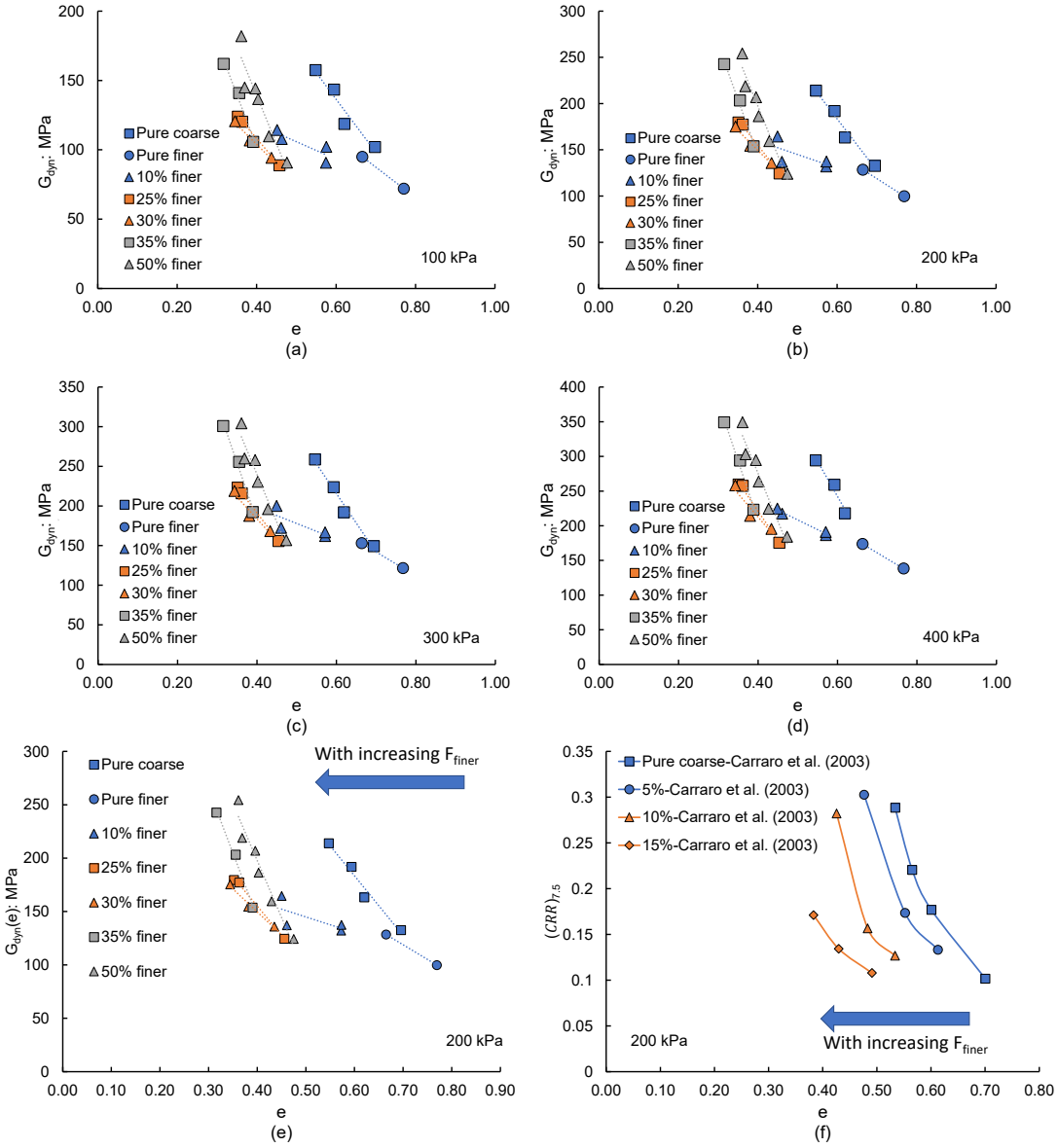


Figure 7.36: Relationship between G_{dyn} and e with four increasing p': (a) p' = 100 kPa; (b) p' = 200 kPa; (c) p' = 300 kPa; (d) p' = 400 kPa; (e) The G_{dyn} versus e when p' = 200 kPa; (f) Cyclic resistance ratio $(CRR)_{7.5}$ versus e (modified from Carraro et al., 2003)

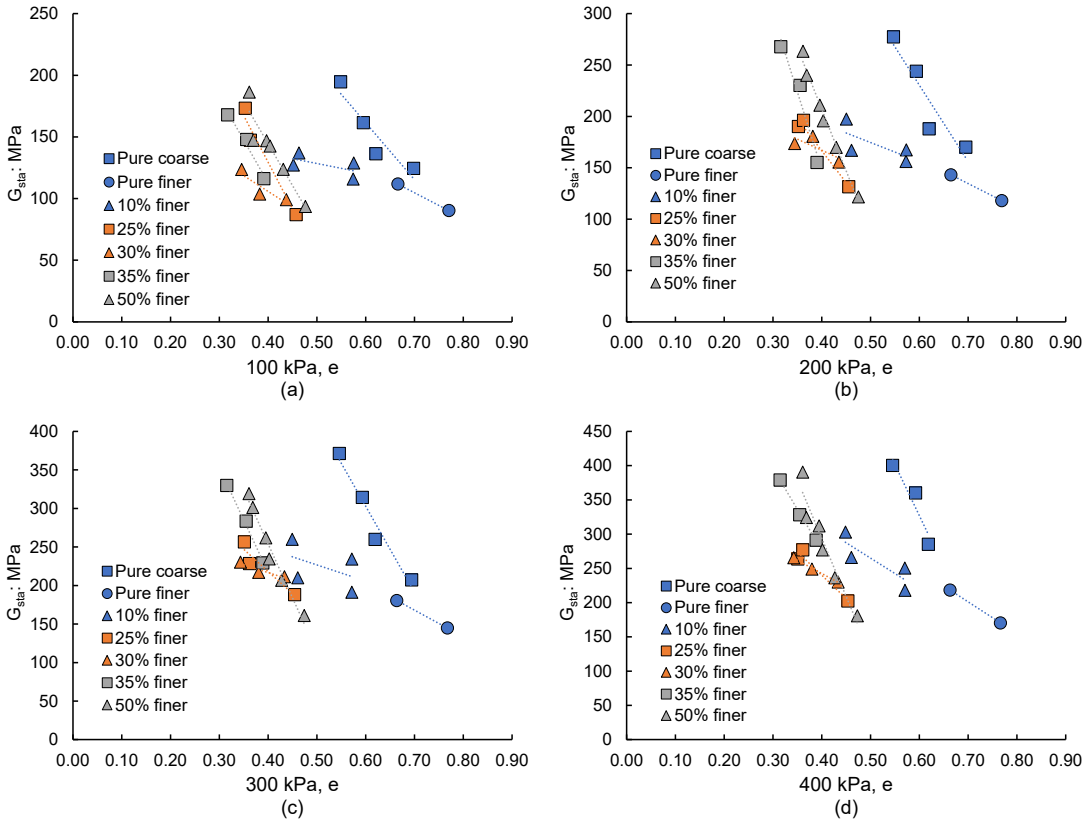


Figure 7.37: Relationship between G_{sta} and e with four increasing p': (a) p' = 100 kPa; (b) p' = 200 kPa; (c) p' = 300 kPa; (d) p' = 400 kPa

7.3.4. Data analysis of the experimental study

To enable a comparison between the experimental and DEM data, a reference was made to the empirical expressions by Hardin & Richart (1963) (i.e. Equation 6.1). Equation 6.2 was employed to describe the variation in G_0 with void ratio, where c is an empirical constant (Hardin & Richart, 1963). To compare the DEM and experimental data, the parameter A in Equation 6.1 determined by regression analysis for each F_{finer} was considered. Following Otsubo (2016) for the smooth spherical grains in the DEM simulations $n = 0.33$ and $c = 1.28$. For the experiments, the sand particles were relatively rounded and so the c value selected was 2.17 following Hardin & Richart (1963). The n value was selected by referring to prior studies using sand with relatively rounded grains. For instance, Carraro et al. (2003) studied the rounded to subrounded Ottawa sand and proposed a n value of approximately

0.437. In addition, Yang & Liu (2016) studied the natural silica sands with the n values ranging from 0.37 to 0.40. In this study, the n is therefore selected as 0.40.

Specimens comprising only coarse particles (F_{finer} = 0%)

The results for the tests for the specimens comprising only coarse grains are presented in Table 7.10 and Figure 7.38, Figure 7.38(a) presents the data obtained using the dynamic method. The state-dependency of the behaviour is clear; both the void ratio and packing density simultaneously affect the stiffness values. Figure 7.38(b) presents the static data and very similar behaviour are observed, with the stiffness values being dependent on the void ratio and packing densities.

Table 7.10: Results for specimens comprising only coarse particles

Specimens	p' (kPa)	e	V_s (m/s)	G_{dyn} (MPa)	G_{sta} (MPa)
Pure coarse-1	100	0.549	302.31	157.6	194.6
	200	0.547	352.21	214.1	277.4
	300	0.546	386.94	258.6	371.4
	400	0.545	412.57	294.1	400.4
Pure coarse-2	100	0.595	292.80	143.5	161.5
	200	0.594	337.47	191.9	243.9
	300	0.593	365.24	223.6	314.4
	400	0.592	393.00	259.0	360.0
Pure coarse-3	100	0.621	268.42	118.7	136.2
	200	0.620	314.80	163.3	187.8
	300	0.619	341.22	192.0	259.8
	400	0.619	363.36	217.8	285.1
Pure coarse-4	100	0.698	254.75	102.0	124.4
	200	0.695	290.26	132.7	170.0
	300	0.694	307.59	149.1	207.2

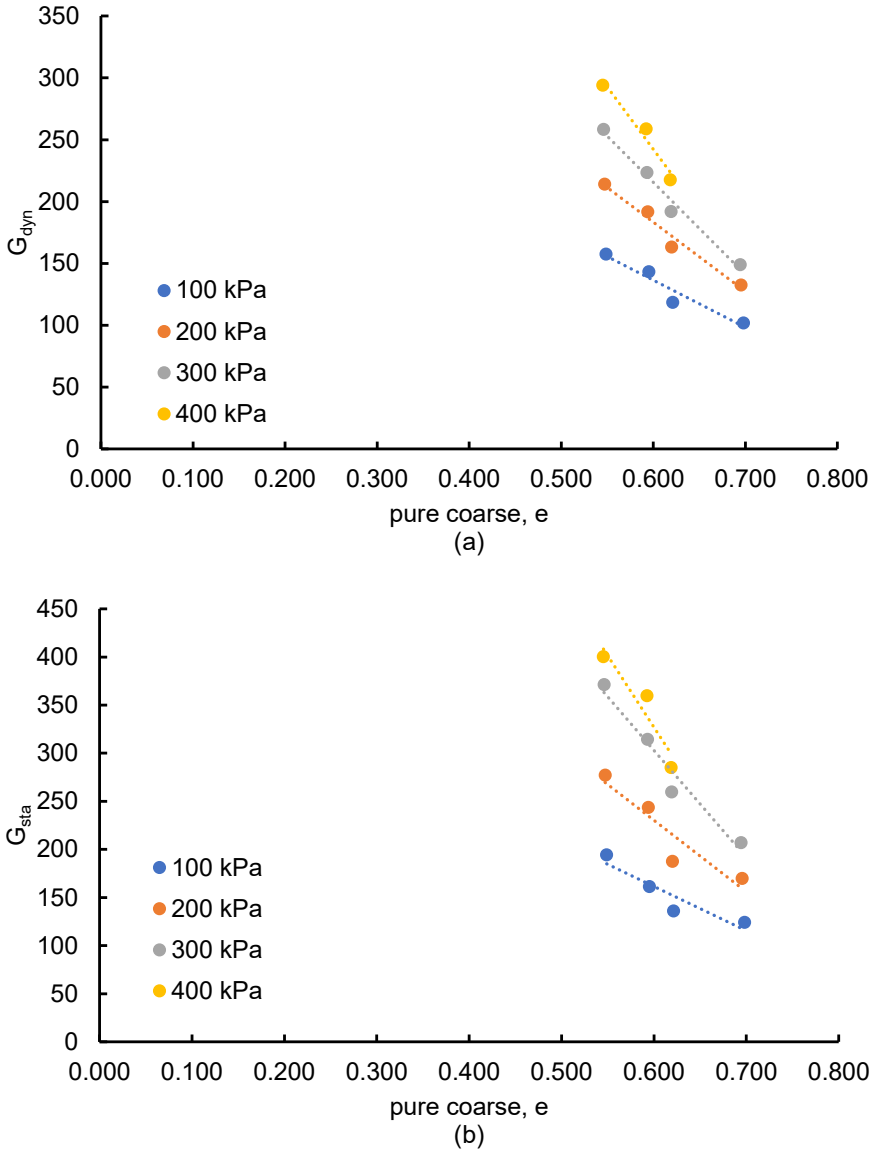


Figure 7.38: The relationship between stiffness values and e for specimens comprising only coarse particles: (a) G_{dyn} versus e; (b) G_{sta} versus e

The comparison between G_{dyn} and G_{sta} for the specimens comprising only coarse particles is presented in Figure 7.39, the void ratio following consolidation was 0.62. This result shows that estimated G_{sta} values are consistently large compared to the corresponding G_{dyn} values.

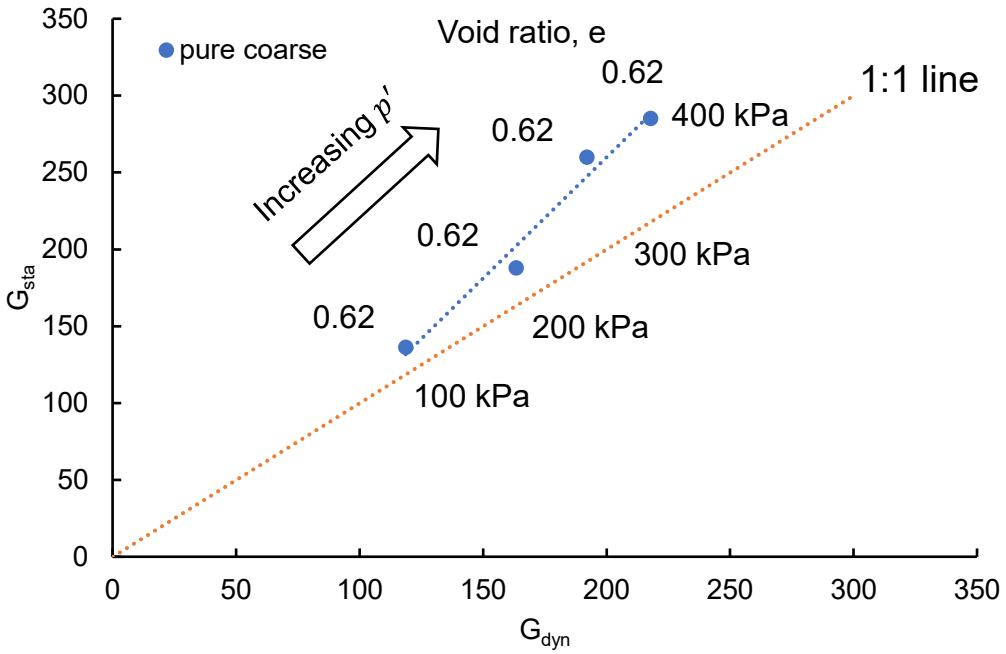


Figure 7.39: The comparison between G_{dyn} and G_{sta} for the specimens comprising only coarse particles

Hardin's equation was applied to the specimens containing only coarse particles, as illustrated in Figure 7.40. Figure 7.40(a) shows the results for G_{dyn}, applying a least square regression and using $MATLAB$, a value of A = 14.28 was obtained (where c = 2.17 and n = 0.4 as discussed above). The R^2 is approximately 0.91, which shows a relatively good performance for the use of the global void ratio to describe the variation in G_0 with state for the specimens comprising only coarse particles. This result agrees with the results identified in Chapter 6 for pure coarse. Figure 7.40(b) shows the optimal surface obtained by fitting the Hardin expression to the G_{sta} data; in this case, the optimal A value was 18.93, again obtained using the least squares regression with c = 2.17 and n = 0.4.

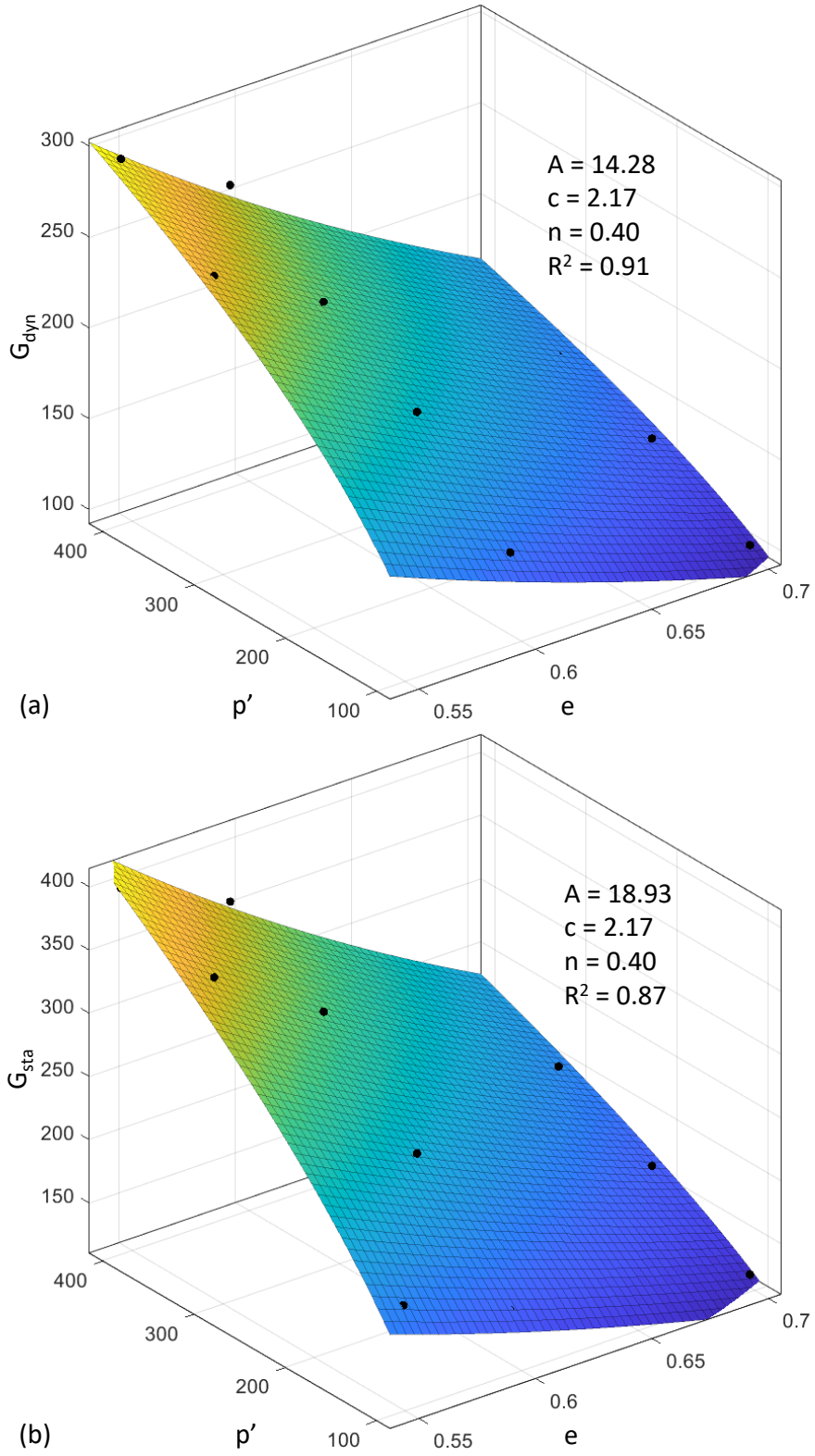


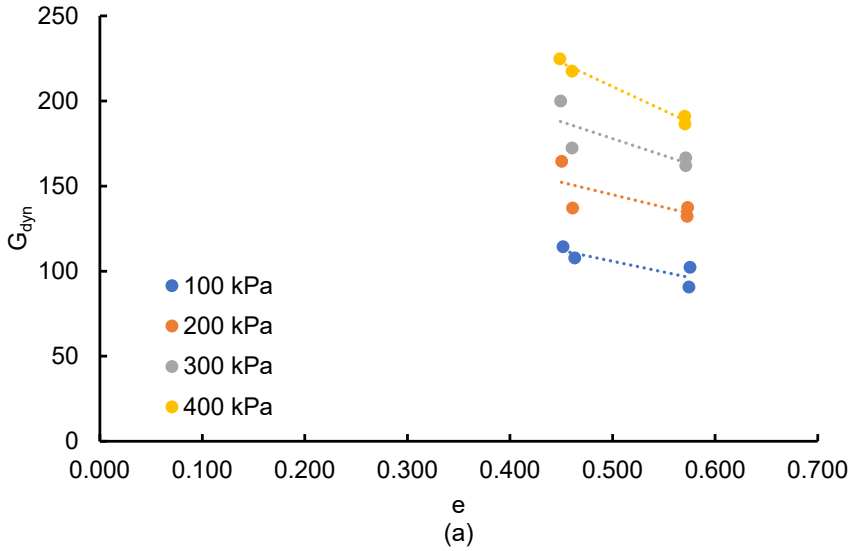
Figure 7.40: Best fit surface obtained by fitting Hardin's equation to the stiffness data for the specimens comprising only coarse particles and assuming c = 2.17 and n = 0.4: (a) G_{dyn} values; (b) G_{sta} values

F_{finer} = 10% (underfilled fabric)

The results for the specimens with F_{finer} = 10% are presented in Table 7.11 and Figure 7.41. For this F_{finer}, a coarse dominant soil behaviour is expected, where most of the finer particles do not transfer stress. Figure 7.41(a) shows the G_{dyn} data, while Figure 7.41(b) presents the G_{sta} data. As before it is clear that both the void ratio and effective confining pressure simultaneously affect the stiffness values so that a state-dependent behaviour is observed for this set of samples.

Table 7.11: Results for specimens with F_{finer} = 10%

Specimens	p' (kPa)	e	V_s (m/s)	G_{dyn} (MPa)	G_{sta} (MPa)
F_{finer} 10%-1	100	0.574	231.28	90.7	115.8
	200	0.573	279.03	132.2	156.0
	300	0.571	308.74	162.0	191.4
	400	0.571	331.16	186.4	218.0
F_{finer} 10%-2	100	0.575	245.64	102.3	128.8
	200	0.573	284.58	137.5	167.3
	300	0.571	313.15	166.6	234.3
	400	0.570	335.23	191.1	250.5
F_{finer} 10%-3	100	0.463	243.10	107.8	137.0
	200	0.461	273.92	137.1	167.0
	300	0.461	307.10	172.4	210.0
	400	0.461	344.90	217.5	266.0
F_{finer} 10%-4	100	0.452	249.37	114.4	127.1
	200	0.450	299.00	164.6	197.4
	300	0.449	329.49	200.0	260.0
	400	0.449	349.21	224.8	303.1



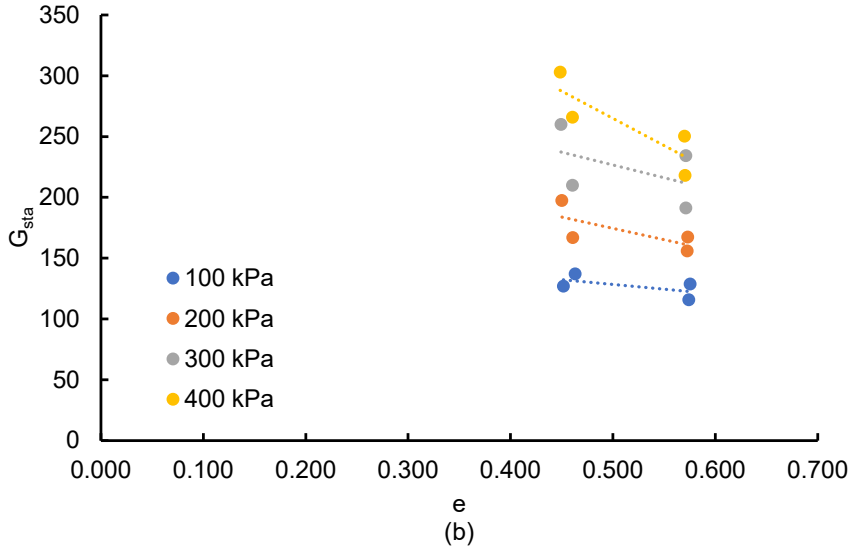


Figure 7.41: The relationship between stiffness values and e for the specimens with F_{finer} = 10%: (a) G_{dyn} versus e; (b) G_{sta} versus e

When F_{finer} is 10%, the comparison between G_{dyn} and G_{sta} is presented in Figure 7.42. The G_{sta} values are consistently large when compared to the corresponding G_{dyn} value.

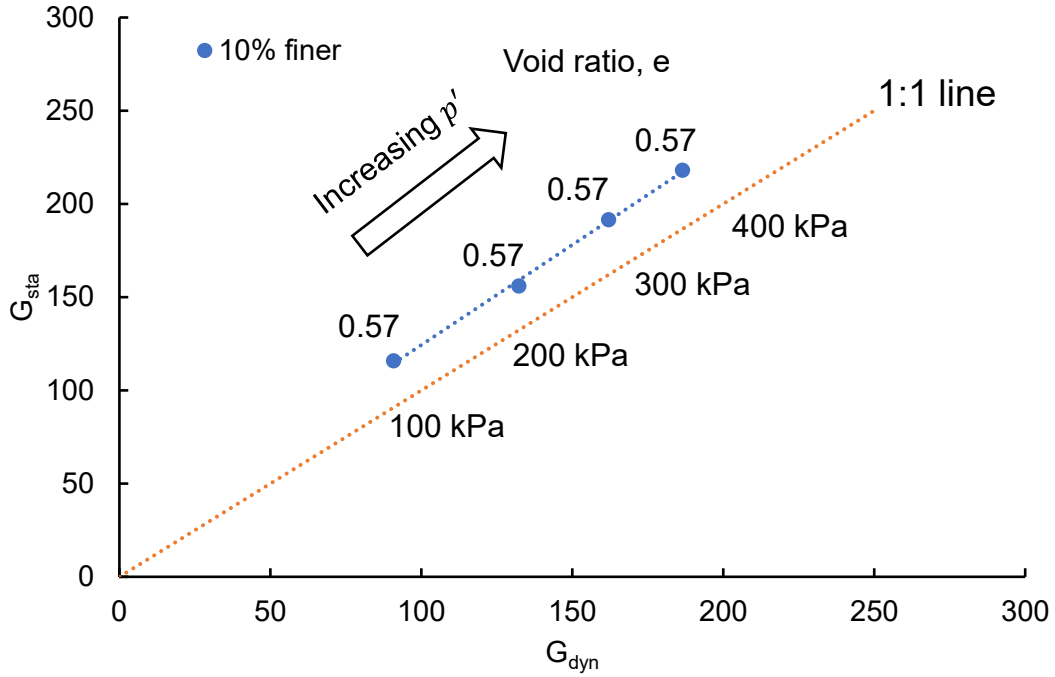


Figure 7.42: The comparison between G_{dyn} and G_{sta} for the specimens with F_{finer} = 10%

When F_{finer} is 10%, Hardin's equation was also used for the data analysis, as illustrated in Figure 7.43, a surface was fitted to the data taking c = 2.17, and n = 0.4 for the G_{dyn} data, the A value obtained was 9.75 from the best-fitting curve. For the G_{sta} data, the A value obtained was 12.21.

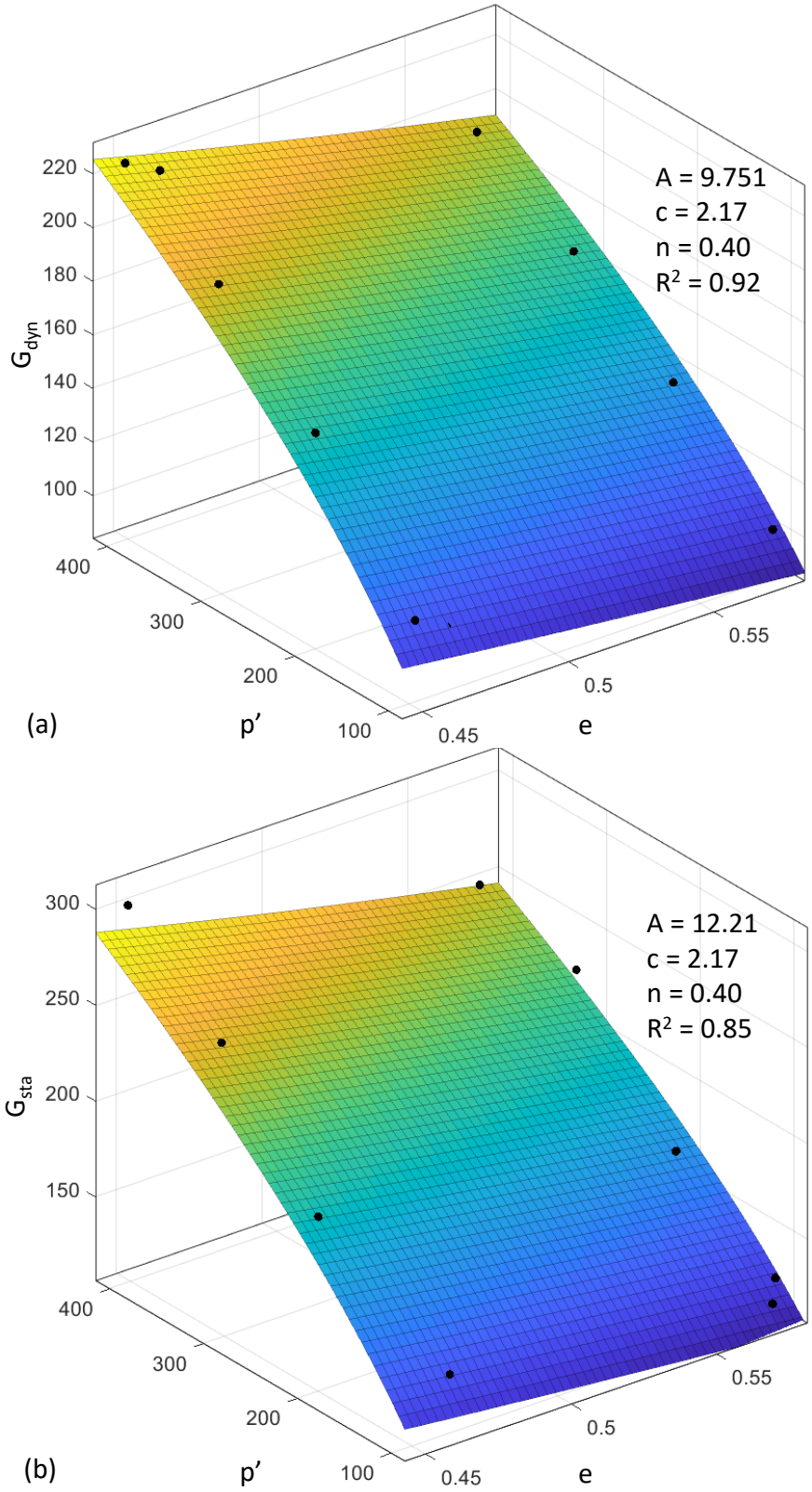


Figure 7.43: Best fit surface obtained by fitting Hardin's equation to the stiffness data for the specimens with F_{finer} = 10% and assuming c = 2.17 and n = 0.4: (a) G_{dyn} values; (b) G_{sta} values

F_{finer} = 25% (density-dependent fabric)

The results for the specimens with F_{finer} = 25% are presented in Table 7.12 as well as Figure 7.44(a) and (b). The G_{dyn} and G_{sta} for specimens with the same state are shown on Figure 7.45. As before, the G_{sta} values are larger than the G_{dyn} values at the same state.

Table 7.12: Results for specimens with F_{finer} = 25%

Specimens	p' (kPa)	e	V_s (m/s)	G_{dyn} (MPa)	G_{sta} (MPa)
F_{finer} 25%-1	100	0.353	250.62	123.9	173.2
	200	0.352	301.61	179.6	190.0
	300	0.351	335.85	222.8	256.5
	400	0.351	362.17	259.2	263.6
F_{finer} 25%-2	100	0.364	247.96	120.4	147.3
	200	0.363	300.80	177.3	196.0
	300	0.362	331.81	215.8	228.5
	400	0.361	362.22	257.3	277.0
F_{finer} 25%-3	100	0.457	220.22	88.8	87.9
	200	0.456	260.54	124.5	131.3
	300	0.454	291.20	155.7	188.0
	400	0.454	308.91	175.3	202.4

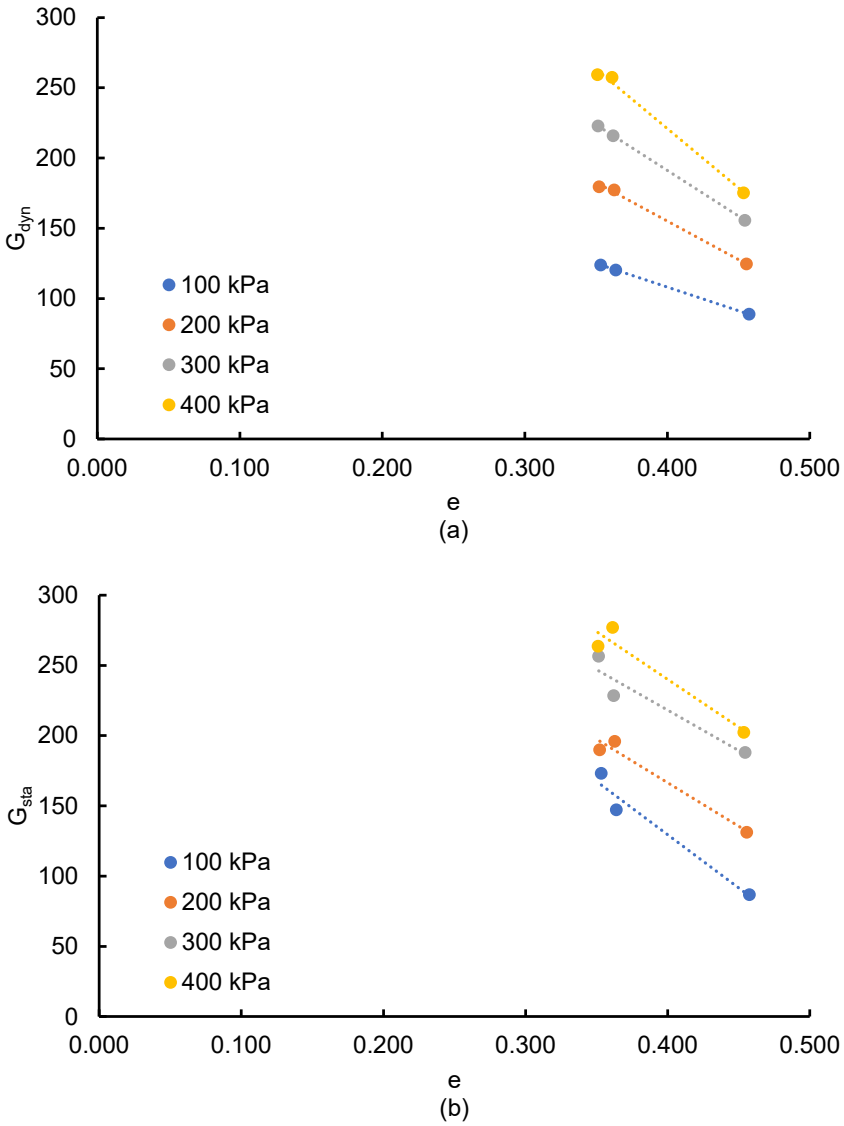


Figure 7.44: The relationship between stiffness values and e for the specimens with F_{finer} = 25%: (a) G_{dyn} versus e; (b) G_{sta} versus e

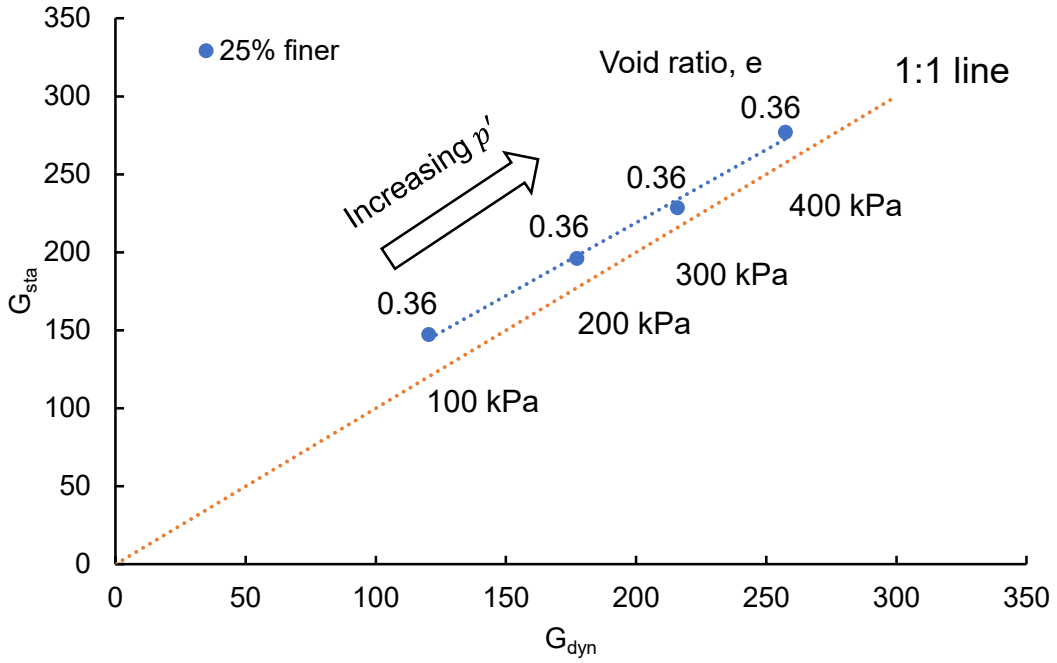


Figure 7.45: The comparison between G_{dyn} and G_{sta} for the specimens with F_{finer} = 25%

When Hardin's equation was fitted to the data for F_{finer} = 25%, (with c = 2.17 and n = 0.40). As illustrated in Figure 7.46, for the G_{dyn} value, an A value of 8.79 was obtained. For the G_{sta} data, the A value obtained was 9.72.

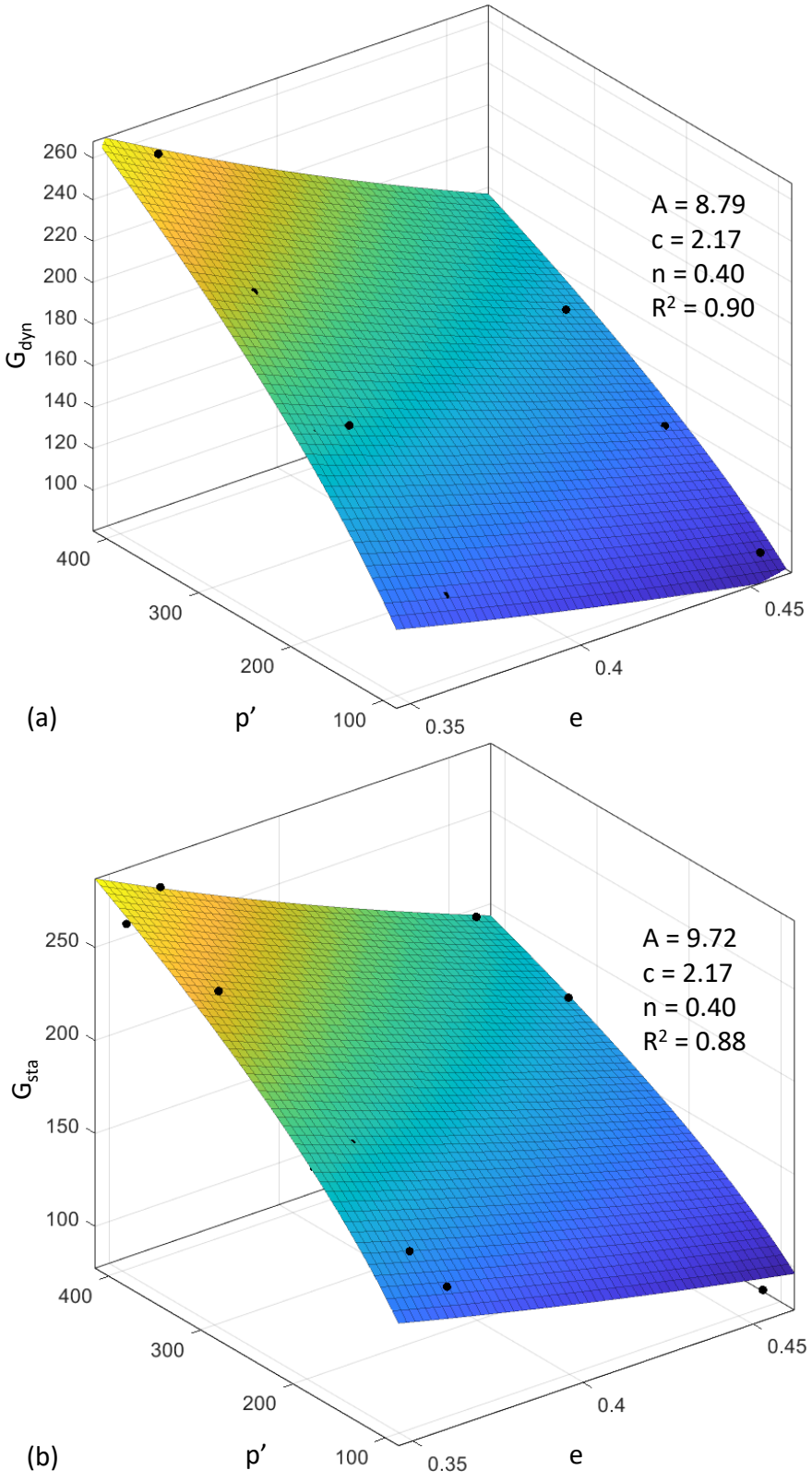


Figure 7.46: Best fit surface obtained by fitting Hardin's equation to the stiffness data for the specimens with F_{finer} = 25% and assuming c = 2.17 and n = 0.4: (a) G_{dyn} values; (b) G_{sta} values

F_{finer} = 50% (overfilled fabric)

The results for the specimens with F_{finer} = 50% are presented in Table 7.13 as well as in Figure 7.47(a) and (b) for the dynamic and static stiffness, respectively. At the same soil state, when the initial void ratio is approximately 0.40, the G_{dyn} and G_{sta} values are similar as illustrated in Figure 7.48. For instance, when the effective confining stress is 100 kPa, the G_{dyn} and G_{sta} are approximately 144.7 and 146.9 MPa, respectively.

Table 7.13: Results for specimens with F_{finer} = 50%

Specimens	p' (kPa)	e	V_s (m/s)	G_{dyn} (MPa)	G_{sta} (MPa)
F_{finer} 50%-1	100	0.361	304.68	182.0	186.3
	200	0.361	360.17	254.4	263.4
	300	0.361	393.80	304.3	319.3
	400	0.361	421.90	349.2	390.7
F_{finer} 50%-2	100	0.370	272.76	145.0	147.2
	200	0.369	335.06	219.0	239.9
	300	0.369	364.99	259.9	301.3
	400	0.368	394.18	303.2	324.4
F_{finer} 50%-3	100	0.397	274.75	144.3	146.9
	200	0.396	328.97	207.0	210.9
	300	0.395	367.12	257.9	261.9
	400	0.395	392.36	294.7	312.1
F_{finer} 50%-4	100	0.404	268.06	136.7	142.6
	200	0.403	313.02	186.5	195.6
	300	0.402	347.90	230.5	234.6
	400	0.401	372.03	263.7	277.0
F_{finer} 50%-5	100	0.431	242.58	109.8	123.7
	200	0.430	292.32	159.6	169.8
	300	0.428	323.64	195.9	206.8
	400	0.427	346.29	224.4	236.3
F_{finer} 50%-6	100	0.476	224.10	90.8	93.5
	200	0.475	262.00	124.3	121.6
	300	0.474	294.20	156.8	161.2
	400	0.473	318.70	184.1	180.9

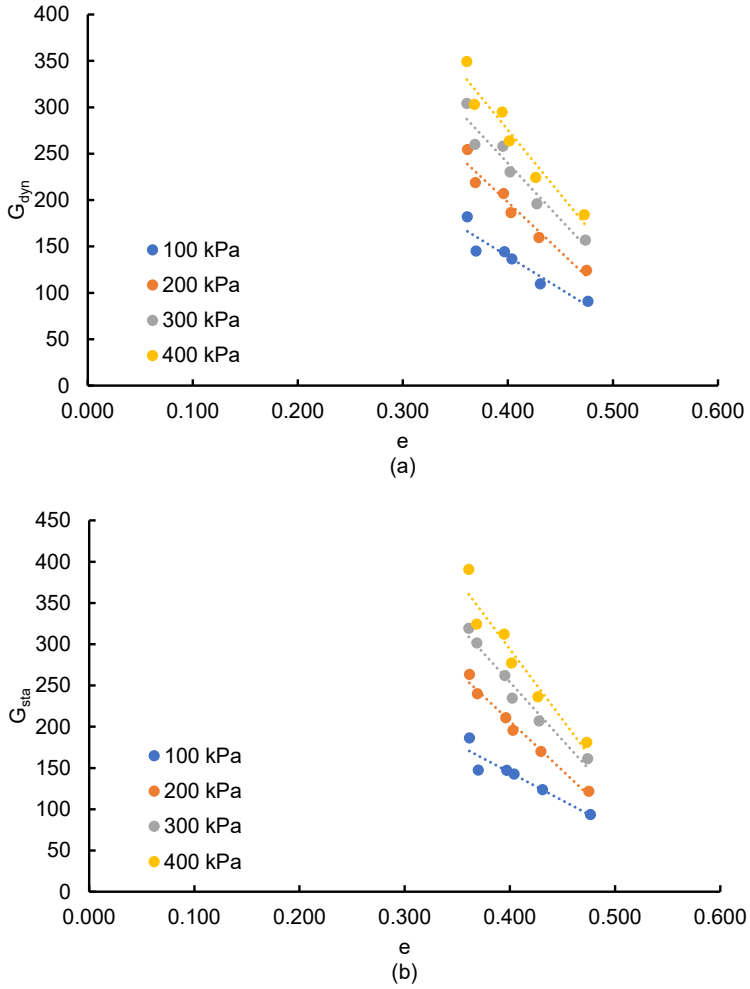


Figure 7.47: The relationship between stiffness values and e for the specimens with F_{finer} = 50%: (a) G_{dyn} versus e; (b) G_{sta} versus e

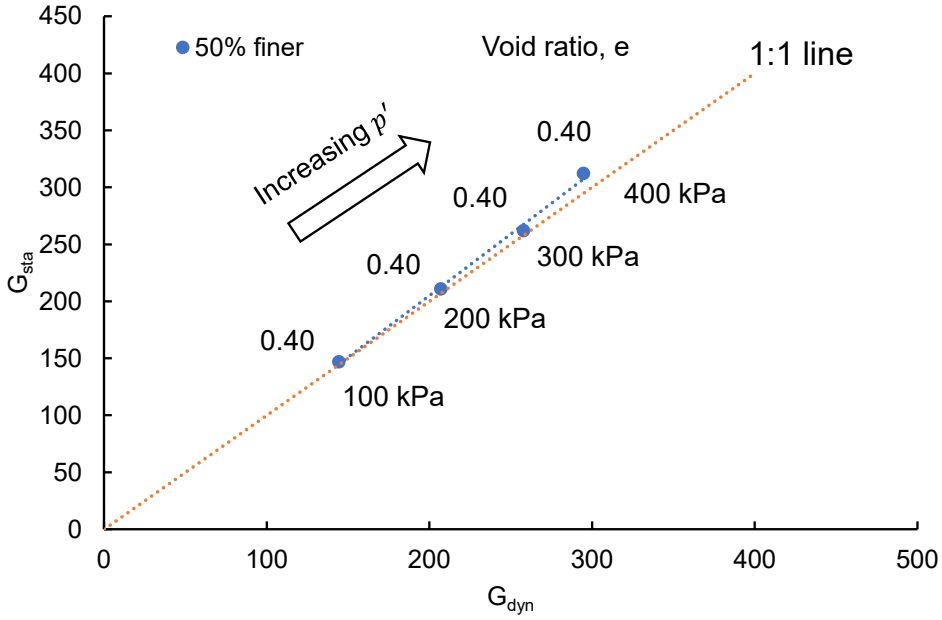


Figure 7.48: The comparison between G_{dyn} and G_{sta} for the specimens with F_{finer} = 50%

When F_{finer} is 50%, the data analysis within Hardin's equation is also illustrated in Figure 7.49, the c value is fixed as 2.17, the n value is fixed as 0.4, for the G_{dyn} value, the A value is obtained as 10.68 from the best-fitting curve. For the G_{sta} value, the A value is then obtained as 11.27.

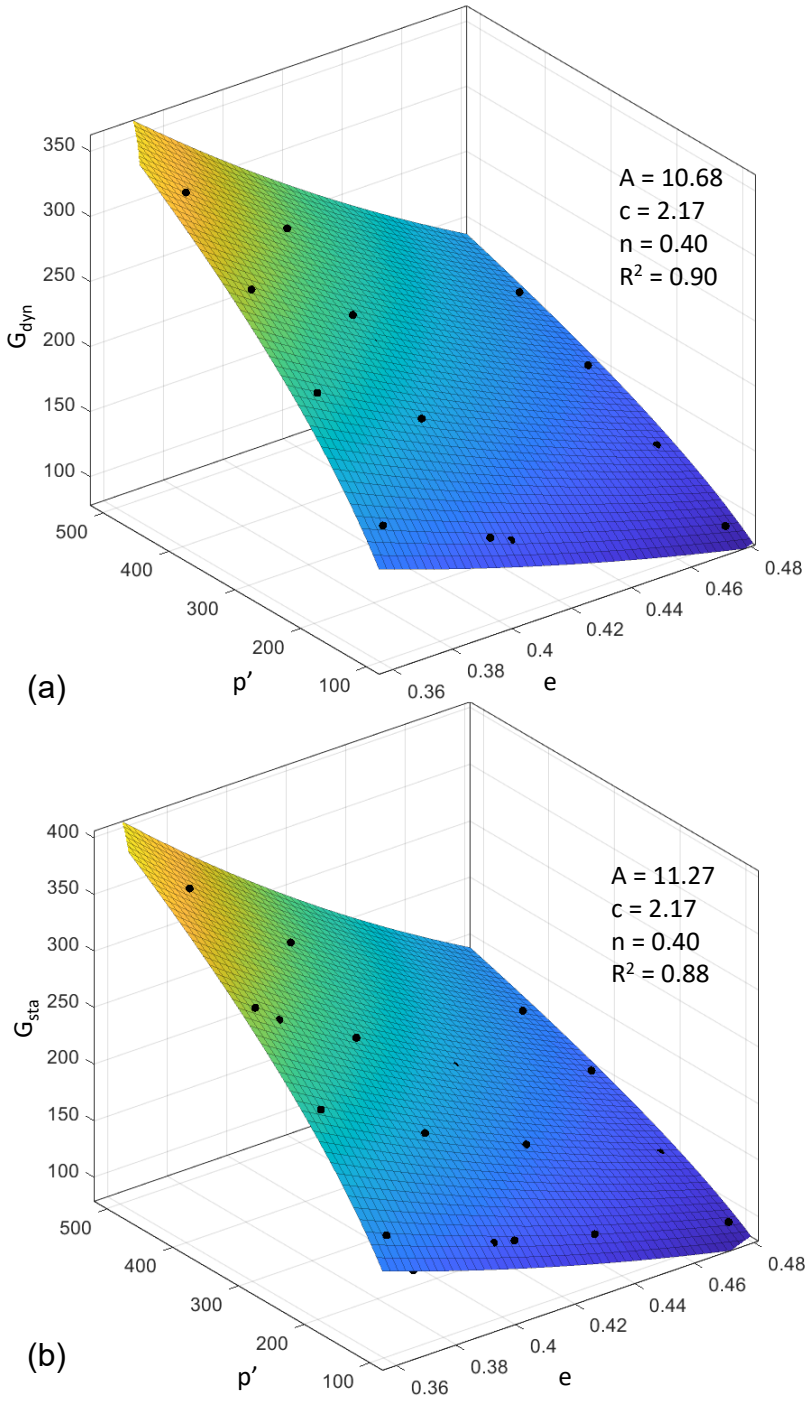


Figure 7.49: Best fit surface obtained by fitting Hardin's equation to the stiffness data for the specimens with F_{finer} = 50% and assuming c = 2.17 and n = 0.4: (a) G_{dyn} values; (b) G_{sta} values

Specimens comprising only finer particles (F_{finer} = 100%)

The results for the tests carried out on the specimens containing only finer particles are illustrated in Figure 7.50 and Table 7.14, Figure 7.50(a) presents two typical cases for the specimens with F_{finer} = 100%. Both void ratio and stress level simultaneously affect the stiffness values. Figure 7.50(b) shows the G_{sta} data and a similar trend is observed.

Table 7.14: Results for specimens comprising only finer particles, i.e. F_{finer} = 100%

Specimens	p' (kPa)	e	V_s (m/s)	G_{dyn} (MPa)	G_{sta} (MPa)
Pure fines-1	100	0.666	243.39	94.9	111.7
	200	0.665	283.06	128.5	143.0
	300	0.664	308.66	152.9	180.5
	400	0.663	328.92	173.7	218.2
Pure fines-2	100	0.771	218.50	72.0	90.2
	200	0.769	257.27	99.9	117.9
	300	0.768	283.64	121.5	144.8
	400	0.766	302.37	138.2	170.3

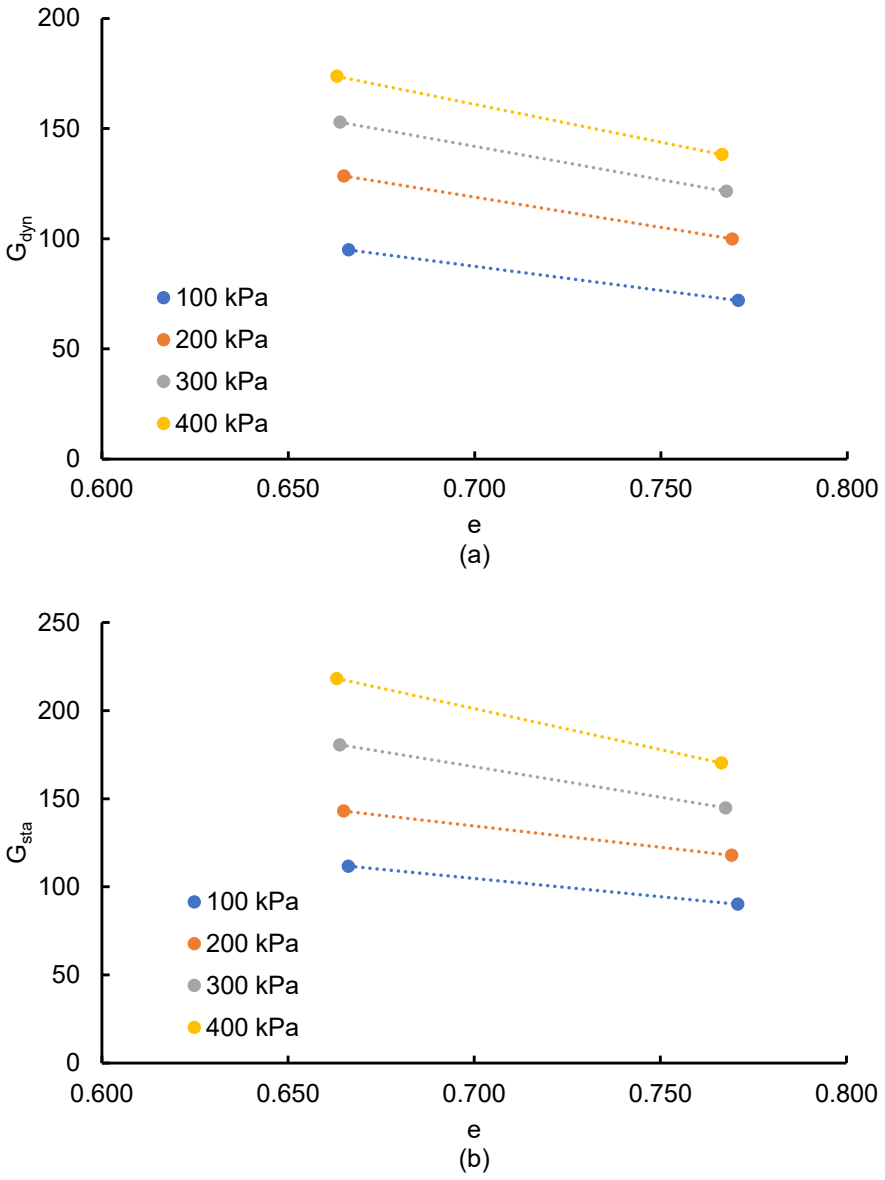


Figure 7.50: The relationship between stiffness values and e for specimens comprising only finer particles: (a) G_{dyn} versus e; (b) G_{sta} versus e

The comparison between G_{dyn} and G_{sta} for the pure finer specimens is presented in Figure 7.51, the void ratio before shearing and the bender element tests was approximately 0.66, four increasing effective confining pressure are presented below. These data show that the estimated G_{sta} values are consistently large compared to the corresponding G_{dyn} values.

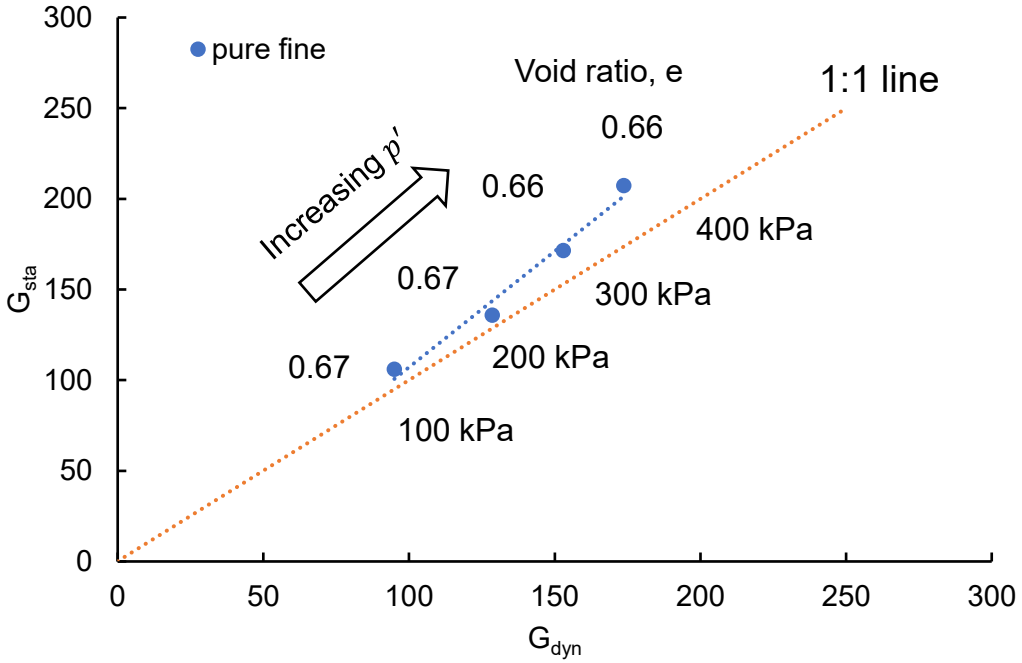


Figure 7.51: The comparison between G_{dyn} and G_{sta} for the specimens comprising only finer particles

When referring to the pure finer specimens, the data analysis within Hardin's equation is also illustrated in Figure 7.52, the c value is fixed as 2.17, the n value is fixed as 0.4, for the G_{dyn} value, the A value is obtained as 11.27 from the best-fitting curve. For the G_{sta} value, the A value is then obtained as 13.54.

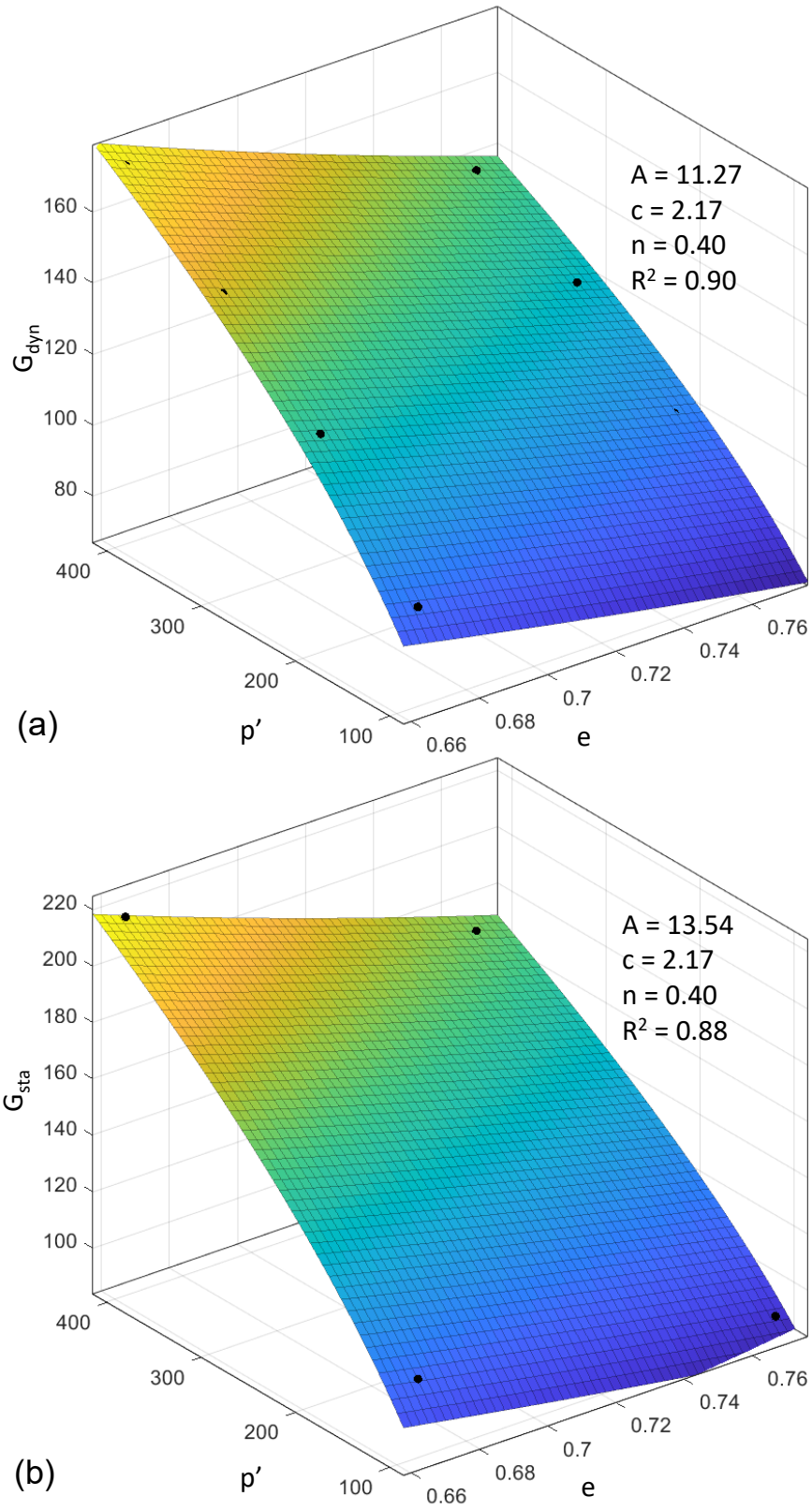


Figure 7.52: Best fit surface obtained by fitting Hardin's equation to the stiffness data for the specimens comprising only finer particles and assuming c = 2.17 and n = 0.4: (a) G_{dyn} values; (b) G_{sta} values

In addition to the data for representative F_{finer} values discussed in more detail above, the data for F_{finer} = 30% and 35% are also presented in Table 7.15 and Table 7.16.

Table 7.15: Results for specimens with F_{finer} = 30%

Specimens	p' (kPa)	e	V_s (m/s)	G_{dyn} (MPa)	G_{sta} (MPa)
F_{finer} 30%-1	100	0.346	246.65	120.7	123.6
	200	0.344	297.13	175.3	173.5
	300	0.343	331.84	218.9	230.3
	400	0.342	360.33	258.2	265.5
F_{finer} 30%-2	100	0.383	235.20	106.8	103.6
	200	0.381	282.77	154.5	180.5
	300	0.381	311.21	187.3	217.1
	400	0.380	332.72	214.2	249.1
F_{finer} 30%-3	100	0.437	225.29	94.3	99.1
	200	0.435	270.20	135.8	155.5
	300	0.433	300.49	168.2	211.4
	400	0.433	323.87	195.4	230.0

Table 7.16: Results for specimens with F_{finer} = 35%

Specimens	p' (kPa)	e	V_s (m/s)	G_{dyn} (MPa)	G_{sta} (MPa)
F_{finer} 35%-1	100	0.317	282.70	162.0	167.9
	200	0.316	345.90	242.7	267.7
	300	0.315	384.92	300.7	329.8
	400	0.315	414.56	349.0	379.1
F_{finer} 35%-2	100	0.356	267.56	140.9	147.9
	200	0.356	321.34	203.4	230.0
	300	0.355	360.09	255.5	283.5
	400	0.355	386.21	294.0	328.3
F_{finer} 35%-3	100	0.391	234.75	105.7	116.0
	200	0.390	282.99	153.8	155.1
	300	0.389	316.17	192.1	229.2
	400	0.388	340.43	222.9	291.3

Key response trends observed from the experimental study

The best-fit A values can be directly compared to the DEM results. As illustrated in Figure 7.53 (a) and (b) for the DEM results, where the G_{dyn} and G_{sta} are used in the regression analysis, A decreases with increasing F_{finer} until F_{finer} ≈25% and then gradually increases with subsequent increases in F_{finer}. As illustrated in Figure 7.53 (c&d), it can be seen that the A values identified in experiments are not exactly the same as those observed in the DEM dataset, The differences may be attributed to the fact that the particle shapes of the real sands and spherical particles differ. Furthermore, the lack of gravity and associated fabric anisotropy in the DEM samples may also contribute to this difference. However, the trend of the variation of A values in experiments is similar to that observed in numerical simulations. The A values

gradually decrease until a F_{finer} of 30%, followed by a gradual increase in A value with increasing F_{finer}. Furthermore, Figure 7.53 also shows that A values fitted from dynamic and static methods show almost the same tendency.

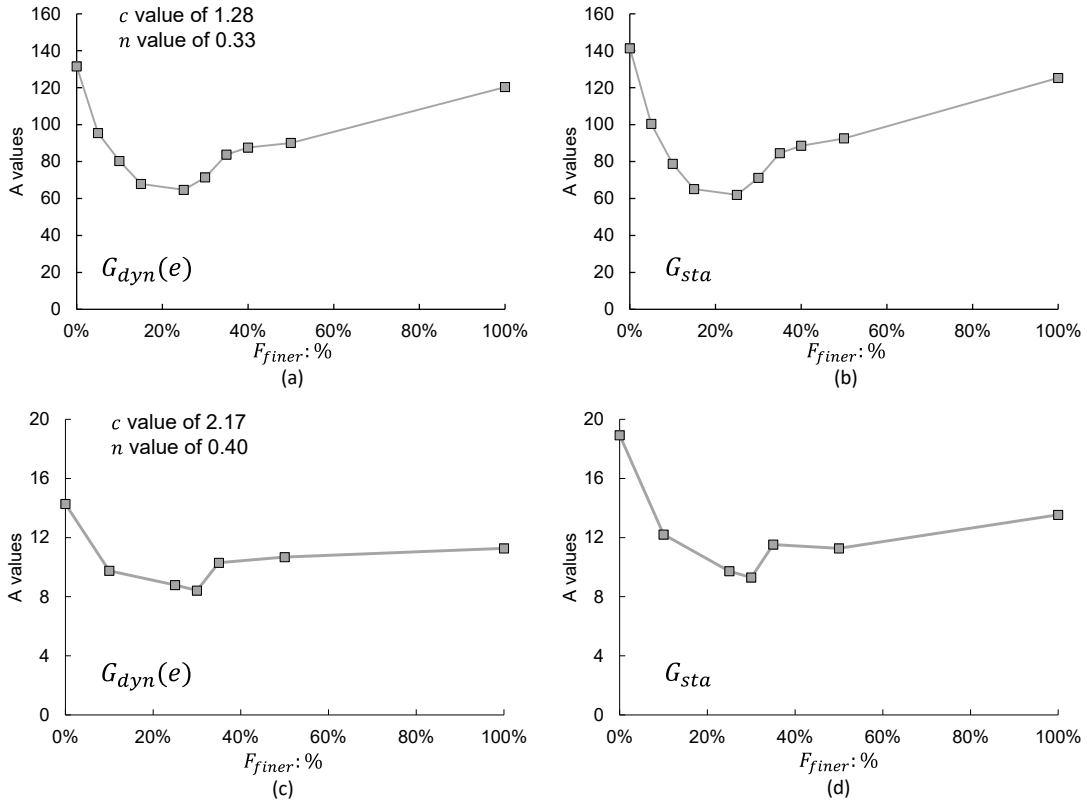


Figure 7.53: Variation in best-fit A value with F_{finer}: (a) $G_{dyn}(e)$ with increasing F_{finer} in DEM; (b) G_{sta} with increasing F_{finer} in DEM; (c) $G_{dyn}(e)$ with increasing F_{finer} in experiments; (d) G_{sta} with increasing F_{finer} in experiments

Figure 7.54 directly compares the G_{sta} and $G_{dyn}(e)$ data for the experiments. When compared to the DEM-generated data presented above, the deviations from the 1:1 line are more significant. The relative difference between G_{sta} and G_{dyn} varies from approximately -30% to 0% with the $RMSD$ value (Section 6.6.3) being approximately 30.26. The average relative difference between G_{sta} and G_{dyn} is approximately 12.4%. This illustrates that the maximum relative difference is larger compared to those identified in DEM results.

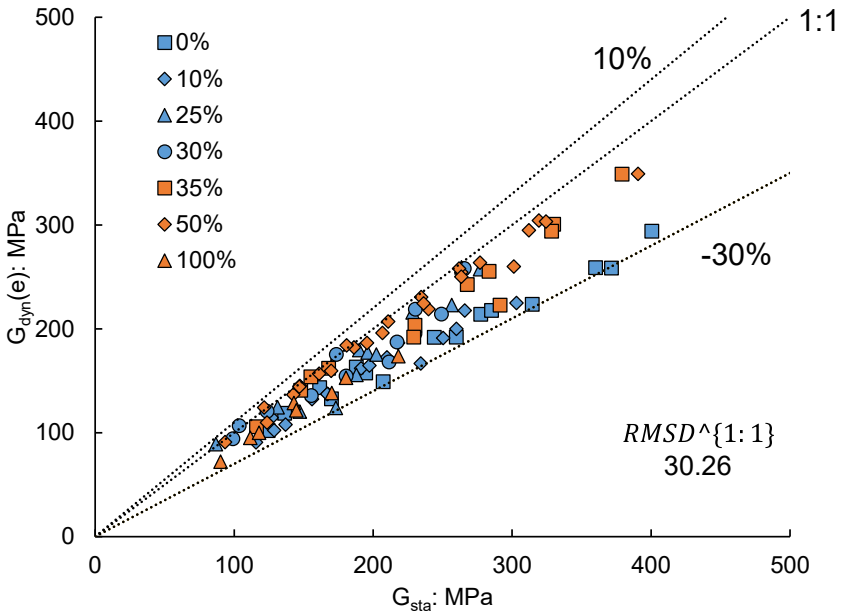


Figure 7.54: The comparison between $G_{dyn}(e)$ and G_{sta} for experimental results

The variation in the ratio of $G_{sta}/G_{dyn}(e)$ with F_{finer} is presented in Figure 7.55, data for the relatively dense and loose conditions are illustrated in Figure 7.55(a) and (b), respectively. In the relatively dense condition, the qualitative trend captured in the experimental data is also evident here. When $F_{finer} \leq 25\%$, the ratio $G_{sta}/G_{dyn}(e)$ reduces with increasing F_{finer}, just as was the case in the DEM dataset. However, the $G_{sta}/G_{dyn}(e)$ values are consistently larger compared to the data obtained in the DEM study. For instance, for the specimen comprising only coarse grains, the ratio $G_{sta}/G_{dyn}(e)$ in the experiments is approximately 1.3, while the ratio $G_{sta}/G_{dyn}(e)$ identified in DEM for pure coarse is only approximately 1.06. When $F_{finer} \geq 25\%$, the ratio $G_{sta}/G_{dyn}(e)$ generally increases with increasing F_{finer}, in line with the DEM dataset, (the data for the case of $F_{finer} = 30\%$ give an outlier datapoint). In the relatively loose condition, slight differences are observed with outlier data points identified when F_{finer} is 30% and 35%. These differences may be attributed to challenges associated with the experimental study. When measuring G_{sta}, the transducers can only measure the displacements of just six points, and consistent measurements cannot always be obtained so that the values of

these transducers may still not be representative of the dimension changes for the whole specimens.

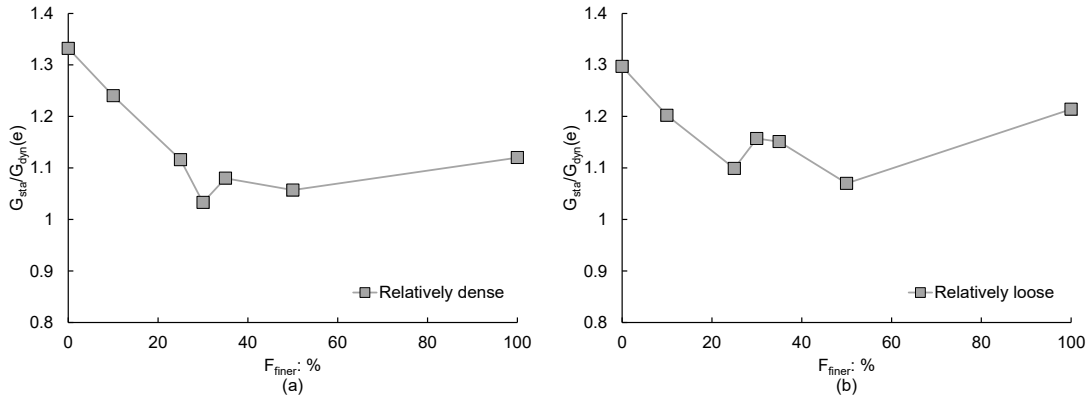


Figure 7.55: The ratio of G_{sta}/G_{dyn} with increasing F_{finer}: (a) Relatively dense condition; (b) Relatively loose condition

Although the trends are less clear than is the case for the DEM-generated dataset, these experimental results indicate that the ratio $G_{sta}/G_{dyn}(e)$ correlates with F_{finer} for gap-graded soils. As discussed before, for $20\% \leq F_{finer} \leq 30\%$, the relatively low values of $G_{sta}/G_{dyn}(e)$ may suggest that a large number of inactive particles may exist for these cases. This trend agrees with the corresponding DEM study. The quantitative differences identified between the DEM and experimental datasets may be attributed to the differences between numerical and experimental conditions. For instance, the anisotropy caused by the gravity, the particle shape and systematic error of the instruments may lead to the differences. Nevertheless, the current results show the possibility to identify the inactive particles in experiments by conducting both static and dynamic methods simultaneously. The trend between the ratio $G_{sta}/G_{dyn}(e)$ and F_{finer} can then be captured, where the relatively low ratio of $G_{sta}/G_{dyn}(e)$ may qualitatively suggest that a large number of inactive particles exist for such a F_{finer}. Despite the challenges of implementation, this approach has a stronger fundamental basis than other purely empirical approaches that have been proposed in the literature, such as looking at e_{min} and e_{max}, or the

intersection of the critical state line with the vertical axis in $e - logp'$ space. However, care should be taken in extrapolating the current results beyond the scope of the scenarios considered here. The results may vary with soil state, intrinsic soil characteristics, etc.

7.4. Summary

This Chapter has put forward an experimental study to verify the hypothesis proposed in Chapter 6. Looking at the difference between the value of the small strain stiffnesses measured in the static method (G_{sta}) and dynamic method (G_{dyn}) can indicate the proportion of inactive particles in a specimen of sand. This hypothesis was tested using data obtained in laboratory tests. A total of 27 triaxial specimens with 108 bender elements and shearing tests (i.e. four increasing p' values) were considered.

(1) The DEM results (Chapter 6) and experimental data for gap-graded specimens with a size ratio (SR) of about 8 exhibited qualitatively similar trends. The comparison between these two datasets could be quantified by considering the fitting parameter A in the empirical equation proposed by Hardin & Richart, (1963). In general, the pattern of variation in the $G_{sta}/G_{dyn}(e)$ of F_{finer} observed in the experimental dataset agrees with the trends observed in the DEM data. Prior studies have summarized several empirical approaches that can be used to assess the contribution of the finer fraction to the overall mechanical behaviour in a gap-graded soil. The approach proposed here presents a viable alternative with a fundamental basis that can easily be explained/understood.

(2) The experimental results presented show similar state-dependent behaviour when compared to the DEM results. Besides, a strong

correlation can be identified for liquefaction resistance on non-plastic soil mixtures even with different soils (Carraro et al., 2003). The current illustrated trends are very similar compared to the cyclic resistance ratio (CRR) behaviour. This may suggest that the fundamental stress transmission may play a much more crucial role in stiffness behaviour and CRR and in turn strongly affect the liquefaction response.

(3) The results illustrated in this study propose the possibility to identify the inactive particles in experiments by conducting both static and dynamic methods simultaneously to quantify the stiffness values for a specimen. However, current conclusions should be carefully extrapolated to more general scenarios. The results may vary with soil state, intrinsic soil characteristics, etc. Besides, the differences in the level of clarity observed in the DEM simulations and the experiments highlight the challenges of experimental research and also the complexity of gap-graded soils, as well as all the possible sources of errors (systematic or random) associated with experiments.

Chapter 8. Conclusions

8.1. Summary

The overall aim of the research presented in this thesis was to study how particle-scale interactions influence the overall continuum-scale mechanical behaviour of granular materials with a broad range of particle size distributions by adopting numerical studies (DEM) and considering experimental data. In particular, the research aimed to understand differences between materials with continuous (linear) particle size distributions and mixtures, comprising either two or three distinct size fractions. The research focussed on developing a better understanding of what might be appropriate state variables to use when predicting soil behaviour by firstly considering how stress is transmitted through the material and then considering implications for predicting the small-strain or elastic stiffness.

The literature review presented in Chapter 2 reviewed prior research that considered gap-graded soils from both experimental and numerical perspectives. This literature review contextualized the research and provided the background material needed to understand the key characteristics of gap-graded soils. The overview focussed on both the shearing behaviour and stiffness characteristics of gap-graded soils. Challenges and research gaps were also identified in this Chapter.

Chapter 3 introduced the DEM code used, and an overview of a verification study for the code was presented. The basic parameters used and the setup of the DEM simulations were presented. An overview of the Hertz-Mindlin contact model used in this research was provided.

Chapter 4 presented a comprehensive DEM investigation on stress transmission in specimens with different types of particle size distribution (PSD). Specimens with a continuous grading as well as bimodal and trimodal gap-graded specimens, comprising two and three size fractions respectively, were considered. This first analysis of these systems took a rather simplistic binary approach, by classifying the particles to be active or inactive, depending on their connectivity. The data presented in Chapter 4 showed that for continuous specimens, the proportion of the overall specimen volume that the inactive particles occupy is non-negligible so that when they are considered to be part of the void space to quantify the material state, there can be significant effects on the traditional measures of state (i.e. void ratio, density), especially in the case of looser specimens. For gap-graded soils, this study showed that the range of materials for which there are limitations to using e as a measure of the state is broader than has hitherto been appreciated. The most significant differences between e and e_m, ρ and ρ_m were observed in the case of the loosest samples considered. For the trimodal specimens, for some combinations of F_{finer}, F_{int} and packing density, a measurable proportion of the finer particles are inactive. This Chapter, therefore, supports the extension of the recent discussions on the unsuitability of global void ratio as a measure of state in bimodal gap graded materials to include more complex mixtures with more than two size fractions.

Chapter 5 presented a DEM investigation into the nature of stress transmission in granular materials. As was the case in Chapter 4, specimens with a continuous grading, bimodal and trimodal specimens were considered. For specimens with a linear grading, there is a clear link between the particle size distribution and the distribution of stress amongst the different size fractions. For bimodal gap-graded specimens, the proportion of stress carried

by the finer grains is significantly lower than the percentage by mass of finer grains in the specimen for all SR values considered when $F_{finer} < 50\%$. For all gap-graded soils, the SR, F_{finer} and density conditions all contribute to determine the relative contribution of finer grains to the stress transmission. The data also indicate a fundamental difference between the nature of stress transmission in the specimens with the lowest SR considered (3.7) and the remaining three specimen types with SR = 8.4, 14.5, and 18.1.

Chapter 6 presented a DEM investigation into the small-strain stiffness of granular materials. Both linear and gap-graded specimens were considered. Analysis of cubic specimens with periodic boundaries subject to quasi-static small amplitude strain probes revealed a clear link between the particle size distribution. The ratio $Z_m/(1+e_m)$, which relies upon particle-scale data has a strong correlation with the overall stiffness for all specimens considered. A new stiffness-matrix approach was proposed to study the overall stiffness contribution of each group of grains. The results show that the $C-C$, $C-F$ and $F-F$ contacts each make measurably different contributions to the overall material stiffness. A new semi-empirical state variable, e_α, was proposed that weights the volume of particles by the proportion of the overall stress they transmit when calculating the material state (void ratio).

Stress wave propagation through cuboidal specimens with a mixture of rigid wall boundaries and periodic boundary conditions enabled exploration of a hypothesis that looking at the difference between the value of the small strain stiffnesses measured in static small strain probes (G_{sta}) and dynamic methods (G_{dyn}) can indicate the proportion of inactive particles in a specimen of sand. For the generated data, a correlation was observed between the ratio $G_{sta}/G_{dyn}(e)$ and the ratios ρ_m/ρ as well as e/e_m. The difference between

G_{sta} and $G_{dyn}(e)$ reflects the difference between ρ and ρ_m, meaning that it can be used to ascertain, as least qualitatively, the proportion of inactive particles. The linear correlation between $G_{sta}/G_{dyn}(e)$ and e/e_α is clearer in comparison with the correlation between $G_{sta}/G_{dyn}(e)$ and e/e_m. This observation highlights the limitation of binary classification of particles as inactive and active which has typically been adopted in the literature.

Chapter 7 presented experimental data from a series of physical laboratory tests that measured the shear stiffness of bimodal gap graded soils using both bender element tests and small amplitude strain probes. The stiffness measured in the static probes, G_{sta} was consistently found to be larger than the corresponding G_{dyn} values measured in the bender element tests. The DEM results (Chapter 6) and experimental data for gap-graded specimens with a similar size ratio (SR) of approximately 8 (Chapter 7) exhibited qualitatively similar trends. In general, the relationship between $G_{sta}/G_{dyn}(e)$ and F_{finer} are similar for both DEM and experimental results. This method is therefore considered a viable approach to indirectly measure the proportion of inactive particles that do not transmit stress in a granular material.

8.2. Key observations

The following key observations were made in this study.

Influence of inactive particles on quantifying the state of granular materials

- Even for materials with continuous PSD, the proportion of inactive particles by volume is finite, i.e. neglecting the active particles can increase the void ratio by up to 60% and reduce the bulk density by up to 14%.

- The large discrepancy between e and e_m in the case of loose materials

is particularly significant as these materials have the greatest susceptibility to liquefaction.

- The relative difference between ρ and ρ_m caused by these inactive particles supported an examination of the implications of this difference on the use of geophysical testing, including bender element tests, to estimate small strain stiffness.

The effect of particle size distribution on stress transmission

- For linear specimens, the cumulative distribution obtained by considering particle stresses has a very similar shape to the particle size distribution.

- For both bimodal and trimodal gap-graded specimens, the relative contribution of the finer grains to the total amount of stress transmitted is dependent upon SR, F_{finer} and packing density.

- For bimodal gap-graded specimens, a network analysis enabled assessment of whether these three types of contact force network ($C-C$, $C-F$, $F-F$) percolate through the entire specimen.

DEM investigation on the small-strain stiffness of gap-graded soils

- For both linear and gap-graded specimens, when compared with the void ratio, e, the ratio $Z_m/(1+e_m)$, has a stronger correlation with G_0.

- A new stiffness-matrix approach was proposed to isolate the contributions of specific groups of particles to the overall stiffness.

- A new semi-empirical state variable e_α was proposed to account for the

non-uniformity in particle stiffnesses arising from the heterogeneity of the contact force within granular materials.

- The distribution of stress amongst the different size fractions has a significant influence on G_0 in the case of gap-graded soils.

- For mixed boundary specimens, a comparison of G_{sta} and $G_{dyn}(e)$ can give an indirect measure of the difference between ρ and ρ_m and therefore the proportion of inactive particles in a material.

Experimental investigation on the small-strain stiffness of gap-graded soils

- The variation in the ratio $G_{sta}/G_{dyn}(e)$ with F_{finer} observed in the experiments quantitively agrees with the trends observed in the DEM data. The experimental dataset, therefore, supports the proposition of using the ratio $G_{sta}/G_{dyn}(e)$ as a means to estimate the proportion of active fines in a gap-graded material.

- The differences observed in the DEM simulations and the experiments highlight the challenges of experimental research and also the complexity of gap-graded materials.

8.3. Recommendations for further research

8.3.1. The influence of particle shape effect on gap-graded soils.

The current research only considered spherical particles in the DEM simulations. In contrast, as illustrated in Chapter 7, the particle morphologies in natural soils are non-spherical, ranging from rounded to angular particles. The effect of particle shape has previously been investigated for narrow, continuous gradings in prior $DEM-$ based research. However, DEM studies that

consider gap-graded materials with non-spherical particles of gap-graded soils are rare, therefore, future studies should focus on the effect of particle shape on the mechanical behaviour of gap-graded soils, considering both the shearing behaviour as well as the small strain stiffness.

8.3.2. The influence of the particle shear modulus of coarse and finer particles on gap-graded soils

The natural gap-graded soils could be mixtures of distinct soils, therefore, the characteristics of these soils may be different. For instance, the particle shear modulus G_p for coarse and finer fractions could be different (G_p for all particles in this thesis was 29.17 GPa). Therefore, further studies could use different G_p values for coarse and finer particles to study the effect of G_p on the mechanical behaviour of gap-graded soils. For the dynamic test simulations, it may also be interesting to vary the particle densities.

8.3.3. The influence of soil fabric on the stiffness

The soil fabric in the case of materials with non-spherical particles in particular, such as the particle orientation, can significantly affect the mechanical behaviour of soils. However, studies of the influence of soil fabric on the stiffness of gap-graded soils are rare. Further studies could use different methods to prepare the specimens with non-spherical particles so that the different particle orientations could be achieved. Then the stiffness values for these specimens could be estimated so that the effect of soil fabric on soil stiffness can be studied.

8.3.4. The link between the soil liquefaction to the current study

As illustrated in Chapter 7, insight into the liquefaction resistance of gap-graded soils may be gained by developing upon the research presented here. The

variation in the cyclic resistance ratio (CRR) behaviour with F_{finer} observed by Carraro et al. (2003) exhibits similar trends to the variation in G_0 with F_{finer} presented here. Future research could investigate the relationship between the particle scale stress distribution and the liquefaction response.

8.3.5. The study of the large strain shearing behaviour

This thesis only focused on the isotropic compression behaviour or the small strain behaviour of gap-graded soils, however, understanding of the response of gap-graded materials to shear deformation at larger strain levels remains incomplete. The current DEM studies were restrained by the ability of HPC, the large strain shearing behaviour has rarely been investigated. However, with improvements in processing power GPU, the ability to run the simulations could be improved in the future. Use of a DEM code that includes a hierarchal grid for contact detection may also be helpful (Shire et al., 2021). Additional insight is needed to improve understanding as to how the concepts of critical state soil mechanics can be applied to gap-graded soils. For instance, the influence of F_{finer} for the critical state lines of gap-graded soils in both $q - p'$ plane and $e - logp'$ plane can be investigated. It will be useful to consider the evolution of the stress distribution in gap-graded soils sheared until the critical state. Based on the study of Sufian et al. (2021), a significant difference may be observed between the initial distribution of stress amongst the different size fractions and the distribution of stress observed at the critical state.

References

Altuhafi, F. N., & Coop, M. R. (2011). Changes To Particle Characteristics Associated With The Compression Of Sands. *Géotechnique*, *61*(6), 459–471.

Altuhafi, F. N., Coop, M. R., & Georgiannou, V. N. (2016). Effect of Particle Shape on the Mechanical Behavior of Natural Sands. *Journal of Geotechnical and Geoenvironmental Engineering*, *142*(12), 04016071.

Altuhafi, F. N., O'Sullivan, C., & Cavarretta, I. (2012). Analysis of an Image-Based Method to Quantify the Size and Shape of Sand Particles. *Journal of Geotechnical and Geoenvironmental Engineering*, *139*(8), 1290–1307.

Alvarado, G., & Coop, M. R. (2011). On The Performance Of Bender Elements In Triaxial Tests. *Géotechnique*, *62*(1), 1–17.

Artigaut, M., Sufian, A., Ding, X., Shire, T., & O'Sullivan, C. (2019). Influence of stress anisotropy on stress distributions in gap-graded soils. *E3S Web Conf.*, *92*, 14007.

Baki, M. A. L., Rahman, M. M., Lo, S. R., & Gnanendran, C. T. (2012). Linkage between static and cyclic liquefaction of loose sand with a range of fines contents. *Canadian Geotechnical Journal*, *49*(8), 891–906.

Barreto, D., & O'Sullivan, C. (2012). The influence of inter-particle friction and the intermediate stress ratio on soil response under generalised stress conditions. *Granular Matter*, *14*(4), 505–521.

Been, K., Jefferies, M. G., & Hachey, J. (1991). The critical state of sands. *Géotechnique*, *41*(3), 365–381.

Been, K, & Jefferies, M. G. (1985). A state parameter for sands. *Géotechnique*, *35*(2), 99–112.

Cabalar, A. F. (2010). Applications of the oedometer, triaxial and resonant column tests to the study of micaceous sands. *Engineering Geology*, *112*(1–4), 21–28.

Carraro, J. A. H., & Prezzi, M. (2008). A new slurry-based method of preparation of specimens of sand containing fines. *Geotechnical Testing Journal*, *31*(1), 1–11.

Carraro, J. A. H., Prezzi, M., & Salgado, R. (2009). Shear Strength and Stiffness of Sands Containing Plastic or Nonplastic Fines. *Journal of Geotechnical and Geoenvironmental Engineering*, *135*(9), 1167–1178.

Carraro, J. A. H, Bandini, P., & Salgado, R. (2003). Liquefaction resistance of clean and nonplastic silty sands based on cone penetration resistance. *Journal of Geotechnical and Geoenvironmental Engineering*, *129*(11), 965–976.

Carrera, A., Coop, M., & Lancellotta, R. (2011). Influence of grading on the mechanical behaviour of Stava tailings. *Géotechnique*, *61*(11), 935–946.

Chang, C. S., & Liao, C. L. (1994). Estimates of elastic modulus for media of randomly packed granules. *Applied Mechanics Reviews*, *47*(1), 197–206.

Cho, G. C., Dodds, J., & Santamarina, J. C. (2006). Particle Shape Effects on Packing Density, Stiffness, and Strength: Natural and Crushed Sands. *Journal of Geotechnical and Geoenvironmental Engineering*, *132*(5), 591–602.

Cubrinovski, M., & Ishihara, K. (2002). Maximum and minimum void ratio characteristics of sands. *Soils and Foundations*, *42*(6), 65–78.

Cuccovillo, T., & Coop, M. R. (1997). The measurement of local axial strains in triaxial tests using LVDTs. *Géotechnique*, *47*(1), 167–171.

Cundall, P. A., & Strack, O. D. L. (1979). A discrete numerical model for granular assemblies. *Géotechnique*, *29*(1), 47–65.

Dash, H. K., Sitharam, T. G., & Baudet, B. A. (2010). Influence of Non-Plastic Fines on the Response of a Silty Sand To Cyclic Loading. *Soils and Foundations*, *50*(5), 695–704.

Dominguez, Q. C., Santiago Q. V., Carraro, J. A. H., Zdravkovic, L., &

Jardine, R. J. (2019). Quality assessment of a new in-mould slurry deposition method for triaxial specimen reconstitution of clean and silty sands. *E3S Web of Conferences*, *92*, 1–6.

Dutta, T. T. (2019). Effects of grain characteristics on the anisotropic mechanical properties evaluated by elastic waves. Ph.D. Thesis, The University of Tokyo, Japan.

Gasparre, A., Nishimura, S., Minh, N. A., Coop, M. R., & Jardine, R. J. (2007). The stiffness of natural London Clay. *Géotechnique*, *57*(1), 33–47.

Goddard, J. D. (1990). Nonlinear elasticity and pressure-dependent wave speeds in granular media. *Proceedings of the Royal Society of London. Series A: Mathematical and Physical Sciences*, *430*(1878), 105–131.

Gong, J., Wang, X., Li, L., & Nie, Z. (2019). DEM study of the effect of fines content on the small-strain stiffness of gap-graded soils. *Computers and Geotechnics*, *112*, 35–40.

Gotoh, K., Jodrey, W. S., & Tory, E. M. (1978). A random packing structure of equal spheres—statistical geometrical analysis of tetrahedral configurations. *Powder Technology*, *20*(2), 233–242.

Goudarzy, M., König, D., & Schanz, T. (2016). Small strain stiffness of granular materials containing fines. *Soils and Foundations*, *56*(5), 756–764.

Goudarzy, M., Rahemi, N., Rahman, M. M., & Schanz, T. (2017). Predicting the maximum shear modulus of sands containing nonplastic fines. *Journal of Geotechnical and Geoenvironmental Engineering*, *143*(9), 6017013.

Gu, X., Yang, J., & Huang, M. (2013). DEM simulations of the small strain stiffness of granular soils: Effect of stress ratio. *Granular Matter*, *15*(3), 287–298.

Guida, G., Einav, I., Marks, B., & Casini, F. (2018). Linking micro grainsize

polydispersity to macro porosity. *International Journal of Solids and Structures*.

Hardin, B. O., & Black, W. L. (1966). Sand stiffness under various triaxial stresses. *Journal of Soil Mechanics & Foundations Div*, *92*(ASCE# 4712 Proceeding).

Hardin, B. O., & Richart, F. E. (1963). Elastic wave velocities in granular soils. *Journal of the Soil Mechanics and Foundations Division*, *89*(1), 33–65.

Hertz, H. (1882). Über die Berührung fester elastischer Körper. *Journal Für Die Reine Und Angewandte Mathematik*, *92*(156–171), 22.

Hight, D. W., & Leroueil, S. (2003). Characterisation of soils for engineering purposes. *Characterisation and Engineering Properties of Natural Soils*, *1*, 255–360.

Hsiao, D. H., & Phan, V. T. A. (2016). Evaluation of static and dynamic properties of sand–fines mixtures through the state and equivalent state parameters. *Soil Dynamics and Earthquake Engineering*, *84*, 134–144.

Huang, X., O'Sullivan, C., Hanley, K. J., & Kwok, C. Y. (2014). Discrete-element method analysis of the state parameter. *Géotechnique*, *64*(12), 954–965.

Huang, X. (2014). *Exploring Critical-state Behaviour Using DEM.* Imperial College London London.

Ishihara, K. (1993). Liquefaction and flow failure during earthquakes. *Géotechnique*, *43*(3), 351–451.

Itasca Consulting Group. (2007). PFC3D Version 4.0 User Manual. Itasca Consulting Group.

Hanley, K., & O'Sullivan, C. (2017). Analytical study of the accuracy of discrete element simulations. *International Journal for Numerical Methods in Engineering*, *109*(1), 29–51.

Johnson, K. L. (1985). Contact mechanics cambridge univ. *Press, Cambridge*,

95, 365.

Ke, L., & Takahashi, A. (2012). Strength reduction of cohesionless soil due to internal erosion induced by one-dimensional upward seepage flow. *Soils and Foundations*, *52*(4), 698–711.

Khalili, M. H., Roux, J. N., Pereira, J. M., Brisard, S., & Bornert, M. (2017). Numerical study of one-dimensional compression of granular materials. II. Elastic moduli, stresses, and microstructure. *Physical Review E*, *95*(3), 1–17.

Kuerbis, R., Negussey, D., & Vaid, Y. P. (1988). Effect of gradation and fines content on the undrained response of sand. *Hydraulic Fill Structures*, 330–345.

Kuerbis, R., & Vaid, Y. P. (1988). Sand sample preparation-the slurry deposition method. *Soils and Foundations*, *28*(4), 107–118.

Kuwano, R., & Jardine, R. J. (2002). On the applicability of cross-anisotropic elasticity to granular materials at very small strains. *Géotechnique*, *52*(10), 727–749.

La, R. L., & Magnanimo, V. (2012). Evolution of the effective moduli of an anisotropic, dense, granular material. *Granular Matter*, *14*(6), 749–757.

Lade, P. V., Liggio, C. D., & Yamamuro, J. A. (1998). Effects of Non-Plastic Fines on Minimum and Maximum Void Ratios of Sand. *Geotechnical Testing Journal*, *21*(4), 336–347.

Lade, P. V, & Yamamuro, J. A. (1997). Effects of nonplastic fines on static liquefaction of sands. *Canadian Geotechnical Journal*, *34*(6), 918–928.

Lings, M. L. (2001). Drained and undrained anisotropic elastic stiffness parameters. *Géotechnique*, *51*(6), 555–565.

Liu, D., O'Sullivan, C., & Carraro, J. A. H. (2021). The influence of particle size distribution on the stress distribution in granular materials. *Géotechnique*, (Ahead of Print), 1–37.

Liu, X., & Yang, J. (2018). Influence of size disparity on small-strain shear modulus of sand-fines mixtures. *Soil Dynamics and Earthquake Engineering*, *115*(February), 217–224.

Liu, Y., Wang, L., Hong, Y., Zhao, J., & Yin, Z. (2020). A coupled CFD‐DEM investigation of suffusion of gap graded soil: Coupling effect of confining pressure and fines content. *International Journal for Numerical and Analytical Methods in Geomechanics*, *44*(18), 2473–2500.

Magnanimo, V., La, R. L., Jenkins, J. T., Wang, P., & Makse, H. A. (2008). Characterizing the shear and bulk moduli of an idealized granular material. *EPL (Europhysics Letters)*, *81*(3), 34006.

Makse, H. A., Gland, N., Johnson, D. L., & Schwartz, L. M. (1999). Why effective medium theory fails in granular materials. *Physical Review Letters*, *83*(24), 5070.

Makse, H. A., Johnson, D. L., & Schwartz, L. M. (2000). Packing of compressible granular materials. *Physical Review Letters*, *84*(18), 4160.

Menq, F. Y. (2003). Dynamic Properties of Sandy and Gravelly Soils. *Philosophy*.

Minh, N. H., & Cheng, Y. P. (2013). A DEM investigation of the effect of particle-size distribution on one-dimensional compression. *Géotechnique*, *63*(1), 44–53.

Mitchell, J. K, & Soga, K. (1976). Fundamentals of Soil Behavior, John Wiley&Sons. *Inc., New York*, *422*.

Miura, K., Maeda, K., Furukawa, M., & Toki, S. (1997). Physical characteristics of sands with different primary properties. *Soils and Foundations*, *37*(3), 53–64.

Murthy, T. G., Loukidis, D., Carraro, J. A. H., Prezzi, M. & Salgado, R. (2007). (2007). Undrained monotonic response of clean and silty sands. *Géotechnique*, *57*(3), 273–288.

Naeini, S. A., & Baziar, M. H. (2004). Effect of fines content on steady-state strength of mixed and layered samples of a sand. *Soil Dynamics and Earthquake Engineering*, *24*(3), 181–187.

Nguyen, H., O'Sullivan, C., & Otsubo, M. (2018). Discrete element method analysis of small-strain stiffness under anisotropic stress states. *Géotechnique Letters*, *8*(3), 183–189.

Nguyen, H., & O'Sullivan, C. (2019). Linking macro-scale yielding and micro-scale response. *E3S Web of Conferences*, *92*, 14008.

Ni, Q., Tan, T. S., Dasari, G. R., & Hight, D. W. (2004). Contribution of fines to the compressive strength of mixed soils. *Géotechnique*, *54*(9), 561–569.

Nocilla, A., Coop, M. R., & Colleselli, F. (2006). The mechanics of an Italian silt: an example of 'transitional' behaviour. *Géotechnique*, *56*(4), 261–271.

O'Sullivan, C. (2015). Advancing geomechanics using DEM. *Geomechanics from Micro to Macro*, 21.

O'Sullivan, C., Cheng, H., & Zhao, J. (2021). *Use of DEM in geomechanics: Special issue associated with the DEM 8 conference*. Elsevier.

Otsubo, M., O'Sullivan, C., & Shire, T. (2017). Empirical assessment of the critical time increment in explicit particulate discrete element method simulations. *Computers and Geotechnics*, *86*.

Otsubo, M. (2016). Particle scale analysis of soil stiffness and elastic wave propagation. Ph.D. Thesis, Imperial College London, London.

Otsubo, M, Dutta, T. T., Durgalian, M., Kuwano, R., & O'Sullivan, C. (2019). Particle-scale insight into transitional behaviour of gap-graded materials–small-strain stiffness and frequency response. *E3S Web of Conferences*, *92*, 14006.

Otsubo, M, Kuwano, R., O'Sullivan, C., & Shire, T. (2021). Using geophysical data to quantify stress transmission in gap-graded granular materials.

Géotechnique, 1–18.

Otsubo, M, & O'Sullivan, C. (2018). Experimental and DEM assessment of the stress-dependency of surface roughness effects on shear modulus. *Soils and Foundations*, *58*(3), 602–614.

Otsubo, M, O'Sullivan, C., Ackerley, S., & Parker, D. (2019). Selecting an appropriate shear plate configuration to measure elastic wave velocities. *Geotechnical Testing Journal*, *43*(6), 1519–1540.

Ouchiyama, N., & Tanaka, T. (1980). Estimation of the average number of contacts between randomly mixed solid particles. *Industrial & Engineering Chemistry Fundamentals*, *19*(4), 338–340.

Papadopoulou, A., & Tika, T. (2008). The effect of fines on critical state and liquefaction resistance characteristics of non-plastic silty sands. *Soils and Foundations*, *48*(5), 713–725.

Parkin, A. K. (1965). On the strength of packed spheres. *Journal of the Australian Mathematical Society*, *5*(4), 443–452.

Payan, M., Khoshghalb, A., Senetakis, K., & Khalili, N. (2016). Effect of Particle Shape and Validity of Gmax Models for Sand: A critical review and a new expression. *Computers and Geotechnics*, *72*, 28–41.

Payan, M., Senetakis, K., Khoshghalb, A., & Khalili, N. (2017a). Characterization of the small-strain dynamic behaviour of silty sands; contribution of silica non-plastic fines content. *Soil Dynamics and Earthquake Engineering*, *102*(September), 232–240.

Payan, M., Senetakis, K., Khoshghalb, A., & Khalili, N. (2017b). Effect of gradation and particle shape on small-strain Young's modulus and Poisson's ratio of sands. *International Journal of Geomechanics*, *17*(5), 4016120.

Pennington, D. S., Nash, D. F. T., & Lings, M. L. (1997). Anisotropy of G_0 shear stiffness in Gault Clay. *Géotechnique*, *47*(3), 391–398.

Petit, J. C., Kumar, N., Luding, S., & Sperl, M. (2020). Additional transition line in jammed asymmetric bidisperse granular packings. *Physical Review Letters*, *125*(21), 215501.

Plimpton, S. (1995). Fast parallel algorithms for short-range molecular dynamics. *Journal of Computational Physics*, *117*(1), 1–19.

Polito, C. P., & Martin II, J. R. (2001). Effects of nonplastic fines on the liquefaction resistance of sands. *Journal of Geotechnical and Geoenvironmental Engineering*, *127*(5), 408–415.

Ponzoni, E., Nocilla, A., & Coop, M. R. (2017). The behaviour of a gap-graded sand with mixed mineralogy. *Soils and Foundations*, *57*(6), 1030–1044.

Potyondy, D. O., & Cundall, P. A. (2004b). A bonded-particle model for rock. *International Journal of Rock Mechanics and Mining Sciences*, *41*(8), 1329–1364.

Powell, J. J. M., Dhimitri, L., Ward, D., & Butcher, A. P. (2016). Small strain stiffness assessments from in situ tests–revisited. In Proc. 5th Intl Conf on Geotechnical and Geophysical Site Characterization ISC'5.

Rahman, M. M., & Lo, S. R. (2008). The prediction of equivalent granular steady state line of loose sand with fines. *Geomechanics and Geoengineering*, *3*(3), 179–190.

Rahman, M. M., Lo, S. R., & Gnanendran, C. T. (2008). On equivalent granular void ratio and steady state behaviour of loose sand with fines. *Canadian Geotechnical Journal*, *45*(10), 1439–1456.

Rahman, M. M., Lo, S. C., & Dafalias, Y. F. (2014). Modelling the static liquefaction of sand with low-plasticity fines. *Géotechnique*, *64*(11), 881–894.

Rollins, K. M., Singh, M., & Roy, J. (2020). Simplified Equations for Shear-Modulus Degradation and Damping of Gravels. *Journal of Geotechnical and Geoenvironmental Engineering*, *146*(9), 4020076.

Salgado, R., Bandini, P., & Karim, A. (2000). Shear strength and stiffness of silty sand. *Journal of Geotechnical and Geoenvironmental Engineering*, *126*(5), 451–462.

Senetakis, K., Anastasiadis, A., & Pitilakis, K. (2012). The small-strain shear modulus and damping ratio of quartz and volcanic sands. *Geotechnical Testing Journal*, *35*(6), 964–980.

Shipton, B., & Coop, M. R. (2012). On the compression behaviour of reconstituted soils. *Soils and Foundations*, *52*(4), 668–681.

Shipton, B., & Coop, M. R. (2015). Transitional behaviour in sands with plastic and non-plastic fines. *Soils and Foundations*, *55*(1), 1–16.

Shire, T., O'Sullivan, C., & Hanley, K. J. (2016). The influence of fines content and size-ratio on the micro-scale properties of dense bimodal materials. *Granular Matter*, *18*(3).

Shire, T., O'Sullivan, C., Hanley, K. J., & Fannin, R. J. (2014). Fabric and Effective Stress Distribution in Internally Unstable Soils. *Journal of Geotechnical and Geoenvironmental Engineering*, *140*(12), 04014072.

Shire, T, & O'Sullivan, C. (2016). Constriction size distributions of granular filters: a numerical study. *Géotechnique*, *66*(10), 826–839.

Shire, T, Hanley, K. J., & Stratford, K. (2021). DEM simulations of polydisperse media: efficient contact detection applied to investigate the quasi-static limit. *Computational Particle Mechanics*, *8*(4), 653–663.

Shirley, D. J., & Hampton, L. D. (1978). Shear‐wave measurements in laboratory sediments. *The Journal of the Acoustical Society of America*, *63*(2), 607–613.

Skempton, A. W., & Brogan, J. M. (1994). Experiments on piping in sandy gravels. *Géotechnique*, *44*(3), 449–460.

Sufian, A., Artigaut, M., Shire, T., & O'Sullivan, C. (2021). Influence of Fabric on Stress Distribution in Gap-Graded Soil. *Journal of Geotechnical and*

Geoenvironmental Engineering, *147*(5), 4021016.

Suzuki, M., Makino, K., Yamada, M., & Iinoya, K. (1981). A study on the coordination number in a system of randomly packed, uniform-sized spherical particles. *Int. Chem. Eng*, *21*(3), 482–488.

Sze, H. Y., & Yang, J. (2013). Failure Modes of Sand in Undrained Cyclic Loading: Impact of Sample Preparation. *Journal of Geotechnical and Geoenvironmental Engineering*, *140*(1), 152–169.

Tastan, E. O., & Carraro, J. A. H. (2013). A new slurry-based method of preparation of hollow cylinder specimens of clean and silty sands. *Geotechnical Testing Journal*, *36*(6), 811–822.

Thevanayagam, S., Shenthan, T., Mohan, S., & Liang, J. (2002). Undrained Fragility of Clean Sands, Silty Sands, and Sandy Silts. *Journal of Geotechnical and Geoenvironmental Engineering*, *128*(10), 849–859.

Thevanayagam, S, & Mohan, S. (2000). Intergranular state variables and stress–strain behaviour of silty sands. *Géotechnique*, *50*(1), 1–23.

Thevanayagam, S. (2000). Liquefaction potential and undrained fragility of silty soils. *Proceedings of the 12th World Conference on Earthquake Engineering*, 1–8.

Thornton, C. (1979). The conditions for failure of a face-centered cubic array of uniform rigid spheres. *Géotechnique*, *29*(4), 441–459.

Thornton, C. (2000). Numerical simulations of deviatoric shear deformation of granular media. *Géotechnique*, *50*(1), 43–53.

Torquato, S., Truskett, T. M., & Debenedetti, P. G. (2000). Is random close packing of spheres well defined? *Physical Review Letters*, *84*(10), 2064.

Tunuguntla, D. R., Weinhart, T., & Thornton, A. R. (2017). Comparing and contrasting size-based particle segregation models. *Computational Particle Mechanics*, *4*(4), 387–405.

Tyler, S. W., & Wheatcraft, S. W. (1992). Fractal scaling of soil particle-size

distributions: analysis and limitations. *Soil Science Society of America Journal*, *56*(2), 362–369.

Vaid, Y. P., Sivathayalan, S., & Stedman, D. (1999). Influence of specimen-reconstituting method on the undrained response of sand. *Geotechnical Testing Journal*, *22*(3), 187–195.

Ventouras, K., & Coop, M. R. (2009). On The Behaviour Of Thanet Sand: An Example Of An Uncemented Natural Sand. *Géotechnique*, *59*(9), 727–738.

Wei, L. M., & Yang, J. (2014). On The Role Of Grain Shape In Static Liquefaction Of Sand–Fines Mixtures. *Géotechnique*, *64*(9), 740–745.

Wichtmann, T., Navarrete H. M. A., & Triantafyllidis, T. (2015). On the influence of a non-cohesive fines content on small strain stiffness, modulus degradation and damping of quartz sand. *Soil Dynamics and Earthquake Engineering*, *69*, 103–114.

Wichtmann, T., & Triantafyllidis, T. (2009). Influence of the Grain-Size Distribution Curve of Quartz Sand on the Small Strain Shear Modulus Gmax. *Journal of Geotechnical and Geoenvironmental Engineering*, *135*(10), 1404–1418.

Wood, D. M., & Maeda, K. (2008). Changing grading of soil: effect on critical states. *Acta Geotechnica*, *3*(1), 3.

Yang, J., & Gu, X. Q. (2012). Shear Stiffness Of Granular Material At Small Strains: Does It Depend On Grain Size? *Géotechnique*, *63*(2), 165–179.

Yang, J., & Liu, X. (2016). Shear wave velocity and stiffness of sand: the role of non-plastic fines. *Géotechnique*, *66*(6), 500–514.

Yang, J., Liu, X., Rahman, M. M., LO, R., Goudarzy, M., & Schanz, T. (2018). Shear wave velocity and stiffness of sand: the role of non-plastic fines. *Géotechnique*, *68*(10), 931–934.

Yang, J., & Luo, X. D. (2015). Exploring the relationship between critical state

and particle shape for granular materials. *Journal of the Mechanics and Physics of Solids*, *84*, 196–213.

Yang, J., & Wei, L. M. (2012). Collapse Of Loose Sand With The Addition Of Fines: The Role Of Particle Shape. *Géotechnique*, *62*(12), 1111–1125.

Yang, J., Wei, L. M., & Dai, B. B. (2015). State variables for silty sands: Global void ratio or skeleton void ratio? *Soils and Foundations*, *55*(1), 99–111.

Yang, S. L., Sandven, R., & Grande, L. (2006). Instability of sand-silt mixtures. *Soil Dynamics and Earthquake Engineering*, *26*(2-4 SPEC. ISS.), 183–190.

Yang, S., Lacasse, S., & Sandven, R. (2006). Determination of the transitional fines content of mixtures of sand and non-plastic fines. *Geotechnical Testing Journal*, *29*(2), 102–107.

Yang, Z. X., Li, X. S., & Yang, J. (2008). Quantifying and modelling fabric anisotropy of granular soils. *Géotechnique*, *58*(4), 237–248.

Yimsiri, S., & Soga, K. (2000). Micromechanics-based stress–strain behaviour of soils at small strains. *Géotechnique*, *50*(5), 559–571.

Youd, T. L. (1973). Factors controlling maximum and minimum densities of sands. In *Evaluation of relative density and its role in geotechnical projects involving cohesionless soils*. ASTM International.

Zhang, F., Li, M., Peng, M., Chen, C., & Zhang, L. (2019). Three-dimensional DEM modeling of the stress–strain behavior for the gap-graded soils subjected to internal erosion. *Acta Geotechnica*, *14*(2), 487–503.

Zhang, X, & Baudet, B. A. (2013). Particle breakage in gap-graded soil. *Géotechnique Letters*, *3*(2), 72–77.

Zhang, X., Baudet, B. A., Hu, W., & Xu, Q. (2017). Characterisation of the ultimate particle size distribution of uniform and gap-graded soils. *Soils and Foundations*, *57*(4), 603–618.

Zhang, X., Baudet, B. A., & Yao, T. (2020). The influence of particle shape and mineralogy on the particle strength, breakage and compressibility. *International Journal of Geo-Engineering*, *11*(1), 1–10.

Zhang, Z. P., Liu, L. F., Yuan, Y. D., & Yu, A. B. (2001). A simulation study of the effects of dynamic variables on the packing of spheres. *Powder Technology*, *116*(1), 23–32.

Zhao, S., Evans, T. M., & Zhou, X. (2018). Effects of curvature-related DEM contact model on the macro- and micro-mechanical behaviours of granular soils. *Géotechnique*, *68*(12), 1085–1098.

Zhao, S., Evans, T. M., & Zhou, X. (2018). Shear-induced anisotropy of granular materials with rolling resistance and particle shape effects. *International Journal of Solids and Structures*, *150*, 268–281.

Zhao, S., Zhao, J., & Guo, N. (2020). Universality of internal structure characteristics in granular media under shear. *Phys. Rev. E*, *101*(1), 12906.

Zhu, Y., Nie, Z., Gong, J., Zou, J., Zhao, L., & Li, L. (2020). An analysis of the effects of the size ratio and fines content on the shear behaviors of binary mixtures using DEM. *Computers and Geotechnics*, *118*, 103353.

Zlatović, S., & Ishihara, K. (1995). On the influence of nonplastic fines on residual strength. *First International Conference on Earthquake Geotechnical Engineering*, *95*, 239–244.

Zuo, L., & Baudet, B. A. (2015). Determination of the transitional fines content of sand-non plastic fines mixtures. *Soils and Foundations*, *55*(1), 213–219.

Zuo, L., & Baudet, B. A. (2020). Normalised behaviour of a non-plastic silt–pumice sand mixture. *Géotechnique*, *70*(9), 822–832.